CONFINED FLOWS WITH AND WITHOUT SWIRL

by

MOHAMED ABDEL-AZIZ MOSTAFA HABIB
B.Sc. (Eng.), M.Sc.

Thesis Submitted for the Degree of
Doctor of Philosophy
in the Faculty of Engineering
University of London

and

for the Diploma of Membership
of Imperial College

Mechanical Engineering Department,
Imperial College of Science and Technology,
London, S.W.7, England

April, 1980

بسم الله الرحمن الرحيم

"الحمد لله
الذى هدانا لهذا
وما كنا لنهتدى لولا أن هدانا الله"

سورة الأعراف، آية ٤٣

In the Name of God, The Most
Gracious, The Most Merciful

"Praise be to God, who hath guided us to this,
never could we have found guidance, had it not
been for the guidance of God"

Qurãn

BIBL.
LONDIN.
UNIV.

ABSTRACT

Velocity characteristics are reported for two types of confined turbulent flows, i.e. confined double coaxial jet with sudden expansion and for two velocity ratios of 3 and 1, and quarl angle expansions with separated boundary layers. The measurements include the mean velocity, Reynolds stresses and probability density distributions of fluctuating velocity and the influence of swirl is determined in both cases. In the confined double coaxial jet, the measurements were obtained by a combination of pressure probe, hot-wire and laser Doppler anemometry and allowed a detailed assessment and precision of the measuring techniques in regions of flow reversal and high turbulence intensity. The measurements without swirl have shown that the larger velocity ratio results in a larger region of recirculation, larger velocity gradients and larger turbulence intensities in the mixing region and downstream of the region of reverse flow. The results with a swirl number of 0.23 in the outer jet for the velocity ratio of 3.0 indicate a region of near recirculation on the centre-line between one and three enclosure diameters downstream of the exit plane. These results and those of the quarl angle expansion indicate the importance of the extra strain rates (any rate of strain other than $\partial\overline{U}/\partial y$) on the generation of the kinetic energy of turbulence particularly in the case of swirl.

A solution procedure has been developed and applied to the prediction of the flow properties in the confined double coaxial jet with sudden expansion. Three turbulence models, that is a mean flow closure (two-equation model) and two Reynolds-stress models, were applied and evaluated. The comparison with experiments showed that the main features of the flow fields are correctly predicted by the

three models with the Reynolds-stress models of better accuracy near and inside the recirculation zone. Discrepancies between measured and calculated flow properties exist, particularly in regions of more than one major component of the velocity-gradient tensor and near the axis of symmetry. The reasons for the discrepancies and the consequent value of the calculation method are discussed. A calculation method for the prediction of the properties of swirling and non-swirling turbulent recirculating flows bounded by curved surfaces in orthogonal curvilinear coordinates is also presented. The procedure was tested for the calculations of wide angle diffusers with different expansion angles and swirl numbers. The results show that the mean velocity was correctly represented by the calculation procedure in the case of zero swirl number: discrepancies were again found between calculated and measured kinetic energy of turbulence and were larger in the case of finite swirl number; they are attributed to the inability of the effective viscosity hypothesis to predict flows with high streamline curvature and to the form of the source in the transport equation of the rate of dissipation.

ACKNOWLEDGEMENTS

This work has been carried out with financial support from the United Kingdom Atomic Energy Research Establishment, Harwell under the supervision of Professor J. H. Whitelaw. It gives me great pleasure to express my gratitude to all persons who have helped me in one way or another during the research of this thesis.

In particular, I wish to acknowledge with gratitude the guidance, advice and constructive criticism provided by my supervisor, Professor J. H. Whitelaw, throughout my research at Imperial College. His critical assessment at all stages of the work was very valuable in bringing the research to a fruitful conclusion.

I also appreciate the help and suggestions of my colleagues including: Dr. Y. Elbanhawy, Mr. M. Noseir, Mr. H. Moneib, Dr. J. Truelove, Dr. D. Durão, Dr. M. Ribeiro, Dr. S. Pope, Mr. A. Attya, Mr. A. Abbas, Mr. Y. Elsaie and Mr. A. Taylor.

The support of the departmental technical staff was vital to the research program; Messrs. O. Vis, F. Bell, J. Laker, M. Roper, J. Pilmer and R. Church were particularly helpful in the experimental part of the work.

Many thanks are also due to Miss E. Archer and the Mechanical Engineering Library staff, to Mr. G. Tindall, to Miss S. Chambers, Miss J. Davies and Mrs. A. Poznanski for their frequent help and support throughout my research work. My thanks are due to Mrs. H. A. Bastin who had the patience to go through every typing detail with great skill.

Finally, I would like to take this opportunity to extend my deepest gratitude to my parents for their support and encouragement throughout my career.

CONFINED FLOWS WITH AND WITHOUT SWIRL

CONTENTS

		Page
ABSTRACT		1
ACKNOWLEDGEMENTS		3
CONTENTS		4
NOMENCLATURE		8
CHAPTER 1	INTRODUCTION	11
1.1	Introductory Remarks	11
1.2	Literature Review	13
1.2.1	Experimental Investigations	13
1.2.2	Computational Investigations	17
1.3	Outline of Thesis	21
PART I	CONFINED DOUBLE COAXIAL JETS WITH SUDDEN EXPANSION	
CHAPTER 2	CONFINED DOUBLE COAXIAL JETS WITH SUDDEN EXPANSION: EXPERIMENTAL INVESTIGATION	24
2.1	Introduction	24
2.2	Flow Configuration and Inlet Conditions	25
2.3	Measurement Techniques	27
2.3.1	Hot-Wire Anemometry	27
2.3.2	Laser Doppler Anemometry	36
2.3.3	Pitot Tube	40
2.3.4	Comparison of the Different Techniques	42
2.4	Velocity Characteristics of the Confined Double Coaxial Jet	51

		Page
2.4.1	Velocity Characteristics of the Confined Double Coaxial Jet Without Swirl	51
2.4.2	Velocity Characteristics of the Confined Double Coaxial Jet With Swirl	60
2.5	Summary and Conclusions	63
CHAPTER 3	CONFINED DOUBLE COAXIAL JETS WITH SUDDEN EXPANSION: COMPUTATIONAL INVESTIGATION	107
3.1	Introduction	107
3.2	The Governing Differential Equations	107
3.2.1	Continuity and Momentum Equations	107
3.2.2	Equations for the Reynolds Stresses	109
3.2.3	Turbulence Models	110
3.2.4	The Inlet and Boundary Conditions	117
3.3	The Solution Procedure	119
3.3.1	The Grid System and Location of Variables	120
3.3.2	The Finite Difference Equation	121
3.3.3	The Solution Algorithm	124
3.3.4	Remarks on the Numerical Procedure	125
3.4	The Calculation of Confined Double Coaxial Jets	129
3.4.1	Presentation and Discussion of the Results	129
3.4.2	Discussion	135
3.5	Summary and Conclusion	139
	PART II	
	FLOW CHARACTERISTICS OF THE QUARL ANGLE EXPANSIONS	
CHAPTER 4	EXPERIMENTAL INVESTIGATION IN QUARL ANGLE EXPANSIONS	157
4.1	Introduction	157

		Page
4.2	Motivation and Objectives	158
4.3	Description of Flow Configuration	159
4.3.1	The Test Section	159
4.4	Measurement Technique and Data Analysis	160
4.5	Presentation and Analysis of Results	161
4.5.1	Measurements of the Mean and rms Velocity of the Flow in Quarl Angle Expansion Without Swirl	161
4.5.2	Measurements of the Mean and rms Velocity of the Flow in Quarl Angle Expansion With Swirl	168
4.5.3	Probability Density Distributions	172
4.6	Summary and Conclusion	174
CHAPTER 5	COMPUTATIONAL INVESTIGATION IN QUARL ANGLE EXPANSIONS	213
5.1	Introduction	213
5.2	The Choice of the Coordinate System and Turbulence Model	213
5.3	Equations in Orthogonal Curvilinear Coordinates	214
5.3.1	The Equation of Continuity	215
5.3.2	The Momentum Equations	215
5.3.3	The Equation of Kinetic Energy of Turbulence	217
5.3.4	The Equation of the Rate of Dissipation of the Kinetic Energy of Turbulence	218
5.4	The Solution Procedure	218
5.5	The Grid Generation Procedure	219
5.6	Comparison with Experiments	223
5.6.1	Numerical Accuracy and Computational Details	223
5.6.2	Calculations of Separated Flows in Expanding Ducts	226

			Page
	5.6.3	The Calculation of the Flow in Quarl Angle Expansion With Swirl	230
	5.6.4	The Effect of Swirl Number	232
5.7	Summary and Conclusion		234
CHAPTER 6	CLOSURE		268
6.1	Achievements of the Present Work		268
6.2	Recommendations for Future Work		271
	6.2.1	Experimental Work	271
	6.2.2	Theoretical Work	272

PART III

SUPPLEMENTARY INFORMATION

APPENDIX A1	REFERENCES	275
APPENDIX A2	EXPERIMENTAL DATA OF QUARL ANGLE EXPANSION WITH SWIRL	286
APPENDIX A3	EQUATIONS IN ORTHOGONAL CURVILINEAR COORDINATES	292
APPENDIX A4	EQUATIONS IN CYLINDRICAL COORDINATES	302
APPENDIX A5	REYNOLDS STRESS EQUATIONS	305

NOMENCLATURE

c's	Constants
D_e	The enclosure inner diameter
d_i	The annulus inner diameter
d_o	The annulus outer diameter (= $2r_2$)
d_p	The inner diameter of the central jet (= $2r_p$)
E	Instantaneous voltage
e	Fluctuating voltage
F ( )	Normalised energy-spectrum of velocity fluctuations
f	Frequency
G, G_K	Production of K
G_{ij}	Production of $\overline{u_i u_j}$
g_{ij}	Metric tensor
$H_i(j)$	Coordinate variation terms
h	Obstacle height, the ratio between the scale factors
h_i	Scale factors
K	Turbulence kinetic energy
K_1 and K_2	Hot-wire calibration constants
k	Wave number
L_x	Longitudinal macroscale
ℓ	Length scale of turbulence proportional to the size of the energy containing motions
ℓ_m	Mixing length scale
N	Number of bursts
P	Mean pressure
P_{tot}	Total mean pressure
P_s	Static mean pressure
p	Fluctuating pressure component
Pe	Peclet number

$P\ (\ )$	Probability density of ( )
R	The inner radius of the enclosure
R_j	The inner radius of the expanding duct at station j
Re	Reynolds number
R_{ij}	Redistribution of $\overline{u_i u_j}$
r	Radius
S	Swirl number
s	Skewness factor, sensitivity factor
T	Turbulence intensity level
U	Axial velocity component
V	Radial velocity component
W	Tangential velocity component
u, v, w	Fluctuating velocity components
U_{eff}	Cooling effective velocity
X	Axial distance
Y	Radial position
$\overline{X}$ and $\overline{Y}$	Cartesian coordinates of the orthogonal grid

Greek Symbols

α	Hot-wire orientation angle, pitch angle
δ_{ij}	Kronecker-delta (= 1 for i = j; = 0 for $i \neq j$)
$\Delta\ (\ )$	Change of ( )
ψ	Stream function
ε	Rate of dissipation of K
ε'	Fluctuating component of ε
Γ	Exchange coefficient
λ_x	Longitudinal microscale
μ_{eff}	Effective viscosity (= $\rho\ \nu_{eff}$)
μ_ℓ	Laminar viscosity (= $\rho\ \nu_\ell$)

μ_t	Turbulent viscosity (= $\rho\ \nu_t$)
ν_D	Doppler frequency
∇ (n)	Divergence operator
Φ	General dependent variable
ϕ	Crossing beam angle;
	Half angle of expansion
ρ	Density
σ	Prandtl/Schmidt number for any variable Φ
τ	Time scale;
	Shear stress
η, ξ	Orthogonal coordinate directions

Subscripts

a	Annulus flow
$\underline{\mathbb{C}}$	Value at the centre-line
cor	Corrected value
m	Measured value, Equations (2.22) and (2.23) and Fig. 2.18;
	Value at the centre-line
o	Axis location at the inlet section
P	Pipe or pipe flow

Superscripts

—	Mean value
~	rms value

CHAPTER 1

INTRODUCTION

1.1 Introductory Remarks

The present work is concerned with the turbulent flows that occur in the developing regions of axisymmetric confined jets and is relevant to those which occur in ducts, furnaces, turbomachines and other practically relevant configurations. Two types of flow are considered in detail, i.e. a confined double coaxial jet with sudden expansion and quarl angle expansions with separated boundary layers. The influence of swirl is determined in both cases and the results are relevant particularly to furnaces and quarl angle burner configurations: computational and experimental investigations for both flows are presented.

Some features of the present flows can be foreseen but require to be quantified. Thus, in the confined double coaxial jet with sudden expansion, the turbulent mixing downstream of the exit of the concentric pipes, between the two coaxial streams and between the forward stream and the reverse flow of the recirculation zone, is similar to that found in furnaces and is known to be important to flame stabilisation and efficient combustion. When swirl is imparted to the outer stream, the initial regions are further complicated by pressure distributions, since the centrifugal effects that follow the sudden expansion of the outer pipe wall establish rapidly changing radial and axial pressure gradients which exert considerable control on the mean velocity field. When these adverse pressure gradients are large, a central re-circulation region is produced and a new region of high turbulent mixing exists.

In the separated flows of the quarl angle expansion, the

adverse pressure gradient causes the boundary layer to slow down and thicken until a reversed flow region occurs and the wall shear stress becomes negative. The resulting recirculation region acts as a concentrated source of turbulence, the subsequent convection, diffusion and decay of which have far-reaching influence on the characteristics of the mean motion. Also the recirculation bubble has the effect of enhancing the momentum transfer to the wall and consequently the behaviour of separated boundary layers in quarl angle expansions is of practical significance in engineering situations, such as diffusers, where the minimum of losses is at a premium. In combustion flows, quarl angle expansions are used in burners and serve an important role in the stabilization of high-intensity combustion; for a given swirl number, they tend to increase the size of the core recirculation zone. The net effect is to improve flame stability and reduce the combustion lengths because of the high rates of entrainment.

Although the above flow features can be deduced from existing knowledge, quantitative information is lacking and the detailed understanding of the flow required to allow more than a general basis for design is not available. Thus, a major purpose of the present contribution was to improve available knowledge by conducting an experimental program. It is intended that this should provide sufficient information to allow interpolation and extrapolation of the particular flows considered and so allow improvements in the design of burner and furnace arrangements.

An ideal vehicle of interpolation and extrapolation of the previous paragraph appears to be the numerical solution of conservation equations in finite difference form. This involves various assumptions and the present thesis describes work carried out to improve and appraise, in relation to the measurements, a calculation method

involving the solution of elliptic differential equations, numerical and turbulence assumptions. The calculation method, as will be discussed, is useful for a wide range of flow configurations but, in particular, may be used to calculate furnace flows based on knowledge of geometry and the flow rates of fuel and air.

The measurement techniques available to allow measurements in the flows of interest include pressure probes, hot-wires and laser Doppler anemometry. Each has advantages and has been used in appropriate regions of the flows. In addition, in high turbulence and recirculating regions, the three methods have been used to allow quantitative comparison. For the calculation of turbulent flows, the time dependent Navier-Stokes equations cannot be closed and the equations for the ensemble averaged velocities contain the Reynolds stresses which must be estimated through turbulence models. Various models have been proposed and represent a family of closures in which the solution difficulties increase with the increase in the complexity of the model. Eddy viscosity and Reynolds-stress closures are examined here.

1.2 Literature Review

This section provides a resumé of previous investigations which are particularly relevant to the present work. References to specific subjects dealt with in the present investigation, and not considered in this review, are introduced in the relevant parts of the text.

1.2.1 Experimental Investigations

Previous experimental investigations of direct relevance to the present work are listed in Table 1.1 and 1.2 for the confined

double coaxial jets and the quarl angle expansion investigations, respectively. In both tables, the measuring techniques and flow configurations are displayed. Reviews of earlier measurements of mean velocities in double coaxial jets are provided by Chedaille et al (1966) and Smithson (1969) and are not reconsidered here. The measurements of Wingfield (1967) encompassed a wide range of burner geometries and inlet conditions and were directed towards the determination of the importance of the size of the annular face between the nozzles of a concentric jet burner on the mean flow field in a model furnace for zero swirl. The results showed that the thickness of the annular face and the velocity ratio of the two jets play an important part in the mixing of the two coaxial streams. The measurements of Mathur and MacCallum (1967) and Beltagui and MacCallum (1976), for swirling flows issuing from annular and hubless vane swirlers respectively, included axial and tangential mean velocity profiles and indicated that a swirl number of 0.275 is required to establish a central recirculation zone and that the spread of the jet up to the impingement point is a function of the swirl number. The velocity measurements were obtained by Pitot tubes and are confined to mean velocities with unknown errors in regions of recirculation and significant flow fluctuations, as discussed for example by Becker and Brown (1974). Similarly, the analysis of hot-wire signals becomes increasingly uncertain as the turbulence intensity increases above around 20%.

The work of Baker et al (1974a) was concerned with demonstrating the use of laser Doppler anemometry in the recirculation region of industrial burners and provided some quantitative information in the presence of combustion. The measurements of mean velocity and turbulence quantities reported by Owen (1976) were made for a low value of sudden expansion ratio of 1.4 and without swirl. The momentum flux

TABLE 1.1

PREVIOUS MEASUREMENTS IN CONFINED, DOUBLE COAXIAL JETS

Author	d_o/D_e	d_i/d_o	d_p/d_i	$\bar{U}_a/\bar{U}_p$	S	L/D_e	Instrumentation
Wi ıgfield (1967)	0.355	0.526 and others	0.327	3.127	0.000	6.0	Pitot probe
Ma :hur and Ma :Callum (1967)	0.402 square duct	0.324	0.000	∞	0.193 0.415 and others	5.0	Pitot probe
Ba ker et al (1974)	0.183	0.218	≃ 1.000	∞ 2.320	0.000 0.520	3.0	L.D.A.
Ba ker et al (1974a)	0.183	0.218	≃ 1.000	2.320	0.500	3.0	L.D.A.
Pai et al (1975)	0.250	0.262	0.800	0.350	0.000	8.5	Prandtl probe and hot-wire anemometer
Owen (1976)	0.700	0.714	≃ 1.000	12.000	0.000	9.6	L.D.A.
Be ltagui and MacCallum (1976)	0.400	1.000	1.000	0.000	0.177 0.385 0.582 1.154	4.0	Pitot probe
Hutchinson et al (1977)	0.183	0.218	≃ 1.000	∞	0.300 0.500	3.0	L.D.A.

of the inner jet was very small and a recirculation region grew in the region of the centre-line both with and without confinement. The confinement increased both the length of the recirculating region and the total mass of recirculating fluid. The measurements of Hutchinson et al (1977) included mean velocity and normal stress profiles in a model furnace with a coaxial burner with a 20° quarl angle and swirl numbers of 0.3 and 0.5. They were obtained by laser Doppler anemometer and concentrated on the region downstream of the exit plane of the quarl.

It is evident that information of the influence of the velocity ratio of the two jets and the degree of swirl on the velocity and turbulence characteristics of the flow field downstream of double coaxial jets is still far from complete. Thus part of the present work is an investigation of these influences and provides additional reliable experimental data, particularly in recirculation zones. In the context of the present calculations, previous experimental investigations are deficient in that values of measured properties were not provided at inlet of the flow domain. The solution of differential equations requires boundary conditions and comparisons between experiments and calculations are imperfect unless the boundary values are known. In the present experimental program, the distributions of the velocity and turbulence quantities were obtained around the physical boundary corresponding to the solution domain.

The study of turbulent flows confined within quarl-angle expansion has formed the subject of numerous publications. The greatest number of these was devoted to low quarl-angle flows, i.e. small angle diffusers were used to obtain high pressure recovery coefficients. For example, the effects of inlet conditions on the performance of two-dimensional subsonic diffusers were studied by, among others, Waitman et al (1961), Kline et al (1959), Livesey and Turner (1965)

and Bradley and Cockrell (1971). Swirling flows in conical diffusers were investigated by McDonald et al (1971), Murakami and Kikuyama (1976) and Senoo et al (1978). These investigations have, however, rarely reported measurements of velocity or turbulence quantities and have been concerned mainly with static-pressure distributions. The flows in wide-angle diffusers, of particular relevance here, have been considered in only a small number of publications as shown in Table 1.2. A review of the swirling flows in quarl-angle expansions, and related to combustion, was given by Syred and Beér (1974) who indicated (see also Chigier and Beér, 1964) that the divergent part of the burner geometry greatly increases the central recirculation zone for a given swirl number.

It can be seen from Table 1.2 that all previous measurements apart from those of Hutchinson et al (1977), which do not provide measurements in the expansion duct, were carried out with pitot probes or hot-wires and are, therefore, subject to unknown errors in regions of recirculation and high values of turbulence intensity. The table also indicates that there are no measurements of turbulence quantities inside expansion ducts with swirling flows. It can be concluded, therefore, that the velocity characteristics and turbulent processes of the flows in quarl-angle expansions with and without swirl require further investigation; quantitative information of the influence of inlet conditions and geometry on downstream flow properties is slight.

1.2.2 Computational Investigations

The calculation of turbulent flows requires the solution of time-averaged forms of the momentum equations in which the Reynolds stresses appear as unknowns. Various methods, or models, for dealing with these extra terms have been proposed and range from the relatively

TABLE 1.2

PREVIOUS MEASUREMENTS IN WIDE-ANGLE EXPANSIONS

Author(s)	Half angle	Swirl number	Instrumentation	Regions of measurement
Kalinske (1946)	3.75 15 90	0.00	Visualisation	Inside and downstream of the expansion duct
Moore and Kline (1958)	3.5 → 8.5	0.00	Flow visualisation	Inside the expansion duct
Chaturvedi (1963)	15 30 45 90	0.00	Hot-wire	Inside and downstream of the expansion duct
Hutchinson et al (1977)	20	0.30 0.50	L.D.A.	Downstream of the expansion duct
Senoo et al (1978)	6 8	0.07 0.12 0.18	Pitot tube	Inside the expansion duct

simple mixing length hypothesis of Prandtl (1925) to the solution of conservation equations for third-order correlations (see Launder and Spalding, 1972, and Bradshaw, 1976). The problem of closure, i.e. of expressing the Reynolds stresses of the momentum equations in terms of functions of known variables, increases in difficulty with the complexity of the model. Whereas boundary layer flows have been dealt with successfully by the mixing-length hypothesis and one-equation models, it has been necessary to use two-equation models to deal with recirculating flows where convection and diffusion of turbulence characteristics are important.

The two-equation model of turbulence requires the solution of equations for turbulence energy, K, and rate of dissipation, ε, and the assumptions of local isotropy and a generalised Boussinesq effective viscosity concept when in practice, all real flows show some degree of anisotropy and, for many of these, the turbulent stress is less directly connected with the mean velocity field than is required by the notion of a turbulent viscosity. Some examples of its use are referred to in Table 1.3. The possibility arises of solving equations for the turbulent stresses but at the cost of introducing additional unknown correlations for which additional approximations in terms of known variables will be required. Such equations have been derived by several authors and were reported, for example, by Harlow and Nakayama (1967), Hinze (1959) and Rodi (1972). A proposal for a model of turbulence in which the Reynolds stresses are determined from the solution of transport equations for these variables and for the turbulence energy dissipation rate was developed by Launder et al (1975) and tested (Reece, 1977) in two-dimensional flows without recirculation, i.e. in axisymmetric plane channel, plane wall jet in stagnant surrounding and in three-

TABLE 1.3

CALCULATIONS OF RECIRCULATING JET FLOWS BY THE K $\sim$ ε MODEL

Author	Flow configuration	Flow properties compared with experiments
Gosman et al (1974)	Axisymmetric expansions	$\overline{U}$ and K
Khalil et al (1975)	Confined flow of an annular jet and sudden expansion	$\overline{U}$, K and $\overline{W}$
Pope and Whitelaw (1976)	Near-wake flow	$\overline{U}$, $\overline{uv}$ and $\overline{u^2}$
Pope (1976)	Flow in a diffuser	-
Hutchinson et al (1977)	Axisymmetric expansion	$\overline{U}$
Moss et al (1979)	Backward-facing step	$\overline{U}$ and K
Durst and Rastogi (1979)	Separated flow of a square obstacle in a channel flow	$\overline{U}$ and K
Gosman et al (1979)	Sudden expansion flows and others	$\overline{U}$, $\overline{W}$ and K
Hyde and Sykes (1979)	Enclosure with divergent quarl angle	$\overline{U}$ and $\overline{W}$
Cebeci et al (1979)	Separated boundary layer flows	$\overline{U}$

dimensional boundary layer flows. It was also applied for the calculation of the near-wake flows by Pope and Whitelaw (1976) who indicated that the Reynolds-stress model revealed that discrepancies, although marginally less than those with the K ∿ ε model, were still prevalent. This model has not previously been applied for the calculation of the flows investigated here.

The aim of the present calculation effort is to establish the ability of the various turbulence models to represent the flow in the confined double coaxial jets with sudden expansion and in quarl-angle expansions by comparison of the calculated results with the present measurements. The numerical method was applied to the sudden expansion and can be applied to small angle-diffusers without modification but as shown by Cebeci et al (1979), the rectangular Cartesian coordinate system is not appropriate to the flow configuration of the separated boundary layer and the present investigation included the extension of the calculation method to orthogonal curvilinear coordinates where the flow and calculation domains are coincident.

1.4 Outline of Thesis

The remainder of the thesis is presented in five chapters. Chapters 2 and 3 are concerned with the measurements and calculations of the turbulent flow in the confined double coaxial jets. The experimental investigation is described in Chapter 2 where the arrangement of the confined jets are presented. The different measurement techniques, their data reduction equations and accuracy are also explained and discussed. The results of the confined double coaxial jet measurements are presented and discussed and brief concluding remarks are given. Chapter 3 is concerned with the computations of the confined coaxial jets. The time-average form of the governing

equations, turbulence models and the solution procedure are described. The results are compared with the experimental data and the main conclusions identified.

Chapters 4 and 5 are concerned with the measurements and calculations of the turbulent flows in quarl-angle expansions. The experimental investigation is described in Chapter 4 where the flow configurations and the measurement technique are described. The results of the different configurations and input conditions are reported and the chapter ends with a summary and the more important conclusions. In Chapter 5, the computational investigation of the turbulent flow in quarl-angle expansions is described. The equations are presented in orthogonal curvilinear coordinates and a precedure for generating the grid is reported. The calculated results are compared with the experiments and concluding remarks presented.

Finally, Chapter 6 summarises the main conclusions of the present work and provides suggestions for future work.

PART I

CONFINED DOUBLE COAXIAL JETS WITH SUDDEN EXPANSION

CHAPTER 2

CONFINED DOUBLE COAXIAL JETS WITH SUDDEN EXPANSION: EXPERIMENTAL INVESTIGATION

2.1 Introduction

The work presented in this chapter describes the measurements which were achieved in confined double coaxial jets. The flow in such configurations is relevant to many practical situations such as furnaces and combustors. The measurements were aimed at providing new information of the velocity and turbulence characteristics of confined coaxial jet flows which would improve understanding of this practically relevant flow. In addition, they aid the evaluation of calculation methods with their turbulence model assumptions.

Measurements of mean velocity and turbulence characteristics in recirculating turbulent flows are difficult to make due partly to the unknown and rapidly varying direction of the velocity vector and partly to the high turbulence intensities associated with such flows. Available measurement techniques include the pitot tube, hot-wire anemometry and laser Doppler anemometry and all are subject to uncertainties in highly turbulent flows. The inaccuracy of each technique is dependent on the flow situation and on the processing method. The measurements reported here were obtained with all three forms of instrumentation and thus the relative advantages of each were exploited. Pitot tubes provide the most convenient and economic technique for mean-velocity measurements; hot-wire anemometry is to be preferred away from regions of recirculation and where the local turbulence intensity is low; and laser Doppler anemometry is advantageous in and around regions of recirculation and where the intensities are higher. The use of all these forms of instrumentations also allows comparison of the results and better assessment and

precision.

The chapter begins with a description of the design of the present confined double coaxial jet, Section 2.2. The three measurement techniques are described in Section 2.3. The hot-wire arrangements and related data processing are described in Subsection 2.3.1 which is followed by Subsection 2.3.2 that presents a description of the optical and electronic instrumentation of the laser Doppler anemometer. The design of the pitot tube is explained in Subsection 2.3.3. The measurements include axial and radial profiles of the axial mean velocity and Reynolds stresses and the corresponding probability density distributions for two velocity ratios with and without swirl and are presented in Section 2.4. The chapter ends with a summary of the more important conclusions.

2.2 Flow Configuration and Inlet Conditions

Fig. 2.1 presents a line diagram of the flow configuration used in the present work. The coaxial jet arrangement in the absence of the present confinement is identical to that used by Durão (1971) for the study of free coaxial jets and a complete description of the rig may be found in the same reference. The coaxial pipe arrangement comprised an inner pipe of inner and outer diameters 16.1 mm and 21.6 mm, respectively and was 2.83 m long. The outer pipe had an inner diameter of 44.5 mm and was 2.0 m long, see Fig. 2.4. The length of the pipes ensured fully developed pipe and annular flows at the exit plane. The air was supplied to the annulus and pipe by two centrifugal fans through two settling chambers. The relative positioning of the two pipes was achieved through two sets of three blades which could be moved in a direction perpendicular to the inner pipe wall. Each set of blades was part of a block rigid with the outer pipe. Symmetry of flow was examined by measuring velocity across two orthogonal diameters

and was found to be satisfied within 1% of the maximum exit-plane velocity.

The flow was confined by a 595 mm long machined and polished perspex cylinder of inner diameter and thickness of 125 mm and 6 mm, respectively. A perspex plate was located flush with the pipe and annulus exit and the confining tube. The confining tube was carried from its free end by a support through an adjusting mechanism which made it possible to move the cylinder free-end in two perpendicular directions. The arrangement was aligned with respect to a laser beam and the axis of the confining tube was coincident with that of the pipe and annulus within 0.05 mm at the upstream and 0.2 mm at the downstream end. Two checks of symmetry are presented on Fig. 2.2. The first was obtained at $x/d_o = 2$ without confinement and the second at 4 mm upstream the end of the confining tube; both with the aid of normal hot-wire and represent four radii in two perpendicular planes.

The measurements without swirl were performed for two velocity ratios, based on the maximum annular and pipe velocity and with the corresponding Reynolds numbers, i.e.:-

$\bar{U}_a/\bar{U}_p$	Re_a	Re_p
3.0	77500	18800
1.0	50500	35500

In the case of swirl, the swirling air was injected into the swirling chamber (see Fig. 2.3) through six equally spaced tangential slots, 4 cm x 2 mm, of 2.0 cm length, located at the outer wall, 7.0 cm upstream of the exit. More details about the swirler may be obtained from Ribeiro (1976). At the outlet of the pipes, the conditions were the following:-

$$\overline{U}_a/\overline{U}_p = 3.0$$

$$Re_a = 76000$$

$$Re_p = 18540$$

Swirl number, defined as:-

$$S = \frac{\int_0^{r_2} r^2\, \overline{U}\, \overline{W}\, dr}{r_2 \int_0^{r_2} r \left(\overline{U}^2 - \frac{1}{2}\overline{W}^2\right) dr} = 0.23 \qquad (2.1)$$

2.3 Measurement Techniques

2.3.1 Hot-Wire Anemometry

This section presents a description of the hot-wire instrumentation and relevant data processing. It is divided into three subsections which present the derivation of the equations relating the signals from the anemometer with the velocity characteristic, a description of the equipment and instrumentation and an error analysis which includes consideration of the calibration method.

(i) Equations of Hot-Wire Anemometry

In a constant temperature anemometer, the relationship between the electrical signal and the effective cooling velocity is given by the formula:-

$$E_o^2 = A + B\, U_{eff}^n \quad * \qquad (2.2)$$

---

* Further modifications to this equation have been suggested by, for example, Davies (1969) but are not necessary

where A and n are constants which depend upon the properties of the hot-wire material and its dimensions. For a linearised system this relation can be written in the form:-

$$E = s\, U_{eff} \qquad (2.3)$$

where s is the sensitivity factor to be determined from the calibration of the hot-wire.

The effective cooling velocity was represented by Hinze (1959) by the following expression:-

$$U_{eff} = (U_n^2 + K_1^2\, U_t^2)^{1/2} \qquad (2.4)$$

where U_n and U_t are the normal and tangential velocity applied to the hot-wire and K_1 is a calibration constant. This relation is not entirely satisfactory because of the influence of the shape and dimensions of the probe. For an approximate compensation for these effects, Rodi (1974) proposed a third term which is a function of the velocity component normal to the plane of the prongs (see Fig. 2.4), i.e.:-

$$U_{eff} = (U_{n,1}^2 + K_1^2\, U_t^2 + K_2^2\, U_{n,2}^2)^{1/2} \qquad (2.5)$$

For a hot-wire located in the x-y plane as shown in Fig. 2.4, the velocities acting on the hot-wire can be resolved into three components; $U_{n,1}$, $U_{n,2}$ and U_t in the three perpendicular directions: normal to the wire in and normal to the plane of the probe and along the wire, respectively. The response equation may be represented as:-

$$E^2 = s^2 \ (U^2_{n,1} + K^2_1 \ U^2_t + K^2_2 \ U^2_{n,2}) \qquad (2.6)$$

Introduction of the following expressions for $U_{n,1}$, U_t and $U_{n,2}$:-

$$\left.\begin{aligned} U_{n,1} &= U_i \cos \alpha + U_j \sin \alpha \\ U_t &= U_i \sin \alpha - U_j \cos \alpha \\ U_{n,2} &= U_k \end{aligned}\right\} \qquad (2.7)$$

where U_i, U_j and U_k are respectively the instantaneous velocity components along and normal to the probe axis in the probe plane and normal to this plane. The response equation can then be expressed as:-

$$E^2 = s^2 \left[(U_i \cos \alpha + U_j \sin \alpha)^2 + K^2_1 \ (U_i \sin \alpha - U_j \cos \alpha)^2 + K^2_2 \ U^2_k\right] \qquad (2.8)$$

or taking the square root:-

$$E = s \ (U_i \cos \alpha + U_j \sin \alpha) \cdot$$

$$\left[1 + \frac{\dfrac{K^2_2}{\cos^2 \alpha} \dfrac{U^2_k}{\overline{U}^2_i} - K^2_1 \left\{\dfrac{U_j}{\overline{U}_i} - \dfrac{u}{\overline{U}_i} \tan \alpha - \tan \alpha\right\}^2}{\left(1 + \dfrac{u}{\overline{U}_i} + \dfrac{U_j}{\overline{U}_i} \tan \alpha\right)^2}\right]^{1/2} \qquad (2.9)$$

This equation shows that the velocity is not linearly related to the anemometer signal and an approximation has to be made in order to

establish a relationship between the values of the moments of the velocity distribution and of the signal. Some of the proposals for such an approximation are described and compared in the following paragraph which is followed by an outline of the method used in this work.

Assessment of the Different Methods

There are two main types of approach. The first is to approximate Equation (2.9) by a series expansion and this method, as discussed by Hinze (1959) and Champagne and Sleicher (1967), starts from the time averaged form of Equation (2.9). It yields a relationship between the mean value of the signal and a polynomial function of the mean value and higher order moments of the velocity field; the mean velocity is obtained directly by neglecting the higher order moments and the rms by subtracting the square of the signal mean value from the average of the square value of the signal.

The second method implies the averaging of Equation (2.8) and relates the mean square of the signal to the mean velocity square and second order moments of the velocity field. The mean value of the signal has to be obtained in a similar manner to the first method. This is called the square method and has been used by Rodi (1974), Durão (1971) and Durão and Whitelaw (1973). It does not entail any approximations for the mean square value but the approximation made to obtain the mean velocity yields some uncertainty in evaluating the rms. Since the Reynolds stress is obtained by subtracting the mean velocity from the sum of the mean value and standard deviation, the error in the Reynolds stresses is proportional to the error in the mean value divided by the turbulence intensity. Therefore, this method leads to large uncertainties at low turbulence intensities.

In contrast, the first method involves a bi-nomial expansion of Equation (2.9) which neglects higher order moments and is valid only for low turbulence intensities (< 20%). To extend this method to higher turbulence intensities, Ribeiro (1976) suggested that the poly-nomial could be approximated through a least square fit of the response equation in the range of values covered by the actual turbulence level. This method implies the reduction of all the higher correlations to second order moments through the assumption of Gaussian behaviour. The complexity of this method increases with the accuracy required.

The Present Method

The use of Equation (2.8) with four configurations of hot-wire corresponding to $\alpha = 0$, $\pi/4$ and $-\pi/4$ with the wire in the x-y plane and $\alpha = \pi/4$ in the y-z plane, allows the quantities $\overline{U}^2 + u^2$, $\overline{V}^2 + \overline{v^2}$, $\overline{w^2}$ and $\overline{UV} + \overline{uv}$ to be determined from four equations. The radial mean velocity may be neglected except in the region of recirculation and the correlations $\overline{v^2}$ and $\overline{uv}$ determined. The values of $\overline{U}$ and $\overline{u^2}$ are determined by the application of the following two approximations to Equation (2.9):-

$$E = s\,(U\cos\alpha + V\sin\alpha)\left[a + b\,\frac{\frac{K_2^2}{\cos^2\alpha}\frac{\overline{w^2}}{\overline{U}^2} - K_1^2\left\{\frac{\overline{V}}{\overline{U}} - \frac{\overline{u}}{\overline{U}}\tan\alpha - \tan\alpha\right\}^2}{\left(1 + \frac{\overline{u}}{\overline{U}} + \frac{\overline{V}}{\overline{U}}\tan\alpha\right)^2}\right] \qquad (2.10)$$

and:-

$$1/\left(1 + \frac{\overline{u}}{\overline{U}} + \frac{\overline{V}}{\overline{U}}\tan\alpha\right)^2 = c + d\left(\frac{\overline{u}}{\overline{U}} + \frac{\overline{V}}{\overline{U}}\tan\alpha\right)$$

allows Equation (2.9) to be reduced to:-

$$E = s\,(U\cos\alpha + V\sin\alpha)\left[a + b\left[\frac{K_2^2}{\cos^2\alpha}\frac{w^2}{\overline{U}^2} - K_1^2\left(\frac{V}{\overline{U}} - \frac{u}{\overline{U}}\tan\alpha - \tan\alpha\right)^2\right]\right.$$
$$\left.\left[c + d\left(\frac{u}{\overline{U}} + \frac{V}{\overline{U}}\tan\alpha\right)\right]\right] \qquad (2.11)$$

where a, b, c and d are obtained from least square fits to experimental data corresponding to Equations (2.10)*. For $\alpha = 0$ with the neglection of terms multiplied by K_1^2, (order of K_1^2 is 0.02) Equation (2.11) reduces to:-

$$E = s\,U\left[a + b\,K_2^2\,\frac{w^2}{\overline{U}^2}\left(c + d\,\frac{u}{\overline{U}^2}\right)\right] \quad ** \qquad (2.12)$$

Neglecting the fourth-order terms, the mean velocity component in the x-direction can be obtained from the relation:-

$$\overline{E} = s\,\overline{U}\left[a + b\,c\,K_2^2\,\frac{\overline{w^2}}{\overline{U}^2}\right] \qquad (2.13)$$

Subtraction of the square of the mean signal in Equation (2.12) from the mean of the square of Equation (2.11), allows the axial normal stress

---

* More information about the evaluation of these constants is provided by Ribeiro (1976).

** The neglection of the terms multiplied by K_1^2 is appropriate except in a thin region of the shear layer surrounding the recirculation zone, where $\overline{U} \to 0$ and $V/\overline{U} \to \infty$.

to be obtained from the equation:-

$$\overline{e^2} = s^2 \overline{U^2} \left[a^2 \frac{\overline{u^2}}{\overline{U^2}} + 2\,a\,b\,K_2^2\,(c+d)\,\frac{\overline{u^2}\,\overline{w^2}}{\overline{U}^2} + 2\,b^2\,c^2\,K_2^4\,\frac{\overline{w^2}^2}{\overline{U}^4} + 2\,b^2 \cdot (K_2^2)^2 \left(5\,c\,d + \frac{3}{2}\,d^2 + \frac{3}{2}\,c^2\right) \frac{\overline{u^2}\,\overline{w^2}^2}{\overline{U}^6} + 8\,b^2\,d^2\,(K_2^2)^2\,\frac{\overline{u^2}^2\,\overline{w^2}^2}{\overline{U}^8} \right] \qquad (2.14)$$

The value of $\overline{u^2}$ obtained by this equation is directly proportional to the measured mean square of the signal fluctuations and it does not, therefore, imply any error propagation.

(ii) Equipment and Instrumentation

Measurements were obtained with DISA single wire probes (Models 55A25 and 55A29) held by probe holders secured to a welded-wire structure which entered the confining tube from its open end and was translatable in three directions by a cathometer and milling-table arrangement, see Fig. 2.4. The wire structure also allowed rotation of the probe about its axis. As a result of this arrangement, hot-wire probes were located within the flow with an accuracy of 0.1 mm. The disturbance caused by the wire structure was investigated at fixed positions by comparing the results with those obtained with a probe held by a single, fixed rod. The maximum difference in measured values of mean velocity was found to be less than 0.5% outside the recirculation region; similar tests inside the recirculation region indicated differences of up to 4% (see Fig. 2.5).

As indicated on the block diagram of Fig. 2.6, the anemometer signal was linearised (DISA 55D10) and supplied to an integrator (DISA 55B30) and root-mean square unit (DISA 55D35) to obtain mean and

rms values. These values were recorded and analysed, in the manner described in the previous subsection, to give values of mean velocity and the components of the Reynolds-stress tensor.

(iii) Error Analysis and Calibration

Error Analysis

The error in the normal and shear stresses arising from a 1% error in $\overline{E^2}$ is represented approximately in Table 2.1 where T is the turbulence intensity. The error associated with the mean velocity $\overline{U}$ and the normal stress $\overline{u^2}$ are directly proportional to the error in the mean and rms of the signal value, respectively.

Calibration

The calibration was directed to the evaluation of the constants s, K_1 and K_2. The hot-wire was calibrated in the potential core of a free jet according to the equation:-

$$E^2 = s^2 U^2 (\cos^2 \beta \cos^2 \theta + K_1^2 \cos^2 \beta \sin^2 \theta + K_2^2 \sin^2 \beta) \qquad (2.15)$$

where β is the complementary to the angle between the flow direction and the probe plane, and θ is the angle between the direction of the flow component in the probe plane and the normal to the wire in the same plane.

The sensitivity factor was determined by plotting $\overline{E}$ against $\overline{U}$ with θ and β equal to zero. K_1 and K_2 are obtained, as shown inset of Fig. 2.6, by drawing $E^2(\theta)/E^2(\theta = 0)$ against $\sin^2 \theta$ with $\beta = 0$ and $E^2(\beta)/E^2(\beta = 0)$ against $\sin^2 \beta$ with $\theta = 0$, respectively.

TABLE 2.1

ERROR PERCENTAGE IN THE MEASURED REYNOLDS STRESSES

The Value	Error Formula	Error at Turbulence Intensity of	
		20%	70%
$\frac{\Delta\,(\sqrt{\overline{v^2}})}{\overline{U}}$	$\frac{T}{2}\left(\frac{0.02 + 0.062\ T^2}{0.03 + 2\ T^2}\right)$	2%	1.7%
$\frac{\Delta\,(\sqrt{\overline{w^2}})}{\overline{U}}$	$\frac{T}{2}\left(\frac{0.04 + 0.15\ T^2}{0.03 + 2\ T^2}\right)$	4%	3.8%
$\frac{\Delta\,(\overline{uv})}{U^2}$	$T^2\left(\frac{0.01 + 0.04\ T^2}{1.94\ T^2}\right)$	6%	2.0%

2.3.2 Laser Doppler Anemometry

This section deals with the laser Doppler anemometer and provides a brief description of its components. In general, the anemometer consists of two main parts, the optical arrangement and the signal processing electronics. For measurements with forward scattered light, as used here, the flow configuration was located between the transmission and collection optical components. The optical arrangement and the signal processing systems are described and the section ends with an error analysis.

(i) Equipment and Instrumentation

The laser Doppler anemometer, see Fig. 2.7, comprised an Argon laser (Spectra Physics Model 164) operated at 488 nm and around 200 mW. The laser beam passed through a water filled acousto-optic cell* which provided zero and first order beams with a frequency difference of 21 MHz, see Durão and Whitelaw (1975). The beams were separated by 71.5 mm, made parallel and focussed to their intersection by a 200 mm focal-length lens. Forward-scattered light was collected with a lens of 150 mm focal length and 100 mm diameter and focussed to a pin-hole in front of a photomultiplier cathode (EMI 9815B). The laser was located and its beam adjusted using a high quality mirror which was secured, with the remaining optical components, to a 2 m

---

* The acousto-optic cells have large frequency shift which suit measurements in highly turbulent flows with separation and regions of reverse flow, as those of the present work. Other optical components such as those without frequency shift or with a rotating diffraction grating cannot be used; the first is only applicable where the instantaneous velocity is unidirectional (see Durst and Whitelaw, 1971 and 1971a) and the second have maximum convenient shifts of around 4MHz which is not sufficient in reverse air-flow experiments if good spatial resolution is to be maintained (see Melling, 1975).

long optical bench located on a milling table which allowed translation in two horizontal directions with a precision of better than 0.1 mm. The milling table also allowed a small range of translation in the vertical direction. The more important characteristics of the optical arrangement are indicated on Table 2.2*.

A small quantity of atomised silicone oil was added to the plenum chambers of the annulus and pipe flow at a distance of about 2 m upstream the inlet to the confinement and so allowed the silicone oil to be uniformly distributed with the air.

TABLE 2.2

OPTICAL CHARACTERISTICS

Half angle between incident beams	11.1 degrees
Frequency difference	21 MHz
Transform relationship	0.752 MHz/m/s
Length of the intersection volume at e^{-2} location	0.3 mm
Diameter of part of intersection volume observed by photodetector	0.095 mm
Magnification of light-collection arrangement	1.5

The signal from the photomultiplier was passed to an oscilloscope and to a spectrum analyser** (Hewlett Packard Model

---

* The reader is referred to Durst et al (1976) for details of the relations required to calculate these characteristics.

** The spectrum analysers resolve the frequency components of the Doppler signal and can be used up to about 100 MHz Doppler frequency at high turbulence intensities; poor signal-to-noise ratios can be accepted with both low and high particle concentrations, but data acquisition and reduction is very slow (see Melling, 1975).

9553B/8552A/141T) which was swept with bandwidths of 30, 100 and 300 KHz depending on the mean frequency. The spectrum analyser measures the probability of the frequency (the number of bursts over some triggering level at certain frequency) at N frequencies equally spaced between the extreme lower and upper frequencies of the Doppler spectrum. The moments of the velocity or Doppler frequency distributions are calculated from the following formulae:-

Mean Velocity

$$\overline{U} = \frac{\lambda}{2 \sin (\phi/2)} \overline{f} = \frac{\lambda}{2 \sin (\phi/2)} \int P(f)\, f\, df$$

Normal Stress

$$\overline{u^2} = \overline{(U - \overline{U})^2} = \left(\frac{\lambda}{2 \sin (\phi/2)}\right)^2 \int P(f)\, (f - \overline{f})^2\, df$$

Skewness Factor

$$\frac{\overline{u^3}}{\overline{(u^2)}^{3/2}} = \left[\left(\frac{\lambda}{2 \sin (\phi/2)}\right)^3 \int P(f)\, (f - \overline{f})^3\, df\right] / \overline{(u^2)}^{3/2}$$

Flatness Factor

$$\frac{\overline{u^4}}{\overline{(u^2)}^2} = \left[\left(\frac{\lambda}{2 \sin (\phi/2)}\right)^4 \int P(f)\, (f - \overline{f})^4\right] / \overline{(u^2)}^2$$

(2.16)

where:-

ϕ is the crossing beam angle

λ is the laser wavelength

$$\int P(f)\, df = 1.0$$

A microprocessor was used to evaluate the probability distributions and calculate the mean and rms according to the above equations. The probability distribution was formed with one pulse per Doppler burst; on the recognition of the arrival of a burst a flag is raised and to be reset by the microprocessor after a maximum time delay of 42 μs which is the sampling rate of the microprocessor*.

(ii) Error Analysis

In general the laser Doppler anemometer with signal processing based on averaging of a number of individual frequency measurements may be subject to errors due to gradient and particle broadening, to the number of signals used to form the average and to non-zero correlation between number of particles and flow velocity. The beam crossing angle was large so that the dimension of the scattering volume aligned with the predominant velocity gradient was not long. This led to the neglect of the first source of error. The second error is caused by the estimation of deriving the statistics, the mean and rms frequencies from the pdf of the Doppler frequency, from a finite sample size. This error was quantified by Yanta (1973) for the mean and rms as given by the following formulae:-

$$e_\mu = \frac{2}{\sqrt{N}} \frac{\tilde{\nu}_D}{\overline{\nu}_D} \qquad (2.17)$$

---

* More details are available in Subsection 2.3.4 and the reader is referred to the work of Durão et al (1978).

$$e_\sigma = \sqrt{2/N} \qquad (2.17)\ \text{(Contd.)}$$

where e_μ and e_σ are the error in the mean and rms values, respectively, and $\bar{\nu}_D$ and $\tilde{\nu}_D$ are the mean and rms values of the Doppler frequency.

The number of signals, N, used to form the averages ranged from 6000 to 25000 and, in accordance with the above equations, implied uncertainties of less than 1.8% in the mean velocity and 1.7% in the rms values, depending on turbulence intensity for the former.

As discussed by McLaughlin and Tiederman (1973), the probability density function of the individual velocity measurements may be biased towards higher velocity because the rate of realizations depends on the instantaneous velocity. However, it was shown by Durão (1976) and Durão and Whitelaw (1979) that the averaging characteristics of the photomultiplier may introduce an opposite bias, i.e. towards lower velocity values. In their recent paper, Durão et al (1980), suggested that this bias tends to cancel that of the velocity-particle-density correlation and the probability distribution formed with one pulse per Doppler burst will lead to the correct values of mean velocities for arrangements with turbulent, instrumentation and particle time scales such as those of the present measurements. Further discussion of this error is given in Subsection 2.3.4.

2.3.3 Pitot Tube

Measurements of the axial mean velocity were obtained using a three-hole pressure probe and compared with those of laser and hot-wire anemometers. The three-hole pressure probe was similar to that described by Hiett and Powell (1962) and is shown diagrammatically on Fig. 2.8. The probe diameter was 6 mm and the three tappings were located as close as possible through a "V" groove arrangement. The two tappings for yaw angle determination lie in one flank of the groove on a 72° angle and the third tapping was on the other flank. The pitot probe was calibrated in the potential core of a round jet

for the range of pitch angle experienced in the confined coaxial jet flows and introduced radially from the circumference of the cylinder. The method of calibration and details of use of the probe are described in the above reference and will be explained briefly in the next paragraph.

The pitch angle parameter, $(P_1 - P_3)/(P_1 - P_2)$, which is an indication of the flow direction relative to the tube axis, was related, through two calibration curves, to the velocity head parameter, $(P_1 - P_2)/V.H.$, which represents the velocity head in a plane normal to the probe axis, see Fig. 2.9. P_1, P_2 and P_3 are the readings of the three tappings; the two yaw tappings are referred to as Nos. 1 and 2 while tapping No. 3 is in the same radial plane as No. 1. V.H. is the total velocity head.

To obtain measurements, the probe was rotated about its axis until the pressures at tappings 1 and 2 were balanced. The tube was then rotated 36° so that hole No. 1 faced the stream. At this setting both the differential pressures $P_1 - P_2$ and $P_1 - P_3$ were measured and the pitch angle and total velocity head determined from the calibration charts (Fig. 2.9).

In turbulent flows, pitot tubes may be subject to errors due to their finite size and to the dependence of their response on the turbulence intensity. In his theoretical study, Goldstein (1936) suggested that the response equation of a pitot tube in a turbulent flow can be given as:-

$$P_{tot} = P_s + \frac{1}{2} \rho \overline{U}^2 \left[1 + \frac{\overline{u^2} + \overline{v^2} + \overline{w^2}}{\overline{U}^2} \right] \qquad (2.18)$$

This formula was criticised by Hinze (1959) who suggested that the total pressure measured by the tube is not equal to the total pressure at the centre of the tube hole due to the finite diameter of the tube

and that the lateral-velocity fluctuations minimize the total-head-tube reading. He suggested the expression:-

$$P_t = P_s + \frac{1}{2} \rho \overline{U}^2 \left[1 + \frac{\overline{u^2} + (1 - \beta) (\overline{v^2} + \overline{w^2})}{\overline{U}^2} \right] \tag{2.19}$$

where β (order of 0.2) is the combined reduction effect of lateral-velocity fluctuations on the measured total and static pressure. More recently, Becker and Brown (1974) obtained the following empirical relation for the directional sensitivity:-

$$P_{tot} = P_s + \frac{1}{2} \rho \vec{V}^2 \left[1 - K (\sin^2 \phi)^m \right] \tag{2.20}$$

where $\vec{V}$ is the total velocity vector and ϕ is defined as:-

$$\cos \phi = (U + u)/(\overline{U}^2 + u^2 + v^2 + w^2)^{1/2} \tag{2.21}$$

and K and m are constants dependent on the pitot tube geometry.

As can be shown from the above relations, the error associated with the pitot tube depends mainly on the probe geometry. An estimation of this error for the present probe will be provided in the next subsection by comparison with laser Doppler and hot-wire results.

2.3.4 Comparison of the Different Techniques

This section presents a comparison of the measurements obtained by the three different techniques described in Subsections 2.3.1, 2.3.2 and 2.3.3. The measurements were performed along the centre-line and along the radius, at the two axial locations x/D_e = 0.616 and 3.67 of the confined coaxial jets described in Section 2.2.

The results are presented and discussed in the following subsections.

(i) Analysis of the Results

Figs. 2.10 and 2.11 allow comparison of the mean velocity and the corresponding normal stress, respectively, between the measurements of laser and hot-wire anemometers for the two different velocity ratios. Fig. 2.10 indicates that the maximum difference in the mean velocity does not exceed 10% of the local velocity for either flow with laser measurements giving the higher values. For the turbulence intensity, Fig. 2.11 indicates a maximum difference between the rms values obtained by the two techniques of the order of 17% of the maximum rms values for each flow. Both figures indicate that the maximum relative differences in both the mean velocity and normal stresses are associated with the higher turbulence intensity levels, $\tilde{u}/\overline{U}$.

In view of the rectification characteristics of the hot-wire, it is to be expected that measured mean values should be high and rms quantities low in regions of turbulence intensity levels greater than around 30%, see Fig. 2.12. Also, the bias of laser Doppler anemometer results due to the correlation between velocity and particle number can cause the mean velocities to be high, depending upon the turbulence level, but have little effect on the second moment. The discrepancies in the mean velocity and normal stress for $x/D_e < 2$, where the turbulence intensity is between 4% and 25%, are probably associated partly with the method of analysing the hot-wire signals and partly from a small overall bias in the laser results. In this region, the correct result for the mean velocity is closer to the hot-wire measurements and that of the normal stress is closer to the laser measurements. In the downstream region, where the turbulence intensity is high,

both sets of mean values may be slightly high and the correct rms values should again be close to the laser measurements.

Radial profiles of the axial component of mean velocity and the corresponding rms values are presented in Figs. 2.13 to 2.16. Figs. 2.13 and 2.14 represent radial profiles at an upstream section, i.e. x/D_e = 0.616. Fig. 2.13 shows that the results obtained by the three measuring techniques are in reasonable agreement provided the hot-wire results, obtained in the region of recirculation, are recognised as corresponding to negative values. The pitot tube measurements indicate higher mean velocity values in the regions of high turbulence intensity due to the effect of turbulence. In the recirculation zone, the difference in the mean velocity increases with increase in the turbulence intensity: the difference in the rms values are considerably larger with the hot-wire, as expected, giving the erroneously low results shown by Fig. 2.14. In Fig. 2.15, the mean velocity values measured by the three techniques are represented at x/D_e = 3.67. The results of hot-wire and laser Doppler anemometer were normalised by the corresponding centre-line value. The mean velocity of the hot-wire at the centre-line was used to normalise the velocity values of the pitot tube measurements. The results of the hot-wire and laser exhibit no further differences along the radius. The pitot tube results indicate higher mean velocity of around 14% near the centre-line and the difference decreases considerably away of the centre-line.

(ii) Discussion

The measurements allow comparison between two obtrusive and one unobtrusive measuring techniques in regions of recirculation. Fig. 2.13 indicates discrepancies in the mean-velocity results in the recirculating region and at the velocity maximum. The hot-wire

results are clearly incorrect but stem from a simple misinterpretation of the flow direction which can readily be appreciated. If rectified, they are in reasonable agreement with the laser anemometer results. The magnitude of the disagreement is of the order of 50% in some regions, due largely to the errors associated with the hot-wire at high values of local turbulence intensity but this represents less than 2% of the maximum velocity and is adequate for many purposes. Similarly, there are discrepancies between the pressure probe and laser anemometer results but they are of the same magnitude at the upstream sections. At least in this flow, the effect of probe interference does not appear to be of major significance. The low values of velocity maximum are due, at least in part, to be spatial average observed by the probe. At a downstream section, $x/D_e = 3.67$, the turbulence intensity is high and the pitot tube indicates higher mean velocities. A correction of the pitot tube results according to Equation (2.19), with a value of $\beta = 1$, shows results which are in reasonable accord with the results of laser anemometer and hot-wire. Another correction obtained by applying Equation (2.18) indicates that Goldstein's formula overestimates the error, see Fig. 2.15.

The differences in the measured values of the rms of the velocity fluctuations between hot-wire and laser anemometer show an expanded trend in the recirculating flow. The hot-wire rectifies negative velocities and leads to values which are low whenever negative velocities are present. This is particularly noticable in the region of recirculation, as previously observed by Bradbury (1976) and Simpson et al (1977), but is also noticable in the regions of the flow where intensities are large. This is also shown by Fig. 2.11. The magnitude of the discrepancies are, however, seldom sufficiently great to permit erroneous fluid mechanic conclusions. Although there are a number of techniques which may be

used to improve the applicability of hot-wires to highly turbulent flows, see for example Downing (1972) and Cook and Redfearn (1976), it seems to be difficult, as indicated by Bradbury (1976), to develop such schemes into practical form. It may be noted here that the pulsed-wire anemometer (Bradbury and Castro, 1971) is not applicable for the measurements of turbulent intensities normal to the mean flow direction in flows of turbulence intensities lower than 50% if reasonable accuracy is to be achieved.

In laser Doppler anemometry, the signal processing based on averaging of a number of individual frequency measurements may be subject to error due to the correlation between velocity and particle number density. This potential error source was discussed by McLaughlin and Tiederman (1973) who argued that a velocity greater or lower than the mean will be associated with a number of particles, per unit time, passing through the control volume which is larger or smaller than the average one. This correlation tends to bias the velocity magnitudes towards higher values. An unbiased result would be obtained if the number of particles contributing to the measured values of velocity were randomly distributed in time and did not, therefore, correlate with the instantaneous velocity. Dimotakis (1976) has shown that the biasing problem can be overcome if the particle arrival rate is high, but this is not practical, in air flow measurements where the number of velocity measurements per second is not high enough for it to be possible to follow turbulence in real time. A one-dimensional correction method was suggested by McLaughlin and Tiederman (1973). Since the particle number density is correlated with the instantaneous velocity vector and not one of its components, this method magnifies the error and gives erroneously high values in highly turbulent flows. A corrected one-dimensional velocity

probability distribution can be obtained from the measured one-dimensional probability distribution using a correction based on the three-dimensionality of the velocity fluctuations. This correction is given by the following equation:-

$$Prob_{cor}\ (U) = Prob_{m}\ (U) * \bar{U}_m/V_m \qquad (2.22)$$

where V_m is the velocity vector value and $\bar{U}_m$ is the measured mean velocity. Along the centre-line of the coaxial jet, the measured velocity probability distribution can be corrected since the velocity components are not correlated; the correct probability distribution is written as:-

$$Prob_{cor}\ (U) = Prob_{m}\ (U).\ \bar{U}_m/(U_m^2 + 2\ v_m^2)^{1/2} \qquad (2.23)$$

This expression is subject to a second order error since U_m and V_m are used rather than the correct values, U and V. Measured and corrected probability density distributions at three different turbulence intensities are shown in Fig. 2.17. The difference between $\bar{U}$ and $\bar{U}_m$ is shown, in absolute percentage form in Fig. 2.18, and may be compared with the one-dimensional correction of McLaughlin et al (1973) which is, as expected, too high. The correction increases in magnitude with the turbulence intensity; it is less than 4% at 0.2 turbulence intensity and increases to a nearly asymptotic value of 21% at turbulence intensity greater than 0.7. It can be anticipated that the magnitude of the correction, at a given turbulence intensity, will depend on the relationship between the velocity components and will increase as the correlation between velocities increases. In most cases, the higher turbulence intensities are associated with low

values of mean velocity and the absolute magnitude of the effect is small. Also, the absolute magnitude of the effect reaches a maximum when the turbulence intensity achieves values which imply negative instantaneous velocity values.

Fig. 2.19 represents the centre-line profile of the inverse of the mean velocity and of the normal stress for the uncorrected and corrected laser measurements values as compared with those of hot-wire results. The figure indicates that the correction in the normal stress is not significant and reaches a maximum of 12% of the local mean velocity at turbulence intensity of around 80%. The figure also indicates that the mean velocity measured by hot-wire is higher, as expected, than the corrected laser values.

Although the correction method explained above is expected to give correct results, it requires simultaneous measurements of the existing velocity components. Similar methods were suggested by Dimotakis (1976), Buchave (1975), Shemer and Einav (1979) and McDougall (1980); Dimotakis has considered the type of LDA which simultaneously measures two perpendicular velocity components and derived a weighting function which can be used for correcting the velocity measurements when the number of velocity measurements per second is low. Buchave and McDougall assumed three-dimensional Gaussian turbulence field to derive a weighting function for correcting the bias. Buchave's method uses the application of $1/|\overline{U}|$ weighting of the data rate and so is inaccurate when the mean velocity, $\overline{U}$, is close to zero. The methods of Dimotakis and McDougall require respectively the simultaneous measurement or estimation of a second velocity component beside the velocity component under consideration. Recently, Durão et al (1979) indicated that the flow velocity influences the signal quality and reported decay of amplitude of the photomultiplier output signal

which will bias the signal towards lower velocities; this bias is opposite to that discussed above. More recently, Durão et al (1980) suggested that the two types of bias tend to cancel each other, but the resulting effect is subject to the type of optical and signal processing arrangement. However, it was shown by Durão (1976) that the signal amplitude decays with the velocity at low frequency values and this decay slows down at higher frequencies which is the case of the present frequency shift of 21 MHz.

A simple way of removing the velocity bias is also available if the laser Doppler anemometer measures both the velocity and the residence time of each particle which passes through the probe volume as discussed for example by Hoesel and Rodi (1977) and Wilson (1978). This method uses a weighting factor which is proportional to the residence time of signal bursts and imply that this time is inversely proportional to the modulus of the velocity vector.

As shown from the above discussion of the different methods of correcting velocity measurements of laser Doppler anemometer, the correction is applied after the measurements have been obtained. Instead of this, an on-line correction weighting function could remove the bias if the time during which a particle is present in the control volume was taken into account in the processing of the signal. Thus unbiased probability distribution would be obtained if it was formed with a number of pulses corresponding to the duration of the burst, see Durão et al (1978). It may be noted here that the biased probability distribution is formed with one pulse per Doppler burst. From now on this is referred to as Method 1 and the former, Method 2. The schemes of the sampling procedure of the two methods are presented and compared in Fig. 2.20*. In Method 1 a flag is

---

* For more details see Laker (1979) and Durão et al (1980).

raised on recognition of the arrival of the burst and is reset by the microprocessor after a maximum time delay of τ_s = 42 μs: the next measurement is obtained from a subsequent Doppler burst. Thus the probability of detection is proportional to (τ_s/τ_p) where τ_p is the time scale of the particle arrival rate and unbiased probability can be obtained only if $\tau_s > \tau_p$. In air flow measurements, τ_p is always larger than τ_s and the measured bursts are usually dependent on the number of particles passing through the control volume, and so formed a biased probability distribution. In the second method, the flag is raised on the arrival of a burst and allows frequencies to be recorded for the duration of the Doppler burst: the probability of detection is proportional to (τ_r) where τ_r is the residence time of a particle which is inversely proportional to the instantaneous velocity vector. Thus this method is expected to result in unbiased probability distribution.

The two methods explained in the above paragraph were compared for the measurements of mean and normal stress of the axial and tangential fluctuating velocity of a swirling flow of 0.93 swirl number in quarl angle expansion (Geometry G2 in Chapter 4). A comparison of the measured probability distribution by Methods 1 and 2 is shown in Fig. 2.21 for positive, zero and negative values of mean velocity. The figure shows that Method 1 results in biased probability only, as expected, for mean velocity values which are not zero. The results of Figs. 2.22 and 2.23 indicate higher amplitudes of the mean velocity measured by Method 1 of about 19% at 90% turbulence intensity which is nearly in accord with the results of correction based upon measurement of all the existing velocity components, Fig. 2.18. The figures also indicate that Method 1 overestimates the normal stresses; for example at 90% turbulence intensity the axial normal stress is overestimated by about 13%.

In conclusion, the comparison between hot-wire and laser

Doppler anemometer measurements, Subsection 2.3.4i, indicated differences between the results of the two techniques in highly turbulent flows. The hot-wire rectifies the negative velocities and leads to higher mean velocities and lower normal stresses. The velocity measurements of laser Doppler anemometer which is based on averaging of a number of individual frequency measurements may be subject to a bias towards higher values. The different methods for correcting this bias were discussed. Two methods were provided, tested and evaluated; the first is a correction of measured probability distribution based on a weighting function of the instantaneous velocity and the second is an on-line correction which takes into account the duration time of the burst. This method was applied for the measurements of Chapter 4; no correction was made for the measurements of the present chapter.

2.4 Velocity Characteristics of the Confined Double Coaxial Jet

This section deals with measurements obtained in the confined double coaxial jets. The measurements were obtained mainly by the laser Doppler anemometer and performed for the velocity ratios 3.0 and 1.0 with zero swirl and for the velocity ratio 3.0 with a swirl number of 0.23 imparted to the annular jet. The mean velocity and normal stresses were measured along the centre-line and along the radius at different x-locations.

2.4.1 Velocity Characteristics of the Confined Double Coaxial Jet Without Swirl

(i) Mean Velocity and Normal Stresses

The centre-line measurements were presented previously in Figs. 2.10 and 2.11 and were normalised by the mean velocity at the

centre-line at the exit plane of the coaxial pipes. Fig. 2.10 indicates that the jets of the higher velocity ratio mix and decay more rapidly than those of $\overline{U}_a/\overline{U}_p$ of unity. The annular jet, in the case of the higher velocity ratio, entrains air from the central jet and causes the centre-line velocity to decrease in the region close to the inlet section. As the spread of the annular jet reaches the centre-line, the velocity begins to increase. This is not the case for the unity velocity ratio where the central jet preserves its momentum and decays at a lower rate.

It is also clear from Fig. 2.11 that the higher velocity ratio is associated with higher normal stress. For the unity velocity ratio there is only one maximum which occurs at the maximum gradient of the mean velocity. Along the centre-line, the production of $\overline{u^2}$ is caused by the term $- 2 \rho \overline{u^2} \partial\overline{U}/\partial x$. In the case of the higher velocity ratio, the maximum normal stress occurs at $x/D_e \tilde{} 2.8$ where the mean velocity gradient is negative. At $x/D_e \tilde{} 1.0$, where the mean velocity gradient is positive, the normal stress is produced at a negative rate. The lost energy is supplied by diffusion from other parts of the flow. It may be also compensated by redistribution among the individual normal stresses by pressure strain terms which can be expressed, as will be shown in Chapter 3 (Subsection 3.2.3), as $- c_{\phi_2} \left(G_{\overline{u^2}} - \frac{2}{3} G_K \right)$ where c_{ϕ_2} is a positive constant and G_K and $G_{\overline{u^2}}$ are the production of K and $\overline{u^2}$, respectively. The occurrence of maximum normal stress at the negative mean velocity gradient and not at the positive gradient is attributed to the eddies moving with a velocity which is higher than the local mean in the former case (negative mean velocity gradient) and lower than the local mean in the latter (positive mean velocity gradient). However, it can be shown from Fig. 2.24 that the turbulence intensity levels, that is the normal stress

normalised by the local mean, are generally higher in the jets of the higher velocity ratio. In the region of $4 < x/d_o < 7$, these values are nearly the same for both velocity ratios and indicate independence of the normalised normal stress on the input conditions in this region.

To investigate the effect of confinement on the velocity structure of the double coaxial jets, the present measurements for unity velocity ratio may be compared with those of Ribeiro (1976) which were carried out in the same coaxial pipe configuration without confinement. Fig. 2.25 represents the comparison of the mean velocity and corresponding normal stress along the centre-line. The figure indicates that the jet penetration is rather less for the confined flows. The axial velocity in the confined and free flows is similar in the upstream region but the former decays much more rapidly down-stream of 5 d_o. The centre-line distributions of the normal stress, Fig. 2.25b , are also in close accord in the upstream region, i.e. to $x/D_e = 1.25$. Downstream of this region and up to $x/D_e = 3.4$, the normal stress exhibits higher values in the confined flow due to larger negative gradients in the mean velocity. Further downstream, the confined jet exhibits lower values for the normal stress. The turbulence intensity levels, that is the normal stresses normalised by local mean velocity values, are greatly increased by the confinement, Fig. 2.25c. This is due to a faster decay of the mean velocity along the centre-line in the confined jet rather than of an increase in the levels of the normal stresses.

Corresponding to Figs. 2.10 and 2.11, radial profiles of mean axial velocity and axial normal stress are presented on Figs. 2.26 and 2.27 at x/D_e of 0.616, 1.43, 2.23 and 3.67 or x/d_o = 1.73, 4.02, 6.25 and 10.6. The mean velocity profiles in the vicinity of the jet exit, Fig. 2.26, can be expected to be similar to those for the corresponding

unconfined flows and, by the first measurement station, the origin of the flow is not detectable at least for the higher velocity ratio. The unity velocity ratio seems to have a low rate of mixing and the profile at x/D_e = 0.616 is still referring to the wall between the two jets at the inlet section. The flow of unity velocity ratio at x/D_e = 0.616 still exhibits two maxima with the one corresponding to the annular jet is higher which is mainly due to the entrained air from the recirculation region. This is not in accord with the free jet for which, as shown by Ribeiro (1976), the outer jet maximum is less than the velocity at the centre-line at x/d_o = 1 and x/d_o = 3. This is attributed to less entrainment in the case of the free jet. From the comparison with the results of Ribeiro (1976), it can be concluded that the flow development in the confined jets is not as dominated by the inlet velocity ratio as in the absence of confinement, for example the radial profiles of mean velocity for the confined arrangements are very similar for values of $x/D_e \geq 1.43$, when the velocity ratio is changed from 1.0 to 3.0.

The normal stress is presented in Fig. 2.27. As for the mean velocity, it is evident that the profiles are influenced by the velocity ratio in the upstream region of $x/D_e \leq 0.616$. However, the difference between the profiles of the two velocity ratios again tends to diminish but at x/D_e values which are comparatively larger than those corresponding to the mean velocity profiles. The figure indicates two maxima of the normal stress at x/D_e = 0.616 for velocity ratio of 3.0 and one maximum for the unity one. These maxima are nearly associated with the main strain, $\partial\bar{U}/\partial y$, through the production of $\overline{u^2}$ directly by $-2\rho\,\overline{uv}\,\partial U/\partial y$ and indirectly through the production of $\overline{uv}$ by $-\rho\,\overline{v^2}\,\partial U/\partial y$. The shear stress, $\overline{uv}$, Fig. 2.28 as measured by hot-wire for $\bar{U}_a/\bar{U}_p$ = 3.0, is negative for $r/R < 0.2$ and positive elsewhere

and its maximum positive value is nearly three times its negative value. These two positions are located at r/R = 0.28 and 0.125, respectively. In both cases, the term $-\rho \overline{uv}\, \partial U/\partial y$ is positive with larger value at r/R = 0.28. At x/D_e = 1.43, the shear stress exhibits only one maximum at about r/R = 0.38. Fig. 2.27 shows that the position of maximum normal stress is the same as the maximum shear stress, Fig. 2.28. At the downstream sections, x/D_e, the maximum of the normal stress is transferred into the centre-line and is not clearly distinguishable. At these sections, the main strain, $\partial\overline{U}/\partial y$ is not high and the production of $\overline{u^2}$ is likely to be more associated with the Reynolds stresses rather than the velocity gradient.

Fig. 2.29 presents the radial distributions of the radial and tangential normal stresses along the radius at x/D_e locations of 0.616, 1.43, 2.23 and 3.67 for the velocity ratio of 3.0. The comparison of these values with those of $\overline{u^2}$, Fig. 2.27, indicates that the rms of the radial and tangential velocity components are comparatively smaller than $\overline{u^2}$ values. The figure also indicates a faster decay of $\overline{v^2}$ near the wall as compared with $\overline{w^2}$.

The mean velocity contours of Figs. 2.30 and 2.31 represent a considerable interpolation of the results of Figs. 2.26 and 2.27 but indicate a recirculation region which increases in length with increased velocity ratio. This increase in length is related to the increase in the total axial momentum and to the higher velocity ratio. The contours of turbulence intensity indicate clearly the extensive region of high values especially for the higher velocity ratio. The pattern of the results is similar to that observed by previous authors, for example, Wingfield (1967) and Baker et al (1974). From examination of these results, Fig. 2.30, it can be deduced that the length of the recirculation region is dependent on velocity ratio and on the dimensions of the geometry. For example, the increase in the velocity

ratio from 1.0 to 3.0 (increase in the total axial momentum by a ratio of 2.067) increases the length from 2.96 D_e to 3.28 D_e which corresponds to 9.2 h and 10.2 h, respectively, where h is equal to $(R - d_o/2)$. The present configuration may be compared with those of previous authors. Since the experimental methods used in early contributions may be subject to uncertainty owing to the instrumentations used, the comparison in Table 2.3 is confined to the mean length of the recirculation region. It shows that this length is strongly dependent on geometry and particularly on the expansion ratio; it is obvious that the length of the recirculation (normalised by h or D_e) decreases with the increase of the expansion ratio d_o/D_e. The present configuration is also similar to the backward-facing step where similarity is held between h and the step height. The comparison is also shown in Table 2.3; the differences are likely to stem from differences in the geometry and the differences in the boundary layer thickness.

(ii) Energy-Spectrum Measurements

Spectral energy was obtained to provide a quantitative indication of the distribution of scale. The measurements were obtained by hot-wire anemometer; the hot-wire signal was fed into a Hewlett-Packard wave analyser with a frequency range of 2.5 to 25000 Hz. The normalised spectrum may be defined as:-

$$F(f) = \frac{\overline{e_f^2}}{\overline{be^2}} \qquad (2.24)$$

with:-

$$\int_0^\infty F(f)\, df = 1 \qquad (2.25)$$

TABLE 2.3

MEASURED VALUES OF

RECIRCULATION ZONE LENGTH

Investigator(s)	Length of Recirculation Zone	Geometrical Configuration	δ/h	d_o/D_e
Chatervedi (1963)	9.4 h	Pipe flow with sudden expansion	0.00	0.500
Wingfield (1967)	7.3 h	Double coaxial jet ($\bar{U}_a/\bar{U}_p = 1.0$)	1.00	0.500
Present (1980)	9.2 h	Double coaxial jet ($\bar{U}_a/\bar{U}_p = 1.0$)	0.55	0.356
Tillman (1945)	13.5 h	Backward-facing step	3.30	
Arie and Rouse (1956)	16.8 h	"	-	
Abbott and Kline (1962)	7.0 h	"	1.00	
Mueller and Robertson (1963)	6.9 h	"	1.00	
Bradshaw and Wong (1972)	6.0 h	"	0.12	
Matthews and Whitelaw (1973)	6.2 h	"	-	
Sakamoto, Moriya and Arie (1975)	13.5 h	"	-	
Moss, Baker and Bradbury (1979)	5.4 h	"	0.70	
Crabb, Durão and Whitelaw (1977)	12.3 h	"	-	
Ota (1975)	4.0 h	Free flow downstream of a circular bluff body	-	
Ota and Itasaka (1976)	12.0 h	" (flat plate)	-	
Moss, Baker and Bradbury (1977)	3.99 h	"	-	
Durão and Whitelaw (1978)	2.90 h	"	-	

where $\overline{e_f^2}$ is the mean of the square of the hot-wire voltage observed through a filter, of bandwidth b, centred at frequency f. In terms of the wave number, k:-

$$F\ (k) = \frac{\bar{U}}{2\pi} F\ (f) \qquad (2.26)$$

with:-

$$k = \frac{2\pi f}{\bar{U}} \quad \text{and} \quad \int_0^\infty F\ (k)\ dk = 1 \qquad (2.27)$$

Distributions of F (f) are presented on Fig. 2.32 for velocity ratio of 3.0 and confirm that the power spectrum is proportional to $k^{-5/3}$ in the inertial subrange. The spectrum may be described by a characteristic frequency at which the spectral density takes on its maximum value. Except for the spectrum corresponding to the pipe exit, which tends to be flat, this peak is well defined and increases with the downstream section.

The measured spectra were extrapolated to zero wavenumber with a parabola as suggested by Corrsin and Uberoi (1951) to provide the longitudinal macro-scale:-

$$L_x = \frac{\pi}{2} \lim_{k \to 0} F\ (k) \qquad (2.28)$$

The microscale was approximated by the expression:-

$$\frac{1}{\lambda_x^2} = \frac{1}{2} \int_0^\infty k^2\ F\ (k)\ dk \qquad (2.29)$$

The distributions of macro- and microscales are shown in Fig. 2.32. The distribution of the macroscale is consistent with the measurements of turbulence energy and mean velocity: the maximum value of macroscale corresponds to the maximum in turbulence energy and to the maximum negative velocity gradient. The measured microscales are intermediate between the large scales which contain most of the energy and the smallest scales which dissipate it.

(iii) Probability Density Distributions

In this subsection, measured probability density distributions of the longitudinal and circumferential velocity fluctuations are presented and discussed. The distributions were obtained along the centre-line and at the radius at x/D_e = 0.616 for velocity ratio 3.0; the various moments are quantified in Table 2.4.

Fig. 2.33 represents the probability density distribution of the longitudinal fluctuations along the centre-line for velocity ratio of 3.0. The probability distributions indicate that the most probable value is not zero and the distribution of skewness factor along the centre-line is represented on Fig. 2.34 together with the mean velocity gradient. It is evident that, for all the points but the last two, the positive mean gradient is associated with positive skewness and vice versa. This supports the suggestion of Ribeiro (1976) that the skewness is related to the dominant occurrence of eddies moving with a velocity either much higher or much lower than the local mean velocity. These eddies are likely to be of large scale created by the mean velocity gradient. As pointed out by Townsend (1956), the skewness is connected with the convection of turbulence energy (large

eddies) by turbulent movements, a process that, as a rule, transfers energy from regions of large intensity to regions of smaller intensity. However, these eddies are affected by the changes in the mean motion inside a finite region of space. This is mostly the case of the downstream two points, x/D_e = 3.84 and 4.32, where the mean velocity gradient is not so high and at these locations, the portion of the small volume, surrounding any of them, where the mean velocity is lower than the local mean, is larger than the portion where the opposite prevails. The flatness factor distribution, Table 2.4, indicates values which are not so far from the Gaussian, 3.0.

The radial distribution of the probability density of the u-fluctuations at x/D_e = 0.616 are presented in Fig. 2.35. The mean velocity gradient was approximated from the contours of Fig. 2.30 and presented with the skewness values on Fig. 2.36. The figure indicates that the skewness is again likely to be connected with the large eddies created by the mean velocity gradient and moving with velocity which is different from the local velocity. Unlike the distributions along the centre-line, the distribution of the skewness along the radius are expected to be affected by the inward or outward transport of the large eddies, created by the mean velocity gradient, by the radial mean velocity. This effect is expected to be small in the regions of small values for the radial velocity as compared with those of the axial velocity. Although the flatness factor, Table 2.4, is not so far from the Gaussian value it is larger than those of the centre-line.

2.4.2 Velocity Characteristics of the Confined Double Coaxial Jet with Swirl

The swirl measurements were made at a swirl number of 0.23 imparted to the annulus jet and for a velocity ratio of 3.0. The

TABLE 2.4

DIFFERENT CHARACTERISTICS OF MEASURED POINTS AT CERTAIN LOCATIONS ($\overline{U}_a/\overline{U}_p$ = 3.0, S = 0.0)

	x/D_e	$\overline{U}$	$\overline{u^2}$	$\overline{w^2}$	$\overline{u^3}/\overline{u^2}^{3/2}$	$\overline{w^3}/\overline{w^2}^{3/2}$	$\overline{u^4}/\overline{u^2}^{2}$	$\overline{w^4}/\overline{w^2}^{2}$
$y = 0$	0.16	14.76	1.13	0.74	- 0.4087	- 0.0671	3.2454	3.380
	0.48	15.95	2.60	2.25	0.8921	- 0.3579	5.2830	3.950
	0.96	31.70	5.60	4.50	0.3267	- 0.0135	3.0000	3.275
	1.44	38.50	5.80	4.96	- 0.3879	0.0631	3.6000	3.480
	1.92	35.10	7.16	5.29	- 0.8312	0.0621	4.0000	3.490
	2.40	27.00	9.10	5.84	- 0.5416	0.0949	3.0000	3.330
	2.88	18.50	9.40	5.65	- 0.3417	0.0688	2.8700	3.090
	3.36	11.90	7.60	4.93	- 0.0149	- 0.0725	2.9230	3.060
	3.84	8.11	5.90	3.75	0.0549	- 0.0136	3.3000	2.835
	4.32	6.37	4.67	2.65	0.1826	- 0.2267	3.9300	3.250
	r/R	$\overline{U}$	$\overline{u^2}$	$\overline{w^2}$	$\overline{u^3}/\overline{u^2}^{3/2}$	$\overline{w^3}/\overline{w^2}^{3/2}$	$\overline{u^4}/\overline{u^2}^{2}$	$\overline{w^4}/\overline{w^2}^{2}$
$x/D_e = 0.616$	0.06	21.60	6.20		0.5750		3.3500	
	0.14	40.00	7.60	4.30	- 0.1630	0.1230	2.7900	3.810
	0.22	50.50	6.80		- 1.4200		5.5500	
	0.30	30.30	11.50	7.30	0.4420	0.0116	2.9500	3.140
	0.38	11.77	9.70		- 0.0082		3.1500	
	0.46	1.57	7.40	4.37	0.3727	0.1380	4.0000	3.490
	0.54	- 1.82	5.36		0.1951		5.1900	
	0.62	- 2.03	6.60	3.47	0.4240	0.1133	6.2200	3.032
	0.70	- 1.20	5.00		- 0.4590		4.2000	
	0.78	- 2.33	4.40	3.18	- 0.3980	- 0.1350	4.5000	2.860
	0.86	- 1.70	5.78		0.1400		3.3000	

measurements were obtained for the mean axial and tangential mean velocities and normal stresses along the centre-line and along the radius at four axial locations; x/D_e = 0.616, 1.43, 2.23 and 3.67. Fig. 2.37 presents the distributions of the mean velocity and normal stresses along the centre-line. The comparison with the flow without swirl in Fig. 2.37 indicates that the maximum along the centre-line is closer to the jet exit plane in the case of swirl and associated with a region of low velocity which exists further downstream as the jet spreads more rapidly away from the centre-line in the present flow. This decrease in the velocity along the centre-line is a direct result of the pressure sink in the transport equation for the axial momentum. The sudden expansion imposes a very high rate of change upon the angular velocity field which affects the pressure field through the centrifugal force, $\overline{W}^2/r$. This produces a positive axial pressure gradient along the centre-line which acts as a sink of the mean velocity.

Fig. 2.37 indicates also that the maximum normal stress is also closer to the jet exit plane in the case of swirl. As previously observed by Ribeiro and Whitelaw (1980) for their corresponding unconfined flow, the axial normal stress exhibits higher values in the upstream region. The axial distribution of the rms values of the two components of fluctuating velocity are similar in form with the circumferential component of very slightly lesser magnitudes. The maxima of the normal stresses are corresponding to the maximum negative gradient of the axial mean velocity where the production of kinetic energy of turbulence by the term $- 2 \rho \overline{u^2} \partial\overline{U}/\partial x$ is very high. The maxima in the intensities are very much larger in the confined flow and are again located to the exit plane. The intensity of the free flow (unconfined jet) asymptotes to a value of around 0.25 and

the present flow exhibits a similar tendency although from higher rather than lower values.

Radial distributions of the axial and circumferential velocity components and the corresponding rms values are presented in Figs. 2.38 and 2.39. They are consistent with the greater spreading rate of the swirling flow. The distributions of mean axial velocity and normal stresses are already near uniform at x/D_e of 3.67. At the upstream stations, the influence of the swirl on the mean velocity is obvious and results in a rapid change in the profile shape between x/D_e of 0.616 and 1.43. In particular, the near zero velocity on the centre-line at x/D_e of 1.43 is accompanied by a relatively high velocity at r/R of 0.8. The normal stress is already uniform at this location; also the tangential normal stress shows a uniform behaviour along the radius; this suggests a strong turbulent diffusion. The distributions of swirl velocity show a similar trend to the axial velocity except near to the pipe exit. It is clear that the value of the swirl velocity decreases at the downstream sections; this corresponds to the distribution of the axial mean velocity where its maxima is reaching the centre-line.

2.5 Summary and Conclusions

In this chapter, the measurements obtained in the confined double coaxial jet with and without swirl were presented and discussed. The measurements were concentrated for the mean velocities and normal stresses. The measurements of non-swirling jets were obtained for velocity ratios of 3.0 and 1.0 and those with swirl number of 0.23 for a velocity ratio 3.0. The results for no swirl were obtained by three different techniques and allowed an assessment of the accuracy of each technique in regions of low and high turbulence intensity and in reverse flow regions.

The measurements indicated discrepancies in the mean-velocity results between hot-wire and laser anemometers in the regions of high turbulence intensities. It was shown that these discrepancies are partly due to the rectification of the hot-wire to the negative velocities which leads to higher values of mean velocity, and partly to the bias towards higher values of mean velocity associated with the laser Doppler anemometer for which the signal processing was based on averaging of a number of individual frequency measurements. With respect to this later error, the different methods that deal with its correction were discussed; two methods were provided and evaluated. It was shown that this error increases with the turbulence intensity; it is less than 4% at 0.2 turbulence intensity and increases to a maximum value of about 20% at 0.90 turbulence intensities. The corresponding error in the normal stress is 13% at 0.9 turbulence intensity. It was also shown that the hot-wire anemometer underestimates normal stress in regions of high turbulence intensity; the hot-wire results are expected to be lower than the correct values by about 50% in the recirculation regions.

The results of this chapter showed that the jets of higher velocity ratio mix and decay more rapidly than those of $\overline{U}_a/\overline{U}_p = 1.0$ and results in steeper mean velocity gradients and large values of normal stress in the mixing region and immediately downstream of the recirculating flow; the corresponding intensities are also large. Comparison with previous results for unconfined flow indicated that the confinement leads to increased value of normal stress in the region downstream the mixing region; the flow properties in the mixing region are not greatly influenced by the confinement.

Interpolation between measured mean velocity profiles indicates that the length of the recirculation zone is approximately

3.28 D_e for the higher velocity ratio and 2.96 D_e for the lower velocity ratio. The presence of this recirculation emphasises the need for a calculation method based on elliptic equations.

The results, with swirl, indicate a region of near-recirculation on the centre-line and between one and three furnace diameters down-stream of the exit plane. Thus as the swirl number is increased from zero, the tendency towards recirculation grows and will ultimately be realised as shown for example by Baker et al (1974) with a swirl number of 0.52. It was shown also that the mixing of the two jets was greatly increased by imparting the swirl; the maxima of the normal stresses were shifted towards the inlet section of the enclosure.

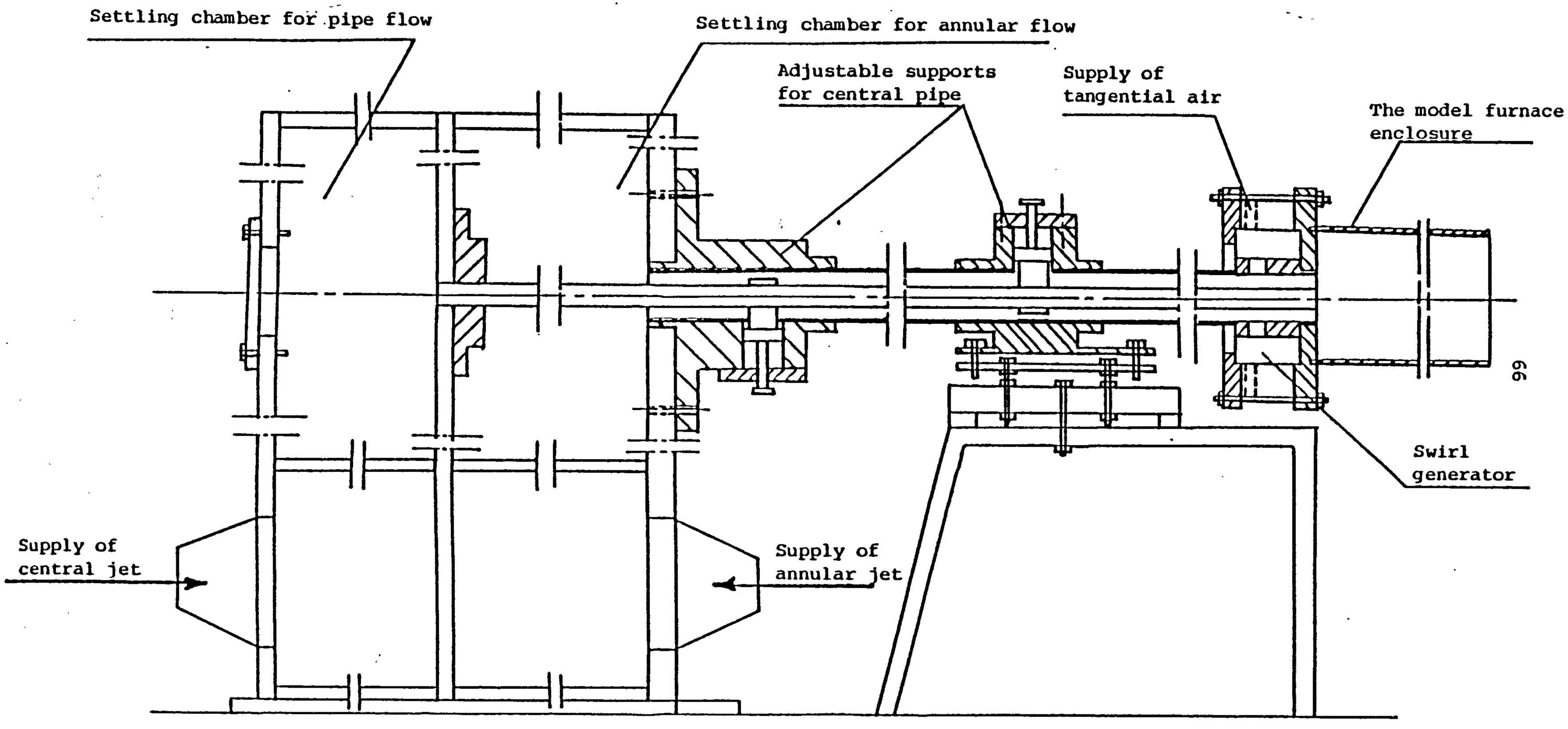
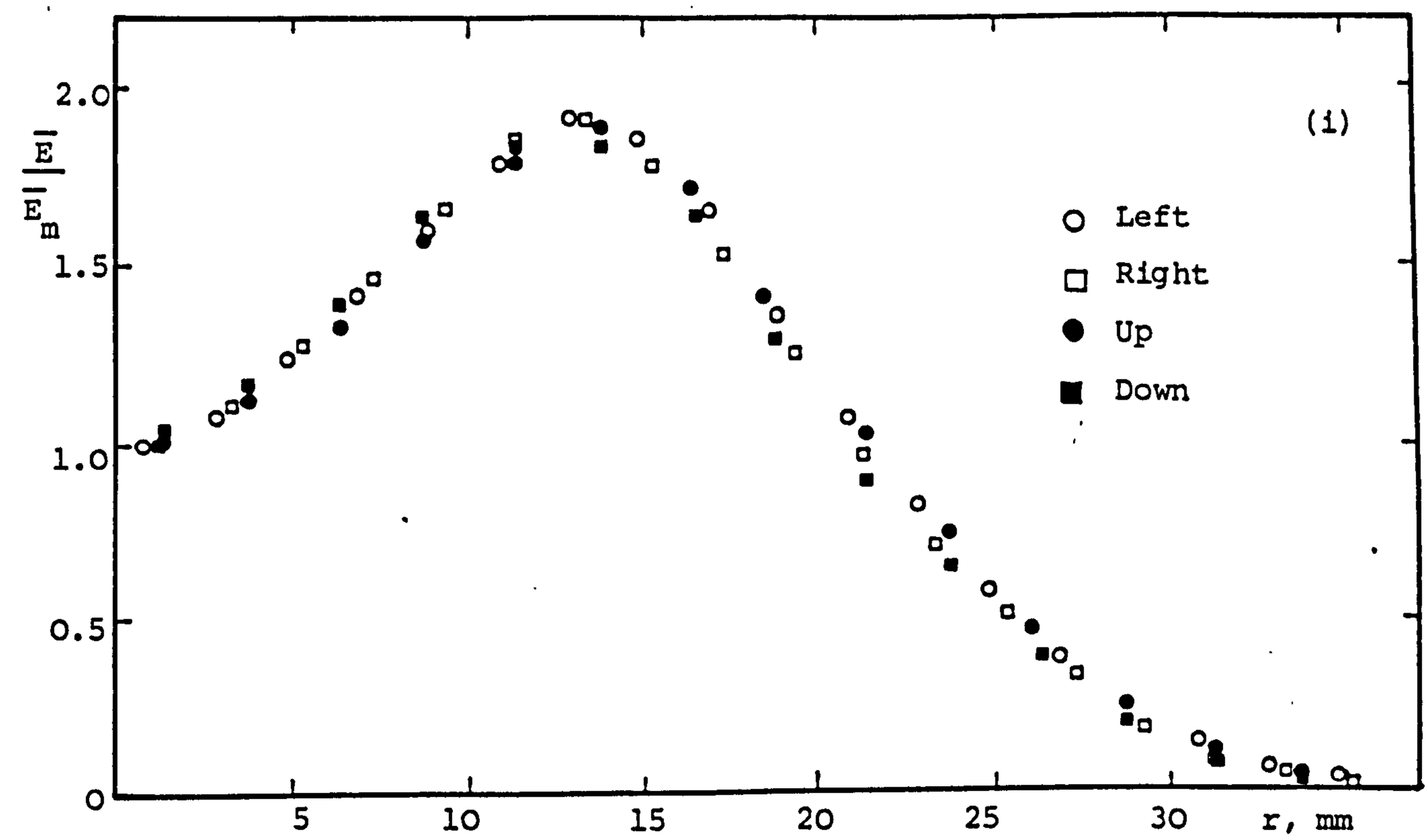


Fig. 2.1 Layout of Apparatus for Confined Double Coaxial Jet



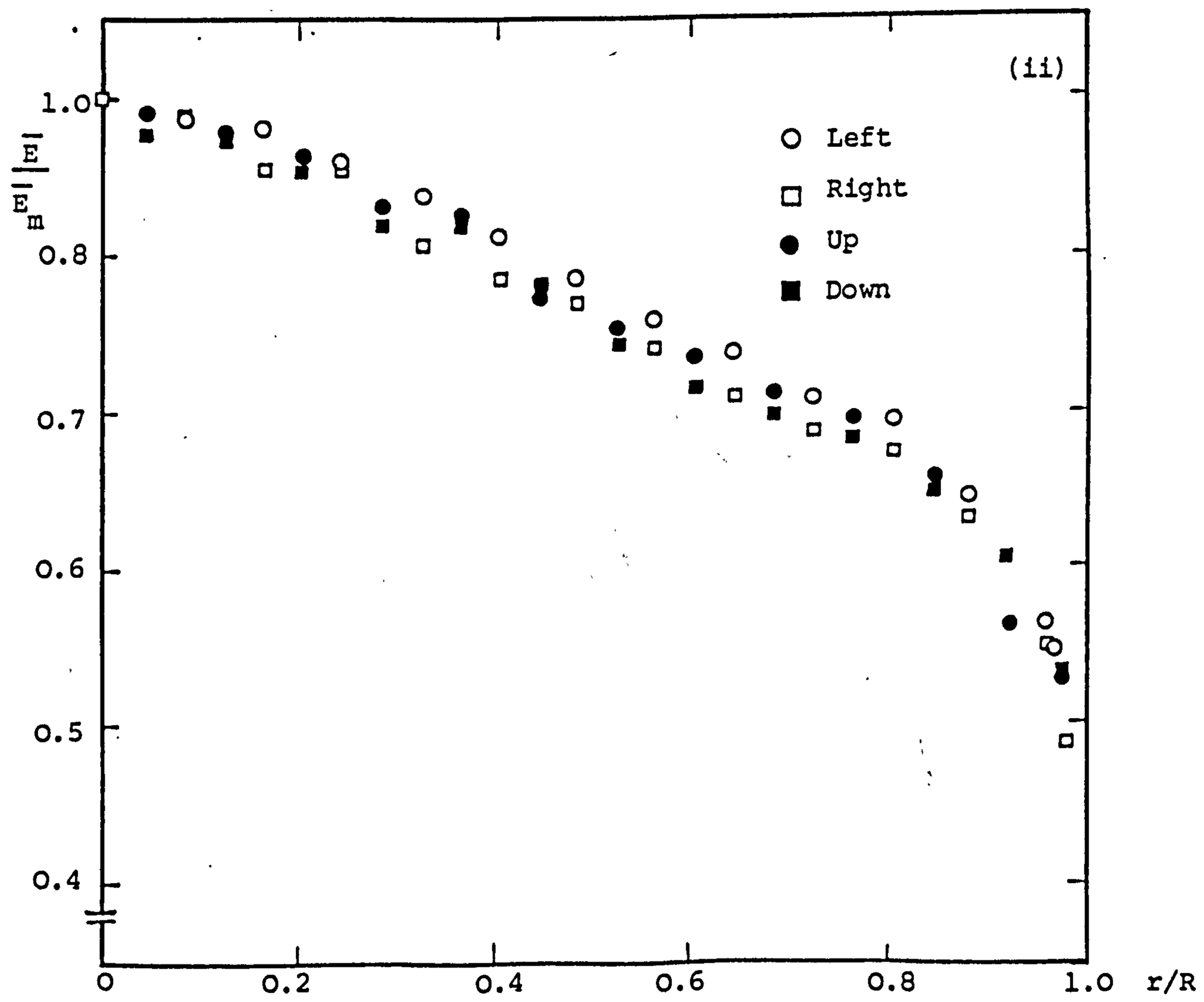
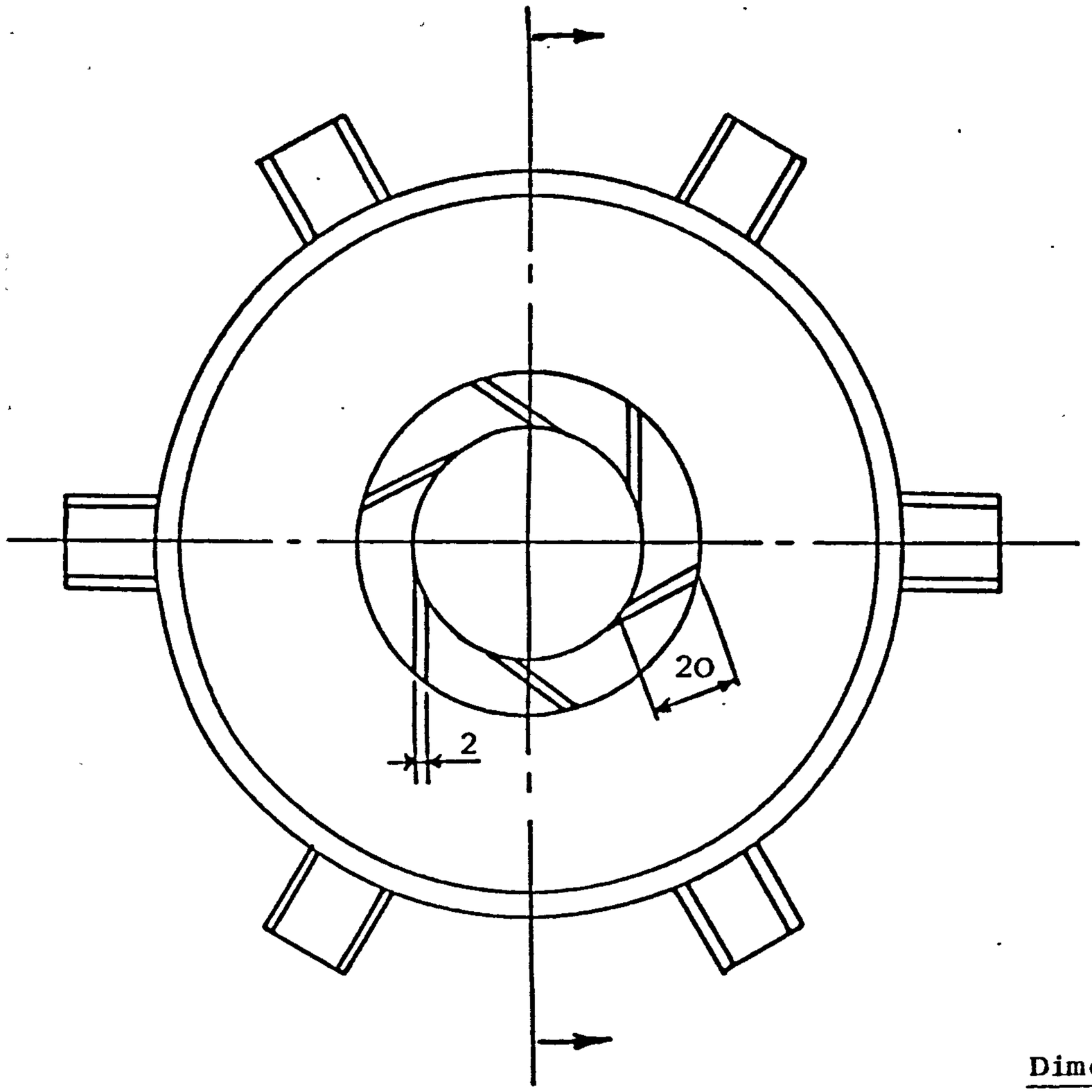
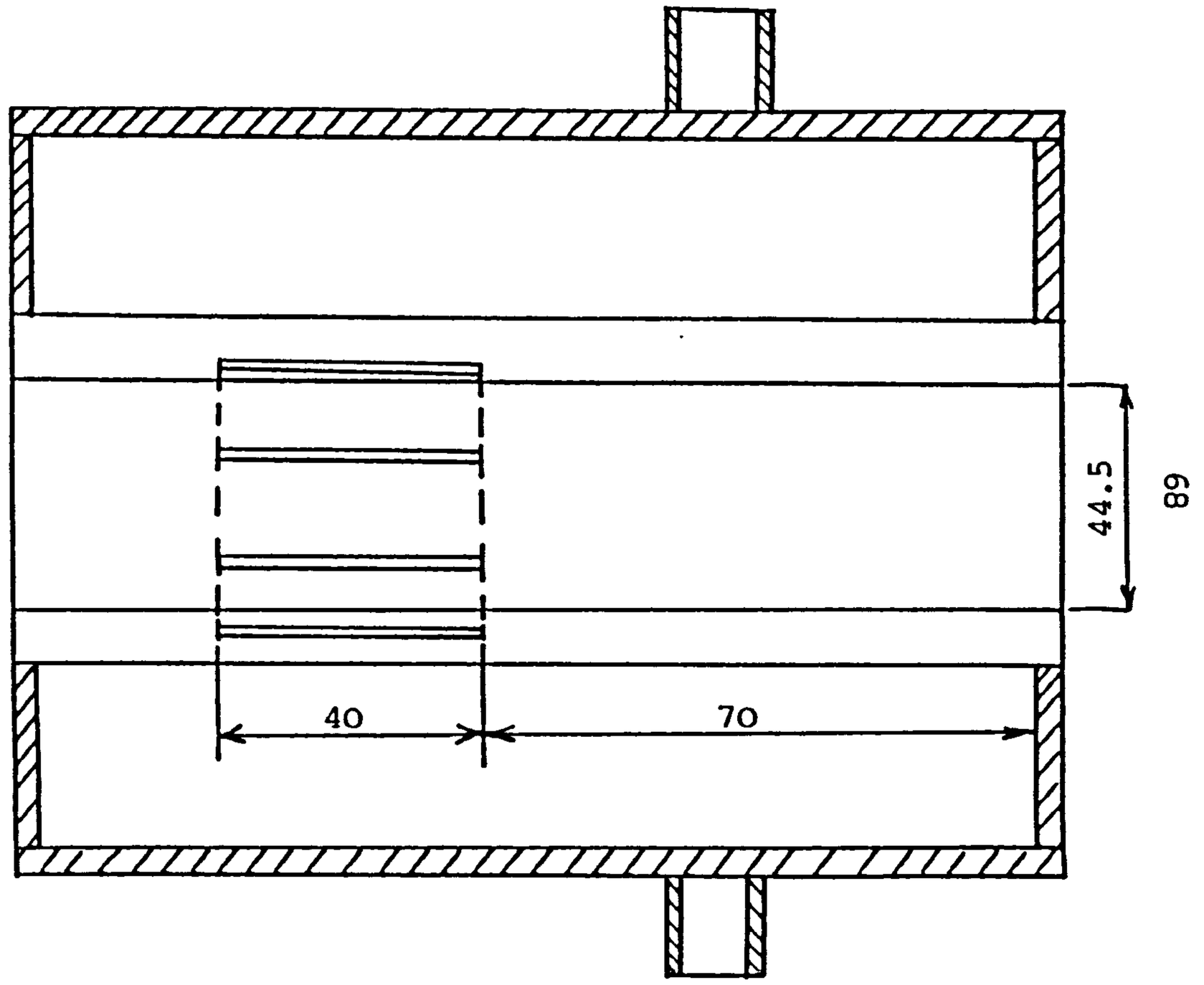


Fig. 2.2 Symmetry Check: Measurements of Mean Values with Normal Hot-Wire along four Radii in Two Perpendicular Planes. (i) At the Outlet of the Coaxial Pipes Without Confinement ($X/d_o \simeq 2$); (ii) At the Outlet of the Confining Tube ($X/D_e \simeq 4.6$)





Dimensions in mm.

Fig. 2.3 Swirl Generator

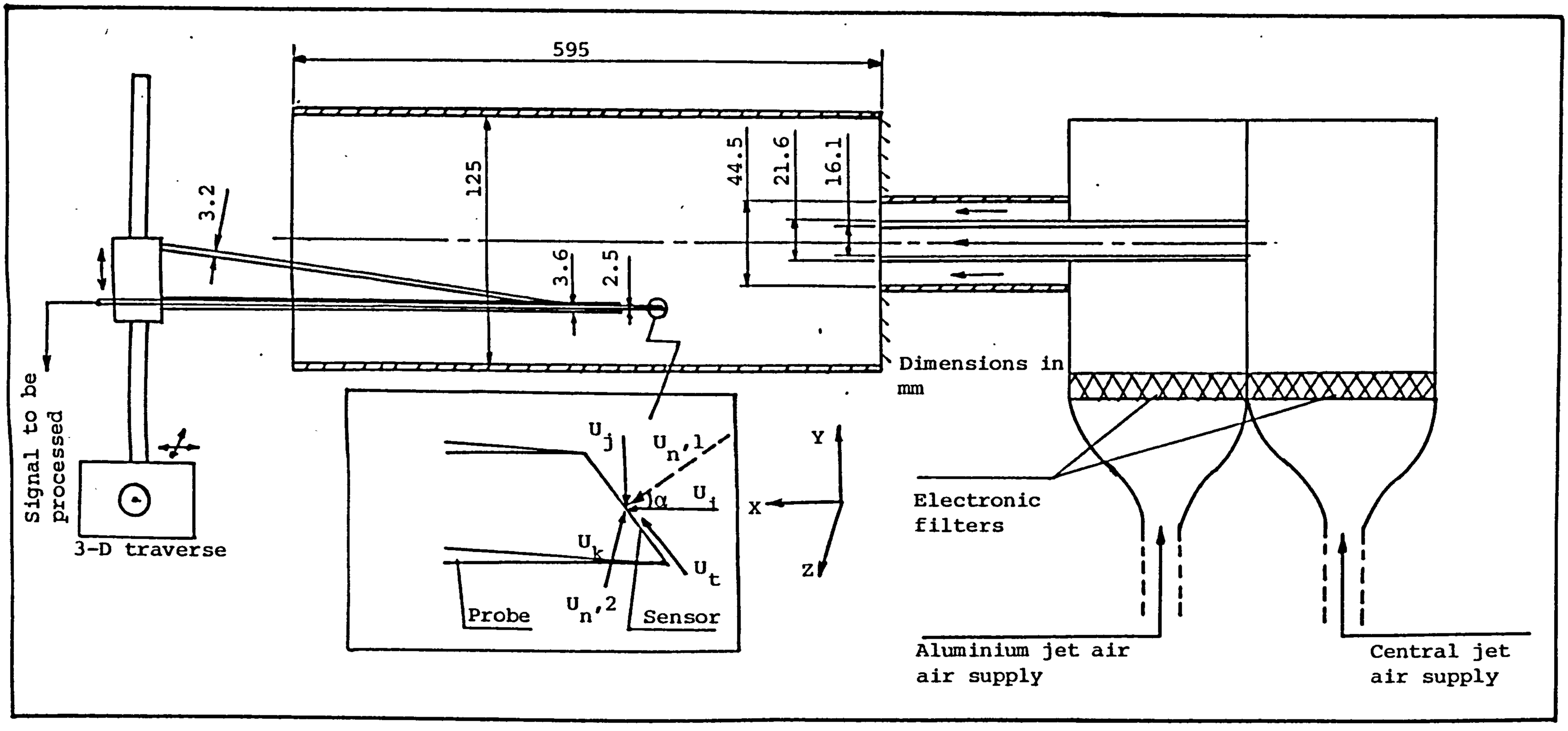


Fig. 2.4 Model for the Confined Flow Measurements Using Hot-Wire Anemometer

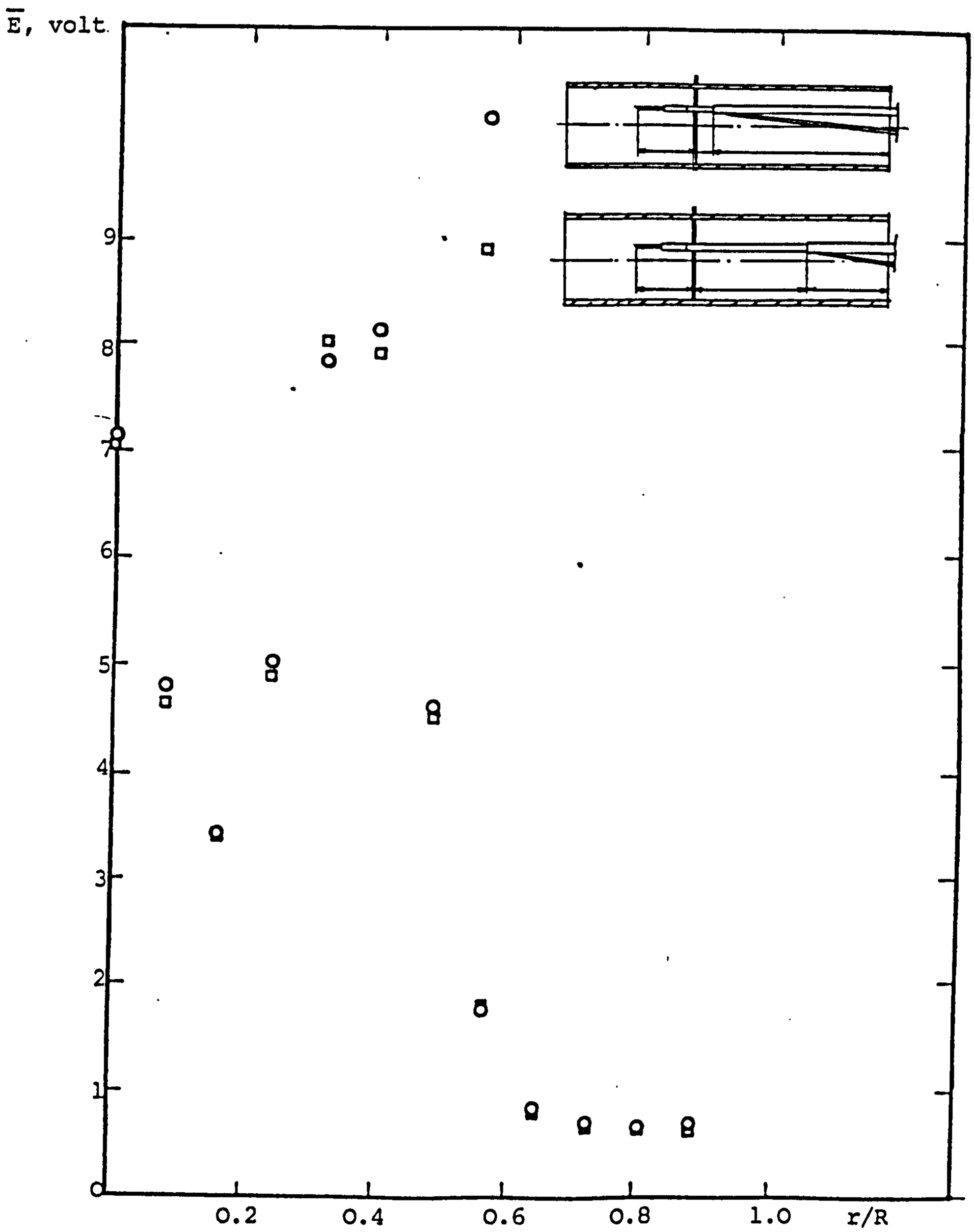


Fig. 2.5 Influence of the Welded Wire Structure on the Readings of the Mean Value; o , The Welded Wire Structure in Near From the Point of Measurement; □ , The Welded Wire Structure is Away From the Point of Measurement.

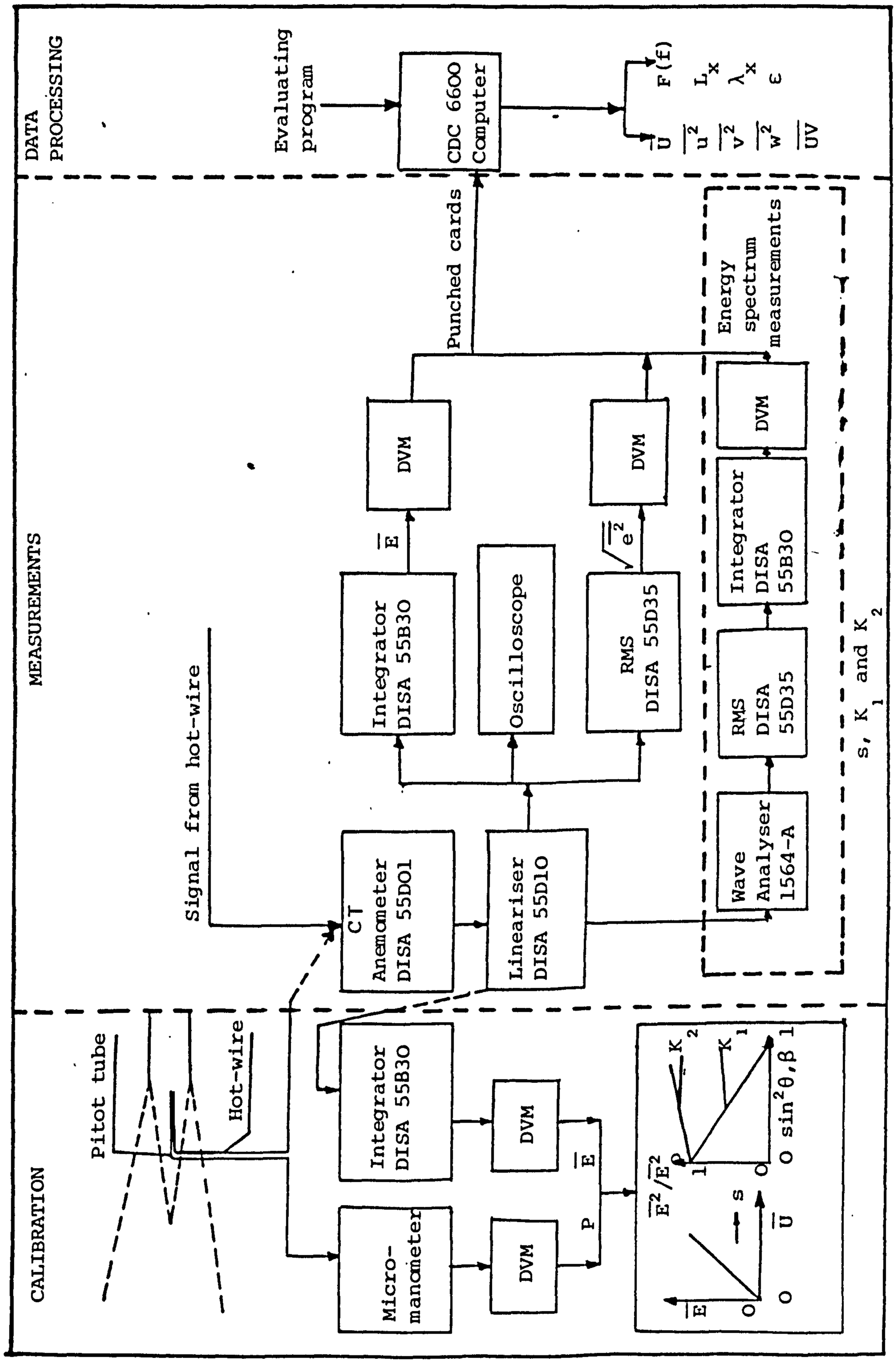
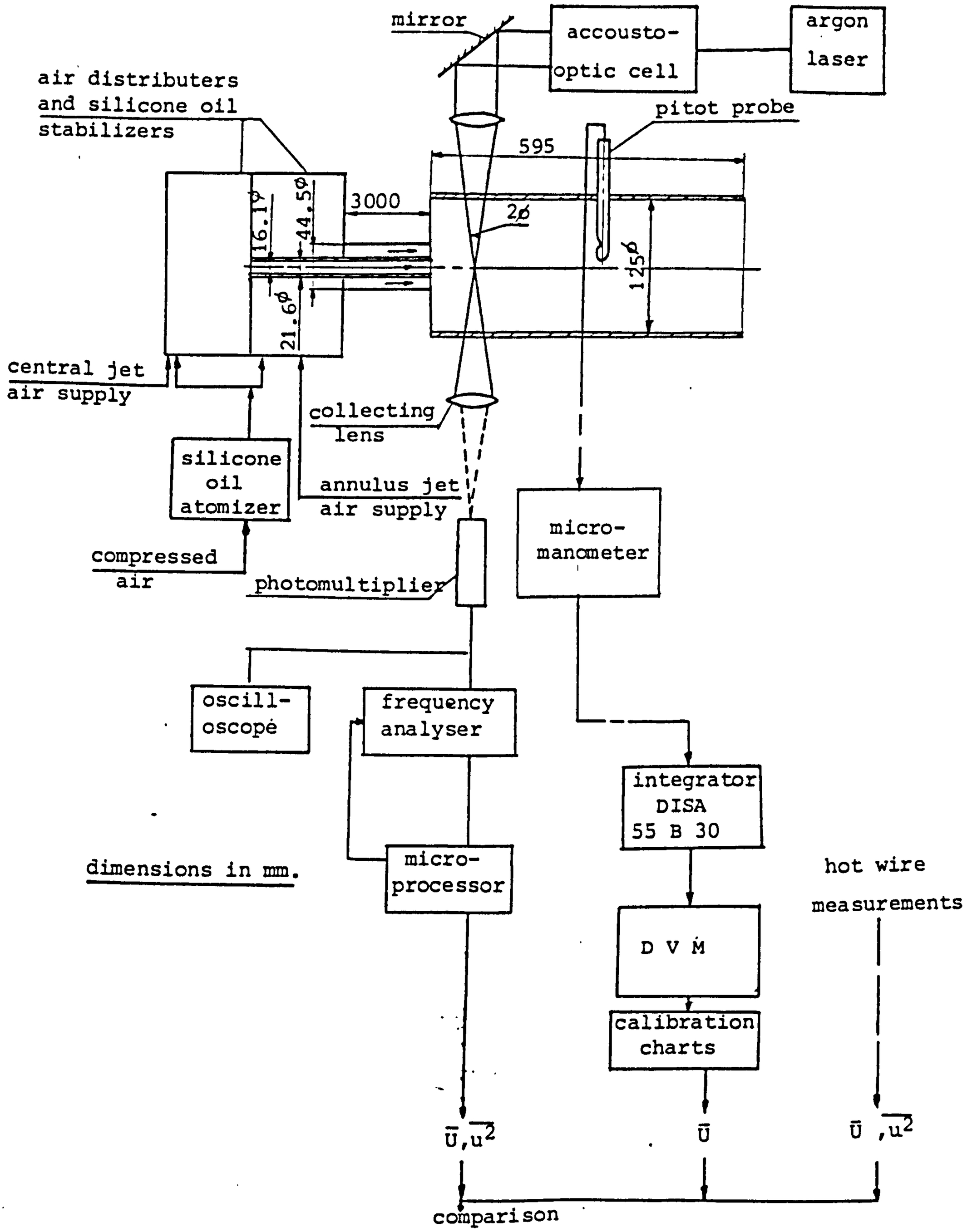


Fig. 2.6 Instrumentation and Data Processing of the Hot-Wire Technique



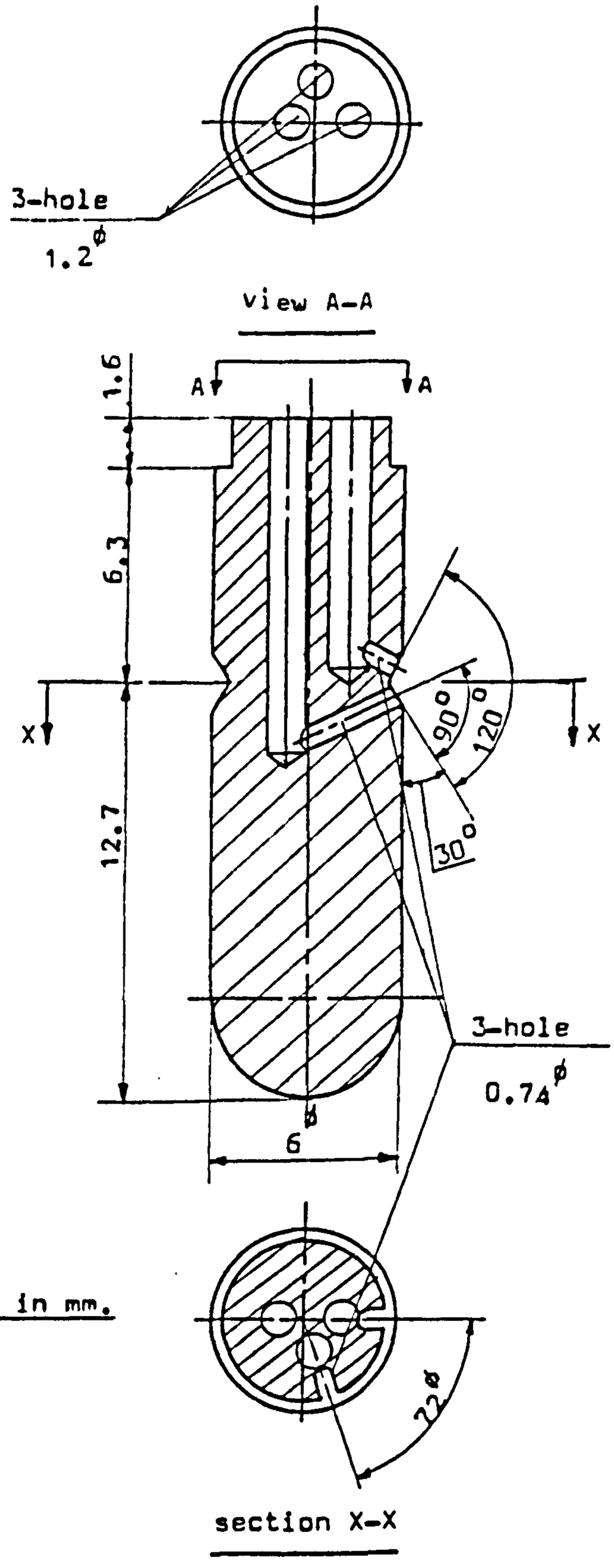
dimensions in mm.

Fig. 2.7 Layout of the Measurement Techniques;

———— Laser-Doppler Anemometry

—— —— Hot-Wire Anemometry

————- Pitot Tube.



dimensions in mm.

section X-X

Fig 2.8 3-Hole Pressure Probe.

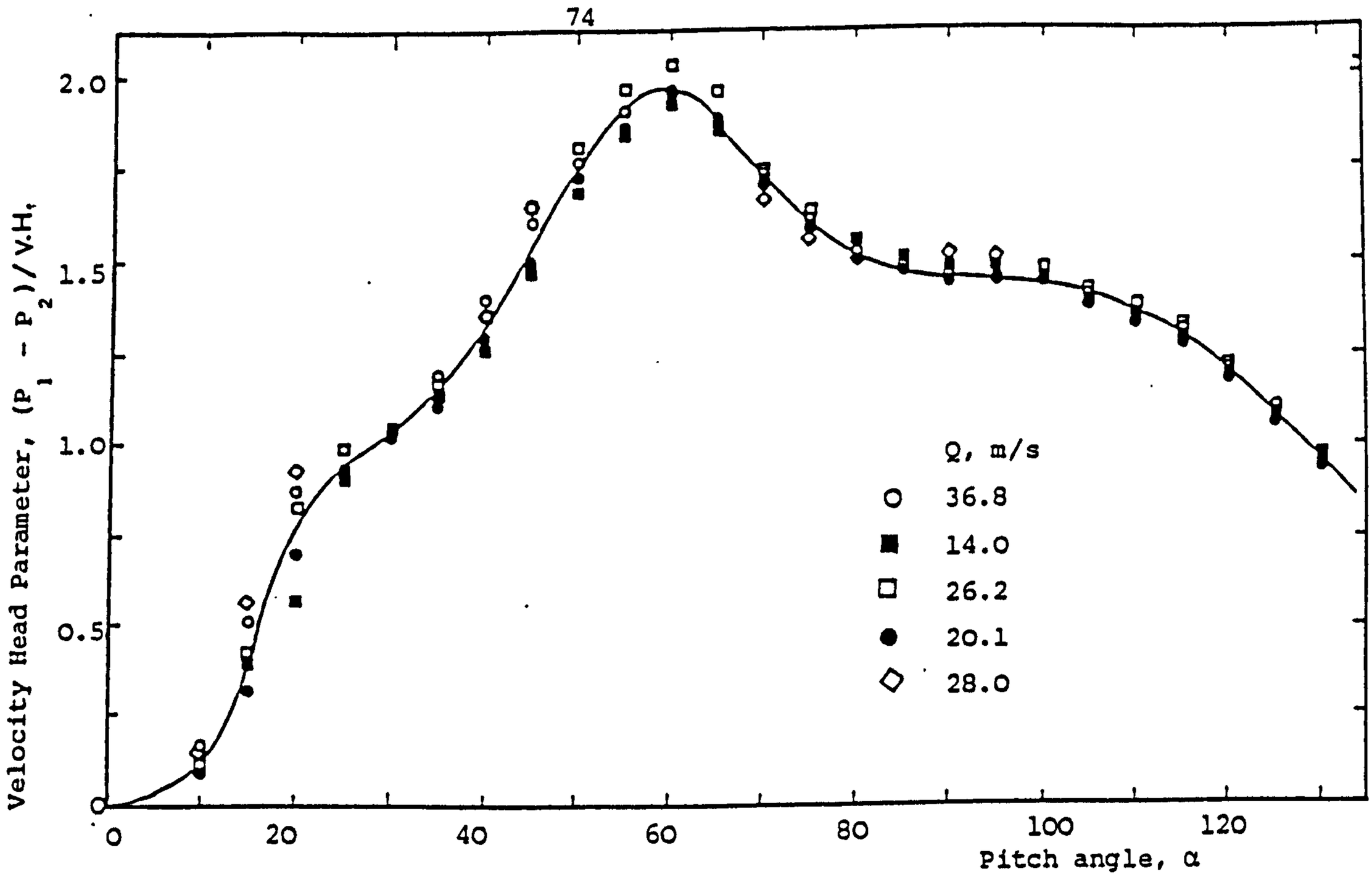


Fig. 2.9 Pitot Tube Calibration

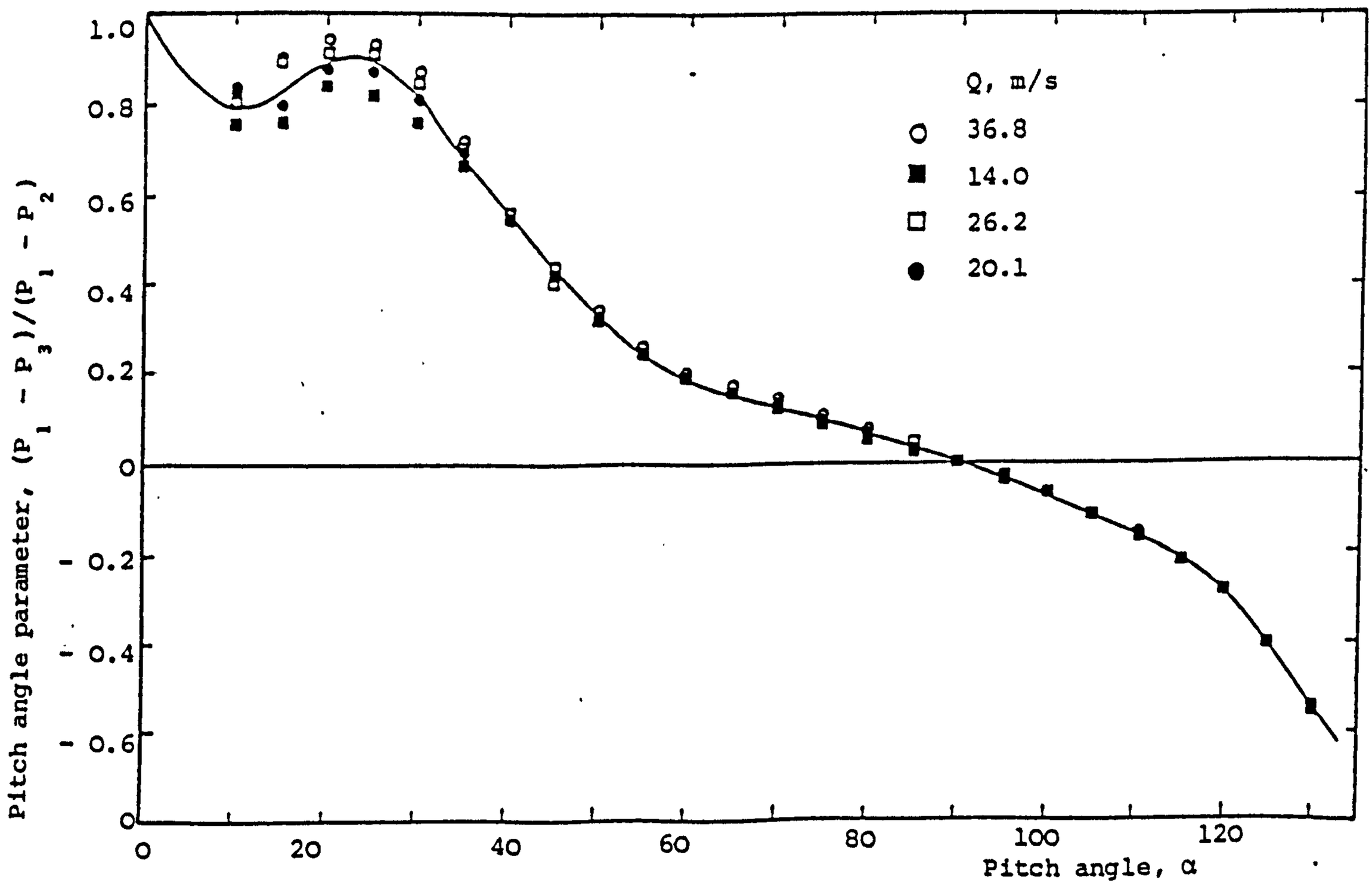


Fig. 2.9 (Continued)

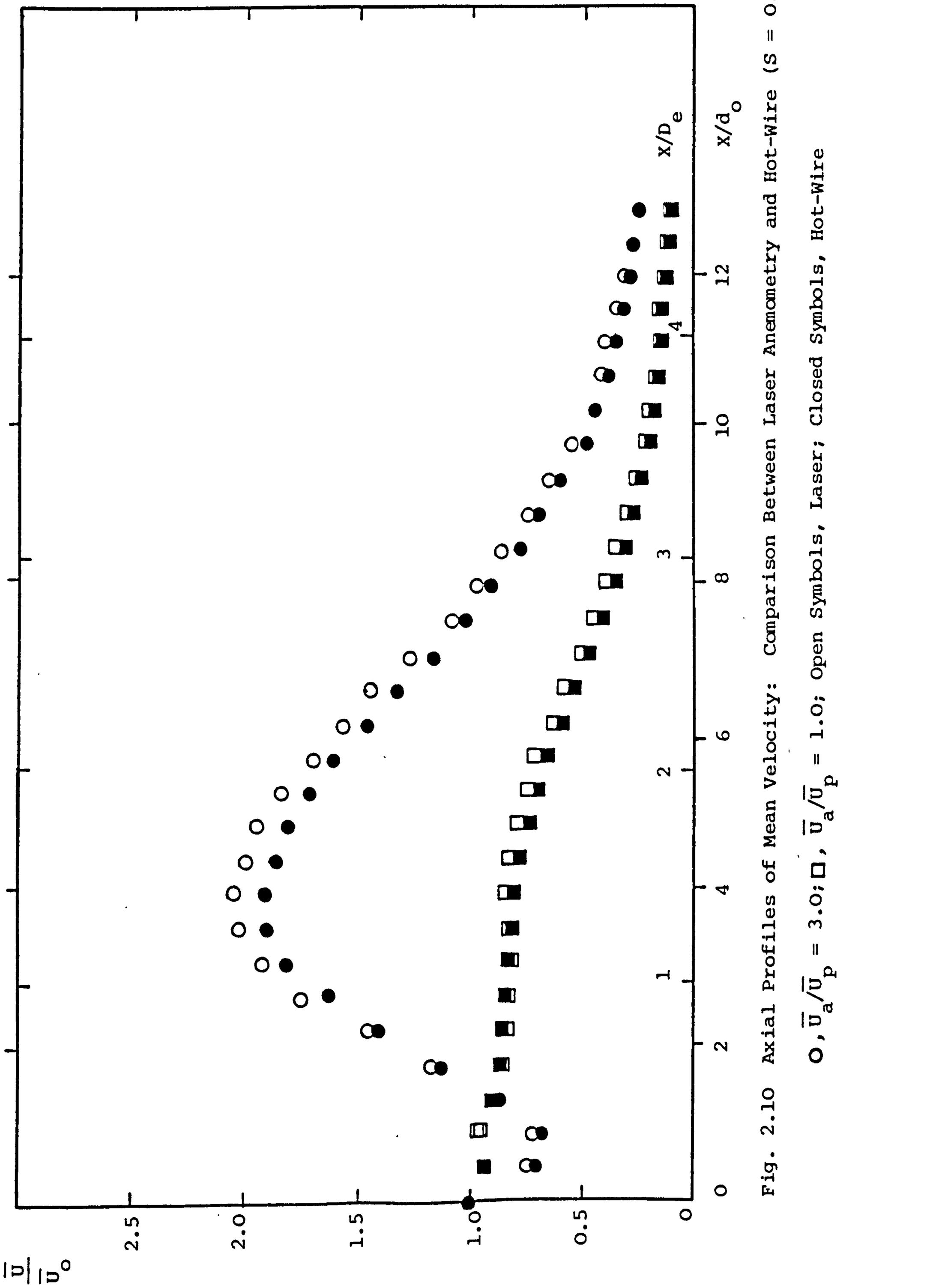


Fig. 2.10 Axial Profiles of Mean Velocity: Comparison Between Laser Anemometry and Hot-Wire (S = 0.0). O, ●, Hot-Wire; ○, ●, Laser; Closed Symbols, Hot-Wire; Open Symbols, Laser; ○, $\bar{U}_a/\bar{U}_p$ = 3.0; □, $\bar{U}_a/\bar{U}_p$ = 1.0; ■, $\bar{U}_a/\bar{U}_p$ = 0.

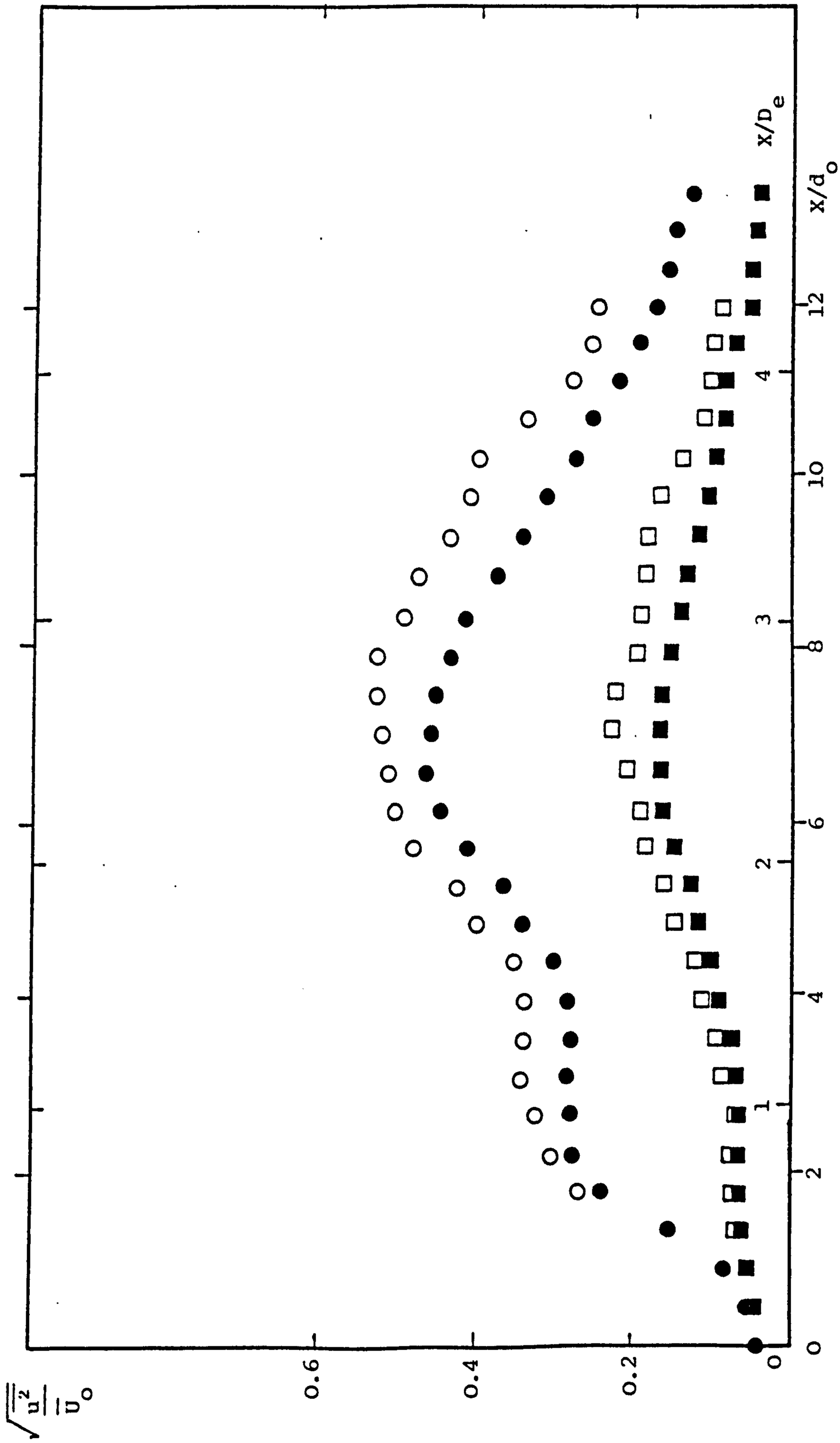


Fig. 2.11 Axial Profiles of Normal Stress: Comparison Between Laser Anemometry and Hot-Wire ($S = 0.0$); Notation as in Fig. 2.10

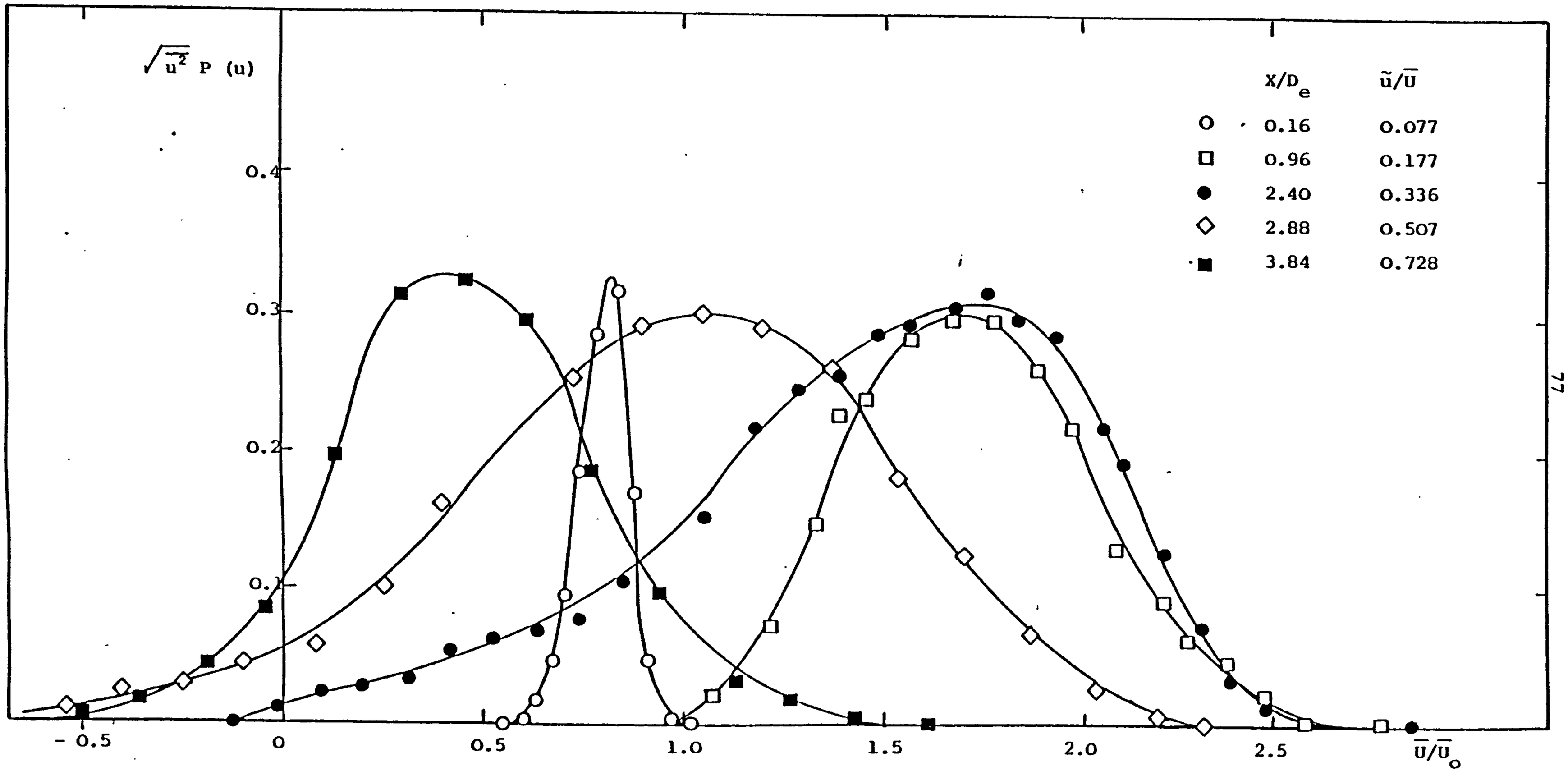


Fig. 2.12 Probability Distributions at Various Locations of Different Turbulence Intensities (the Increase of the Directional Intermittency with the Turbulence Intensity)

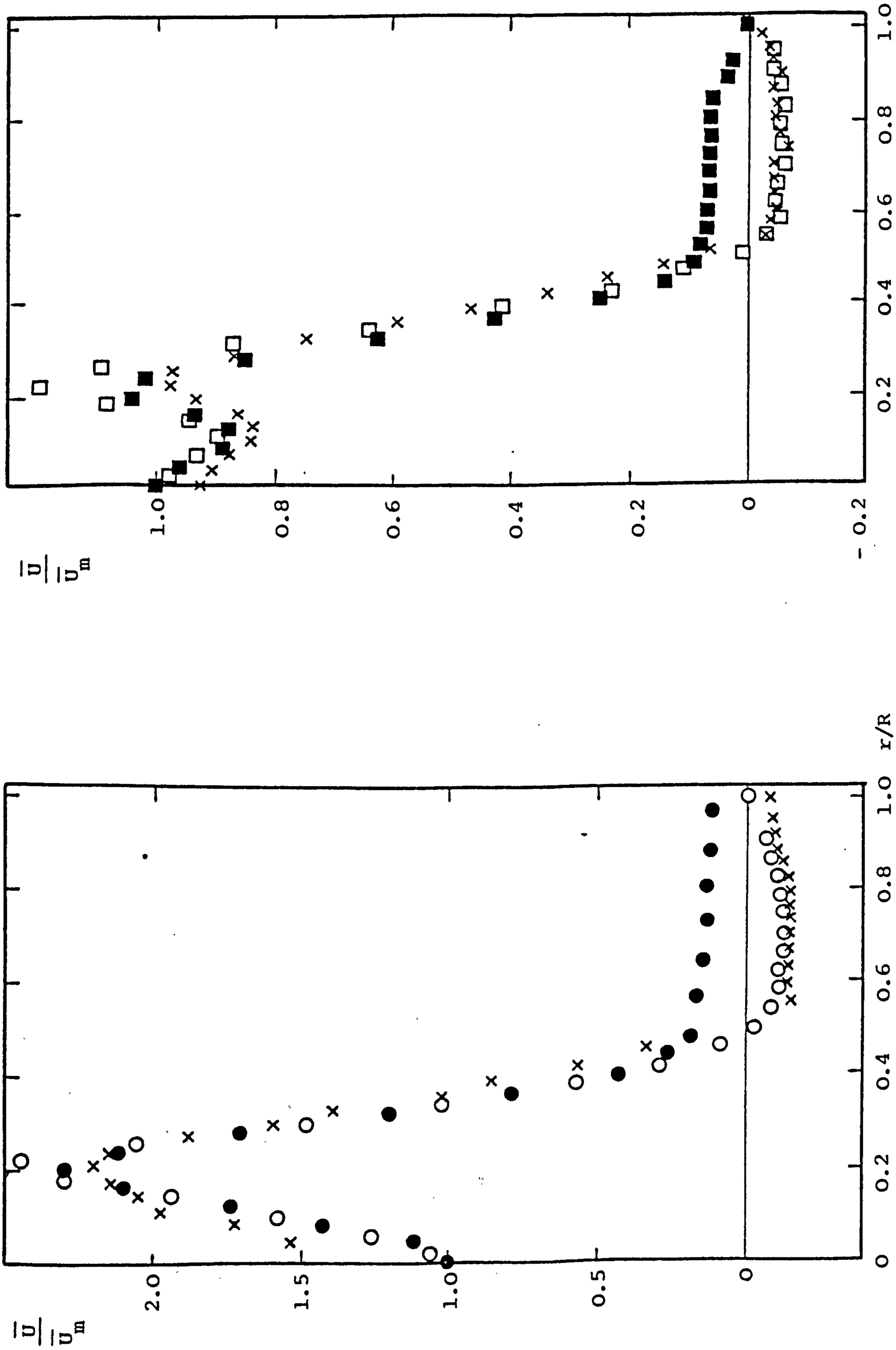


Fig. 2.10 Comparison Between Laser Anemometry, Hot-Wire and Pitot Tube; ■, □, ●, ○, Laser Anemometry; x, Pitot Tube; Otherwise as in Fig. 2.10

Fig. 2.13 Radial Profiles of Mean Velocity: Pitot Tube (S = 0.0, X/D_e = 0.616)

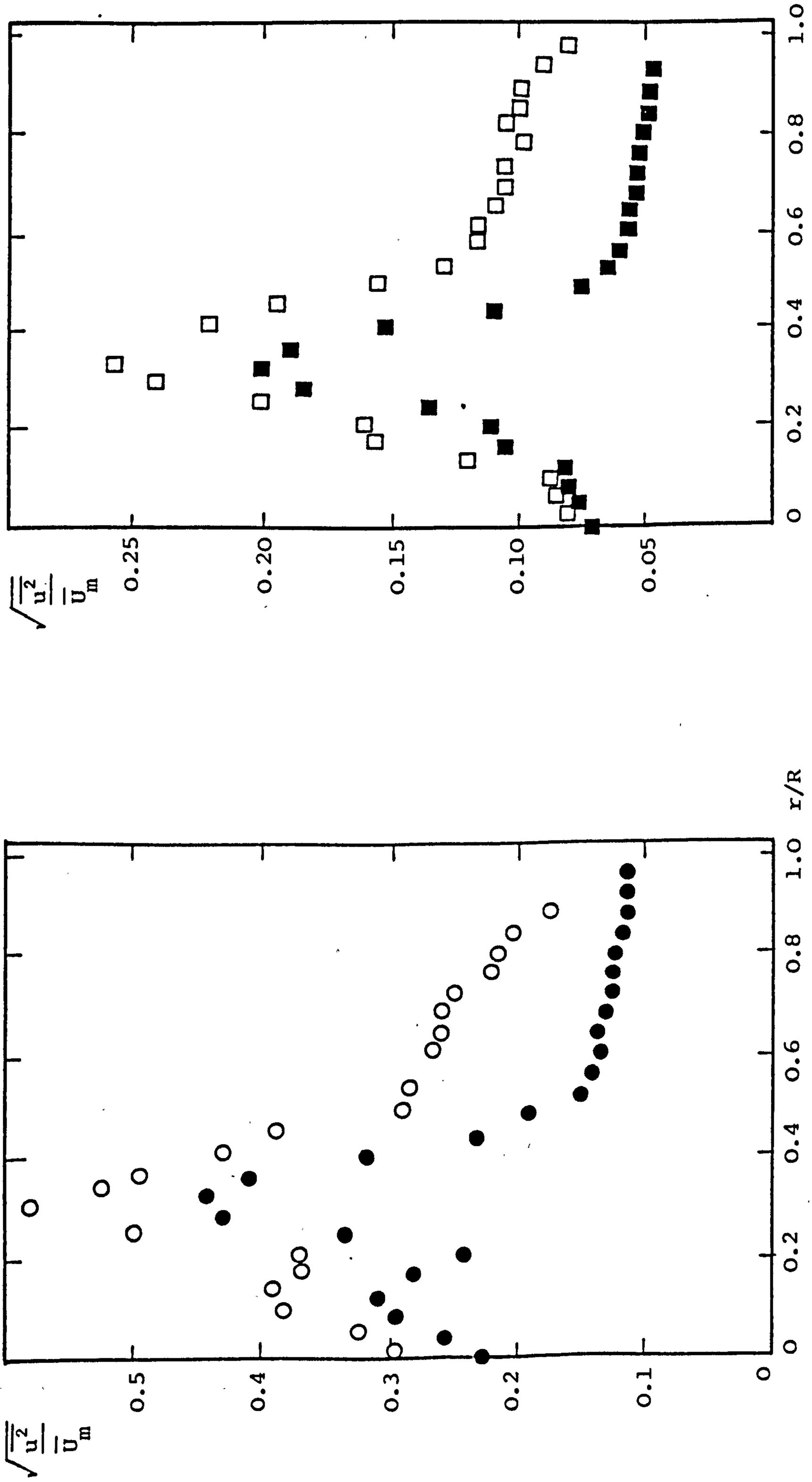


Fig. 2.13 Comparison Between Laser Anemometry and Hot-Wire Results: Comparison Between Laser Anemometry and Hot-Wire Results in Fig. 2.10

Fig. 2.14 Radial Profiles of Axial Normal Stress ($S = 0.0$, $X/D_e = 0.616$); Notation as in Fig. 2.10

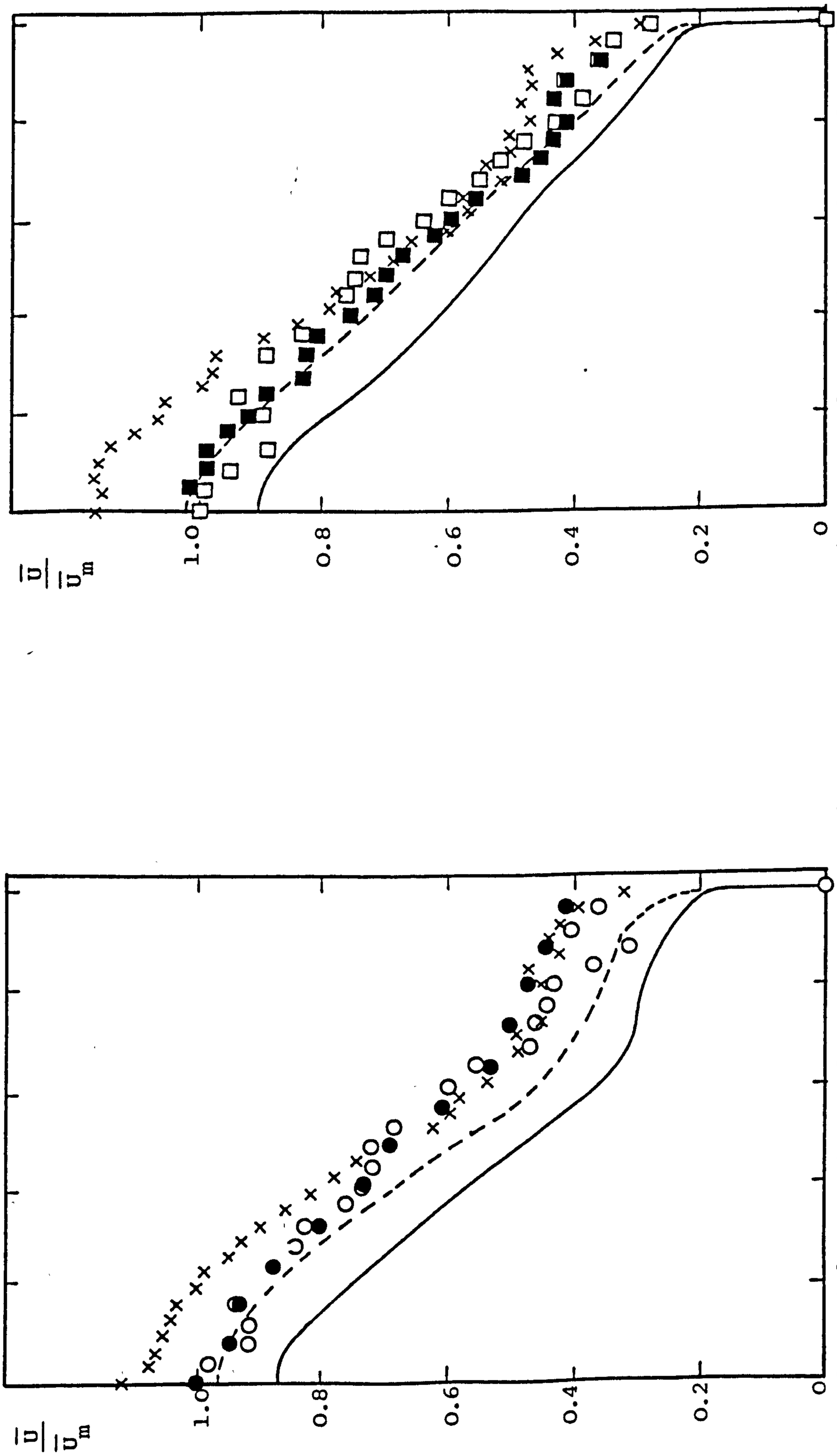


Fig. 2.15 Radial Profiles of Mean Velocity: Comparison Between Laser Anemometry, Hot-Wire and Pitot Tube
(S = 0.0, X/D_e = 3.67); x, Pitot Tube; Otherwise as in Fig. 2.10

- - - - - -, Pitot Tube results corrected according to Equation (2.19) β = 1

———, Pitot Tube results corrected according to Equation (2.18)

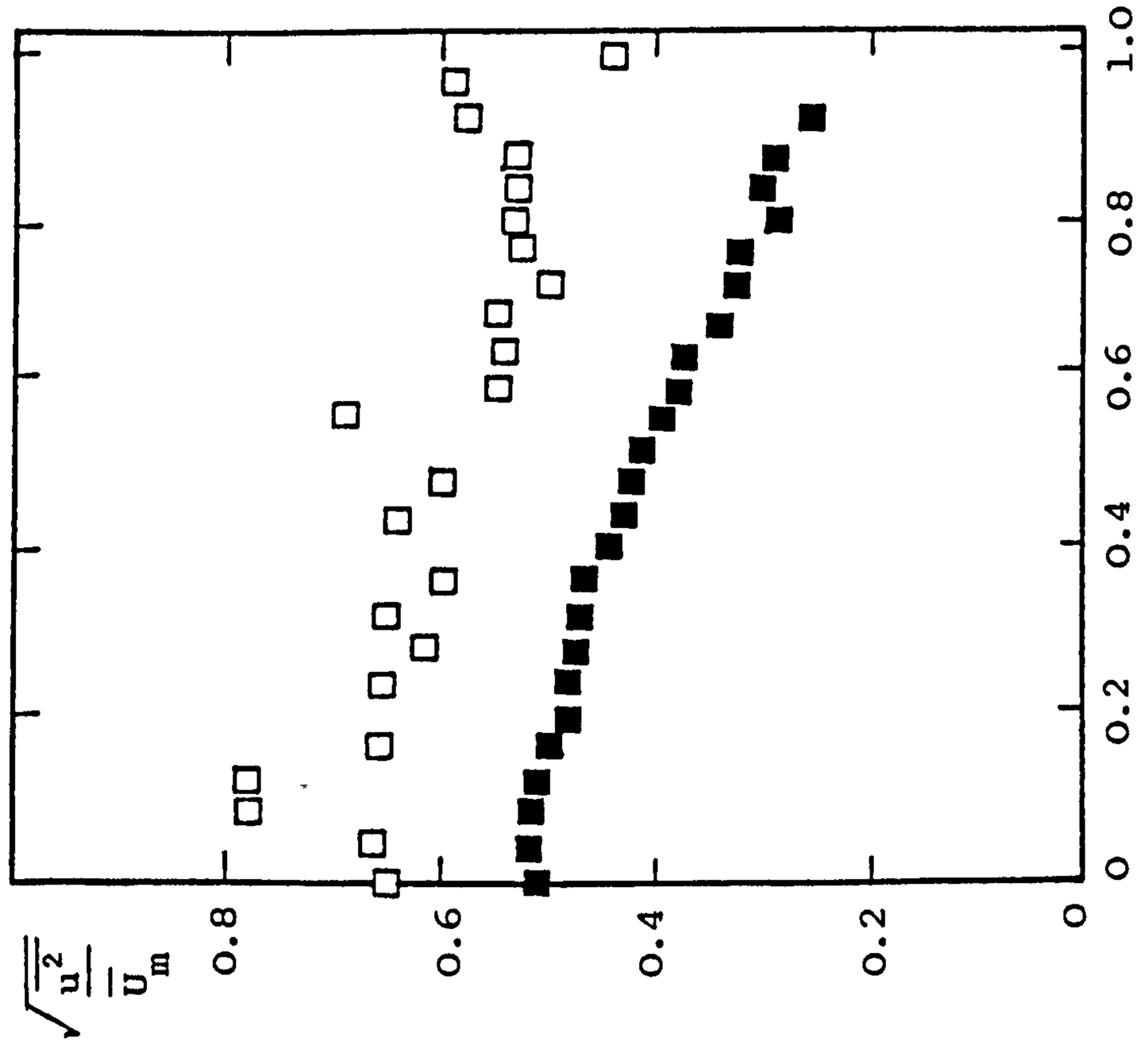


Fig. 2.15: Comparison Between Laser Anemometry and Hot-Wire Measurements; Notation as in Fig. 2.10

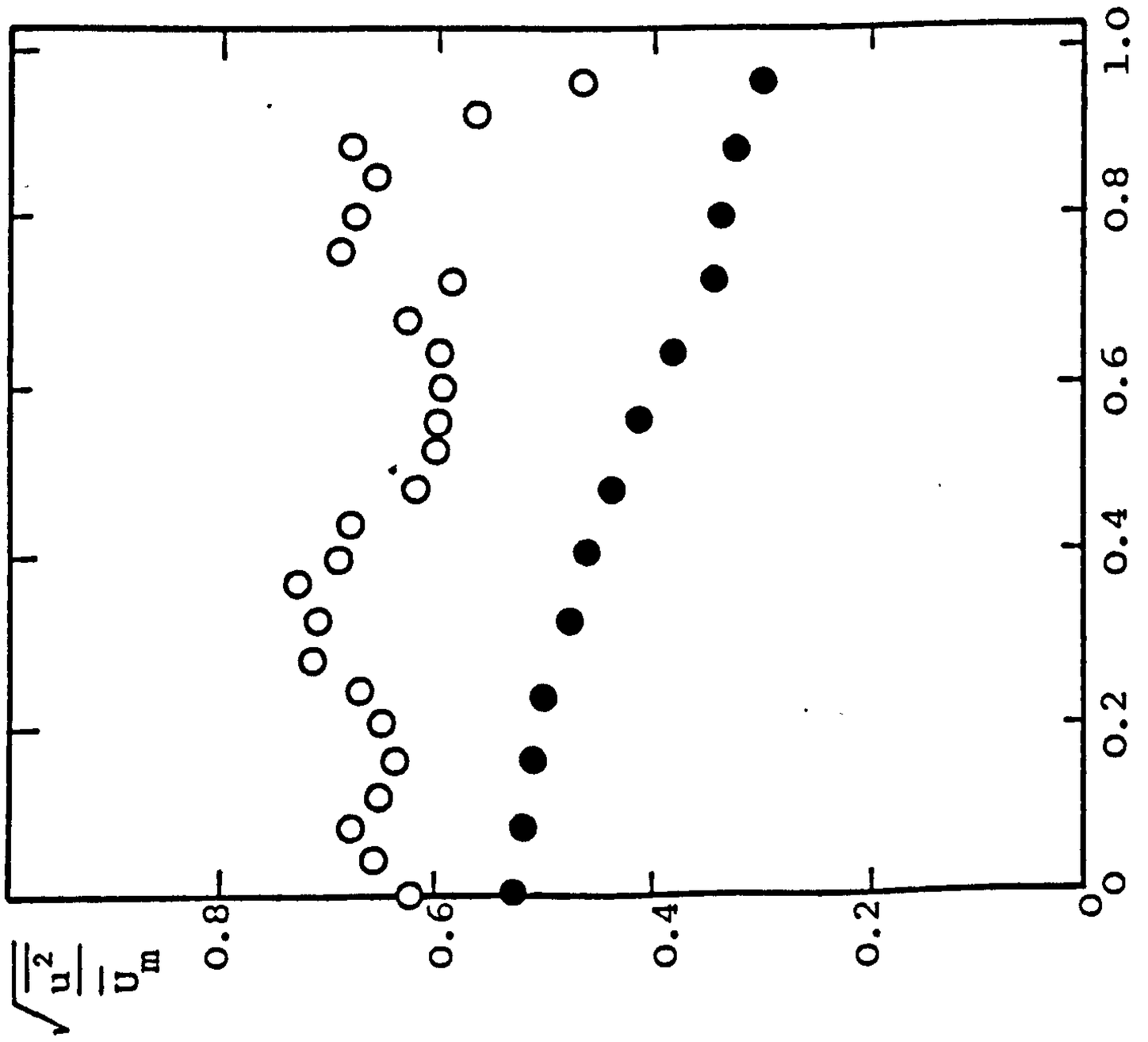


Fig. 2.16 Radial Profiles of Axial Normal Stress ($S = 0.0$; $X/D_e = 3.67$); Notation as in Fig. 2.10

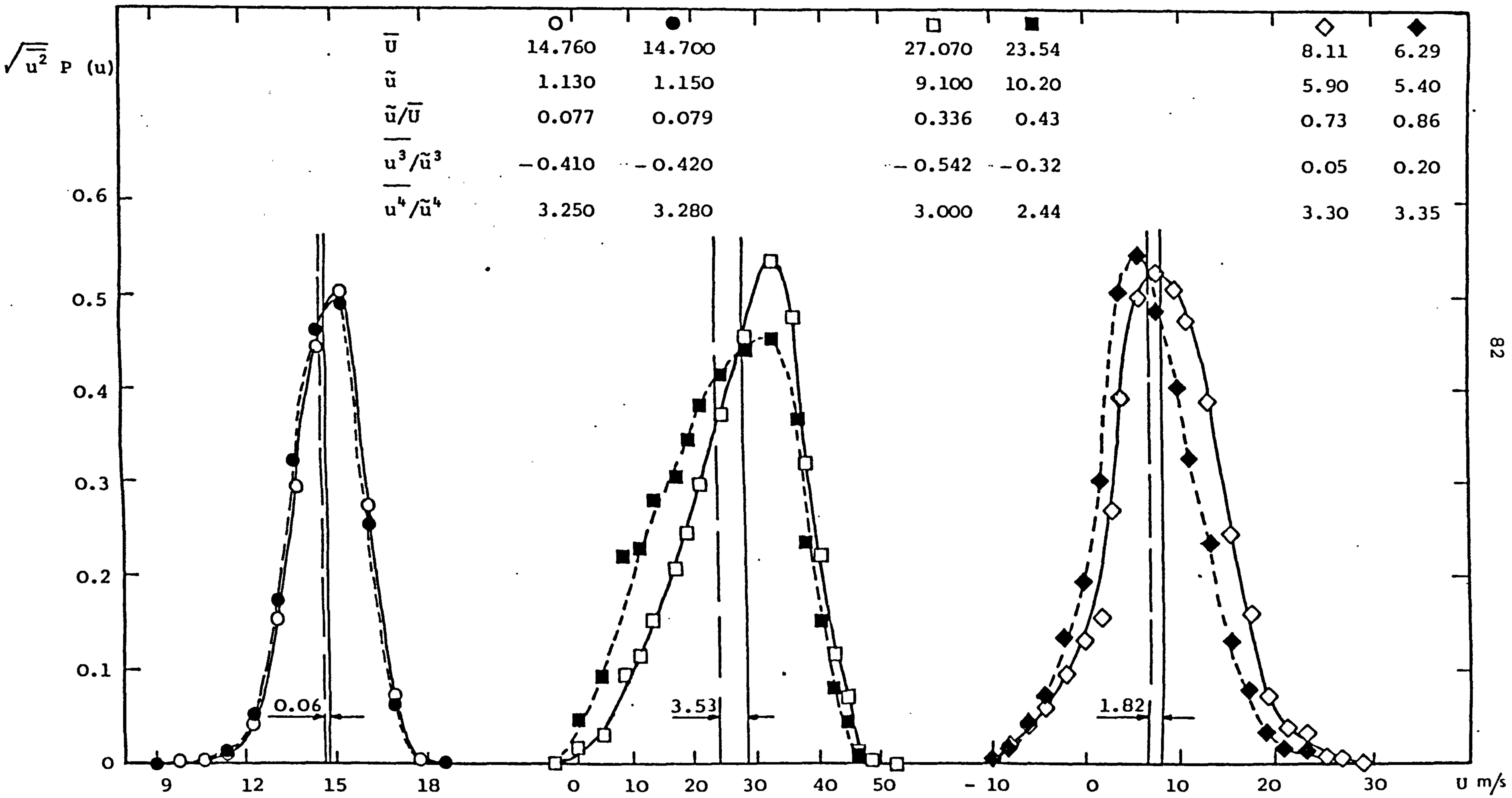


Fig. 2.17 Measured and Corrected Probability Density Distributions; Open Symbols, Measured Distributions; Solid Symbols, Corrected Distributions

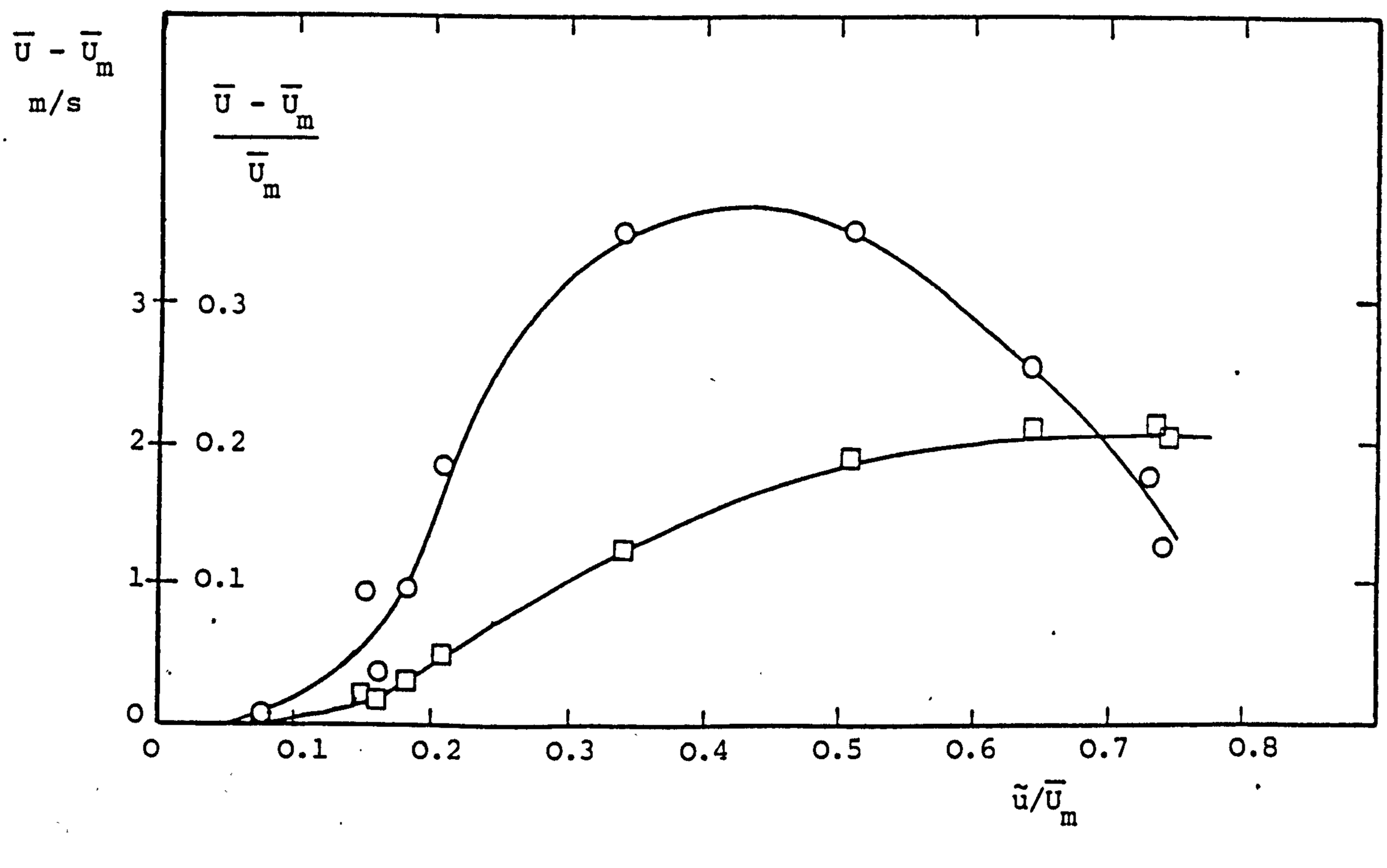
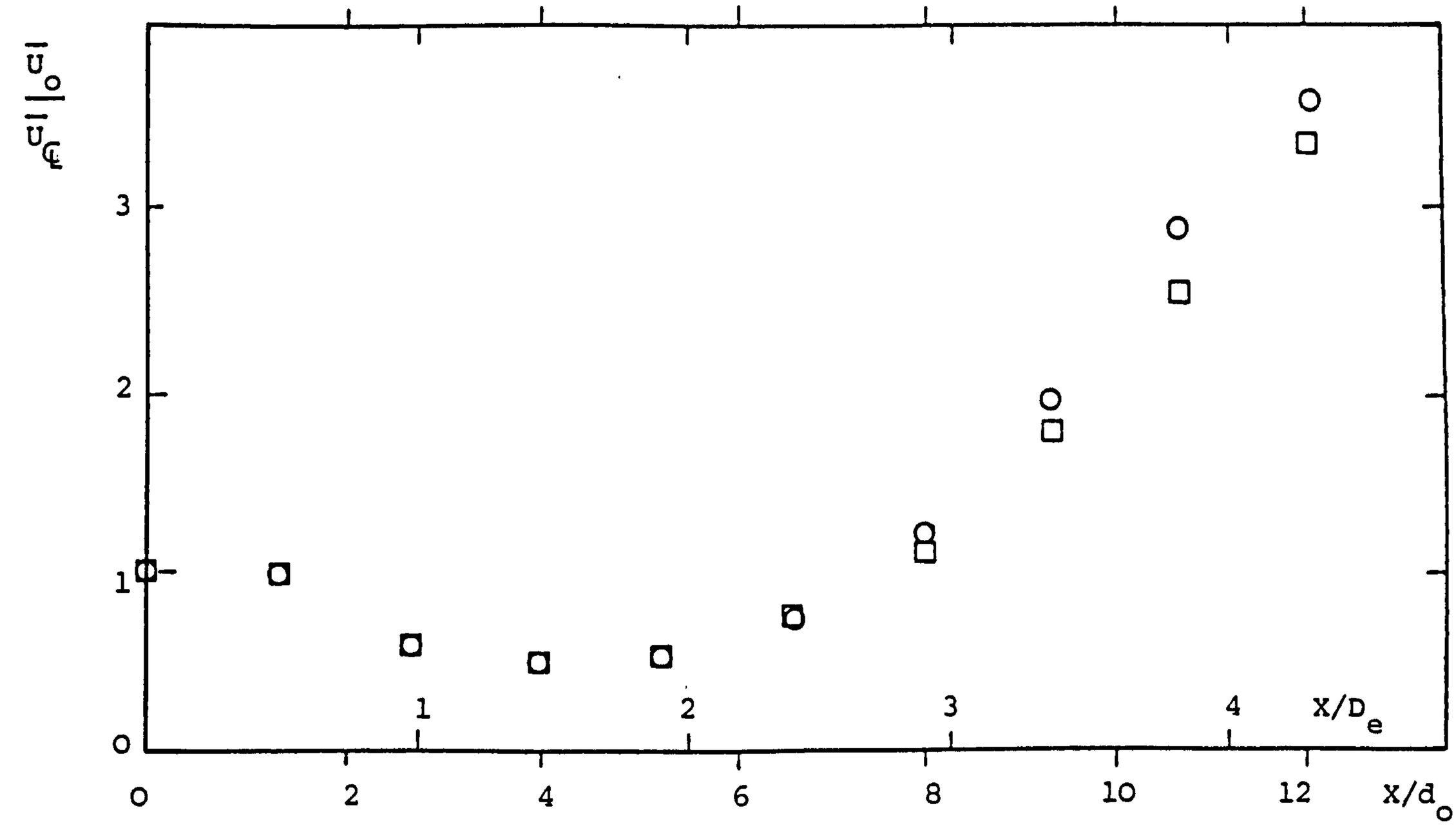


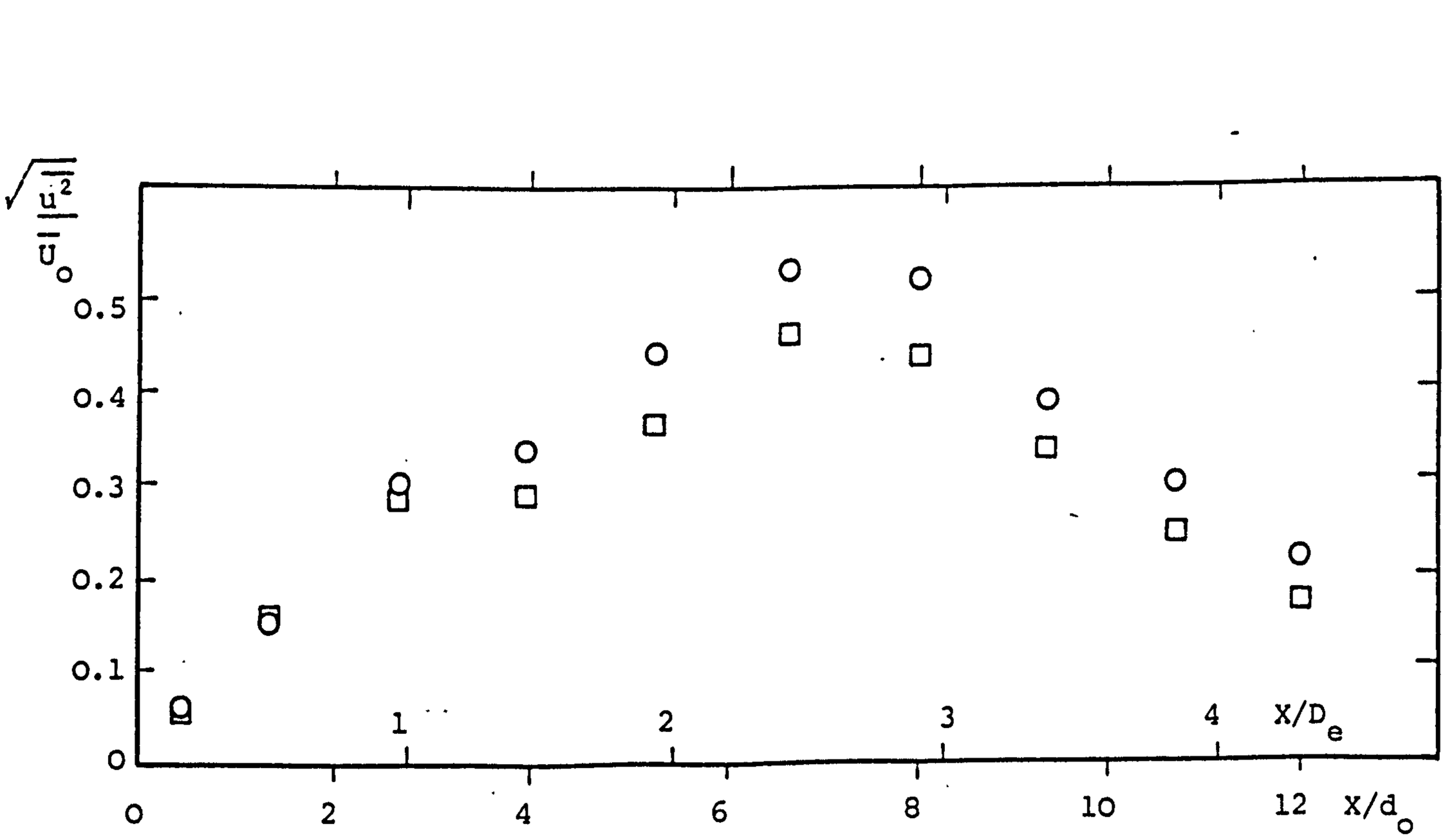
Fig. 2.18 Effect of Turbulence Intensity on the Magnitude of the Error Correction

○, $\overline{U} - \overline{U}_m$

□, $(\overline{U} - \overline{U}_m)/\overline{U}_m$



(i)



(ii)

Fig. 2.19 Axial Profiles (S = 0.0, $\overline{U}_a/\overline{U}_p$ = 3.0)

O , Corrected Laser results ; □ , Hot-Wire results

(i) Axial Mean Velocity ; (ii) Axial Normal Stress

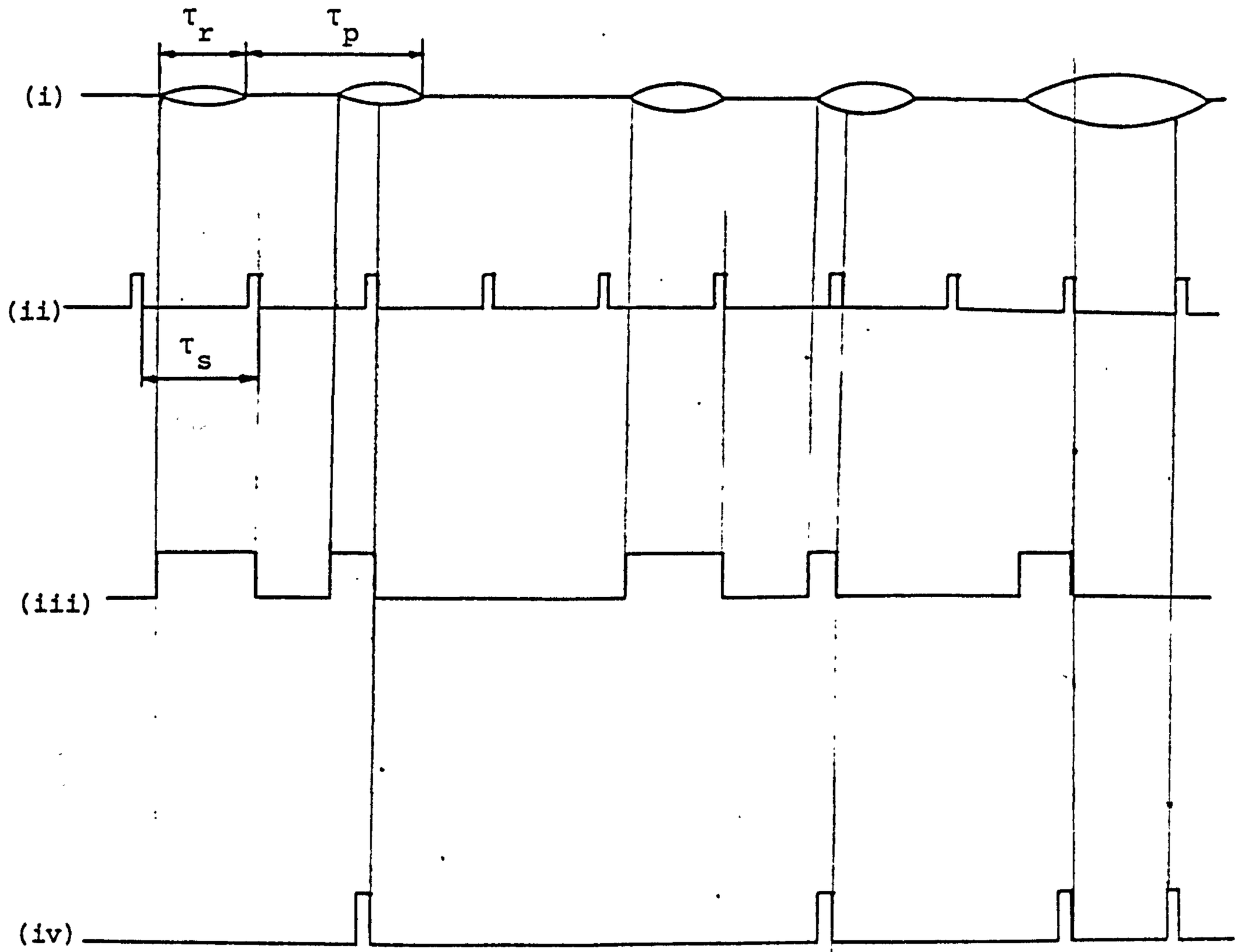


Fig. 2.20 Schemes of Sampling Procedure

(i) Arbitrary Number of Bursts
(ii) Microprocessor Sampling Rate
(iii) Method 1
(iv) Method 2

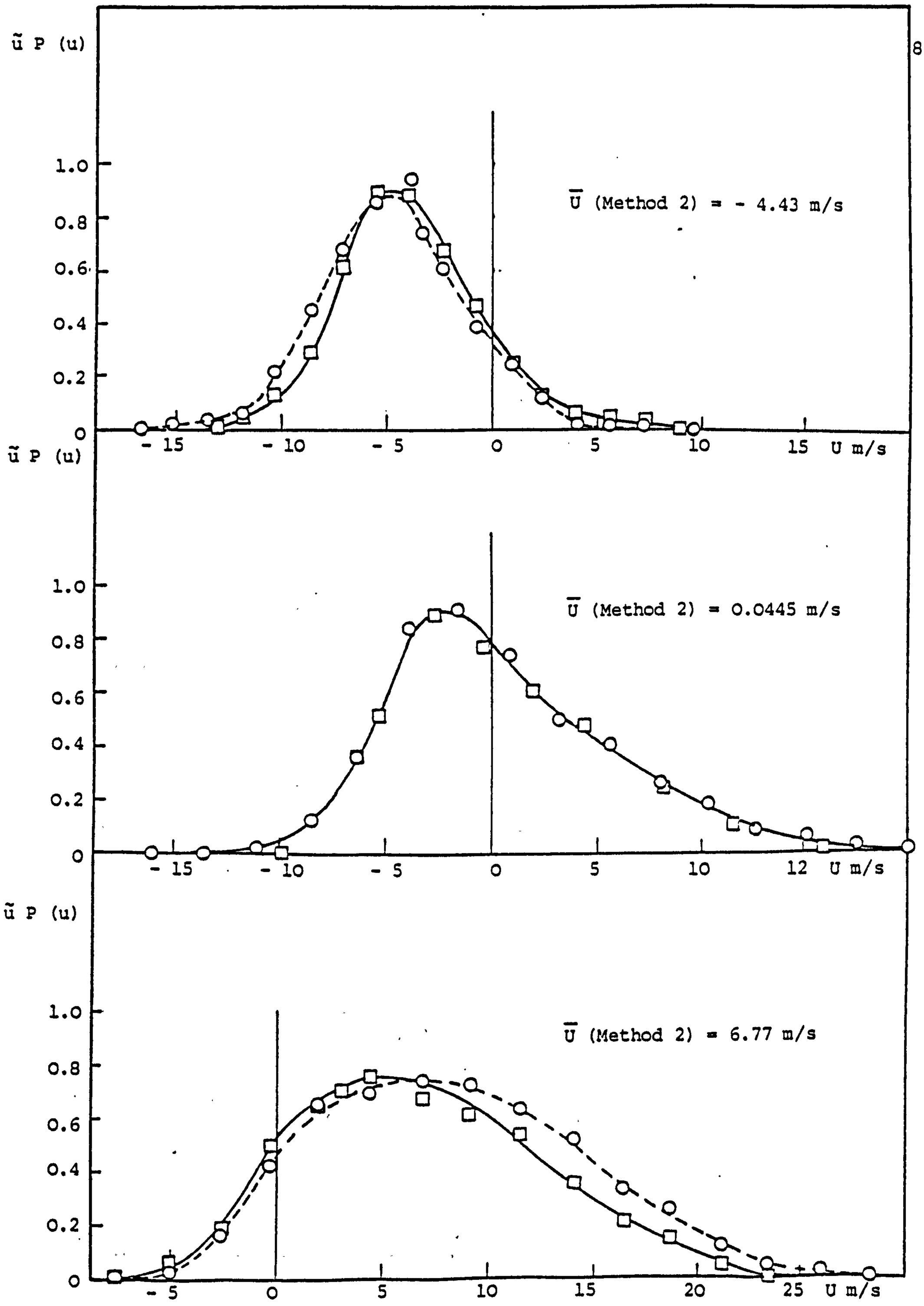


Fig. 2.21 Comparison Between Biased (Method 1) and Unbiased (Method 2) Probability Distributions

---O-, Method 1 ; —□—, Method 2

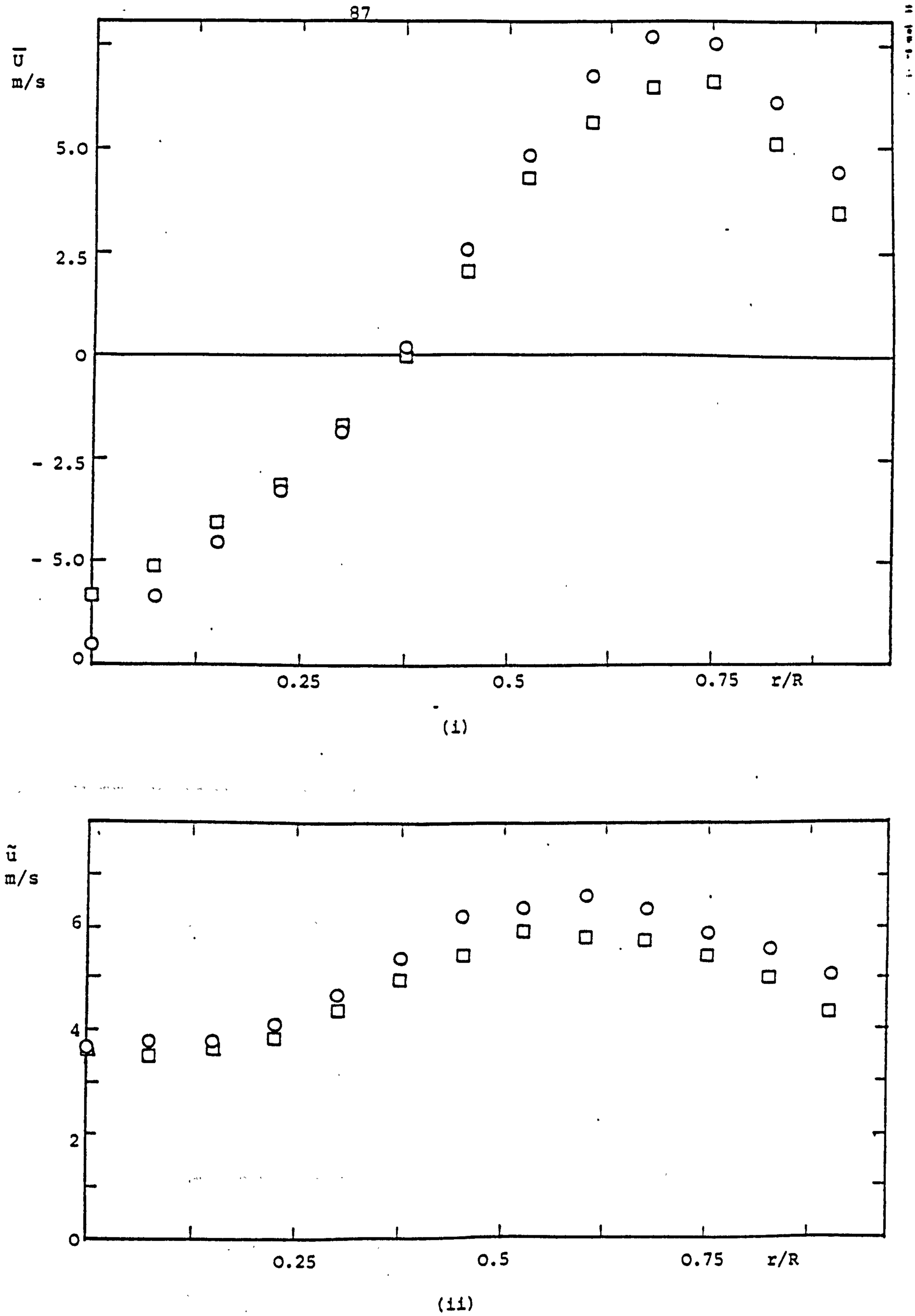
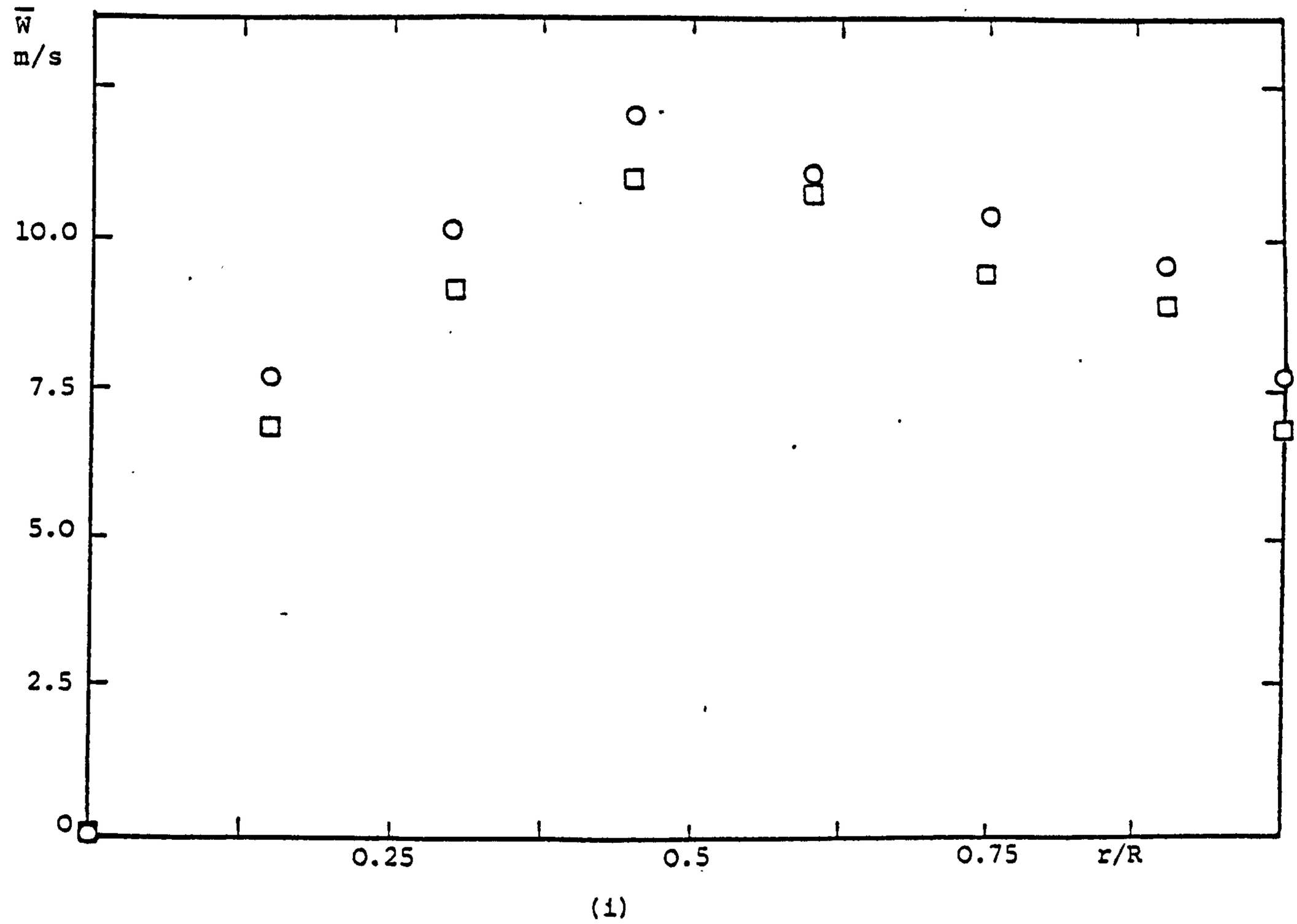
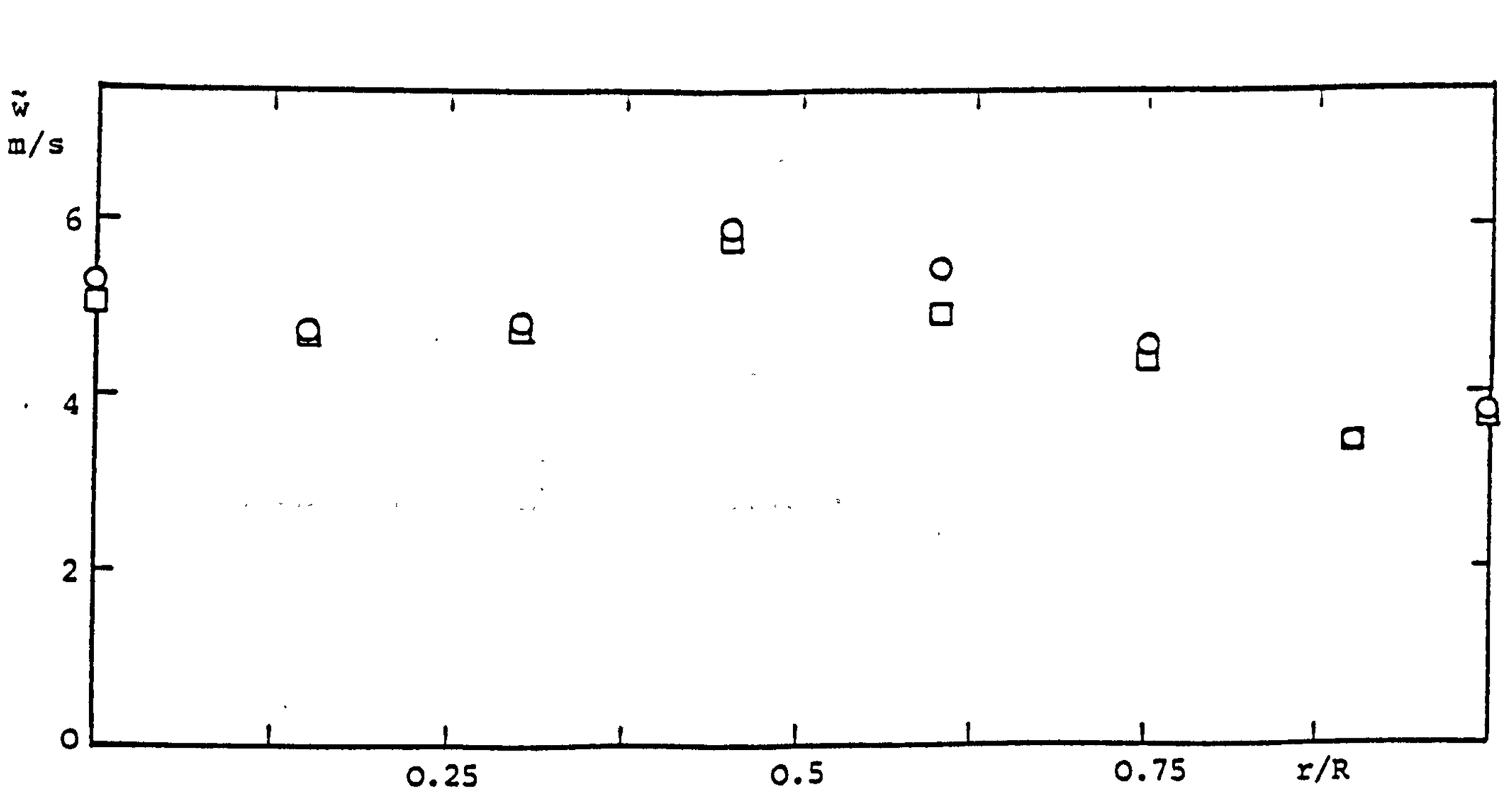


Fig. 2.22 Measured Mean and rms Values of the Axial Fluctuating Velocity; , Biased Values (Mode 1); , Unbiased Values (Mode 2); (i) Mean Velocity; (ii) Normal Stress



(i)



(ii)

Fig. 2.23 Measured Mean and rms Values of the Tangential Velocity Fluctuations; , Biased Values (Mode 1); , Unbiased Values (Mode 2); (i) Mean Velocity, (ii) Normal Stress

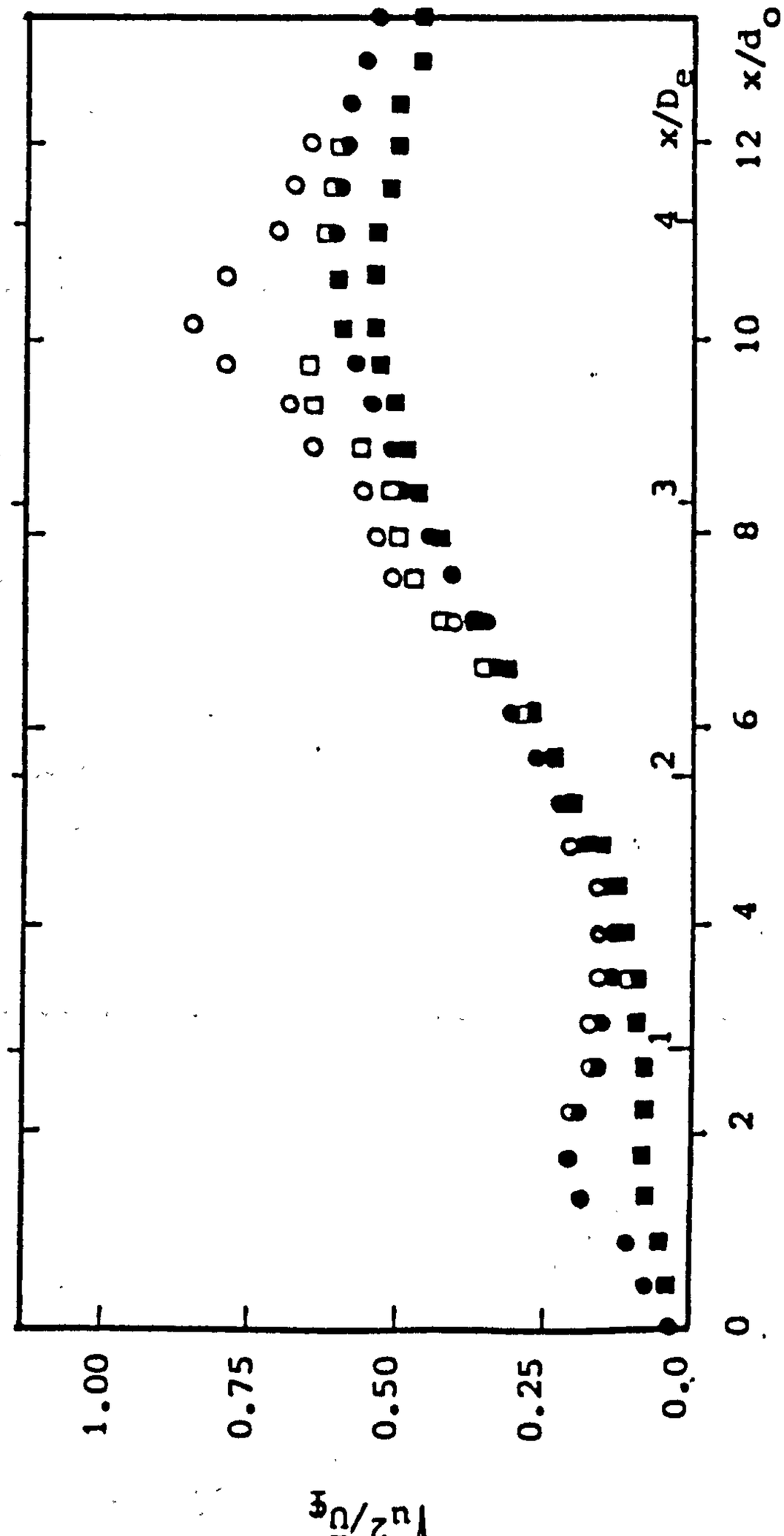


Fig. 2.24 Axial Profiles of the Turbulence Intensity (S = 0.0); Notation as in Fig. 2.10

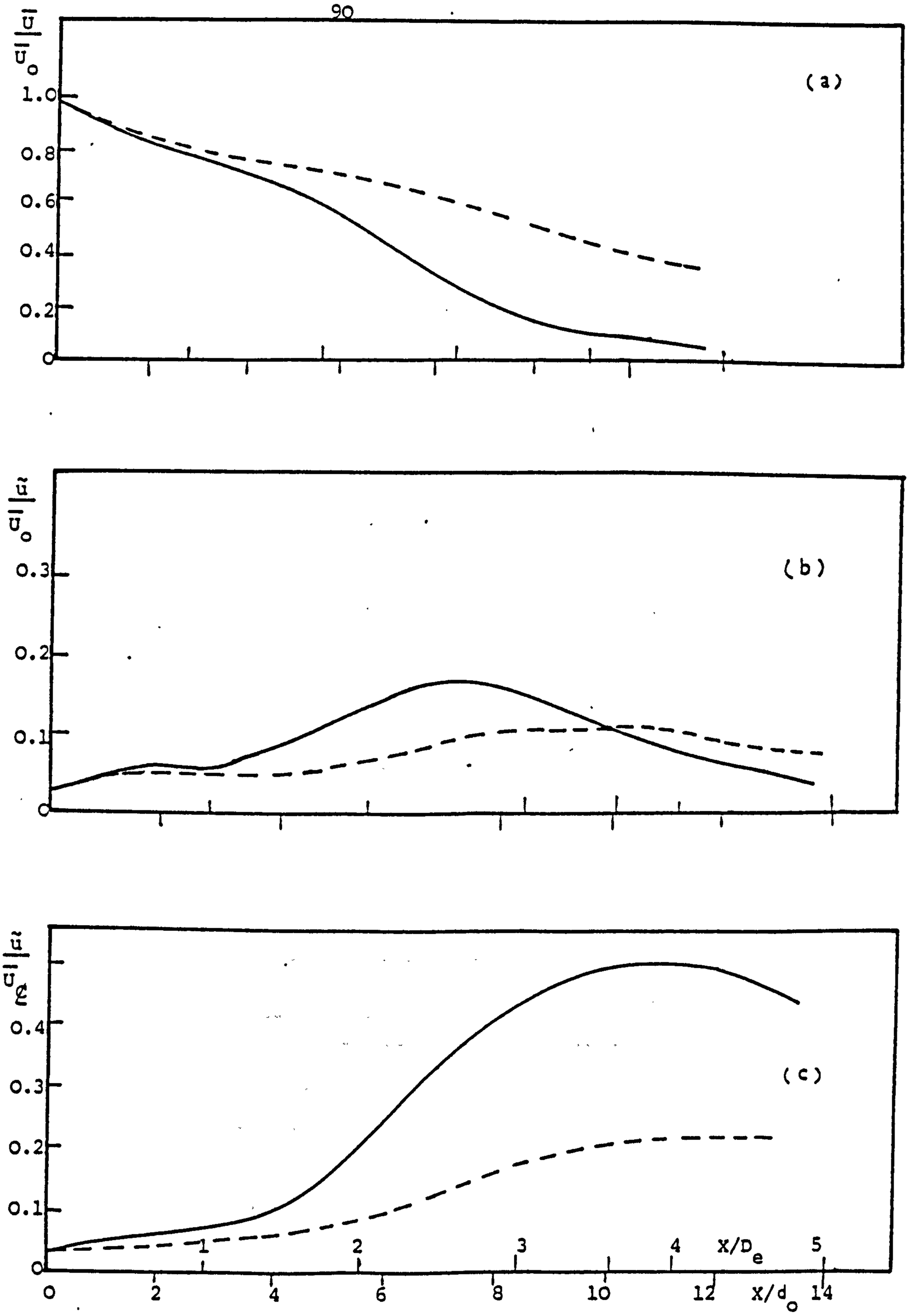


Fig. 2.25 Axial Distributions of Mean, rms and Turbulence Intensity of the Axial Fluctuating Velocity (U_a/U_o = 1.0), ——, Present Measurements; - - -, Free Jets, Ribeiro (1976)

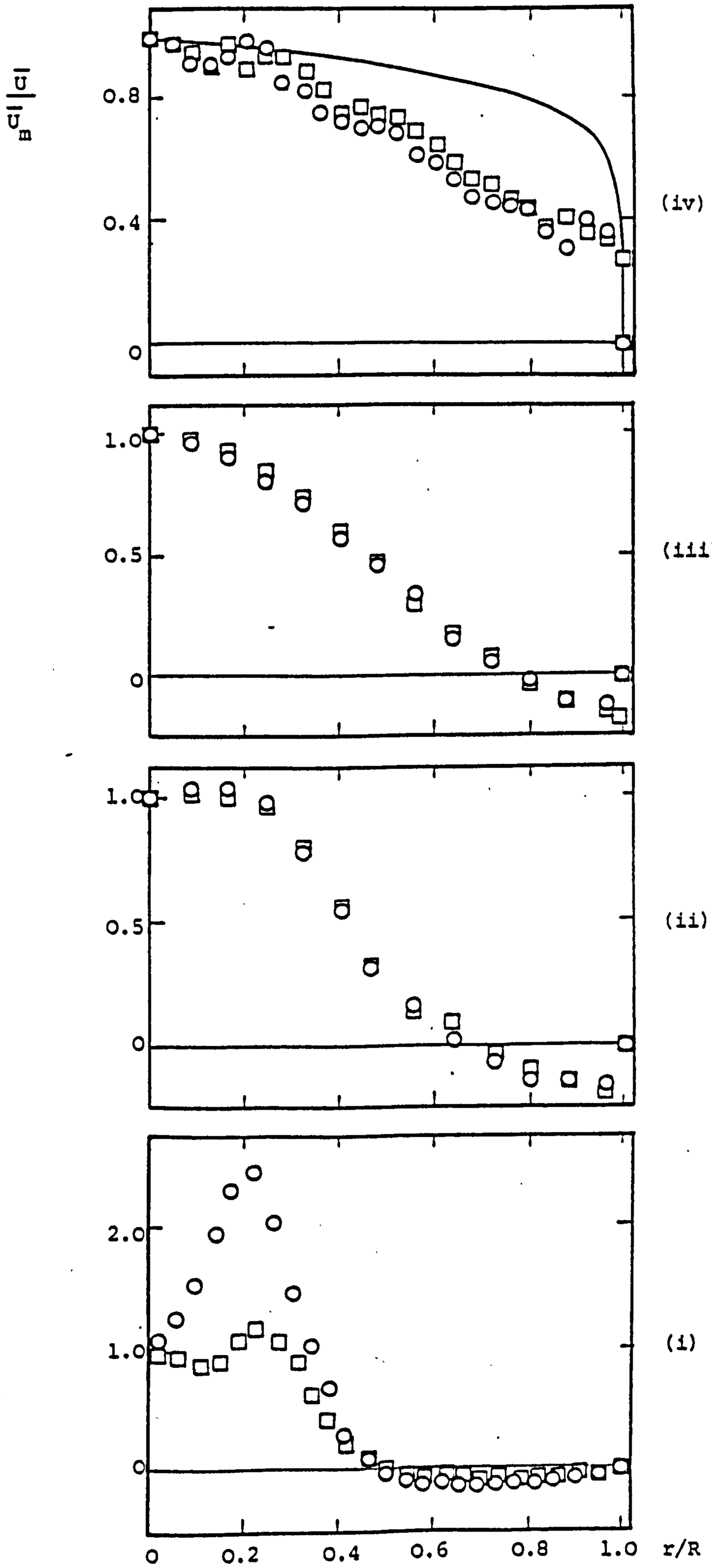


Fig. 2.26 Radial Profiles of Mean Velocity (S = 0.0)

(i) X/D_e = 0.616; (ii) X/D_e = 1.43;

(iii) X/D_e = 2.23; (iv) X/D_e = 3.67

———, Fully Developed Pipe Flow; Other Notations as in Fig. 2.10

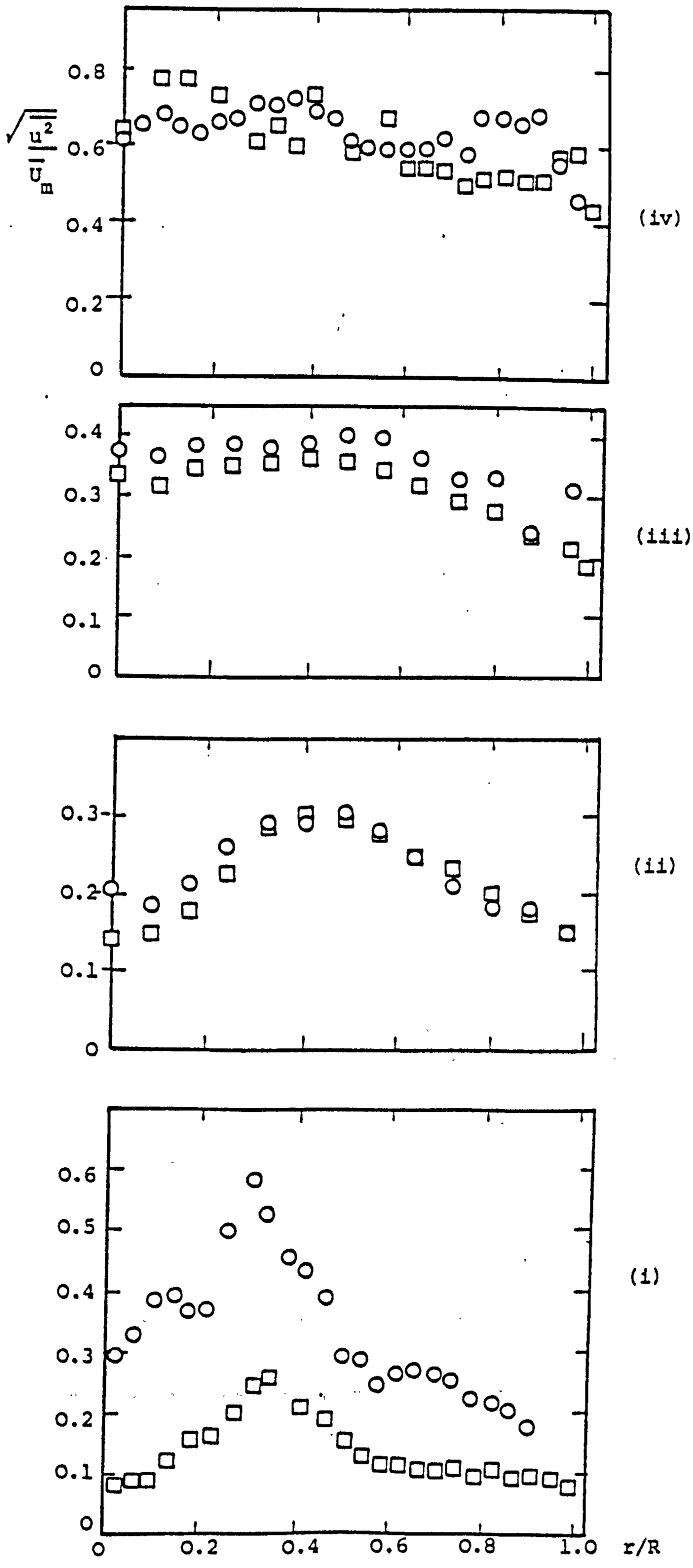


Fig. 2.27 Radial Profiles of Normal Stress (S = 0.0); Notation as in Fig. 2.26

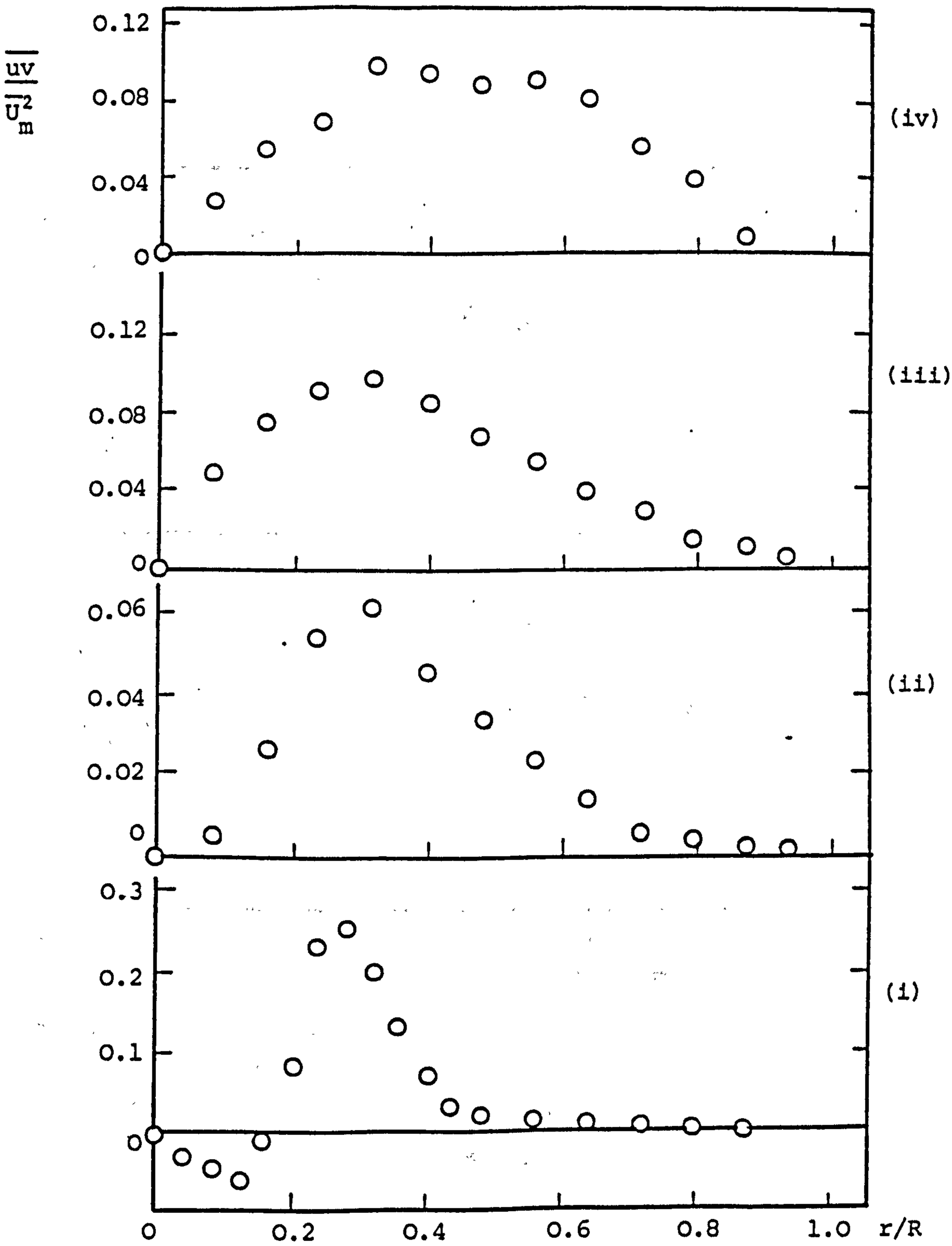


Fig. 2.28 Shear Stress Distributions (S = 0.0, $\overline{U}_a/\overline{U}_p$ = 3.0); Notation as in Fig. 2.26

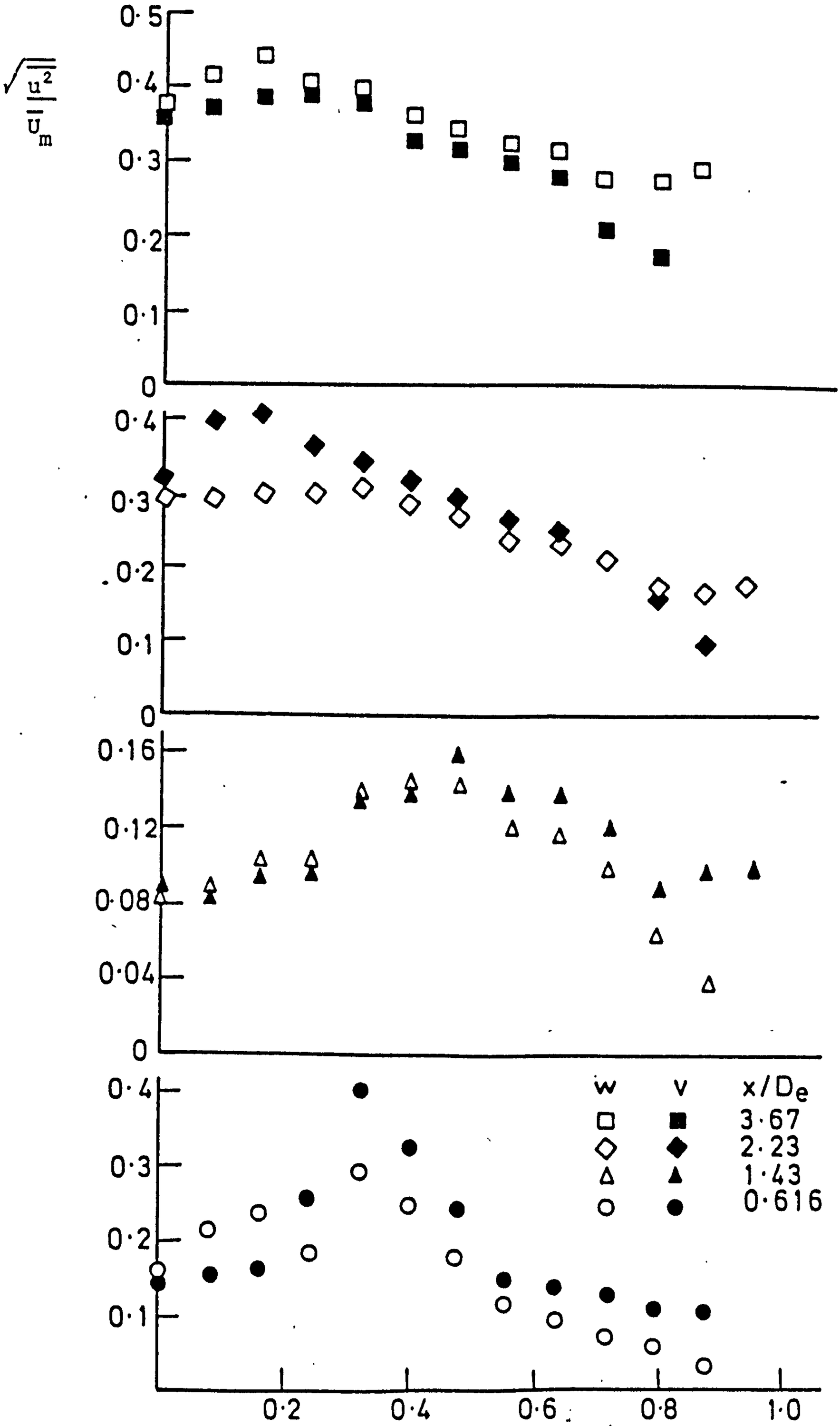
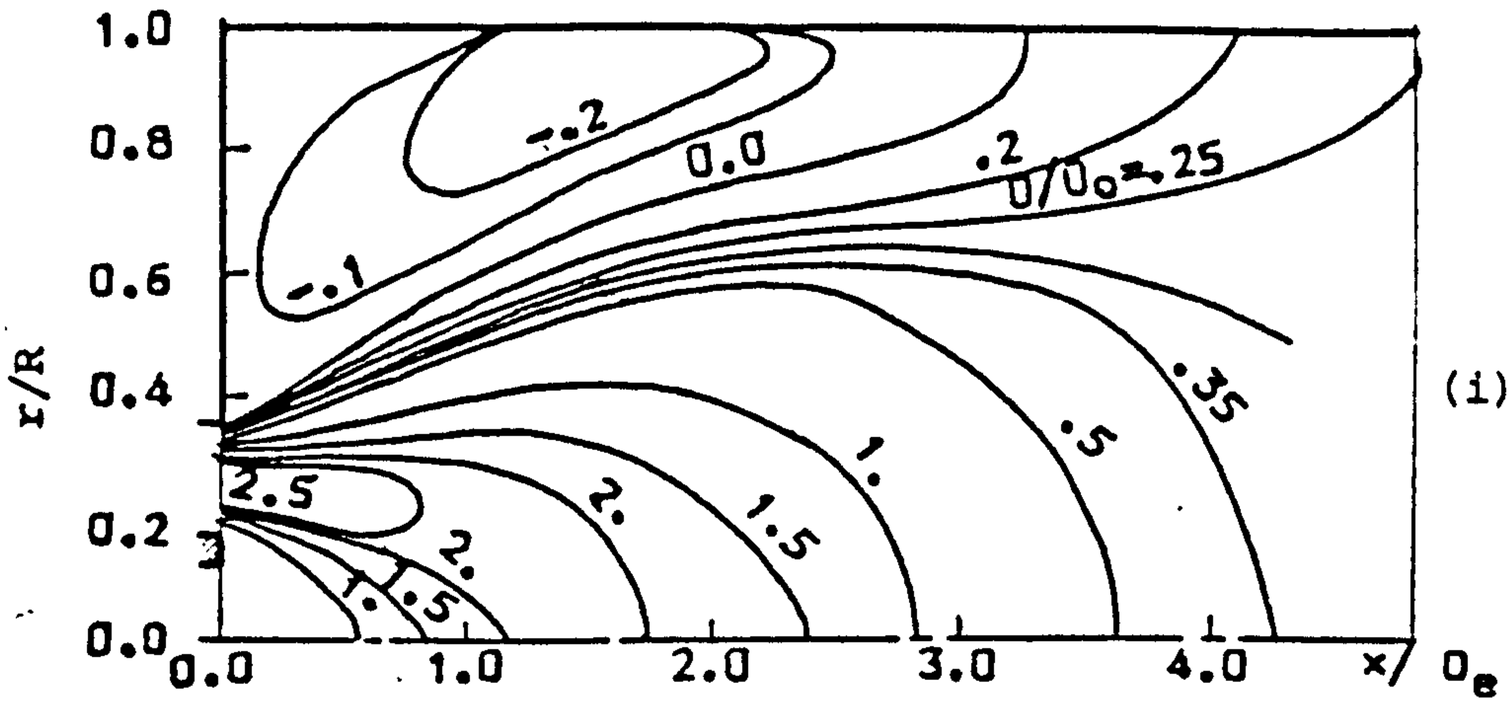


Fig. 2.29 Radial and Tangential Normal Stresses (S = 0.0; $\overline{U}_a/\overline{U}_p$ = 3.0)



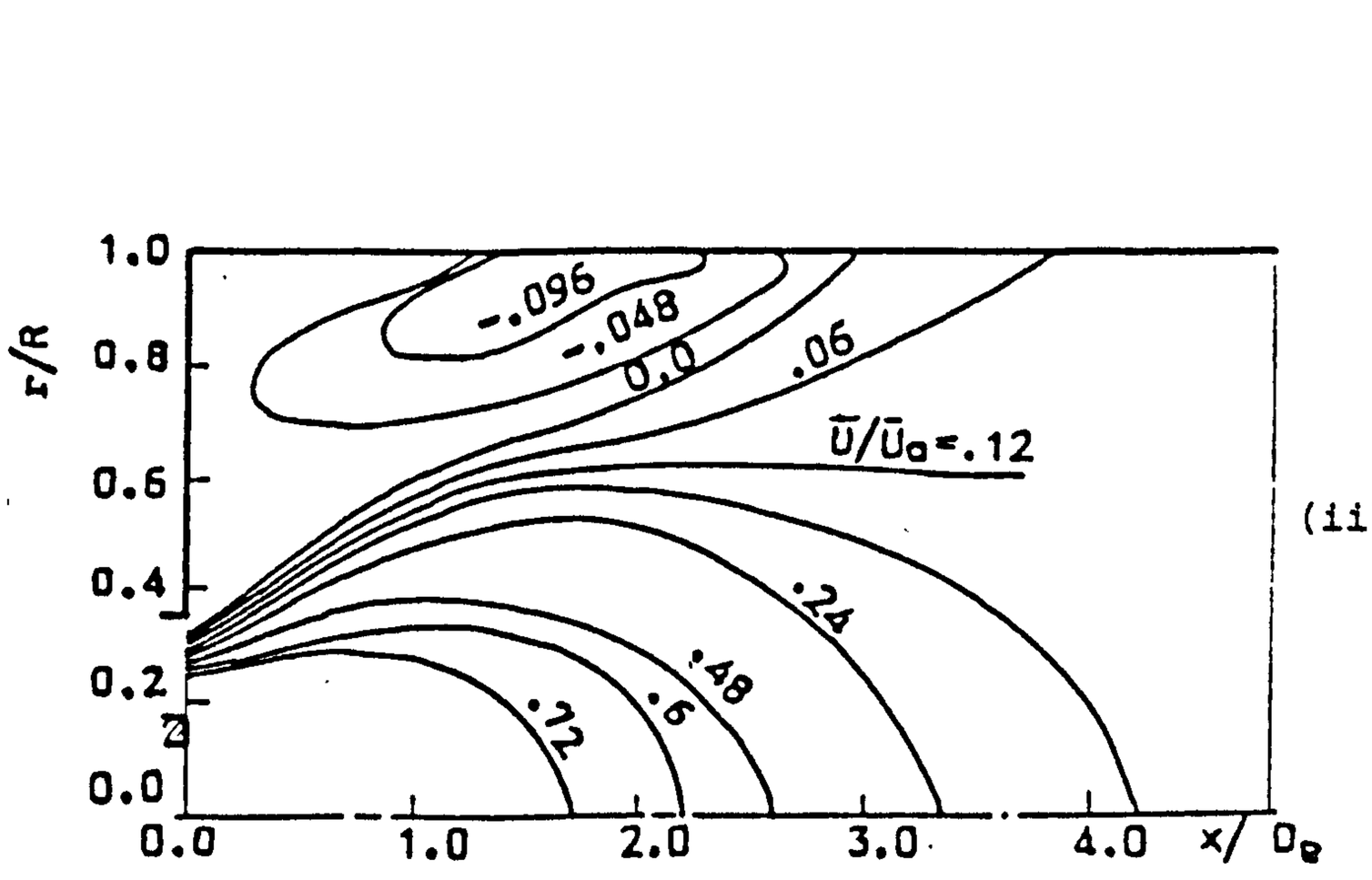
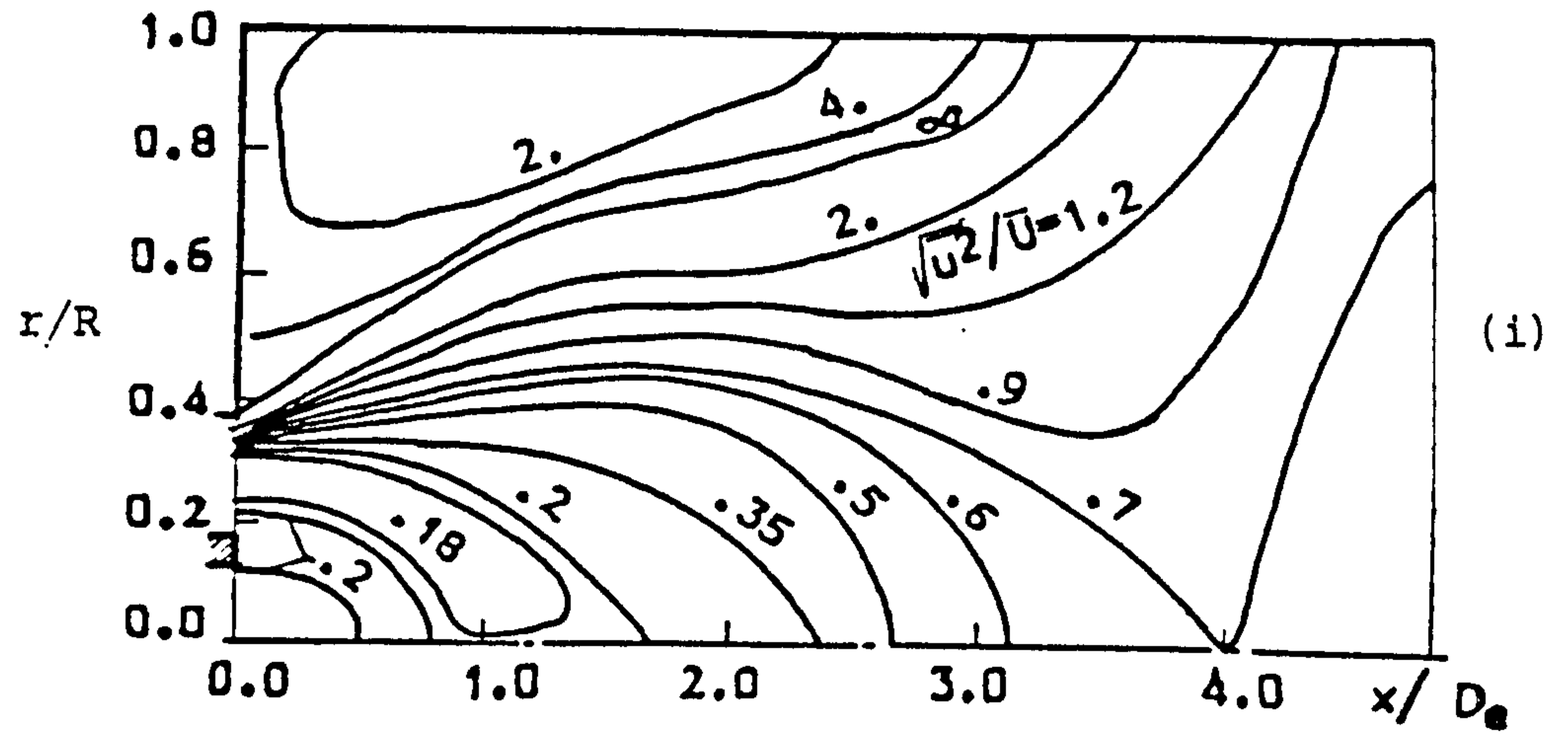
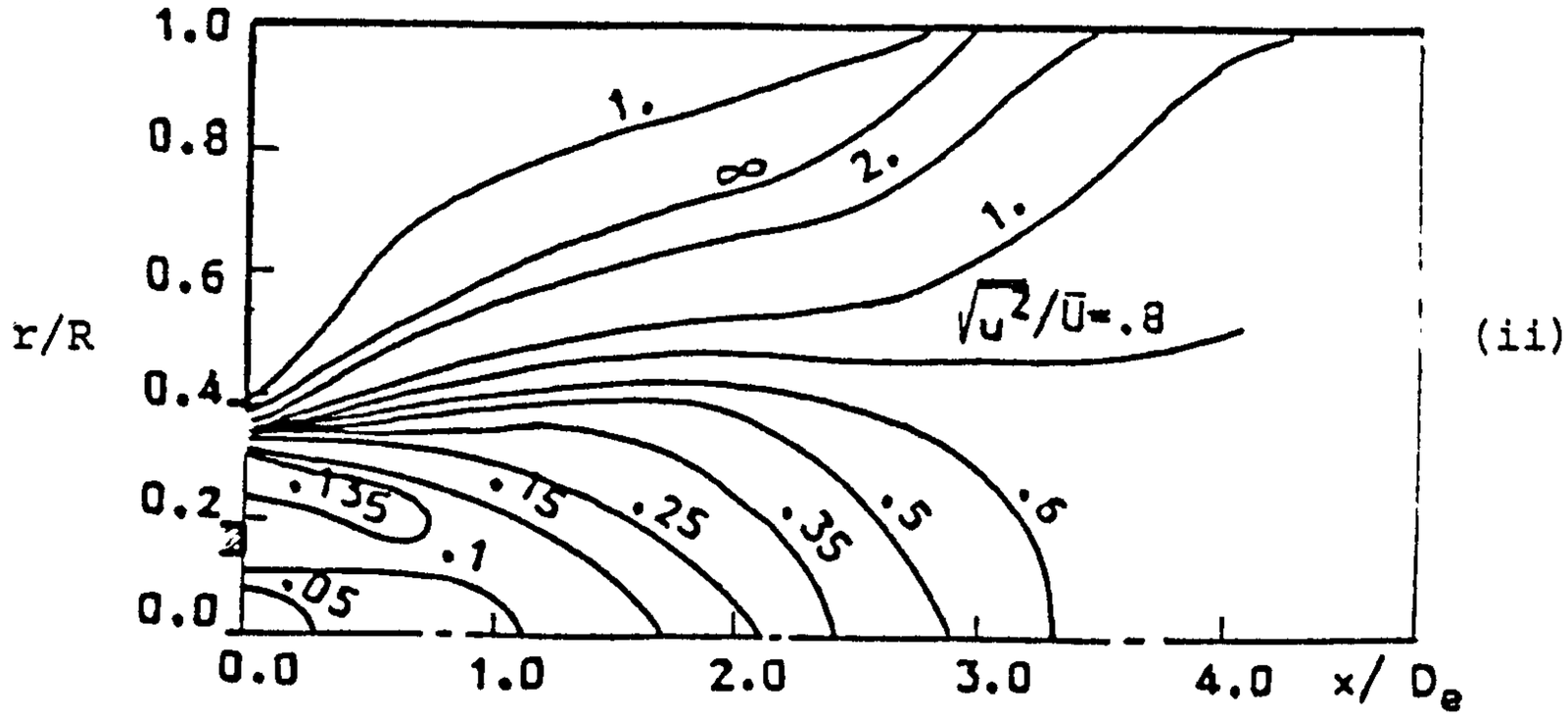


Fig. 2.30 Contours of the Mean Velocity (S = 0.0);

(i) $\overline{U}_a/\overline{U}_p = 3.0$; (ii) $\overline{U}_a/\overline{U}_p = 1.0$



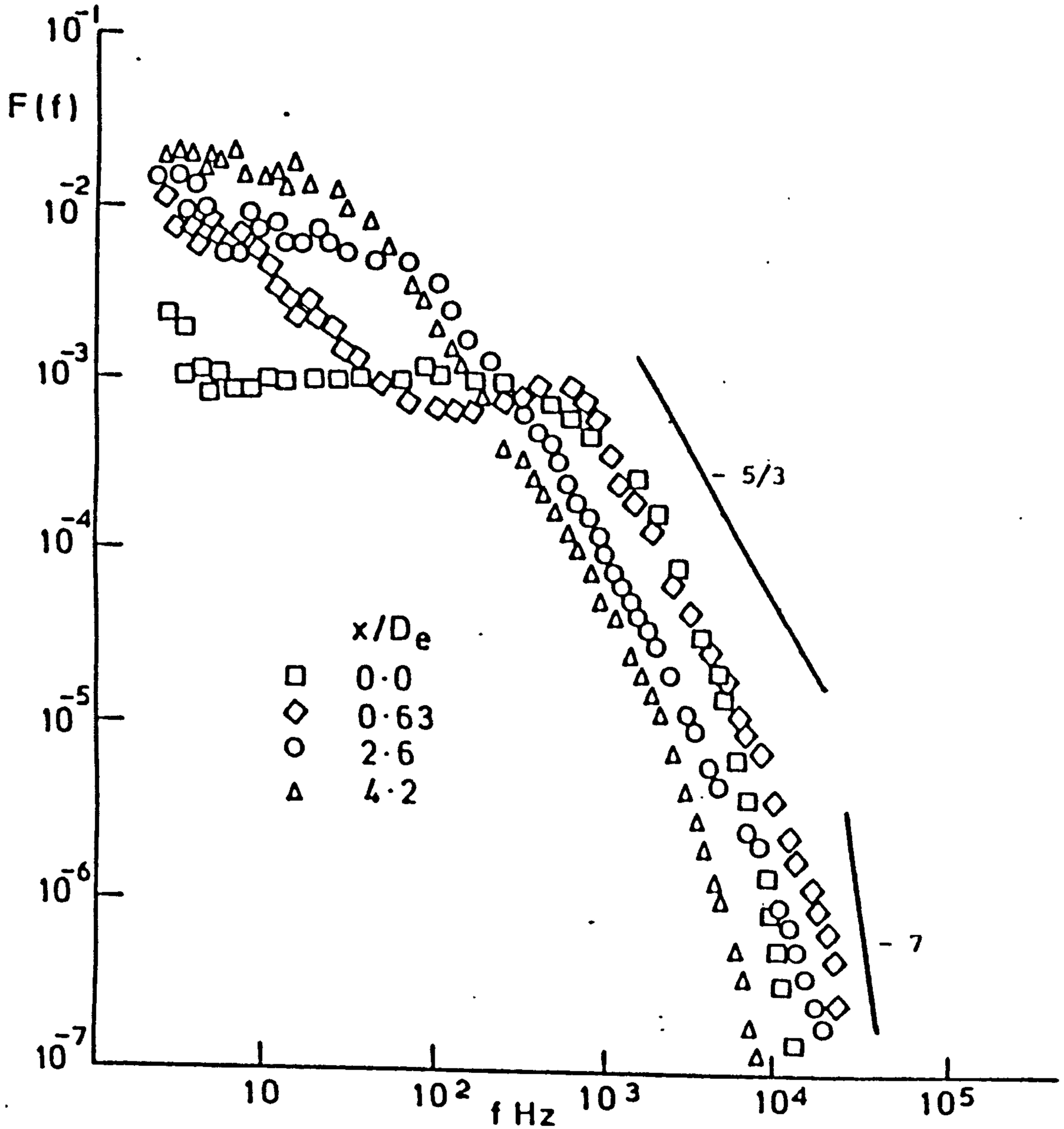
(i)



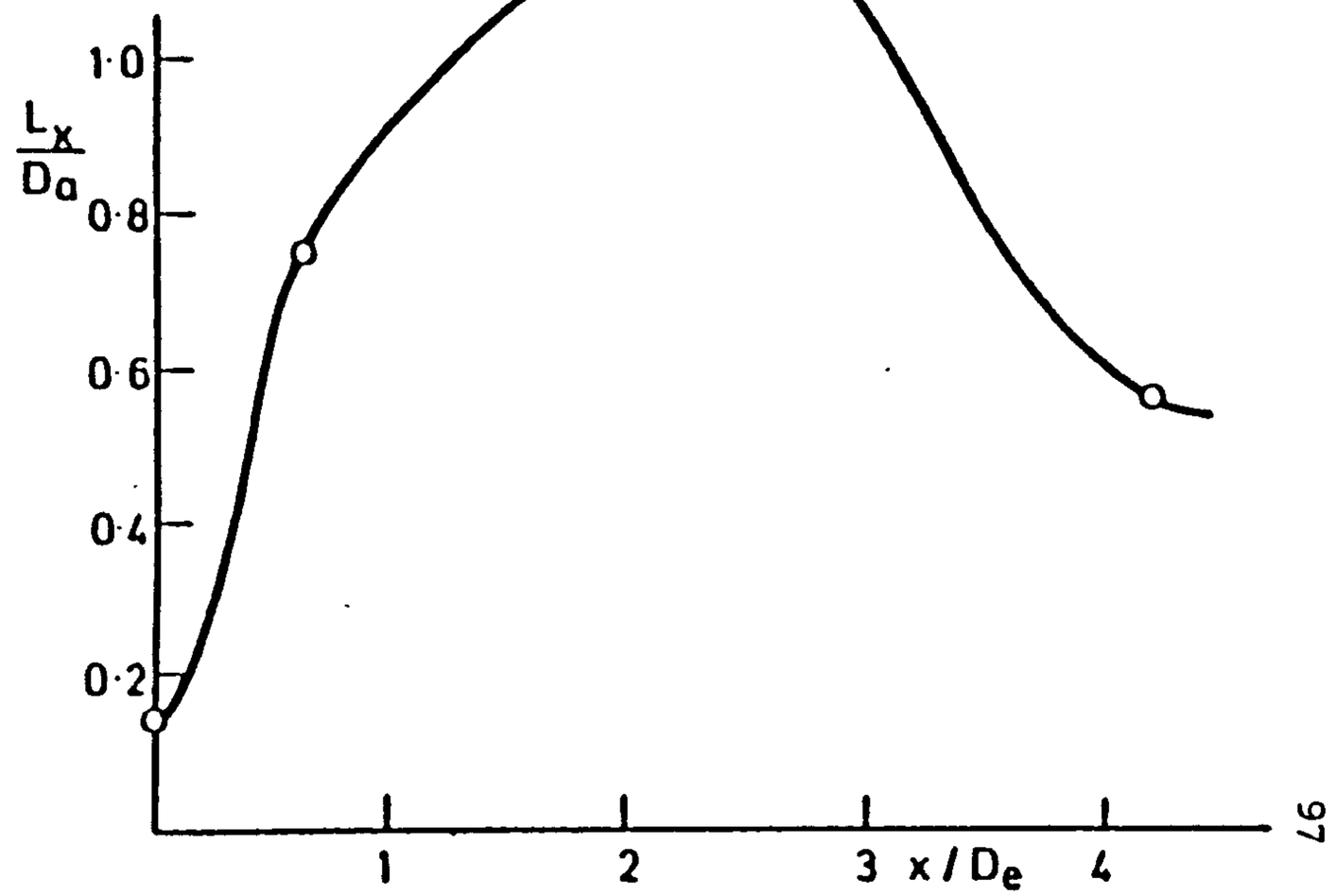
(ii)

Fig. 2.31 Contours of Turbulence Intensity (S = 0.0);

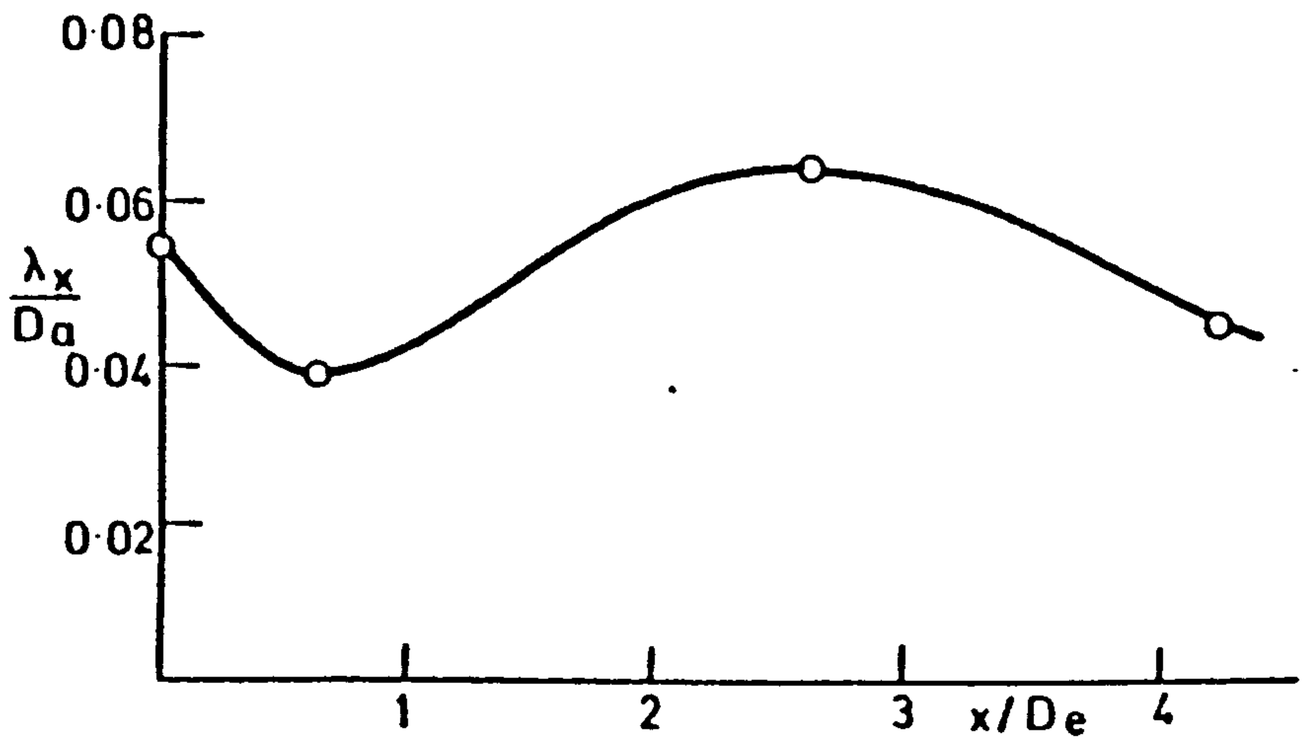
(i) $\bar{U}_a/\bar{U}_p = 3.0$; (ii) $\bar{U}_a/\bar{U}_p = 1.0$



(i) NORMALIZED ENERGY SPECTRA.

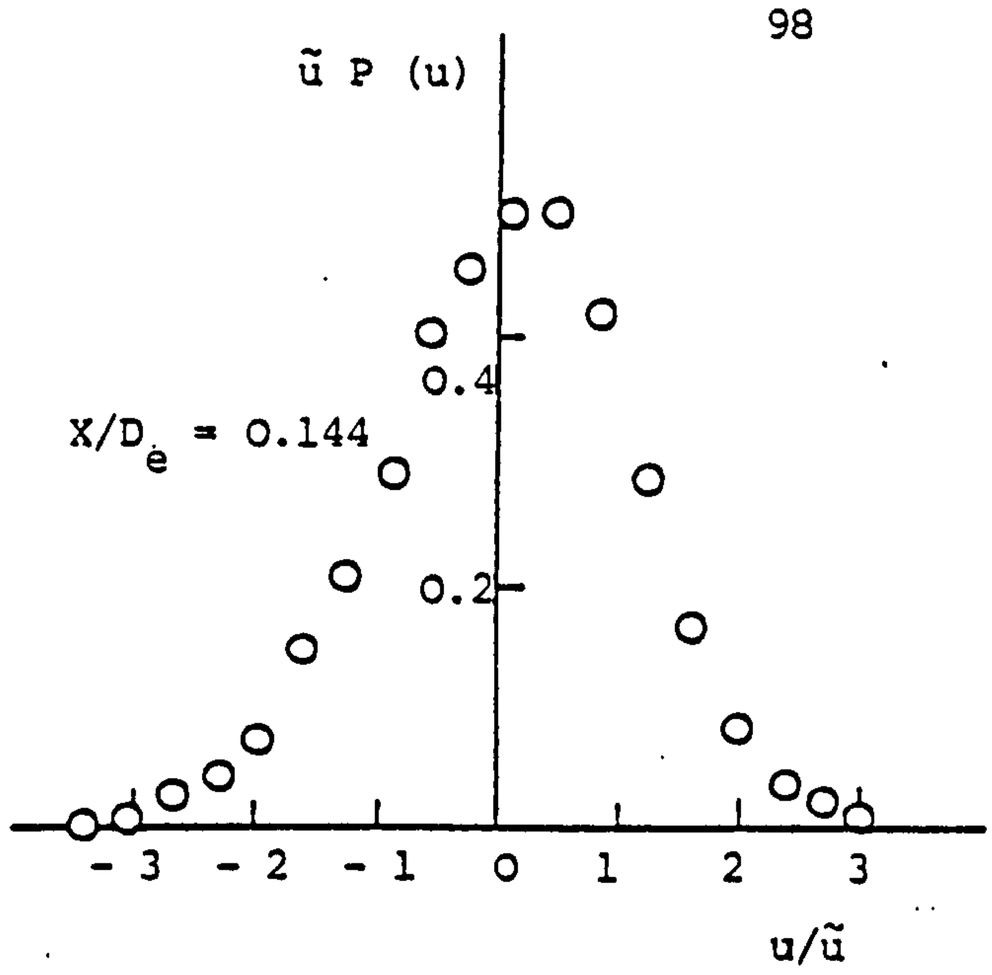


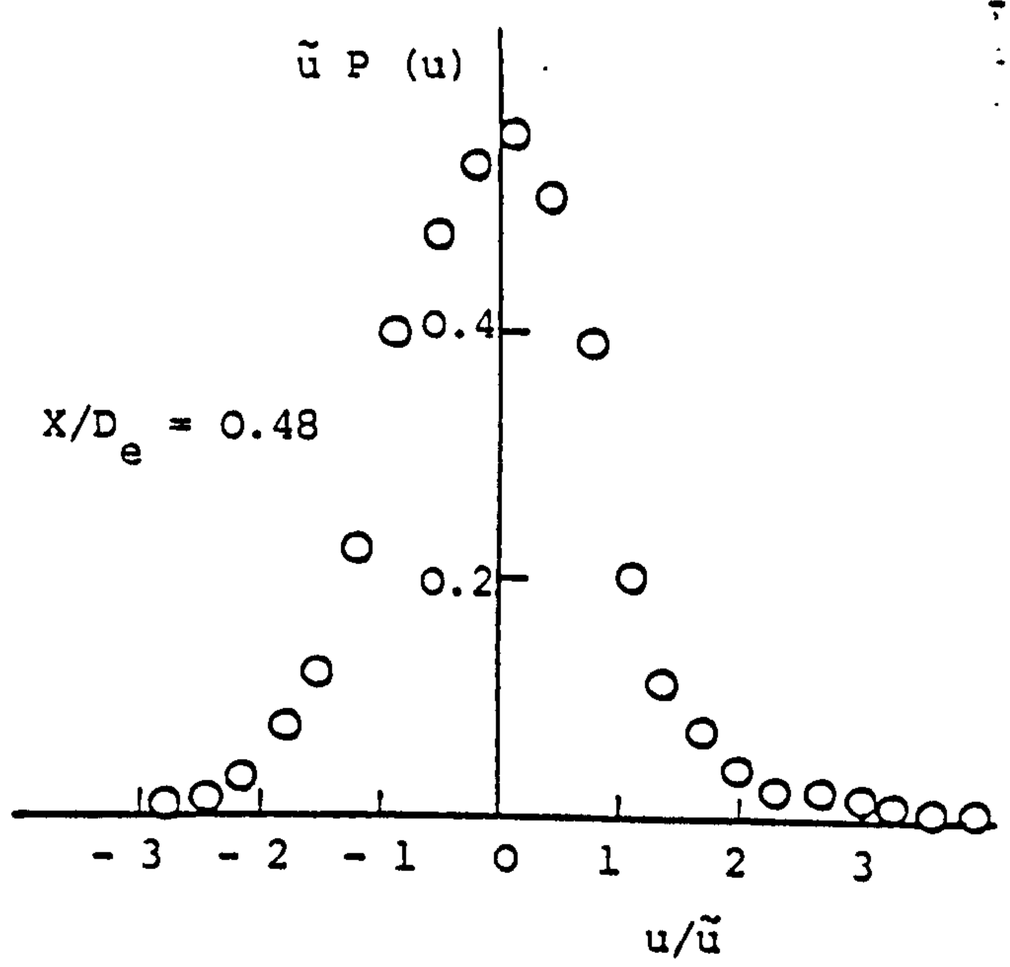
(ii) DISTRIBUTION OF THE LONGITUDINAL MACROSCALES

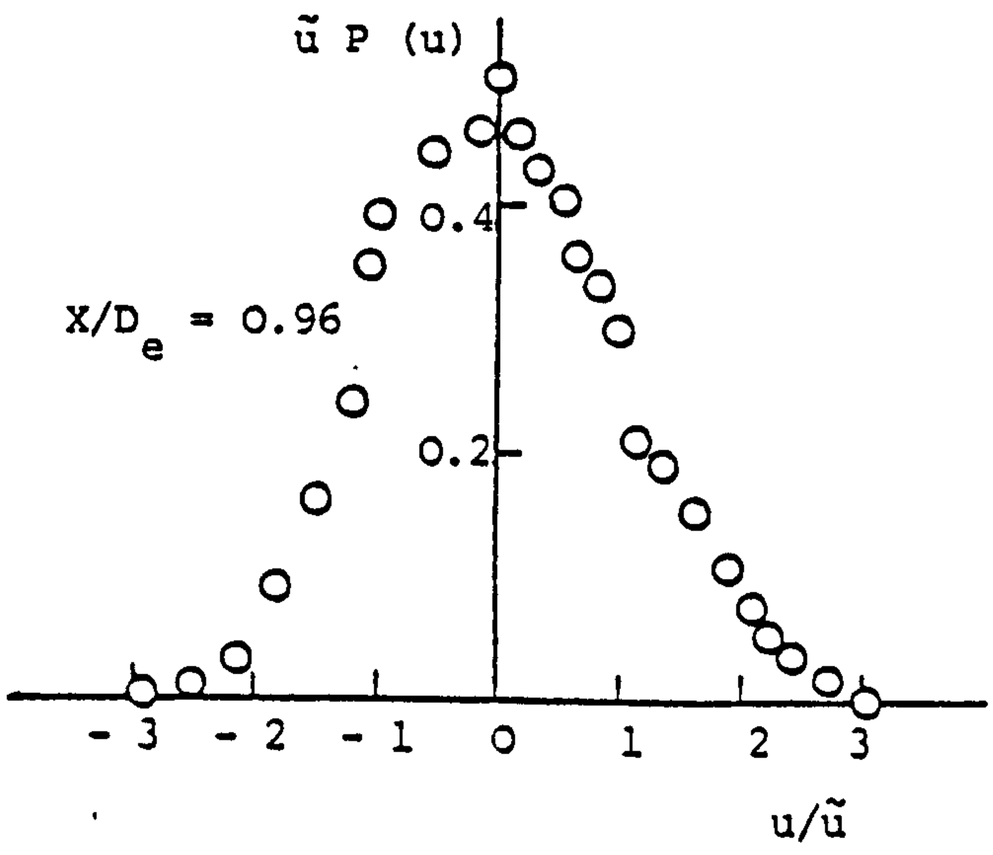


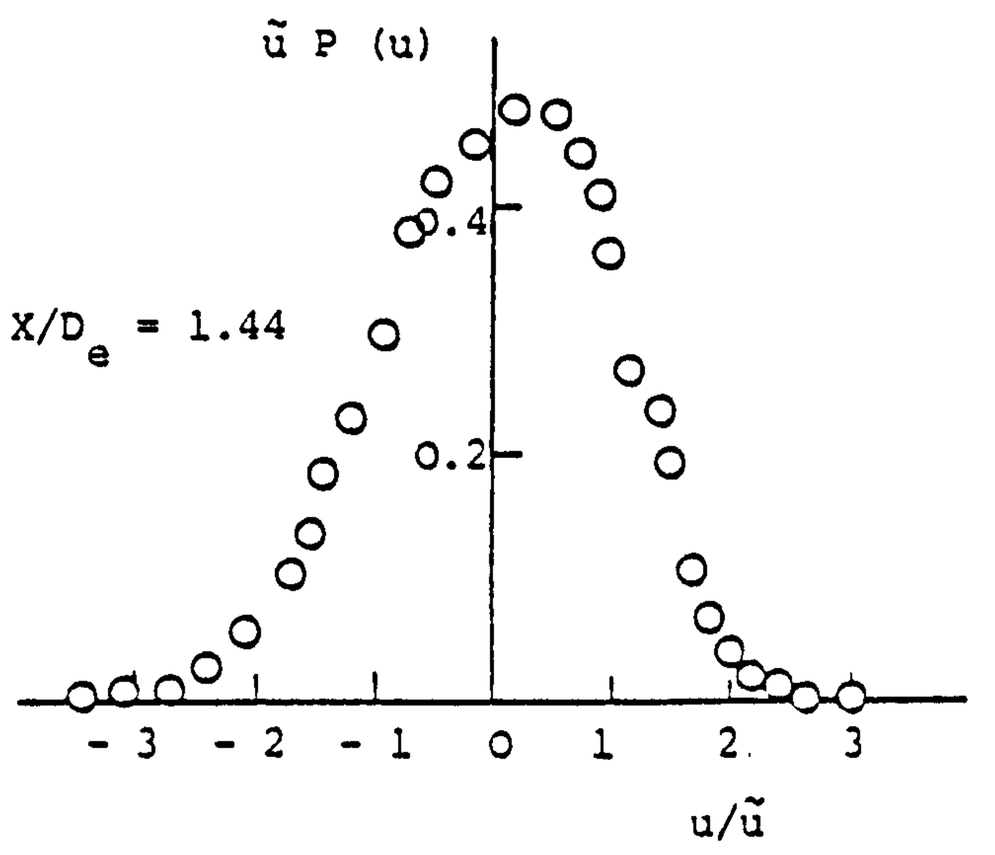
(iii) DISTRIBUTION OF THE LONGITUDINAL MICROSCALES

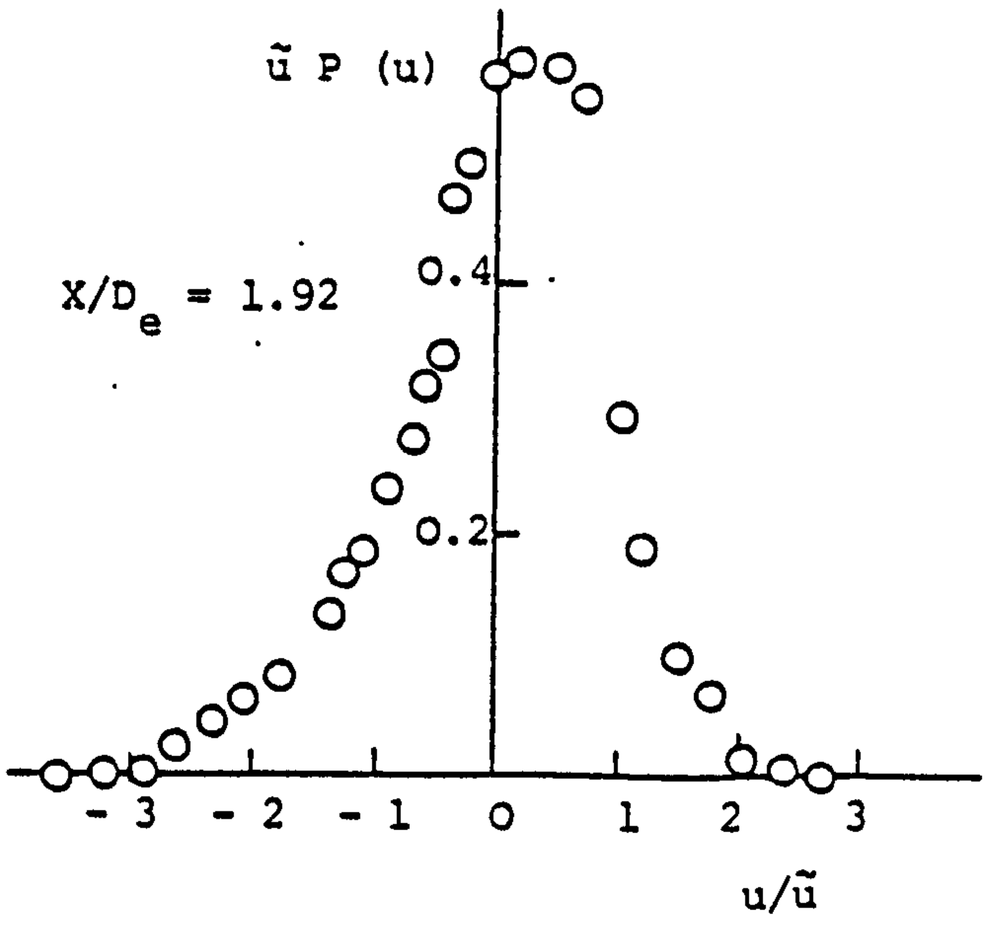
Fig. 2.32 Energy Spectra and Corresponding Longitudinal Scales Distributions Along the Centre-Line ($\bar{U}_a/\bar{U}_p$ = 3.0)











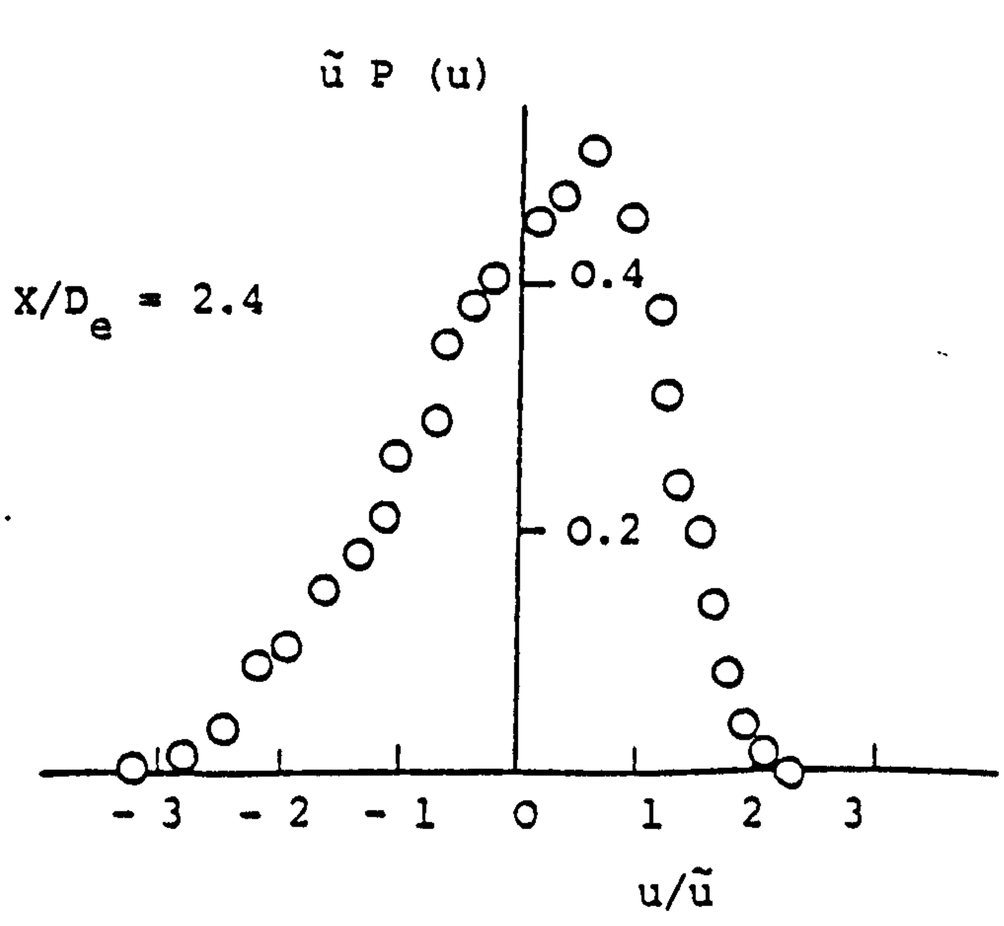
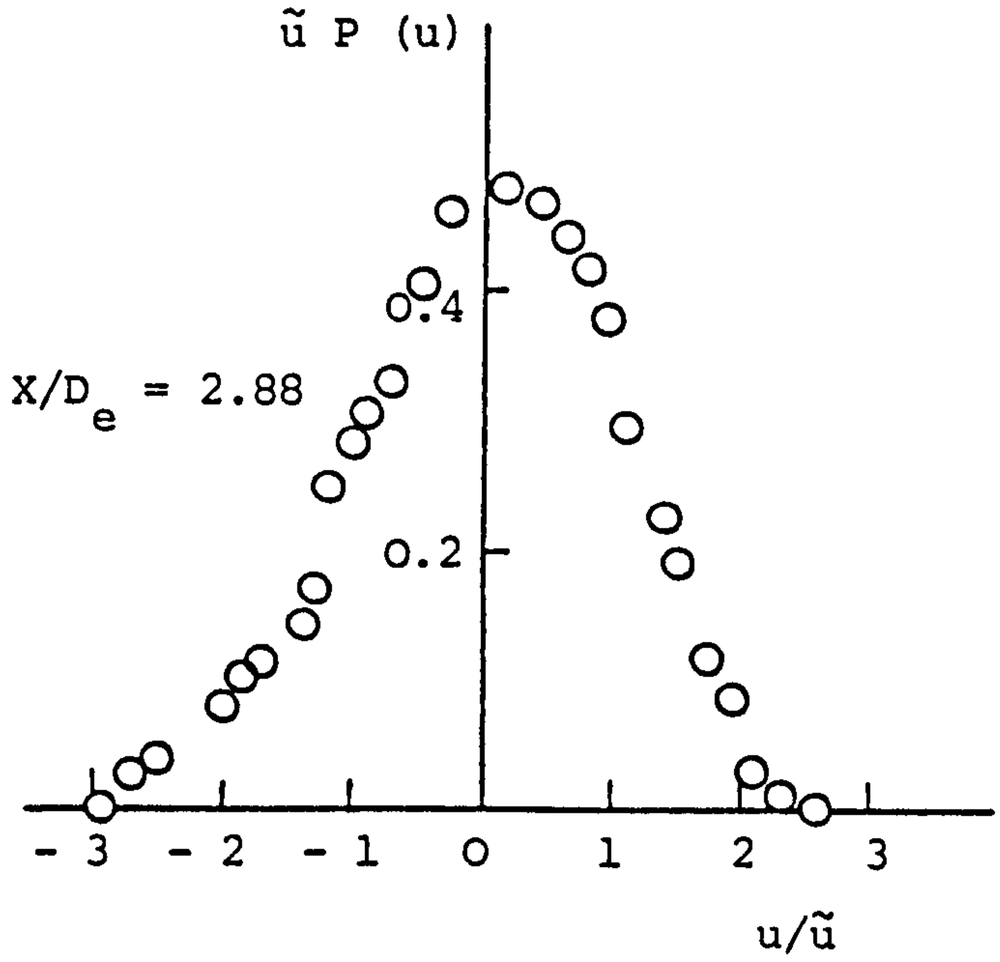
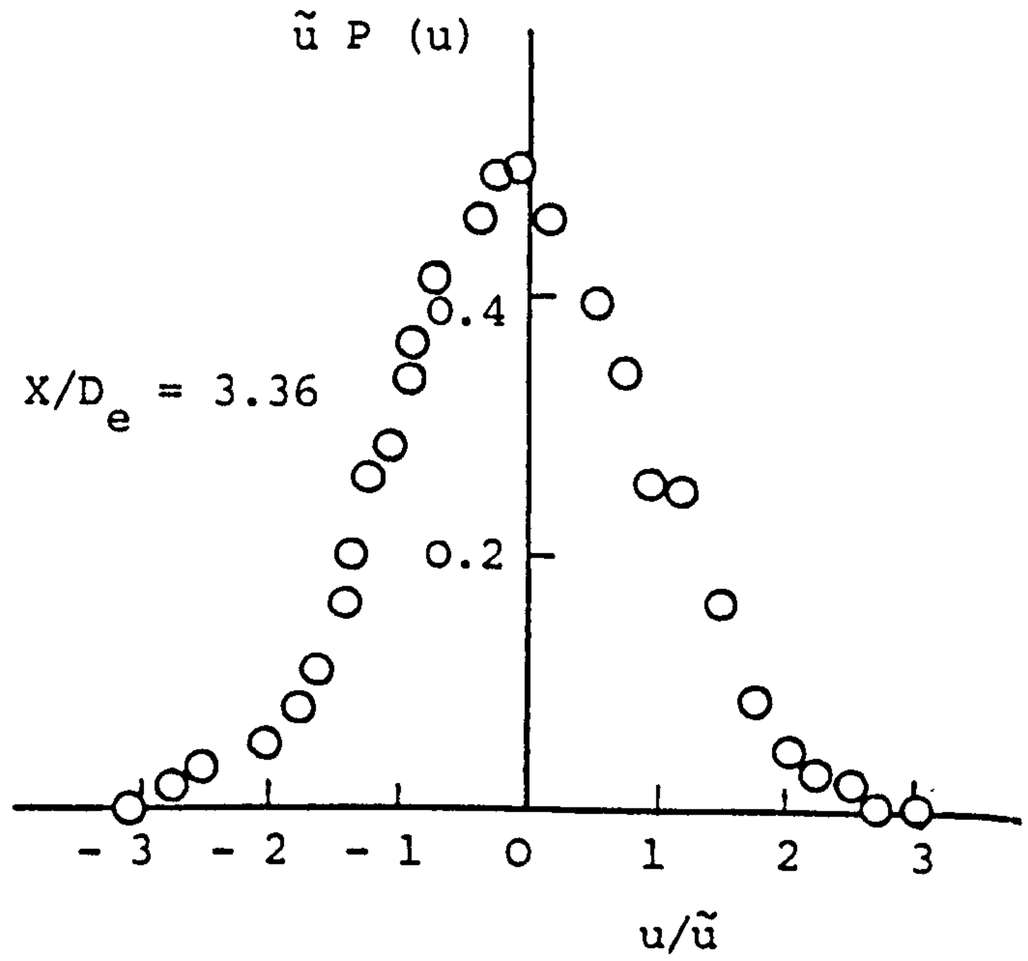
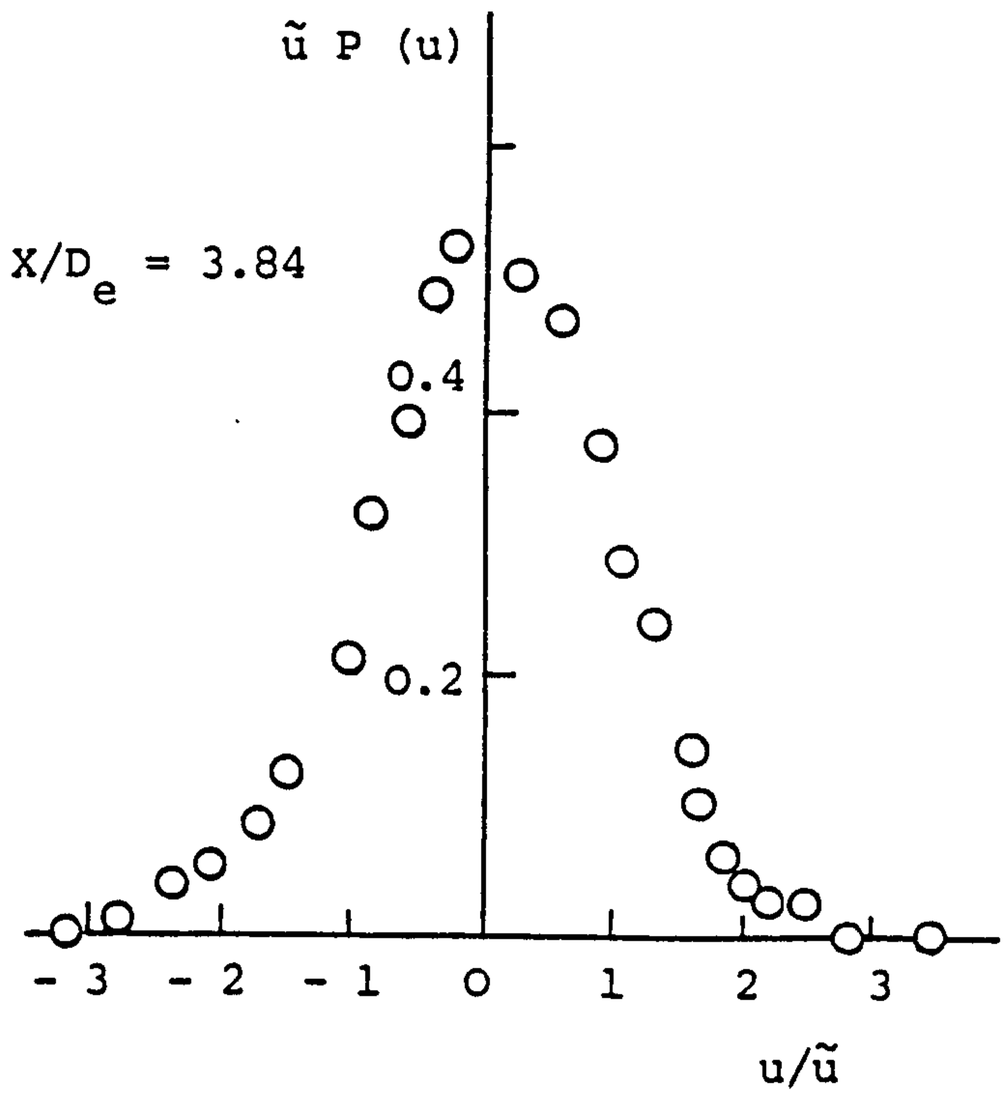


Fig. 2.33 Probability Distributions Along the Centre-Line (S = 0.0, $\overline{U}_a/\overline{U}_p$ = 3.0)







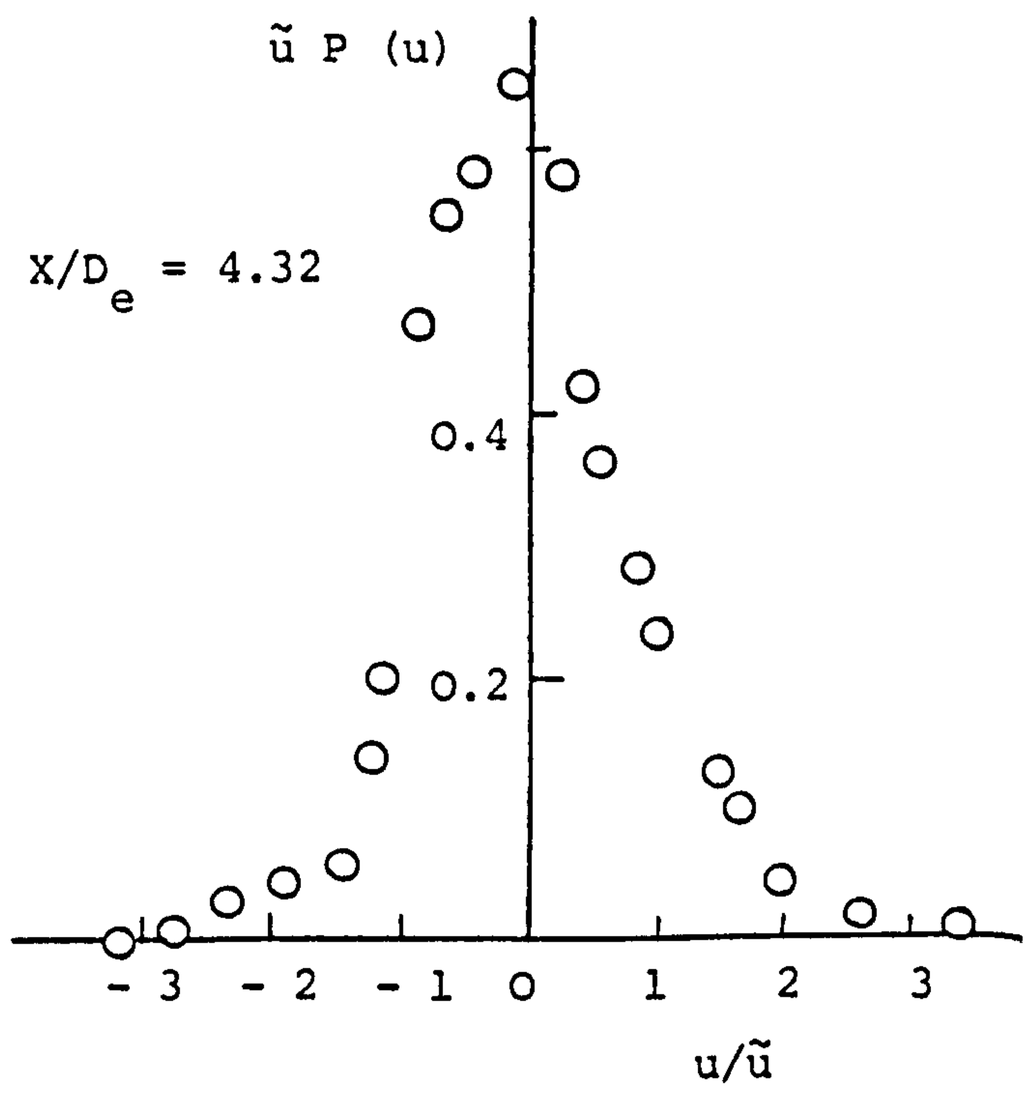


Fig. 2.33 (Continued)

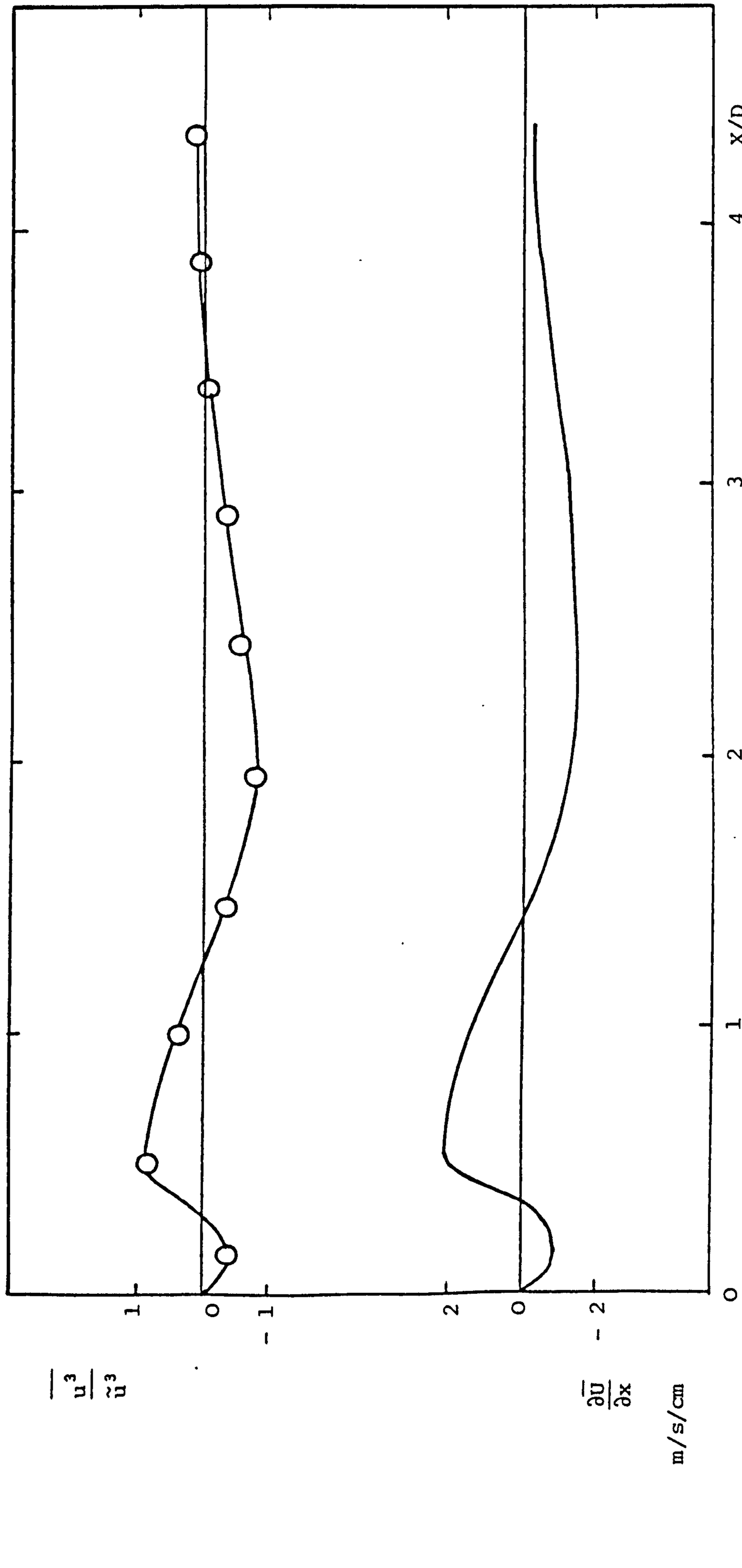


Fig. 2.34 Axial Distributions of Skewness Factor and Axial Velocity Gradient ($S = 0.0$, $\bar{U}_a/\bar{U}_p = 3.0$)

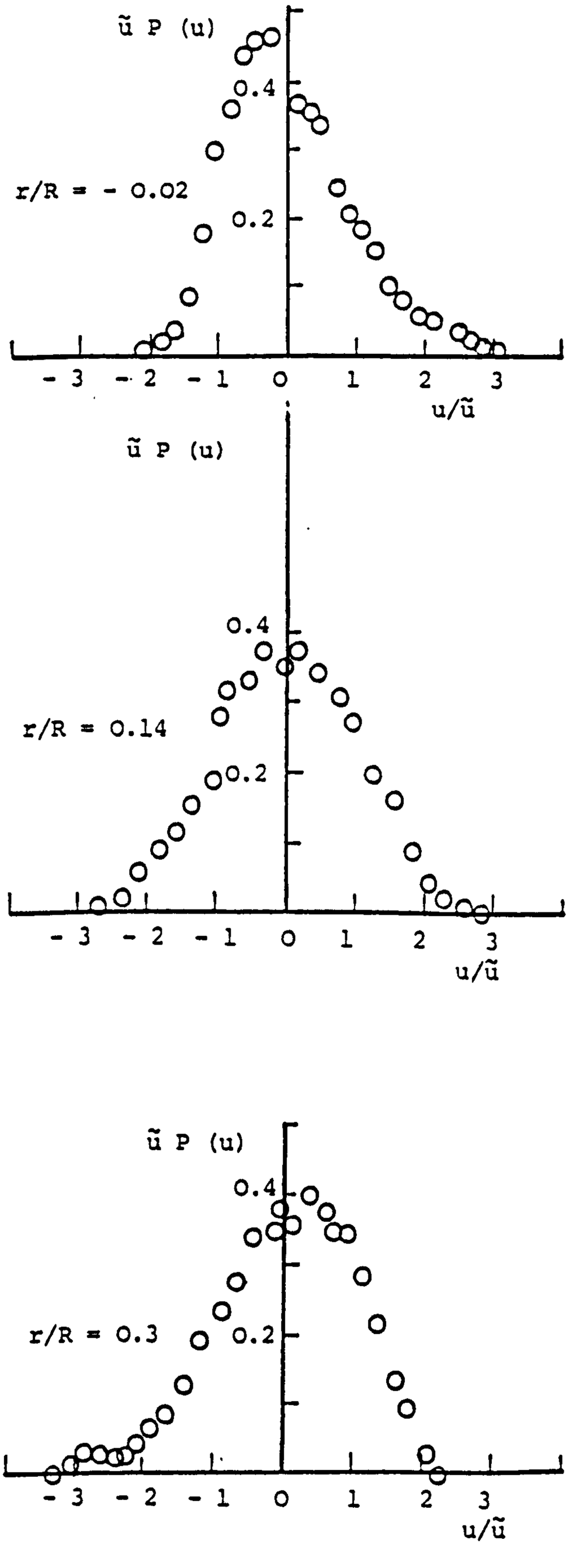
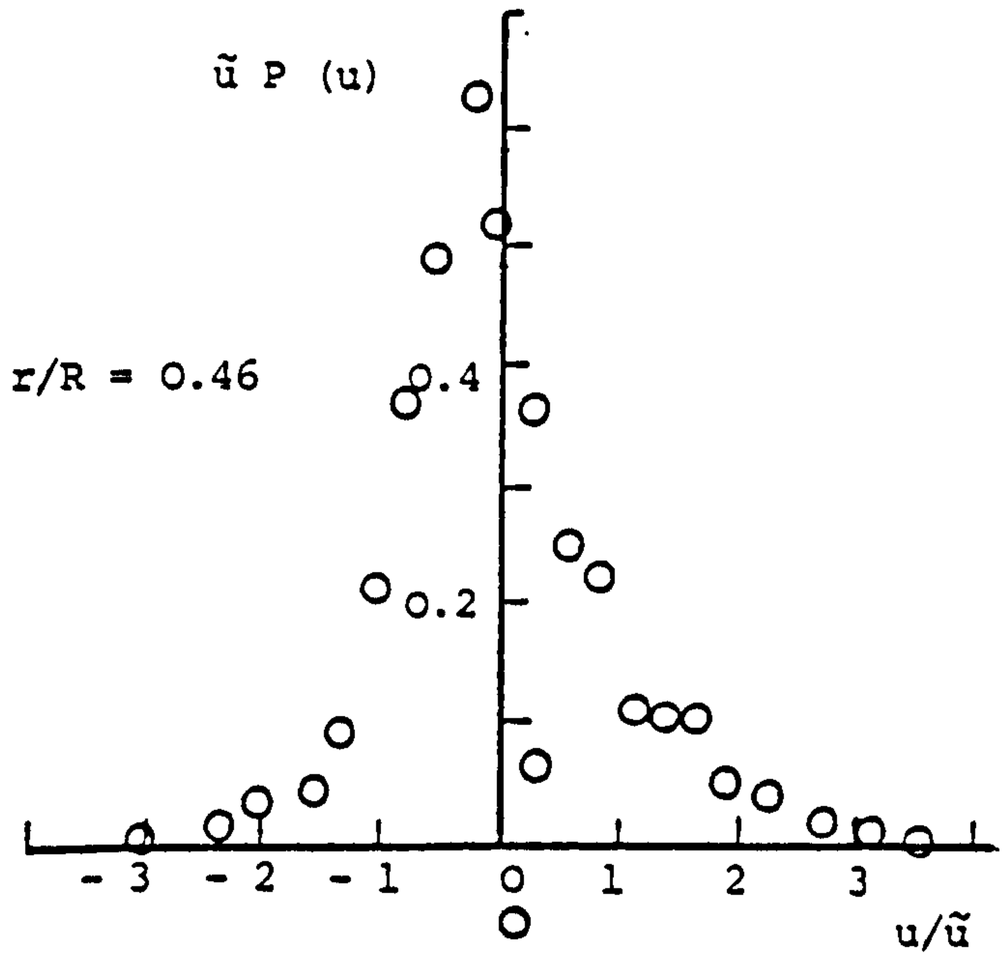
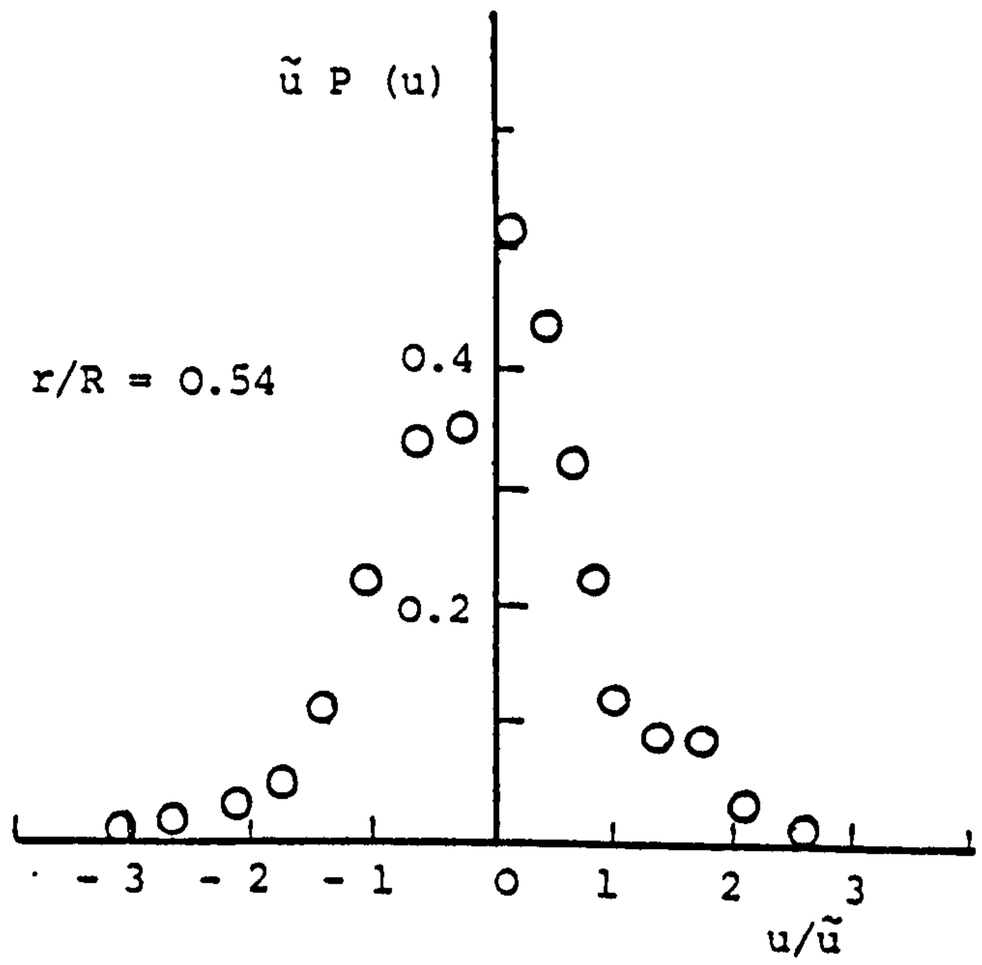
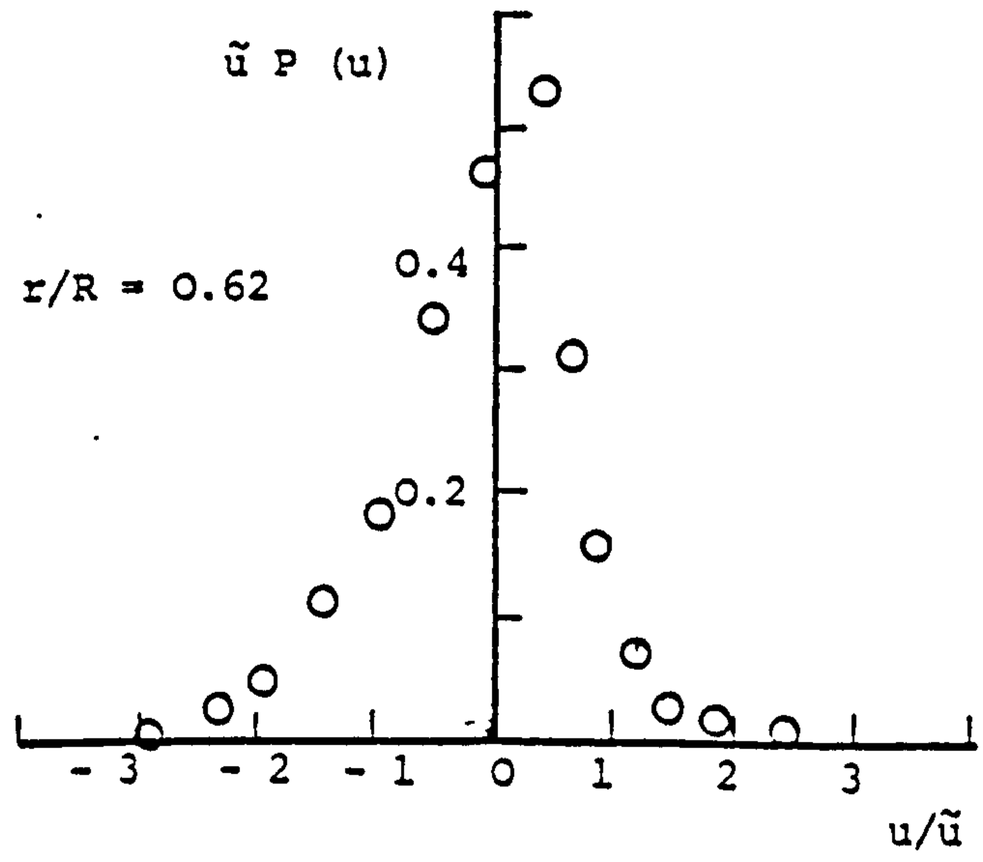
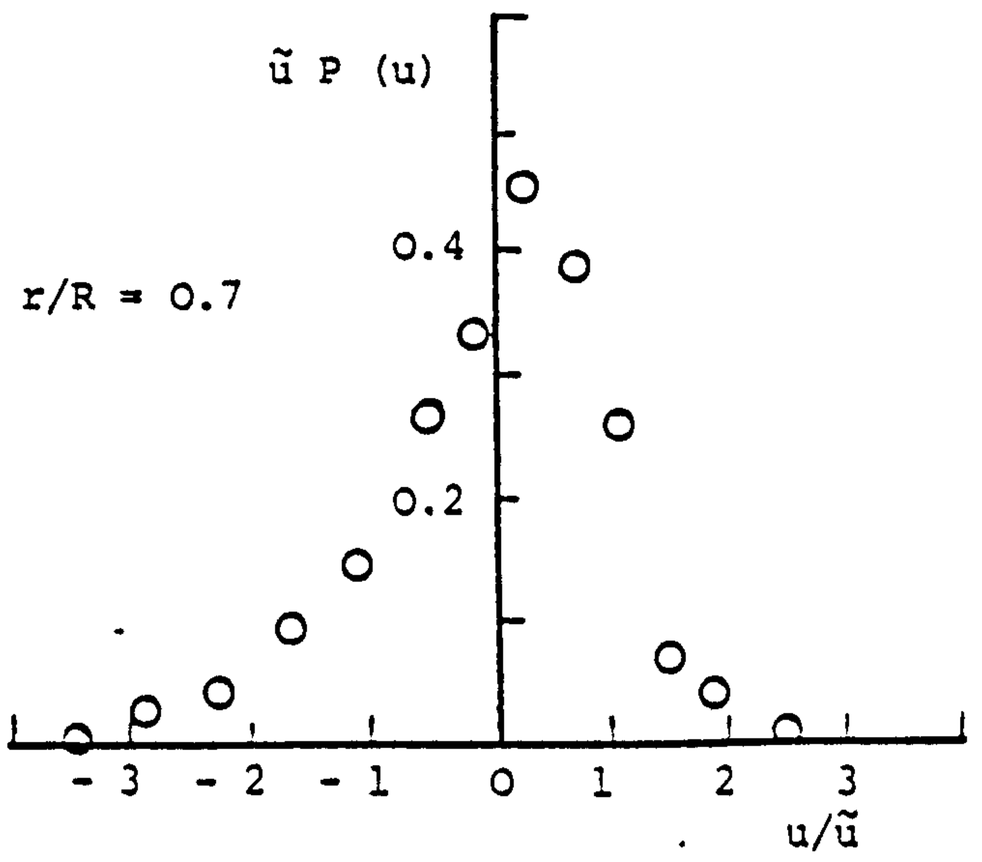


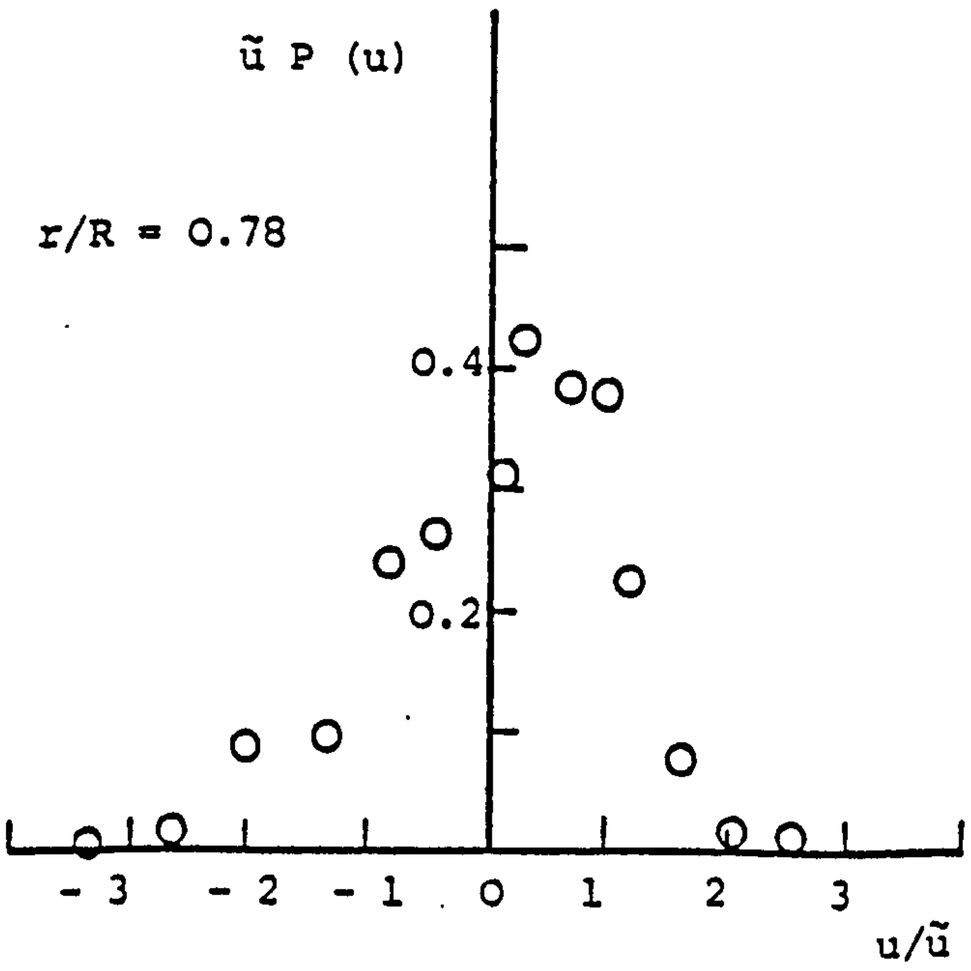
Fig. 2.35 Radial Distributions of the Probability Density of the Axial Velocity Fluctuations ($\bar{U}_a/\bar{U}_p$ = 3.0, X/D_e = 0.616)











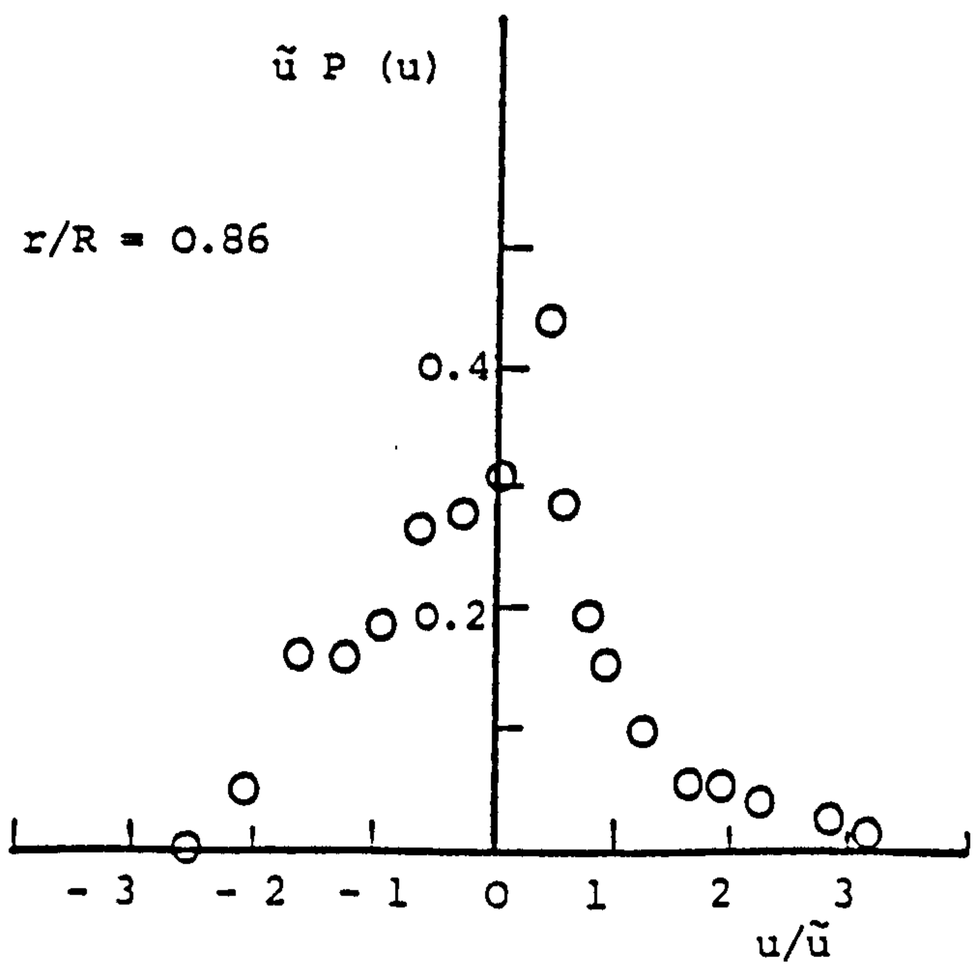


Fig. 2.35 (Continued)

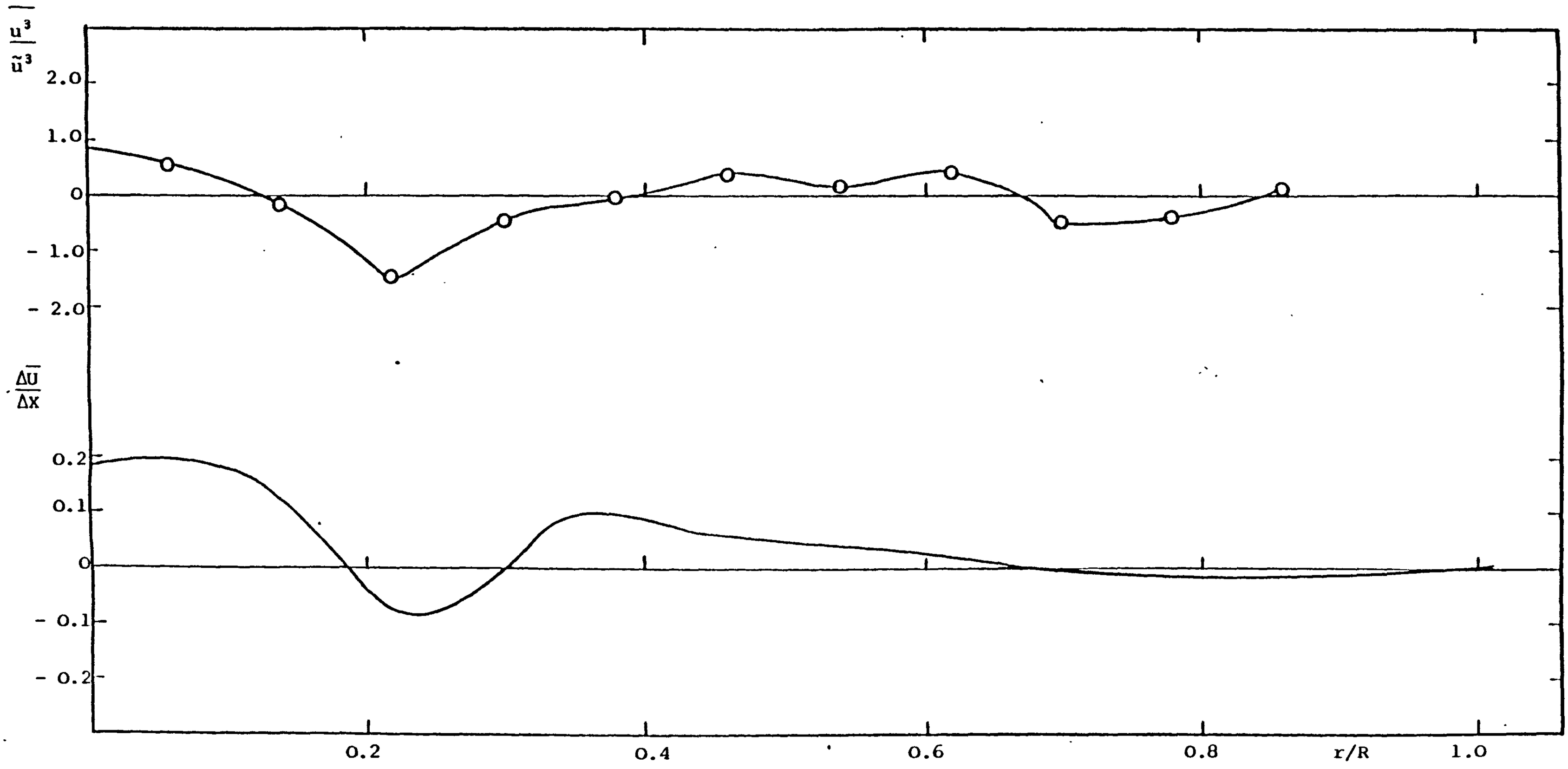


Fig. 2.36 Radial Distributions of Skewness Factor and Axial Velocity Gradient ($S = 0.0$, $U_a/\overline{U}_p = 3.0$, $X/D_e = 0.616$)

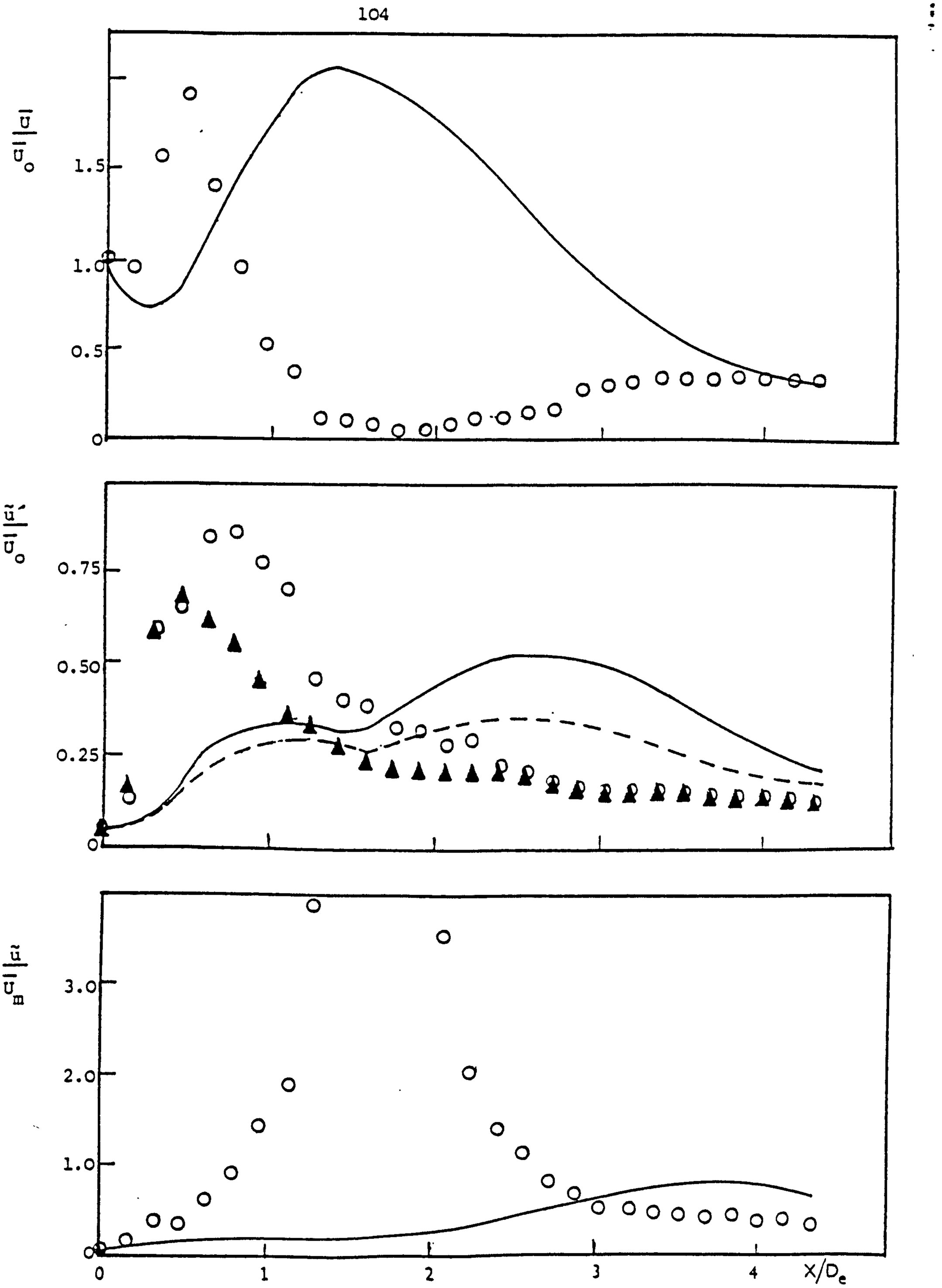


Fig. 2.37 Axial Distributions ($\overline{U}_a/\overline{U}_p$ = 3.0)

O, $\overline{u^2}$; ▲, $\overline{v^2}$ and $\overline{w^2}$ (S = 0.23)

——, $\overline{u^2}$;----, $\overline{v^2}$ and $\overline{w^2}$ (S = 0.0)

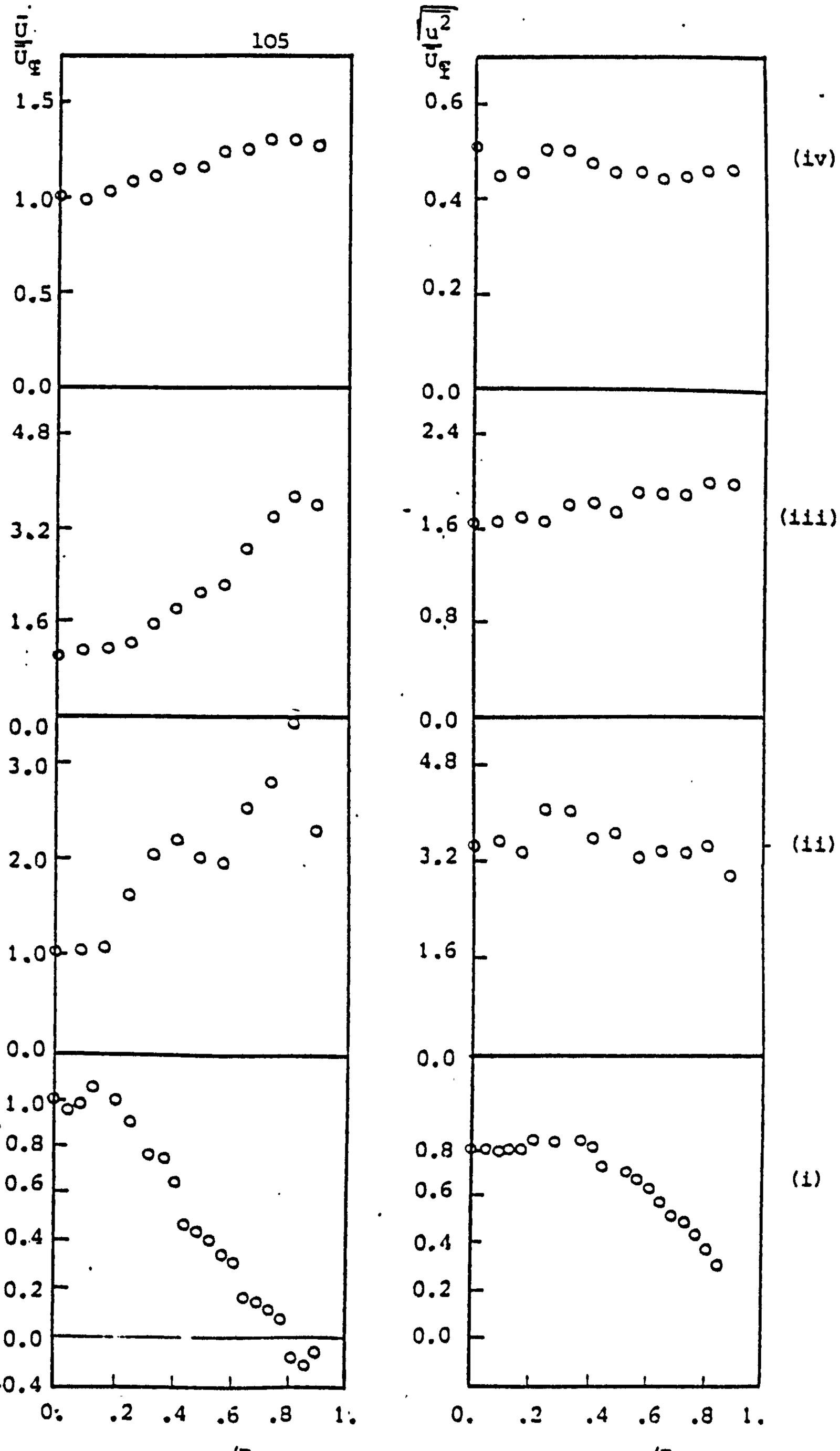


Fig. 2.38 Radial Distributions of The Axial Mean Velocity and Normal Stress (S=0.23) ;notation as in figure 2.26

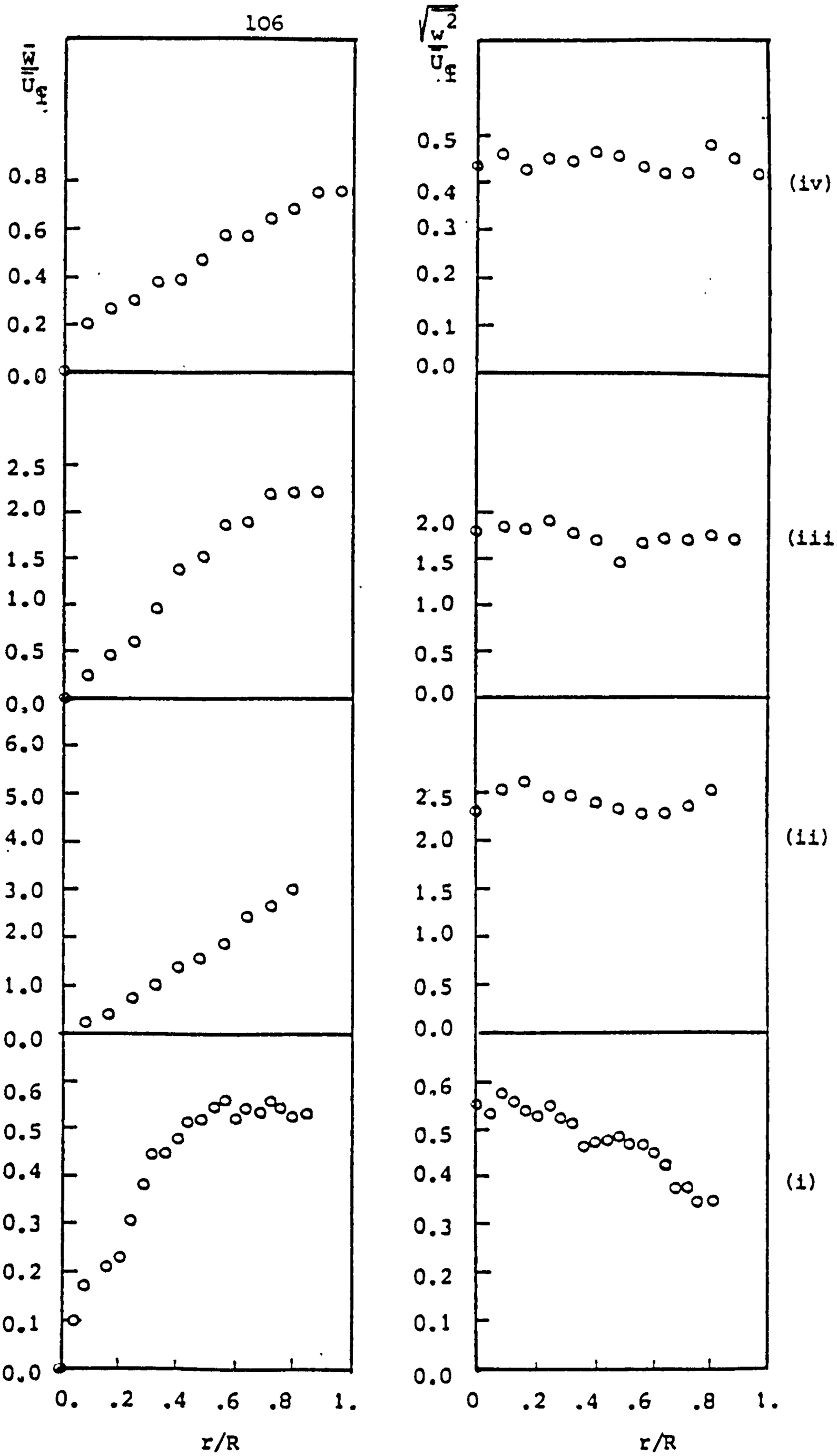


Fig. 2.39 Radial Distributions of Tangential Velocity and Normal Stress (S=0.23) ; notation as in figure 2.26

CHAPTER 3

CONFINED DOUBLE COAXIAL JETS WITH SUDDEN EXPANSION: COMPUTATIONAL INVESTIGATION

3.1 Introduction

This chapter describes the formulation of the mathematical problem and consists first of the differential equations which govern the transport of mass and momentum together with the equations which comprise the turbulence models. Three turbulence models have been used and are evaluated: the first requires the solution of the differential equations of the kinetic energy of turbulence and its dissipation rate; the second and third models require the solution of differential equations which govern the transport of the Reynolds stresses and the rate of dissipation of the kinetic energy of turbulence. The procedure for solving the equations is explained in Section 3.3 where the general form of the differential equations is represented and solved in a finite difference form with the help of boundary and inlet conditions which are explained in the same section. The section ends with an assessment of the accuracy of the solution procedure. The results of the calculations are then described and discussed in Section 3.4 which includes comparison between the calculated values of the mean velocity and turbulence components and the experimental results. The chapter ends with a summary of the more important concluding remarks.

3.2 The Governing Differential Equations

3.2.1 Continuity and Momentum Equations

For a Newtonian fluid with constant density and viscosity,

the conservation equations of mass and momentum which govern the turbulent motion of this fluid are:-

Mass Conservation: Continuity Equation

$$\frac{\partial U_j}{\partial x_j} = 0 \tag{3.1}$$

Momentum Conservation: Navier-Stokes Equation

$$\frac{\partial U_i}{\partial t} + \frac{\partial}{\partial x_j}(U_i\ U_j) = -\frac{1}{\rho}\frac{\partial P}{\partial x_i} + \nu_\ell \frac{\partial^2 U_i}{\partial x_j^2} \tag{3.2}$$

These conservation equations which describe the instantaneous motion of a turbulent flow cannot be solved numerically (as opposed to the same equations for laminar flows) because of the inability of setting-up a grid fine enough to describe the flow. Small scale motions in a turbulent flow occur in eddies about 10^3 times smaller than a typical flow field dimension, thus requiring a number of nodes for adequate solution of the conservation equations far in excess of that available from present generation computers. The problem is circumvented by solving for the time-averaged properties of the flow only. It is fortunate that the design engineer is not interested in every detail of the turbulent motion, but mainly in the time-averaged velocity and pressure.

Thus, time-averaging Equations (3.1) and (3.2), the continuity and momentum equations could be expressed (Hinze, 1959) as:-

$$\frac{\partial \overline{U}_j}{\partial x_j} = 0 \tag{3.3}$$

Momentum Equation

$$\frac{\partial}{\partial x_j}(\overline{U}_i\,\overline{U}_j) = -\frac{1}{\rho}\frac{\partial P}{\partial x_i} + \frac{\partial}{\partial x_j}\left(\nu_\ell \frac{\partial \overline{U}_i}{\partial x_j} - \overline{u_i u_j}\right) \tag{3.4}$$

These are two very important equations; they govern the mean motion and will, therefore, in one form or another, be part of any prediction method which does not solve the time-dependent equations. The new term $\overline{u_i u_j}$ represents the transfer of momentum by the turbulent motion. The appearance of this correlation introduces an additional unknown in each equation. In order to close the set of equations a means for evaluating $\overline{u_i u_j}$ must be found.

3.2.2 Equation for the Reynolds Stresses

An equation for $\overline{u_i u_j}$ can be obtained, see Hinze (1959), if Equation (3.4) is subtracted from Equation (3.2) for both the components i and j, multiplying the resulting equations for i and j components by u_j and u_i, respectively and summing the two equations and averaging. The resulting equation for $\overline{u_i u_j}$ can be expressed as:-

$$\overline{U}_k \frac{\partial \overline{u_i u_j}}{\partial x_k} = \frac{\partial}{\partial x_k}\left[\nu_\ell \frac{\partial \overline{u_i u_j}}{\partial x_k} - \overline{u_i u_j u_k} - \overline{\frac{p}{\rho}(\delta_{jk}\,u_i + \delta_{ik}\,u_j)}\right] -$$

Convection Diffusion

$$- \left[\overline{u_j u_k}\frac{\partial \overline{U}_i}{\partial x_k} + \overline{u_i u_k}\frac{\partial \overline{U}_j}{\partial x_k}\right] + \overline{\frac{p}{\rho}\left(\frac{\partial u_i}{\partial x_j} + \frac{\partial u_j}{\partial x_i}\right)} - 2\nu_\ell \overline{\frac{\partial u_i}{\partial x_k}\frac{\partial u_j}{\partial x_k}} \tag{3.5}$$

Production Pressure strain Dissipation

This equation, in turn, introduces new unknowns in the form of the higher order correlations represented in the turbulent diffusion, pressure-strain and dissipation terms. Transport equations can be derived from the Navier-Stokes equations for these higher order correlations, however, correlations of the next higher order will appear.

3.2.3 Turbulence Models

In order to obtain the value of $\overline{u_i u_j}$ in the momentum equation and close the system of the equations some of the correlations are usually approximated in terms of quantities that can be calculated. These approximations form the basis for turbulence modelling. A convenient classification of turbulence models uses the number of equations which must be solved in addition to the continuity and momentum equations; zero-, one- and two-equation models are often called "effective viscosity" models and directly approximate the value of $\overline{u_i u_j}$ as a function of the mean rate of strain through the Boussinesq (1877) equation:-

$$- \rho \overline{u_i u_j} = \mu_t \left(\frac{\partial \bar{U}_i}{\partial x_j} + \frac{\partial \bar{U}_j}{\partial x_i} \right) - \frac{2}{3} \rho K \delta_{ij} \qquad (3.6)$$

The effective viscosity is the sum of the molecular viscosity, μ_ℓ and the turbulent viscosity, μ_t. All the terms in Equation (3.6) are known except the turbulent viscosity which has to be specified. Zero-equation models usually specify μ_t through the length scale which is, in turn, prescribed in algebraic form and a characteristic velocity scale which is equal to $\ell \left|\partial U/\partial y\right|$ and so the expression for μ_t is:-

$$\mu_t = \rho \ell^2 \left| \frac{\partial U}{\partial y} \right| \qquad (3.7)$$

One-equation models employ $K^{1/2}$ as the velocity scale where $K \equiv \frac{1}{2}\overline{u_i^2}$ is the turbulence kinetic energy; thus:-

$$\mu_t = \rho K^{1/2} \ell \qquad (3.8)$$

ℓ is specified algebraically but K is to be found by solving a transport equation which can be obtained from Equation (3.5) by the summation of equations for $\overline{u_i^2}$. If ℓ is to be obtained by solution of a transport equation, the model will be called a two-equation model. Only one two-equation model will be discussed; more details may be found in Rodi (1972). The models of turbulence used in the present calculations are explained in the following two subsections.

(i) Two-equation Model

If, in Equation (3.8), ℓ is expressed as:-

$$\ell = c_\mu K^{3/2}/\varepsilon \qquad * \qquad (3.9)$$

where ε is the rate of dissipation of the turbulence energy and c_μ is a constant, then the turbulent viscosity can be expressed as:-

$$\mu_t = \rho c_\mu K^2/\varepsilon \qquad (3.10)$$

---

* This equation is valid for flows of high Reynolds number, where the rate of energy dissipation is supposed to be dependent on ℓ and K. For dimensional consistency, it follows that the length scale is of the form given (see Launder and Spalding, 1972).

To close the set of equations, transport equations for K and ε can be derived as follows.

K-equation

The exact form of the equation of the kinetic energy of turbulence, in high Reynolds number, is easily obtained from Equation (3.5) by summing the correlations $\overline{u_i u_i}$:-

$$\frac{\partial K\bar{U}_j}{\partial x_j} = \frac{\partial}{\partial x_j}\left[\nu_\ell \frac{\partial K}{\partial x_j} - \overline{u_j\left(\frac{u_i u_i}{2} + \frac{p}{\rho}\right)}\right] - \overline{u_i u_j}\frac{\partial \bar{U}_i}{\partial x_j} - \overline{\nu_\ell \left(\frac{\partial u_i}{\partial x_j}\right)^2} \qquad (3.11)$$

Convection Diffusion Production Dissipation

It should be noted that the pressure strain term which distributes the energy among the Reynolds stress components has disappeared in the above equation and only the diffusion term is modelled, by analogy with laminar transport and the assumption that K diffuses down its gradient, as:-

$$\nu_\ell \frac{\partial K}{\partial x_j} - \overline{u_j\left(\frac{u_i u_i}{2} + \frac{p}{\rho}\right)} = \left(\nu_\ell + \frac{\nu_t}{\sigma_K}\right)\frac{\partial K}{\partial x_j} \qquad (3.12)$$

where σ_K is a diffusion constant.

The dissipation of turbulent kinetic energy occurs predominantly in the smallest eddies and, at high Reynolds numbers, these eddies are very much smaller than the energy containing motions. Then, the rate at which energy is fed into these eddies (which is equal to the rate of dissipation) is governed by the larger eddies. At large Reynolds numbers, the rate of dissipation, $\varepsilon \equiv \overline{\nu_\ell (\partial u_i/\partial x_j)^2}$, is, therefore, independent of the molecular viscosity and can be

expressed (Kolmogorov, 1942) in the form:-

$$\varepsilon = c_\mu K^{3/2}/\ell \tag{3.13}$$

Introduction of Equations (3.12) and (3.13) into Equation (3.11), yields an equation for the kinetic energy of turbulence:-

$$\frac{\partial}{\partial x_j}(K\bar{U}_j) = \frac{\partial}{\partial x_j}\left[\frac{\nu_{eff}}{\sigma_K}\frac{\partial K}{\partial x_j}\right] - \overline{u_i u_j}\frac{\partial \bar{U}_i}{\partial x_j} - \varepsilon \tag{3.14}$$

with $\overline{u_i u_j}$ determined from Equation (3.6).

ε-equation

An exact equation for the rate of dissipation can be obtained by taking the derivative of equation of motion for u_i with respect to x_ℓ, then multiplying through by $2\nu\ \partial u_i/\partial x_\ell$ and ensemble averaging (see Daly and Harlow, 1970), i.e.:-

$$\bar{U}_j\frac{\partial \varepsilon}{\partial x_j} = \underbrace{\frac{\partial}{\partial x_j}\left[\nu_\ell\frac{\partial \varepsilon}{\partial x_j} - \overline{u_j\varepsilon'} - \overline{\frac{2\nu_\ell}{\rho}\frac{\partial u_j}{\partial x_\ell}\frac{\partial p}{\partial x_\ell}}\right]}_{\text{Diffusion}} - \underbrace{2\nu_\ell\overline{\frac{\partial u_i}{\partial x_j}\frac{\partial u_i}{\partial x_\ell}\frac{\partial u_j}{\partial x_\ell}}}_{\text{Production}} - \underbrace{2\overline{\left(\nu_\ell\frac{\partial^2 u_i}{\partial x_j \partial x_\ell}\right)^2}}_{\text{Destruction}}$$

$$\underbrace{- 2\nu_\ell\left[\overline{\frac{\partial u_i \partial u_j}{\partial x_\ell \partial x_\ell}} + \overline{\frac{\partial u_\ell \partial u_\ell}{\partial x_i \partial x_j}}\right]\frac{\partial \bar{U}_i}{\partial x_j} - 2\nu_\ell\,\overline{u_j\frac{\partial u_i}{\partial x_\ell}}\frac{\partial^2 \bar{U}_i}{\partial x_j \partial x_\ell}}_{\text{Other terms (to be omitted at high Reynolds number)}} \tag{3.15}$$

An order of magnitude analysis made by Tennekes and Lumley (1972) shows that the generation and destruction terms in Equation (3.15) far outweigh all other terms; their difference, however, is of same magnitude

as the diffusion term. At high Reynolds number, the diffusion term and the difference between the generation and destruction in Equation (3.15) were approximated (see Launder and Spalding, 1972 and Hanjalic and Launder, 1972) and the equation for ε expressed as:-

$$\bar{U}_j \frac{\partial \varepsilon}{\partial x_j} = \frac{\partial}{\partial x_j}\left(\frac{\nu_{eff}}{\sigma_\varepsilon}\frac{\partial \varepsilon}{\partial x_j}\right) + c_{\varepsilon_1}\frac{\varepsilon}{K}\overline{u_i u_j}\frac{\partial \bar{U}_i}{\partial x_j} - c_{\varepsilon_2}\frac{\varepsilon^2}{K} \qquad (3.16)$$

The first term on the right hand side represents the diffusive transport while the last two terms represent the difference between the production and destruction terms in Equation (3.15). c_{ε_1}, c_{ε_2} and σ_ε are constants.

Equations (3.14) and (3.16) constitute a two-equation model which forms, together with the continuity and momentum equations, Equations (3.3) and (3.4) and the auxiliary relations Equations (3.6) and (3.10), a closed set of equations. The two-equation model is suitable for many flows because of its comparatively smaller computing time and core size required for the solution of a number of equations which is small in this model compared with higher order closures (Rodi, 1972). However, the more important assumption of isotropic-viscosity becomes progressively worse as the flow departs from homogeneity. On the other hand, it has been found that it is difficult to specify fixed values of the constants incorporated in the model to specify more general flows; for example, the same set of constants cannot be used for the prediction of plane and round jets (see Rodi, 1972 and Spalding, 1975).

(ii) Five-equation Models

Models of this type incorporate a separate transport equation for each of the three normal stresses, the shear stress and the dissipation rate. The exact forms of these equations are given

by Equations (3.5) and (3.15). Both of the two equations include unknown terms of higher order moments which need to be expressed by known quantities. Two models (will be called hereafter Model II and Model III)* will be discussed; they differ only in the modelled form of the pressure-strain term of Equation (3.5). The first modelled form of the pressure-strain term (incorporated in Model II) was proposed by Rotta (1951) and Launder et al (1975) as:-

$$R_{ij} \equiv \overline{\frac{p}{\rho}\left(\frac{\partial u_i}{\partial x_j} + \frac{\partial u_j}{\partial x_i}\right)} = - c_1 \left(\frac{\varepsilon}{K}\right)\left(\overline{u_i u_j} - \frac{2}{3}\delta_{ij} K\right) - c_2\left(G_{ij} - \frac{2}{3} G \delta_{ij}\right) \tag{3.17}$$

The second (incorporated in Model III) was also proposed by Launder et al (1975) as:-

$$R_{ij} \equiv \overline{\frac{p}{\rho}\left(\frac{\partial u_i}{\partial x_j} + \frac{\partial u_j}{\partial x_i}\right)} = - c_1 \left(\frac{\varepsilon}{K}\right)\left(\overline{u_i u_j} - \frac{2}{3}\delta_{ij} K\right) - \frac{c_2 + 8}{11}\left(G_{ij} - \frac{2}{3} G \delta_{ij}\right) -$$

$$\frac{30\, c_2 - 2}{55} K \left(\frac{\partial \bar{U}_i}{\partial x_j} + \frac{\partial \bar{U}_j}{\partial x_i}\right) - \frac{8\, c_2 - 2}{11}\left(D_{ij} - \frac{2}{3} G \delta_{ij}\right) \tag{3.18}$$

where:-

$$\left.\begin{aligned} G_{ij} &= - \left[\overline{u_i u_k}\frac{\partial \bar{U}_j}{\partial x_k} + \overline{u_j u_k}\frac{\partial \bar{U}_i}{\partial x_k}\right] \\ D_{ij} &= - \left[\overline{u_i u_k}\frac{\partial \bar{U}_k}{\partial x_j} + \overline{u_j u_k}\frac{\partial \bar{U}_k}{\partial x_i}\right] \\ G &= \frac{1}{2} G_{ii} \\ &\text{and } c_1 \text{ and } c_2 \text{ are constants} \end{aligned}\right\} \tag{3.19}$$

---

* The two-equation model is referred to as Model I.

The common part of the two forms has a magnitude proportional to the anisotropy. The second term in the right hand side of the two forms tends to counteract anisotropy by diminishing the effects of anisotropic production.

The diffusion term in Equation (3.5), $(\partial/\partial x_k)\ (\overline{u_i u_j u_k})$, is connected to the convection of the turbulence energy by turbulent movements and was obtained from employing the gradient diffusion hypothesis proposed by Daly and Harlow (1970) (also by severe simplification of the exact transport equation for $\overline{u_i u_j u_k}$ by Launder et al, 1975) as:-

$$-\overline{u_i u_j u_k} = c_s \frac{K}{\varepsilon} \overline{u_k u_\ell} \frac{\partial \overline{u_i u_j}}{\partial x_\ell} \qquad (3.20)$$

where c_s is a constant.

Neglecting the remaining diffusion terms, which represent the transport by molecular interactions and pressure-induced diffusion:-

$$\frac{\partial}{\partial x_k}\left(\nu \frac{\partial \overline{u_i u_j}}{\partial x_k}\right) \quad \text{and} \quad \frac{\partial}{\partial x_k}\left(\overline{\frac{p}{\rho}(\delta_{jk} u_i + \delta_{ik} u_j)}\right) \quad \text{respectively}$$

the final equation for the Reynolds stresses can be expressed as:-

$$\frac{\partial}{\partial x_\ell}(\bar{U}_\ell\ \overline{u_i u_j}) = c_s \frac{\partial}{\partial x_k}\left(\overline{u_\ell u_k} \frac{\partial \overline{u_i u_j}}{\partial x_k}\right) + G_{ij} + R_{ij} - \frac{2}{3}\varepsilon\ \delta_{ij} \qquad (3.21)$$

The dissipation equation was developed from its exact form, Equation (3.15), by Hanjalic and Launder (1972):-

$$\frac{\partial}{\partial x_j}(\bar{U}_j\,\varepsilon) = c_\varepsilon \frac{\partial}{\partial x_j}\left(\frac{K}{\varepsilon}\overline{u_j u_\ell}\frac{\partial \varepsilon}{\partial x_\ell}\right) - c_{\varepsilon_1}\frac{\varepsilon}{K}\overline{u_i u_j}\frac{\partial \bar{U}_i}{\partial x_j} - c_{\varepsilon_2}\frac{\varepsilon^2}{K} \qquad (3.22)$$

It differs from the form of the two-equation model, Equation (3.16), in the modelled form of the diffusion term.

Equation (3.21) as presented for three normal stresses and one shear stress together with Equation (3.22) and the continuity and momentum equations of Equations (3.3) and (3.4) represent two Reynolds-stress models.

The equations* of the three models described in (i) and (ii) were solved in the manner which is described in Section 3.3 to yield three different solutions of the flow in the confined double coaxial jet. The results of the three models are compared and evaluated with the experimental results of Chapter 2 in Section 3.4. The solution of the above equations required the specification of the appropriate inlet and boundary conditions.

3.2.4 The Inlet and Boundary Conditions

In addition to the set of equations represented in (i) and (ii) of Subsection 3.2.3, the complete specification of the mathematical problem requires the determination of the inlet and boundary conditions.

(i) Inlet Conditions

All the variables have to be specified at the inlet to the furnace model. The distributions of experimentally-determined

---

* The equations quoted here in terms of Cartesian tensors are expanded in cylindrical-polar coordinates in Appendices A4 and A5.

velocities at the inlet to the model furnace were supplied as a function of radial position and the maximum pipe (or annulus) inlet velocity, Fig. 3.1a. The kinetic energy distribution was also specified as a function of the grid position according to the results of measurements, Fig. 3.1b. The dissipation rate was determined on the basis of a mixing length, i.e.:-

$$\varepsilon = c_\mu \frac{K^{3/2}}{\ell}$$

where $\ell = 0.03\ R$. In the case of five-equation turbulence models, the kinetic energy was divided between the three normal stresses while the shear stress was determined from the experimental measurements, Fig. 3.1c.

(ii) Boundary Conditions

All axial gradients ($\partial/\partial x$) were presumed zero in the exit plane of the confining tube, $x/D_e \tilde{\sim} 4.8$; this assumption presumes developed boundary-layer flow at the exit section which is confirmed by the measurements, see Fig. 2.30, Chapter 2. A symmetry axis was specified with $\overline{V} = \overline{uv} = 0$ and $\partial/\partial y$ of all other quantities = 0 on $y = 0$. Zero velocities were specified on all solid surfaces.

Partly to economize computer time requirements, logarithmic wall functions were used to link the near-wall grid lines to wall boundaries, see Launder and Spalding (1973), thus:-

$$\tau_w = \frac{\overline{U}_p}{y_p} \frac{\mu_\ell\ \kappa\ y_p^+}{\ell n\ (E_1\ y_p^+)} \quad , \quad \text{where } y_p^+ = c_\mu^{1/4}\ K_p^{1/2}\ y_p/\nu_\ell \qquad (3.23)$$

where subscript, p, refers to the near-wall node. κ and E_1 are the

wall law constants and take the values 0.419 and 9.8 respectively.

The value of the kinetic energy of turbulence at point p, K_p, is calculated from the transport equation of K with the flux of energy to the solid wall set to zero. The corresponding value of the dissipation of K, ε, was prescribed by:-

$$\varepsilon_p = (c_\mu^{1/2} K_p)^{3/2}/\kappa y_p \tag{3.24}$$

and the integral of ε from the wall to y_p, which is required for the kinetic energy or the Reynolds stress equations is given by:-

$$\int_0^{y_p} \varepsilon \, dy = (c_\mu^{1/2} K_p)^{3/2} \frac{1}{\kappa} \ell n \, (E_1 y_p^+) \tag{3.25}$$

The values of constants used in the above subsections are shown in Table 3.1. The constants of Model I are identical to those of Launder et al (1972) and were used for the prediction of recirculating flows, see for example Khalil et al (1975). The choice of these constants is based on a comparison between some solutions and the appropriate experimental data, Launder and Spalding (1972). The coefficients of Models II and III were derived by making comparison with the data of grid turbulence, shear flow turbulence and a wide range of two-dimensional boundary layers, Launder et al (1975), and were applied to axisymmetric flow cases by Naot and Launder (1975) and to recirculating flow behind bluff body by Pope and Whitelaw (1976).

3.3 The Solution Procedure

From the preceding sections we see that the differential equations are non-linear and coupled. In most practical situations

TABLE 3.1

CONSTANTS OF EQUATIONS

OF SUBSECTION 3.2.3

Constant \ Model	I	II	III
c_μ	0.09	-	-
σ_K	1.00	-	-
σ_ε	1.22	-	-
c_s	-	0.25	0.25
c_ε	-	0.15	0.15
c_1	-	2.50	1.50
c_2	-	0.40	0.40
c_{ε_1}	1.44	1.45	1.45
c_{ε_2}	1.92	1.92	1.92

there is no possibility of obtaining analytical solutions to them and numerical methods are required. In this section, details are provided of a numerical scheme which was used to solve for the velocity and pressure fields. The numerical scheme is similar to that described by Patankar et al (1972) and is based upon the derivation of finite difference equations by integrating the differential equations over finite control volumes. The features of the present computational procedure are explained in the following subsections.

3.3.1 The Grid System and Location of Variables

A rectangular field is considered, with the coordinates x

and y in the axial and radial directions respectively and the x-axis is taken along the axis of symmetry. The finite difference grids are formed over the region of interest by lines running parallel to both the x-axis and the y-axis. Where the two sets of perpendicular grid lines intersect are the "nodes", where flow properties (except $\overline{U}$, $\overline{V}$ and $\overline{uv}$) are to be evaluated. Fig. 3.2 shows part of a finite difference grid where the variables are assumed known at the nodes P, N, S, E and W. Near the boundaries, the side of the finite difference grid coincides with the domain boundary. As shown from the figure, the $\overline{U}$ and $\overline{V}$ nodes are located at the boundaries of the scalar cells. This "staggered grid" system has the advantage that the variables $\overline{U}$, $\overline{V}$ and P are stored such that the pressure gradients which drive the velocities $\overline{U}$ and $\overline{V}$ are easy to be evaluated. Moreover, the velocities are located where they are needed for the calculation of convective fluxes. The location of $\overline{uv}$ node at the corner of the cell was found (Pope and Whitelaw, 1976) to preserve a strong link between the stress and rate of strain and so provide numerical stability in the solution of the Reynolds-stress equations, Models II and III. The finite difference grids for $\overline{U}$ and $\overline{V}$ and $\overline{uv}$ near the boundaries are extended to cover the calculation domain as shown in Fig. 3.3.

3.3.2 The Finite Difference Equations

The equations of Section 3.2 may be expressed in the general form:-

$$\frac{\partial}{\partial x}(\rho\overline{U}\Phi) + \frac{1}{r}\frac{\partial}{\partial r}(r\rho\overline{V}\Phi) - \frac{\partial}{\partial x}\Gamma_x\left(\frac{\partial\Phi}{\partial x}\right) - \frac{1}{r}\frac{\partial}{\partial y}\left(r\Gamma_y\frac{\partial\Phi}{\partial r}\right) = S_\Phi \qquad (3.26)$$

where Φ stands for the time averaged value of any of the variables mentioned earlier, Γ_x and Γ_y are the corresponding exchange

coefficients and S_Φ is the source term of Φ. Equation (3.26) may be integrated over the indicated control volume of Fig. 3.2 to give:-

$$\left[\int_{y^-}^{y^+} r\left(\rho\bar{U}\Phi - \Gamma_x \frac{\partial\Phi}{\partial y}\right) dy\right]_{x^-}^{x^+} + \left[\int_{x^-}^{x^+} r\left(\rho\bar{V}\Phi - \Gamma_y \frac{\partial\Phi}{\partial y}\right) dx\right]_{y^-}^{y^+} =$$

$$= \int_{y^-}^{y^+}\int_{x^-}^{x^+} S_\Phi \, r \, dx \, dy \qquad (3.27)$$

The following approximations may be made for the convection terms:-

$$\int_{y^-}^{y^+} r\rho\bar{U}\Phi \, dy\Big|_{x^-} = \rho\bar{U}\Big|_{x^-}\left[f_w \Phi_P + (1 - f_w)\Phi_W\right]\int_{y^-}^{y^+} r \, dy = c_{x^-}\left[f_w \Phi_P + (1 - f_w)\Phi_W\right]$$

(3.28)

For the diffusion terms*:-

$$\int_{y^-}^{y^+} r\Gamma_x \frac{\partial\Phi}{\partial x} dy\Big|_{x^-} \simeq \Gamma_{x^-} \frac{\Phi_P - \Phi_W}{x_p - x_w}\int_{y^-}^{y^+} r \, dy = D_{x^-}(\Phi_P - \Phi_W) \qquad (3.29)$$

Source terms are expressed by linear relation:-

$$\int_{y^-}^{y^+}\int_{x^-}^{x^+} rS_\Phi \, dx \, dy \simeq S_u + S_p \Phi_P \qquad (3.30)$$

---

* The same treatment cannot be applied to the Reynolds stress closures because they do not provide an explicit relationship between stress and rate of strain. Consequently, the terms of the Reynolds stress gradients $\partial(u_i u_j)/\partial x_j$ is included in the source and the diffusivities are set to zero. This modification of the numerical scheme of Patankar and Spalding (1972) was found necessary in the solution of the Reynolds stress equations, Pope and Whitelaw (1976).

where f_w is the weight factor relating the position of the finite difference grid boundary to the location of the points p and E. Similar approximations can be obtained for all the remaining terms of Equation (3.26) to give:-

$$A'_W \Phi_{x^-} + A'_E \Phi_{x^+} + A'_S \Phi_{y^-} + A'_N \Phi_{y^+} = (A'_W + A'_E + A'_S + A'_N) \Phi_P$$

$$= S_u + S_p \Phi_P \qquad (3.31)$$

where $A'_W = -D_{x^-} + (1 - f_w) c_{x^-}$, $A'_E = D_{x^+} - f_e c_{x^+}$, etc., and f_w, f_e, etc. are the corresponding weighting factors for the different sides.

The finite difference coefficients are modified to a hybrid scheme, Gosman et al (1974), to compensate for unrealistic effects which result from the assumption of linear relation of Φ between the nodes. Accordingly, the coefficients can be expressed as:-

$$A_E = D^*_{x^+} - f_e c_{x^+}$$

where $D^*_{x^+} = \max \left[D_{x^+}, -(1 - f_e) c_{x^+}, f_e c_{x^+} \right]$ and the finite difference equation becomes:-

$$\Phi_P \left(\sum A_i - S_p \right) = \sum A_i \Phi_i + S_u \qquad (3.32)$$

In this method the exact expression (Gosman and Ideriah, 1976) was approximated by employing central difference for $-2 < Pe < 2$ and upwind differencing for $2 \leq Pe \leq -2$, so as the flux for the west boundary, for example, can be expressed as:-

$$\dot{q}_w = c_{x^+} \left(f\ \Phi_W + (1 - f)\ \Phi_P \right) \tag{3.33}$$

where:-

$$f = \frac{1}{2}\left(1 + \frac{1}{Pe}\right) \qquad \text{for } -2 < Pe < 2$$

$$f = 1 \qquad \text{for } Pe \geq 2$$

$$f = 0 \qquad \text{for } Pe \leq -2$$

where Pe is the Peclet number defined as $\rho\ \bar{U}_w\ \delta_x/\mu_{eff}$ where δ_x is a characteristic dimension of the cell in the velocity direction.

3.3.3 The Solution Algorithm

Equation (3.32), written for each variable at each grid node with the pressure known, yields a closed set of algebraic equations. These equations can be solved by tri-diagonal algorithm which is an iterative, line-by-line procedure (Patankar and Spalding, 1972). With guessed or assumed pressure values, P*, the momentum equations can be solved to obtain a first estimate of the velocity field. However, there was no guarantee that the resultant velocity field, $\bar{U}^*$ and $\bar{V}^*$, would satisfy the continuity equation. Thus, if the correct velocities and pressure, $\bar{U}$, $\bar{V}$ and P are defined as:-

$$\left.\begin{aligned} \bar{U} &= \bar{U}^* + \bar{U}' \\ \bar{V} &= \bar{V}^* + \bar{V}' \\ P &= P^* + P' \end{aligned}\right\} \tag{3.34}$$

and substituted into the momentum equation, a pressure correction

equation will be obtained (for more details see Patankar and Spalding, 1972); $\overline{U}'$, $\overline{V}'$ and P' are the corrections. The resulting equation can be solved and the values of pressure and velocities corrected. The procedure is repeated until convergence is obtained.

3.3.4 Remarks on the Numerical Procedure

(i) Stability

Because of the non-linearities of the partial differential equations and the strong inter-linkages between them, numerical instability may develop leading to divergence of the solution during the computations. In general, the initial conditions were chosen in a way to minimize the instability in the first number of iterations, for example, the mean velocity was ensured to satisfy the continuity along the furnace model. In the case of the Reynolds-stress models, the initial values were taken as the result of the solution by K-ε model to increase the stability of the procedure: as indicated by Fig. 3.4, the solution of the Reynolds stress models was begun with initial values obtained from the solution by Model I with a convergence factor, defined below, of 2%. Under-relaxation factors were used to suppress the large fluctuations in the Φ's values as follows:-

$$\Phi = \Phi_{old} + (1 - \alpha)\ \Phi_{new} \qquad (3.35)$$

where α is the under-relaxation factor ; these are given for each variable in Table 3.2.

(ii) Convergence

The solution procedure used an iterative method and convergence

TABLE 3.2

VALUES OF UNDER-RELAXATION FACTORS

	U and V	K	ε	$\overline{u^2}$	$\overline{v^2}$	$\overline{w^2}$	$\overline{uv}$	μ_{eff}
α (K $\sim$ ε model)	0.5	0.7	0.7	-	-	-	-	0.7
α (Reynolds-stress models)	0.5	-	0.4	0.3	0.3	0.3	0.2	-

was assessed at the end of each iteration with a convergence factor which equals the residual source of each finite difference equation normalised by the fixed flux of the relevant extensive property fed into the domain of calculation. The results were considered accurate when the convergence factor was less than 0.1%; the under-relaxation factors explained above were helpful to improve the convergence. The convergence factor is plotted against the number of iterations for the 24 x 18 grid on Fig. 3.4. It is clear from the figure that the number of iterations and, consequently, the computation time required by the Reynolds-stress models is larger than that of the K $\sim$ ε model to achieve the same convergence. The figure indicates also that the rate of decay is much larger in the case of the solution of Model I which is probably due to the lesser number of equations interconnected in the model.

(iii) Accuracy

The accuracy of the calculation method is a function of convergence and grid. With the small convergence factor considered above, the errors due to this source are very small and the changes

in the variables from one iteration to another are less than 0.01%. The second error occurs when Peclet number is large and the flow is inclined to its mesh with resulting "false diffusion" which is caused by the truncation error incurred in the Taylor series expansion from which the finite difference equations are implicitly derived and by large cross-stream spatial variations of velocity. The effect on calculations can be serious where the mean flow component is not aligned with the grid direction. The problem has been examined by, among others, Wolfshtein (1969), Gosman et al (1969) and Raithby (1976). The last author has provided a critical evaluation of the problem, particularly in connection with upwind differencing. Thus, Raithby (1976) shows that the most serious source of numerical diffusion for types of flows considered here arise, in situations where convection occurs at an angle to the grid lines and when the cell Peclet number is large. For $|Pe| < 2$, the hybrid-difference scheme (Gosman and Pun, 1974) incorporated in the present numerical procedure reduces to a central-difference scheme for which numerical diffusion becomes small (see Raithby, 1976).

An estimate of the ratio of false (or numerical) to real diffusion can be shown to be given by the expression (Gosman et al, 1969):-

$$\frac{(\mu/\rho)_f}{(\mu_{eff}/\rho)} = \frac{0.36\ hV\rho}{\mu_{eff}} \sin(2\alpha) = 0.36\ R_{\ell oc} \left(\frac{\mu_\ell}{\mu_{eff}}\right) \left(\frac{h}{L}\right) \sin 2\alpha \qquad (3.36)$$

h is the distance between grid lines in an equally spaced two-dimensional grid and V is the resultant velocity at an angle α to the grid lines. $R_{\ell oc} \equiv \rho VL/\mu_\ell$ is a Reynolds number based upon a typical length L of the problem considered.

False diffusion may be important, particularly for laminar flows with large values of $R_{\ell oc}$. When $R_{\ell oc}$ is large, the flow becomes turbulent, and then the effect will be diminished, for in turbulent flows μ_{eff} is usually much larger than μ_{ℓ}. For the present calculations, the flow was turbulent with high $R_{\ell oc}$ and high values for the effective viscosity. The present calculated results were obtained with a grid distribution comprising 24 x 18 nodes with concentrations of the nodes in the upstream region, in the vicinity of the exits from the pipe and in the near wall regions. This number of nodes and their distribution were selected after experiments with fewer nodes and different distributions had indicated that the present arrangement led to results which are reasonably free from numerical errors. Thus, an increase in the number of grid nodes from 396 to 432 led to differences in calculated dependent variables which did not exceed 3% and the trend in values was monotonic for a number of nodes greater than 256.

Grid-dependent tests made with fewer (18 x 14) and larger (30 x 22) number of nodes than those of the present (24 x 18) grid are shown in Figs. 3.5 to 3.8. The figures show calculated values (obtained by Model I for velocity ratio of 3.0) of the mean axial velocity and the kinetic energy of turbulence along the centre-line and at the radial profile of $x/D_e = 0.616$. The results show that the numerical accuracy is reasonable even with a 18 x 14 grid.

(iv) Economy

The finite-difference equations were solved iteratively by a TEACH Fortran program on a CDC 6600 digital computer. The storage and time requirements differed from one model to another. The time consumption by each model is shown in Table 3.3; the increase in time in the Reynolds stress models, II and III, is due to the fact that the procedure solves for eight dependent variables rather than

TABLE 3.3

COMPUTING TIME TO ACHIEVE CONVERGENCE

Model	Number of Iterations	Total Time sec.	Time per Iteration per grid node sec.
I	277	198	0.0017
II	299	373	0.0028
III	333	422	0.0029

for five. The storage requirements by the two-equation model was 73% of that required by the Reynolds-stress models. The values shown in Table 3.3 are taken for the case of 3.0 velocity ratio: the values of time consumptions in the case of unity velocity ratio were slightly lesser.

3.4 The Calculation of Confined Double Coaxial Jets

3.4.1 Presentation and Discussion of the Results

In this section, a comparison is provided between the calculated results of the procedure described above and the data reported in Chapter 2. The calculations were obtained using three turbulence models; the first is a mean flow closure (two equation model, I), Equations (3.14) and (3.16) and the second, II and third, III are the two Reynolds-stress models with Equations (3.21) and (3.22). The two Reynolds-stress models differ from each other only in the redistribution terms, as explained above. The Reynolds-stress models are well-known but have not been evaluated for the prediction of recirculating flows, apart from the calculation of near-wake flows

of Pope and Whitelaw (1976).

The calculations with the three models were compared with the experimental measurements of Section 2.4 of Chapter 2 for the two velocity ratios, 3.0 and unity. The comparisons are made along the centre-line and at the two radial profiles, x/D_e = 0.616 and 3.67. They relate to the axial mean velocity, corresponding normal stress, kinetic energy of turbulence and shear stress. The general characteristics of the two flows investigated here are shown in Fig. 3.9 where mean velocity and kinetic energy contours are presented isometrically. The near-wall region of the flows is not well demonstrated by Fig. 3.9 but the mixing of the two jets and the decay of the velocity maxima are clearly represented. The higher velocity ratio jets mix and decay more rapidly than those for $\overline{U}_a/\overline{U}_p$ of unity. This is the same as indicated by experiments in Section 2.4.

The axial distributions of the axial mean velocity, normalised by the mean velocity value on the axis at the exit plane of the coaxial jets are compared with the measurements on Fig. 3.10. The calculated centre-line velocity distribution is in reasonable accord with the measurements except in the region immediately downstream of the exit in the case of the higher velocity ratio where the velocity is underpredicted especially with models II and III. Further downstream and at around x/d_o = 4.0, and again for the higher velocity ratio, the mean velocity maximum is underpredicted by about 15%. The discrepancy in the calculation by Model I has been attributed (see Habib and Whitelaw, 1979) to the incorrect representation of the turbulent diffusion process as a result of the isotropic-viscosity hypothesis and Fig. 3.10 shows that the same discrepancy occurs with the Reynolds-stress models. This may suggest that the mixing of the two jets is underpredicted since the increase in the mean velocity along the centre-line in the case of the higher velocity ratio is attributed to the diffusion of the flow

of the outer jet towards the centre-line. The discrepancies may be partly attributed to numerical accuracy in the calculation procedure. As can be shown from Fig. 3.5 that the numerical diffusion could be affecting the results slightly, thus accounting for some of the discrepancy appearing between calculation and experimental values: the decrease in the grid size led to more accurate distribution and the discrepancies were decreased slightly in regions at x/d_o of 0.5, 4.0 and 11. However, Fig. 3.10 indicates that the mean velocity in the case of unity velocity ratio is calculated more accurately than that of the higher velocity ratio.

Fig. 3.11 represents the distribution of the rms of the axial velocity fluctuations along the centre-line. The normal stress is underpredicted by all models; with the Reynolds-stress approach giving better accuracy in most regions. The differences between the three models are, however, small. The agreement improves in the downstream region where discrepancies are less than 10% at $x/D_e = 4.0$. The normal stress distributions predicted by the two Reynolds-stress models are nearly the same and are not affected by the difference in the forms of the redistribution terms. This difference was also observed to be small in the calculation of near-wake flows by Pope and Whitelaw (1976). It can be seen that the mean velocity and normal stress calculated by the two Reynolds-stress models are very similar, especially in the case of the unity velocity ratio.

The calculated values of the kinetic energy of turbulence are presented on Fig. 3.12 and apart from the upstream region, $x/D_e < 0.5$, the kinetic energy of turbulence is underpredicted by all the three models: the maximum value at $x/D_e \tilde{} 2.5$ is underpredicted by about 25%. However, the three models give the same result in the downstream region and the calculated values are more precise in that

region. The differences between calculated and experimental results may be attributed partly to numerical diffusion and partly to the forms of the diffusion and dissipation terms in the transport equations of K in model I or $\overline{u_i u_i}$ in models II and III. As can be shown from Fig. 3.6, the decrease in the grid size increased the value of K in most regions and the discrepancy in the calculated maximum value was decreased by the increase in the number of nodes. However, the discrepancies due to the grid size are not significant enough to explain the differences between calculations and measurements in Fig. 3.12. The form of the diffusion terms will be discussed later and it remains now to study the behaviour of the calculated rate of the dissipation of the turbulence kinetic energy.

The distribution of the rate of dissipation along the centre-line may be obtained from the microscales of Fig. 2.32 in Chapter 2 through the relation of isotropic turbulence, i.e.:-

$$\varepsilon = 15\ \nu_\ell\ \overline{u^2}/\lambda_x^2$$

These values of the rate of dissipation are presented on Fig. 3.13 together with the calculated values. The values along the centre-line are normalised by the value which is calculated from the measurements on the axis at the exit plane of the coaxial pipe arrangement. The rate of dissipation is overpredicted by the three models with the Reynolds-stress models of less discrepancies. Down-stream the location $x/d_o \simeq 10$, the calculations show good agreement with experiments. These results are consistent with those of Fig. 3.10 and the overprediction in the values of the rate of dissipation may explain the underestimated values of K along the centre-line. The overprediction of ε and underprediction of K near the centre-line are expected to decrease the transport in the momentum equation by

diffusion processes through the decrease in the effective viscosity, μ_{eff} ($\equiv \mu_t + \mu_\ell$) as shown from the relation $\mu_t = \rho\, c_\mu\, K^2/\varepsilon$, in model I and through the decrease in the level of the normal stresses in models II and III. This may clarify the underpredicted mixing of the two jets shown by Fig. 3.10 and discussed above.

Fig. 3.13 indicates that the inlet distribution of length scale has a large effect on the ε-distribution in the upstream region where the diffusion terms have a large effect in the momentum equations; it has no significant effect in the downstream region where the diffusion effects are smaller. Although the mixing length distribution formula by Nikuradse (see Launder and Spalding, 1972, p. 37):-

$$\ell_m/r_{p,a} = 0.14 - 0.08\,(r/r_{p,a})^2 - 0.06\,(r/r_{p,a})^4$$

where r_p, r_a are the characteristic radii of the pipe and annulus, respectively and with $\ell_o = c_\mu^{1/4}\ell_m$ as given by Launder and Spalding (1972) represents correctly the pipe flow value of rate of dissipation it results in an erroneously higher value downstream the exit plane. On the other hand, the formula relating the length scale to the radius of the confinement, although much higher than the pipe flow rate of dissipation, gives the best result.

Figs. 3.14 to 3.19 represent the radial profiles of the calculated and measured flow properties at $x/D_e = 0.616$. The comparison of the mean velocity, Figs. 3.14 and 3.15, indicates that the two Reynolds-stress models have nearly the same distribution for both the two velocity ratios. It can be concluded that the difference in the forms of the redistribution terms has no significant effect on the mean velocity distribution along the radius. The results of the Reynolds-stress models are more precise for unity velocity ratio and show better agreement than in the case of the higher velocity ratio. The $K \sim \varepsilon$ model predicts the velocity maximum in the 3 : 1 velocity

ratio case more accurately, but shows greater discrepancies in the region of rapid velocity decay, $0.4 < y/R < 0.6$. The width of the recirculation region is underpredicted by the three models with the Reynolds-stress models giving slightly smaller discrepancies and better representation of the mean velocity near the wall.

The rms of the axial fluctuating velocity is presented on Figs. 3.16 and 3.17 for the velocity ratios of 3.0 and unity, respectively. The normal stress is represented more precisely by the Reynolds-stress models in the case of unity velocity ratio and is underpredicted in the vicinity of the axis of symmetry, particularly for the higher velocity ratio. Pope and Whitelaw (1976) observed similar discrepancies in their calculations for the near-wake flows near the axis of symmetry. This may be explained, as noted by Spalding (1975), that the gradient assumption in any of the turbulence models breaks down near an axis of symmetry. The profiles of shear stress, Figs. 3.18 and 3.19, show that the changes in sign are correctly represented and that no one model can be identified as a clear improvement over any other. The discrepancy in the calculated shear stress around $r/R = 0.6$ may explain the corresponding discrepancy in the prediction of the mean velocity, Figs. 3.14 and 3.15.

The grid size distribution may be partly contributing to the deficiency near the centre-line: as shown by Figs. 3.7 and 3.8 that although the increase in the number of nodes from 24 x 18 to 30 x 22 has nearly no effect on the mean velocity it led to an increase in the value of $\sqrt{K}/\overline{U}_m$ by about 10% on the centre-line.

Figs. 3.20 to 3.25 allow comparison of the calculated flow properties with the measurements at a downstream section, x/D_e = 3.67 and show agreement with the experiments within 20% in the mean velocity and 50% in the normal stresses. The Reynolds stress models

represent the normal stress and the shear stress more precisely than the $K \sim \varepsilon$ model and the shear stress is predicted within 20% of the experimental value.

Figs. 3.26 and 3.27 present the distributions of the kinetic energy of turbulence for velocity ratio of 3.0 along the radii at x/D_e = 0.616 and 3.67, respectively. The experimental values were obtained by the summation of the individual normal stresses; $\overline{v^2}$ was assumed equal to $\overline{w^2}$. The $K \sim \varepsilon$ and Reynolds-stress models underpredict the kinetic energy of turbulence particularly near the centre-line in the upstream section.

3.4.2 Discussion

In the preceding subsection, the calculation procedure presented in Sections 3.2 and 3.3 was applied to the prediction of the flow of the confined double coaxial jets. Three models of turbulence, mean flow closure and two Reynolds-stress models, were evaluated in different flow conditions.

The calculations showed that the mean velocity was accurately represented by the three models with the maxima along the centre-line and radius underpredicted by around 20%, Figs. 3.10, 3.14 and 3.15. These discrepancies were attributed to the underprediction of the turbulent diffusion and this was confirmed by the underestimation of normal and shear stresses and their gradients as shown by Figs. 3.11, 3.16 - 3.19 and 3.22 - 3.25, particularly near the centre-line. The underestimation of the Reynolds stresses is likely to stem from incorrect representation of their values by the turbulence models.

In the case of the $K \sim \varepsilon$ model, the effective viscosity formulation (Boussinesq equation) is incorporated and assumes that the principal axes of the Reynolds stress tensor are parallel to the

principal axes of the strain rate tensor so that any change in the strain rate is directly felt in the stresses. This instantaneous change of the Reynolds stresses with the strain rates is not supported by the experimental observations because the Reynolds stresses, being due to the vorticity fluctuations, require some time to adjust to the new strain rates (Warsi and Amilicke, 1976; Rotta, 1979 and Bradshaw, 1973). The isotropic-viscosity formulation is, therefore, expected to lead to incorrect representation of the Reynolds stresses (or K) in the regions of high velocity gradients (regions of high rate of strains).

In the case of the Reynolds-stress models, the under-estimation of the Reynolds stresses may be attributed to the incorrect representation of the diffusive mechanism. It was suggested in Chapter 2 and from the results of Ribeiro (1976) that the diffusive mechanism is associated with the larger scales of the motion and not represented by any of the Reynolds-stress models. This is particularly true in regions of high velocity gradients where the local turbulent field is strongly asymmetric and, therefore, the third order correlations play an important role on the transport of the Reynolds stresses. These correlations were determined by the second order terms and their gradients. This may result in inability of these models to predict such complex shear flows.

The calculations showed also that the rate of dissipation of the kinetic energy of turbulence is overpredicted by the three models. This is attributed to the strong link between ε and the mean flow field incorporated in the models and represented by the term $G\varepsilon/K$. This link is inappropriate since the dissipation occurs in the finest scales of motion and these do not reflect the local mean strain field. This connection tends to increase the local level of

ε, and consequently decreases the level of the kinetic energy of turbulence. The replacement of G by εA (A being the anisotropy of stresses defined as $\left(\overline{u_i u_j} - \frac{2}{3}\delta_{ij} K\right)^2 / K^2$, Zaman and Lumley (1979), seems physically better but does not work as well in practice (Launder and Whitelaw, 1977). The form of the dissipation equation was also criticised by Bradshaw (1973) and Pope and Whitelaw (1976) particularly in relation to flows with streamline curvature.

In complex flows, where there is more than one major component of the velocity gradient tensor, extra strain rates are added to the generation terms. Bradshaw (1973) suggested that the Reynolds stresses are observed to change by values which are much larger than the direct effect of these strains and that neither of the effective viscosity model nor the Reynolds stress models represent these changes correctly. In the case of $K \sim \varepsilon$ model, the changes in the shear stresses are directly related to the strain rates through a factor f ($\equiv \mu_t$ ($\partial\bar{U}/\partial y$ + e) where e represents any other strain rather than $\partial\bar{U}/\partial y$) which is very small with respect to the real factor, F ($\equiv \mu_t$ ($\partial\bar{U}/\partial y + \alpha e$), order of α is 10, Bradshaw, 1975). In the case of the Reynolds stress models, changes of the order of F are to be applied to the destruction, redistribution and turbulent diffusion transport terms in addition to changes of f in the generation terms. This can be achieved in the present models by specifying empirical formulae for the different constants in the models which are related to a parameter that can represent streamline curvature, such as Richardson number.

It may be noted here that the effect of the extra strain rates is especially important in the regions of $\partial\bar{U}/\partial y = 0$, near the axis for example (Spalding, 1980). These effects are expected to attribute to the underprediction of the Reynolds stresses near the

centre-line, Figs. 3.11 and 3.12 and 3.16 to 3.19. It may be anticipated also that these effects are of more importance in the case of the higher velocity ratio and explain the better agreement between the calculations and experimental results in the case of unity velocity ratio, as mentioned in Subsection 3.4.1 (see also Figs. 3.10, 3.16 and 3.17).

The form of the dissipation equation is common to the three models and, since it is based on unproven assumptions, it is expected as mentioned above to be a major source of errors in the present calculations. Recent trials were made to modify the dissipation equation to be suitable for the prediction of flows with streamline curvature. Morse (1979), for example, found it necessary to make the dissipation equation constant c_{ε_1} a function of the Richardson number to increase the rate of spread in his free-swirling flows. A modification of the dissipation equation was also made by Rodi (1979) in which one of the empirical constants in the equation is made a function of the flux Richardson number based on the extra production of the lateral fluctuations of $\overline{v^2}$. Such modifications were shown to be useful in the predictions of swirling jets (Rodi, 1979) and are expected to decrease the discrepancies between measurements and predictions in the present context. Furthermore, more satisfactory practice appears to be offered by devising stress equations for different slices of wave number (Hanjalic et al, 1979) thus employing two or more independent time scales which characterise the rates of progress of different turbulent interactions. Such schemes can be introduced easily in the present models. However, they are expected to require much more computer time.

Finally, a note is given to the performance of the models used for the calculations achieved in the present context. Although

the storage and time requirements of the Reynolds-stress models are greater than those of the two-equation model by about 35% and 90% respectively, they showed better agreement in most of flow regions; for example, the size of recirculation zone and the velocity distribution of the reverse flow region were better estimated by the Reynolds-stress models. The results showed also that the difference in the calculations of the two Reynolds-stress models due to the difference in the forms of the redistribution term are insignificant.

3.5 Summary and Conclusion

In the preceding sections of this chapter, a calculation procedure was presented and applied to the prediction of the flow properties in a confined double coaxial jets with sudden expansion. The elliptic form of the continuity equation and equations for two components of momentum and the rate of turbulence dissipation have been solved numerically together with equations for turbulence kinetic energy or the four Reynolds-stress equations.

The solution procedure has been applied to the prediction of the flow properties of the confined double coaxial jet for two different velocity ratios and the results compared with corresponding experimental data; comparisons indicate that the general features of the flow fields are correctly predicted by the three models. The extent of the agreement between experimental data and predicted results of the three models are found to vary according to the flow conditions. For example, the mean velocity distribution near and inside the recirculation zone was better predicted by the Reynolds-stress models than the eddy-viscosity model.

The comparison with experiments showed that significant discrepancies exist between measurements and predictions; the size of

the recirculation zone was underpredicted by the three models with the Reynolds-stress models giving lower discrepancy. Also, the normal stress was underestimated by the three models particularly near the centre-line and the rate of dissipation overestimated and again with the Reynolds-stress models of less deficiency. The discrepancies were attributed to streamline curvature and the need for the different terms in the Reynolds stress equations and the equation of the rate of dissipation to account for the changes in the Reynolds stresses due to changes in the generation terms.

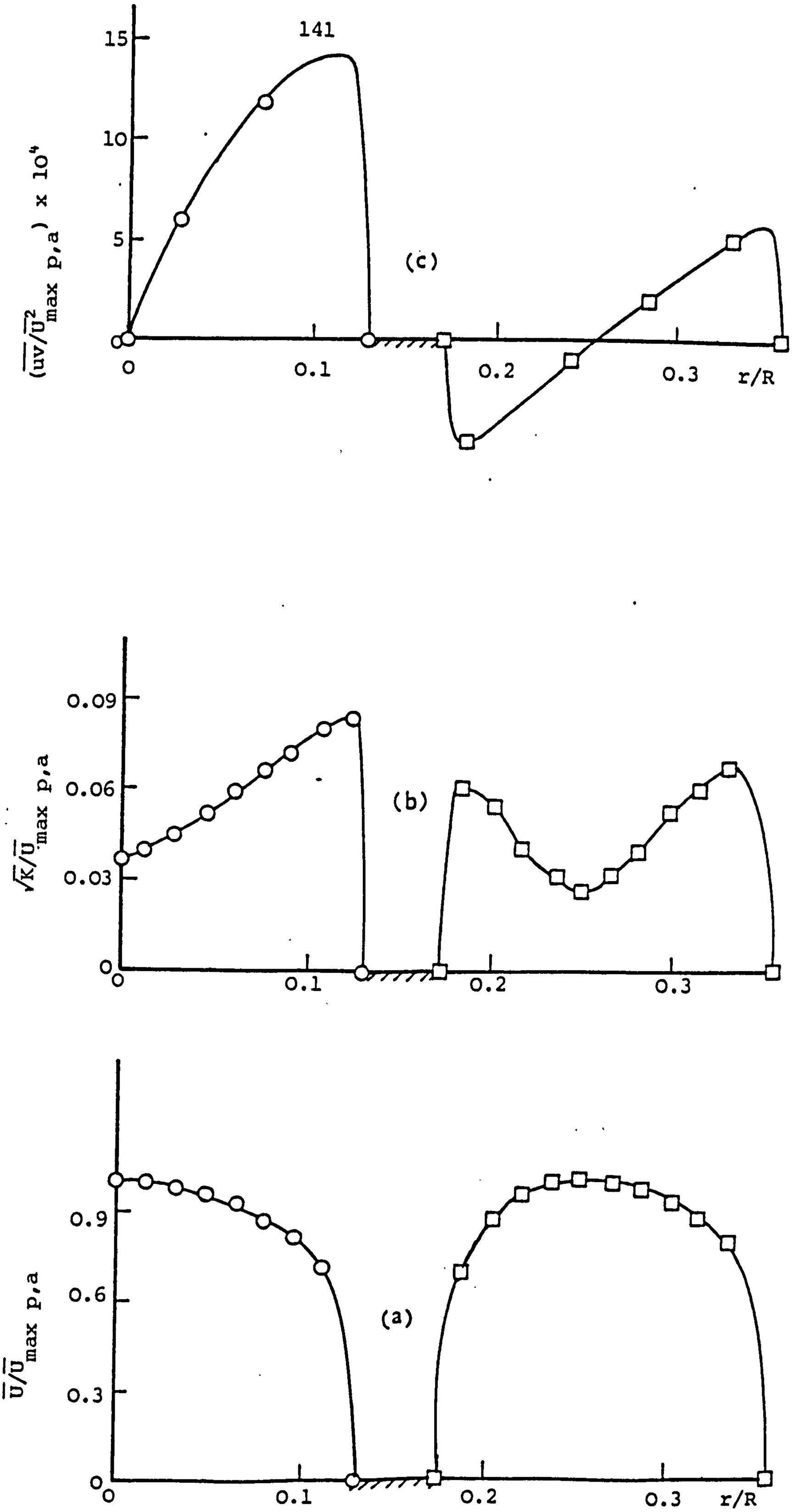


Fig. 3.1 Input Radial Profiles

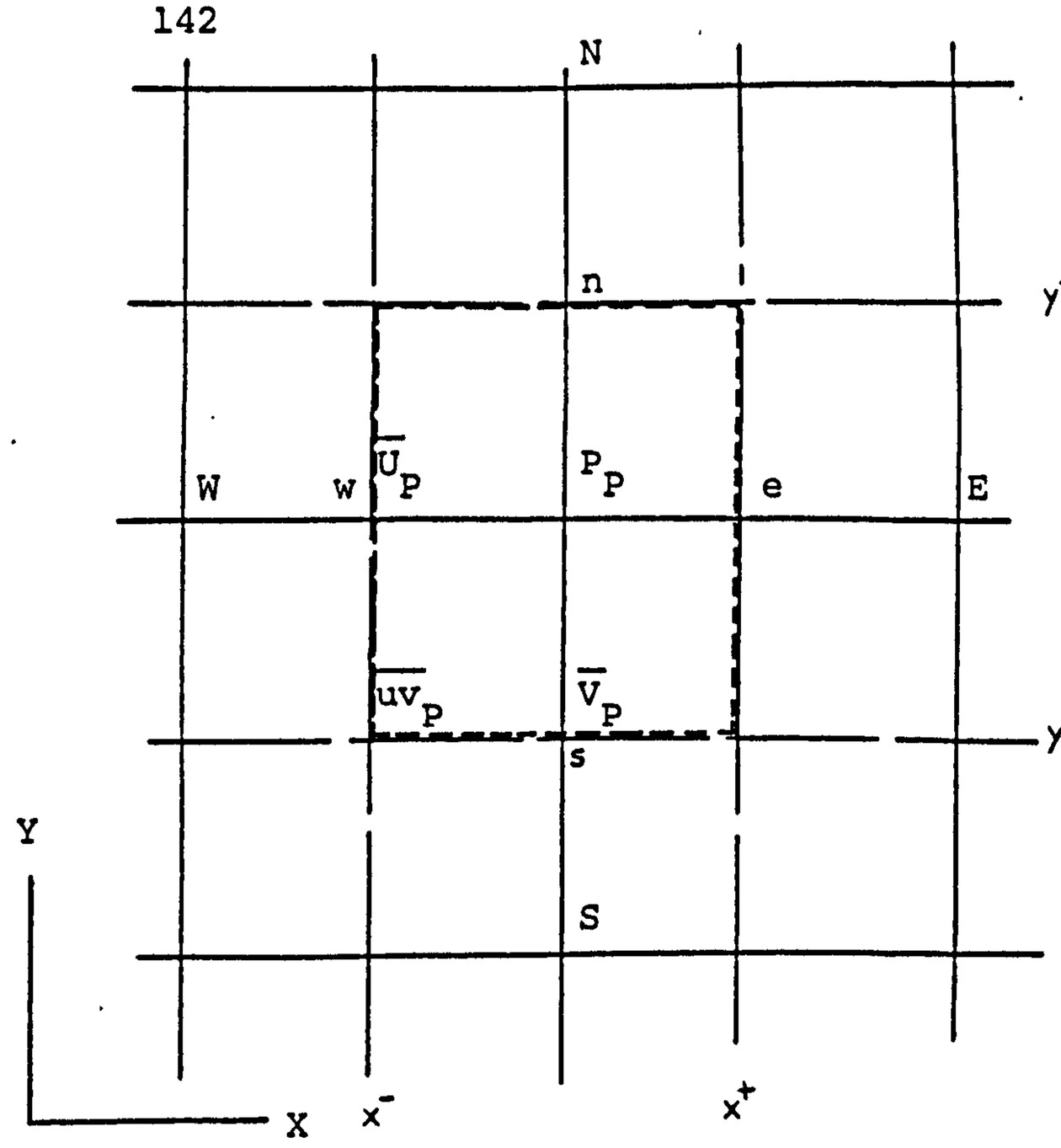


Fig. 3.2 Location of Grid Nodes

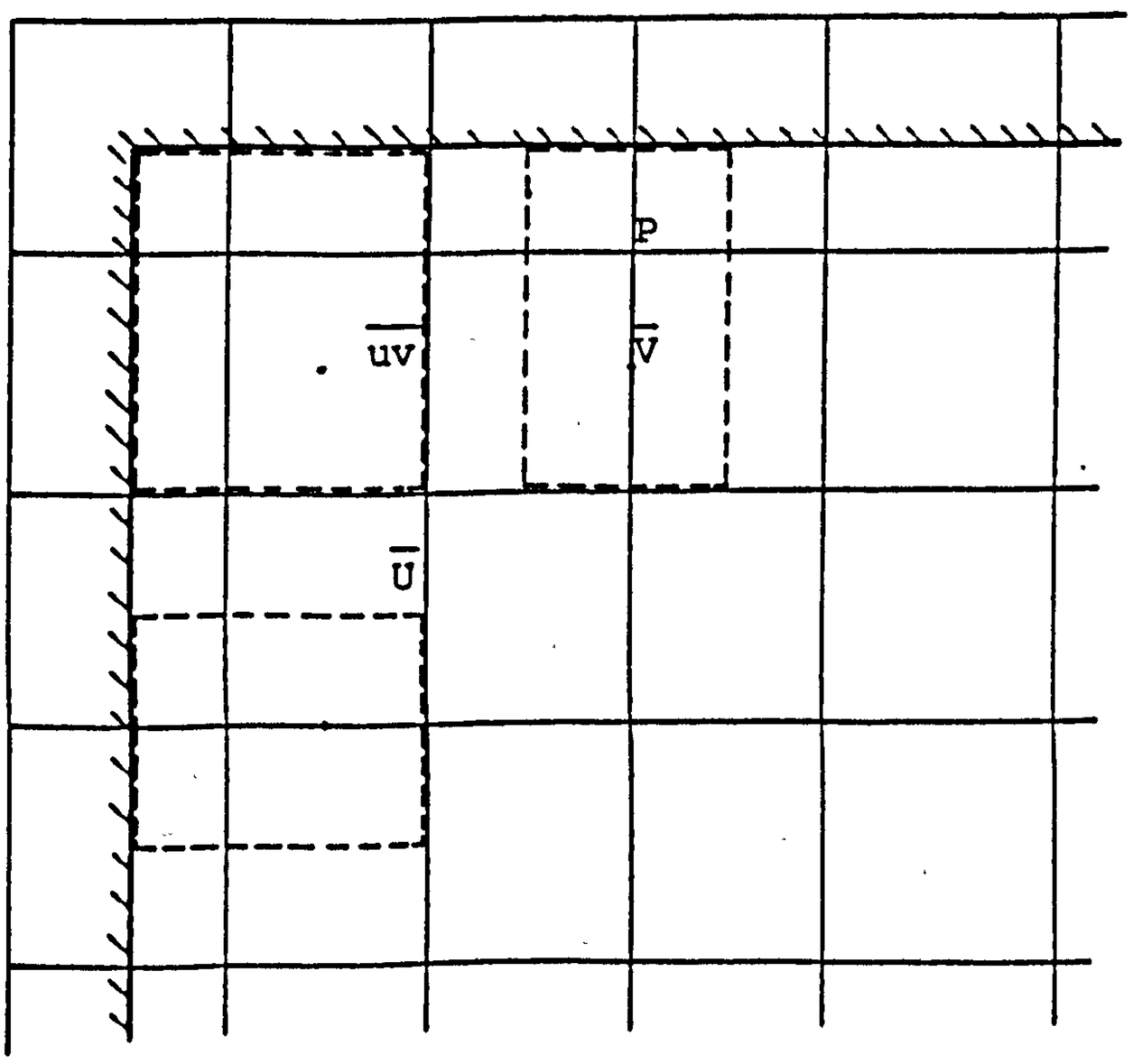


Fig. 3.3 Treatment of Control Volumes Near the Wall

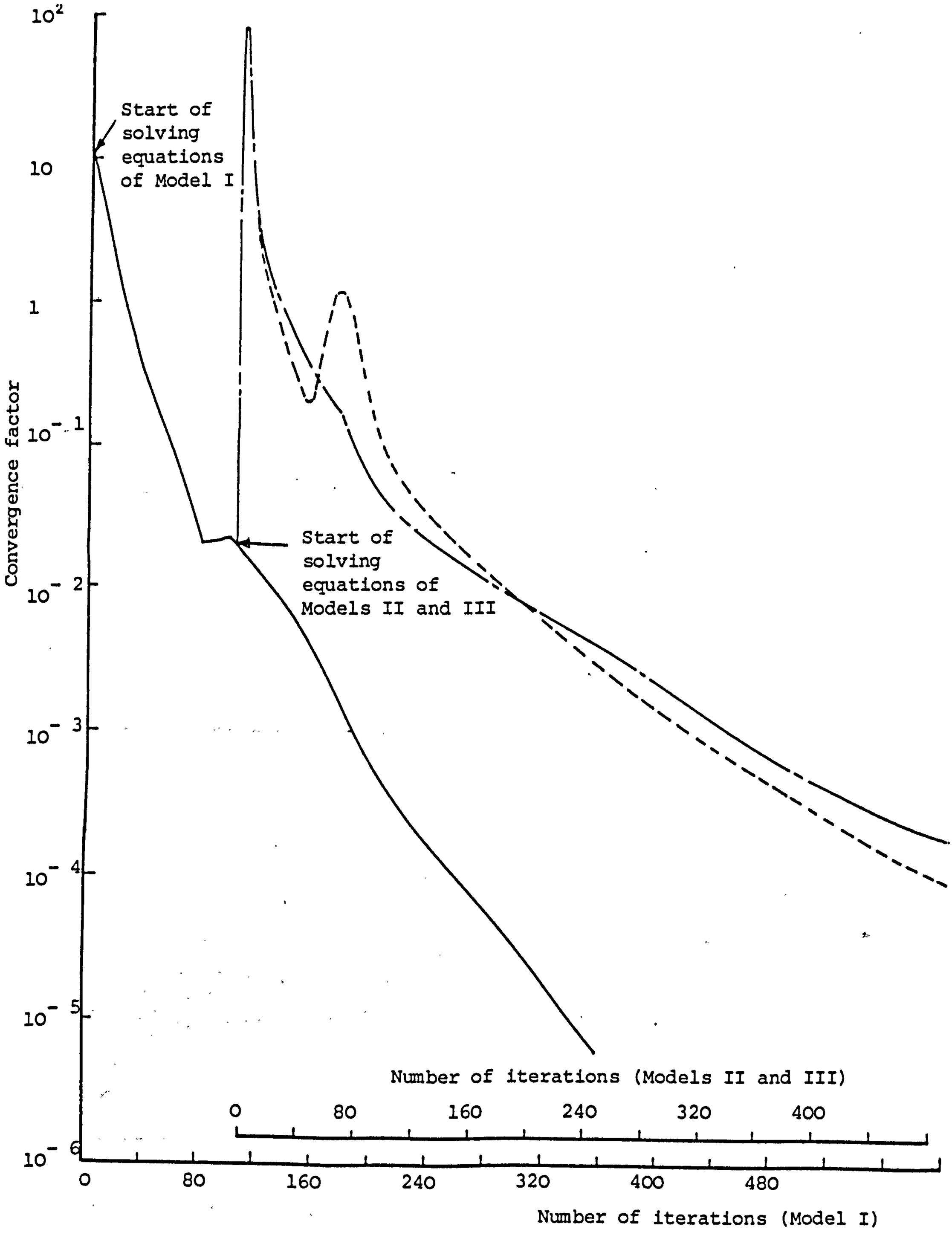


Fig. 3.4 The Convergence of the Solution Procedure

———,Model I;------,Model II;———--,Model III

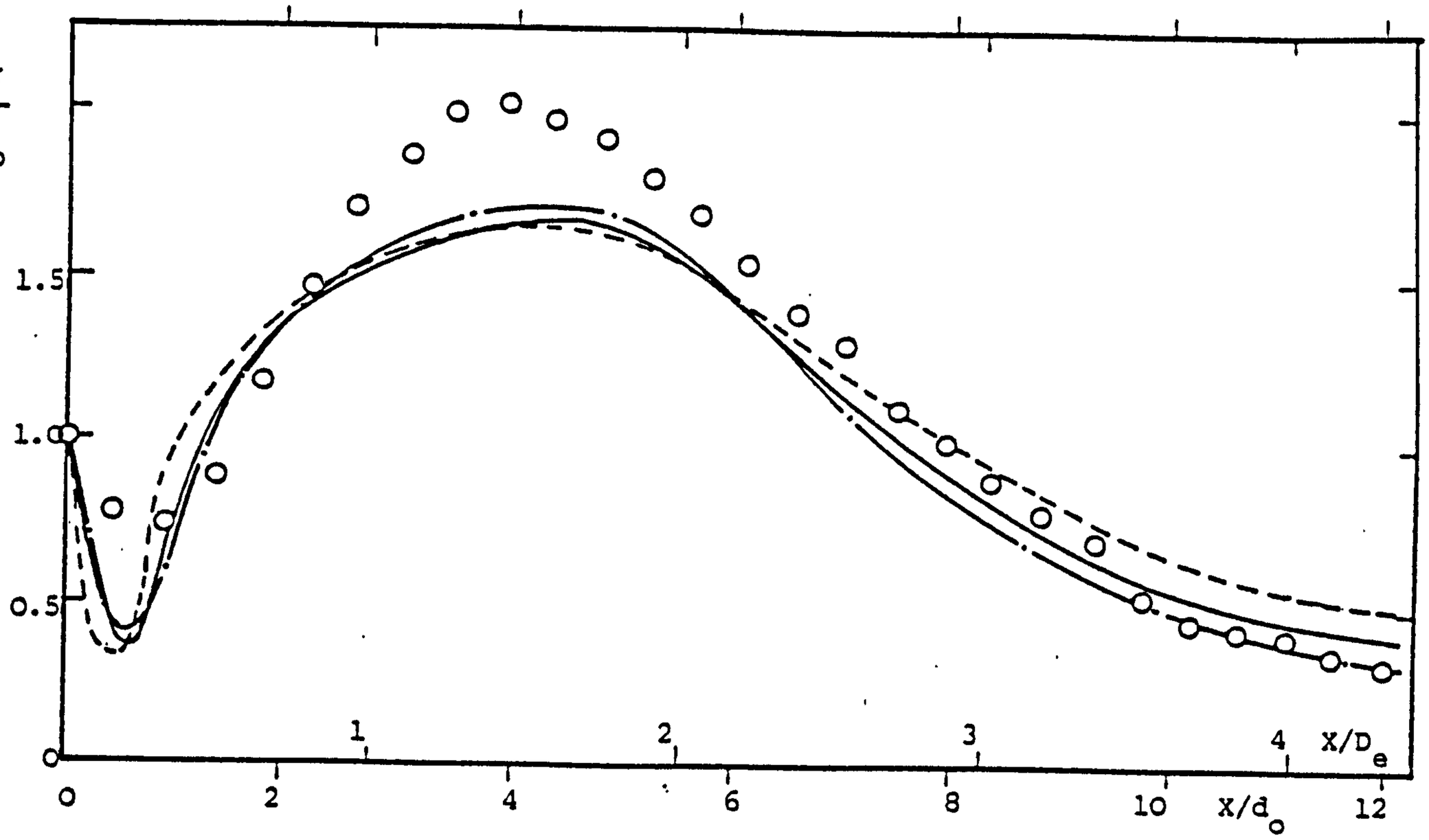


Fig. 3.5 Effect of Grid Size on the Mean Velocity Distribution (S = 0.0, $\overline{U}_a/\overline{U}_p$ = 3.0)

– – – –, 18 x 14 ; ————————, 24 x 18 ; ——·——·——, 30 x 22

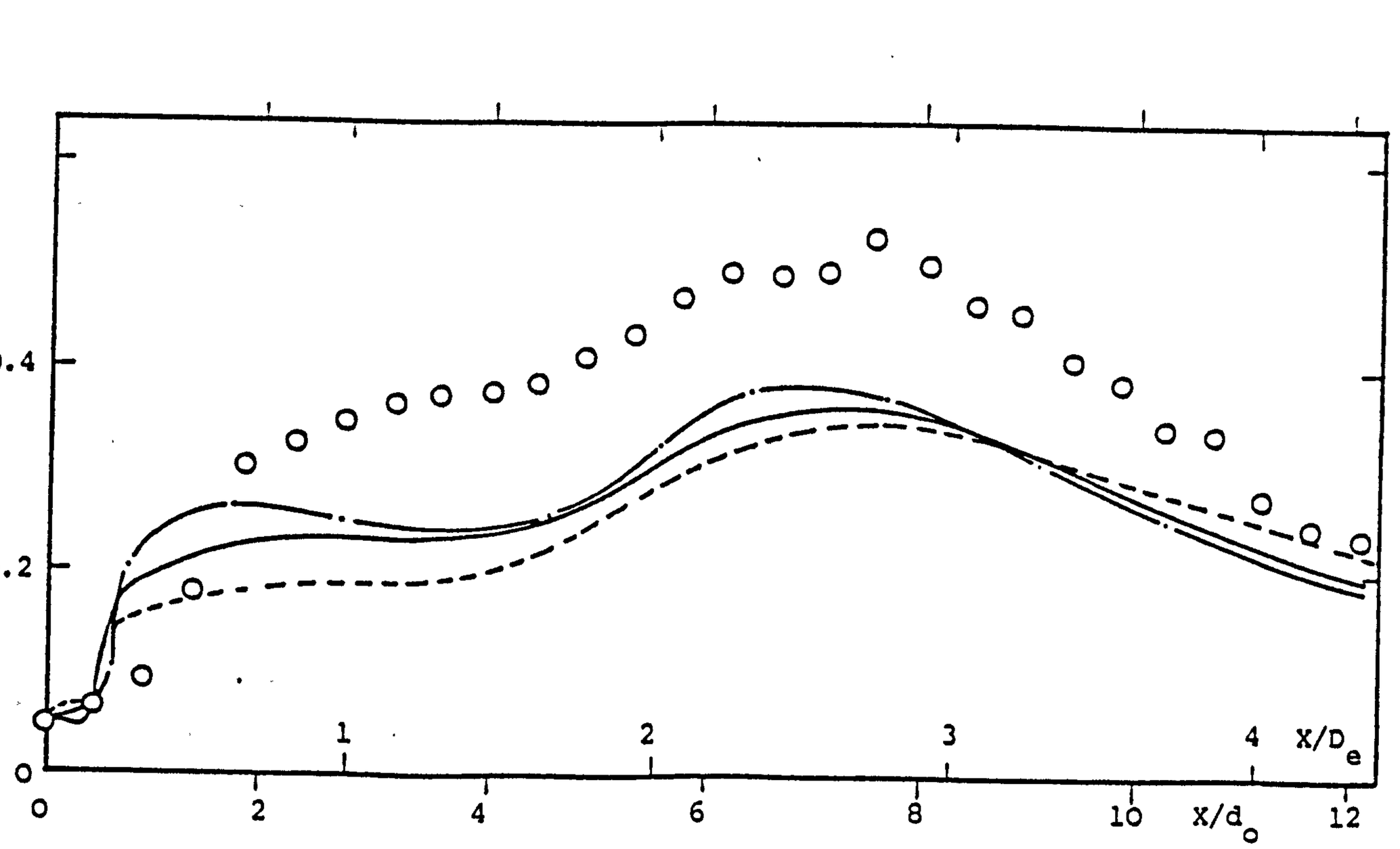


Fig. 3.6 Effect of Grid Size on the Distribution of the Kinetic Energy of Turbulence; Notation as in Fig. 3.5

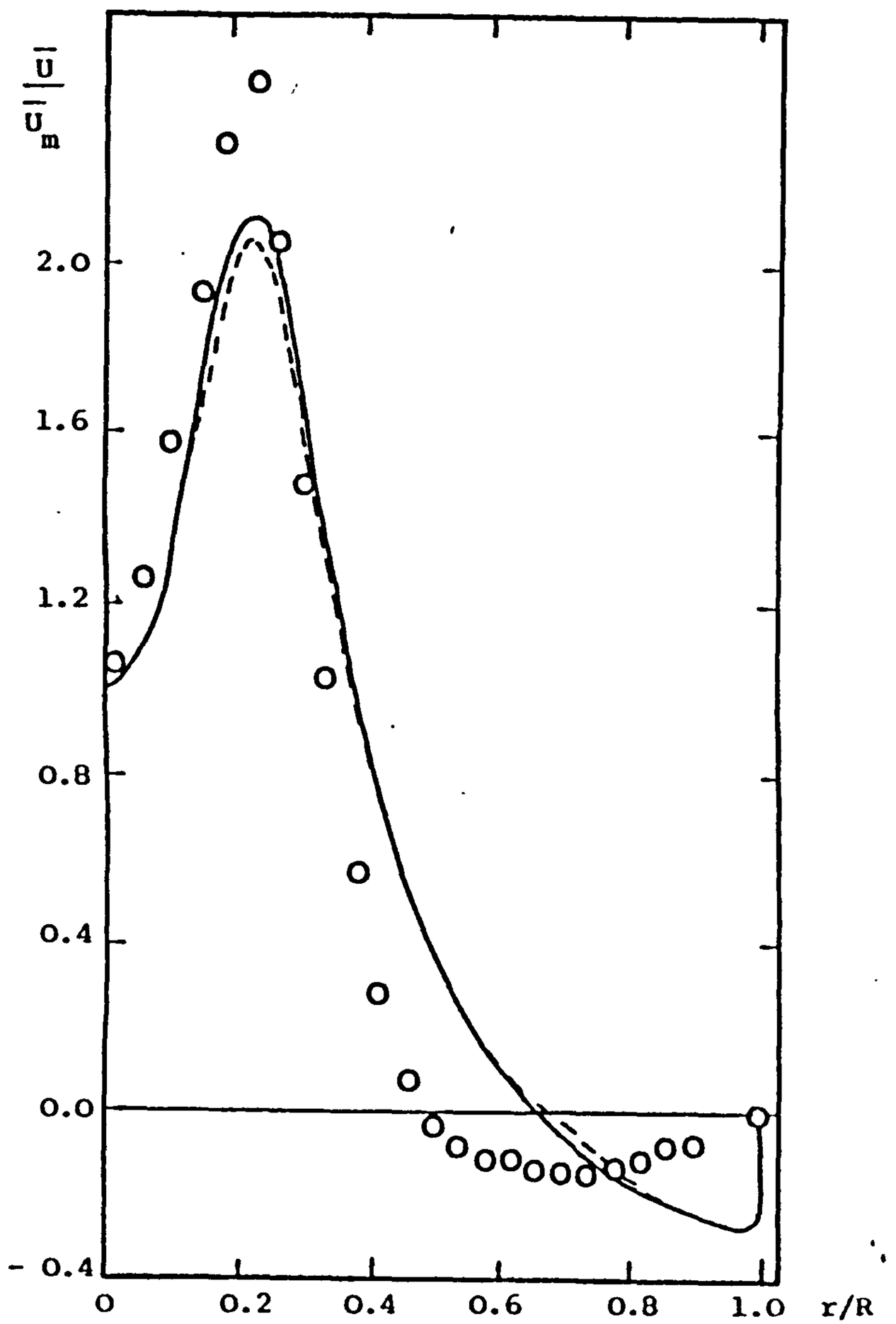


Fig. 3.7 Effect of Grid Size on the Mean Velocity Values Along the Radius (X/D_e = 0.616); Notation as in Fig. 3.5

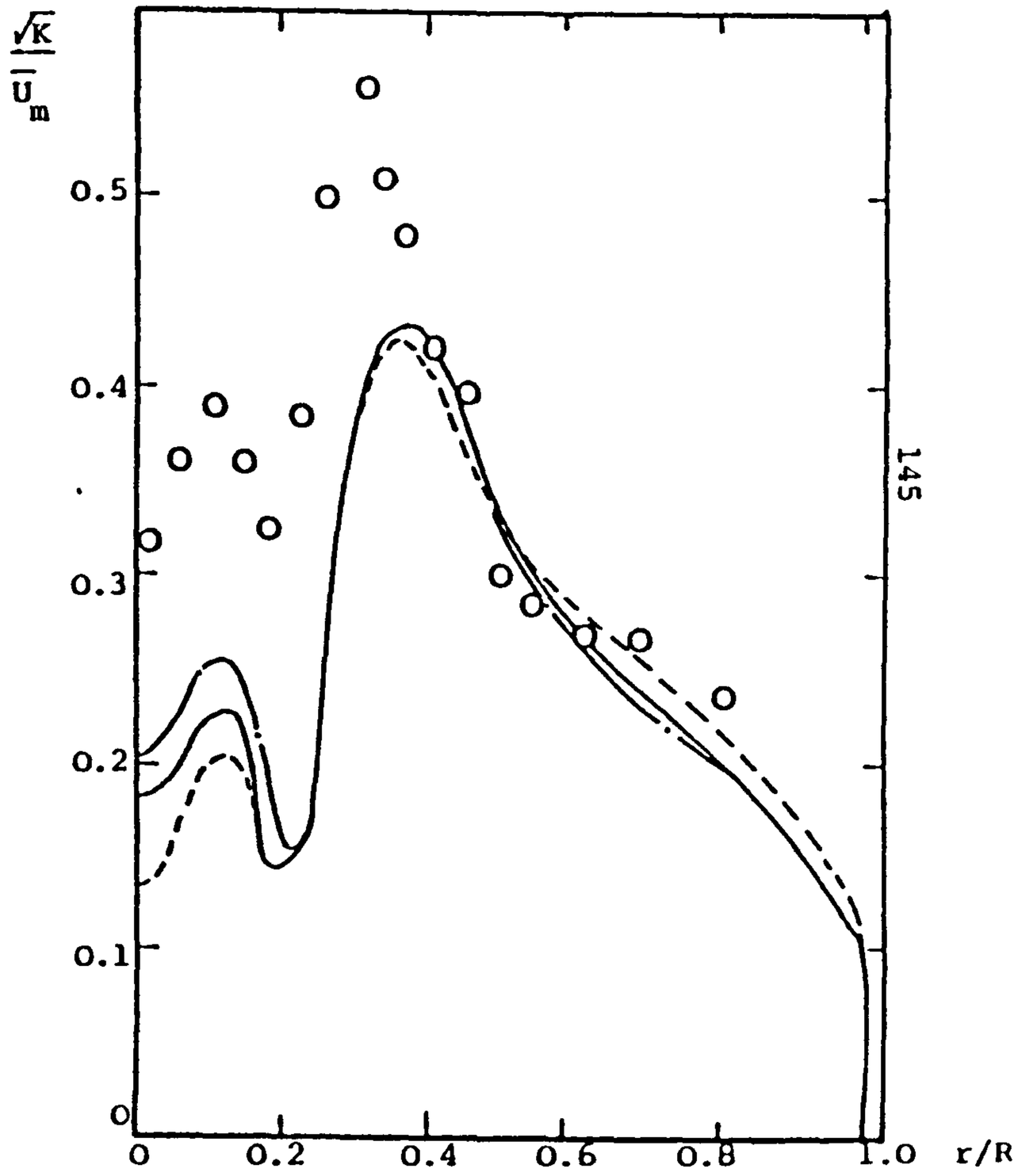


Fig. 3.8 Effect of Grid Size on the Values of the Kinetic Energy of Turbulence Along the Radius (X/D_e = 0.616); Notation as in Fig. 3.5

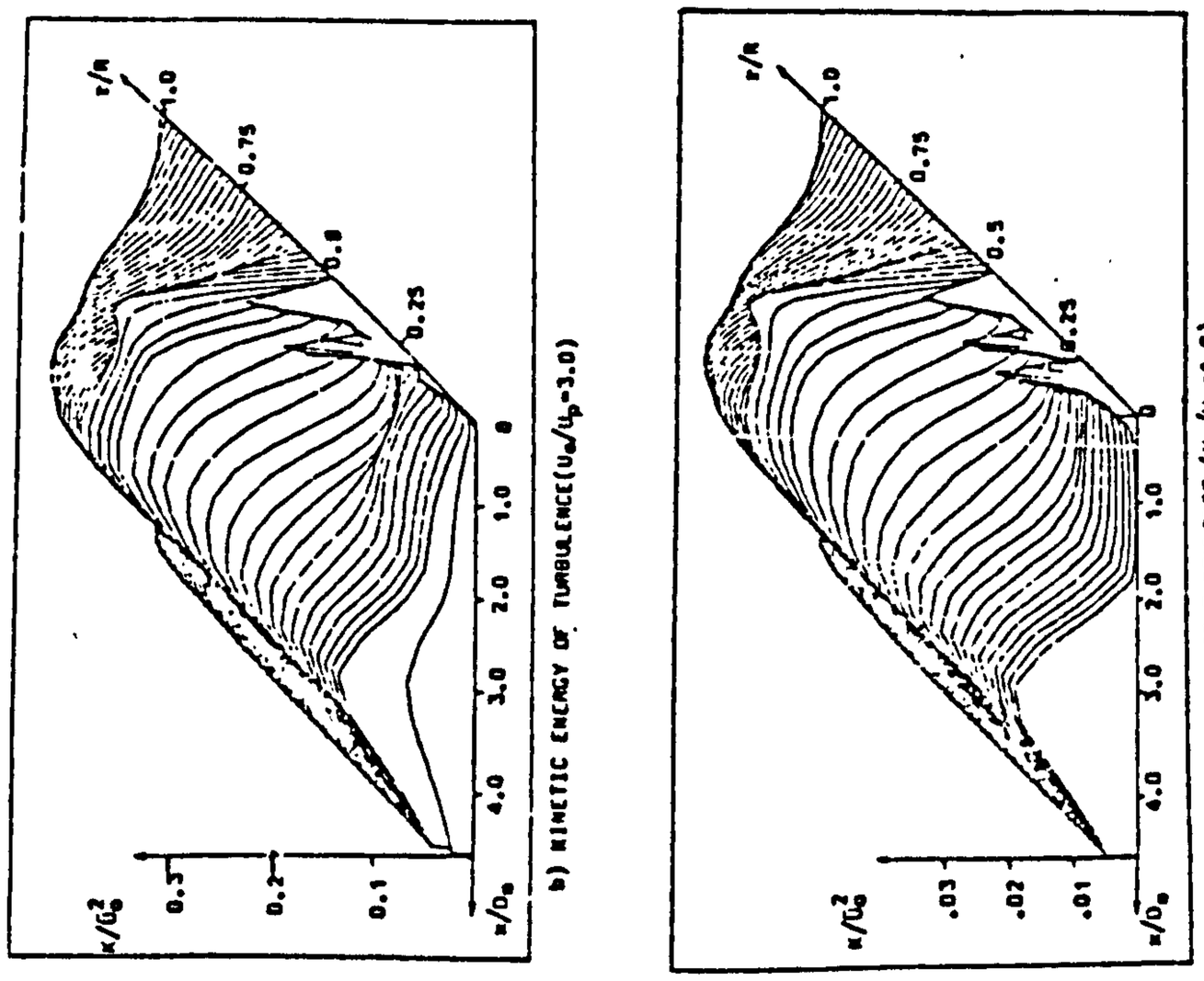


Fig. 3.9 The Predicted Distributions of the Axial Mean Velocity and the Turbulence Kinetic Energy

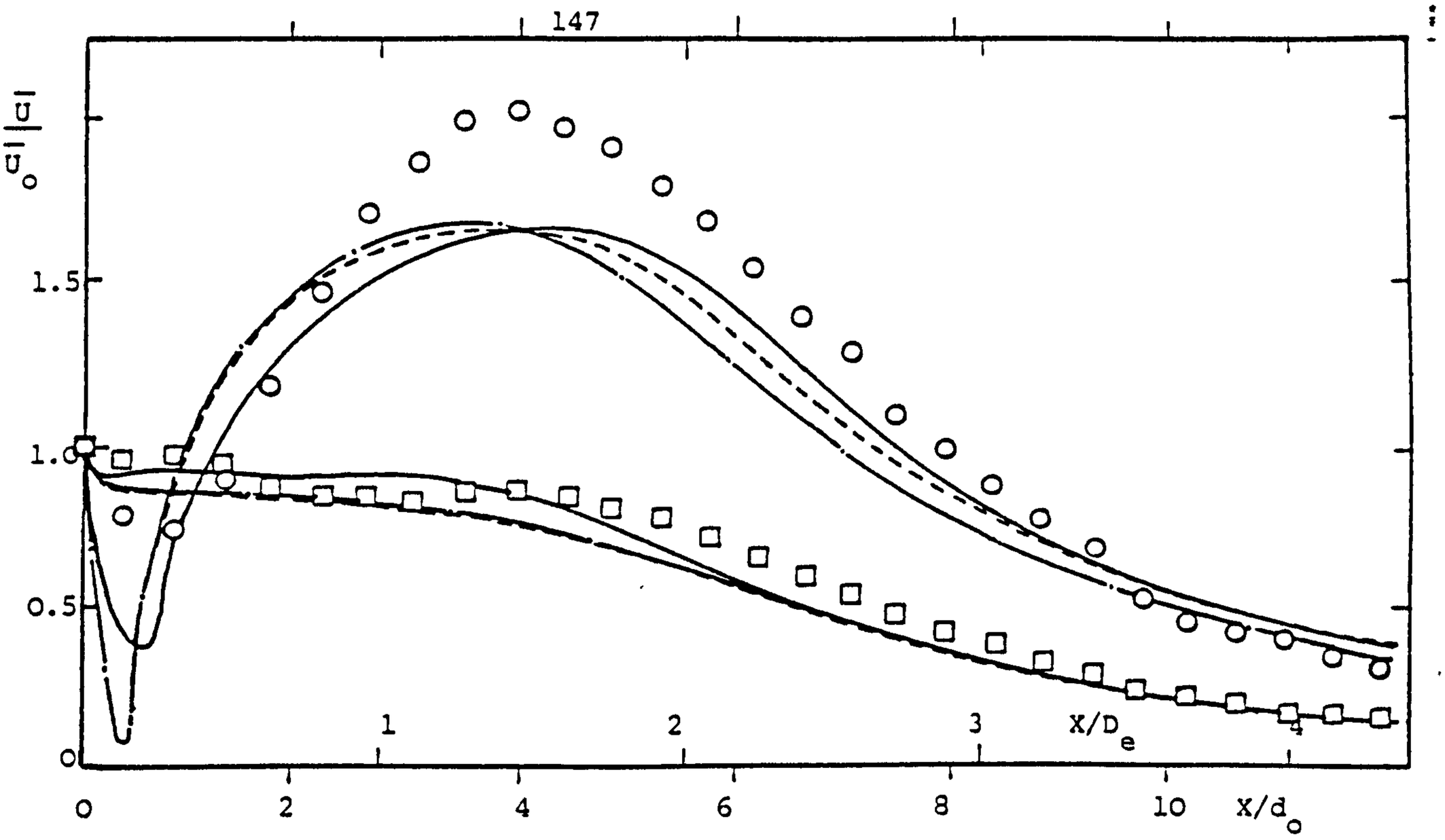


Fig. 3.10 Axial Distribution of Axial Mean Velocity

O , measurements, $\overline{U}_a/\overline{U}_p$ = 3.0; □ , measurements, $\overline{U}_a/\overline{U}_p$ = 1.0;

———, calculations, Model I; – – – –, calculations, Model II;

———·———, calculations, Model III

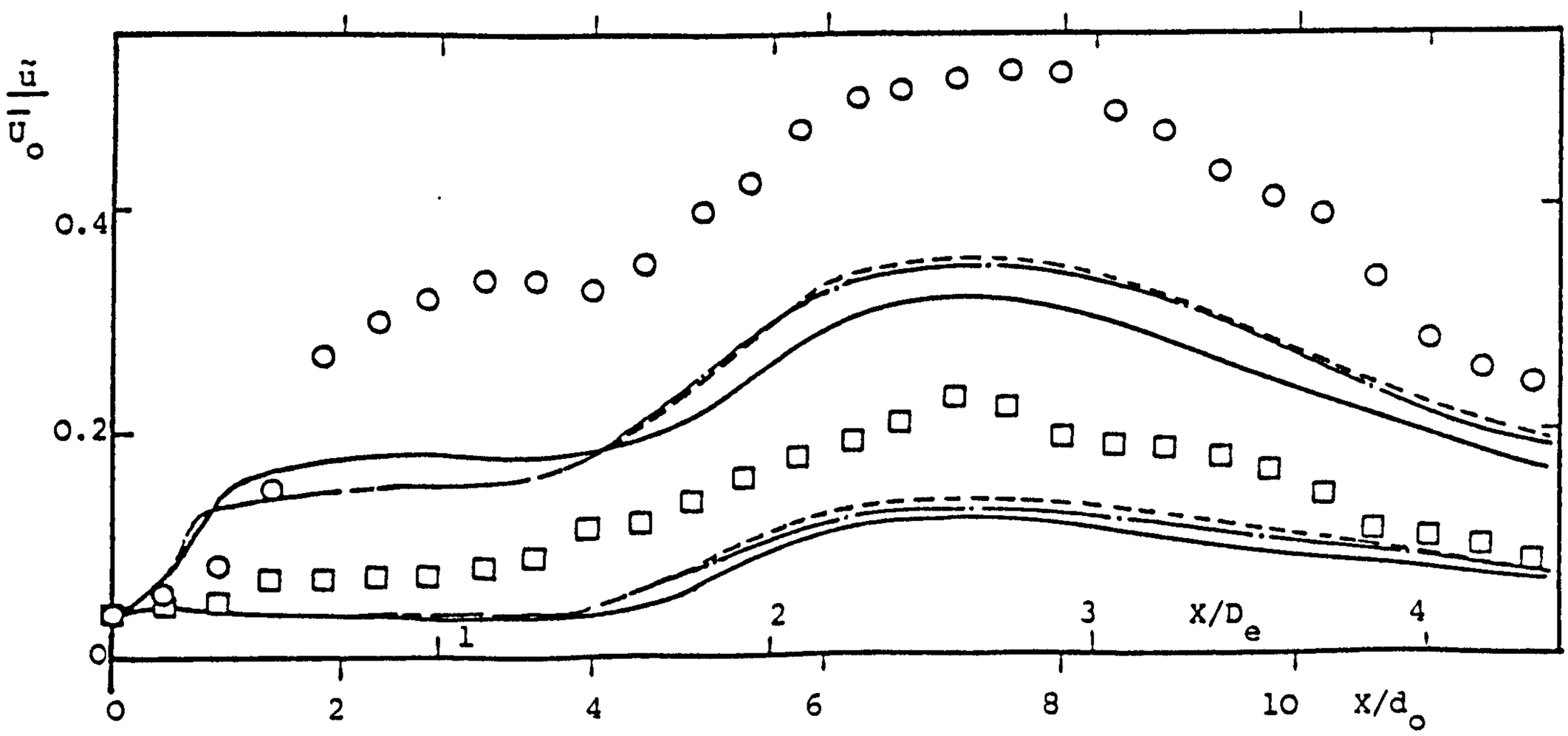


Fig. 3.11 Axial Distributions of Axial Normal Stress; Notation as in Fig. 3.10

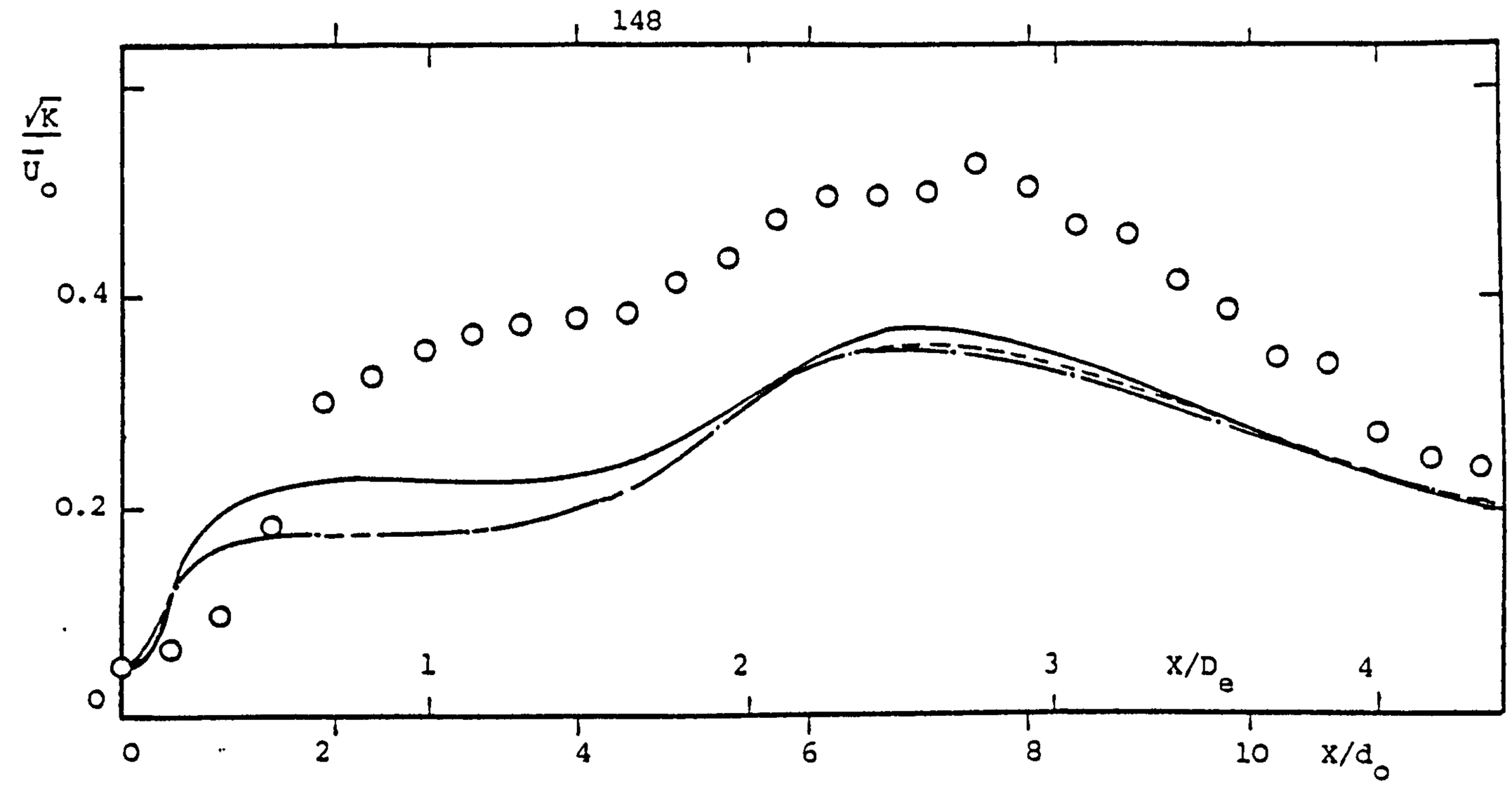


Fig. 3.12 Axial Distributions of the Kinetic Energy of Turbulence; Notation as in Fig. 3.10

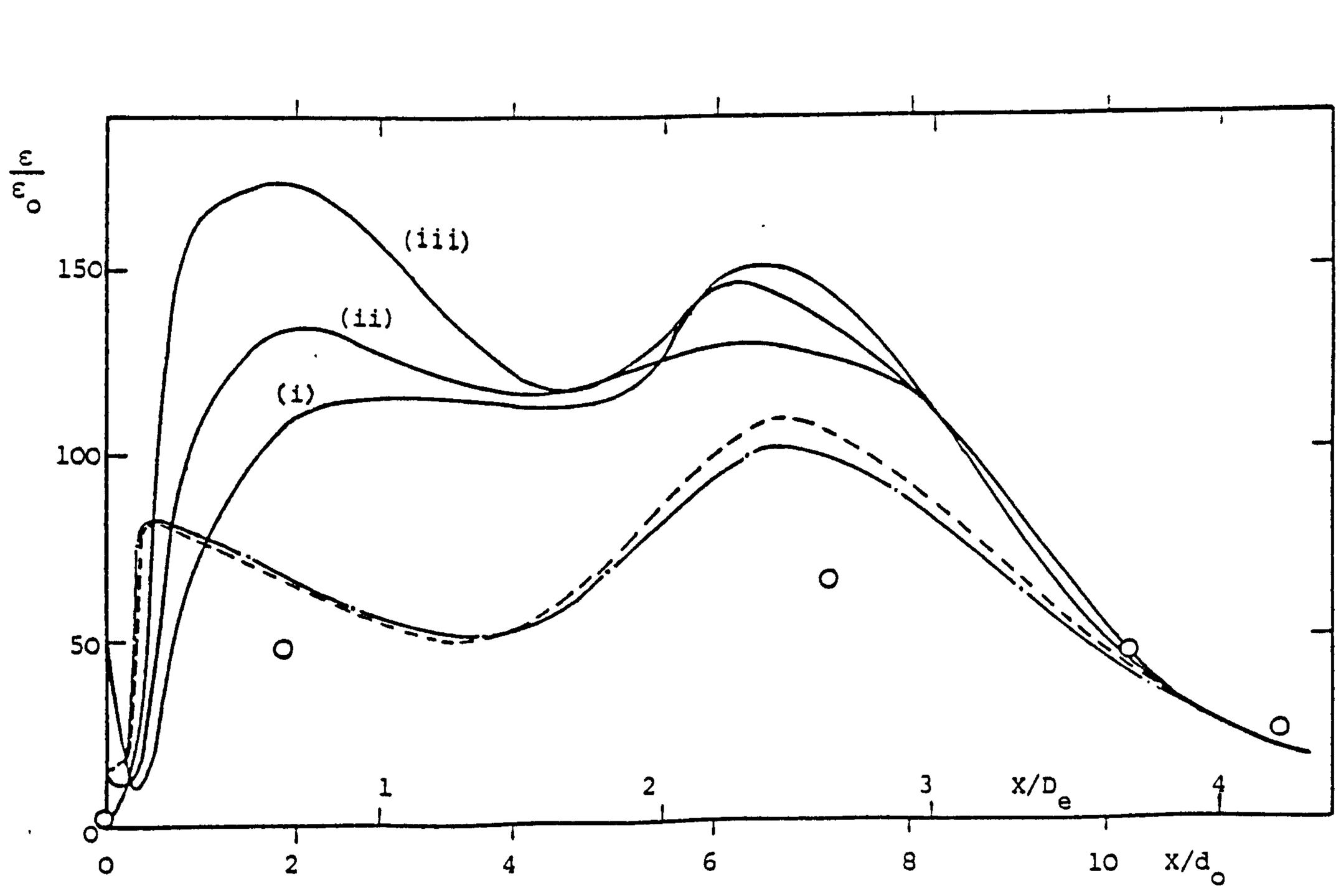


Fig. 3.13 Axial Distributions of the Dissipation Rate of the Kinetic Energy of Turbulence; (i) $\ell_o = 0.01\ c_\mu\ R$; (ii) $\ell_o = 0.03\ r_{p,a}$; (iii) $\ell_o = c_\mu^{1/4}\ \ell_m$. Otherwise as in Fig. 3.10

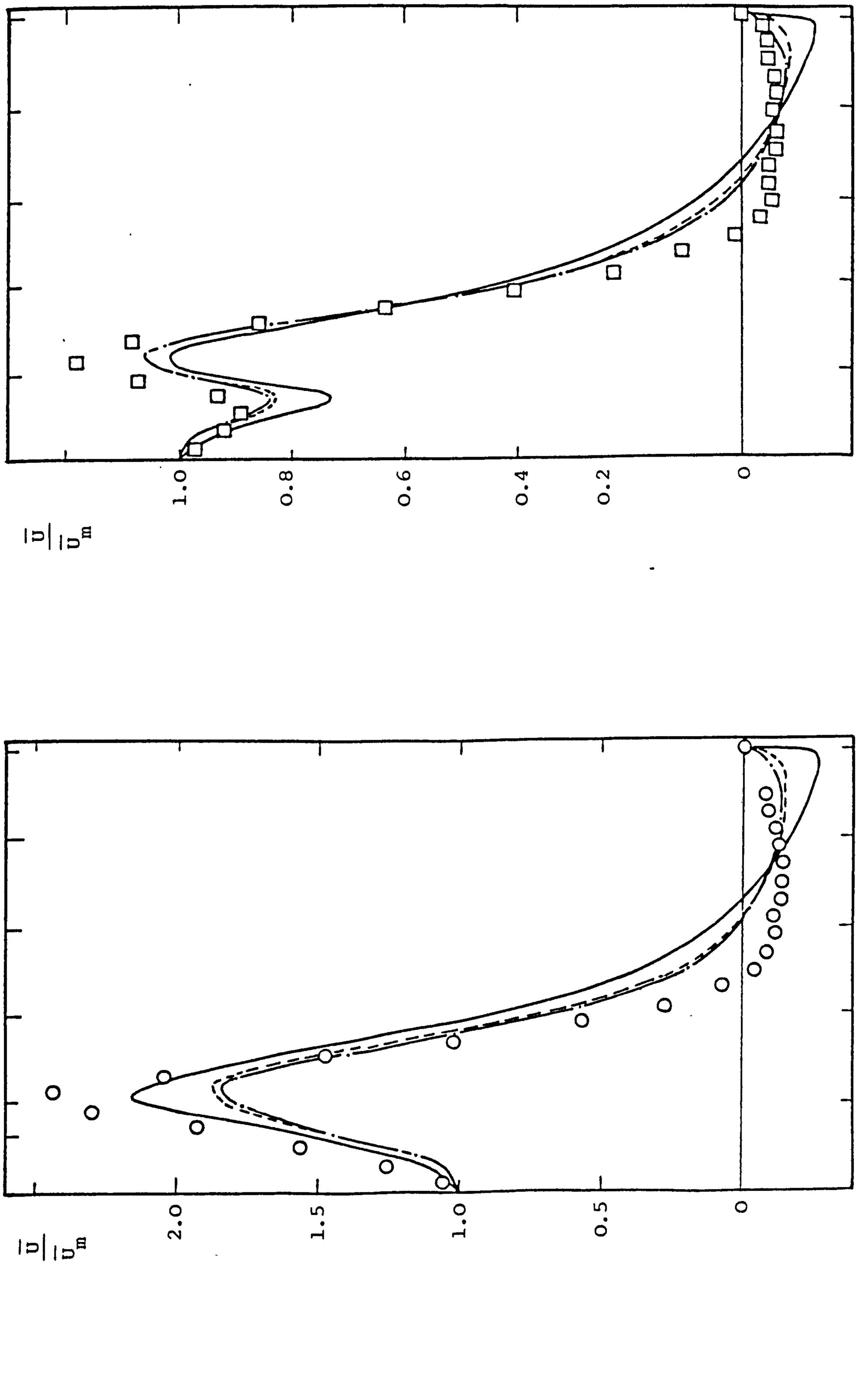


Fig. 3.15 Radial Profiles of Axial Mean Velocity ($X/D_e = 0.616$, $\bar{U}_a/\bar{U}_p = 1.0$); Notation as in Fig. 3.10

Fig. 3.14 Radial Profiles of Axial Mean Velocity ($X/D_e = 0.616$, $\bar{U}_a/\bar{U}_p = 3.0$); Notation as in Fig. 3.10

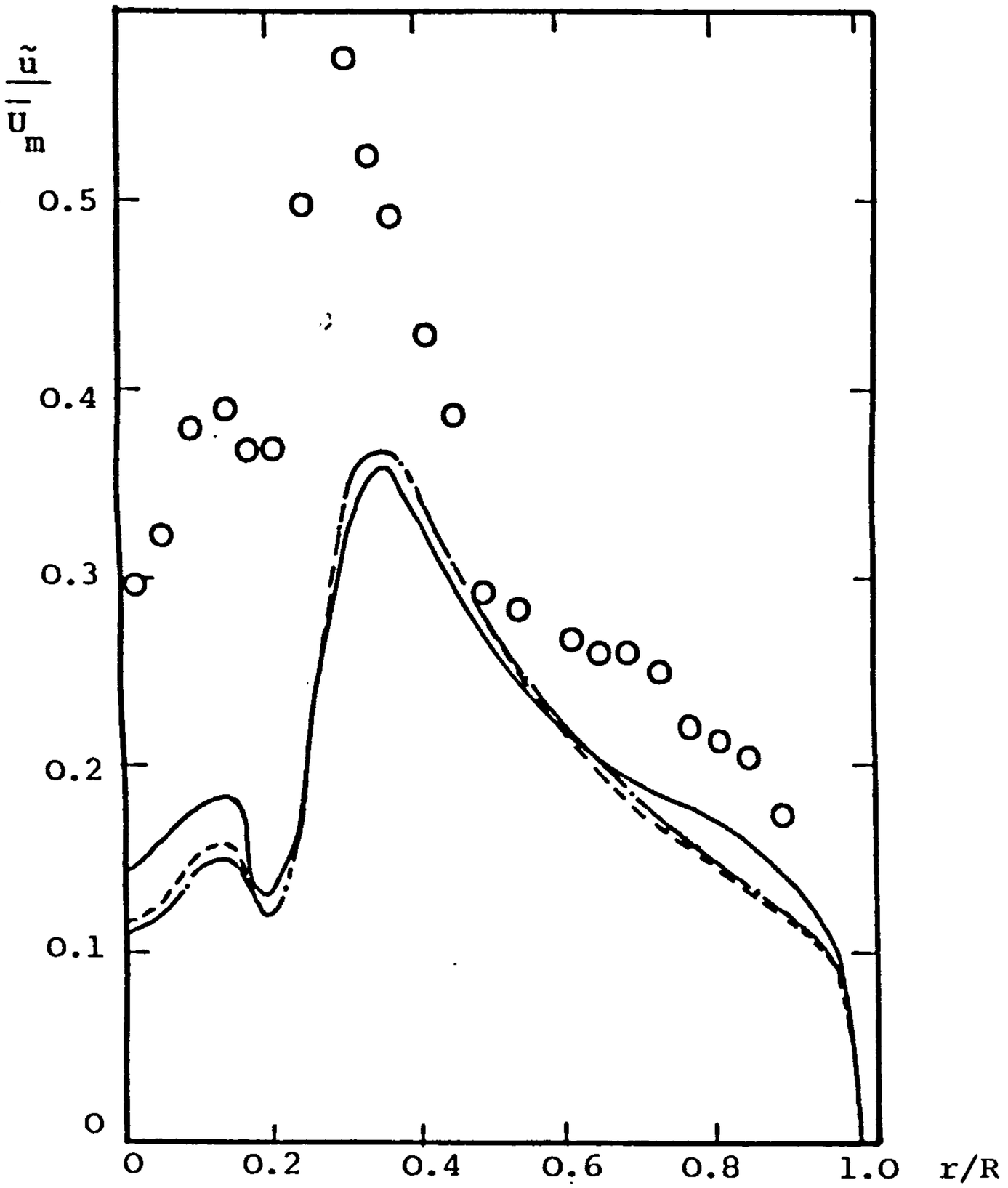


Fig. 3.16 Radial Profiles of Axial Normal Stress (X/D_e = 0.616, $\bar{U}_a/\bar{U}_p$ = 3.0); Notation as in Fig. 3.10

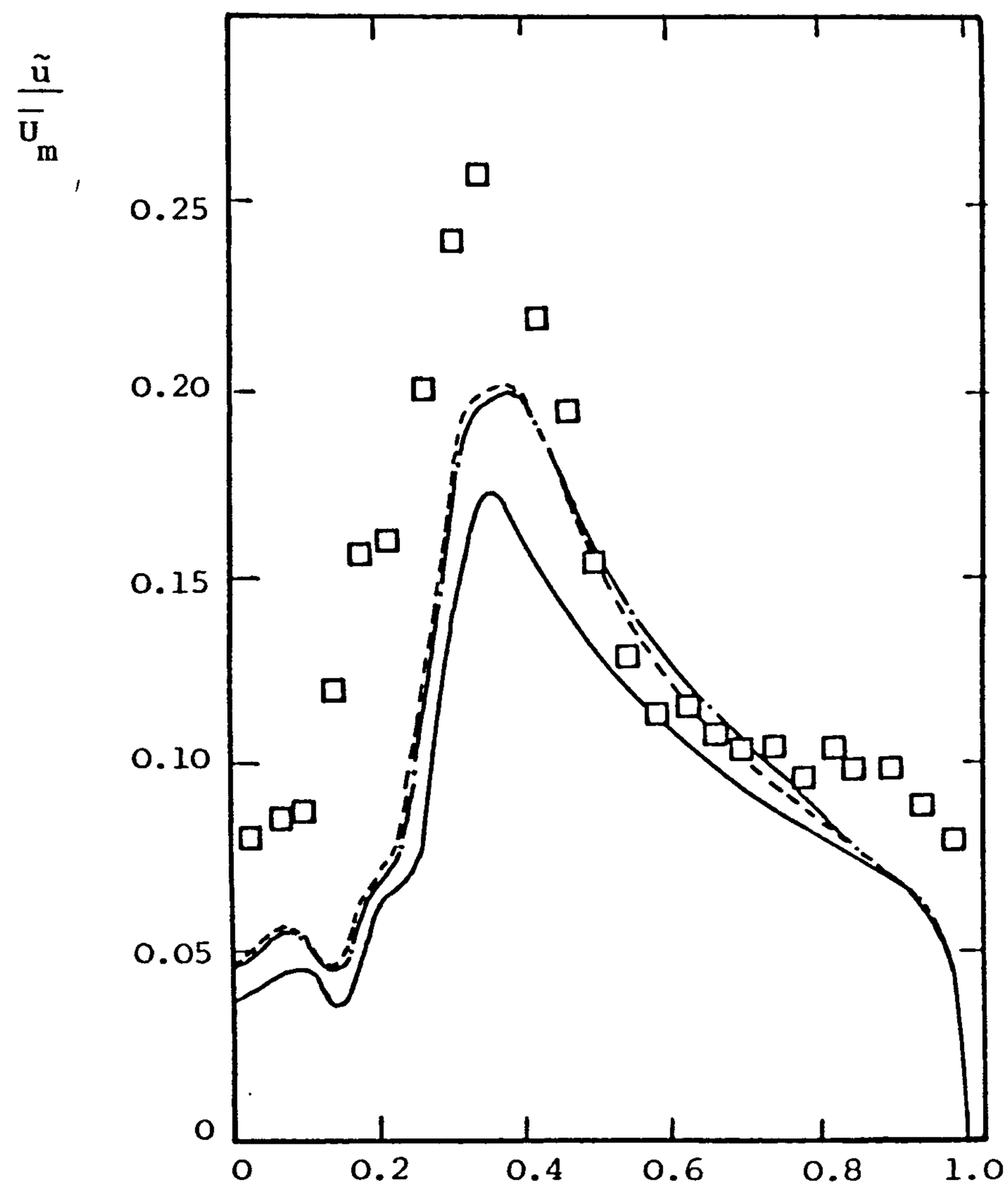


Fig. 3.17 Radial Profiles of Axial Normal Stress (X/D_e = 0.616, $\bar{U}_a/\bar{U}_p$ = 1.0); Notation as in Fig. 3.10

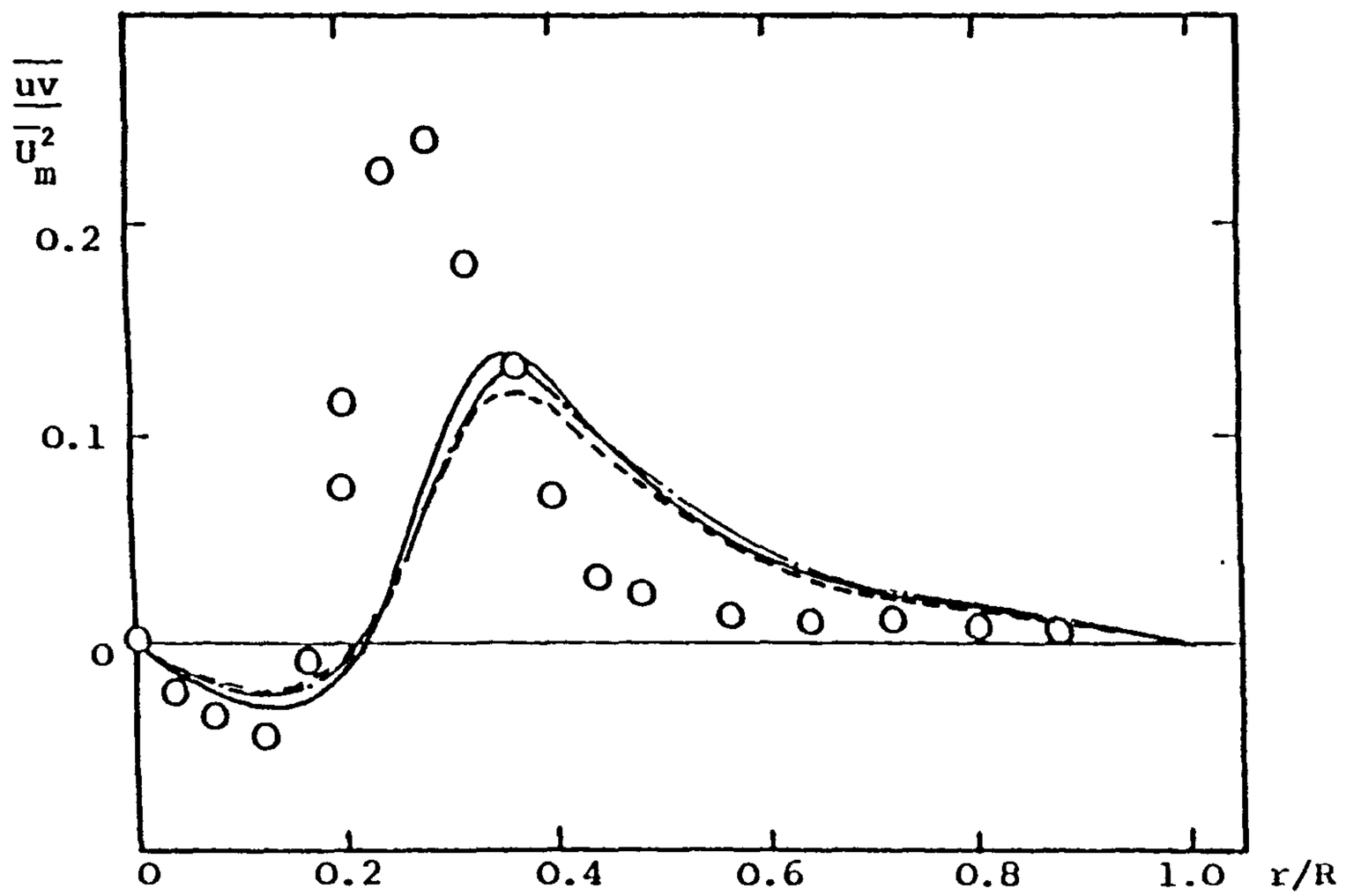


Fig. 3.18 Radial Distributions of Shear Stress (X/D_e = 0.616, $\bar{U}_a/\bar{U}_p$ = 3.0); Notation as in Fig. 3.10

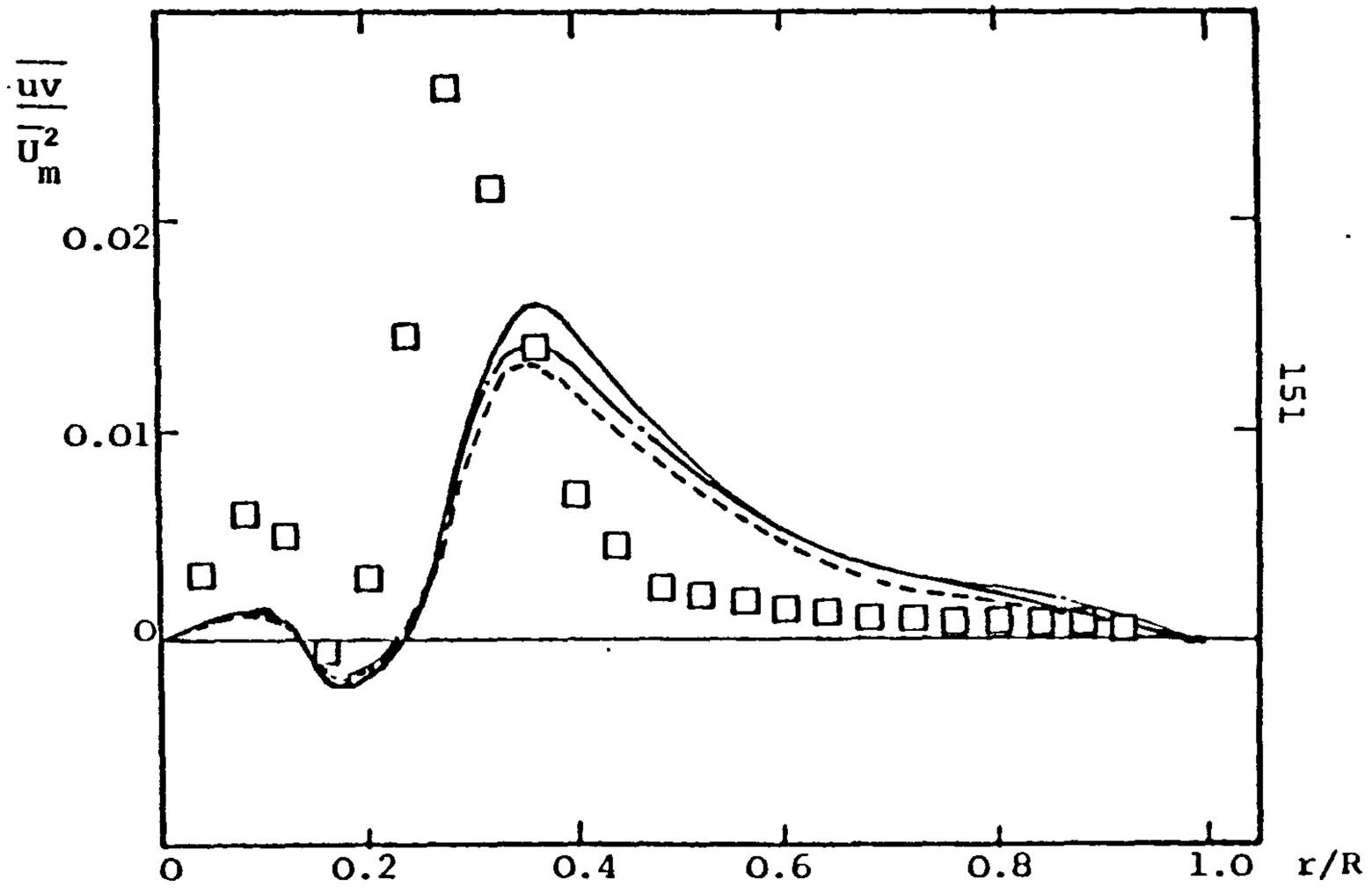


Fig. 3.19 Radial Distributions of Shear Stress (X/D_e = 0.616, $\bar{U}_a/\bar{U}_p$ = 1.0); Notation as in Fig. 3.10

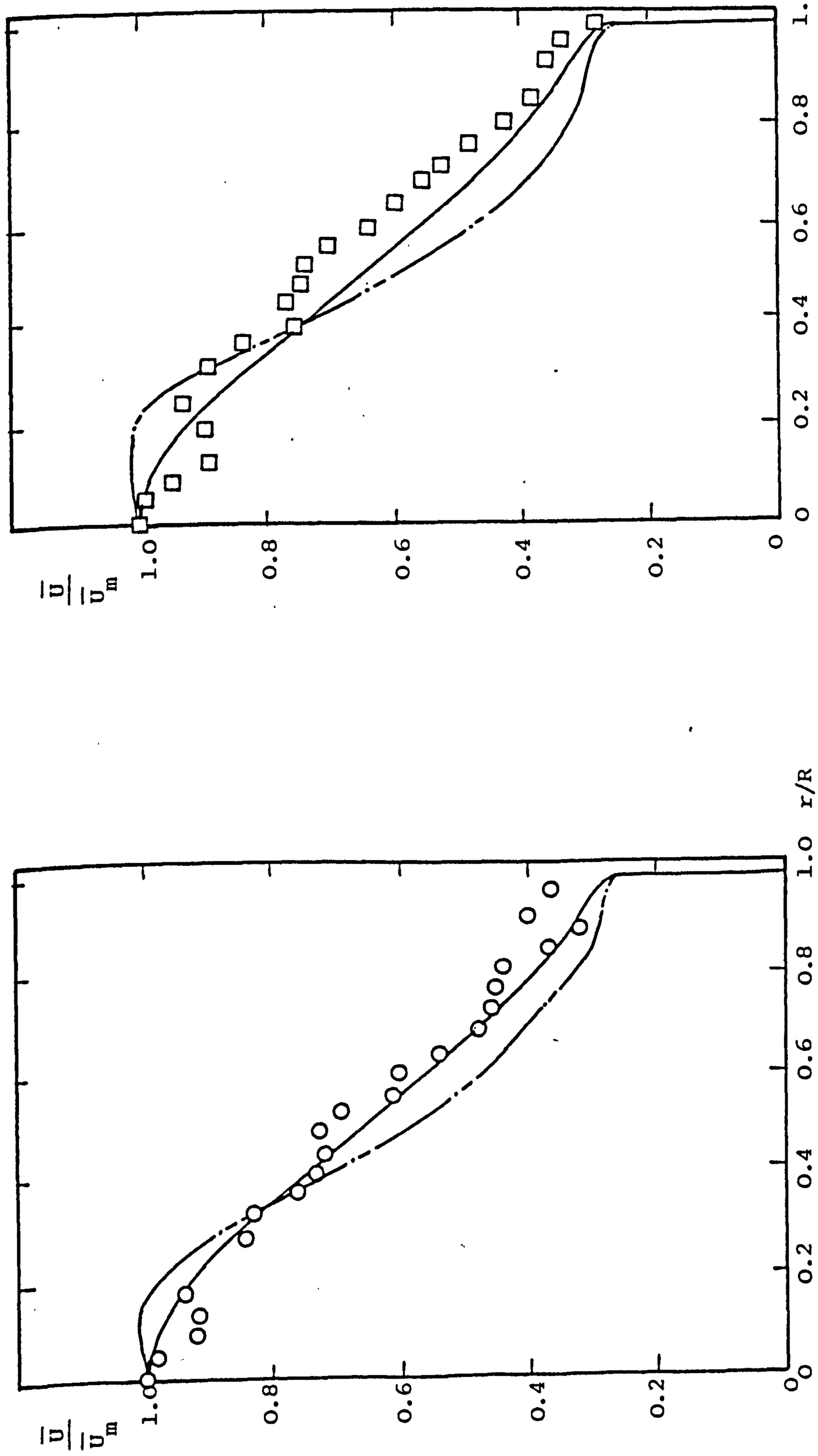


Fig. 3.21 Radial Profiles of Axial Mean Velocity ($X/D_e = 3.67$, $\bar{U}/\bar{U}_a = 1.0$); Notation as in Fig. 3.10

Fig. 3.20 Radial Profiles of Axial Mean Velocity ($X/D_e = 3.67$, $\bar{U}/\bar{U}_a = 3.0$); Notation as in Fig. 3.10

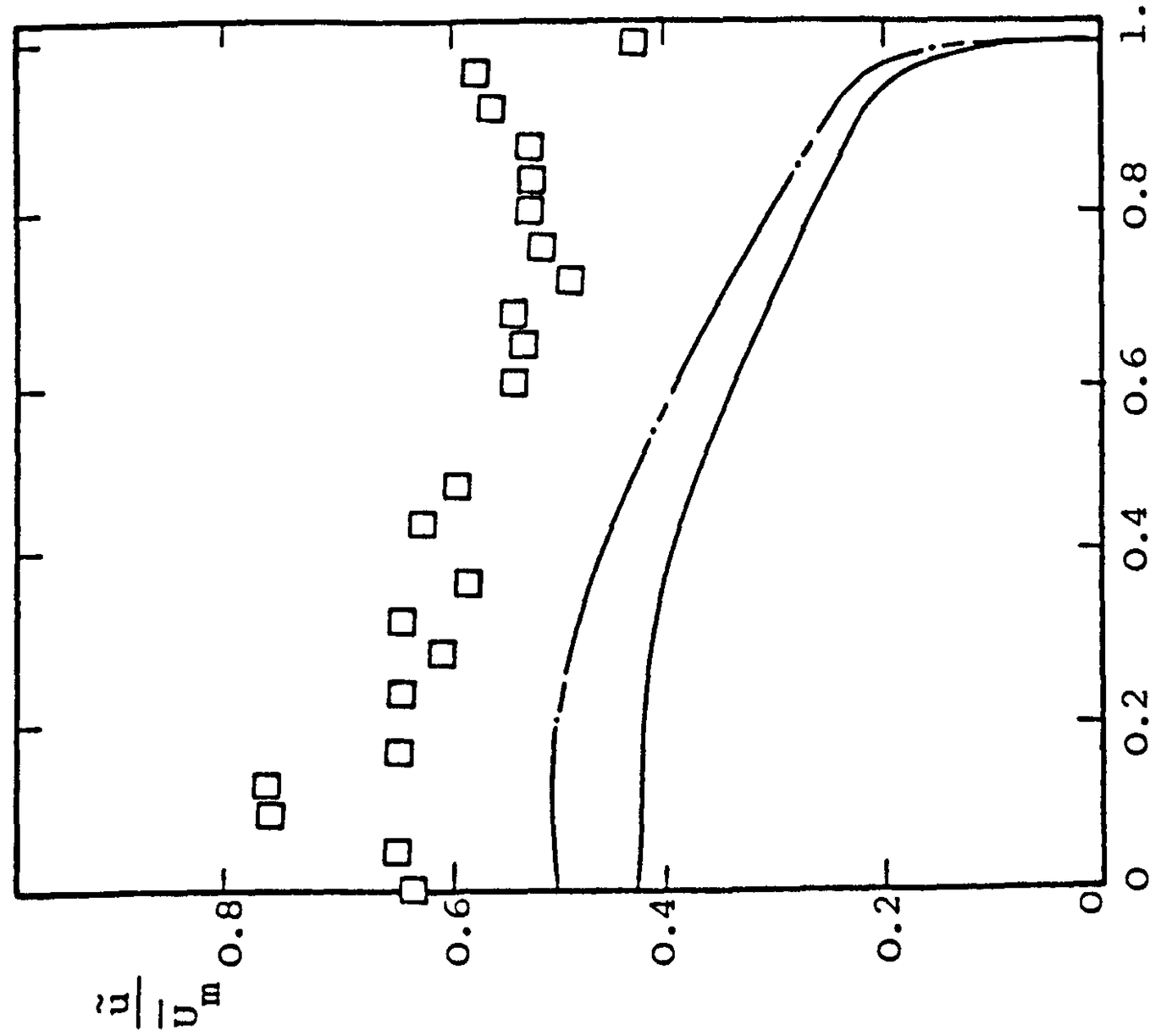


Fig. 3.23 Radial Profiles of Axial Normal Stress (X/D_e = 3.67, $\bar{U}_a/\bar{U}_p$ = 1.0); Notation as in Fig. 3.10

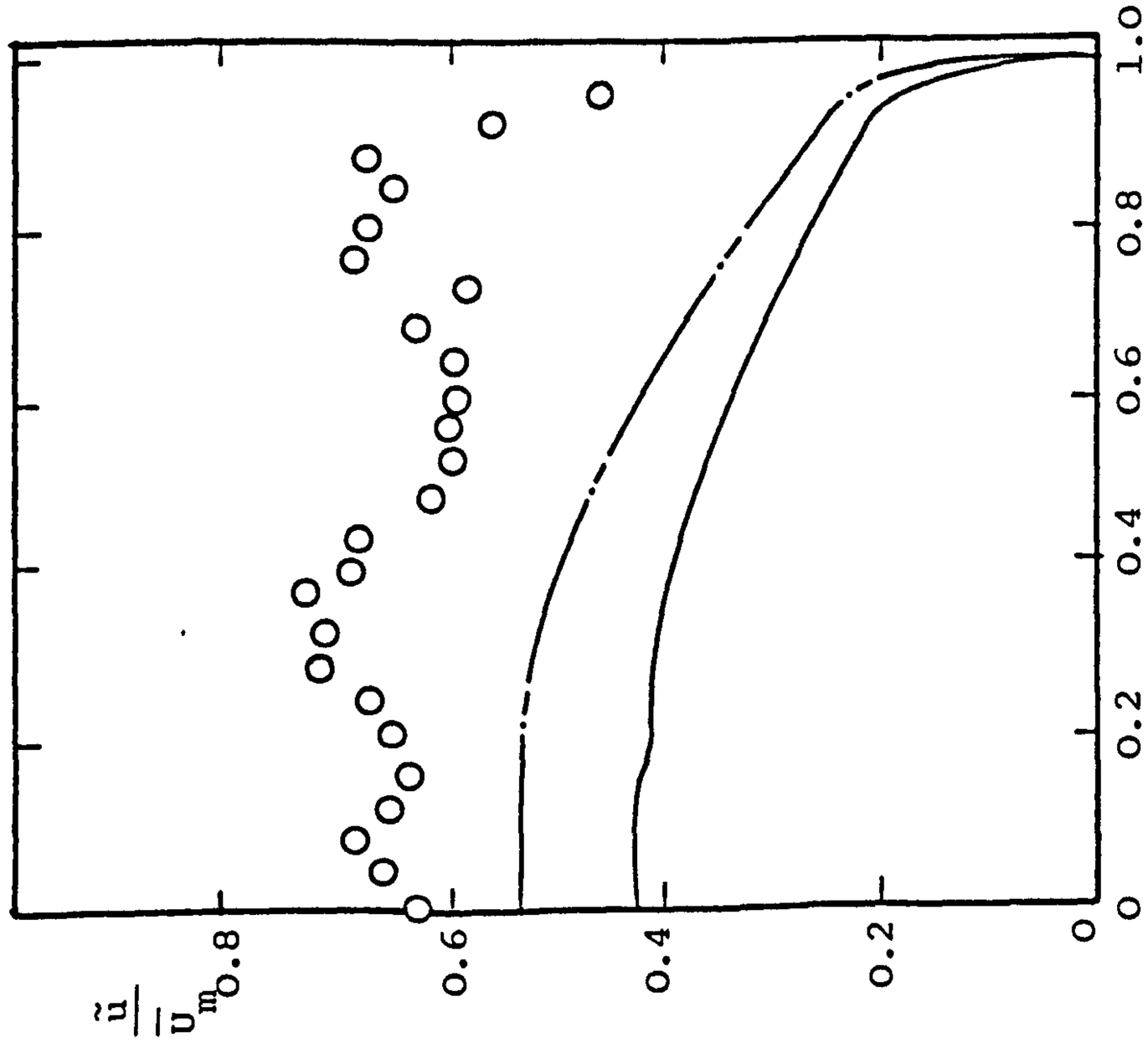


Fig. 3.22 Radial Profiles of Axial Normal Stress (X/D_e = 3.67, $\bar{U}_a/\bar{U}_p$ = 3.0); Notation as in Fig. 3.10

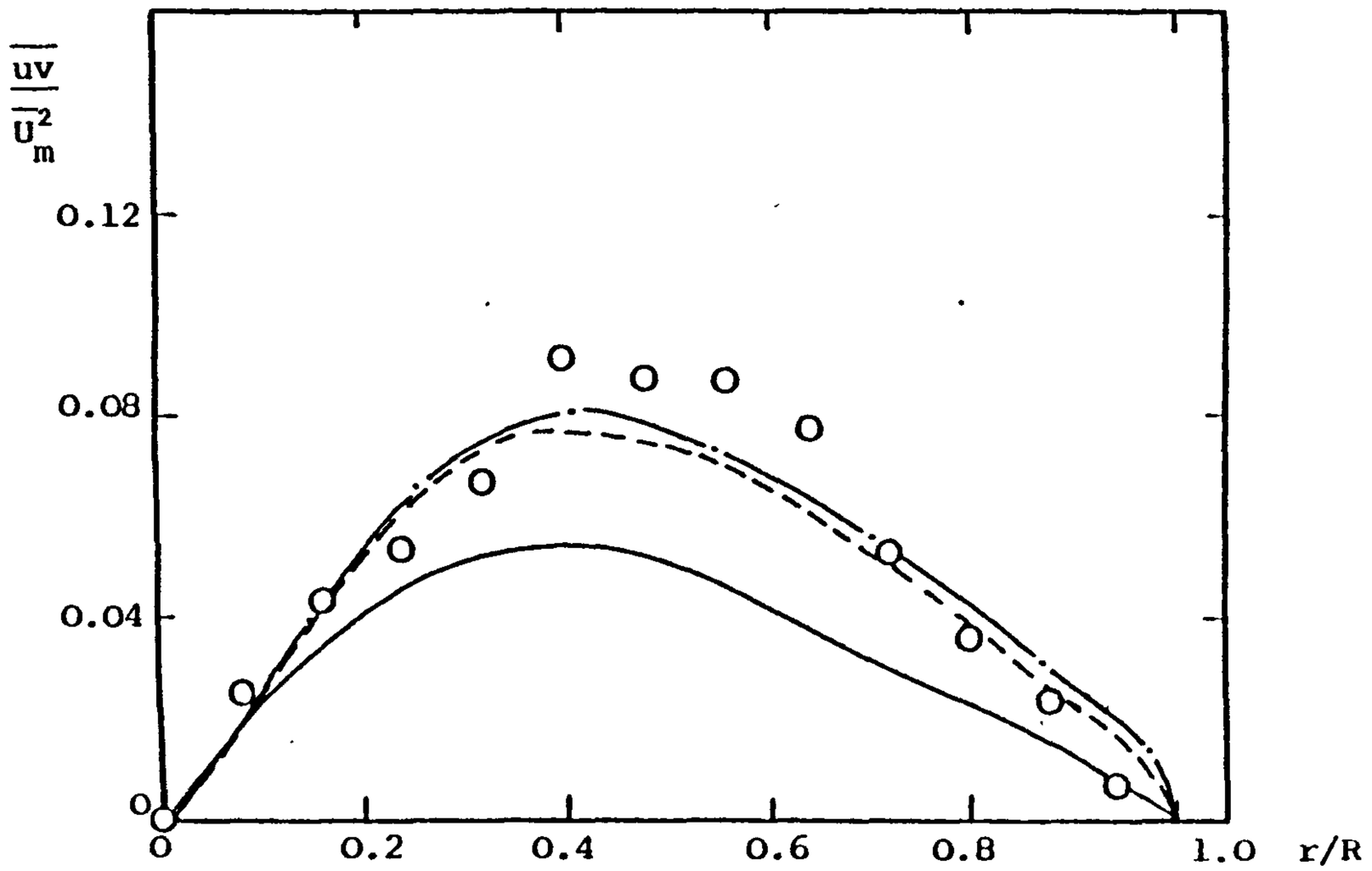


Fig. 3.24 Radial Profiles of Shear Stress (X/D_e = 3.67, $\overline{U}_a/\overline{U}_p$ = 3.0); Notation as in Fig. 3.10

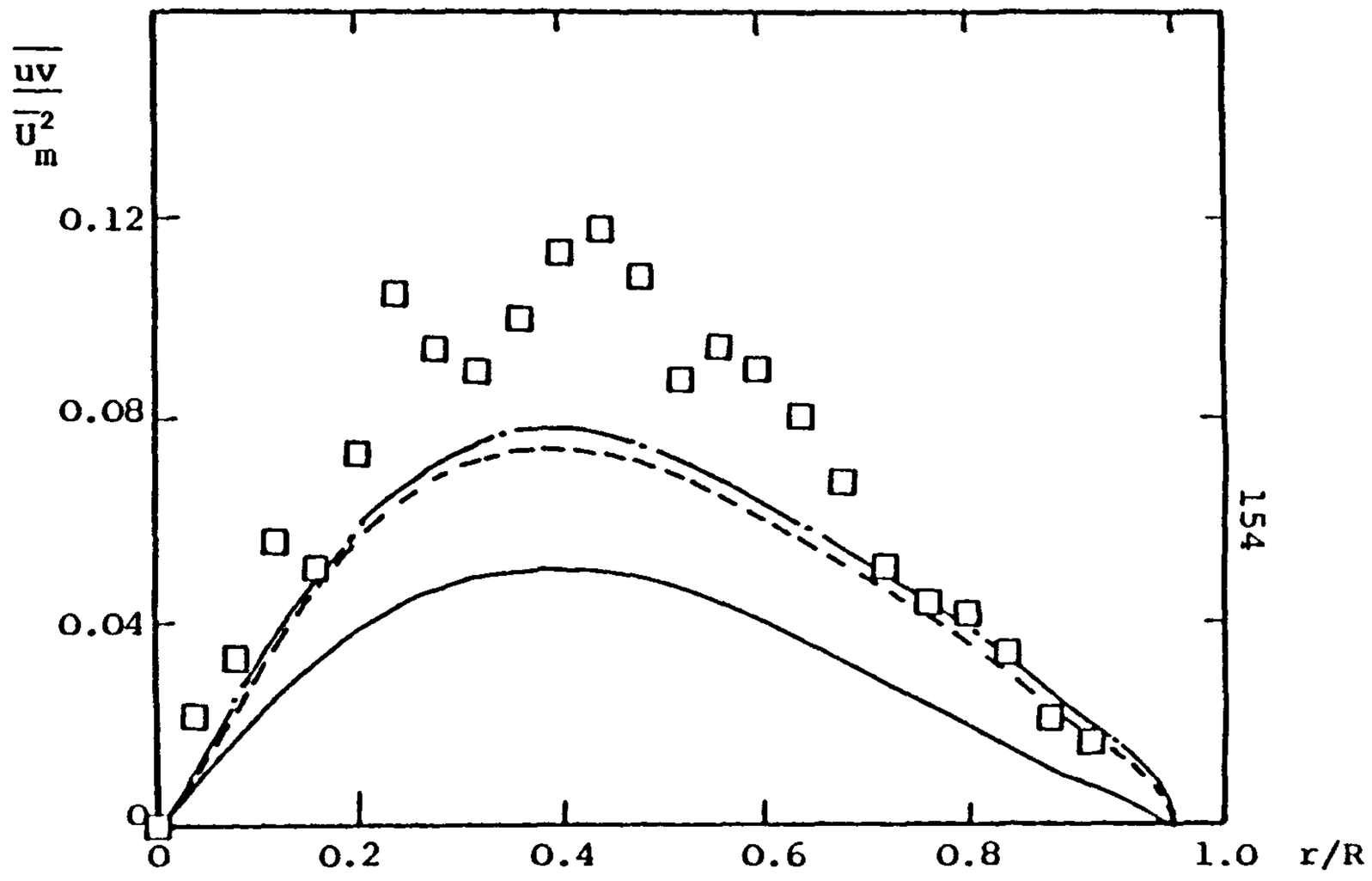


Fig. 3.25 Radial Profiles of Shear Stress (X/D_e = 3.67, $\overline{U}_a/\overline{U}_p$ = 1.0); Notation as in Fig. 3.10

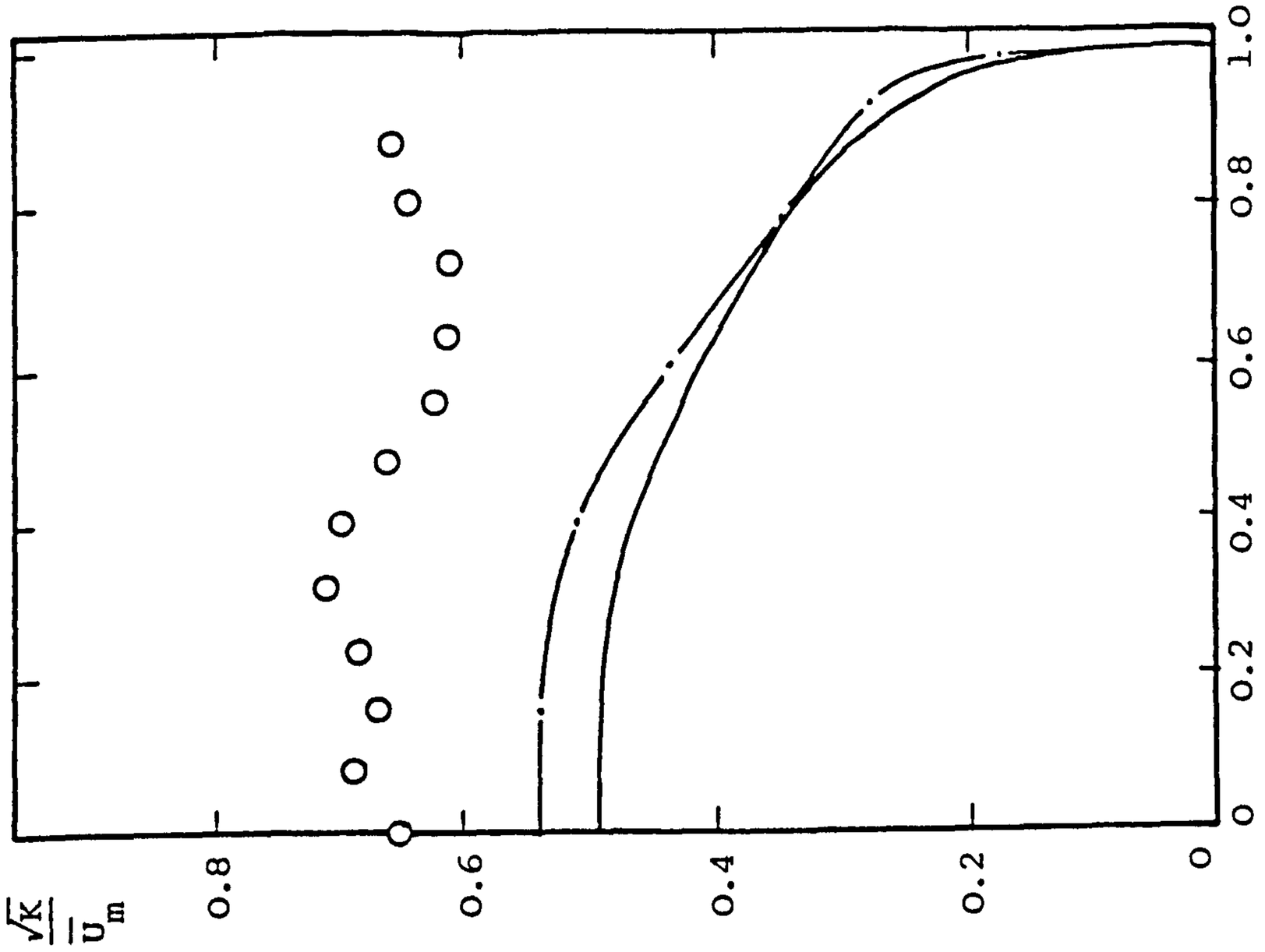


Fig. 3.27 Radial Profiles of Kinetic Energy of Turbulence (X/D_e = 3.67, $\bar{U}_a/\bar{U}_p$ = 3.0); Notation as in Fig. 3.10^a

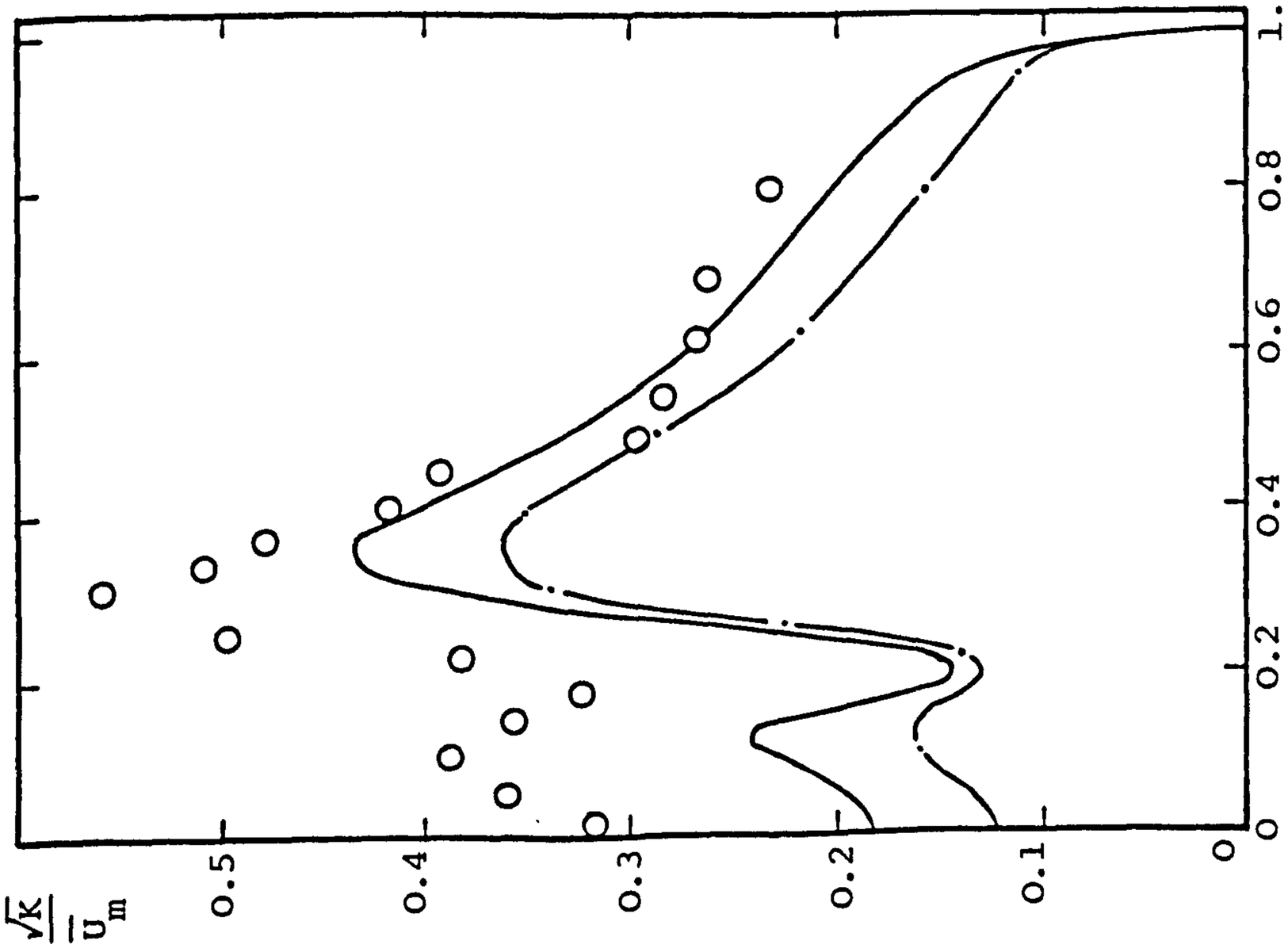


Fig. 3.26 Radial Profiles of Kinetic Energy of Turbulence (X/D_e = 0.616, $\bar{U}_a/\bar{U}_p$ = 3.0); Notation as in Fig. 3.10^a

PART II

FLOW CHARACTERISTICS OF THE QUARL ANGLE EXPANSIONS

CHAPTER 4

EXPERIMENTAL INVESTIGATION IN QUARL ANGLE EXPANSIONS

4.1 Introduction

The study of the flow field and turbulence characteristics of axisymmetric expansions is relevant to a number of practical flows which may be divided into two groups, the first with expansions of small total angle (5° - 10°) as in the diffusers of gas turbines and the second with large total angle such as quarl angle burners. The latter flows are of more interest in this chapter.

Certain general characteristics of separated flows in axisymmetrical expansions should be noted. The surface of separation is one of high velocity gradient and intense shear and occurs in an adverse pressure gradient. These conditions promote turbulence production which, in turn, involves entrainment of fluid lying outside the main stream of the flow. The region between separation and reattachment can be considered as a concentration source of turbulence with the subsequent convection, diffusion and decay of having a far-reaching influence on the characteristics of the mean motion.

In combustion, the presence of a divergent outlet for a burner plays an important part in the stabilization of high-intensity combustion and has a disproportionate effect on the recirculated mass flow; thus for a given swirl number, it has a strong tendency to increase the size and strength of the core recirculation zone. This increase in recirculating mass improves the flame stability, due to the heat transferred by the recirculating combustion products and to the reduced velocity again in the neighbourhood of the burner where the stabilization of the flame speed and flow velocity can be matched. It also reduces the length of the combustion region by producing

higher rates of entrainment of the ambient fluid and faster mixing close to the exit nozzle and on the boundaries of recirculation zone. On the other hand, the presence of a divergent burner outlet, with high swirl, reduces the pressure loss coefficient and, although the magnitude of this pressure recovery is not large, it improves the combustion efficiency since the reaction rate is proportional to the square of the pressure.

The aim of this chapter and the following one is to study flow and turbulence characteristics of quarl expansion ducts. In Chapter 5, a computational investigation is reported and in this chapter, the corresponding experimental program and results are described for two geometries of a burner model each with and without swirl. The motivation for the experimental program is outlined in the following section and the geometric configuration and design of the rig are presented in Section 4.3. The measuring technique and data-reduction devices are described in Section 4.4. The results are presented and discussed in Section 4.5 and summary conclusions presented in the final section.

4.2 Motivation and Objectives

The experimental investigation has two main purposes. First, to obtain detailed information and understanding of the flow in axi-symmetric expansions and thereby to assess the extent to which the flow in a model furnace is affected by the inlet and boundary conditions. Secondly, the experimental study was formulated to help the development and testing of a computational procedure for sudden-expansion and quarl-type flows so as to allow the calculation of furnace flow properties starting from a knowledge of the burner geometry and the mass flow of fuel and air.

4.3 Description of the Flow Configuration

As shown in Fig. 4.1, laboratory compressed air was supplied through two main pipes to provide the main flow to the test section and to atomize silicone oil required for seeding purposes. The seeded flow was introduced to the main flow through four inlet tubes at right angles to each other and to the main flow pipe. The flow passed through an orifice-meter, to measure the mass flow rate which was fixed for all the experiments with uncertainty of less than 0.5% and to a straight brass tube of one inch inside diameter and 1.5 meter length which was located immediately upstream of the test section.

4.3.1 The Test Section

The measurements were performed for the two different geometries, G1 and G2, as shown in Figs. 4.2 and 4.3 respectively. All parts of the test section were manufactured from perspex to allow laser Doppler anemometer measurements. The common part of the two geometries was manufactured from a perspex solid rod which was machined and polished to form a pipe of one inch inside diameter and 5 cm length ending with a diffuser part of total angle of 40° and length of 36.6 mm. This part was cut from its measuring side, as shown in the figure, to 2 mm thickness to minimize the loss of laser-beam intensity through the walls. The second part of the test section is an enclosure of 52 mm inside diameter for the first geometry and of 80.5 inside diameter for the second. The first geometry was designed so that the enclosure would fit directly to the end of the diffuser while, in the second, a circular flange was made to connect the enclosure to the diffuser part. The smaller cylinder of the first geometry was 3 mm thick and the larger one 5 mm thick; both were

391 mm long.

The composite system was adjusted coaxially using a pressure dial which ensured the surfaces of the brass tube, pipe part of the diffuser and the enclosure were parallel within 0.1 mm. The composite system was mounted on a traverse mechanism which was capable of moving in two perpendicular horizontal directions with precision of ± 0.1 mm.

The swirl was generated by a cascade of vane swirler which had two blades of 2 mm thickness inclined at 60° to the main direction of the flow. The swirler was 2.54 cm diameter and 10 cm long and was inserted into the brass tube, Fig. 4.1, so that its outlet section was about 5 cm upstream the expanding conduit inlet section. The swirl number, as defined by the ratio between the angular momentum of the air flow through the swirler and the axial momentum multiplied by a characteristic radius, is given by:-

$$S = \frac{\int_{r_i}^{R} \rho \, \overline{U} \, \overline{W} \, r^2 \, dr}{R_1 \int_{r_i}^{R} \rho \, \overline{U}^2 \, r \, dr} = 0.93 \qquad (4.1)$$

where r_i, ≡ 1.5 mm, and R_1 are the inner and outer radii of the swirler and $\overline{U}$ and $\overline{W}$ are the axial and tangential mean velocity components, respectively.

4.4 Measurement Technique and Data Analysis

The optical arrangement was similar to that described in Subsection 2.3.2, except that a 5 mW helium-neon laser replaced the argon one. As described in Subsections 2.3.2 and 2.3.4, a micro-processor was used to evaluate the probability distributions and to

calculate the mean and rms values according to Equation (2.16). The probability distribution was formed with a number of pulses corresponding to the duration time of the burst. Thus, the mean velocity is obtained according to the following formula, see Durão et al (1979):-

$$\bar{U} = \frac{\sum_{n=1}^{N} (U\tau)_n}{\sum_{n=1}^{N} (\tau)_n} \qquad (4.2)$$

where τ is the duration time of the Doppler burst and N is their number.

4.5 Presentation and Analysis of Results

In this section the measurements obtained for the two geometries each with and without swirl are presented and analysed. They were performed for one input flow rate corresponding to a Reynolds number of 32000, based on the average pipe flow velocity at the 1" diameter pipe outlet. The first part of the section presents the flow properties without swirl while those with a swirl number of 0.93 are presented in the second subsection, Subsection 4.5.2. The measurements were obtained along the axis and along the radii at the ten axial stations shown in Table 4.1: R_j is the radius of the confining tube at each station.

4.5.1 Measurements of the Mean and rms Velocity of the Flow in Quarl-Angle Expansion Without Swirl

(i) The Flow in Geometry G1

The radial profiles of axial mean velocity and the

TABLE 4.1

LOCATION OF MEASUREMENT STATIONS

Station	1	2	3	4	5	6	7	8	9	10
Distance from inlet section, cm	0.00	1.50	2.50	5.50	7.00	10.00	13.00	19.00	22.00	25.00
R_j (G1) mm	12.70	18.16	21.80	26.00	26.00	26.00	26.00	26.00	26.00	26.00
R_j (G2) mm	12.70	18.16	21.80	40.25	40.25	40.25	40.25	40.25	40.25	40.25

corresponding normal stress are shown in Figs. 4.4 and 4.5. They have not been normalised for two reasons; the first is that all the measurements were obtained for one input velocity distribution and, secondly, it was difficult to specify a normalisation parameter which is common for zero and finite swirl. The half angle of expansion was 20° which is high enough to cause separation from the wall and this separation is confirmed by the radial profile at Station 2 of Fig. 4.4. The profile at Station 1 corresponds to fully developed pipe flow and the boundary layer has separated between the two stations. The description of turbulent boundary layer separation is not clear cut as in a steady laminar flow, where separation is presumed to occur at a location along the flow where the wall shear vanishes. Sandborn and Kline (1961), Spangenberg et al (1967) and Simpson et al (1977) have shown that turbulent separation, or intermittent separation, occurs at the upstream point (the turbulent separation point or the intermittent separation point) at the wall where backflow begins on an intermittent basis. This region exists in the adverse pressure gradient, where the mean velocity in the boundary layer near the wall decreases at a greater rate than the turbulent fluctuations decrease and the turbulence intensity exceeds 0.3. In this region, the turbulent fluctuations appear to become predominant and, as separation is approached, more negative turbulent excursions exceed the local forward velocity in absolute value so that, in the limit, the turbulent fluctuations will exist with no forward flow. After this occurs, the weakened driving force of the stresses within the fluid becomes less than the retarding effects of the adverse pressure gradient so that the separation ensues.

The width of the recirculation increases with the increase in duct diameter, as shown at Stations 3 and 4 in Fig. 4.4. On the

other hand, the mean velocity values near the centre-line decrease with axial distance. The decrease of the mean velocity near the centre-line is mainly due to the transfer of eddies, created near the boundaries of the recirculation zone, inside it and near the wall into the centre-line. These eddies have relatively low forward velocities, and, as they mix with the rapidly moving central part of the stream, the fast-moving fluid is gradually slowed down. This is shown by Fig. 4.4 where the centre-line velocity decreases with the distance from the entrance to the expanding duct and up to the last station.

Downstream of Station 4, the width of the recirculation zone decreases as shown at Station 5 until reattachment before Station 6 where the near-wall velocity increases with the near centre-line velocity decreasing and the flow develops towards a fully developed pipe flow.

The radial profiles of the axial normal stress are presented in Fig. 5.5 for the same axial locations as the mean velocity. They indicate that, at the upstream sections, the maxima of the normal stress profiles are close to the maximum gradients of the axial mean velocity. This link breaks down gradually at the downstream sections. As described by Spangenberg et al (1967) in flows with adverse pressure gradient, the contribution to the turbulence production shifts its emphasis from the velocity gradient to the Reynolds stress. In other words, the maximum turbulence-production rate, in separating flows, coincides with the region of maximum Reynolds stress tensor rather than with the region of high local velocity gradient. The production of K may be expressed as:-

$$G_K = - \rho \left[\overline{uv} \left(\frac{\partial \bar{U}}{\partial y} + \frac{\partial \bar{V}}{\partial x} \right) + \overline{u^2} \frac{\partial \bar{U}}{\partial x} + \overline{v^2} \frac{\partial \bar{V}}{\partial y} + \frac{\bar{w^2} \bar{v}}{r} \right]$$

and that of $\overline{u^2}$ is:-

$$G_{\overline{u^2}} = - 2\rho \left(\overline{u^2} \frac{\partial \bar{U}}{\partial x} + \overline{uv} \frac{\partial \bar{U}}{\partial y} \right)$$

As can be shown from the results in Chapter 2 and by Kalinske (1967), the production of $\overline{u^2}$ in turbulent shear flows where the axial velocity is predominant represents the major part of the production of the kinetic energy of turbulence and the magnitude of the axial normal stress is the major contribution for the kinetic energy of turbulence. The longitudinal strain, $\partial\bar{U}/\partial y$, plays an important part in the production of $\overline{u^2}$ directly through $- 2\overline{uv}\ \partial\bar{U}/\partial y$ and indirectly through the production of $\overline{uv}$ by $- \overline{v^2}\ \partial\bar{U}/\partial r$. In this situation $\partial\bar{U}/\partial r$ is of large negative value and consequently, the production of $\overline{u^2}$ is large. In the upstream region, Stations 2 to 6, $\partial\bar{U}/\partial r$ is much greater than $\partial\bar{U}/\partial x$ and the production due to the extra strain $\partial\bar{U}/\partial x$, although significant, is small compared with that of the main strain, $\partial\bar{U}/\partial r$. Thus, in the upstream region, the maximum production of K is strongly connected to the maximum of the shear stress while it is associated with the maximum of $\overline{u^2}$ at the downstream stations.

The results of Chaturvedi (1963), for diffusers with half angles of 15° and 30°, indicate that the maximum production of the kinetic energy occurs at the separation surface (or the boundary of the recirculation zone) at the beginning of separation. At the downstream sections, these results show that the position of the maximum production moves away from the separation region towards the centre-line and this is supported by the present measurements where

the location of the maximum normal stress is created initially near the separation line, see Fig. 4.5, and moves gradually towards the centre-line until it is completely transferred to the axis of symmetry at Station 6. It is thought that the energy containing eddies created near the separation at the upstream sections are moved into the main stream flow and the turbulence energy produced near separation is diffused through its gradients inside the main stream flow. It may be noted that the rate at which energy is supplied to the energy cascade is determined by the largest elements (range of energy extraction). These eddies are created in the regions of high velocity gradients. However, the eddies of maximum kinetic energy are those of higher wave number (see Reynolds, 1974) and are formed from tearing the large eddies by shear. The movements of these comparatively smaller eddies cause the transfer behaviour mentioned above. This may also explain the increase in the width of the radial profile of the normal stress near the maximum value with the axial distance as shown from Fig. 4.5.

Fig. 4.5 shows that the normal stress values downstream of Station 6 have decreased and at a higher rate near the centre-line. This is mainly due to rapid decrease in the maximum shear stress and the velocity gradient near the point of the maximum shear stress, which occurs downstream of the reattachment, and is consistent with the results of Mueller and Robertson (1963) and Bradshaw and Wong (1972) and to the positive rate of strain, $\partial\overline{U}/\partial x$, near the wall and the consequent production of $\overline{u^2}$ at the negative rate of $-2\rho\,\overline{u^2}\,\partial\overline{U}/\partial x$. The decrease of $\overline{u^2}$ downstream of the region of reattachment was also observed by Moss et al (1979) in their measurements in backward-facing step. The comparison with the mean velocity distributions of Fig. 4.4 indicates that the mean flow is developing faster than the turbulence.

This results in the conclusion that the diffusion in the momentum equations is becoming of less influence at the downstream sections.

(ii) The Flow in Geometry G2

The radial distributions of the mean axial velocity at different x-locations in the geometry G2 are presented in Fig. 4.6. The general features of the mean velocity distribution in the angled expansion are very similar to those in the first geometry, G1. The figure allows comparison of the mean velocity distributions in the upstream sections for the two different geometries and shows the extent of the upstream influence of the downstream recirculation region, associated with the sudden expansion. The existence of downstream sudden expansion has caused a decrease in the mean velocity gradient at Stations 2 and 3 with smaller magnitudes of the velocity near the centre-line and in the recirculation zone, and the width of the recirculation has decreased. In the downstream stations the main stream retains its high momentum with the growth of the boundary layer thickness outside the recirculation. This may be attributed to the entrained air from the recirculation zone. Further downstream, Station 6, the flow develops towards a boundary layer flow with the reattachment point near to Station 8.

The radial distributions of the rms of the axial velocity fluctuations are presented on Fig. 4.7 which indicates that the normal stress in the upstream sections is reduced by the imposed sudden expansion. This is in accord with the decrease in the mean velocity gradients mentioned above since the production of the normal stress is mainly connected to the mean velocity gradient in the upstream stations as discussed in (i) above. As the normal stress produced at the expanding duct diffuses to the centre-line, its

distribution becomes more uniform in the sections downstream the sudden expansion. Fig. 4.7 also indicates that the normal stresses at Stations 4, 5 and 6 are low by comparison with those of the first geometry, Fig. 4.5. Further downstream, the continuous production of the kinetic energy of turbulence near the boundary of the re-circulation zone in the flow of the second geometry, G2, minimises its decay and results in higher values for the normal stress at the downstream Stations 7, 8 and 10, by comparison with the flow of the first geometry.

The radial profiles of Figs. 4.4 to 4.7 were interpolated to form the contours of the axial mean velocity and corresponding normal stress for both the geometries, see Figs. 4.8 and 4.9. Fig. 4.8 shows that the flow of G2 is associated with a higher rate of decay of the mean velocity along the centre-line in the expanding duct and with lower decay in the downstream region. It is clear also that the velocity magnitudes in the recirculation region are larger for the flow of G1 with respect to those of G2. Fig. 4.9 shows that the rates of increase and decay of the normal stress values are much larger in the case of the flow of G1.

4.5.2 Measurements of the Mean and rms Velocities of the Flow in Quarl-Angle Expansion With Swirl

In this subsection, the measurements obtained in the geometries of the previous subsection are represented for a swirl number of 0.93. The properties of the flow in G2 are presented and analysed in the following paragraphs while those of G1 are used for comparison only; further details are available in Appendix A2.

The development of the axial mean velocity across the centre-line is shown in Fig. 4.10 which indicates a central

recirculation zone with a width of $r/R \tilde{\sim} 0.21$ at the inlet section. The zero-velocity location moves radially outward and the recirculation zone covers a significant portion of the enclosure radius and reaches a maximum value of $r/R = 0.62$ at Station 2. It can be seen from Station 4 that the radial profile has a wall recirculation zone in addition to the central one. Further downstream, both recirculation zones diminish and the wall recirculation region disappears completely as indicated by Station 6. The point of maximum positive velocity moves towards higher radii with a decrease in its value at downstream stations.

Corresponding to the mean velocity distribution, the rms of the axial velocity fluctuations are presented in Fig. 4.11. As described in Subsection (i) the maximum normal stress is associated with the maximum mean velocity gradient; the swirling flows are associated with new shear stresses, $\overline{uw}$, $\overline{vw}$, however. The generation of $\overline{u^2}$ is still mainly connected to the shear stress $\overline{uv}$ and the rate of strain $\partial\overline{U}/\partial y$ as it can be expressed as:-

$$G_{\overline{u^2}} = -2\rho\left(\overline{u^2}\frac{\partial\overline{U}}{\partial x} + \overline{uv}\frac{\partial\overline{U}}{\partial y}\right)$$

It is expected, therefore, that the location of the maximum normal stress will be related to the maximum rate of strain, $\partial U/\partial y$, in the region of high shear as in the case of no swirl. This is confirmed by the radial profiles at Stations 1, 2, 3 and 4. The energy of turbulence generated at locations of high rate of strain at the upstream stations, diffuses towards the centre-line at the downstream sections. At Station 6, the normal stress exhibits two maxima; the first lies on the centre-line and the second is near the wall. The

latter is likely to be associated with the region of high mean velocity gradient, $r/R \tilde{} 0.8$. This maximum decays in the downstream region and the radial profiles of the normal stress exhibit one maximum on the centre line. The production of the kinetic energy of turbulence may be expressed as:-

$$G_K = - \overline{u^2} \frac{\partial \bar{U}}{\partial x} - \overline{uv} \frac{\partial \bar{U}}{\partial r} - \overline{uv} \frac{\partial \bar{V}}{\partial x} - \overline{v^2} \frac{\partial \bar{V}}{\partial r} - \overline{uw} \frac{\partial \bar{W}}{\partial x} - \overline{vw} \frac{\partial \bar{W}}{\partial r} + \frac{\bar{W}}{r} \overline{vw} - \frac{\bar{V}}{r} \overline{w^2}$$

It is unlikely that the maximum on the centre-line can be attributed to the axial rate of strain, $\partial \bar{U}/\partial x$, since the rate of change of $\bar{U}$ with x is small, as indicated by Fig. 4.10. It is more probable that the generation of K is due to the high rates of strain, $\partial \bar{W}/\partial r$, $\partial \bar{U}/\partial r$ and $\partial \bar{V}/\partial r$, as may be shown by Figs. 4.10 and 4.12. It is expected that these rates of strain represent a source of energy production in the region around the centre-line.

Fig. 4.12 presents the radial profiles of the tangential mean velocity components which reveal a forced vortex distribution of the tangential velocity and a consequent high centrifugal force which stems from high values of the pressure gradient as can be seen from an overall momentum balance. The size of the central recirculation zone is dependent on the value of this pressure gradient. The effect of the divergent part is to develop this centrifugal force and so it tends to increase the size of the central recirculation zone. The stations downstream the sudden expansion exhibit uniform $\bar{W}$-distributions away from the axis with very steep gradients near the centre-line and support the results of Beltagui and MacCallum (1976) in sudden expansion geometries.

The distributions of the rms of the tangential velocity fluctuations are presented in Fig. 4.13. The maxima of the profiles

are connected to the maxima in the tangential mean velocity gradient. The production of $\overline{w^2}$ is related directly to the rate of strain $\partial\overline{W}/\partial r$ and indirectly by the generation of $\overline{vw}$ through the term $-\overline{v^2}\,\partial\overline{W}/\partial r$. The maxima is transferred from locations near to the wall, Stations 2 and 3, towards the centre-line, Stations 4, 6, 7 and 9. The latter stations exhibit two maxima, on the centre-line and near to the wall; the first is largely due to the high rates of strain in the region around the axis of symmetry and the second is probably due to the destruction of the v-fluctuations near the wall by irrotational vortex to u and w-fluctuations. The latter was also indicated by Moss et al (1979) and Bradshaw and Wong (1972).

A comparison of the rms of the axial and tangential velocity fluctuations is presented in Fig. 4.14 and provides a measure of the anisotropy associated with swirling flows. The figure indicates high degree of anisotropy, in general, with the similar trend of the two normal stresses in the downstream region reducing the degree of anisotropy. This suggests that turbulence models which are based on the homogeneity assumption are inadequate for calculation of the swirling flows.

In order to study the effect of the presence of a sudden expansion on the flow properties, the axial mean velocity and the corresponding normal stress are compared with those of the first geometry in Figs. 4.15 and 4.16 respectively. Fig. 4.15 indicates that the sudden expansion in geometry G2 led to an increase in the length of the recirculation zone; this increase in the size of the central recirculation zone is associated with higher values of the negative velocity. It led also to the transfer of the region of maximum negative velocity towards the inlet section and, as a result, a strong shear layer is formed outside the recirculation zone in the

expanding conduit region. This shear layer resulted in high turbulence levels in that region for the case of the second geometry, G2, Fig. 4.16. This energy level diffuses in the downstream section and the flow of the G1 exhibits higher levels of turbulence.

4.5.3 Probability Density Distributions

Probability density distributions of the longitudinal and tangential velocity fluctuations for the flows in the second geometry, G2, are presented in this subsection. They are presented along the centre-line and along the radius at different x-locations for swirl numbers of zero and 0.93.

Fig. 4.17 represents the probability density distributions of the longitudinal velocity fluctuations along the centre-line for S = 0.0. The distributions are normalised by the rms of the fluctuations and show that the distributions are skewed, although not significant, with high probability of occurrence on the side of positive u-values. These results are in accord with those of Chapter 2 and indicate that the skewness is related to the dominant occurrence of eddies moving with a velocity much larger or much lower than the local mean velocity. In this situation, fluctuations with an axial momentum much larger than the local mean are transported to the points under consideration. This is also confirmed by the distributions of the probability density along the radius at Stations 2, 3, 6 and 7, presented in Figs. 4.18, 4.19, 4.20 and 4.21 respectively. The figures indicate negative skewness near the centre-line, where the transport is outward ($\overline{v}$- velocity component is positive) with the centre-line of higher axial velocity values. Away of the centre-line and at larger values of r/R_j, the probability distributions are more affected by slow motions from the wall region; at large radii, the

skewness exhibits positive values with the most probable value negative (for example, at r/R_j = 0.9, Station 3 and r/R_j = 0.82 and 0.969 at Station 6 and r/R_j = 0.745 and 0.894 at Station 7).

For the swirl number of 0.93, the probability density distributions of the longitudinal velocity fluctuations are presented in Figs. 4.22 to 4.26. Along the centre-line, they exhibit nearly Gaussian behaviour with low values of the skewness factor and the most probable value is zero. Along the radii, Stations 3, 4, 5 and 7, the distributions are positively skewed with the tail of the probability distribution longer in the positive side. This is clearly illustrated by the radial profiles, particularly in the near wall points where the abnormality of the distributions is greatly increased, r/R_j = 0.944 at Station 7. Corresponding probability density distributions of the tangential velocity fluctuations are presented in Figs. 4.27 to 4.30. Fig. 4.27 shows that the probability density exhibits bimodal behaviour along the centre-line. The figure shows the occurrence of two peaks for all the points on the centre-line. The spacing between the peaks remains nearly the same downstream of X/R_1 = 0.63 and, consequently, the amplitude of the motion does not change significantly. This is not the case for the upstream points, where the spacing between the peaks was decreased from the first station to the second. This may be explained by the lower steep gradient of the W-velocity near the centre-line in the expansion part with respect to the downstream locations. The radial distributions indicate that the probability distributions are nearly Gaussian in the region away from the centre-line and up to the near-wall locations where slow motions tends to skew the distributions with the most probable w-value negative.

4.6 Summary and Conclusion

The main purpose of the experimental investigation of this chapter was to provide new and useful information for developing, expanding flows in two geometries of practical interest. Thus, measurements of mean velocity, the corresponding normal stresses and probability density distributions are reported for two different swirl numbers in two geometries by means of a laser Doppler velocimeter. In these measurements, the signal processing was based on averaging of a number of individual frequency measurements in which the probability distribution was formed with a number of pulses corresponding to the duration of the burst. Thus, the results were free of any bias due to the correlation between particle number and velocity. The data allow improved understanding of turbulence and aspects of turbulence modelling procedure to predict increasingly more complex flows.

The cases investigated were turbulent flow with zero and 0.93 swirl numbers in an expanding duct ending with and without sudden expansion to a confinement, G2 and G1, respectively. Each of the four flows displayed strong ellipticity; a wall recirculation zone was formed in the case of zero swirl while in the 0.93 swirl number case, a central region of reverse flow was indicated in both of the two geometries. The elliptic nature of the flow in any of swirl or no swirl cases showed that the difference in the flow properties in the cylindrical confinement, due to the difference in geometry between G1 and G2, led to corresponding differences in the expanding duct. For example, the mean velocity gradients, width of the recirculation zone and value of maximum normal stress, were smaller in the flow of G2 in the expanding conduit region for the zero swirl number case. Also, in the 0.93 swirl number flows, the central

recirculation zone was shifted towards the inlet section with higher magnitudes of negative velocities in the flow of G2.

The results of Section 4.4 for zero swirl number showed that the Reynolds stress generation is connected to the main rate of strains, $\partial\overline{U}/\partial y$, in the upstream region. This connection breaks down in the downstream region and the production of $\overline{u^2}$ is connected to the maximum value of the Reynolds stress. The results showed also the importance of the extra strain-rate terms, any terms other than $\partial\overline{U}/\partial y$, on the generation of the kinetic energy of turbulence. As suggested by Bradshaw (1973), the effect of these high strain on the Reynolds stresses are not well presented by any of the present turbulence models. It is suggested that these models will become inadequate to represent the flow properties as the value of the lateral rates of strain increase.

1 Cylindrical tube
2 Diffuser section } Test section
3 Brass tube
4 Brass tube
5 Standard orifice meter
6 Supply of atomized silicone oil
7 Supply of compressed main flow
8 Traverse mechanism
------- Refers to Geometry G2

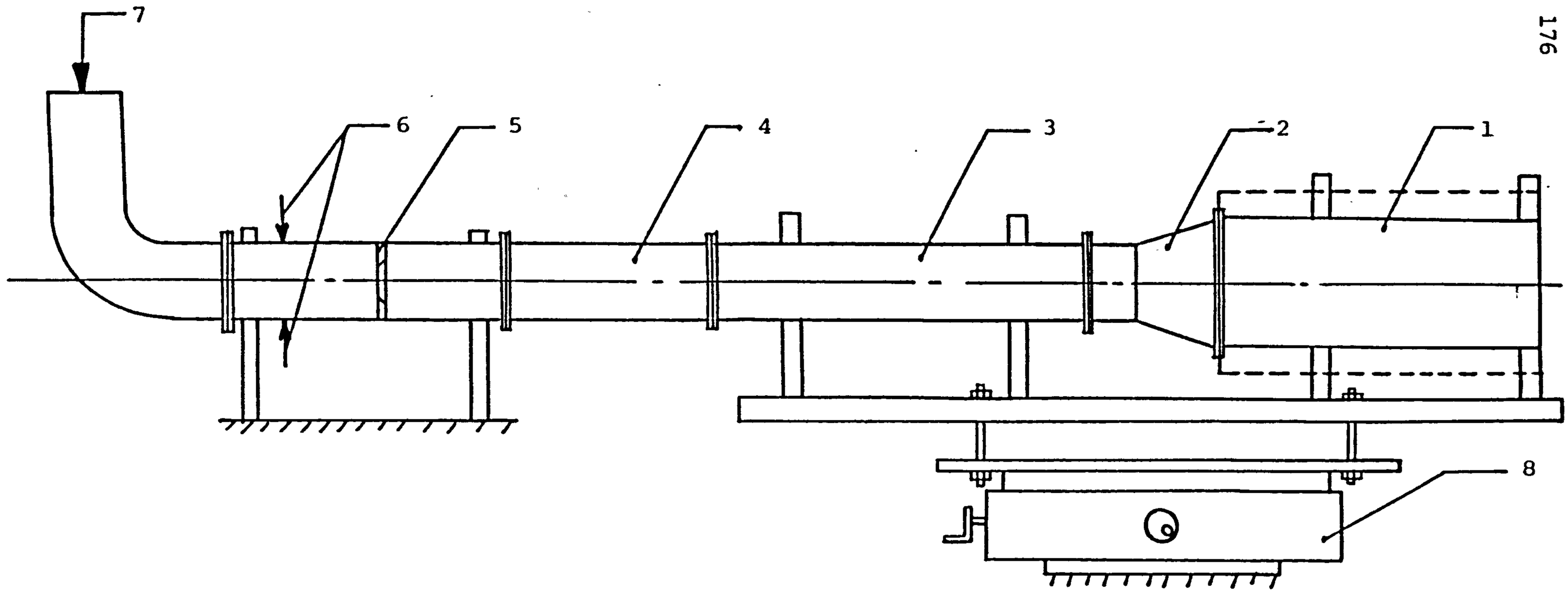
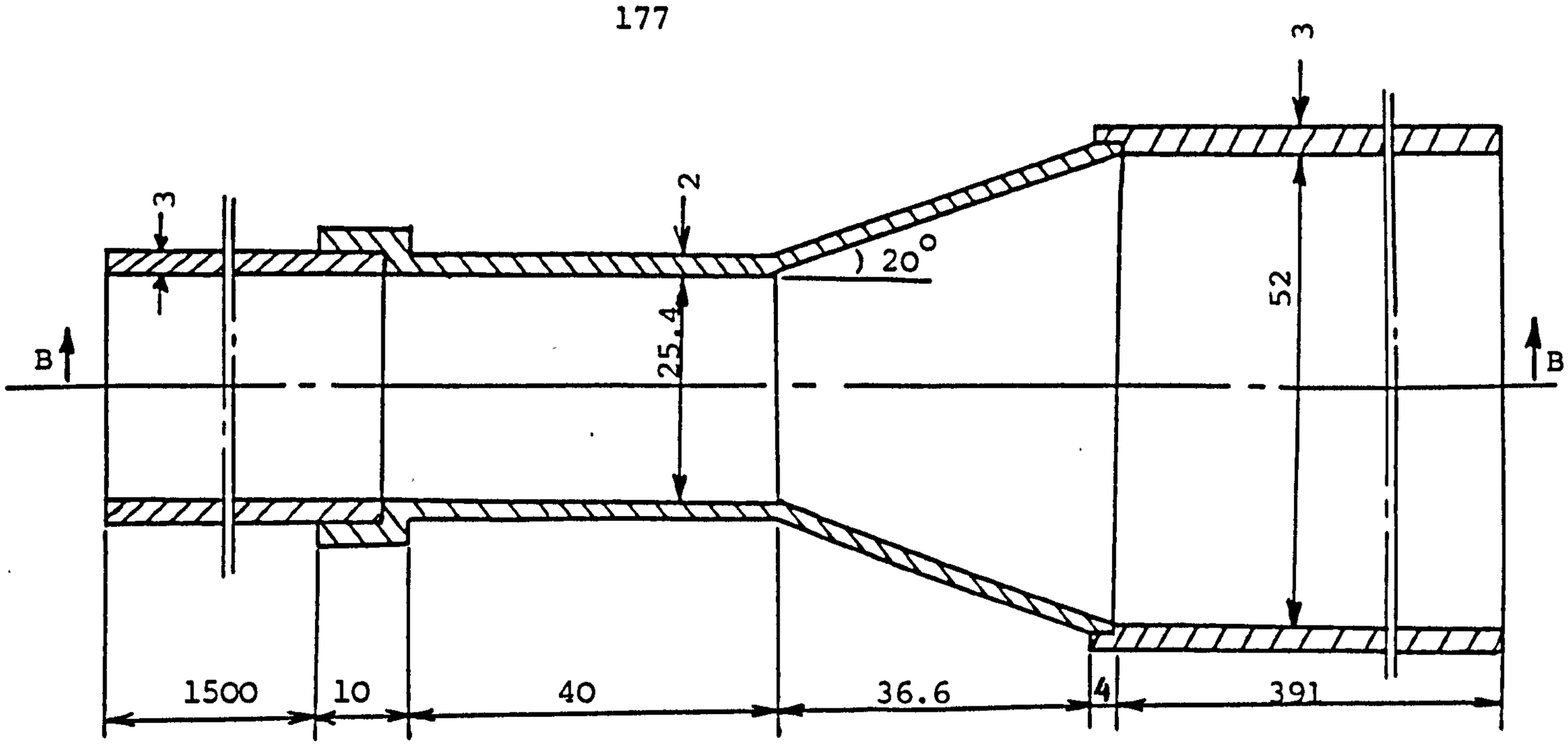
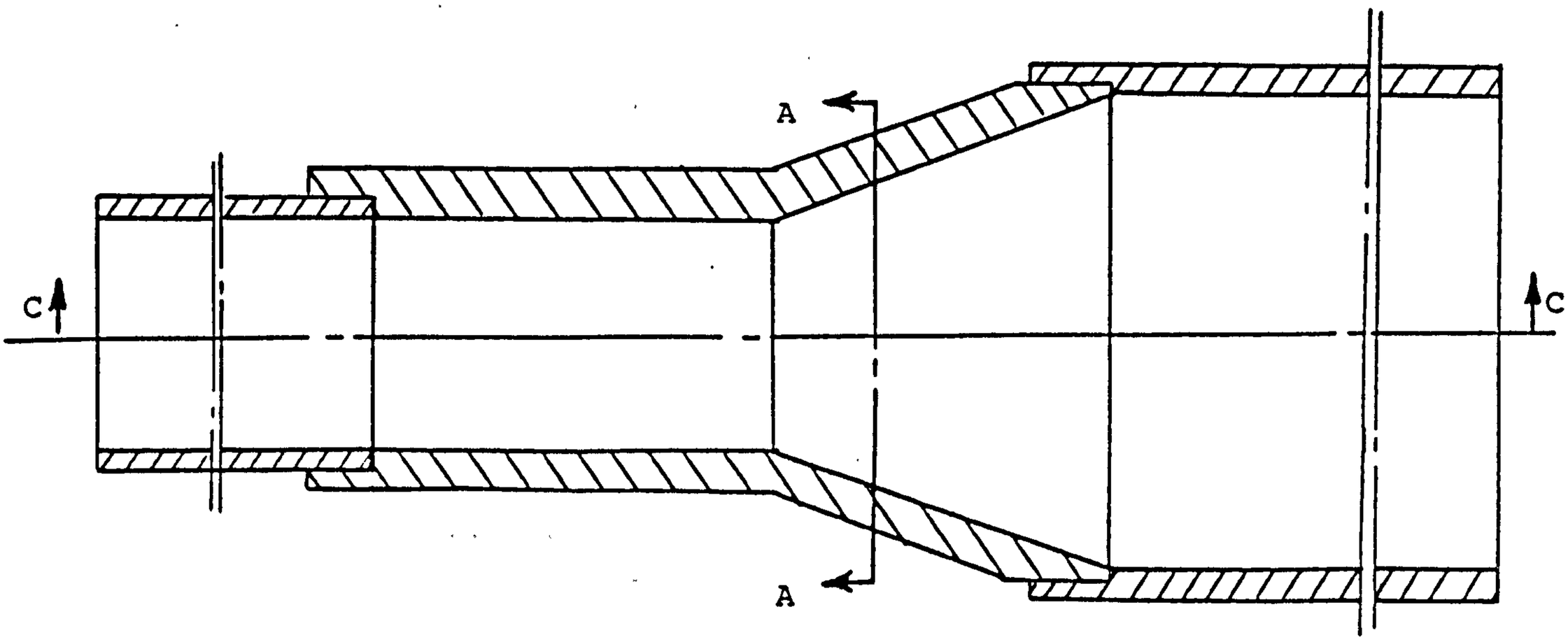


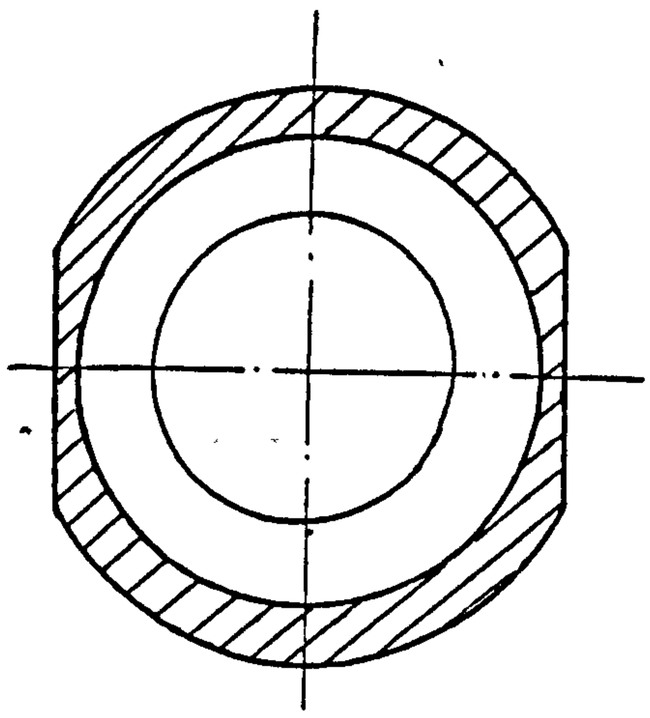
Fig. 4.1 Assembled View of the Experimental Rig



Section C-C



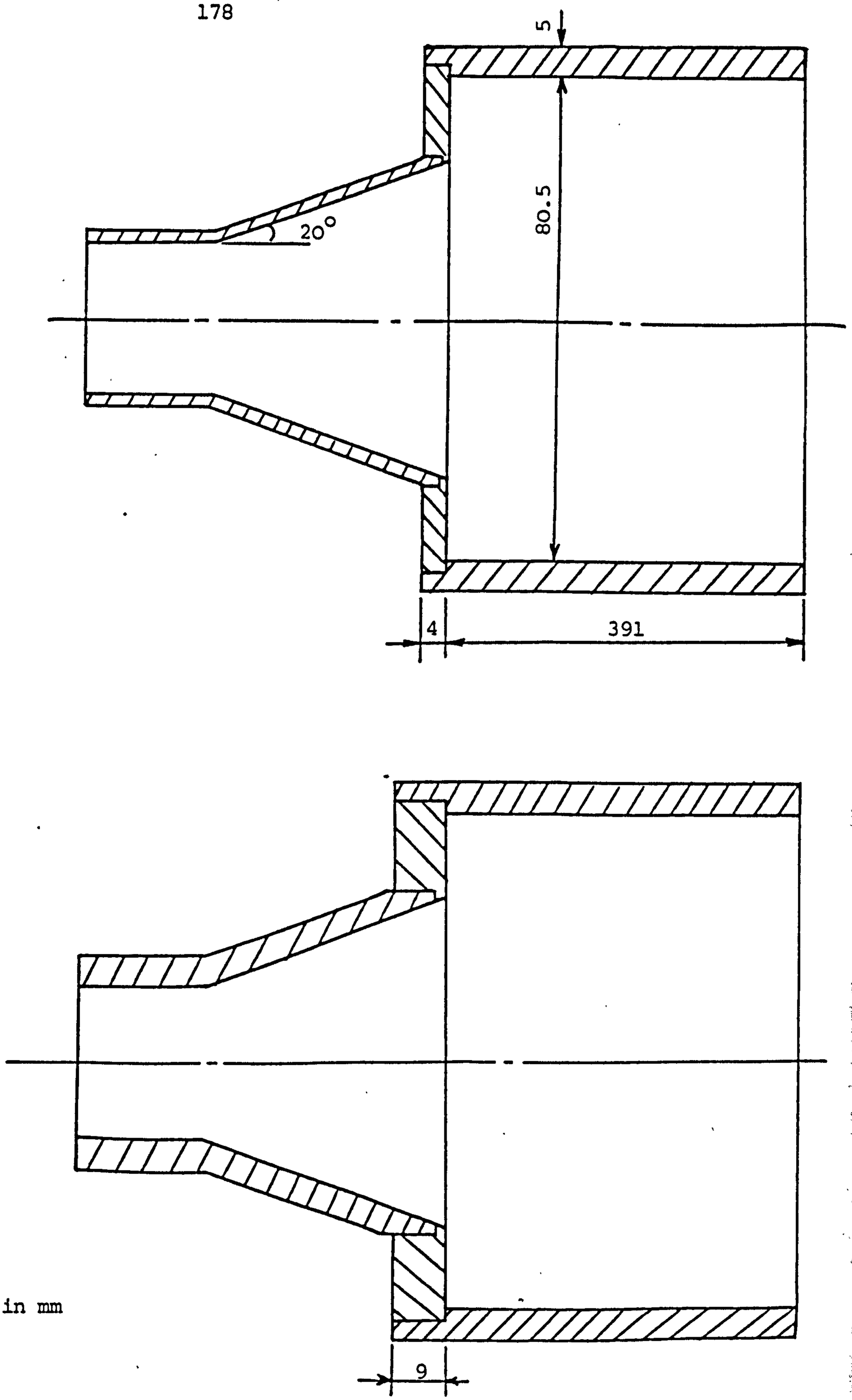
Section B-B



Cross-Section at A-A

Dimensions in mm

Fig. 4.2 Construction Views of the Test Section, Geometry G1



Dimensions in mm

Fig. 4.3 Construction View of Test Section, Geometry G2

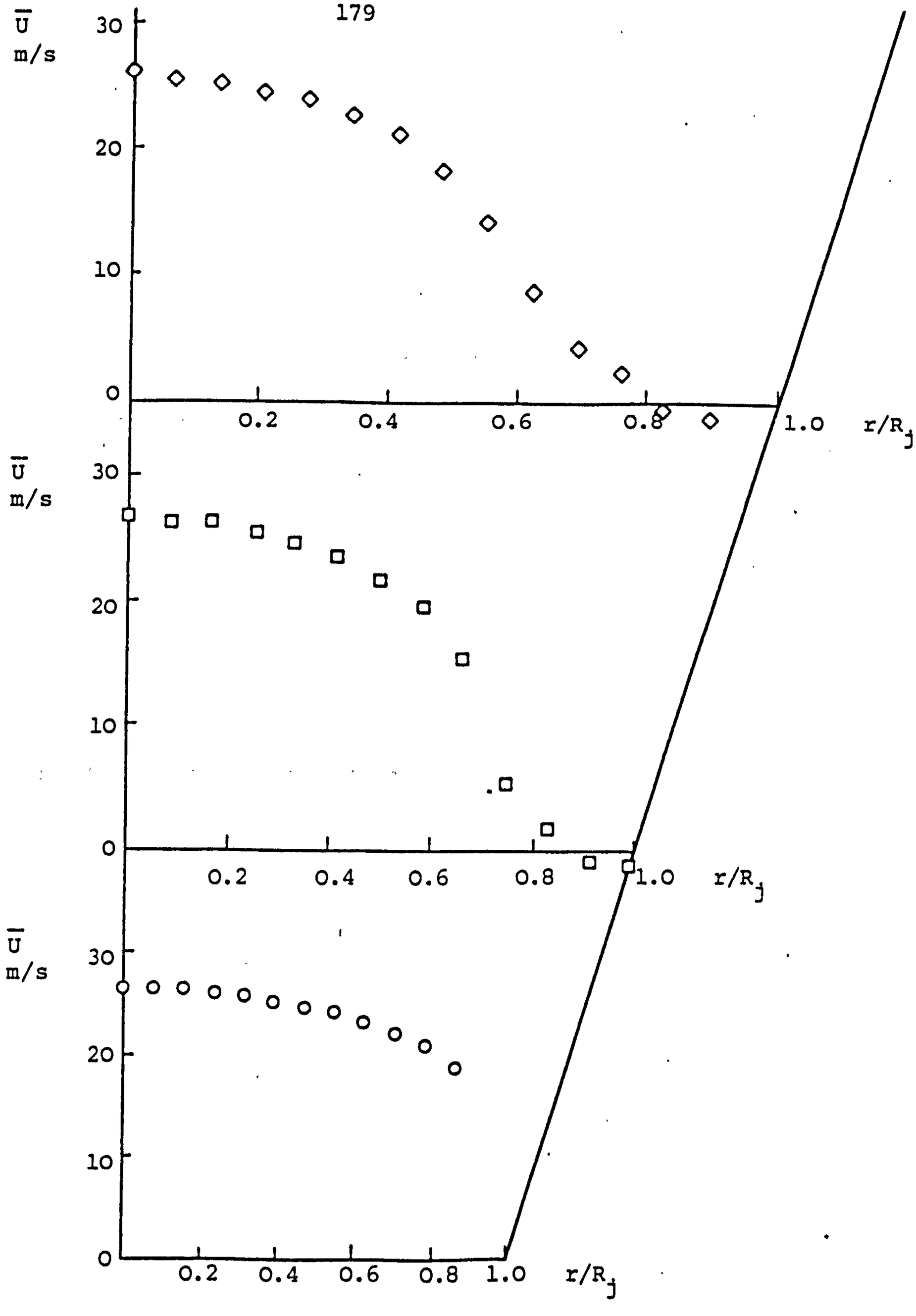


Fig. 4.4 Development of Velocity Profiles Across the Centre-Line of G1 (S = 0.0)

Symbol	○	□	◇	▽	△
Station No.	1	2	3	4	5
Symbol	●	■	◆	▼	▲
Station No.	6	7	8	9	10

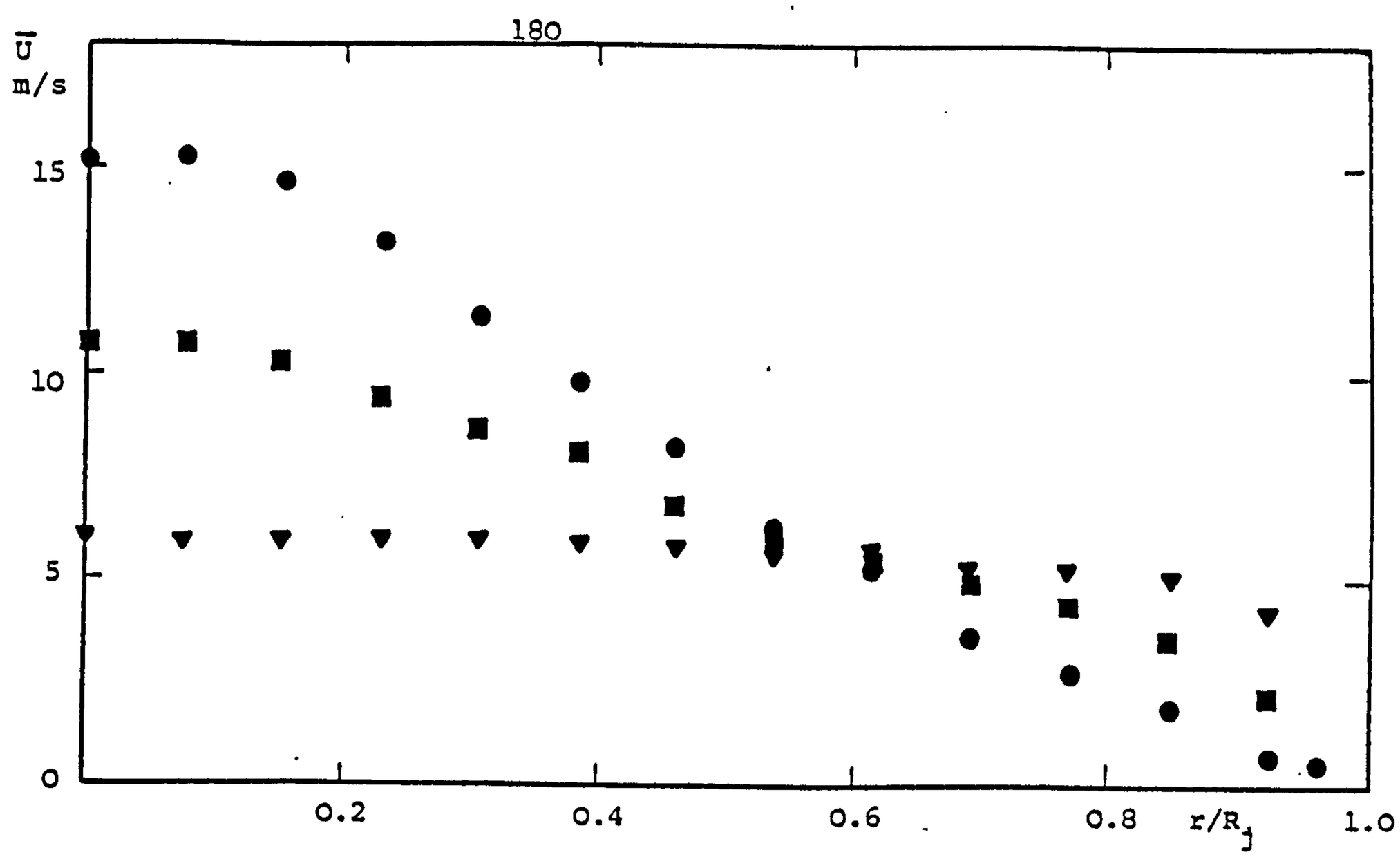


Fig. 4.4 (Continued)

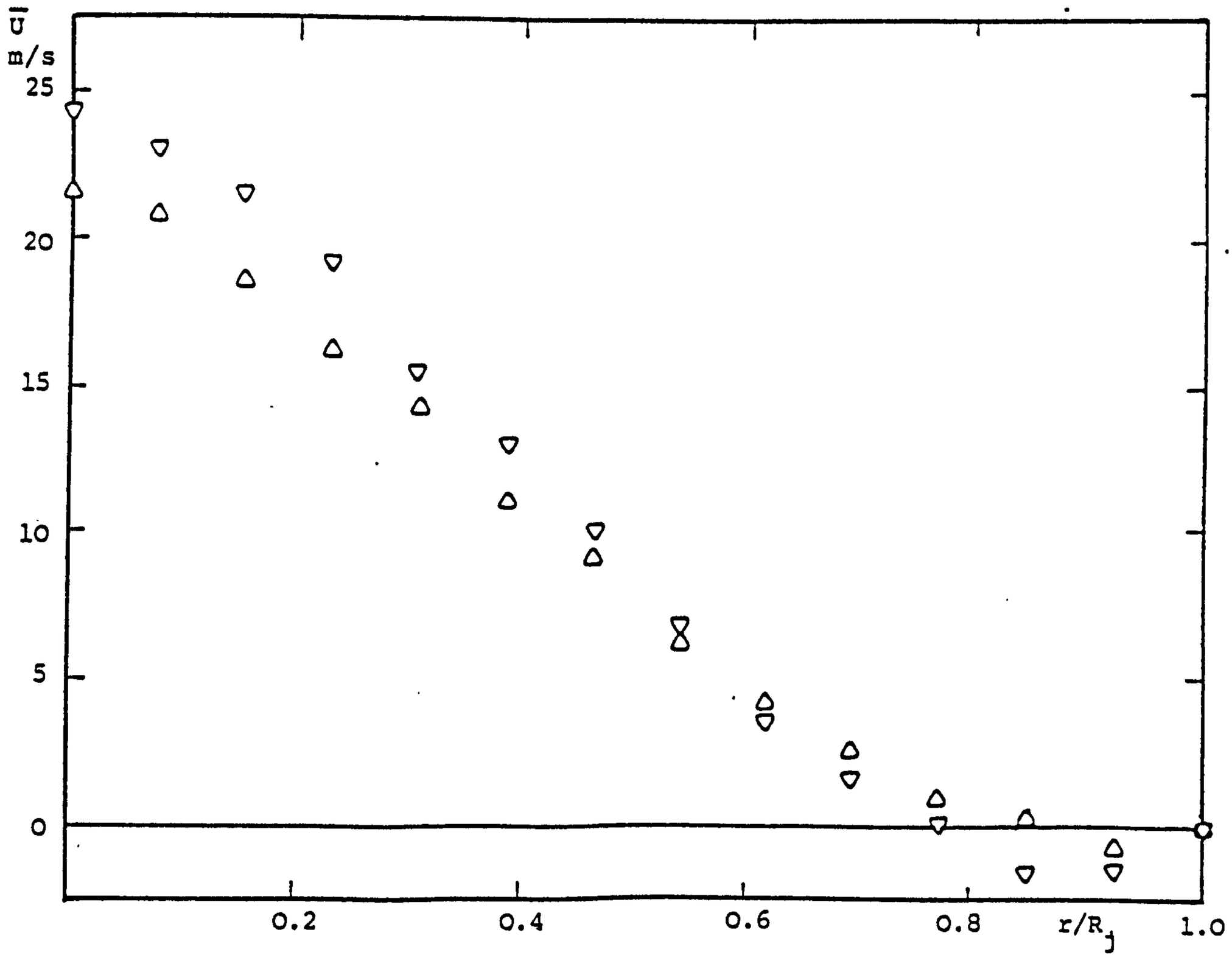


Fig. 4.4 (Continued)

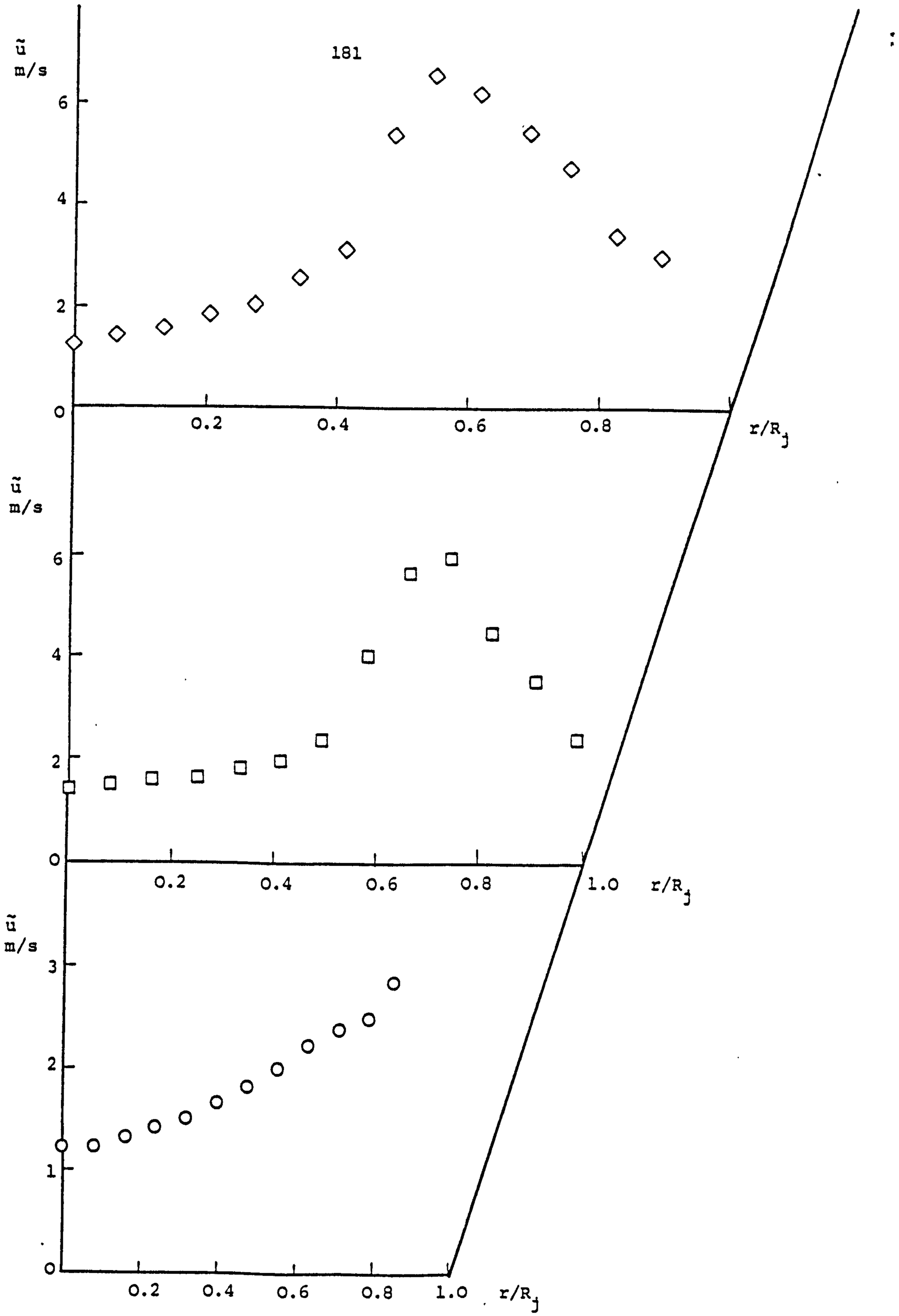


Fig. 4.5 Development of the Axial Normal Stress Across the Centre-Line of G1 (S = 0.0); Notation as in Fig. 4.4

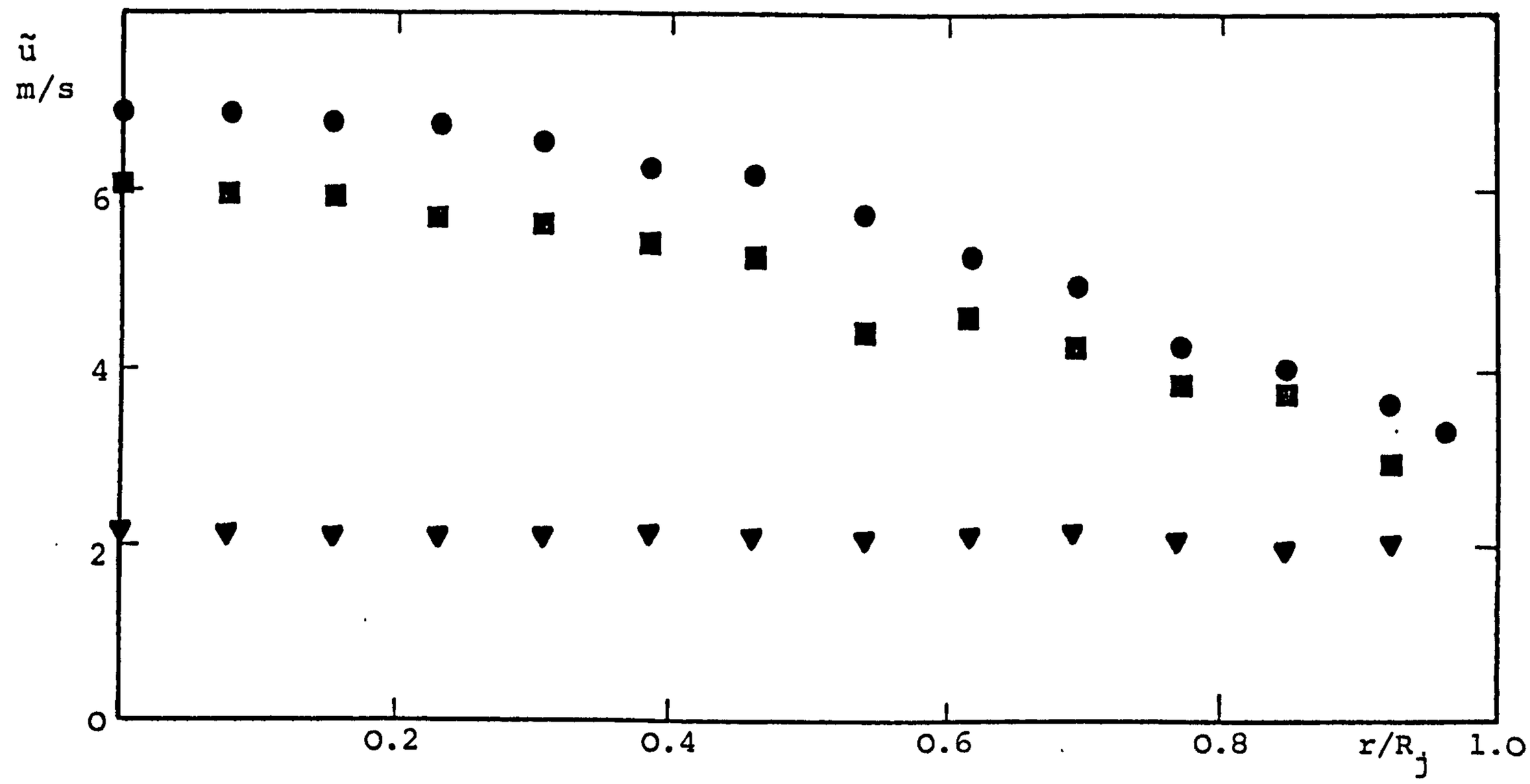


Fig. 4.5 (Continued)

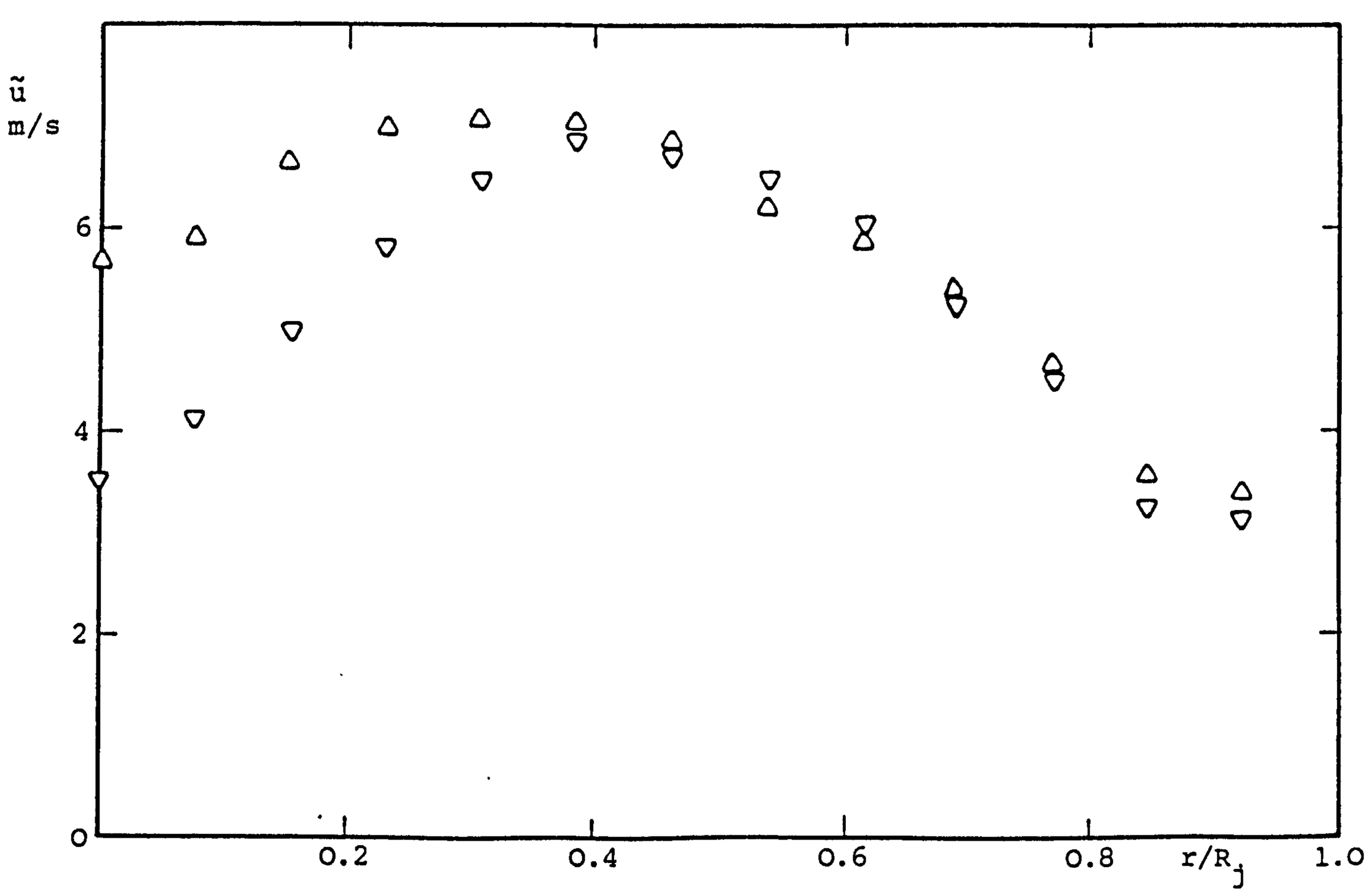


Fig. 4.5 (Continued)

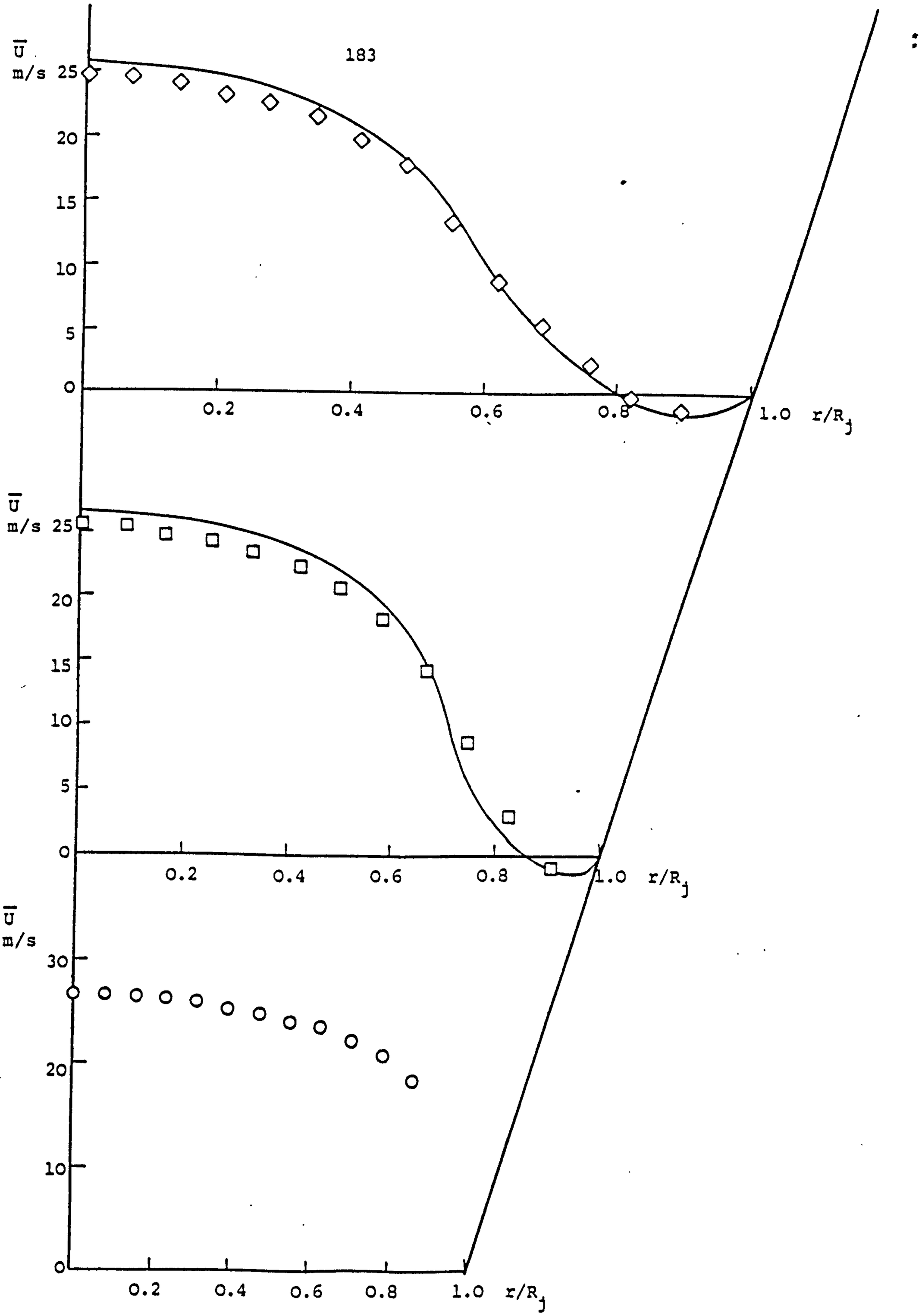


Fig. 4.6 Development of the Axial Mean Velocity Across the Centre-Line of G2 (S = 0.0); ———— , Corresponding Distributions for G1; Otherwise as in Fig. 4.4.

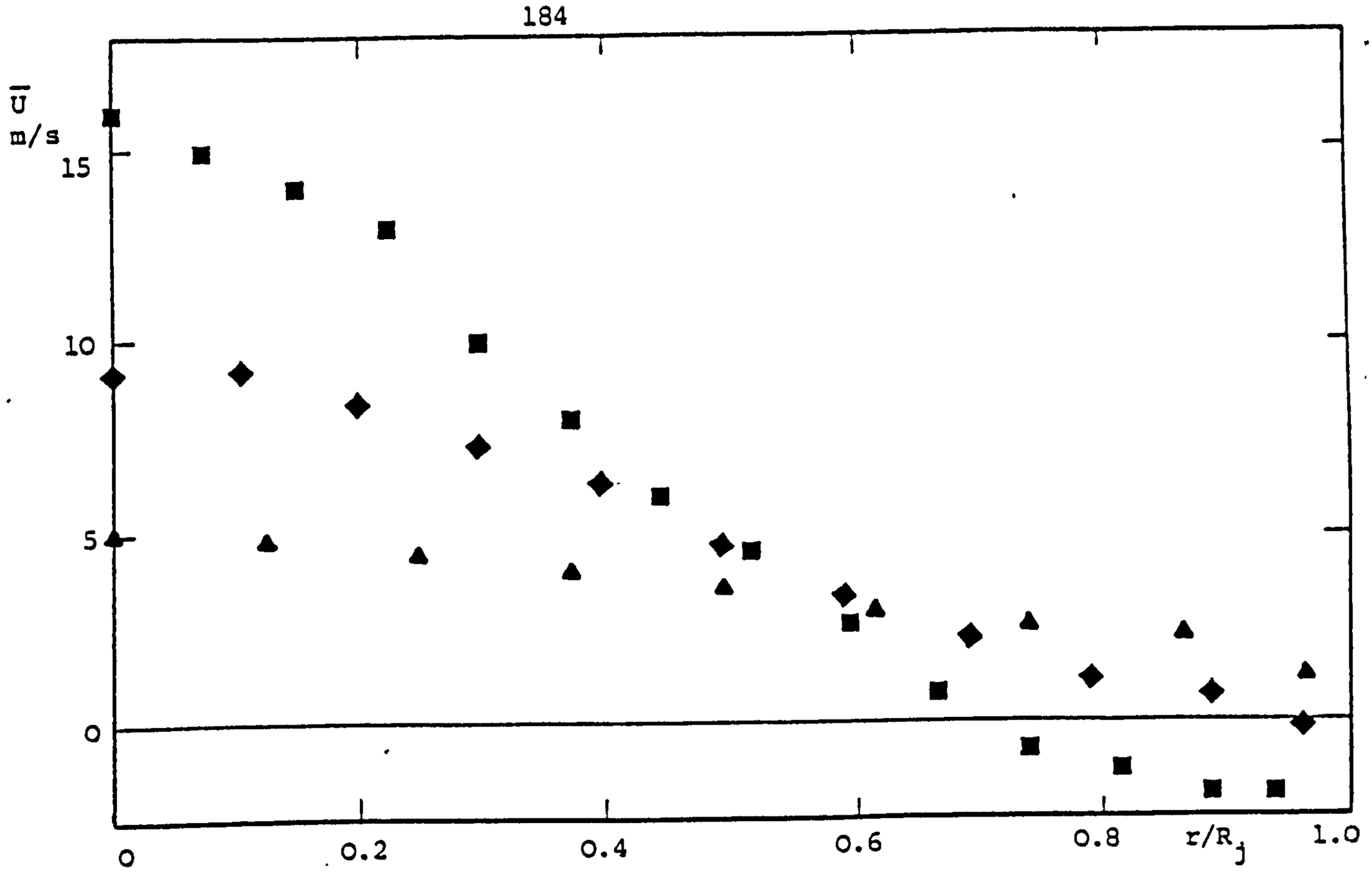


Fig. 4.6 (Continued)

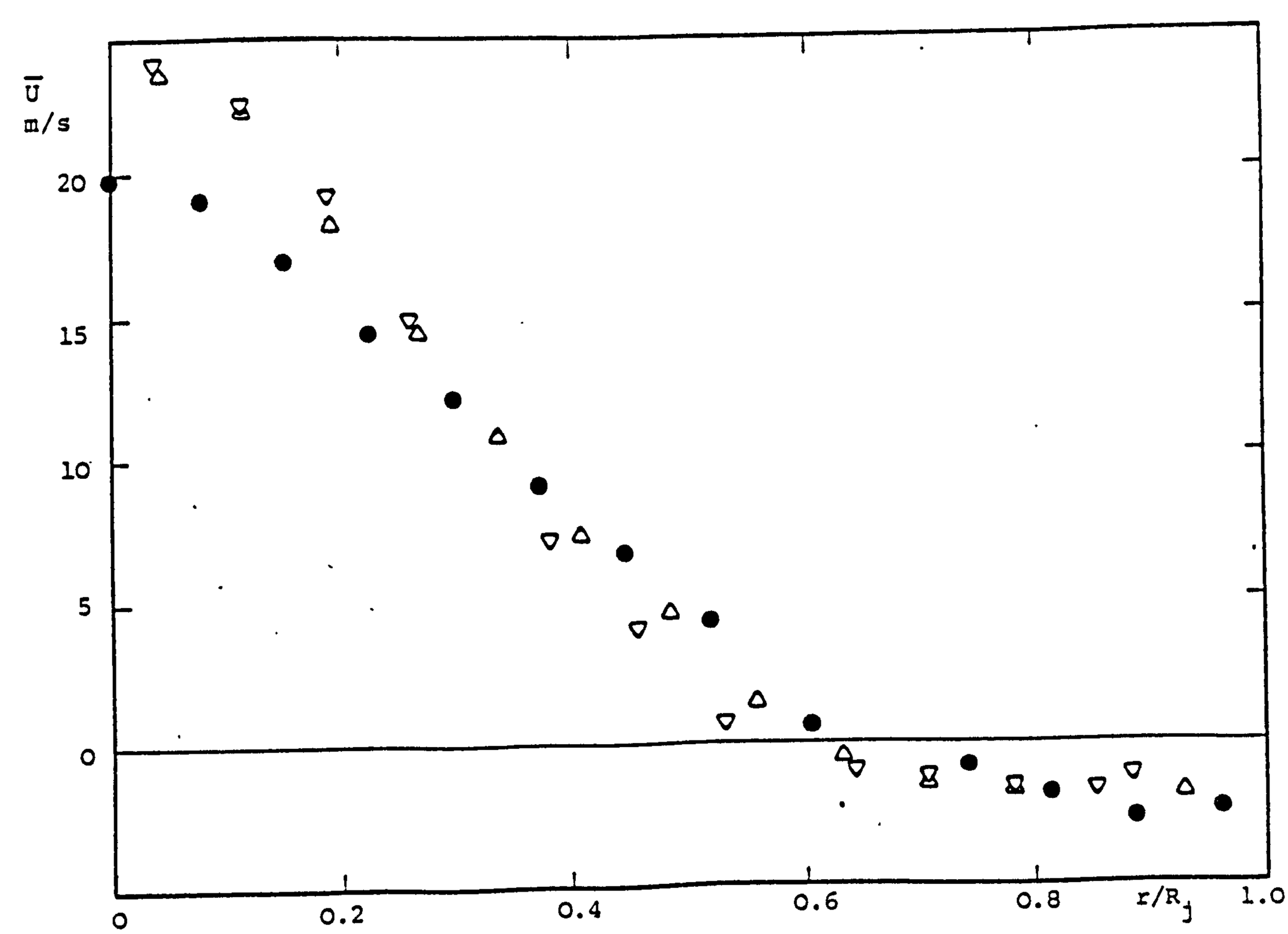


Fig. 4.6 (Continued)

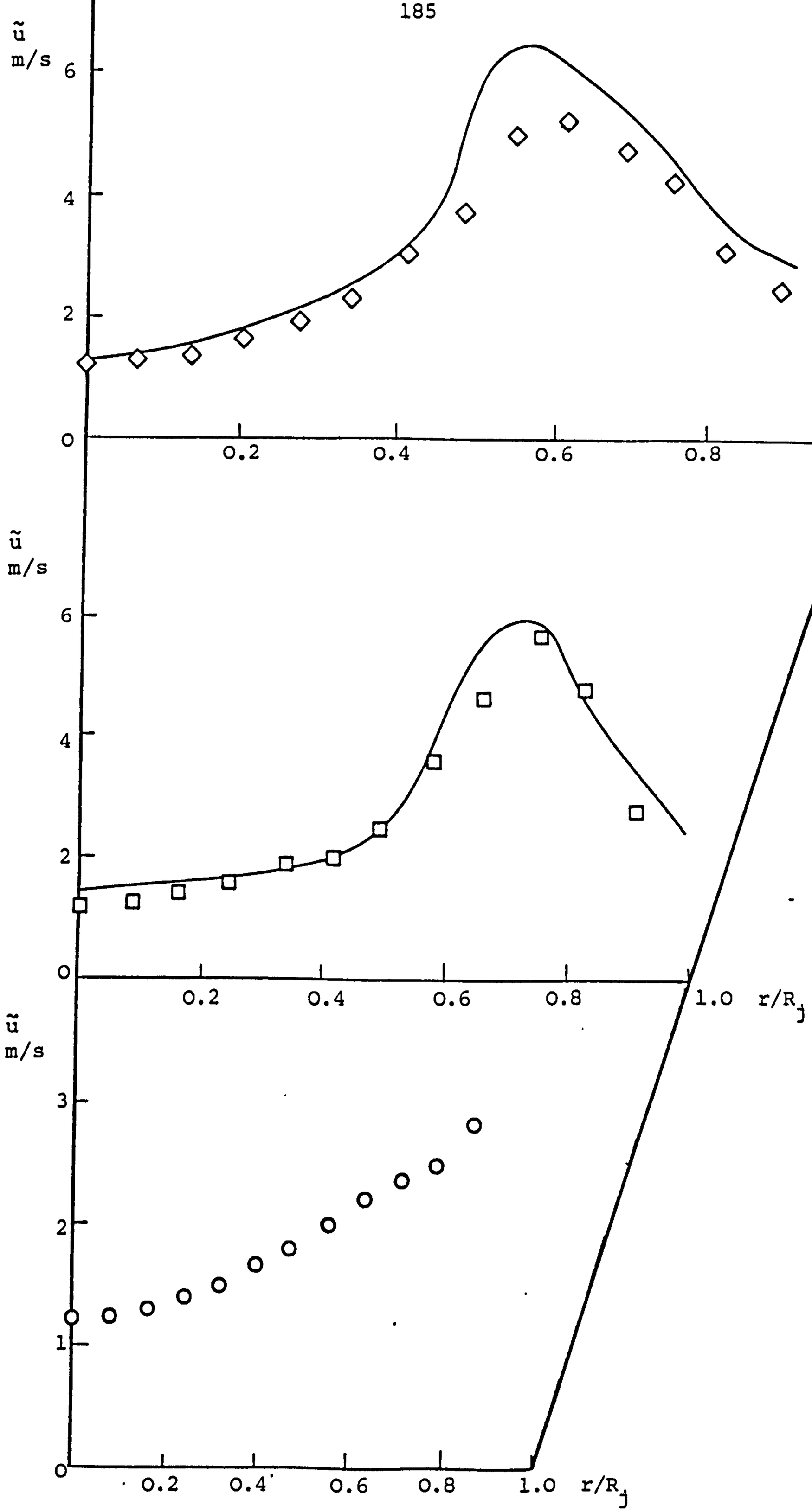


Fig. 4.7 Development of the Axial Normal Stress Across the Centre-Line of G2 (S = 0.0); ———, Corresponding Distributions for G1; Otherwise as in Fig. 4.4

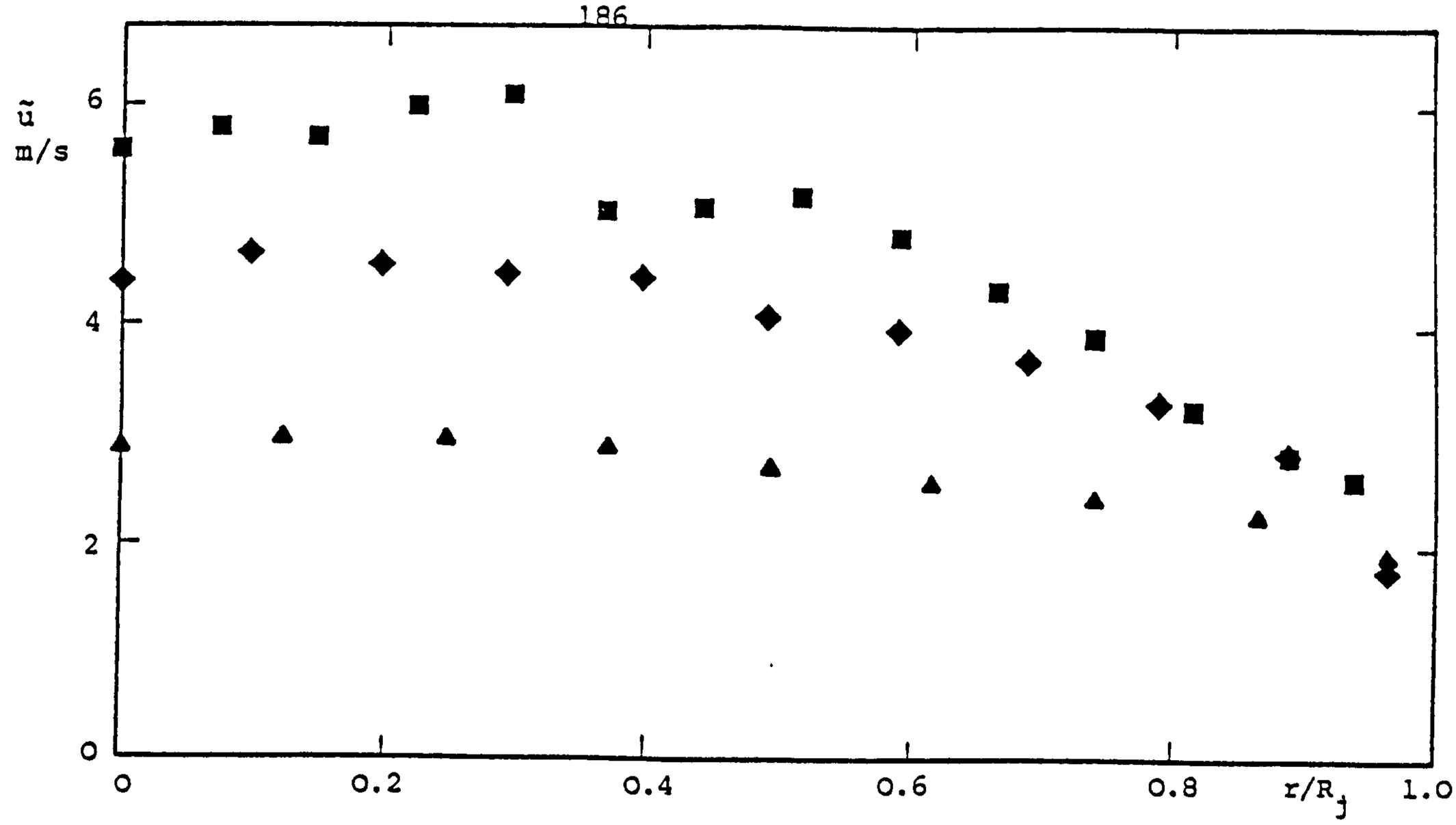


Fig. 4.7 (Continued)

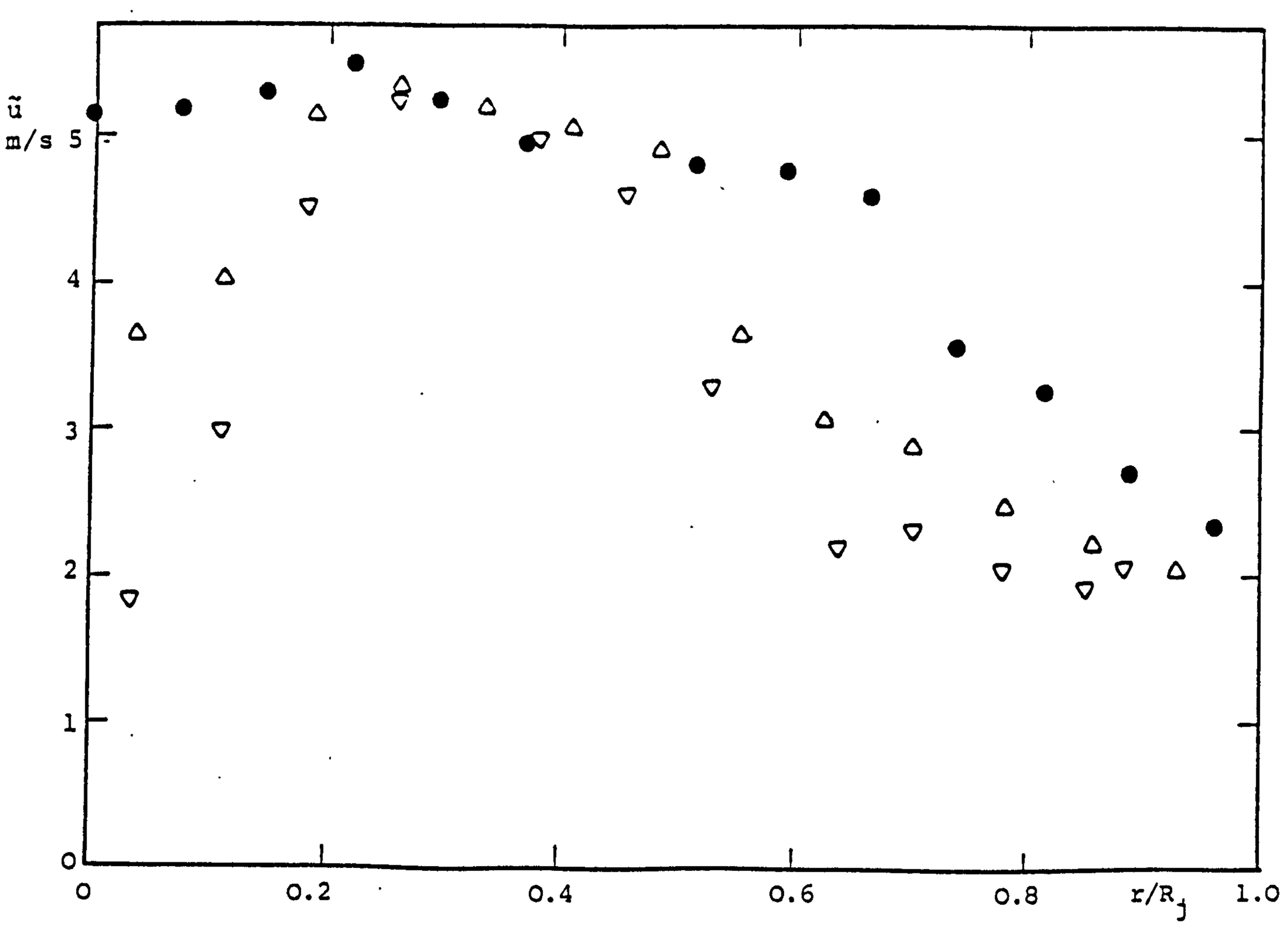


Fig. 4.7 (Continued)

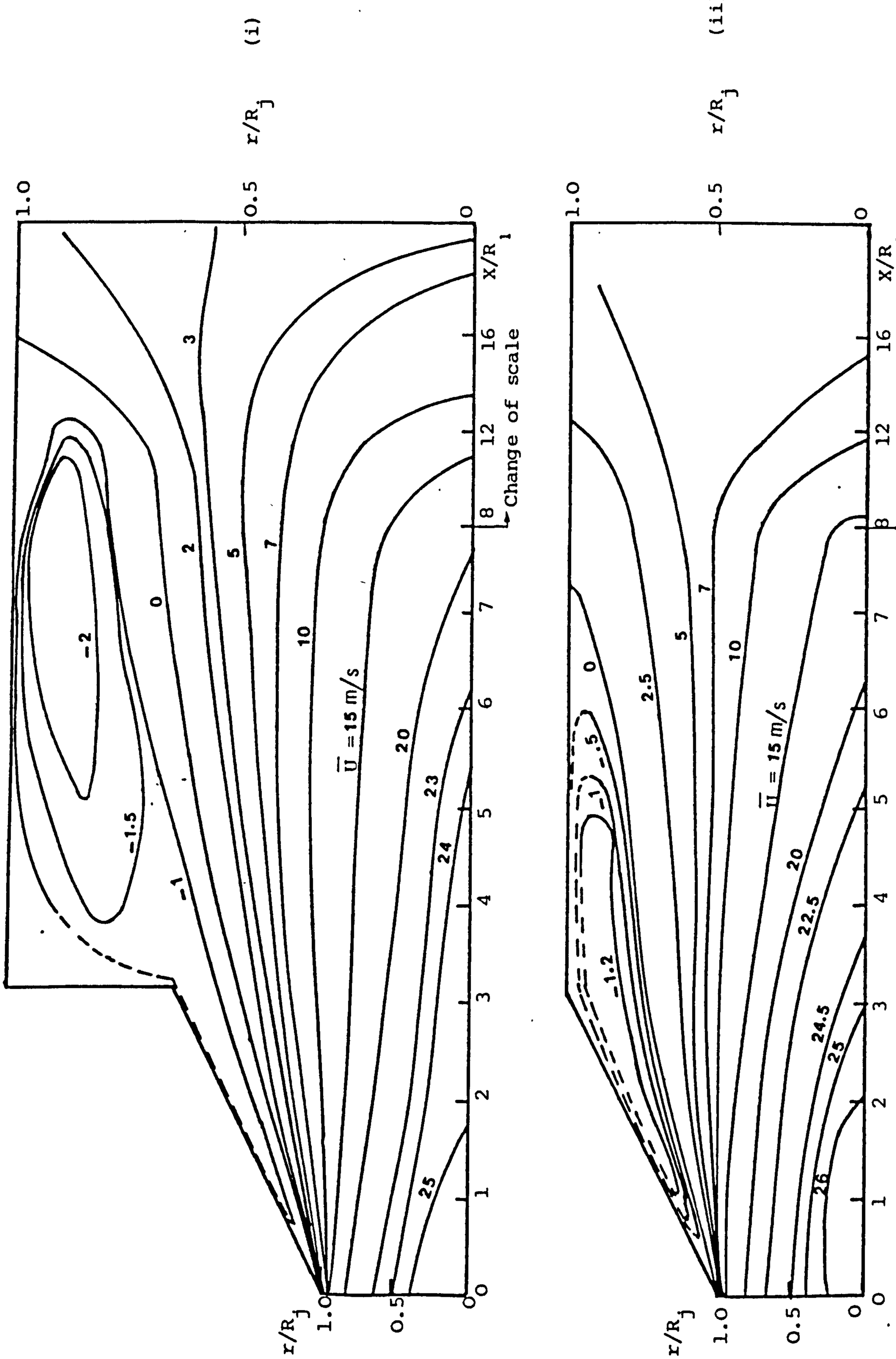


Fig. 4.8 Axial Mean Velocity Contours (S = 0.0); (i) Geometry G2; (ii) Geometry G1

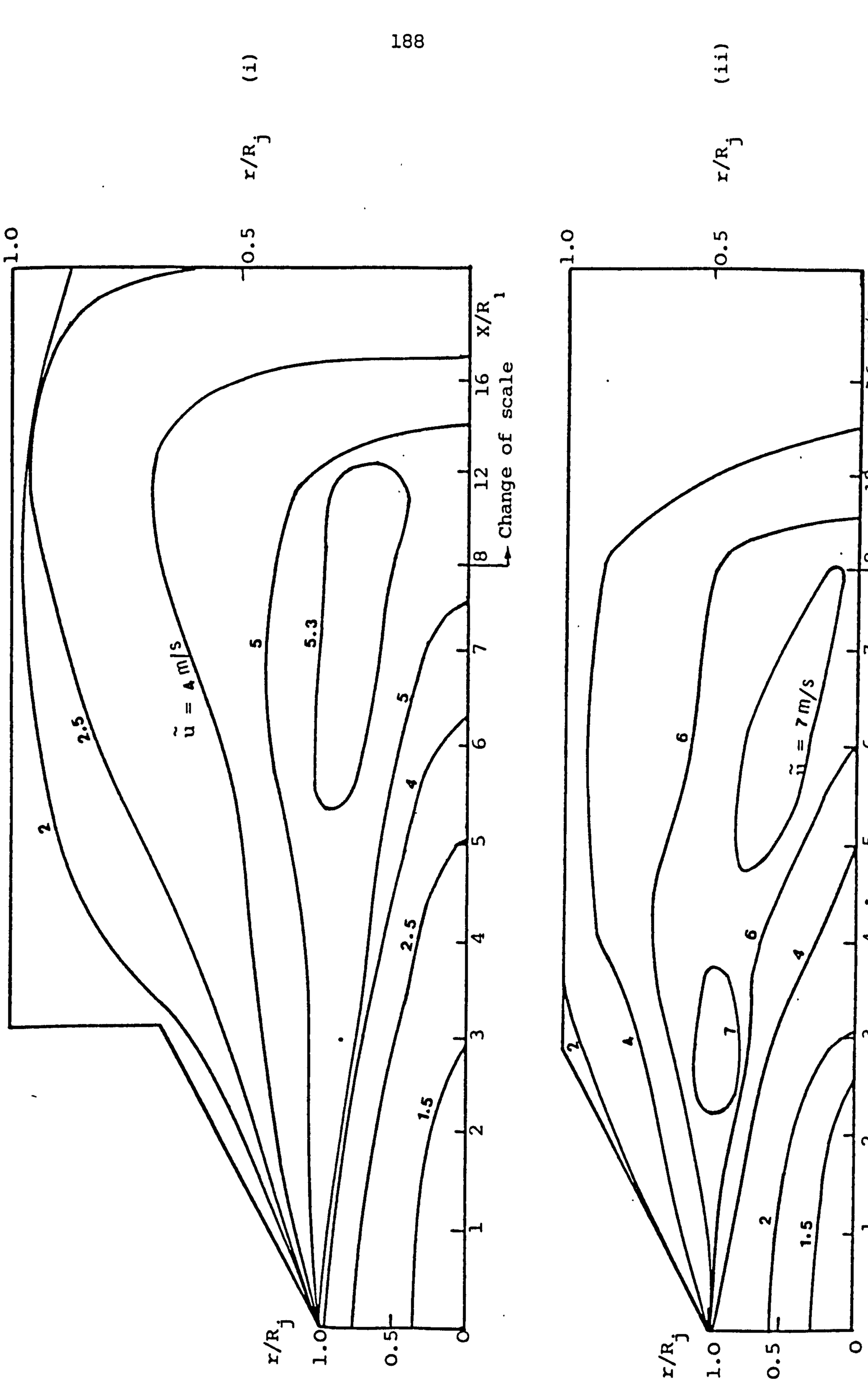


Fig. 4.9 Contours of the Axial Normal Stress (S = 0.0); (i) Geometry G2; (ii) Geometry G1

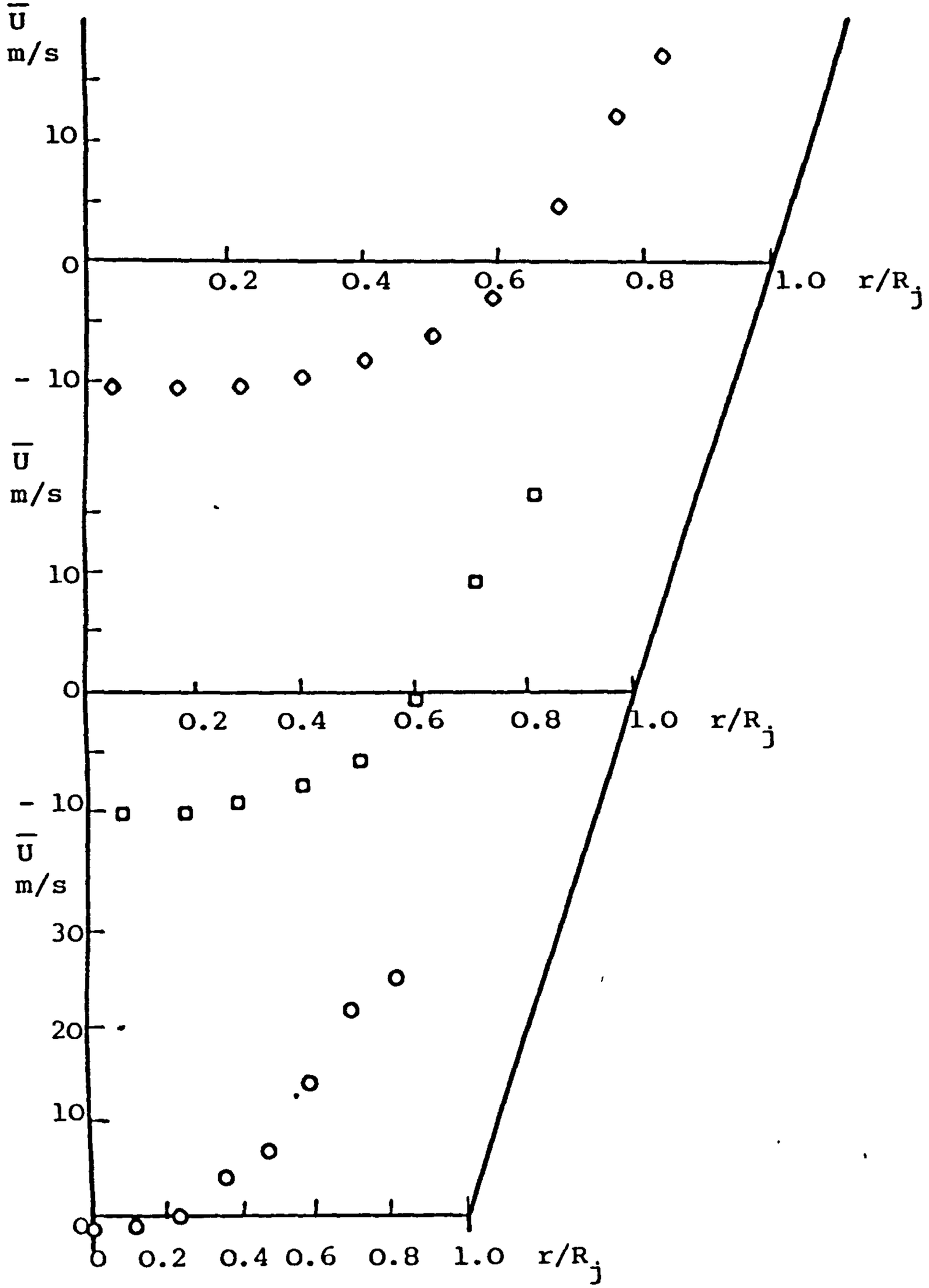


Fig. 4.10 Development of the Axial Mean Velocity Across the Centre-Line of G2 (S = 0.93); Notation as in Fig. 4.4

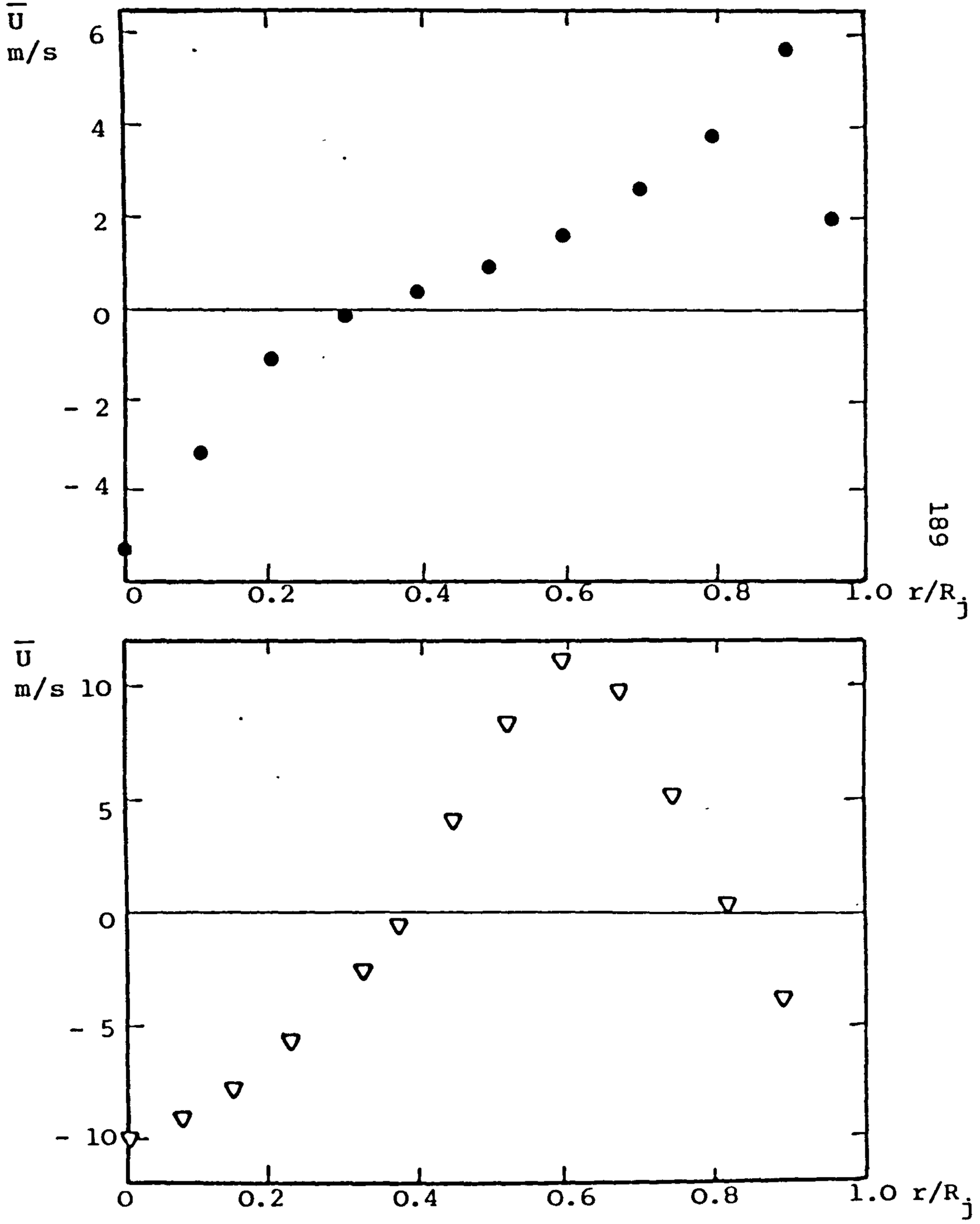


Fig. 4.10 (Continued)

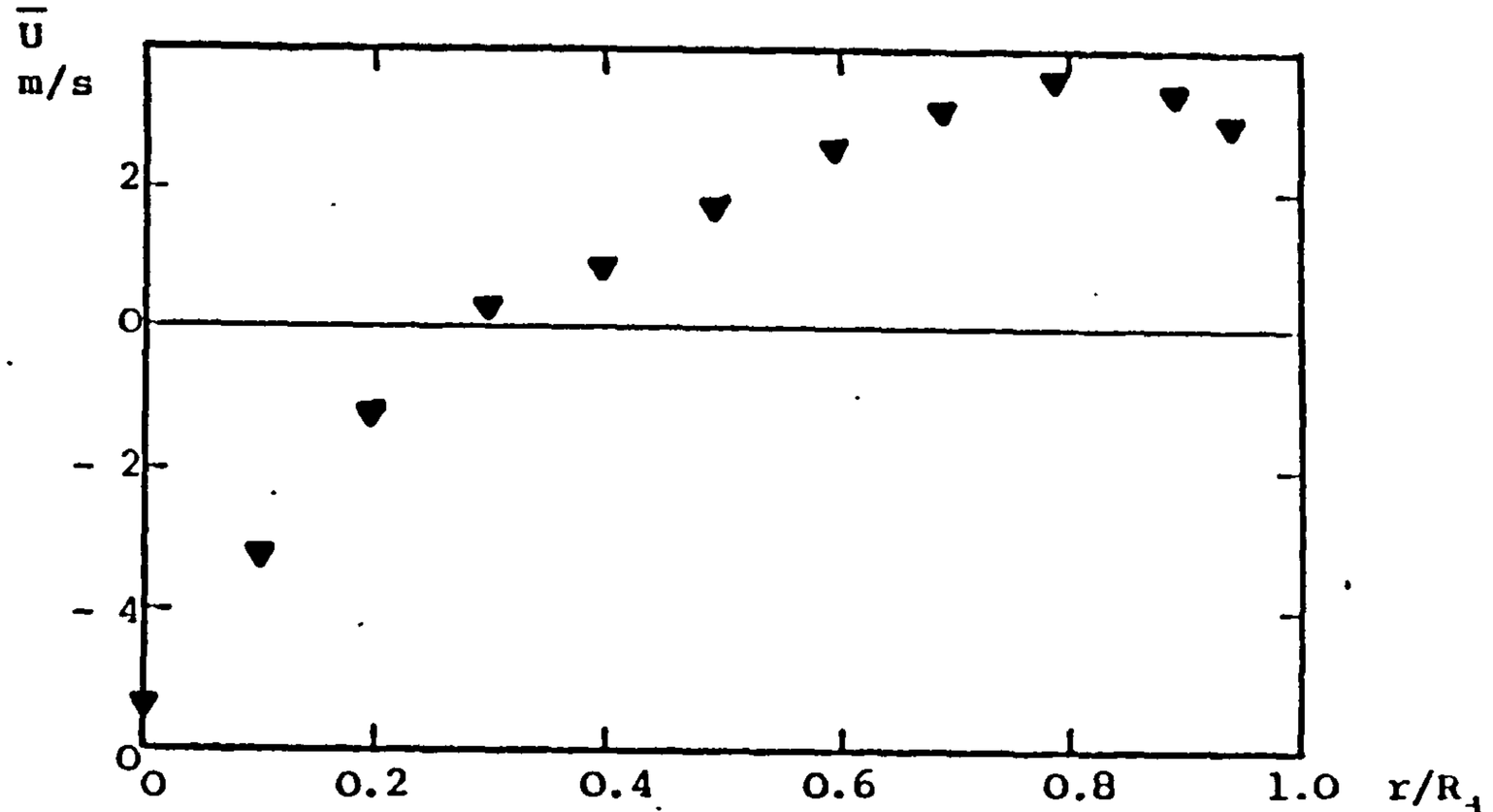


Fig. 4.10 (Continued)

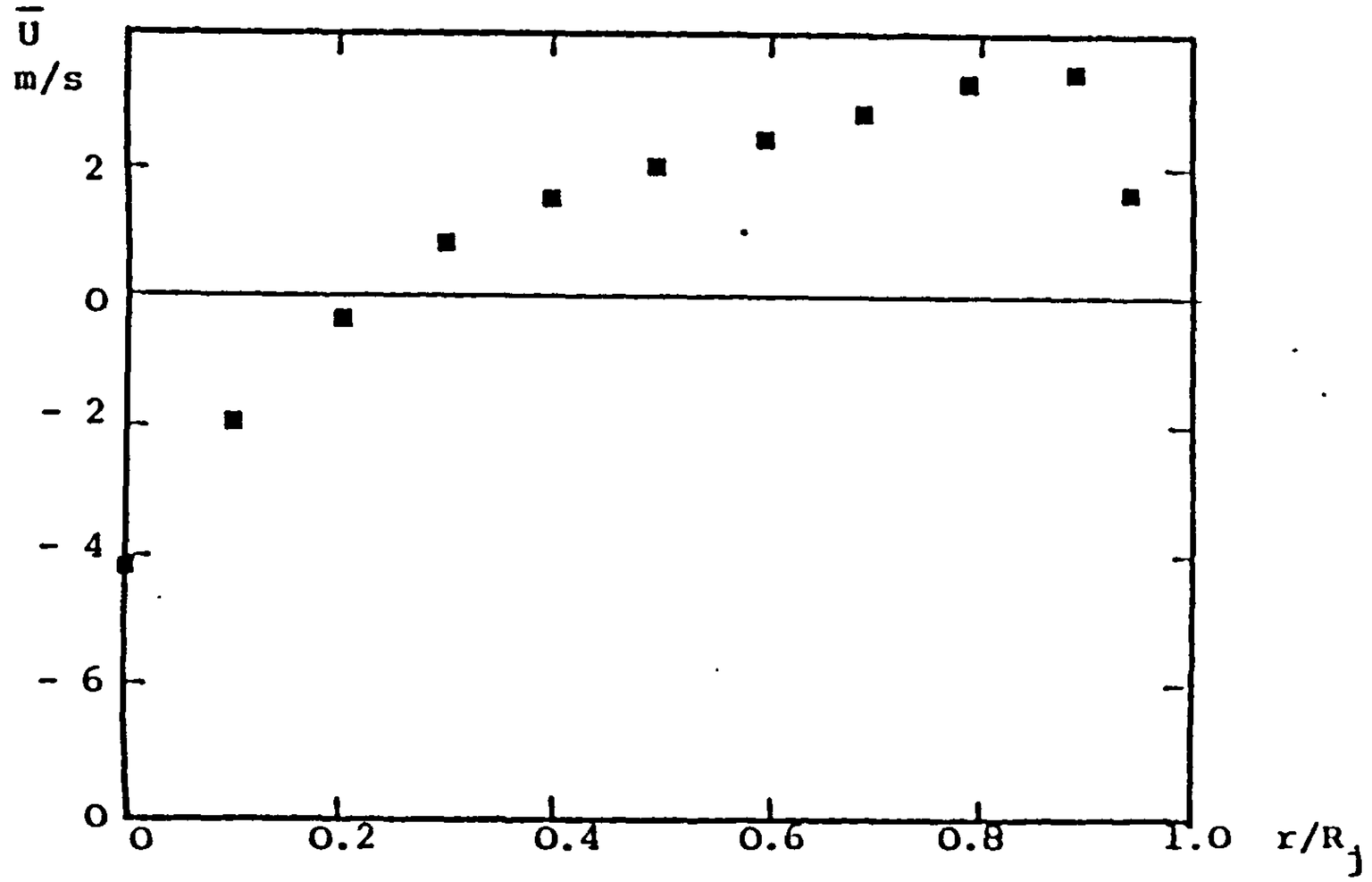


Fig. 4.10 (Continued)

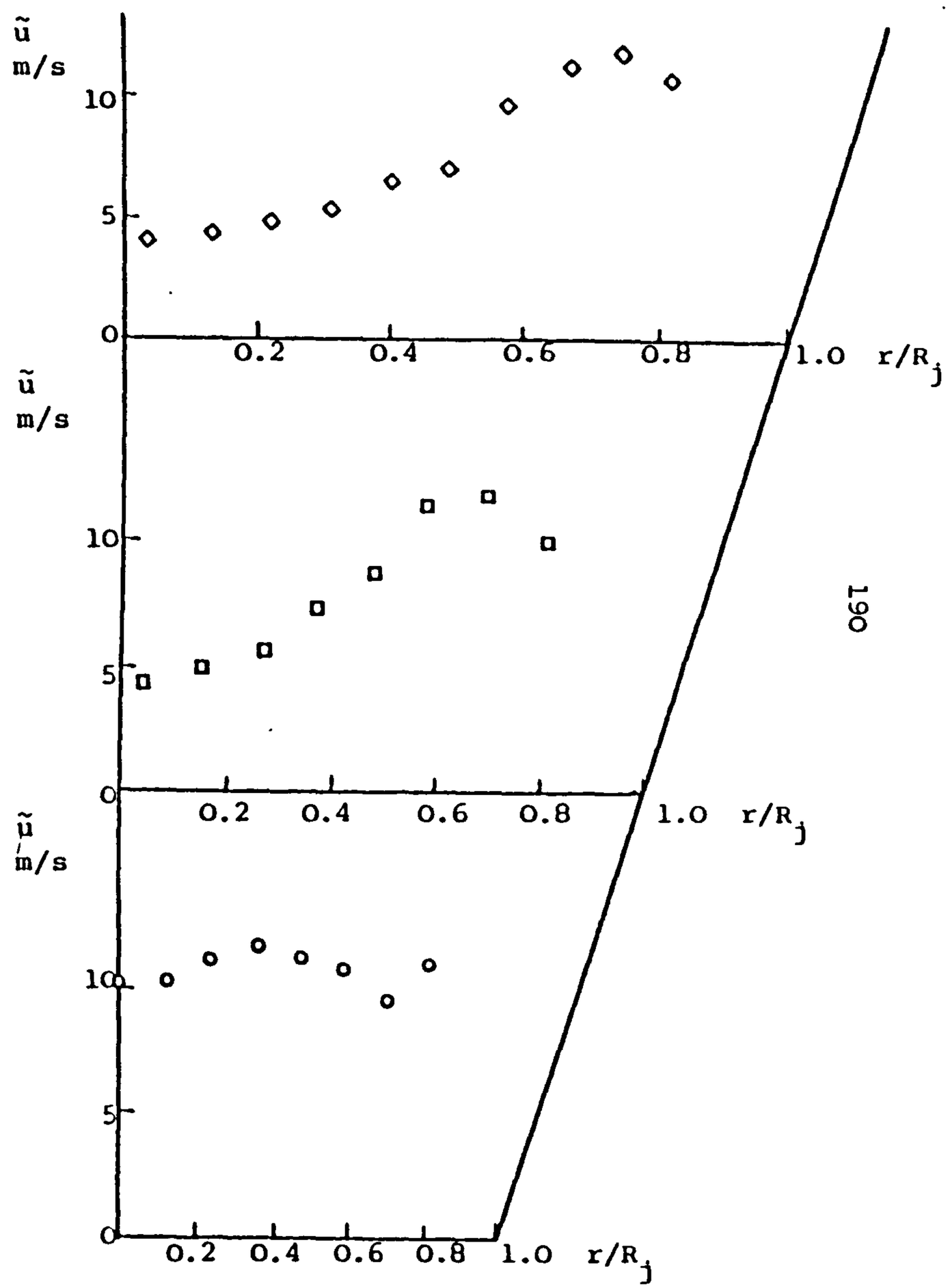


Fig. 4.11 Development of the Axial Normal Stress Across the Centre-Line of G2 (S = 0.93); Notation as in Fig. 4.4

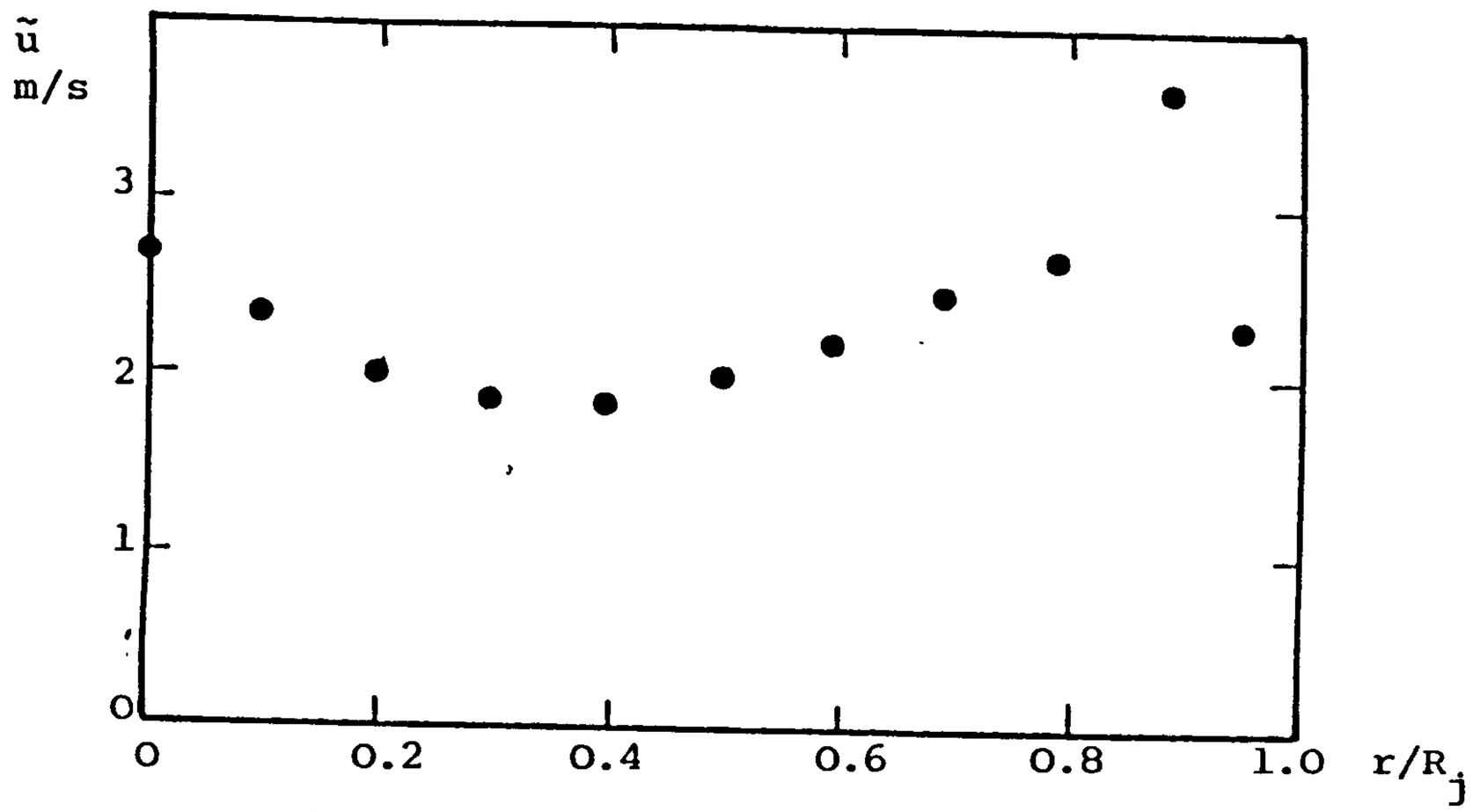


Fig. 4.11 (Continued)

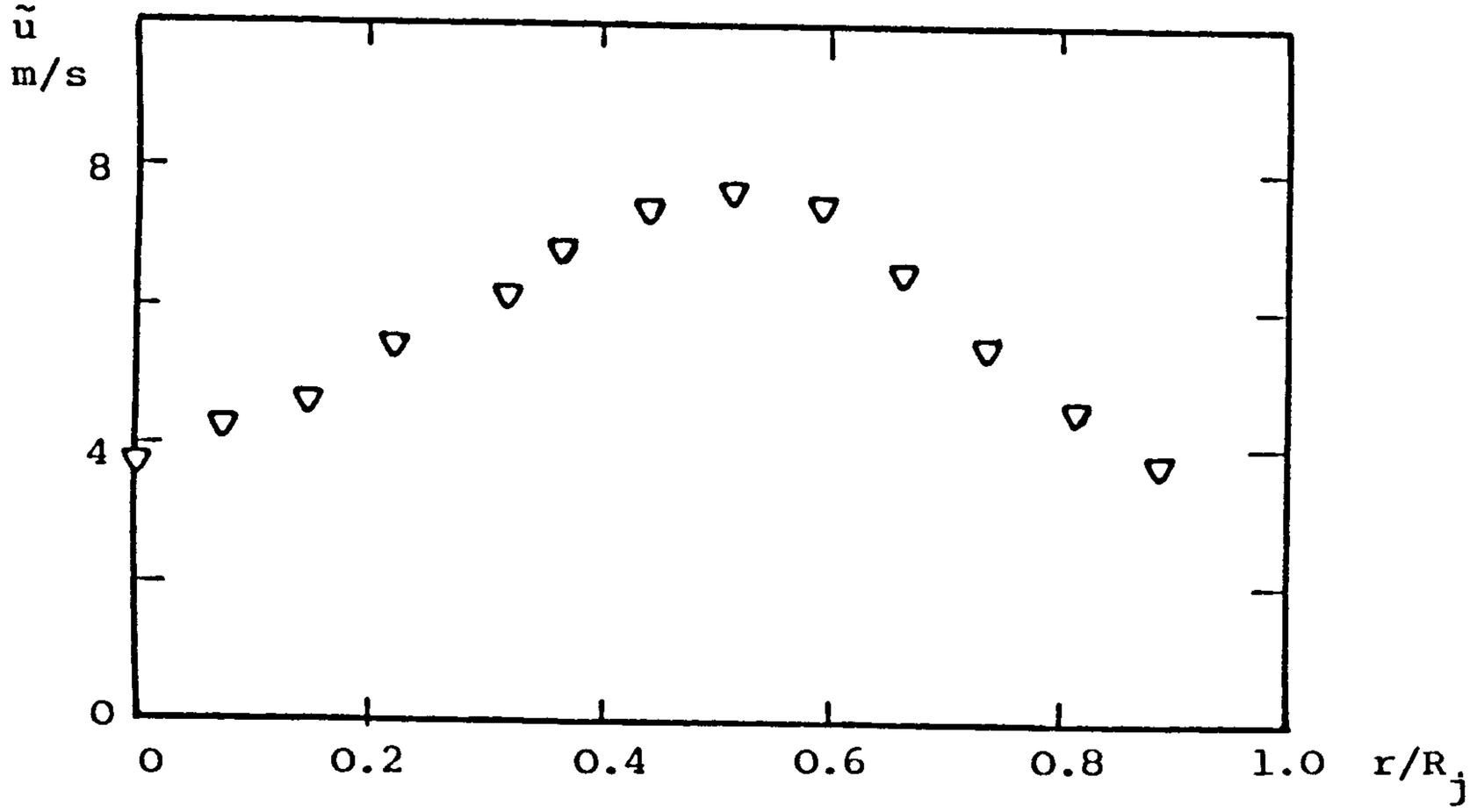


Fig. 4.11 (Continued)

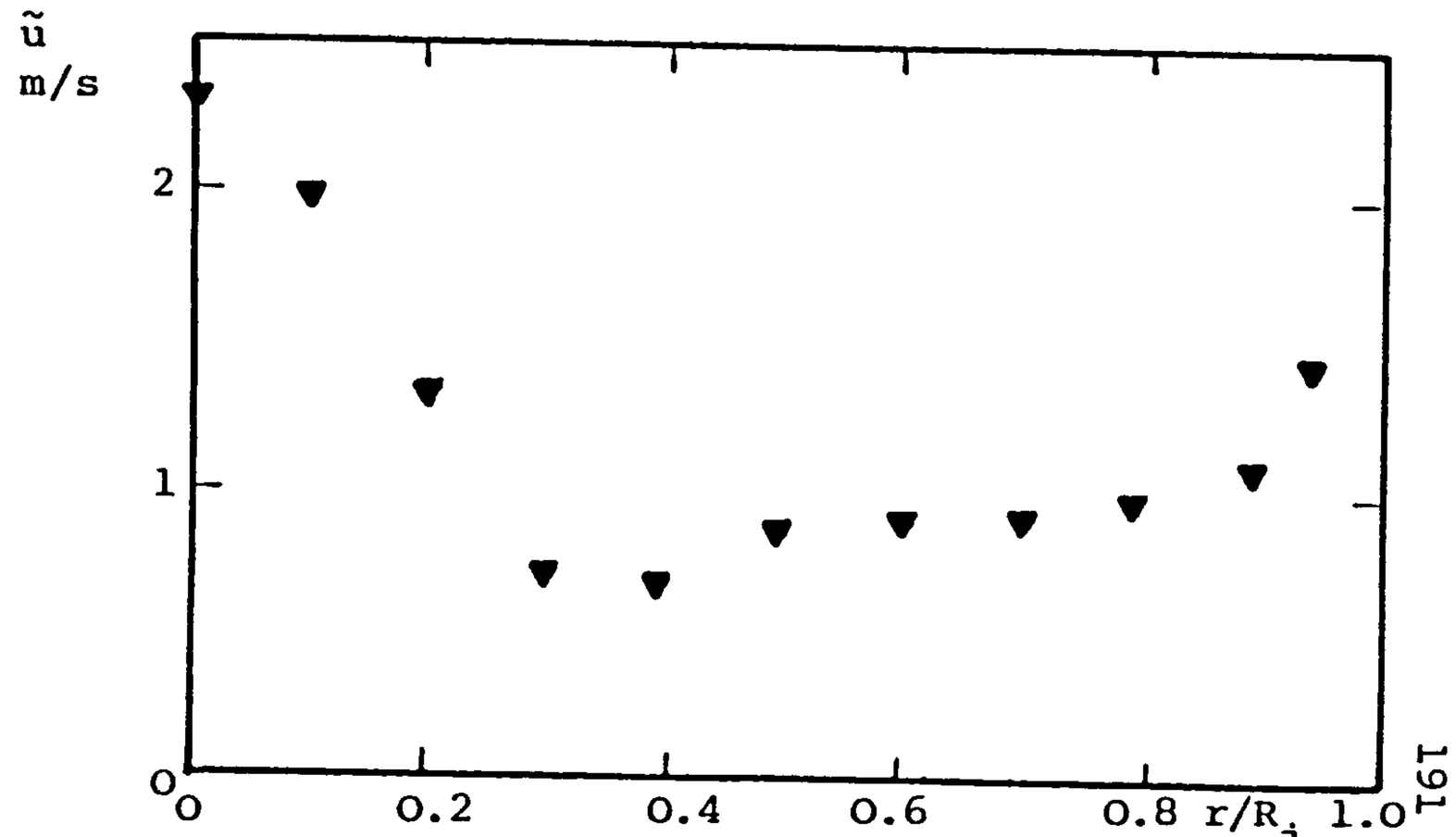


Fig. 4.11 (Continued)

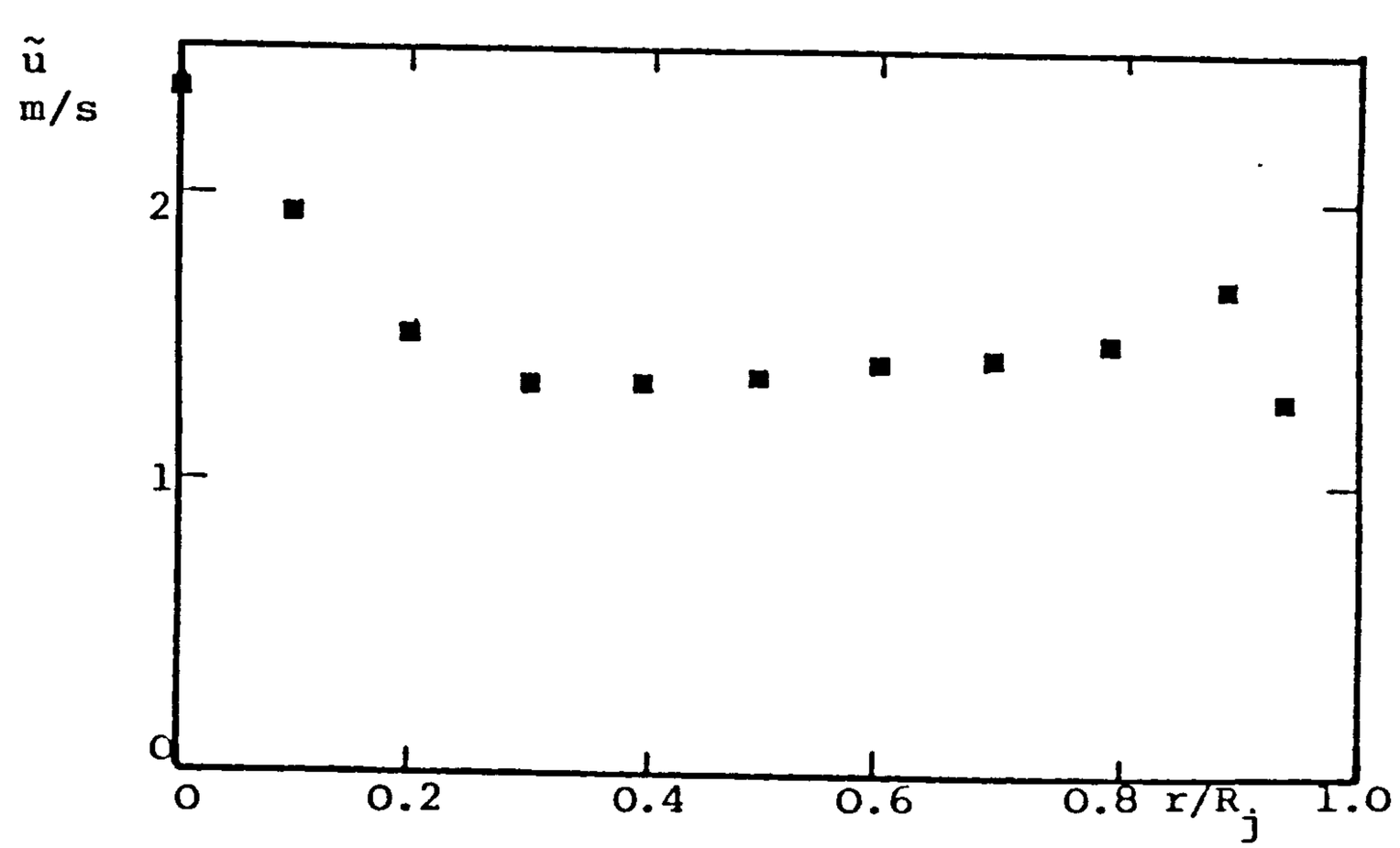


Fig. 4.11 (Continued)

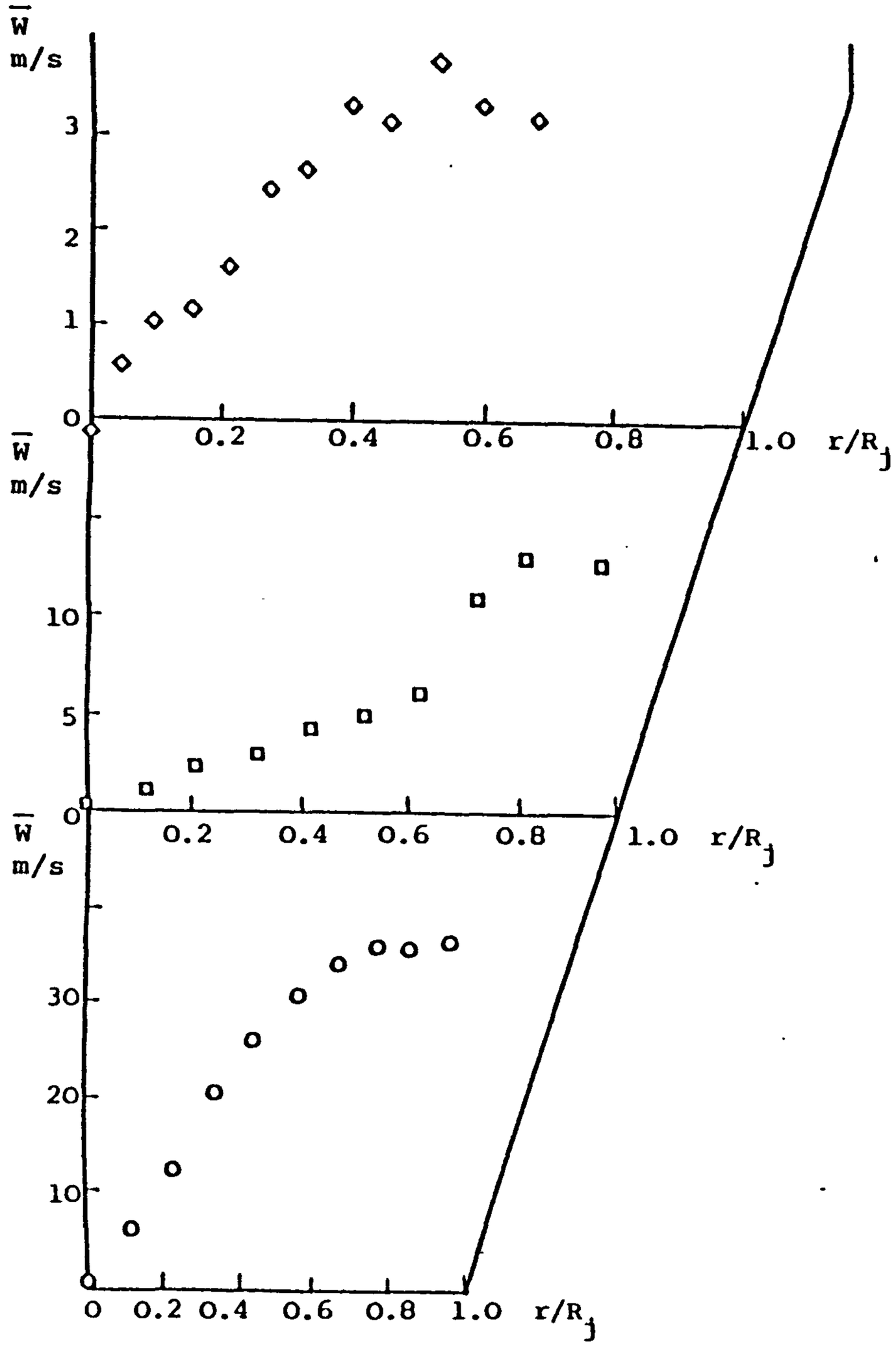


Fig. 4.12 Development of the Tangential Mean Velocity Across the Centre-Line of G2 (S = 0.93); Notation as in Fig. 4.4

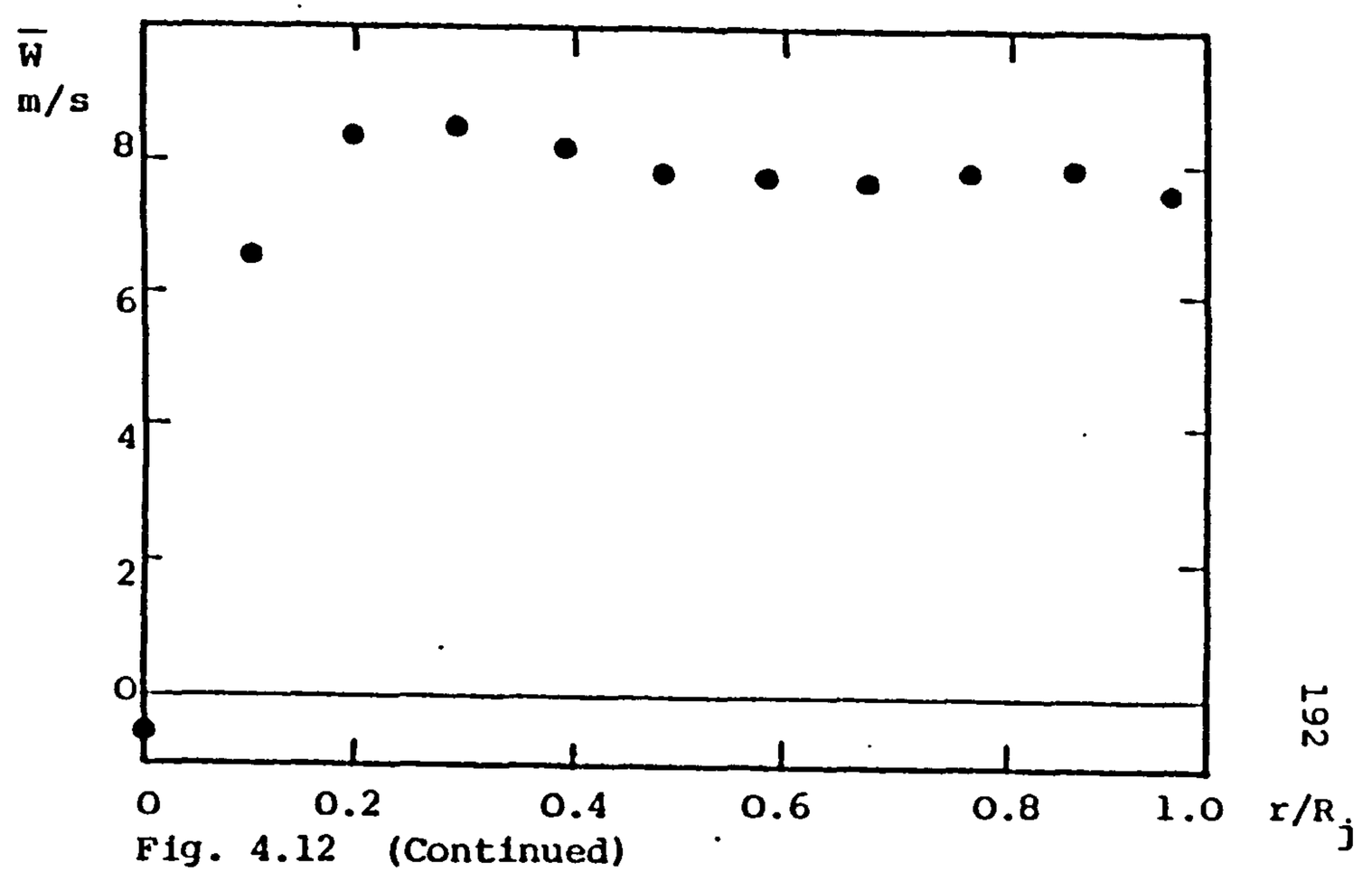


Fig. 4.12 (Continued)

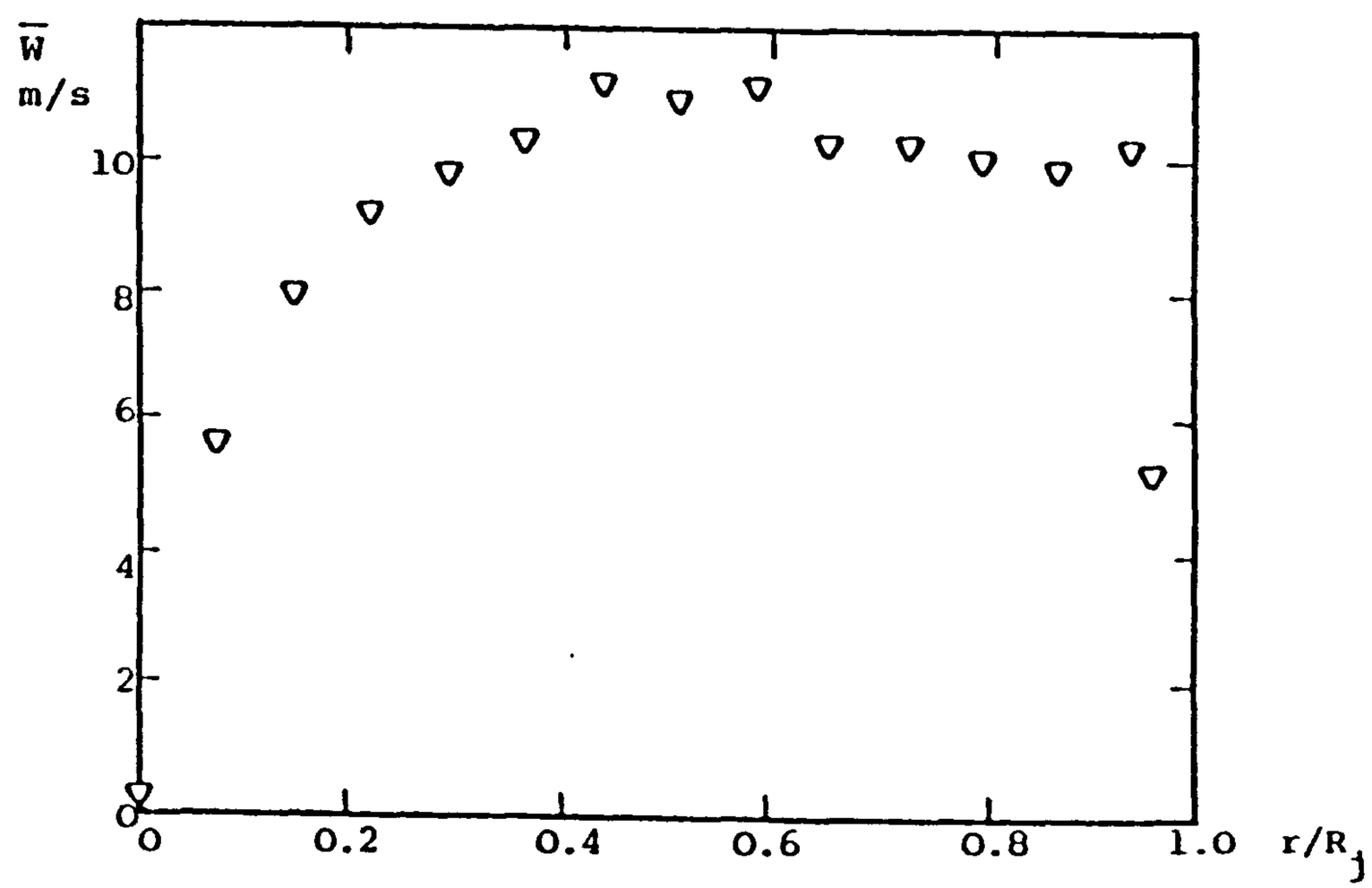


Fig. 4.12 (Continued)

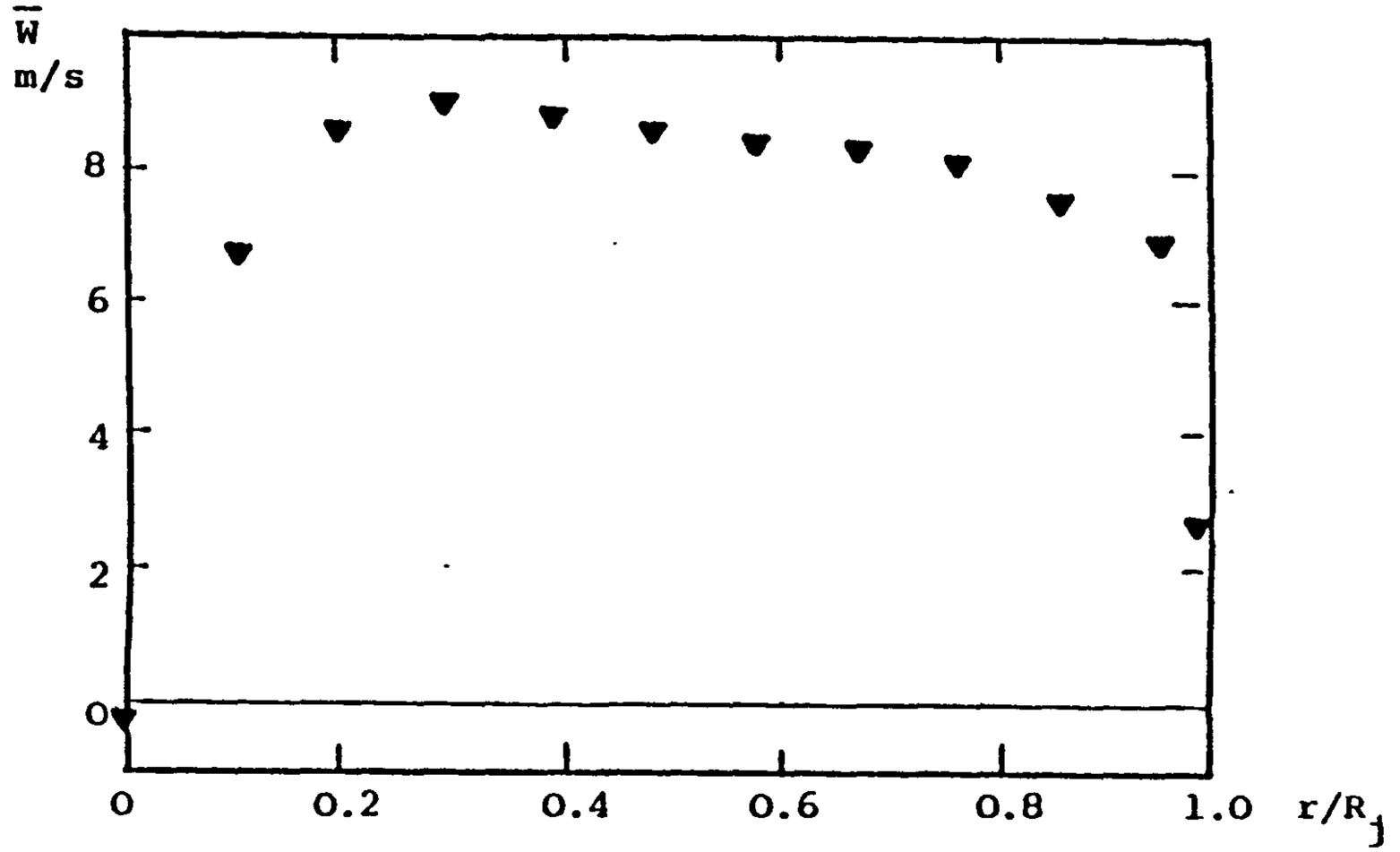


Fig. 4.12 (Continued)

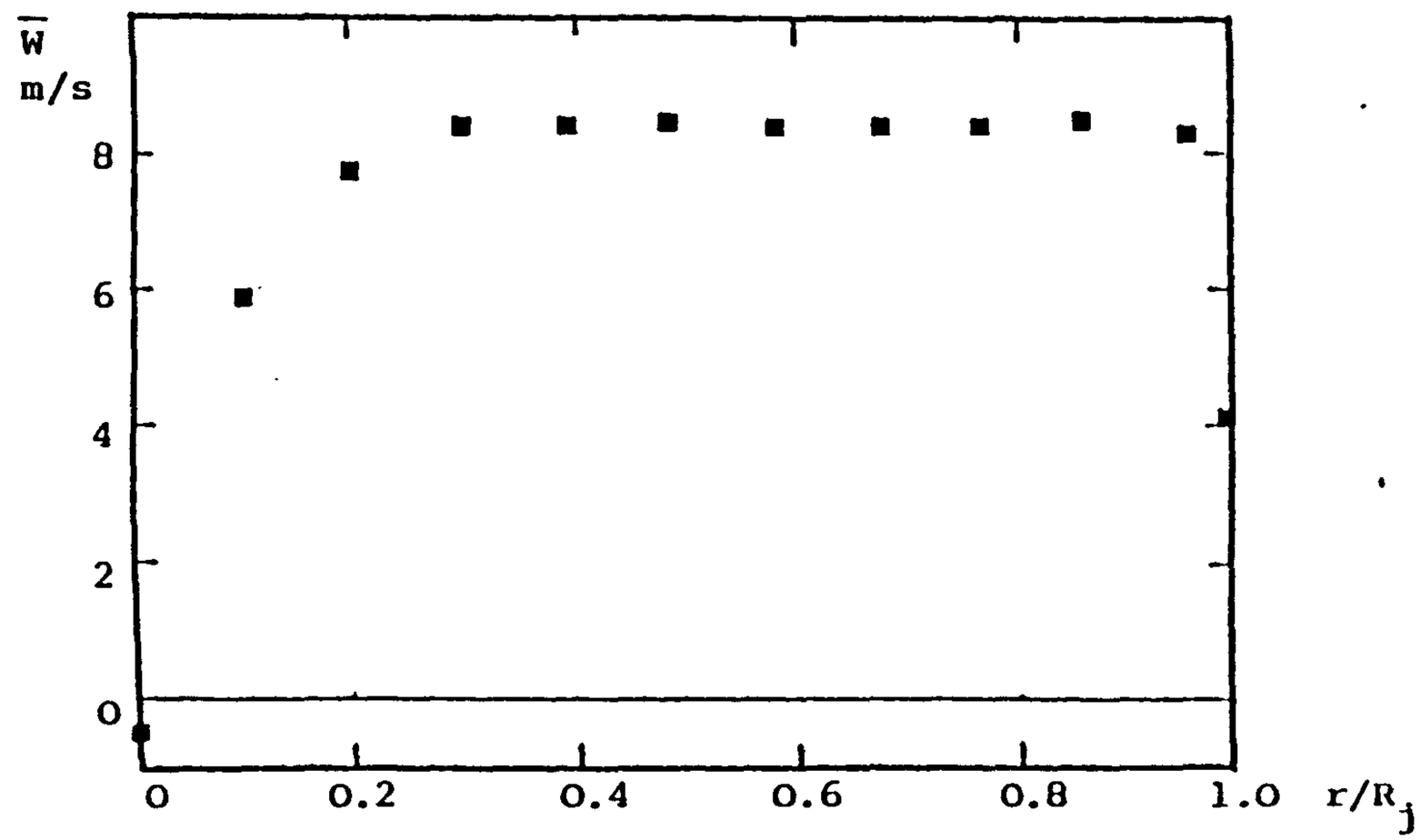


Fig. 4.12 (Continued)

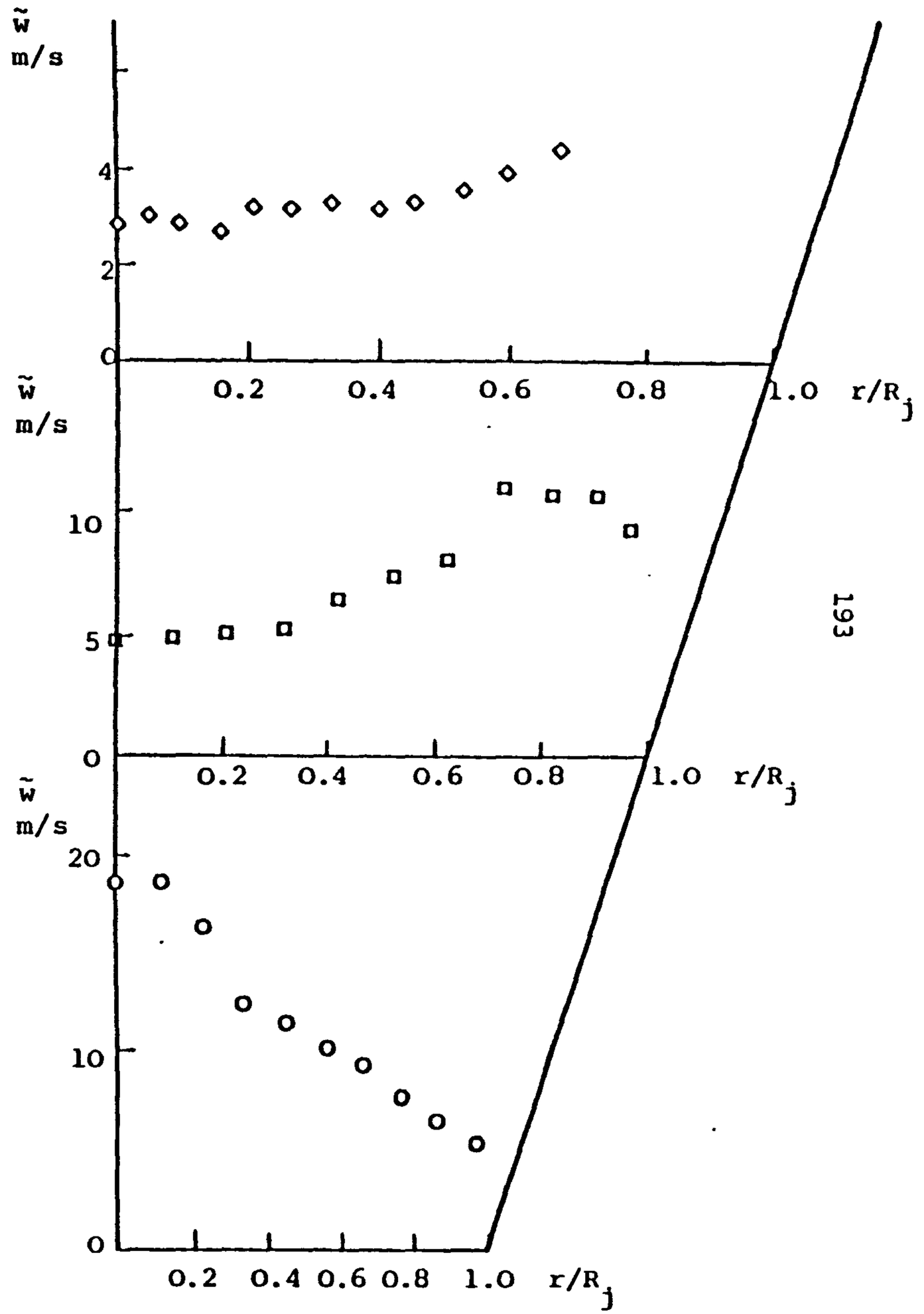


Fig. 4.13 Development of the Tangential Normal Stress Across the Centre-Line of G2 (S = 0.93); Notation as in Fig. 4.4

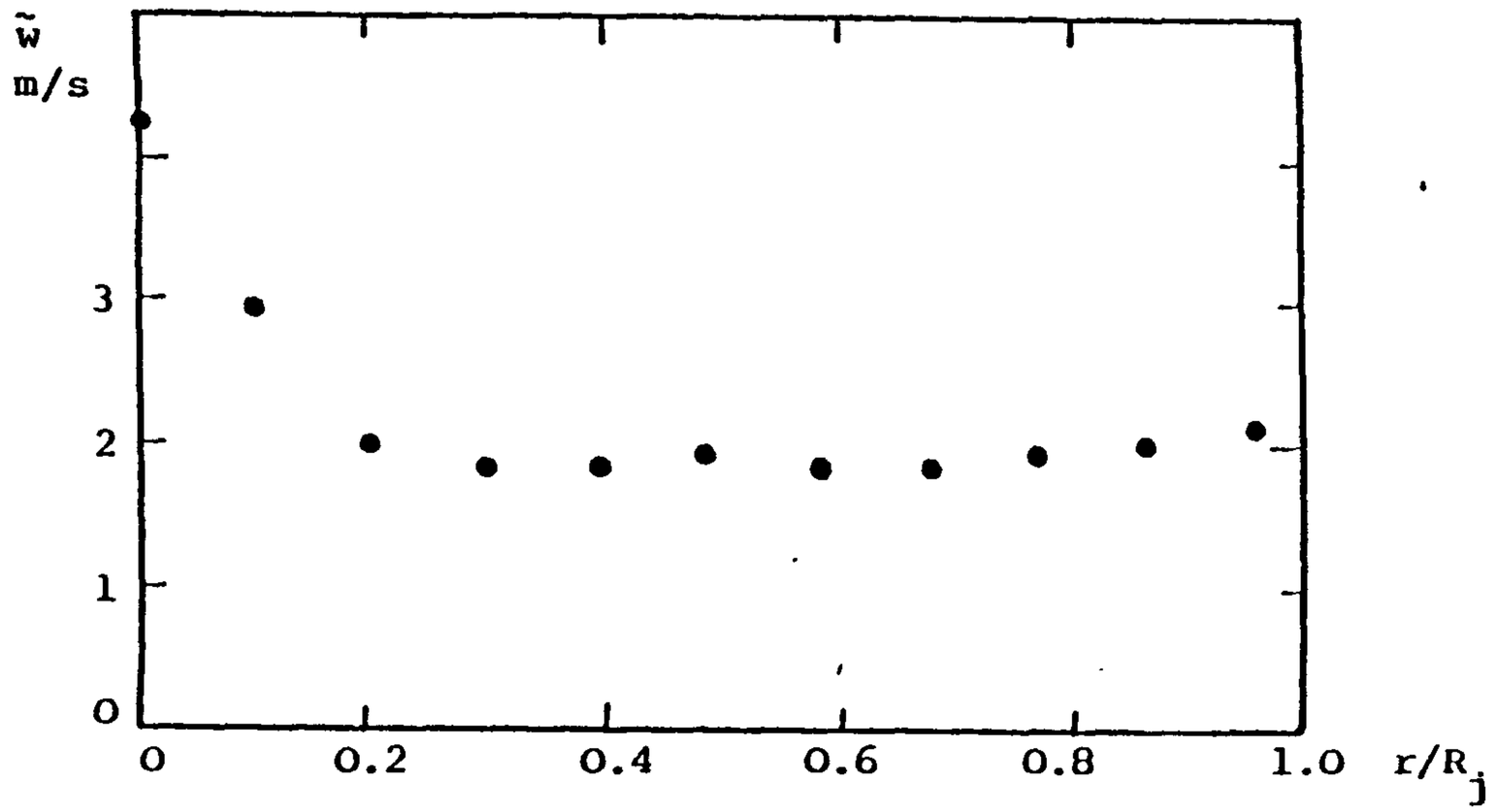


Fig. 4.13 (Continued)

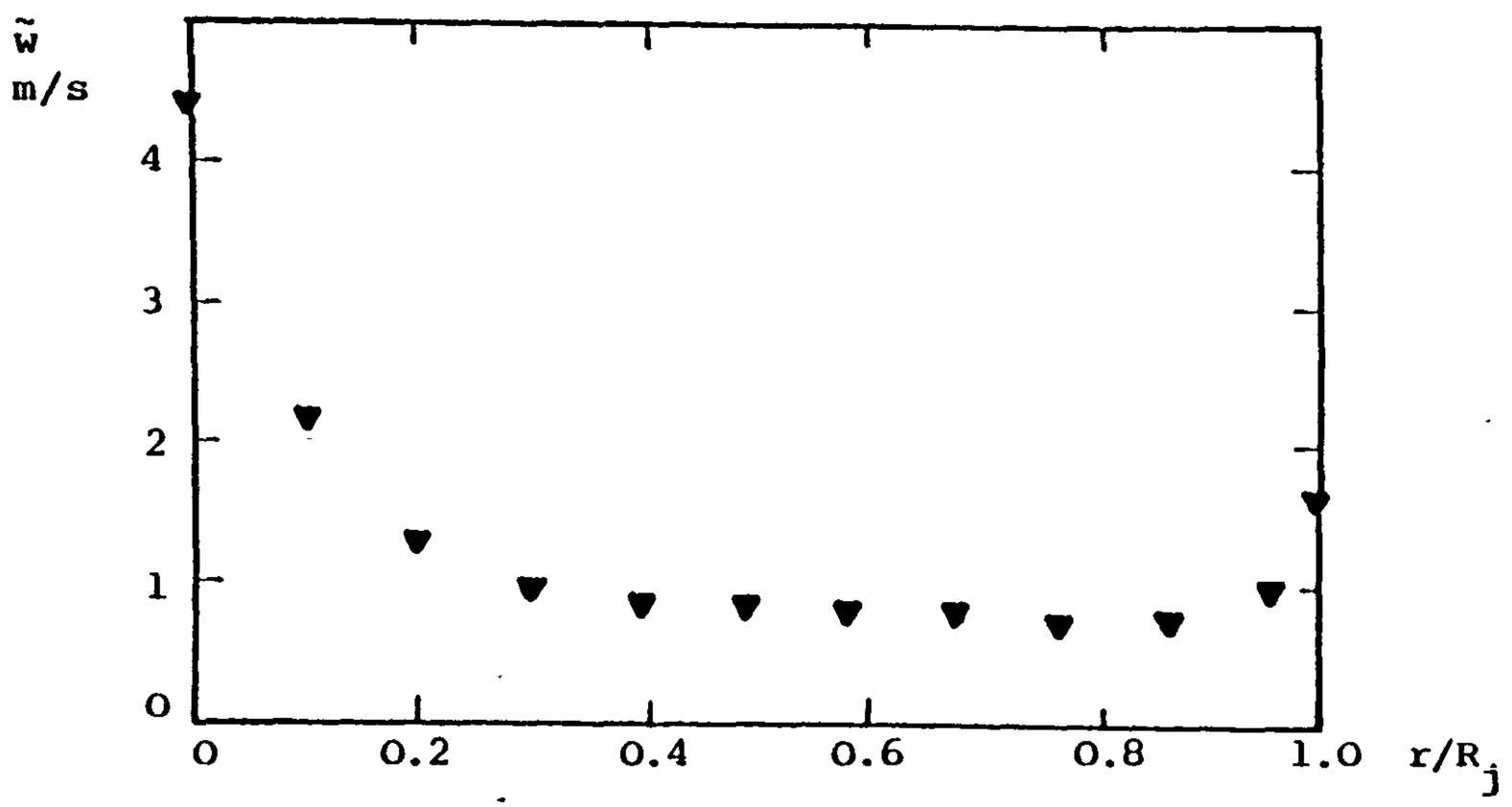


Fig. 4.13 (Continued)

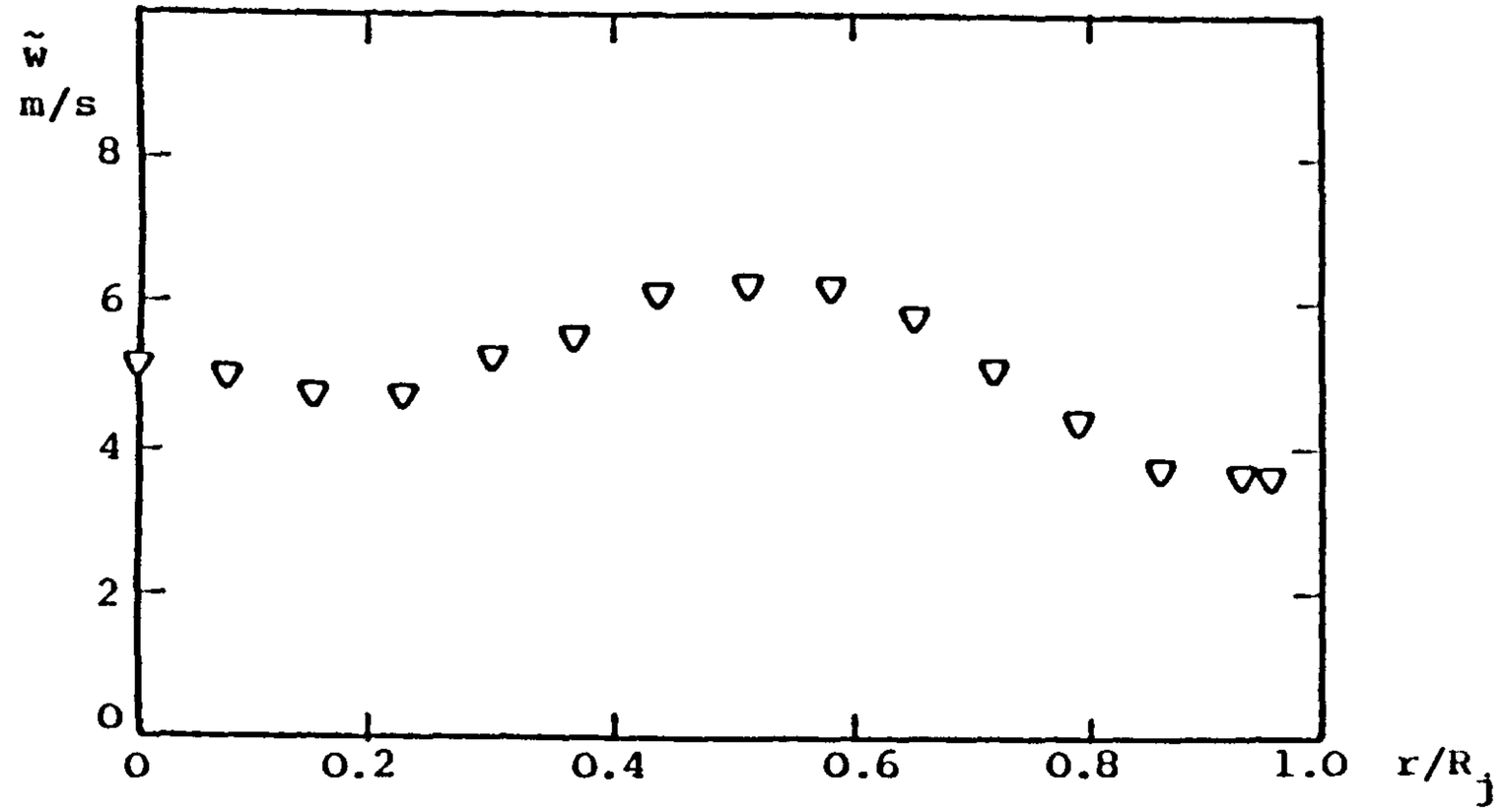


Fig. 4.13 (Continued)

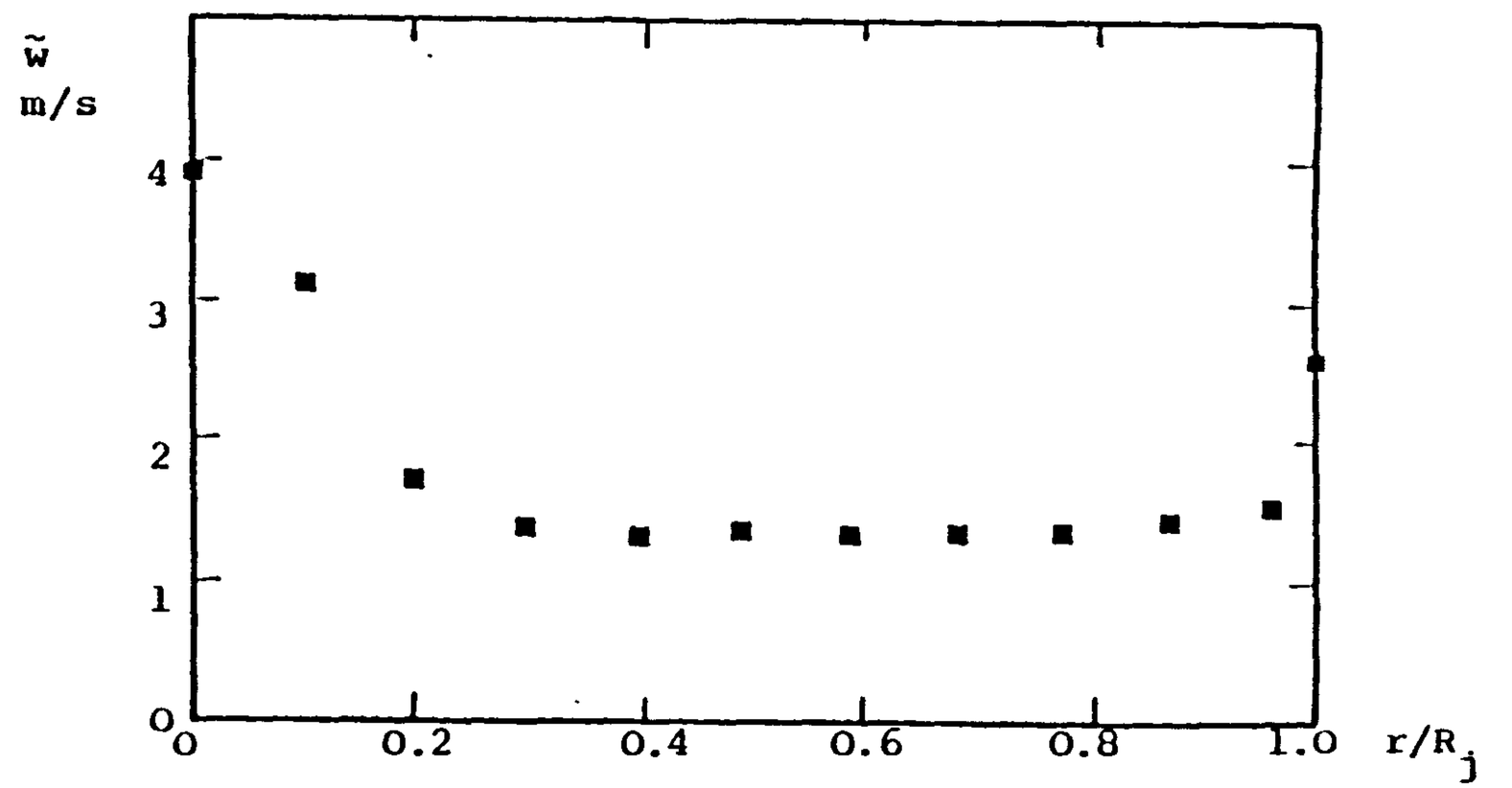
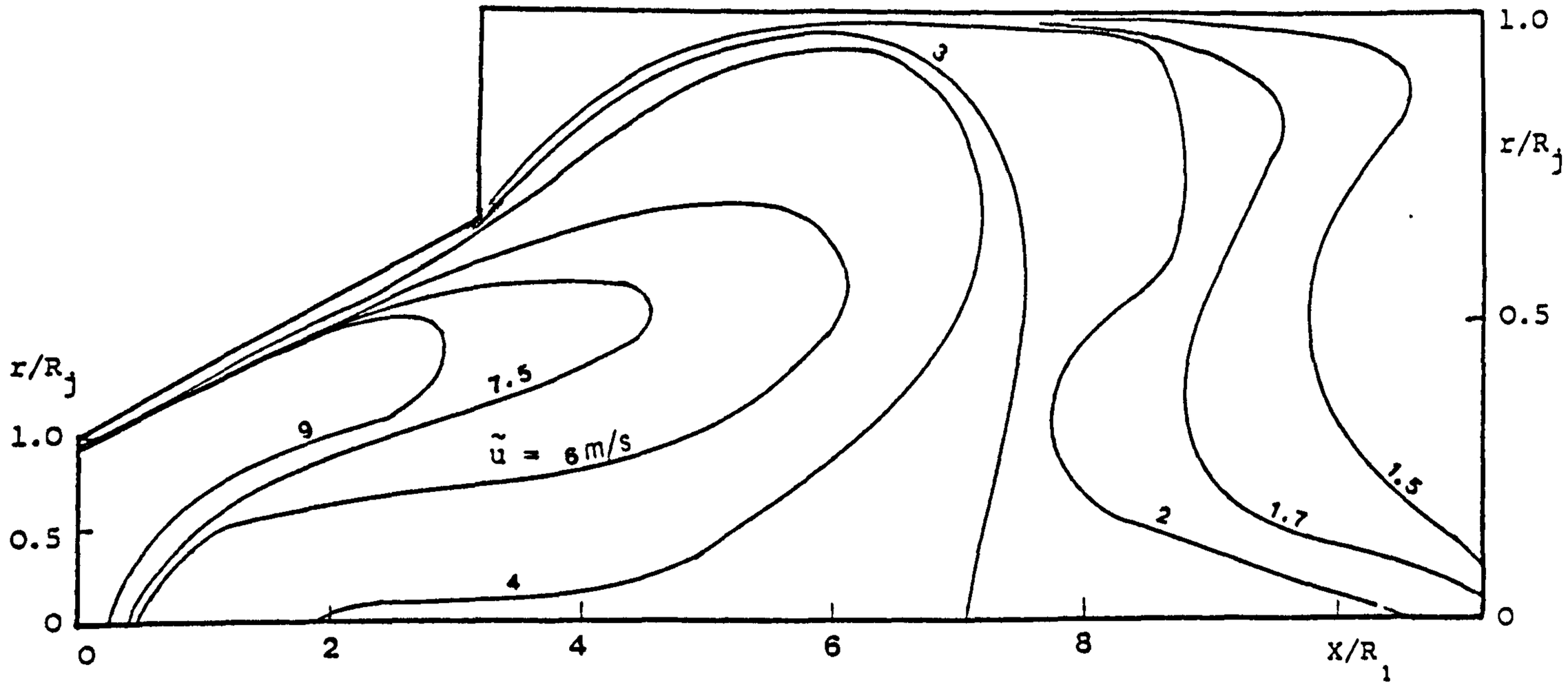
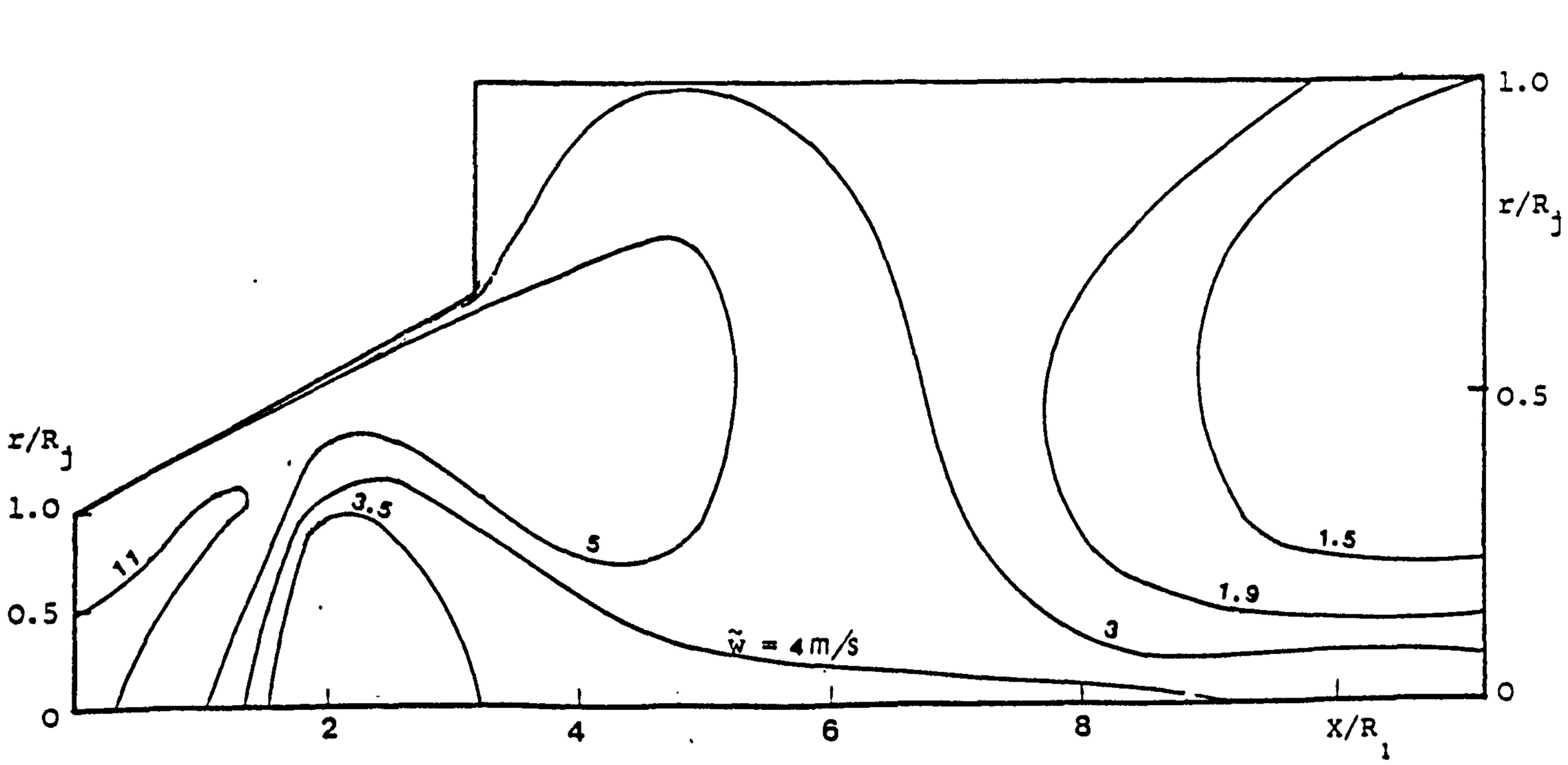


Fig. 4.13 (Continued)

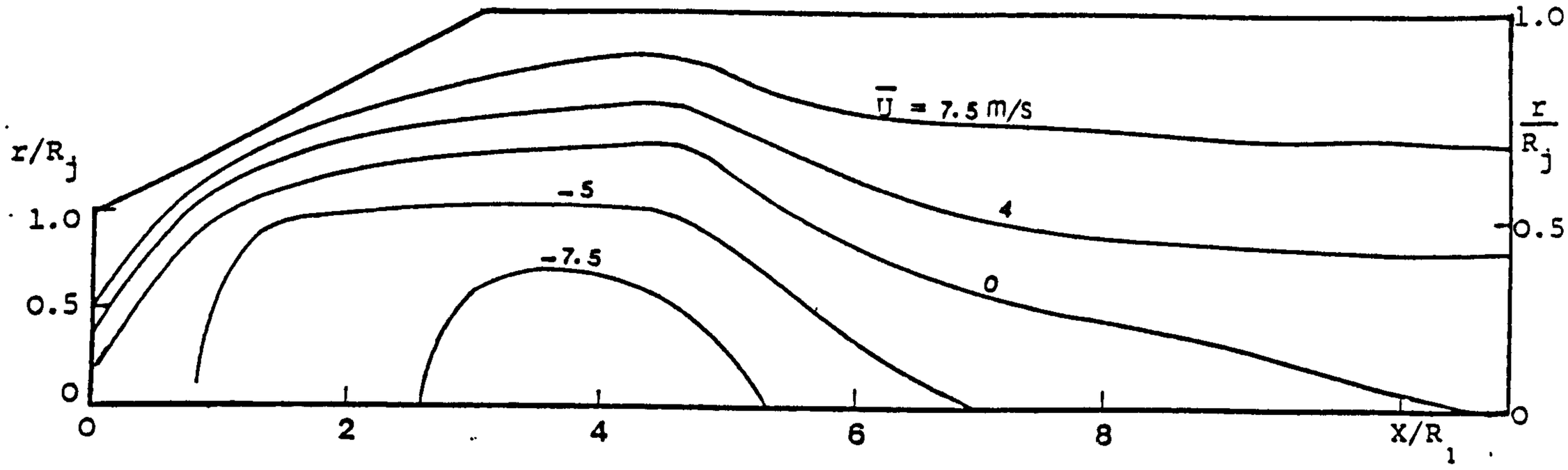


(i)

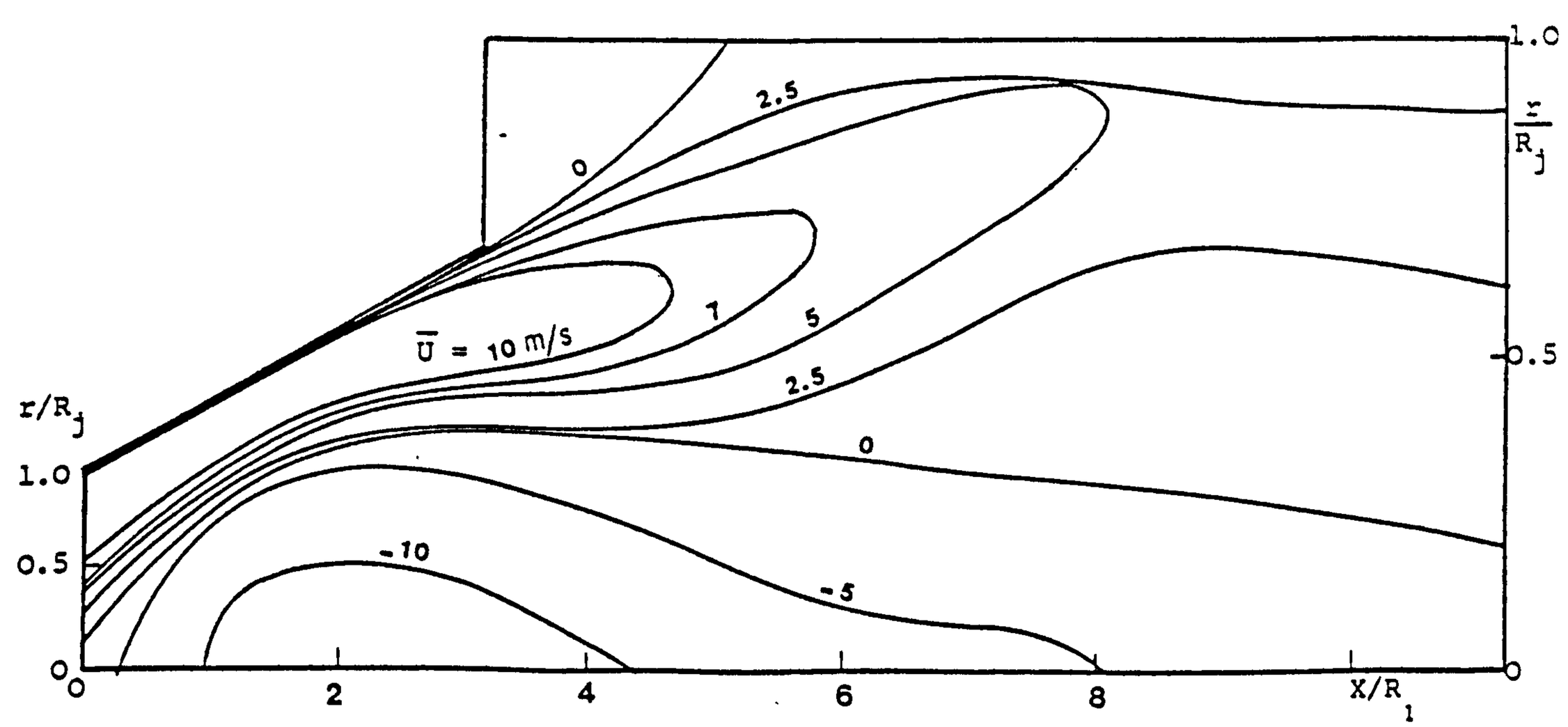


(ii)

Fig. 4.14 Contours of the rms of the Axial and Tangential Velocity Fluctuations of the Flow in G2 (S = 0.93); (i) $\tilde{u}$; (ii) $\tilde{w}$

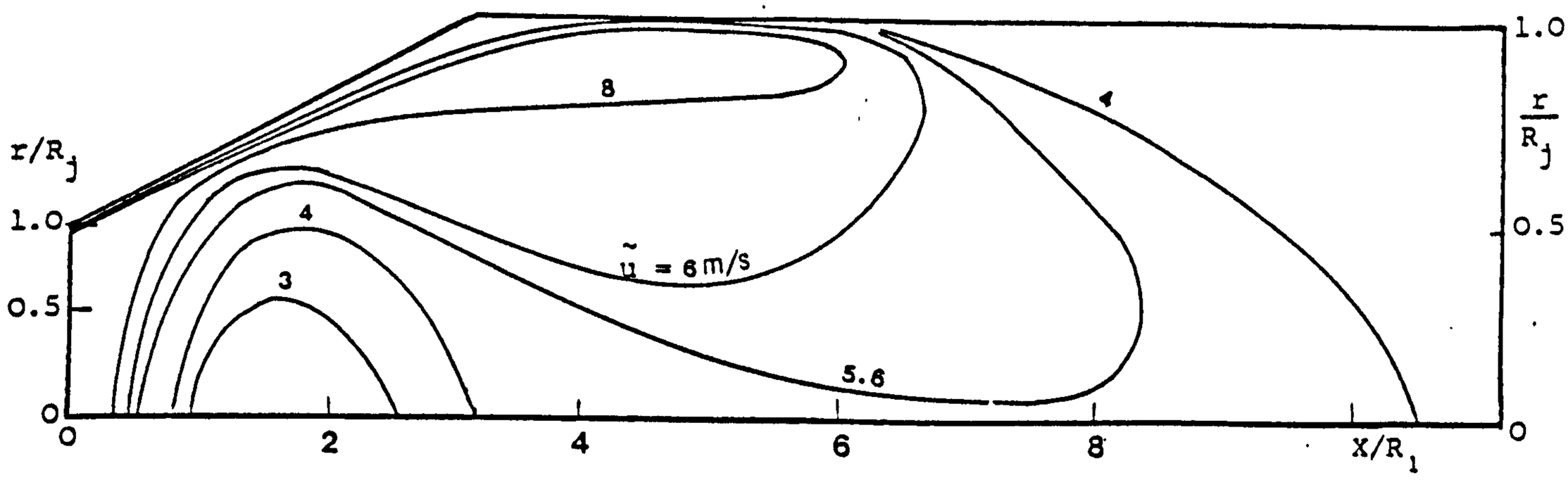


(i)

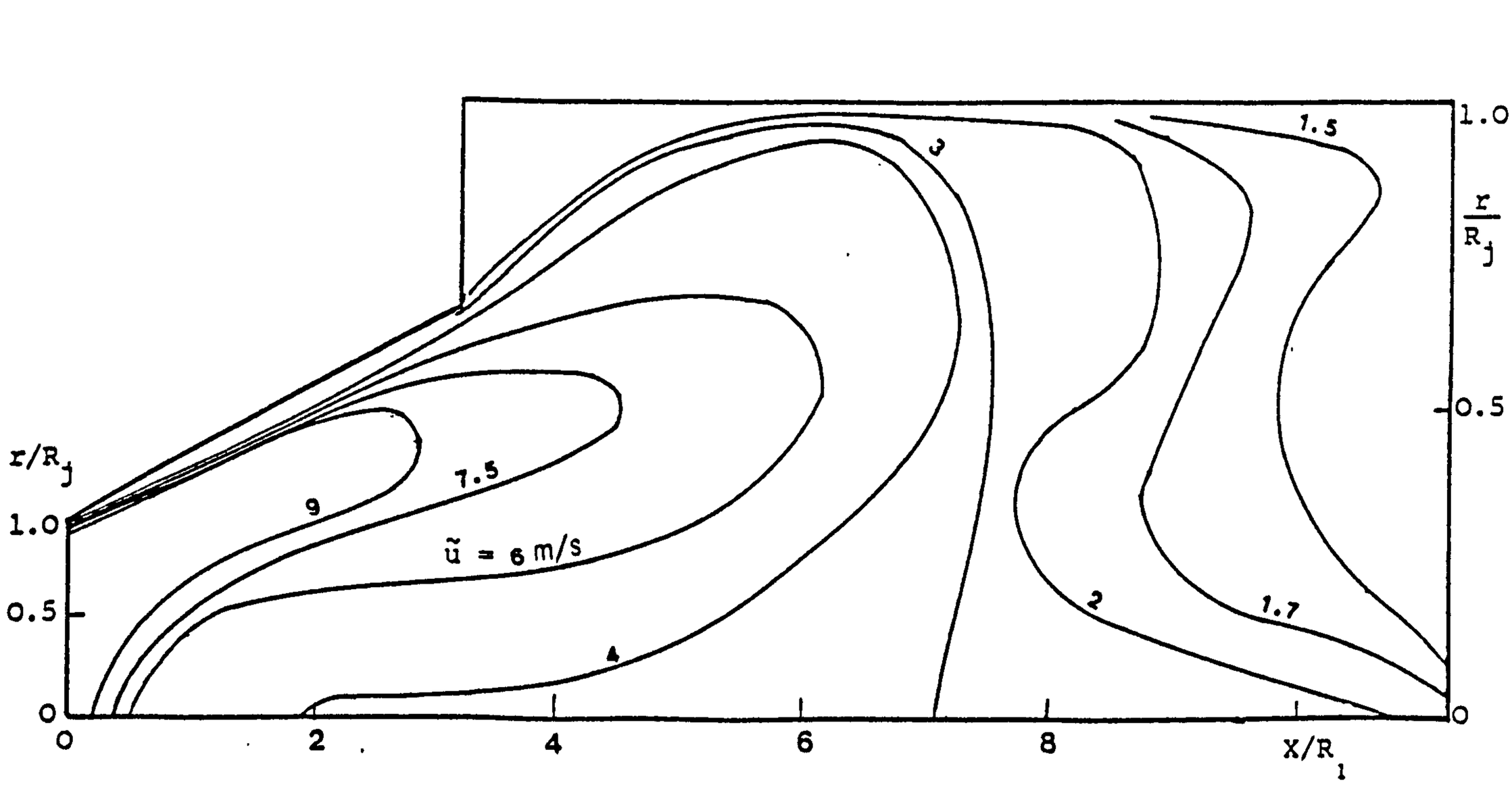


(ii)

Fig. 4.15 Mean Velocity Contours (S = 0.93); (i) Flow of G1; (ii) Flow of G2



(i)



(ii)

Fig. 4.16 Contours of the Axial Normal Stress (S = 0.93); (i) Flow of G1; (ii) Flow of G2

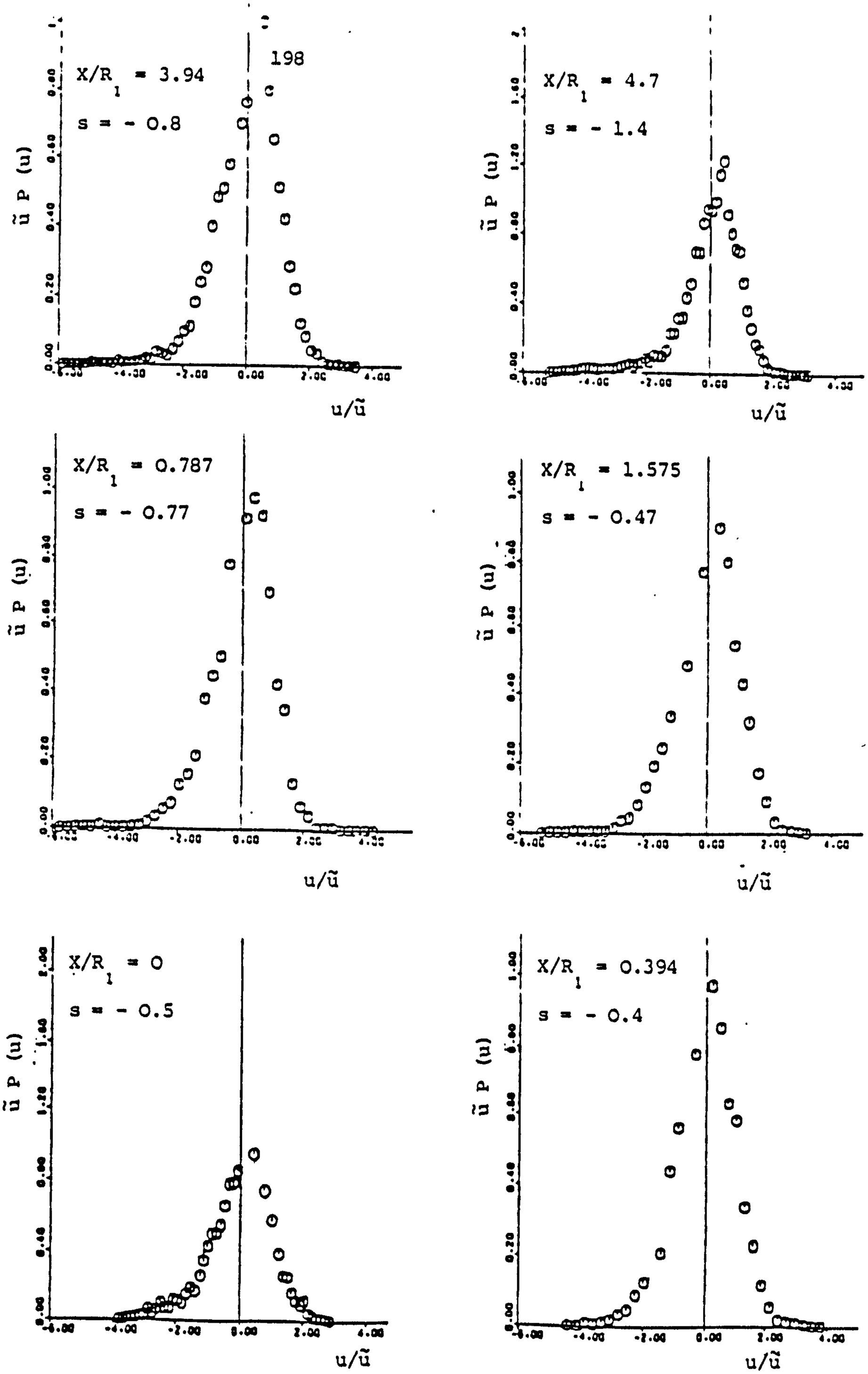
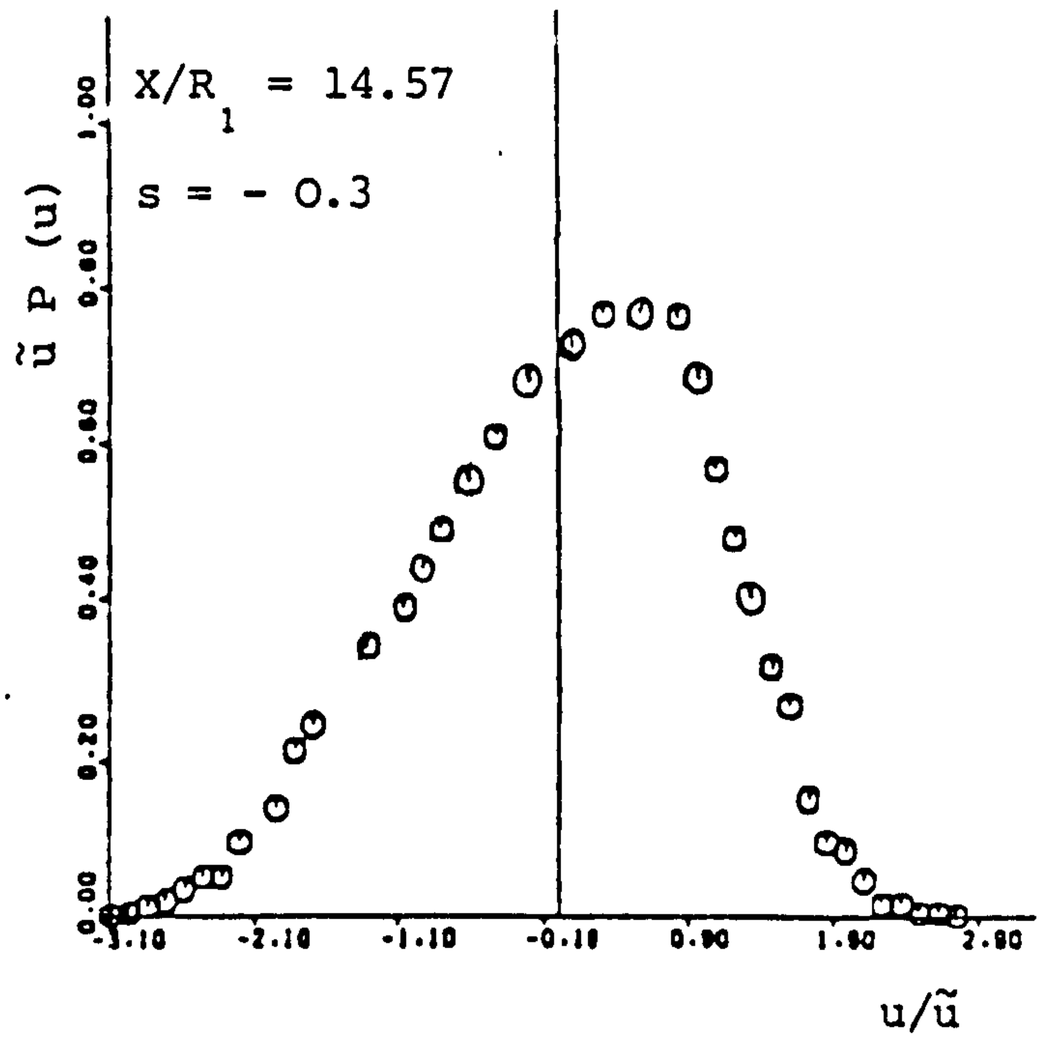
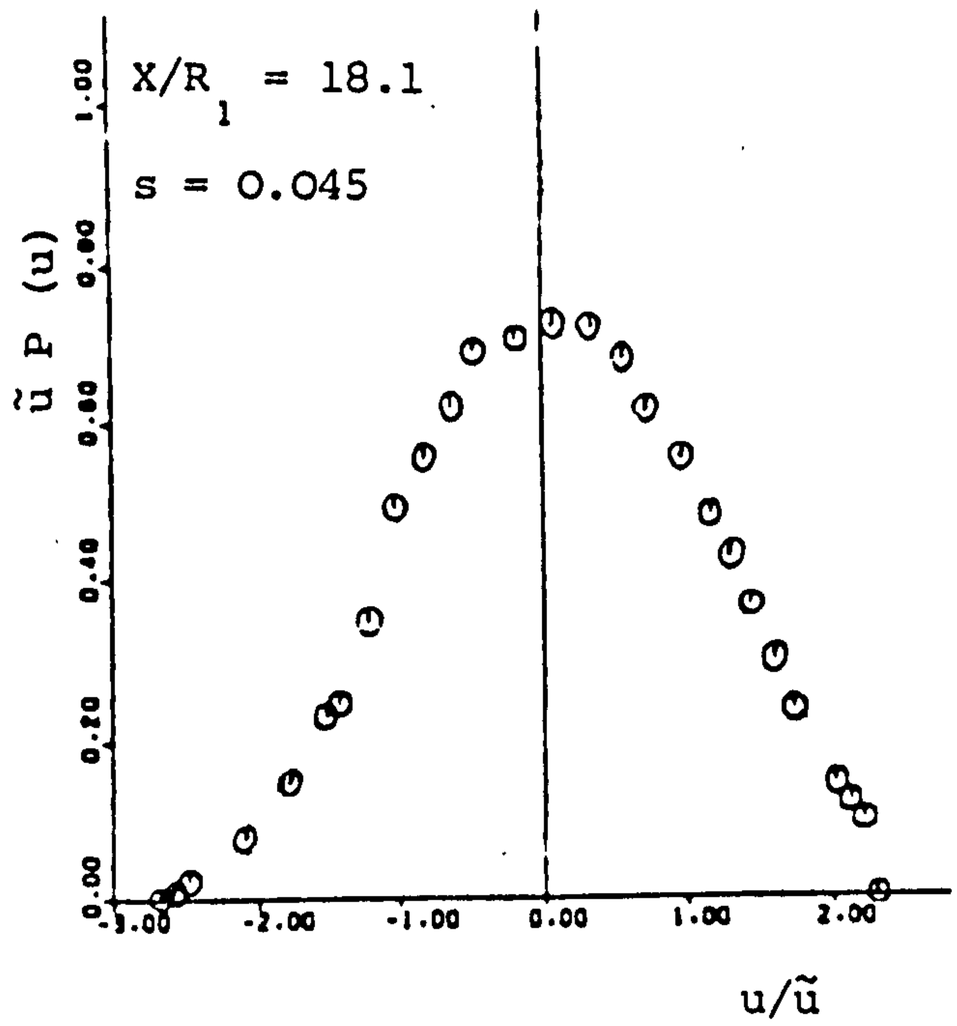
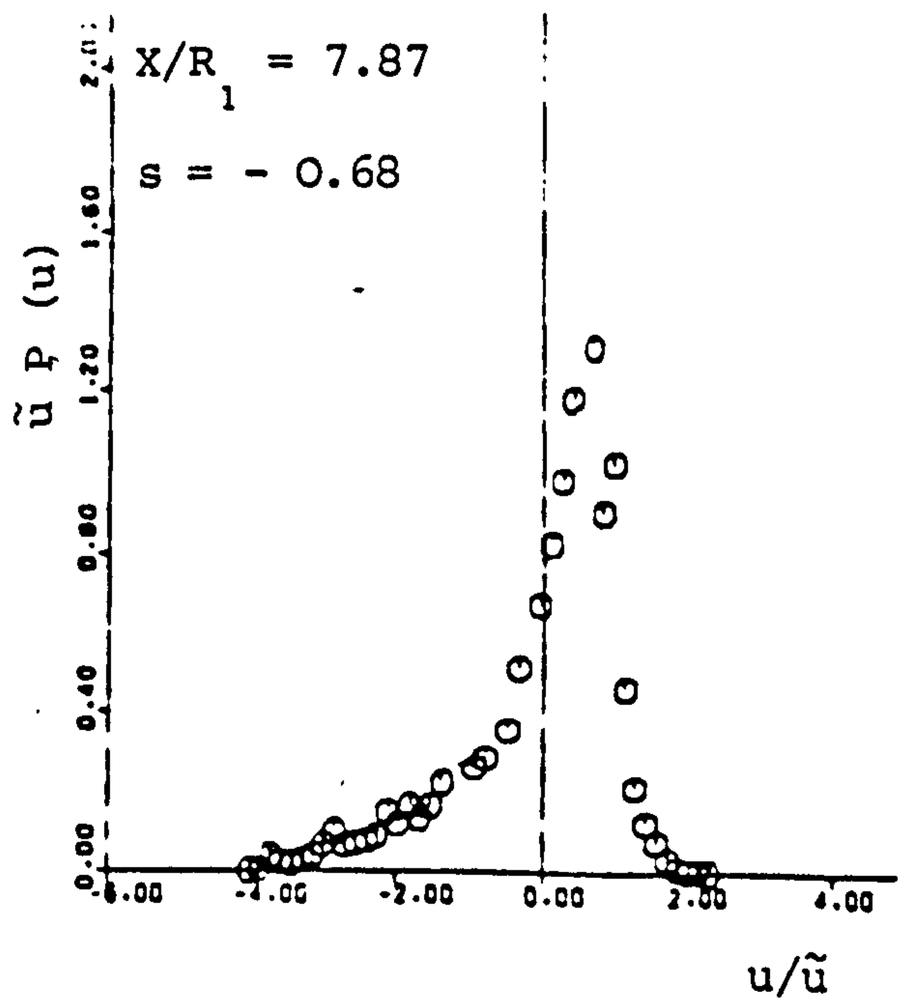


Fig. 4.17 The Probability Density Distribution of the Axial Velocity Fluctuations Along the Centre-Line of G2 (S = 0.0)







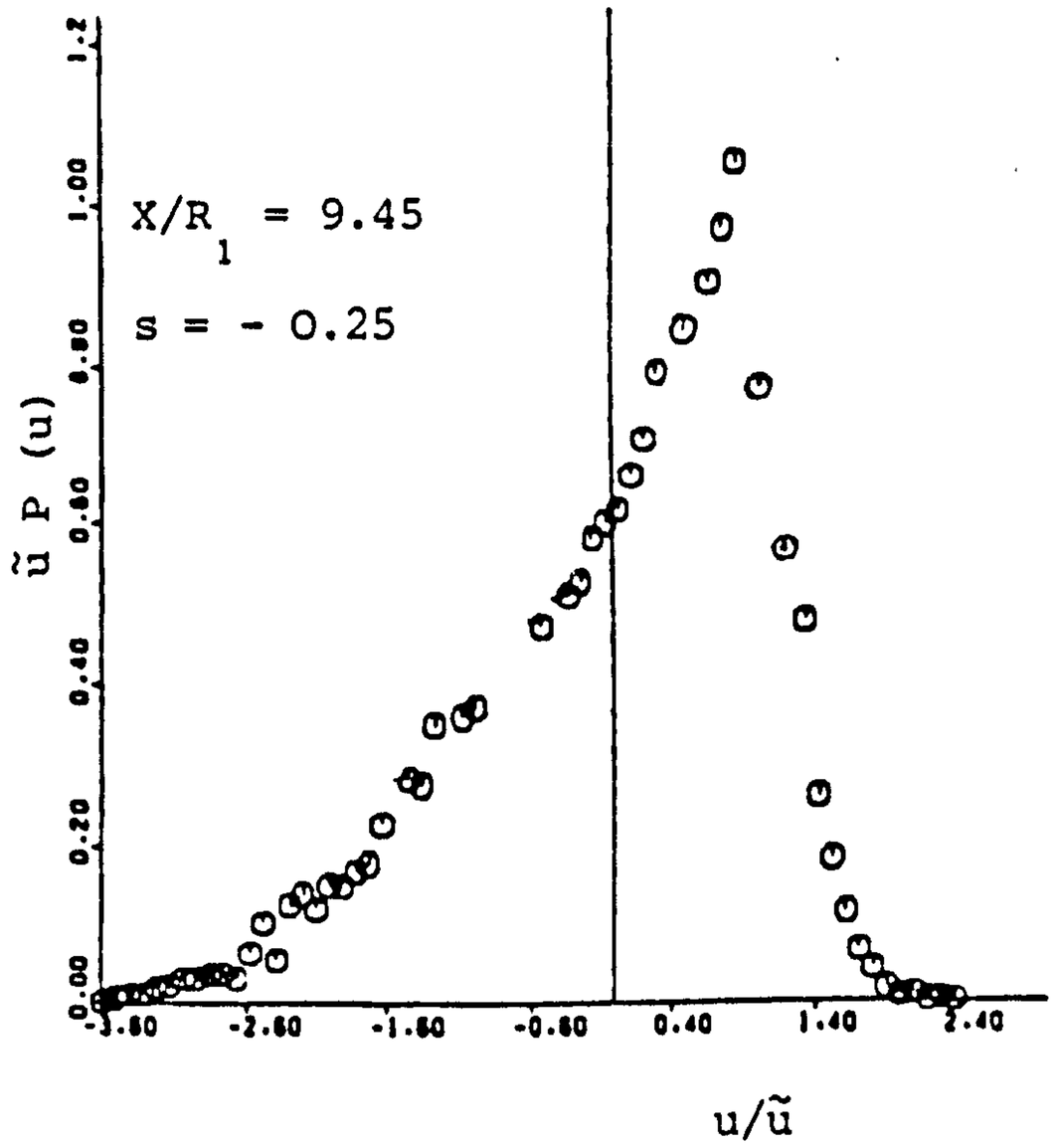
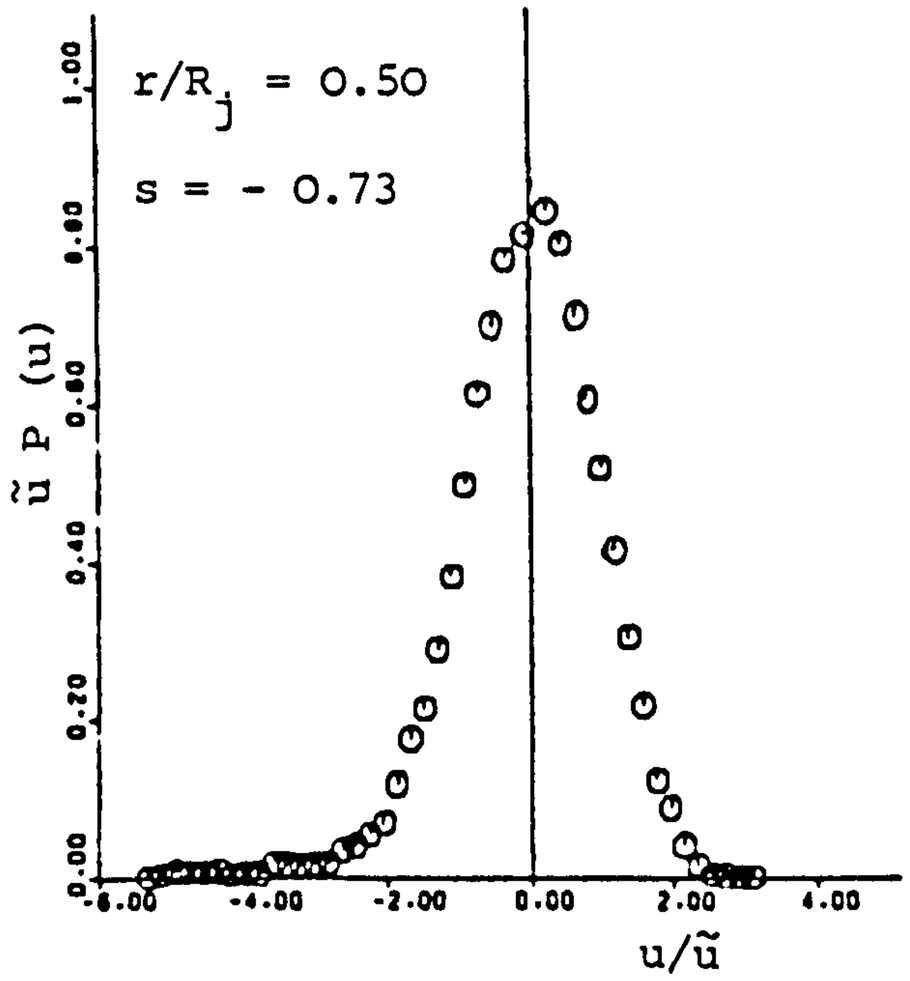
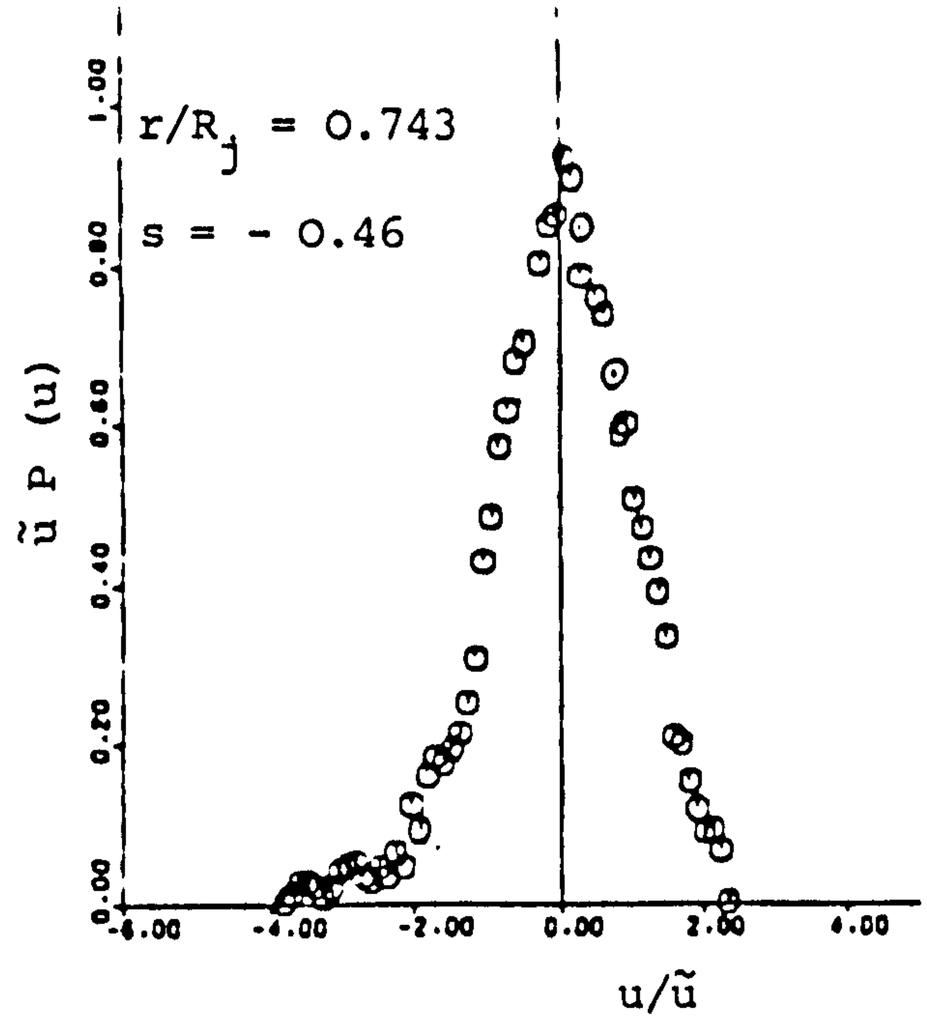
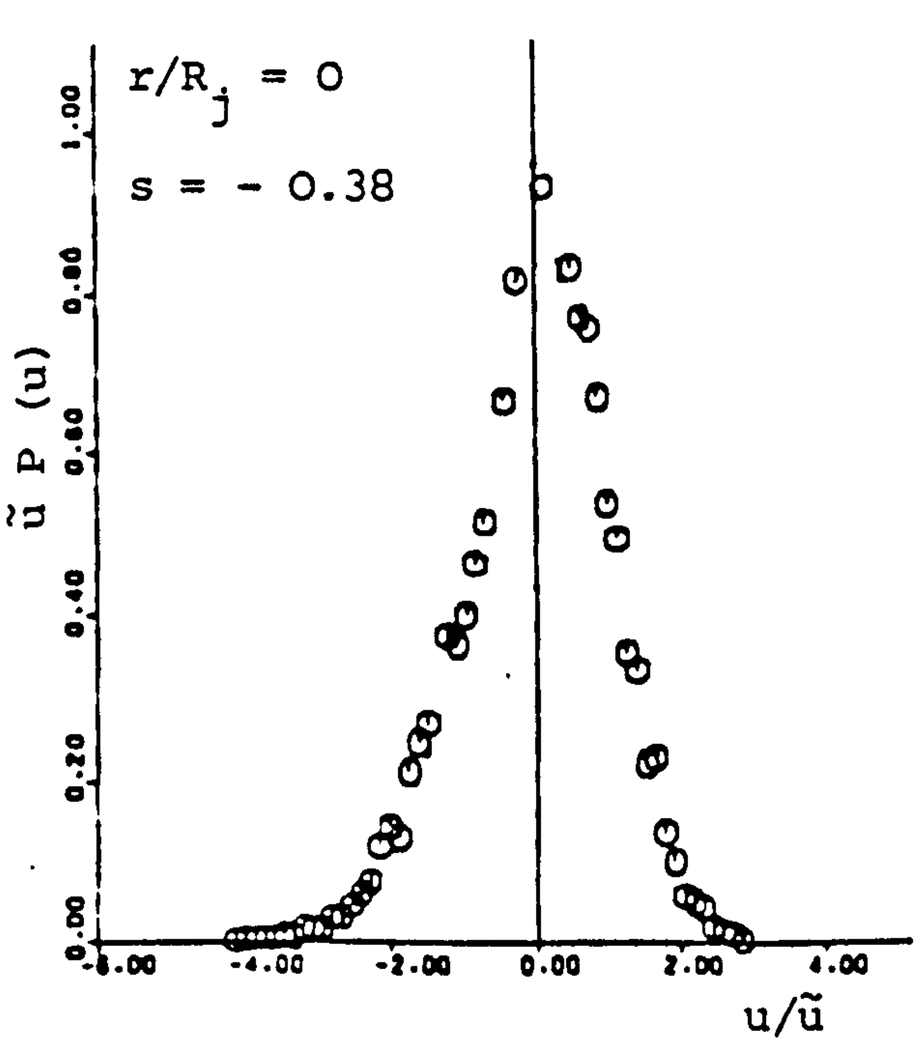


Fig. 4.17 (Continued)







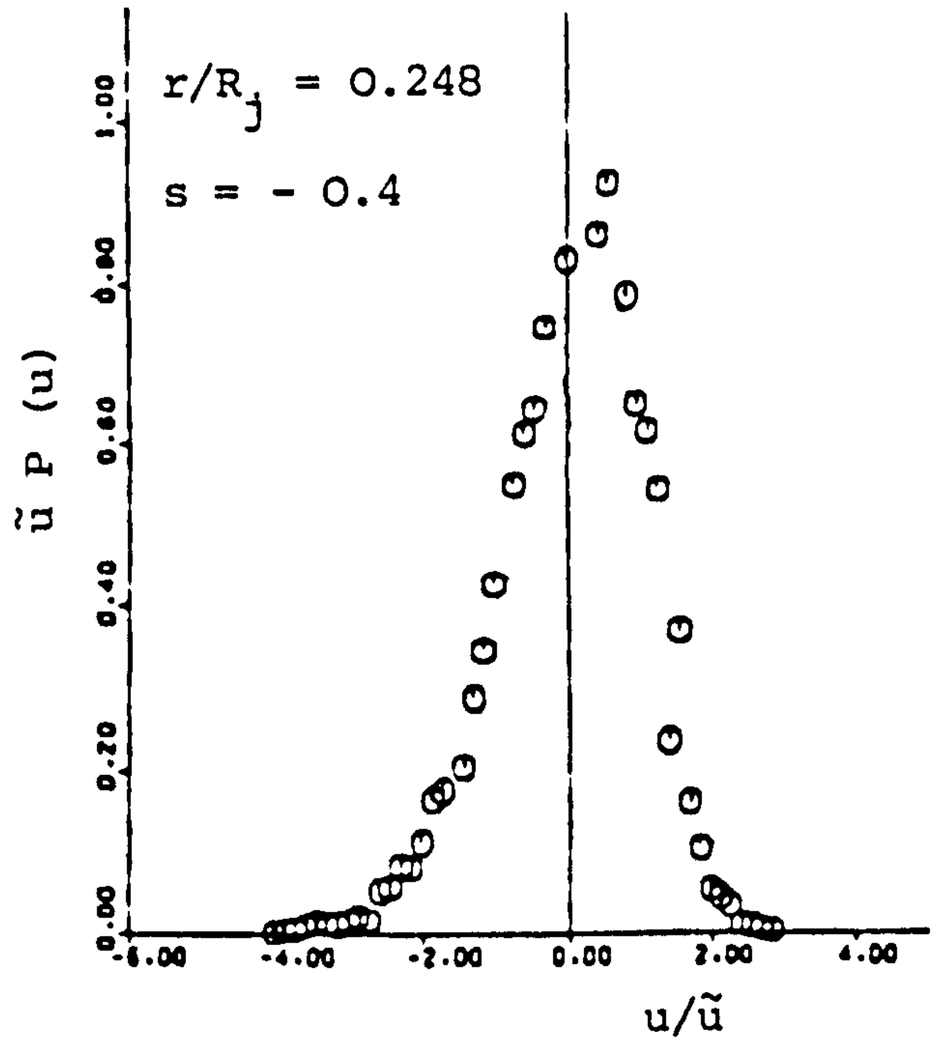


Fig. 4.18 The Probability Density Distribution of the Axial Velocity Fluctuations Along the Radius of G2 (S = 0.0, Station 2)

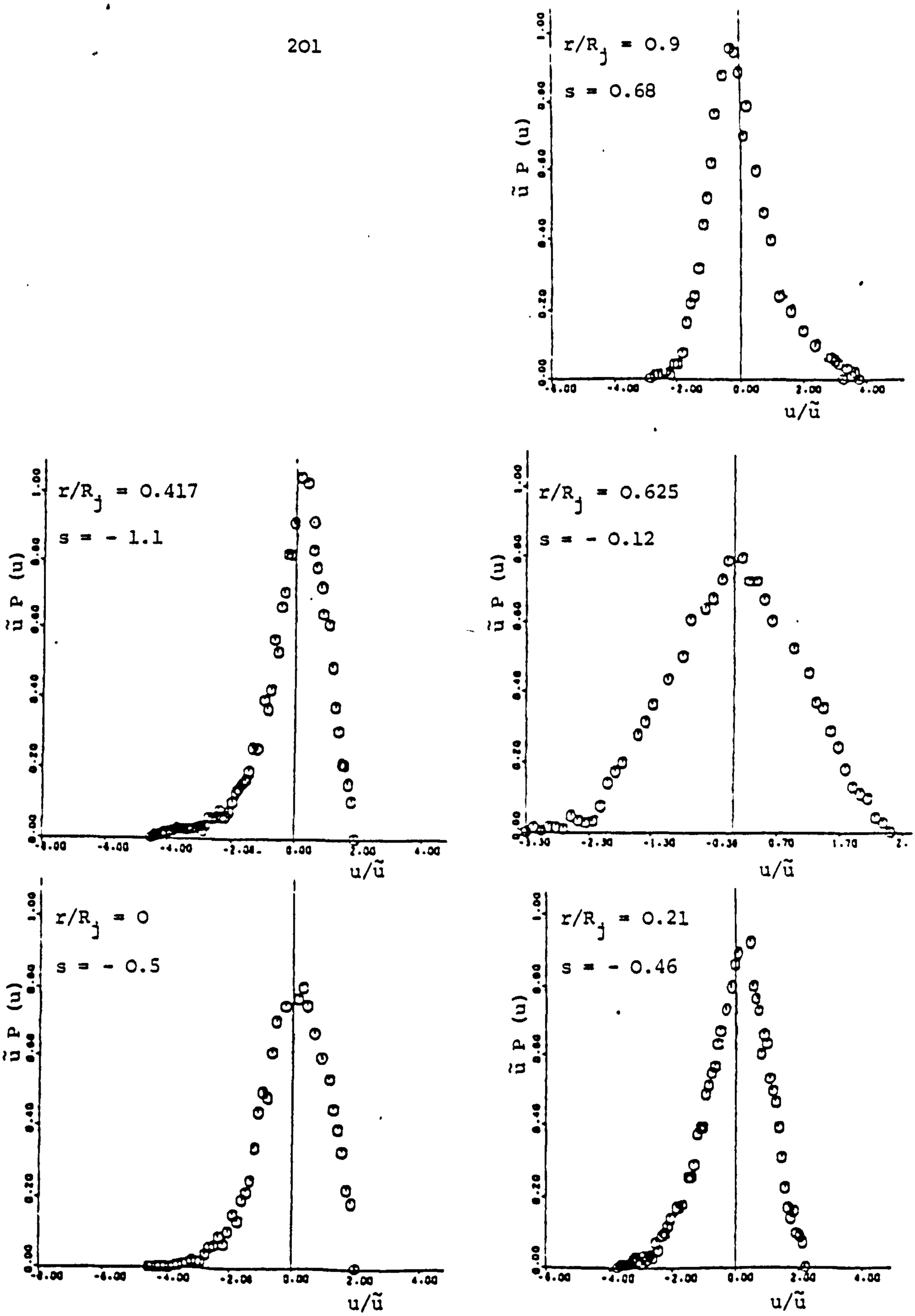


Fig. 4.19 The Probability Density Distribution of the Axial Velocity Fluctuations Along the Radius of G2 (S = 0.0, Station 3)

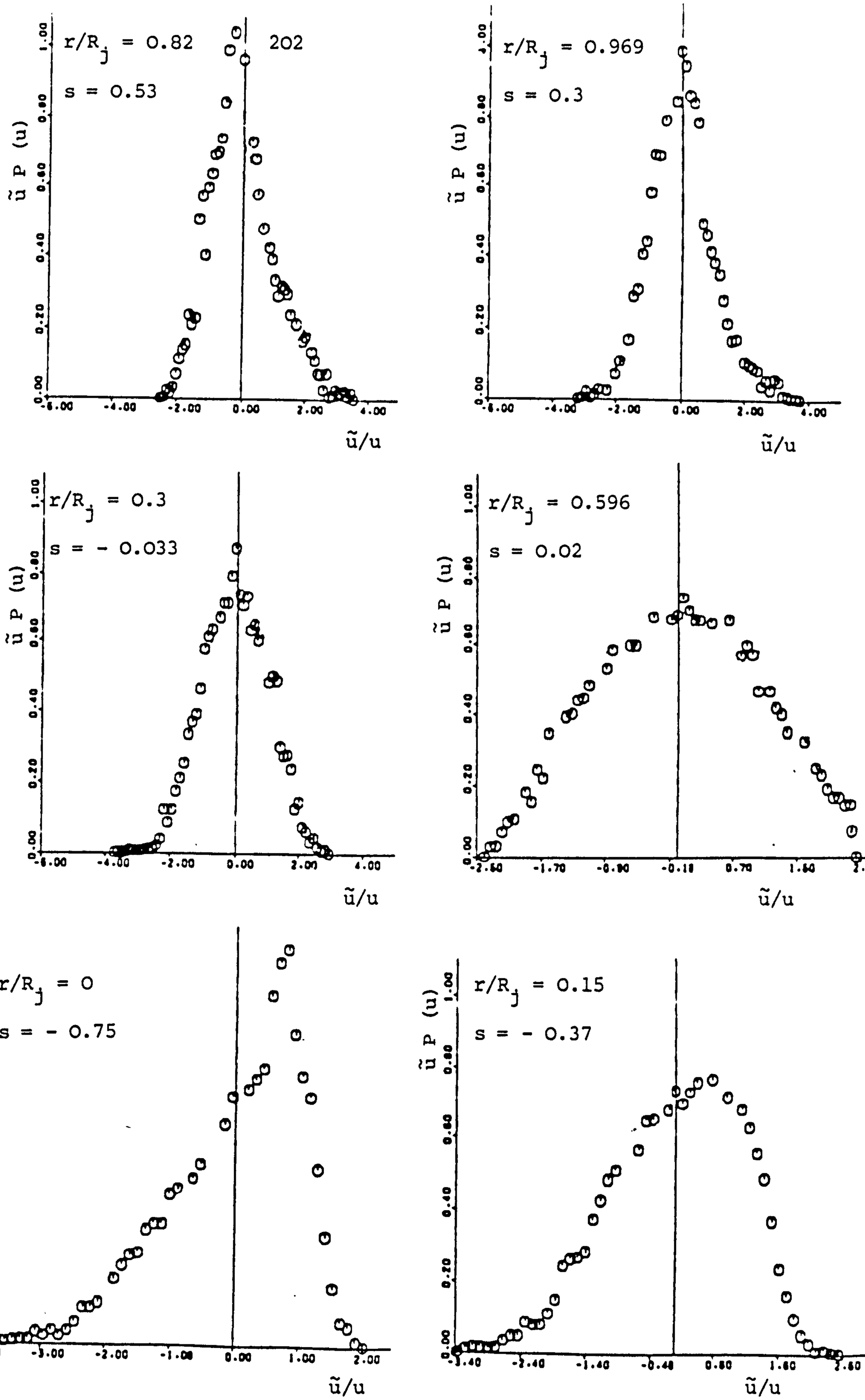
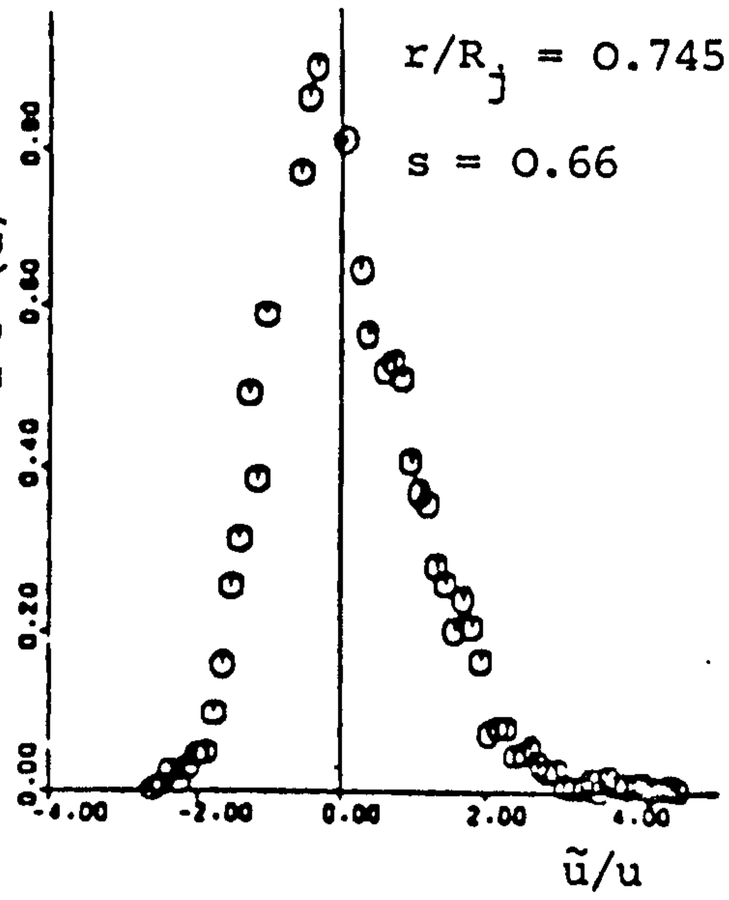
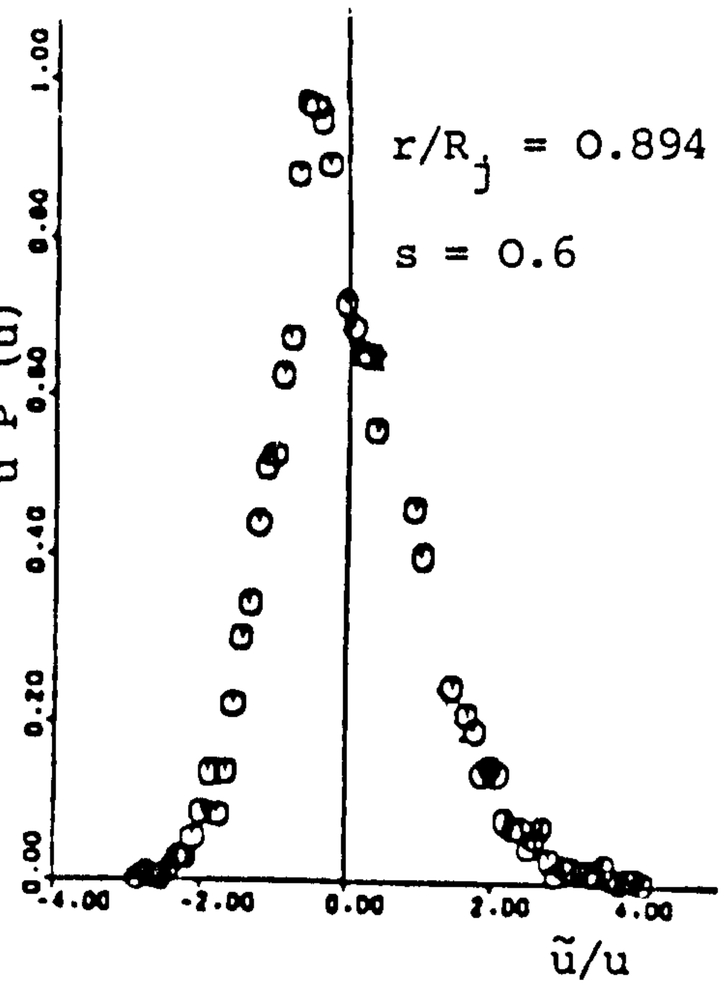
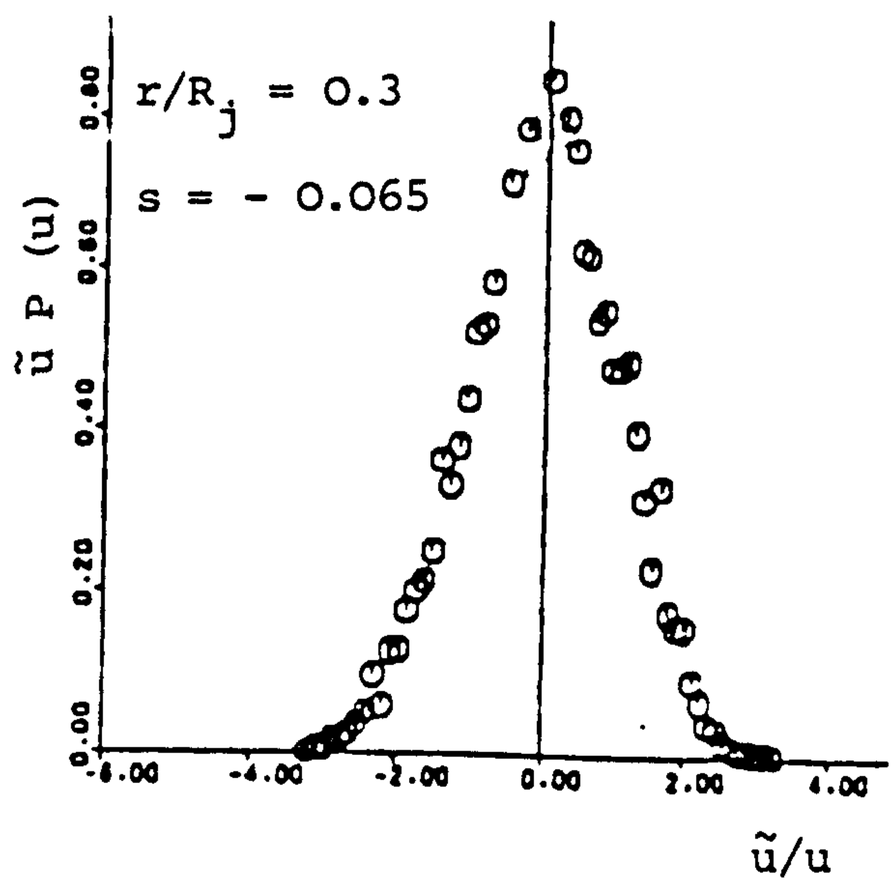
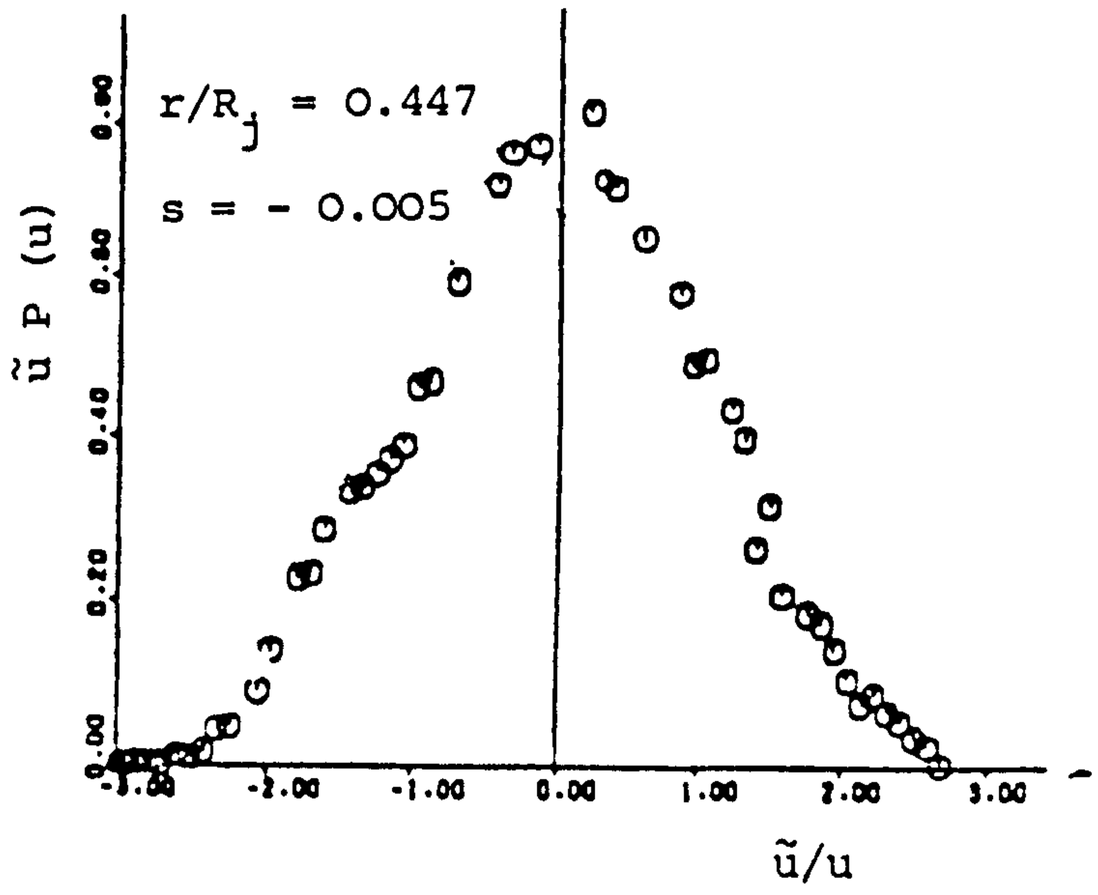


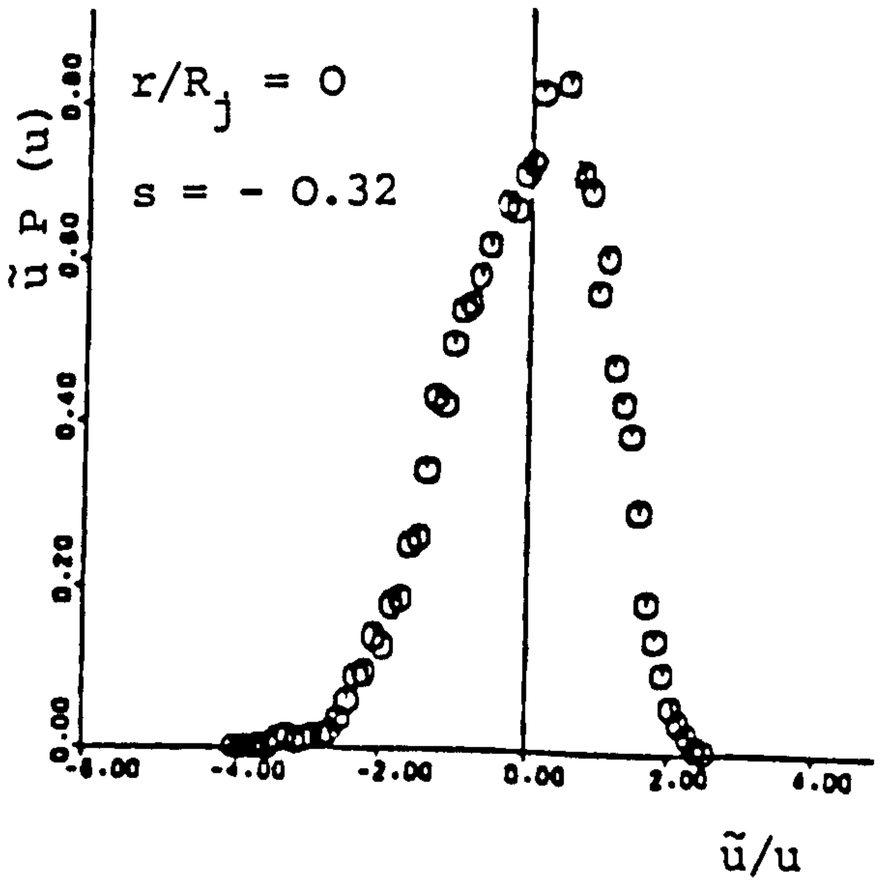
Fig. 4.20 The Probability Density Distributions of the Axial Velocity Fluctuations Along the Radius of G2 (S = 0.0, Station 6)











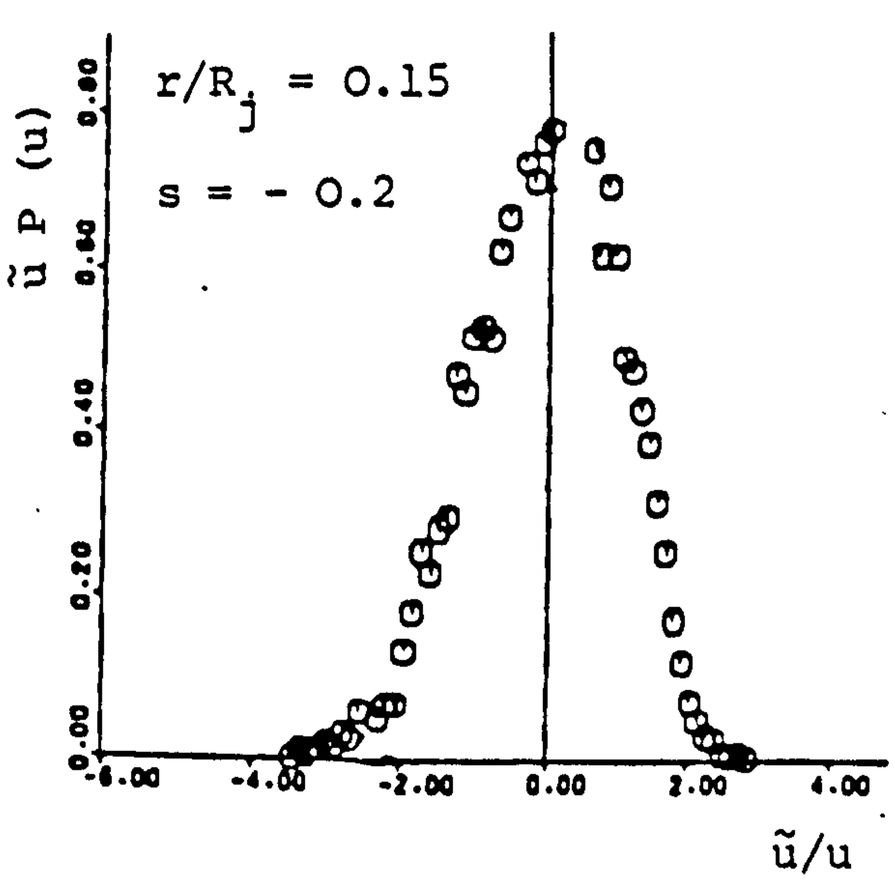
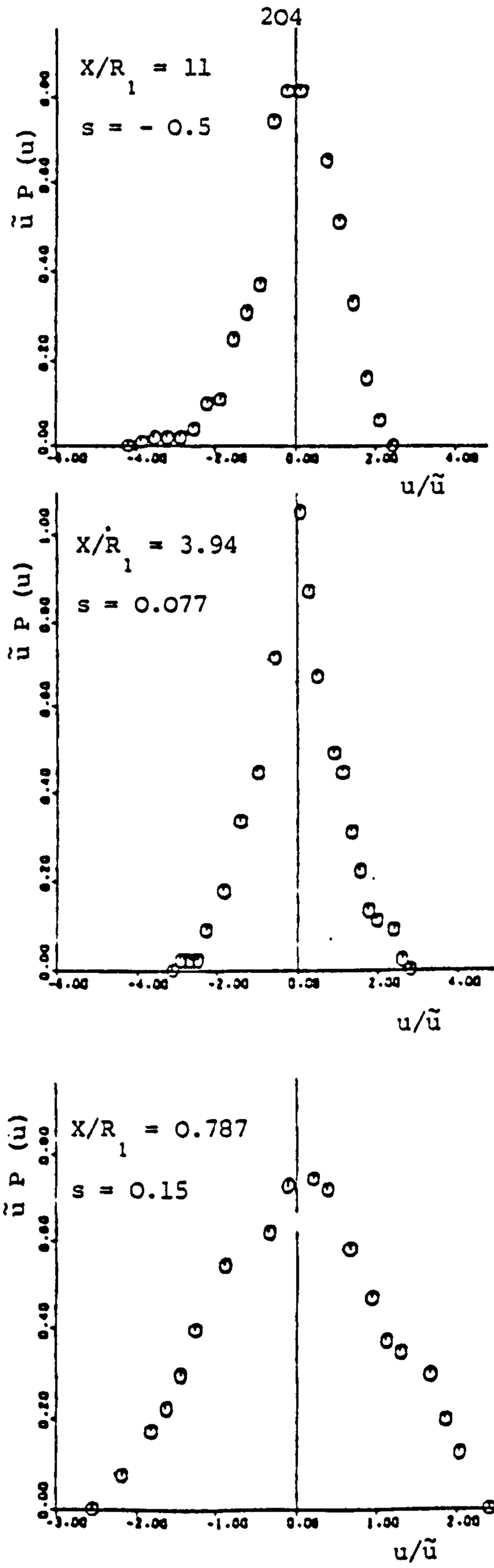


Fig. 4.21 The Probability Density Distribution of the Axial Velocity Fluctuations Along the Radius of G2 (S = 0.0, Station 7)



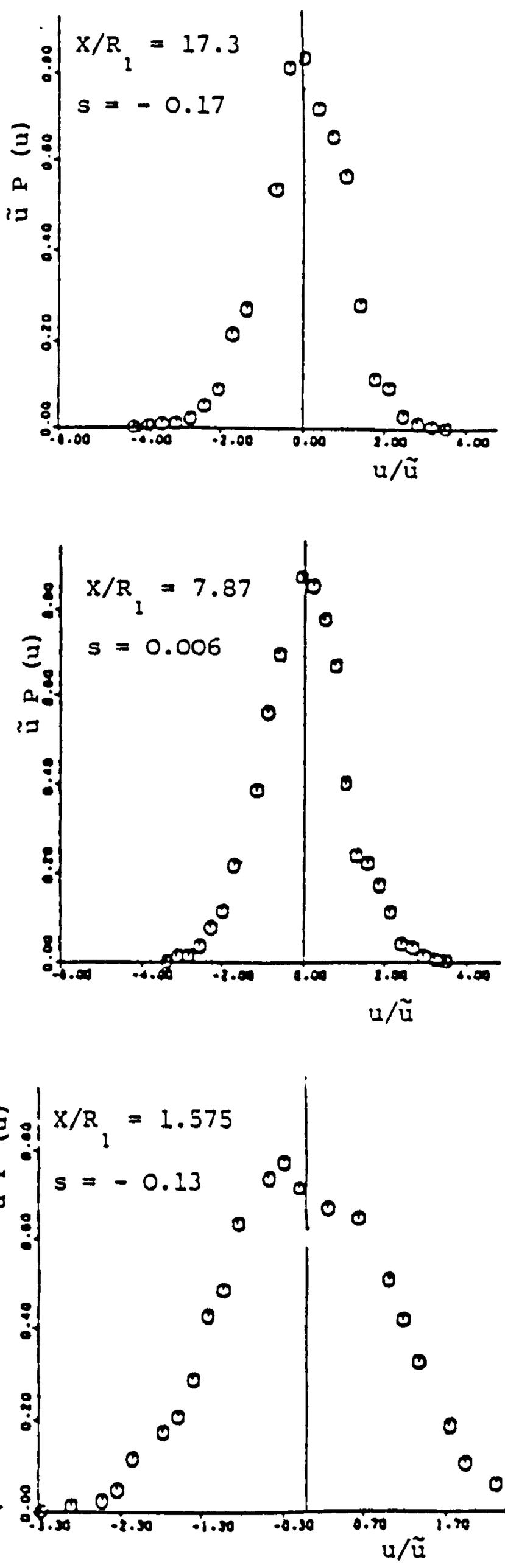
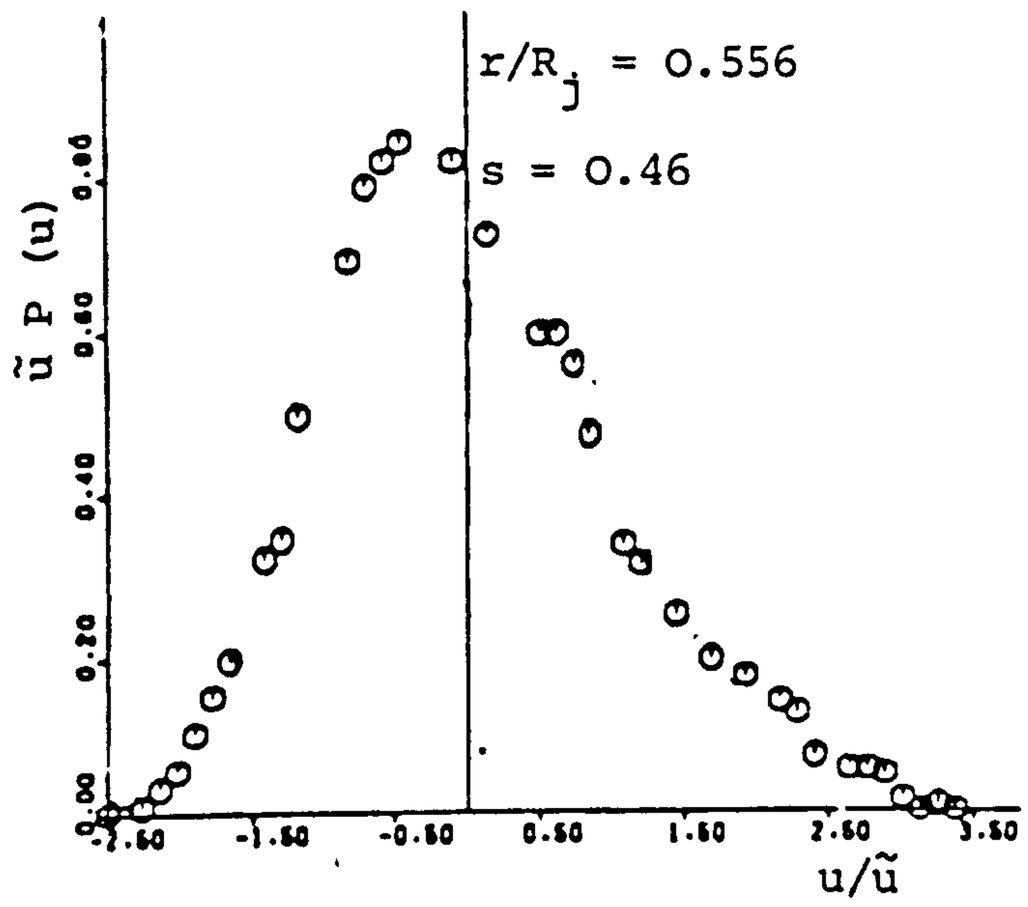
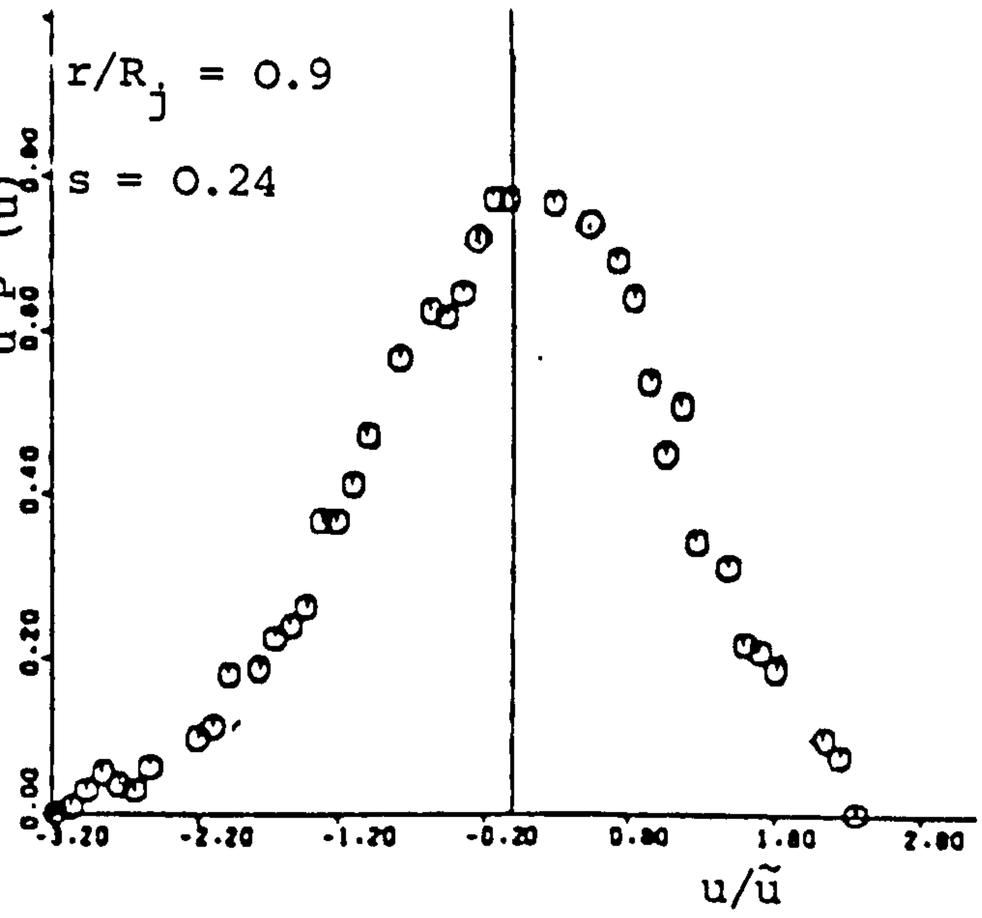
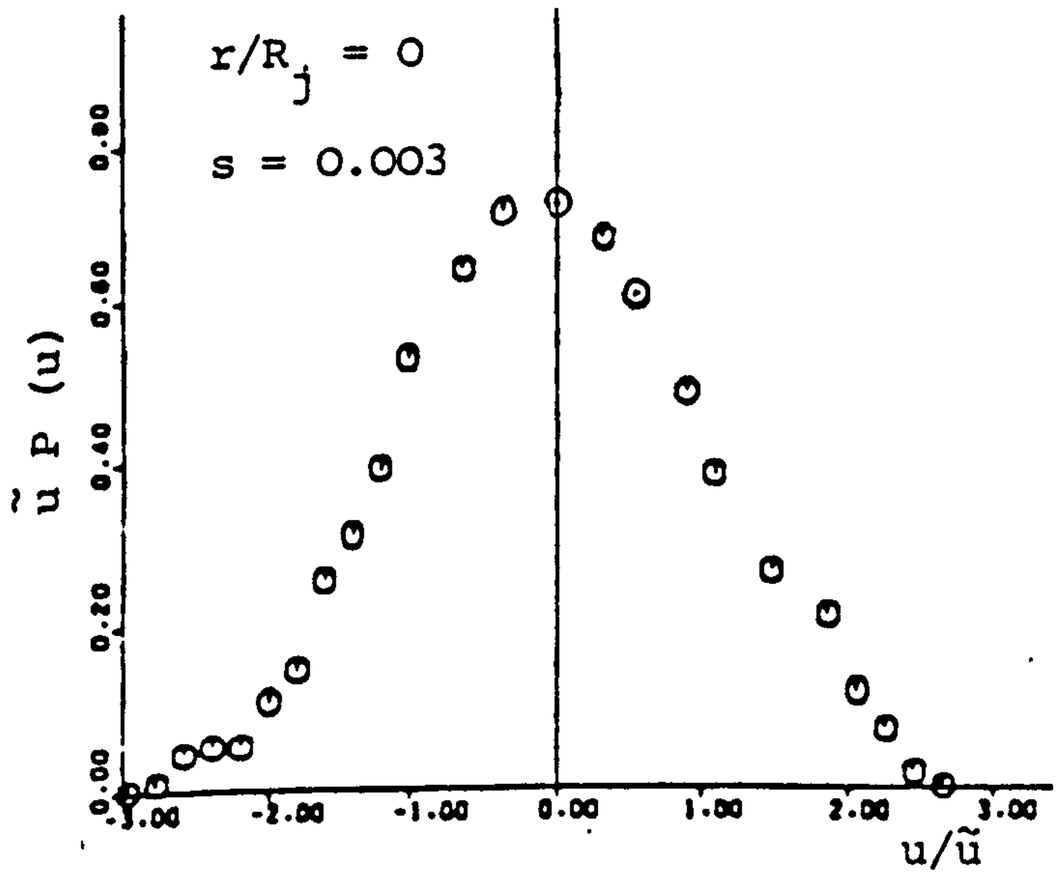


Fig. 4.22 The Probability Density Distributions of the Axial Velocity Fluctuations Along the Centre-Line of G2 (S = 0.93)







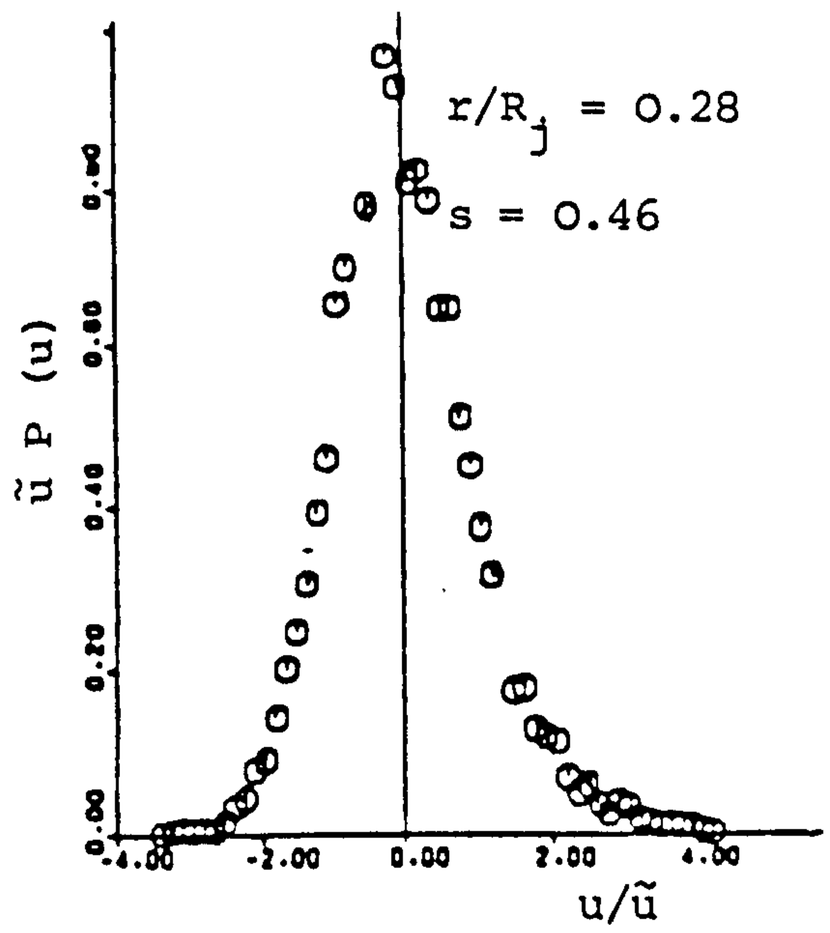


Fig. 4.23 Radial Distributions of u-Probability Density of the Flow of G2 (S = 0.93, Station 3)

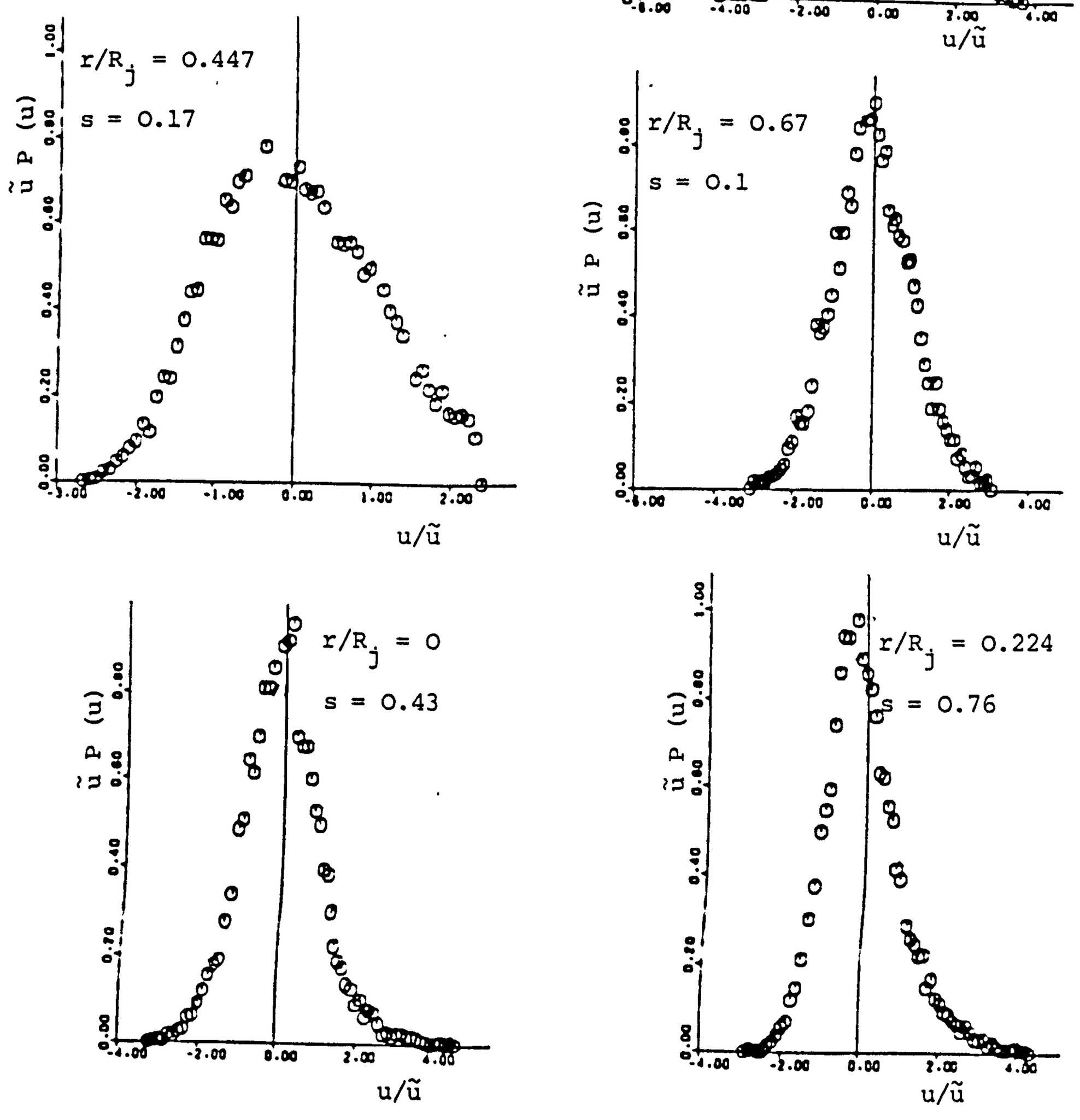
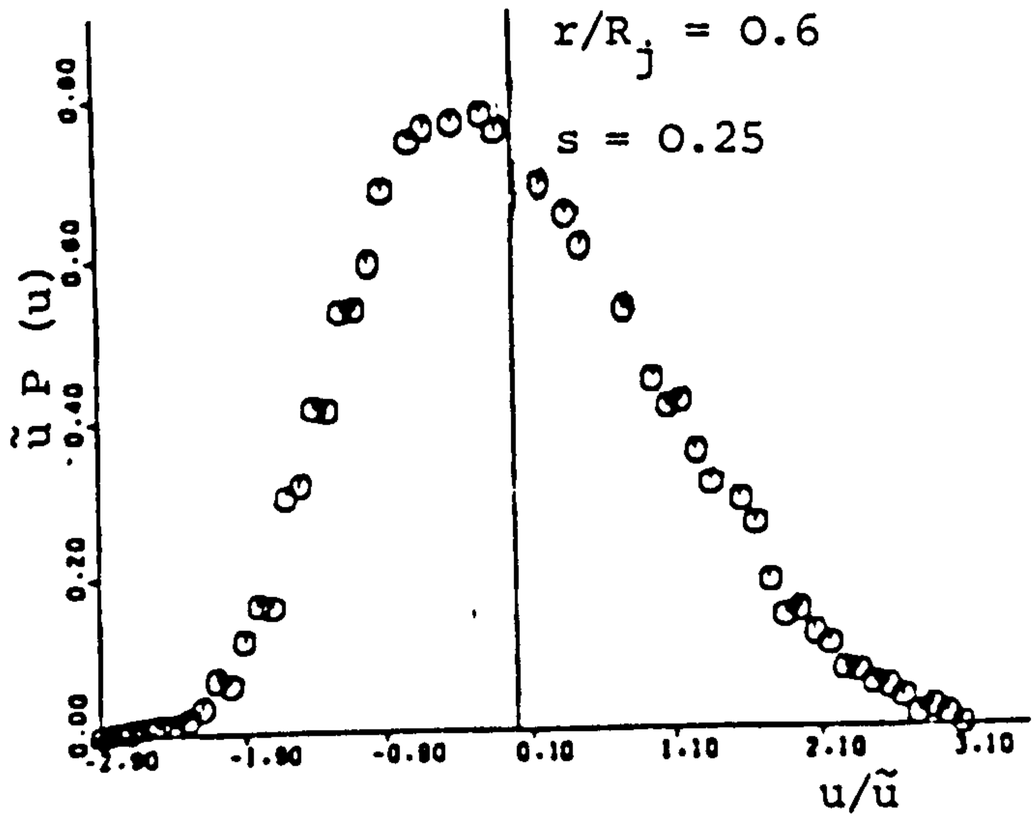
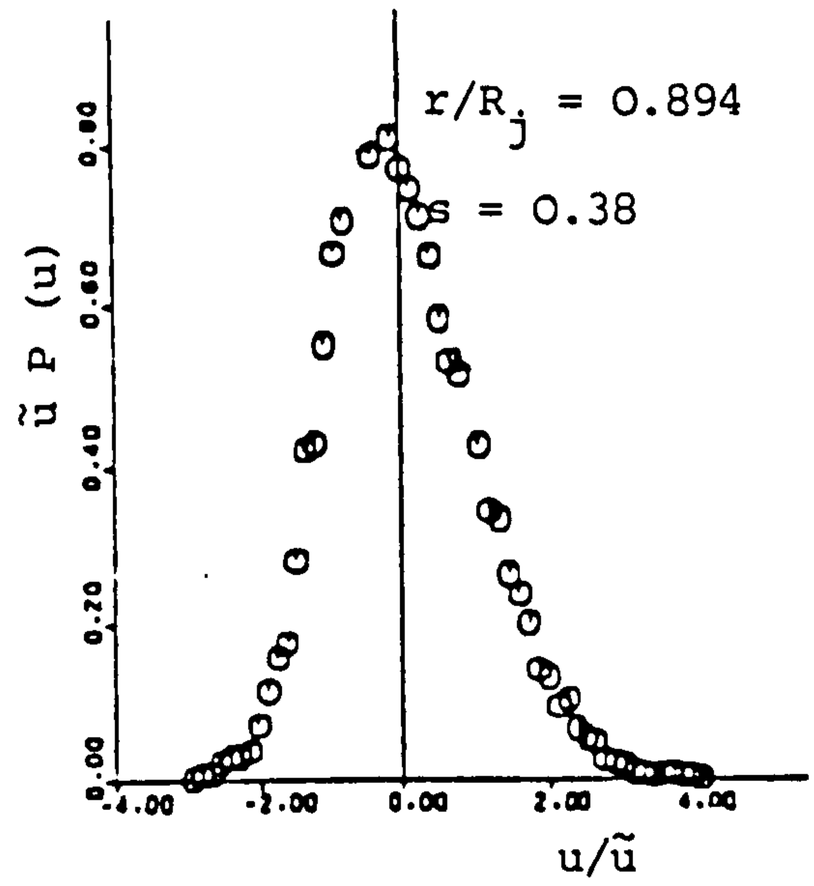
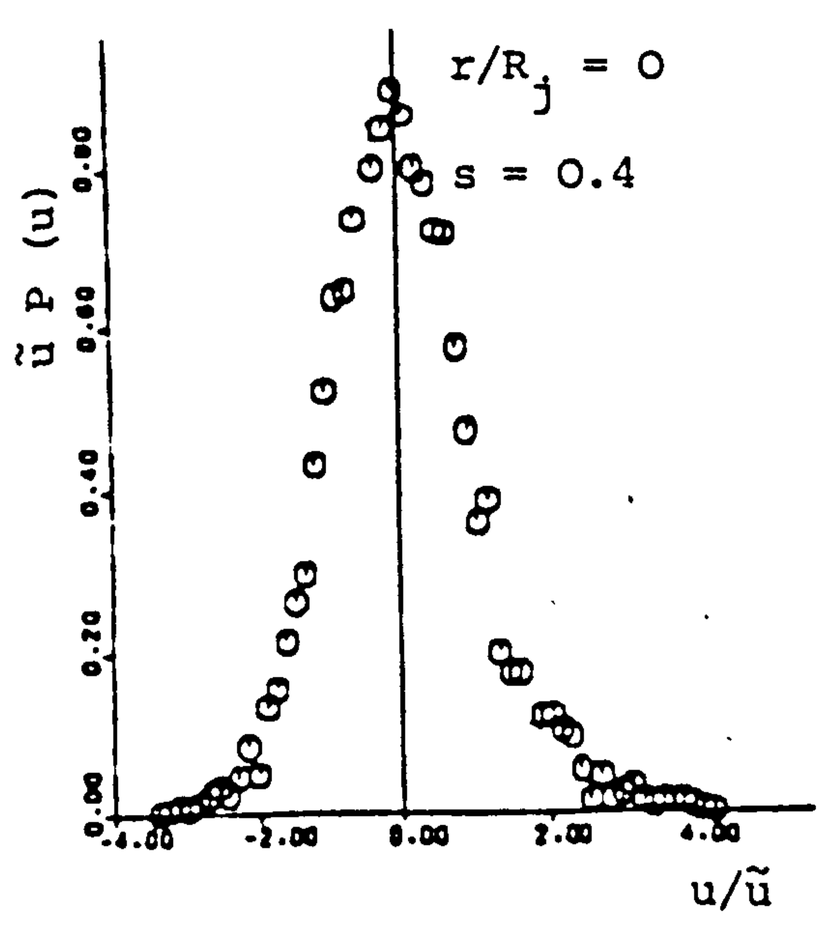


Fig. 4.24 Radial Distributions of u-Probability Density of the Flow of G2 (S = 0.93, Station 4)







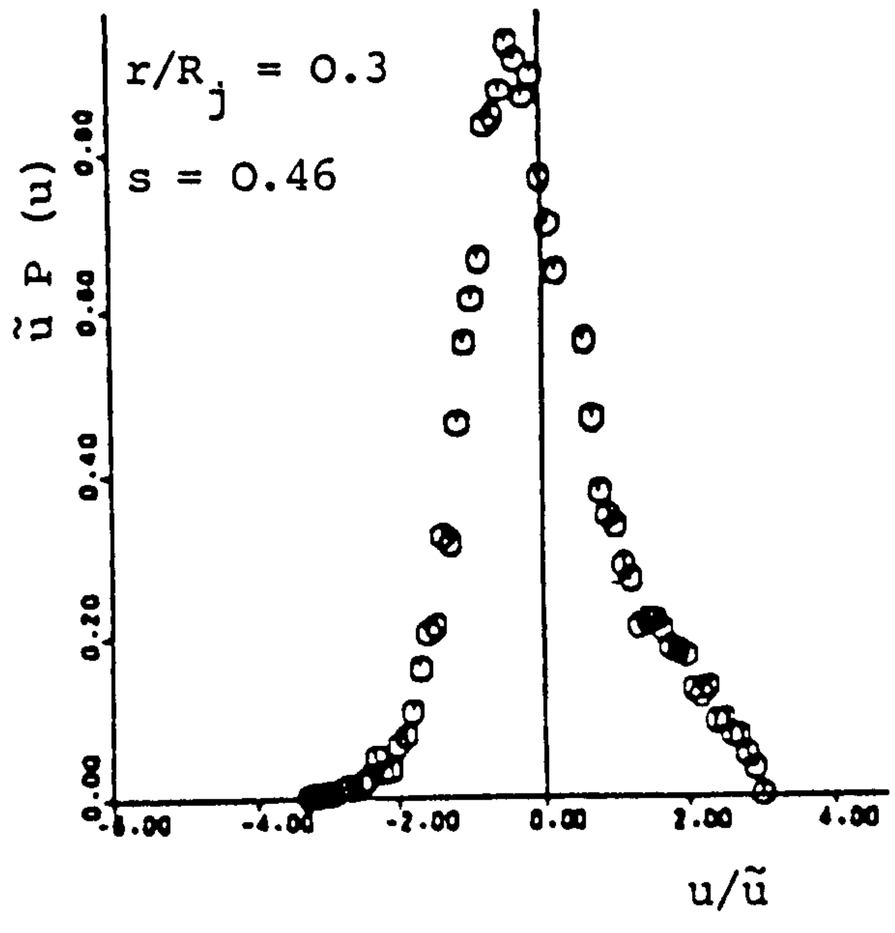


Fig. 4.25 Radial Distributions of u-Probability Density of the Flow of G2 (S = 0.93, Station 5)

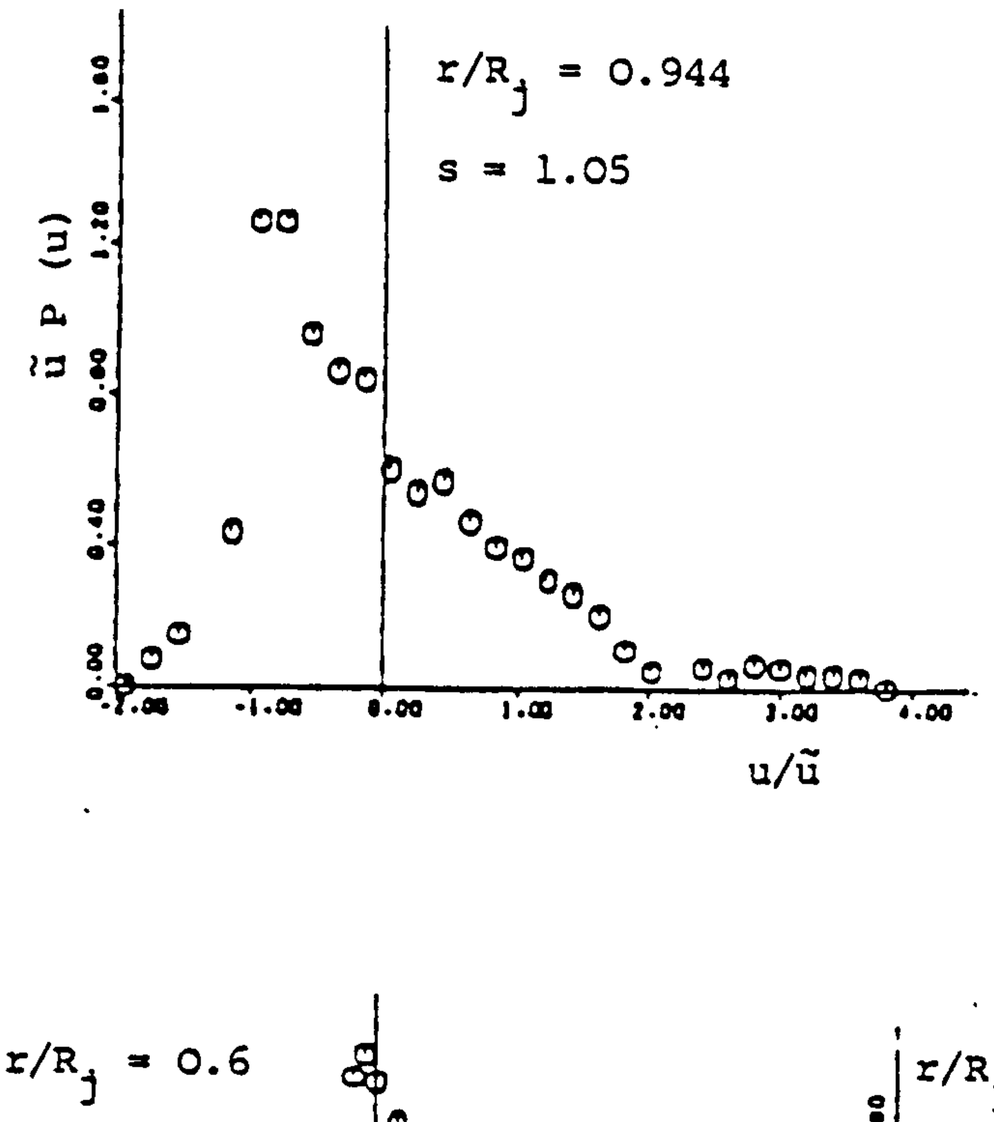
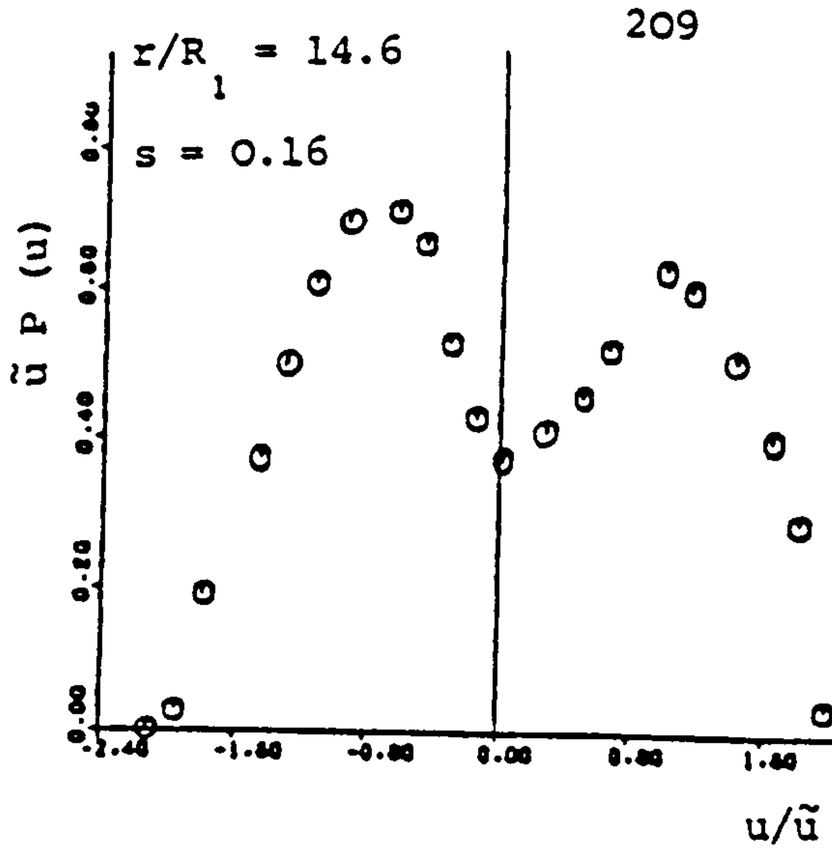
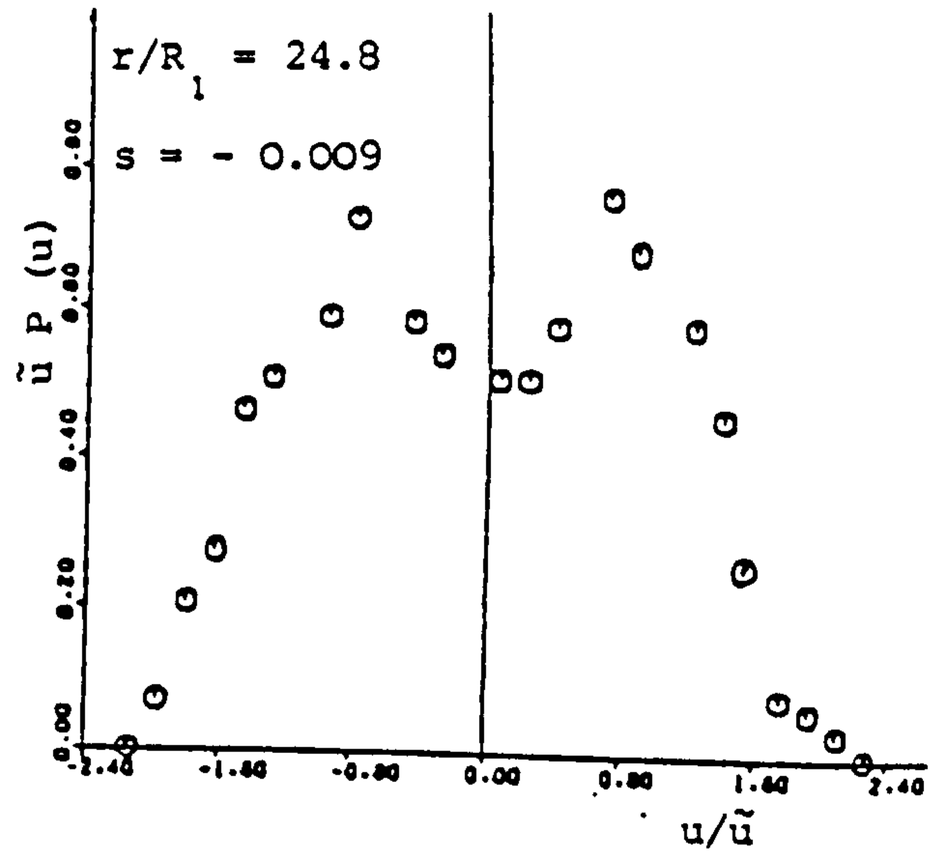
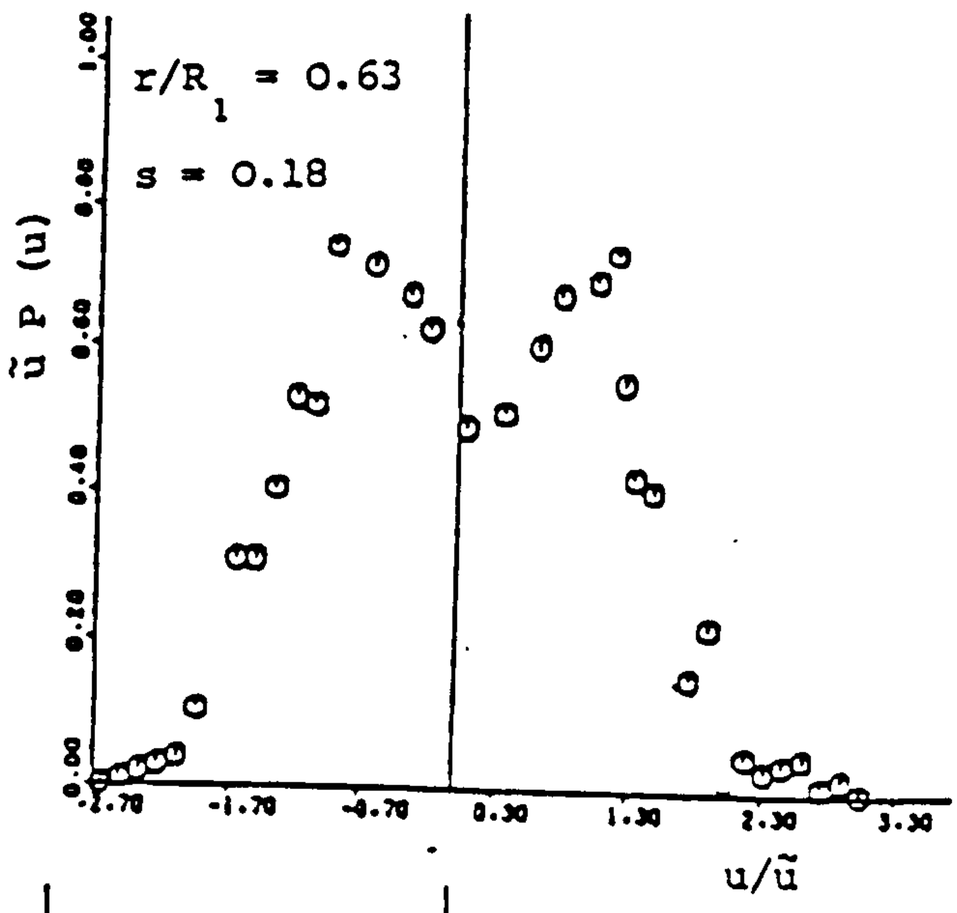
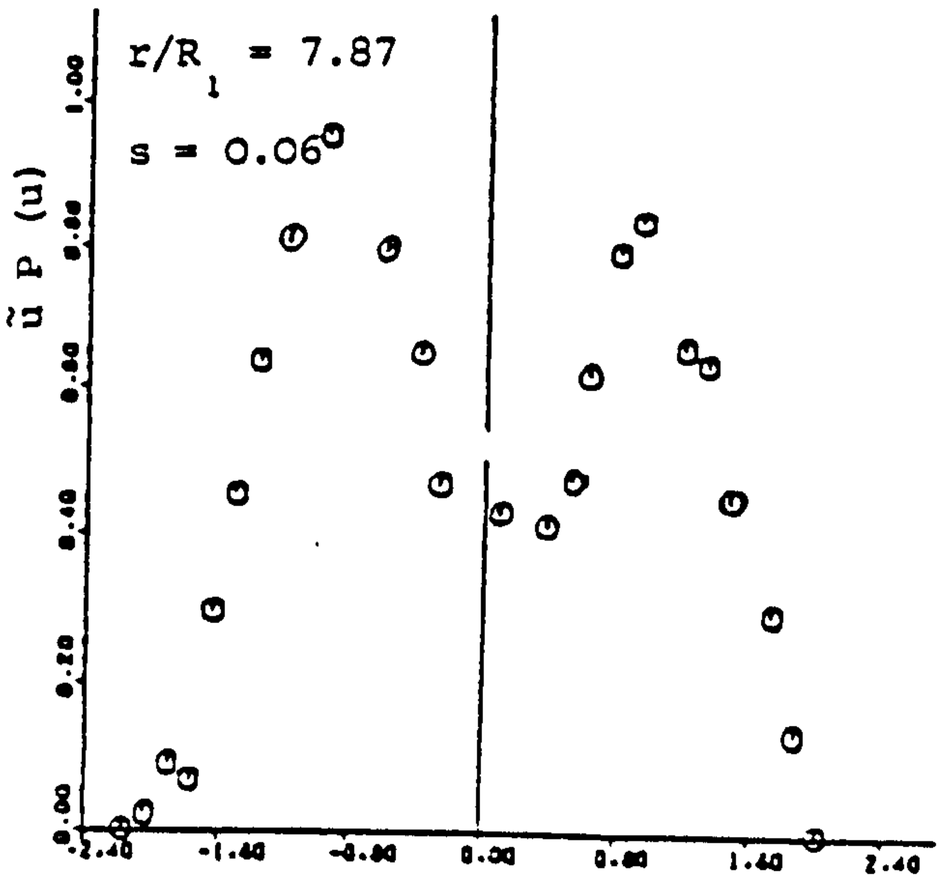


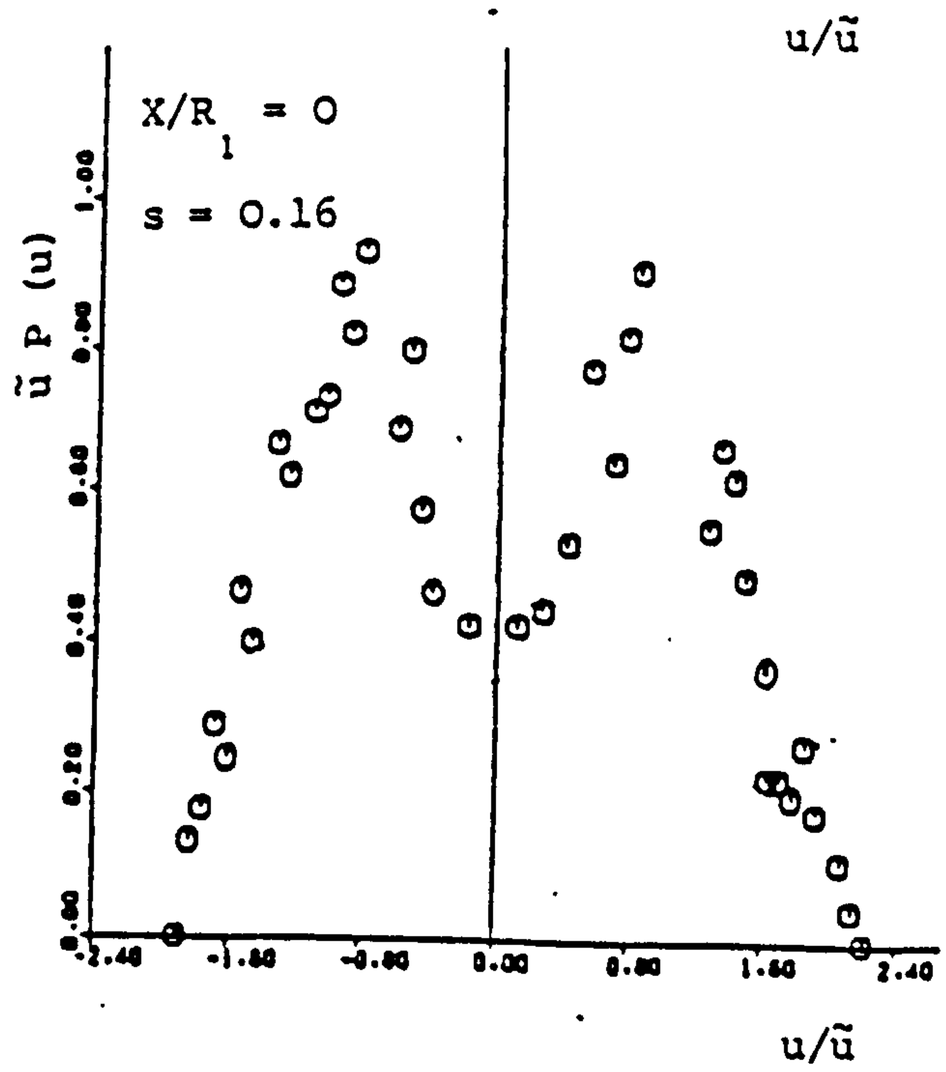
Fig. 4.26 Radial Distributions of u-Probability Density of the Flow of G2 (S = 0.93, Station 7)











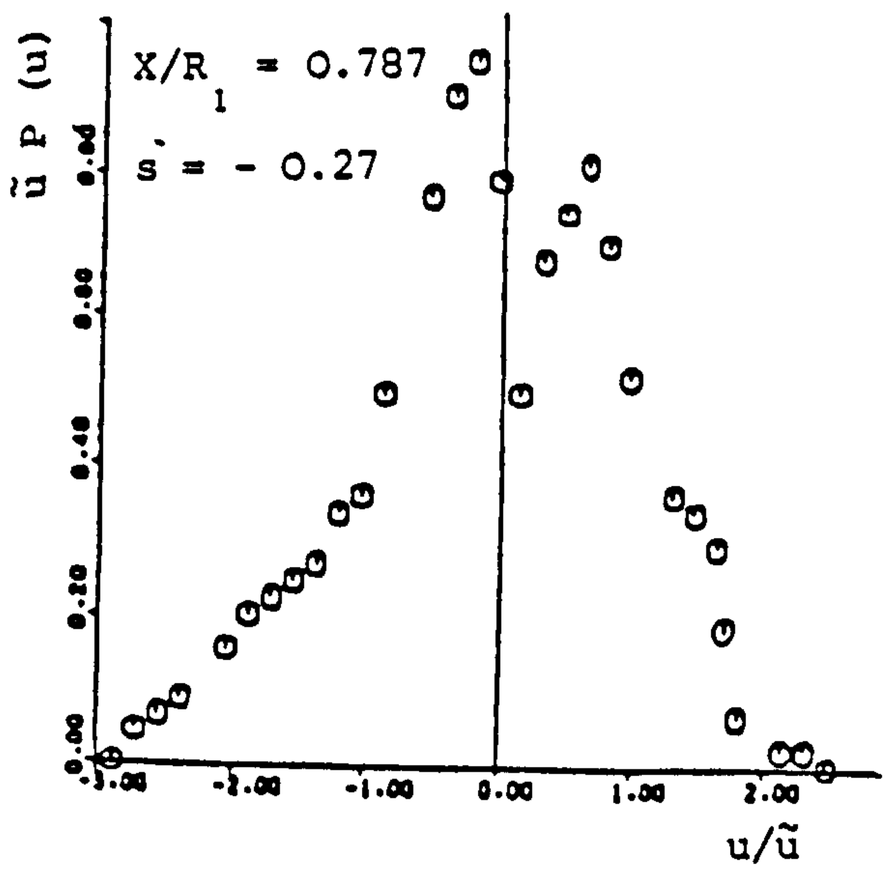


Fig. 4.27 Axial Distributions of w-Probability Density of the Flow of G2 (S = 0.93)

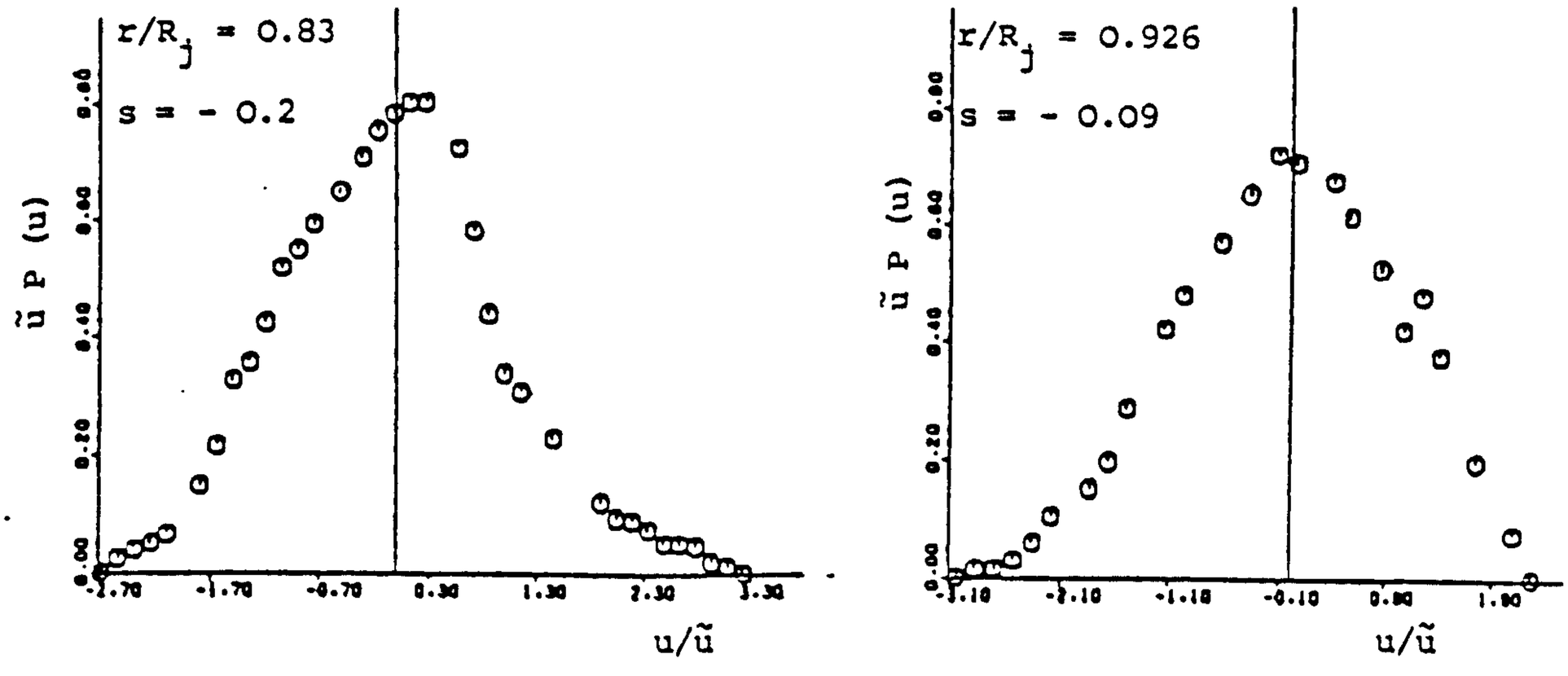


Fig. 4.28 Radial Distributions of w-Probability Density of the Flow of G2 (S = 0.93, Station 2)

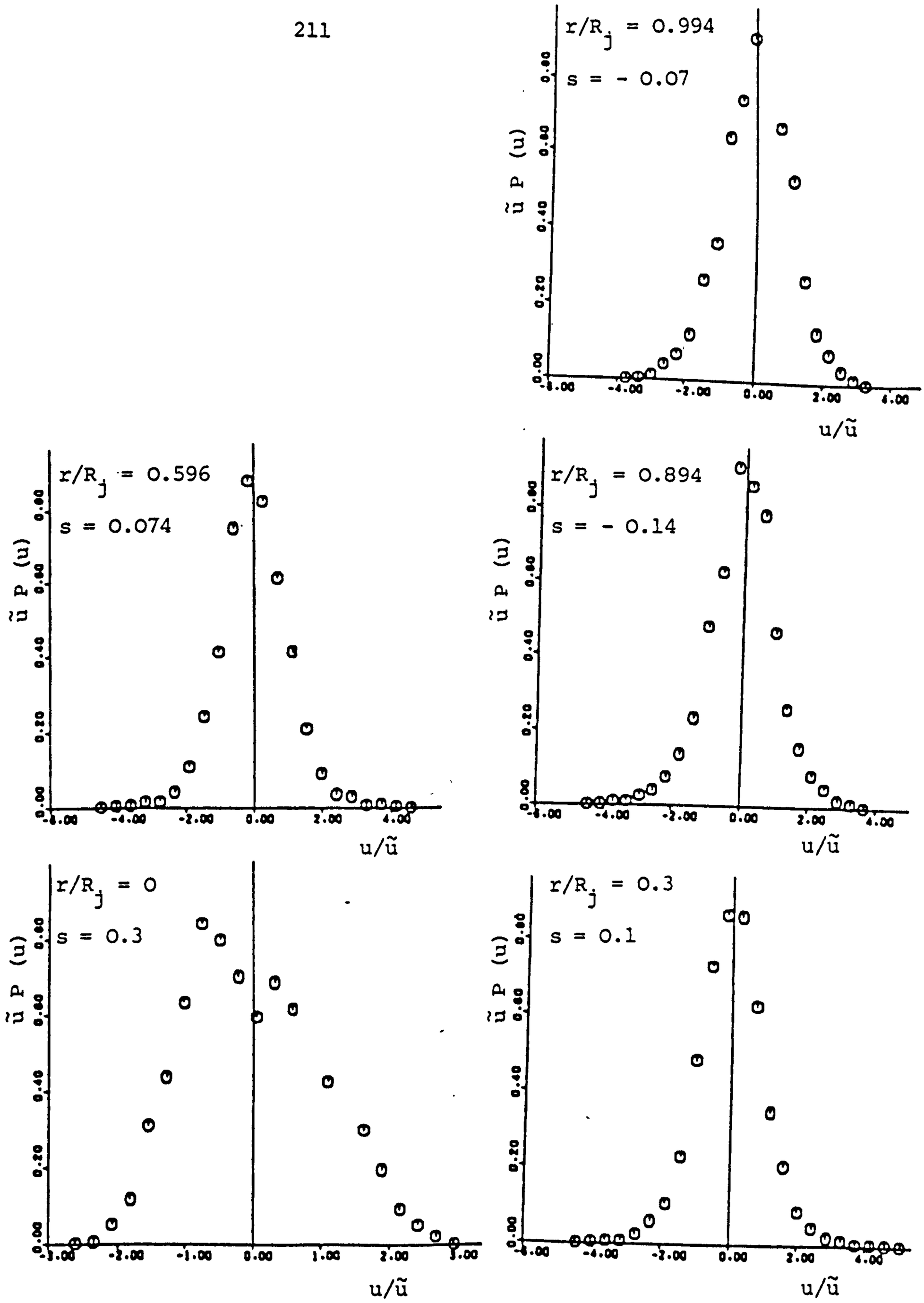


Fig. 4.29 Radial Distributions of w-Probability Density of the Flow of G2 (S = 0.93, Station 6)

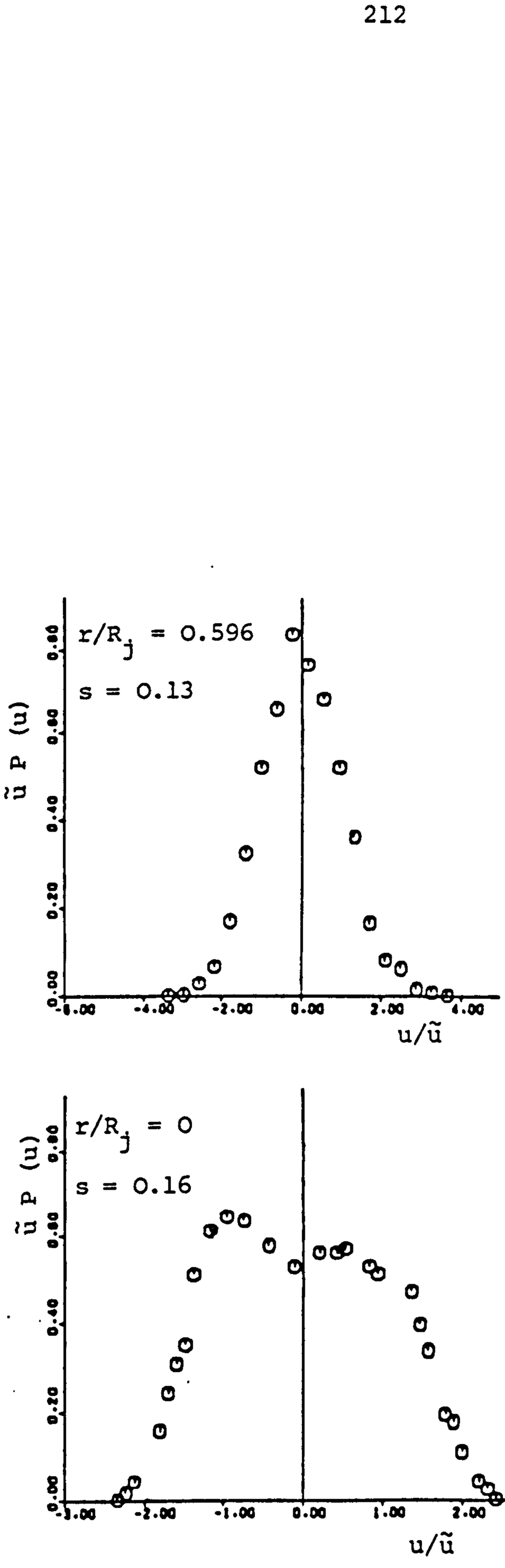


Fig. 4.30 Radial Distributions of w-Probability Density of the Flow at G2 (S = 0.93, Station 9)

CHAPTER 5

COMPUTATIONAL INVESTIGATION OF QUARL ANGLE EXPANSIONS

5.1 Introduction

This chapter is concerned with the numerical calculation of the flow in axisymmetric expansions with and without swirl. Section 5.2 deals with the consideration and choice of the coordinate system and turbulence model. The partial differential equations, which govern the transport of mass and momentum and those which comprise the turbulence model are derived, in Section 5.3, for two-dimensional, axisymmetric flows, in a curvilinear coordinate system. The solution procedure is described in Section 5.4. A method for generating the orthogonal curvilinear grid is developed and described in Section 5.5.

The appraisal of the computational method is achieved by comparison with measurements in Section 5.6 in which a parametric study of the effect of the important parameters is described. The chapter ends with a summary of the more important conclusions.

5.2 The Choice of the Coordinate System and Turbulence Model

The computations presented in this chapter were achieved using orthogonal curvilinear coordinates which were used for two reasons. The first is that orthogonal curvilinear coordinates are more appropriate for the presentation of the expanding geometries since the coordinate lines can be arranged coincident with the flow boundaries. Consequently, the finite difference solution domain lay entirely within the flow field and the grid could be selectively refined in order to retain numerical accuracy in regions of high gradients, close

to boundaries*. Also, the coincidence of the boundaries with coordinate lines greatly simplified the specification of boundary conditions. The second reason for the choice of the orthogonal curvilinear coordinates is their superior generality over rectangular coordinates (for example, when different expansion angles are to be considered). It may be noted that the use of general curvilinear coordinates instead of orthogonal ones is complicated and entails additional expense in terms of computer resources.

The use of the orthogonal curvilinear grids has increased the terms in the dependent variable equations, as will be seen in Section 5.3, and so increased the amount of computations. Consequently, the required storage was also increased. For these reasons, the two-equation model, Subsection 3.2.3, in which the equations of kinetic energy of turbulence, K, and its rate of dissipation, ε, were solved, is considered appropriate for the calculations of the present chapter.

5.3 Equations in Orthogonal Curvilinear Coordinates

There are a variety of ways in which the equations of Chapter 3 can be expressed in general orthogonal coordinates and many ways of performing the transformations. The method explained here is to write the equations for Cartesian coordinates in general tensor notation and then work out the appropriate tensor transformations to the required set of coordinates which are here the orthogonal curvilinear axi-symmetric coordinates.

---

* In the Cartesian coordinate system, the curved surface passes through the finite-difference grid at an angle, hindering the accurate imposition of boundary conditions, introducing numerical diffusion and preventing the selective refinement of the grid near the surface.

The steady state differential equations are written below in orthogonal curvilinear coordinates; corresponding transformations are provided in Appendix A3.

5.3.1 The Equation of Continuity

$$\nabla_x (\rho\bar{U}) + \nabla_y (\rho\bar{V}) = 0 \qquad (5.1)$$

where ∇_x and ∇_y are defined as:-

$$\nabla_x = \frac{1}{h_2}\frac{\partial}{\partial x} h_2 \qquad \text{and} \qquad \nabla_y = \frac{1}{rh_1}\frac{\partial}{\partial r} rh_1 \qquad (5.2)$$

and h_i are the scale factors and are given by:-

$$h_i = (g_{ii})^{1/2} \qquad \text{(no summation on i)} \qquad (5.3)$$

and g_{ij} is the metric tensor, see Appendix A3. $\bar{U}$, $\bar{V}$ and $\bar{W}$ are the time mean velocity components in the directions x, y and θ, respectively.

5.3.2 The Momentum Equations

(i) The U-Momentum Equation

$$\nabla_x (\rho\bar{U}^2) + \nabla_y (\rho\bar{U}\bar{V}) - \nabla_x \left(\mu_{eff} \frac{\partial\bar{U}}{\partial x}\right) - \nabla_y \left(\mu_{eff} \frac{\partial\bar{U}}{\partial y}\right)$$

$$= -\frac{\partial P}{\partial x} + \nabla_x \left(\mu_{eff} \left(\frac{\partial\bar{U}}{\partial x} + 2\bar{V} H_1(2)\right)\right) + \nabla_y \left(\mu_{eff} \left(\frac{\partial\bar{V}}{\partial x} - H_1(2)\,\bar{U} - H_2(1)\,\bar{V}\right)\right) +$$

$$+ H_2(1) \left(\rho\bar{V}^2 - \mu_{eff} \left(2\frac{\partial\bar{V}}{\partial y} + 2\bar{U} H_2(1)\right)\right) + H_3(1) \left(\rho\bar{W}^2 - \mu_{eff} \left(2\bar{U} H_3(1) + 2\bar{V} H_3(2)\right)\right)$$

$$- H_1(2) \left[\rho\overline{u}\overline{v} - \mu_{eff} \left[\frac{\partial \overline{u}}{\partial y} + \frac{\partial \overline{v}}{\partial x} - H_1(2)\ \overline{u} - H_2(1)\ \overline{v}\right]\right] \qquad (5.4)$$

(ii) The V-Momentum Equation

$$\nabla_x\ (\rho\overline{u}\overline{v}) + \nabla_y\ (\rho\overline{v}^2) - \nabla_x \left[\mu_{eff}\ \frac{\partial \overline{u}}{\partial x}\right] - \nabla_y \left[\mu_{eff}\ \frac{\partial \overline{u}}{\partial y}\right]$$

$$= - \frac{\partial P}{\partial y} + \nabla_y \left[\mu_{eff} \left[\frac{\partial \overline{v}}{\partial y} + 2\overline{u}\ H_2(1)\right]\right] + \nabla_x \left[\mu_{eff} \left[\frac{\partial \overline{u}}{\partial y} - H_2(1)\ \overline{v} - H_1(2)\ \overline{u}\right]\right] +$$

$$+ H_1(2) \left[\rho\overline{u}^2 - \mu_{eff} \left[2\ \frac{\partial \overline{u}}{\partial x} + 2\overline{v}\ H_1(2)\right]\right] + H_3(2) \left[\rho\overline{w}^2 - \mu_{eff} \left[2\overline{v}\ H_3(2) + 2\overline{u}\ H_3(1)\right]\right]$$

$$- H_2(1) \left[\rho\overline{u}\overline{v} - \mu_{eff} \left[\frac{\partial \overline{v}}{\partial x} + \frac{\partial \overline{u}}{\partial y} - H_2(1)\ \overline{v} - H_1(2)\ \overline{u}\right]\right] \qquad (5.5)$$

(iii) The W-Momentum Equation

$$\nabla_x\ (\rho\overline{u}\overline{w}) + \nabla_y\ (\rho\overline{v}\overline{w}) - \nabla_x \left[\mu_{eff}\ \frac{\partial \overline{w}}{\partial x}\right] - \nabla_y \left[\mu_{eff}\ \frac{\partial \overline{u}}{\partial y}\right]$$

$$= - \nabla_x \left[\mu_{eff}\ H_3(1)\ \overline{w}\right] - \nabla_y \left[\mu_{eff}\ H_3(2)\ \overline{w}\right] - H_3(1) \left[\rho\overline{u}\overline{w} - \mu_{eff}\ \frac{\partial \overline{w}}{\partial x} + \mu_{eff}\ H_3(1)\ \overline{w}\right]$$

$$- H_3(2) \left[\rho\overline{v}\overline{w} - \mu_{eff}\ \frac{\partial \overline{w}}{\partial r} - \mu_{eff}\ H_3(2)\ \overline{w}\right] \qquad (5.6)$$

$H_i(j)$ are the coordinate variation terms, defined as:-

$$H_i(j) = \frac{1}{h_i} \frac{\partial h_i}{\partial x_j} \qquad (5.7)$$

5.3.3 The Equation of the Kinetic Energy of Turbulence

$$\nabla_x (\rho\bar{U}K) + \nabla_y (\rho\bar{V}K) - \nabla_x \left(\frac{\mu_{eff}}{\sigma_K} \frac{\partial K}{\partial x}\right) - \nabla_y \left(\frac{\mu_{eff}}{\sigma_K} \frac{\partial K}{\partial y}\right) = G - \rho\varepsilon \qquad (5.8)$$

where G is the production of the kinetic energy of turbulence and is given by:-

$$G = \frac{1}{2\mu_{eff}} \left[\tau_{xx}^2 + \tau_{yy}^2 + \tau_{\theta\theta}^2 + 2\left[\tau_{xy} + \tau_{y\theta} + \tau_{\theta x}\right]^2\right] \qquad (5.9)$$

and τ_{xx}, τ_{yy} .... etc. are given by:-

$$\left.\begin{aligned}
\tau_{xx} &= 2\mu_{eff}\left(\frac{\partial\bar{U}}{\partial x} + \bar{V}\,H_1(2)\right)\\
\tau_{yy} &= 2\mu_{eff}\left(\frac{\partial\bar{V}}{\partial y} + \bar{U}\,H_2(1)\right)\\
\tau_{\theta\theta} &= 2\mu_{eff}\left(\bar{U}\,H_3(1) + \bar{V}\,H_3(2)\right)\\
\tau_{xy} &= \mu_{eff}\left(\frac{\partial\bar{U}}{\partial y} + \frac{\partial\bar{V}}{\partial x} - H_1(2)\,\bar{U} - H_2(1)\,\bar{V}\right)\\
\tau_{y\theta} &= \mu_{eff}\left(\frac{\partial\bar{W}}{\partial r} - H_3(2)\,\bar{W}\right)\\
\tau_{\theta x} &= \mu_{eff}\left(\frac{\partial\bar{W}}{\partial x} - H_3(1)\,\bar{W}\right)
\end{aligned}\right\} \qquad (5.10)$$

σ_k is a diffusion constant; its value is the same as in Chapter 3.

5.3.4 The Equation of the Rate of Dissipation of the Kinetic Energy of Turbulence

$$\nabla_x (\rho\bar{U}\varepsilon) + \nabla_y (\rho\bar{V}\varepsilon) - \nabla_x \left(\frac{\mu_{eff}}{\sigma_\varepsilon} \frac{\partial\varepsilon}{\partial x}\right) - \nabla_y \left(\frac{\mu_{eff}}{\sigma_\varepsilon} \frac{\partial\varepsilon}{\partial y}\right) = \frac{\varepsilon}{K} (c_{\varepsilon_1} G - c_{\varepsilon_2} \rho\varepsilon) \tag{5.11}$$

c_{ε_1}, c_{ε_2} and σ_ε are constants; their values are the same as in Chapter 3.

5.4 The Solution Procedure

Equations (5.1), (5.3), (5.4), (5.5) and (5.7) may be expressed in the general form:-

$$\nabla_x \left(\rho\bar{U}\Phi - \frac{\mu_{eff}}{\sigma_\Phi} \frac{\partial\Phi}{\partial x}\right) + \nabla_y \left(\rho\bar{V}\Phi - \frac{\mu_{eff}}{\sigma_\Phi} \frac{\partial\Phi}{\partial y}\right) = S_\Phi \tag{5.12}$$

where Φ stands for any of the dependent variables; $\bar{U}$, $\bar{V}$, $\bar{W}$, K and ε.

The above equations (with $\mu_{eff} = \rho\, c_\mu\, K^2/\varepsilon$ and c_μ a constant given in Chapter 3) represent a complete set of equations which can be solved numerically by the method explained in Chapter 3: the finite difference equations are obtained by integrating the differential equations over the two-dimensional volume indicated on the finite difference grid, Fig. 5.1.

Attention is focussed here on the computational problems posed by the curvilinear grid. The cell-face areas, the distance between grid nodes and cell volumes cannot be calculated from x and y as was the case in Cartesian coordinates but require evaluation from, or storage as, two-dimensional quantities. The first method, that is to store only the Cartesian coordinates of the grid line intersections and to calculate the geometric parameters each time they are required, is computationally expensive. The method used here is based on the

storage of the distance between each intersection of all the lines (both full and broken) as well as the volumes of each of the four "quarter cells" surrounding the pressure node, see Fig. 5.2. Thus, the cell-face areas appropriate to any node ($\overline{U}$, $\overline{V}$ or P) are given by the sum of two of these lengths (these are shown as dotted distances in Fig. 5.2) and the cell volumes are given by the sum of four quarter cell volumes. This method required twelve storage locations per triad of nodes and a minimum of computational time.

5.5 The Grid Generation Procedure

The equations presented in Section 5.3 were presented in orthogonal curvilinear coordinates and their solution requires that an orthogonal curvilinear grid be generated and the equations integrated over its control volume . Thus a procedure is required to determine the Cartesian coordinates of the nodes of an orthogonal grid. One approach is due to Barfield (1970) who developed a method for generating an orthogonal grid which is based on conformal mapping of the boundary of a closed two-dimensional region on the perimeter of a rectangular polygon in which is inscribed an orthogonal rectangular grid. Since numerical solutions are required, the solution of the Laplace equation, see also Pope (1976) and Hung and Brown (1977), is a more convenient method for generating the Cartesian coordinates of the orthogonal grid nodes and is discussed here. Thus, the locations of the coordinate line intersections are determined by a numerical procedure similar to that used in Chapter 3 and, by approximating the coordinate lines between the nodes as straight lines, the grid distances can be calculated.

The following numerical procedure was developed to generate the orthogonal curvilinear coordinate system (η, ξ) which maps the

irregular region (the flow domain) R into a rectangular region R´ (Fig. 5.3). The geometry of the flow domain is prescribed by the function g(x, y). For computational flow simulations, a simple orthogonal curvilinear mesh can be taken from an inverse solution of the Laplace equations which can be derived as follows. Fig. 5.4 is a sketch of an orthogonal coordinate system where the orthogonal coordinates, η and ξ are shown relative to Cartesian coordinates $\bar{x}$ and $\bar{y}$. From the condition of orthogonality, the distances in Cartesian coordinates can be expressed as:-

$$\left.\begin{aligned} d\bar{x} &= h_1\, d\eta \cos\theta + h_2\, d\xi \sin\theta \\ d\bar{y} &= -h_1\, d\eta \sin\theta + h_2\, d\xi \cos\theta \end{aligned}\right\} \qquad (5.13)$$

From the equation of the coordinate transfer motion:-

$$d\bar{x}^j = \frac{\partial \bar{x}^j}{\partial \eta^i}\, d\eta^i \qquad (5.14)$$

it follows that:-

$$\frac{\partial \bar{x}}{\partial \eta} = \frac{h_1}{h_2}\frac{\partial \bar{y}}{\partial \xi} \quad , \quad \frac{\partial \bar{y}}{\partial \eta} = -\frac{h_1}{h_2}\frac{\partial \bar{x}}{\partial \xi} \qquad (5.15)$$

Thus Laplace's equation can be written as:-

$$\nabla^2 \bar{x} = 0 \quad \text{and} \quad \nabla^2 \bar{y} = 0 \qquad (5.16)$$

where:-

$$\nabla^2 = \frac{1}{\sqrt{g}} \sum_j \frac{\partial}{\partial \eta^j} \left(\frac{\sqrt{g}}{h_j^2} \frac{\partial}{\partial \eta^j} \right) \tag{5.17}$$

h_j are the scale factors and $\sqrt{g}$ is the product of the scale factors and represents the volume ratio between the coordinate systems.

Defining h as the ratio between h_1 and h_2, Equations (5.15) may be expressed as:-

$$\frac{\partial^2 \overline{x}}{\partial \eta^2} + h^2 \frac{\partial^2 \overline{x}}{\partial \xi^2} = 0 \tag{5.18}$$

$$\frac{\partial^2 \overline{y}}{\partial \eta^2} + h^2 \frac{\partial^2 \overline{y}}{\partial \xi^2} = 0 \tag{5.19}$$

In order to solve Equations (5.18) and (5.19) eight boundary conditions (two on each side of the flow domain) are required and the constant h which is unique for a given set of boundary conditions in each space is determined. One boundary condition is provided from the geometry g (x, y) of the wall while another is deduced from the integration of any of Equations (5.15) by:-

$$\left.\begin{aligned} \overline{x}_2 - \overline{x}_1 &= h \int \left(\frac{\partial \overline{y}}{\partial \xi} \right) d\eta \\ \text{or:-} & \\ \overline{y}_2 - \overline{y}_1 &= - h \int \left(\frac{\partial \overline{x}}{\partial \xi} \right) d\eta \end{aligned}\right\} \tag{5.20}$$

Further, since $\overline{x}$ and $\overline{y}$ are known at each corner, h can be determined from the above relations.

Equations (5.18) and (5.19) were solved together with the boundary conditions by a finite difference method involving five-point scheme to obtain the Cartesian coordinates of the orthogonal grid. Thus Equation (5.18), for example, expressed as follows:-

$$\nabla^2 \bar{x} = \frac{1}{\sqrt{g}} \left(\frac{\partial}{\partial \eta} \left(h \frac{\partial \bar{x}}{\partial \eta} \right) + \frac{\partial}{\partial \xi} \left(\frac{1}{h} \frac{\partial \bar{x}}{\partial \xi} \right) \right) = 0 \qquad (5.21)$$

can be written in the finite difference form as:-

$$A_p \bar{x}_p = \sum A_i \bar{x}_i \qquad (5.22)$$

where the coefficients A_p and A_i are functions of h and the distances in region R´. The subscript i refers to the nodes, E, W, N and S and P is the node under consideration. Equation (5.22) and similar one for $\bar{y}_p$ were solved by a tri-diagonal algorithm (Patankar and Spalding, 1972) which is an iterative line-by-line procedure and after each iteration the boundary conditions and the value of h are updated.

A large number of grid lines with even spaces were produced by the above method from which interpolation was made to produce other grid lines with the required number of grids to suit computation economy and the numerical accuracy. In this interpolation, the grids were concentrated in the regions where large variations of flow properties were expected. Fig. 5.5 shows an example of the grids produced by the above method. For the 32 x 32 grid of Fig. 5.5, a time of 0.30 seconds per iteration was required on a CDC 6600 with a storage requirement of 8200 locations and a number of iterations of 200. A check of orthogonality at all the nodes was made and the maximum error was 5 degrees while the average error, made all over the total number of nodes, was less than 0.1 degree.

5.6 Comparison With Experiments

The calculated values of the various dependent variables are compared, in this section, with the available experimental data. The comparison is held on for four different cases, see Table 5.1, which covered:-

(i) flows in expanding ducts for two different angles of expansion, Cases 1 and 2, respectively, and;

(ii) flows in expanding ducts followed by sudden expansion with and without swirl, Cases 3 and 4, respectively.

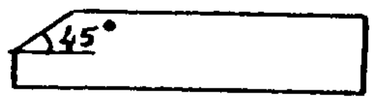
Numerical accuracy of the solution procedure and computational details are given in Subsection 5.6.1 which is followed by the calculations of the test cases 1, 2 and 3 in Subsection 5.6.2. Subsection 5.6.3 deals with the calculation of flows in G2 with swirl, test case 4. The section ends with a parametric investigation of the effect of swirl number on the calculated flow properties of G2 in Subsection 5.6.4.

5.6.1 Numerical Accuracy and Computational Details

Fig. 5.6 presents two samples of the computational grid line and node distributions used in the present calculations. These are the geometries of test cases 2 and 3 or 4. These distributions were selected after experiments with fewer nodes and different distributions had indicated that the present arrangement led to results which were reasonably free from numerical errors. A sample of the different distributions used in the grid independence tests is shown in Fig. 5.7 and comprises three distributions of 20 x 15, 28 x 20 and 34 x 24. The test was made in an expanding duct of 45° half expansion angle (the

TABLE 5.1

DETAILS OF THE CALCULATIONS

Test Case	Geometry	Source of Experimental Data	Swirl Number	Computing Time per Iteration per Grid Node	Number of Iterations	Number of Grid Lines	Comments
1	 , G1	Chapter 4	0.00	0.0014	128	28 x 20	-
2		Chaturvedi (1963)	0.00	0.0014	128	28 x 20	-
3	 , G2	Chapter 4	0.00	0.0014	300	28 x 24	-
4	 , G2	Chapter 4	0.93	0.0025	550	28 x 24	Calculations were made and presented for other swirl numbers to investigate the influence of swirl number on the flow properties of G2

geometry of test case 2) and the results were evaluated against the measurements of Chaturvedi (1963) at two different sections for the mean velocity and kinetic energy of turbulence. The results are shown in Fig. 5.8 and indicate the smearing effect inherent in the finite-difference method and shown clearly by Fig. 5.8a where the mean velocity distribution is smeared by the grid 20 x 15. However, as shown from Fig. 5.8, the trend of the results of the three grid distributions is monotonic and the differences between the results of 28 x 20 and 34 x 24 grids are much smaller compared with those of 20 x 15 and 28 x 20. It may be concluded that the differences between the calculated and measured values are partly attributed to the grid size and node distribution but, as will be discussed in the next sub-sections, more related to errors in the experimental data and turbulence modelling.

The boundary conditions required for the solution procedure at x = 0 were taken when possible from experiments and are described separately for each test case. In all the test cases, the rate of dissipation at the inlet section was not available and consequently obtained, as shown in Chapter 3, from the relation:-

$$\varepsilon = c_\mu K^{3/2}/\ell \qquad \text{where } \ell = 0.03\ R_1$$

where R_1 is the radius of the pipe upstream the expansion. All the axial gradients ($\partial/\partial x$) were presumed zero in the exit plane of the confining tube. The wall functions required to link the near-wall grid nodes to wall boundaries are the same as described in Chapter 3. The computing times and number of iterations required by each test case to reach a convergence factor of 0.1 are indicated in Table 5.1.

5.6.2 Calculations of Separated Flows in Expanding Ducts

(i) The Flow in a Confinement With an Expansion of 20° Half Angle (Test Case 1)

The measurements in the separated boundary layer of Chapter 4 were obtained partly to aid evaluation of the present calculation method. The measured inlet velocity values, see Fig. 4.4, were used as initial conditions with the inlet distribution of kinetic energy of turbulence presumed similar to that of the normal stress with the value of K at the centre-line equal to 0.003 $\overline{U}_o^2$, where $\overline{U}_o$ is the mean velocity at the centre-line.

The experimental and predicted results, for the axial velocity and the kinetic energy of turbulence at different axial distances from the inlet section to the expanding conduit, are shown in Figs. 5.9 and 5.10. The calculated mean velocity in the expanding conduit, Stations 2 and 3 (see Table 4.1, Chapter 4), are in reasonable accord with the measurements with a maximum discrepancy of 14% located nearly at the region of maximum normal stress, see Fig. 4.5. The width of the recirculation is correctly predicted by the solution procedure. Downstream of the expanding duct and at Stations 4, 5 and 6, the calculations are in better agreement with a maximum discrepancy of around 8%.

The kinetic energy distributions are compared with the experimental data in Fig. 5.10. The experimental values of the kinetic energy of turbulence were approximated from the measured axial normal stress, $\overline{u^2}$ with the values of $\tilde{v}$ and $\tilde{w}$ taken equal to 0.60 $\tilde{u}$, see Kalinske (1946). In general, Fig. 5.10 indicates that the location of the maximum of the kinetic energy is correctly predicted but its value is underpredicted at most of the x-locations with maximum deficiency of 30% at Station 7. The discrepancies are likely to stem partly from

expected overprediction in the rate of dissipation due to the incorrect representation of the source term in its transport equation and partly due to the effect of the extra strain terms on the calculation of both the Reynolds stresses and rate of dissipation. These two sources of errors were explained in Chapter 3. It can be noted here that the underprediction of the maximum value of the kinetic energy is partly participating in the underestimation of K near the centre-line since the turbulent diffusion of K towards the centre-line is expected to be underestimated. The underestimation of K near the centre-line, Stations 4, 5 and 6 of Fig. 5.10, is also attributed to the effect of the extra strain terms on the validity of the gradient assumption of Boussinesq equation as explained in Chapter 3.

Contours of the calculated mean velocity and the kinetic energy of turbulence are shown in Fig. 5.11: mean streamlines and velocity vector distributions are also shown in the same figure. The streamline function is defined as:-

$$\psi_1 = \frac{\int_R^r \bar{U} r dr}{\int_R^O \bar{U} r dr} \qquad (5.23)$$

The comparison of the calculated mean velocity contours with those of experiments, Fig. 5.11a, indicates that the length of the recirculation zone and the flow pattern are predicted accurately. Fig. 5.11 shows that the maximum value of the mean velocity in the reverse direction is slightly larger than 1.2 m/s (the maximum input velocity is 27 m/s) and the maximum value of the reverse flow rate is approximately 0.12 of the total mass flow rate and is located slightly downstream the

end of the expanding conduit. Fig. 5.11c represents the velocity vector distributions and gives an indication of the jet spread and entrainment process near the recirculation zone. In Fig. 5.11d, the contours of the kinetic energy of turbulence are represented and indicate clearly diffusion towards the centre-line. The location of maximum production of the kinetic energy of turbulence is near the recirculation zone in the upstream sections and moves gradually towards the centre-line in the downstream stations.

(ii) The Flow in a Confinement With an Expansion of 45° Half Angle (Test Case 2)

The experimental data of this case were reported by Chaturvedi (1963) and comprised mean velocity and kinetic energy distributions. The measurements were obtained by hot-wire anemometer and, therefore, are subject to possible errors in the regions of high turbulence intensities and in reverse flow regions. The mean velocity was constant at the intake section and the turbulence level was nearly zero.

The experimental and predicted values of the mean velocity and kinetic energy of turbulence are presented in Figs. 5.12 and 5.13. It is indicated from Fig. 5.12 that the general features of the flow are accurately predicted. However, large discrepancies are shown in the region of high velocity gradient and near the boundaries of the recirculation zone. They are partly due to sources of calculation errors similar to those indicated in (i) and partly due to the errors associated with the measurements. As indicated in Chapter 2, the hot-wire measurements are subject to errors in regions of high rate of velocity gradients. Downstream of the recirculation zone and at $x/D_1 = 6$ and 8 (D_1 is the diameter of the pipe upstream the expansion) the discrepancies in

both experiments and calculations are decreased and the agreement is more reasonable.

The kinetic energy distributions are shown in Fig. 5.13. The agreement is reasonable in the upstream sections apart from the recirculation region where the experiments are subject to large errors and as shown in Chapter 2, the hot-wire underestimates the normal stress by around 50% in the recirculation region. At $x/D_1 = 3$ and 4 the kinetic energy of turbulence is underpredicted near the centre-line. This is most likely to stem from, as shown before in Chapter 3, the inability of the Boussinesq equation to represent the flow near the axis of symmetry where the extra strain rates (any strain other than $\partial\overline{U}/\partial y$) are of particular importance.

(iii) The Calculation of the Flow in G2 Without Swirl (Test Case 3)

The calculations of the flow in a confinement with an expanding entry of 20° half angle, followed by a sudden expansion, are compared with the experimental results of Chapter 4 in Figs. 5.14 and 5.15. The inlet conditions are the same as in (i). The calculated mean velocities are in good agreement with the experiments apart from small discrepancies in the region near the boundaries of the recirculation.

Comparison of the calculated and measured kinetic energy of turbulence shows the same behaviour as explained in (i). The calculations are in accord with measurements in that the location of the maximum kinetic energy of turbulence is transferred towards the centre-line and in general, the kinetic energy of turbulence is underestimated by the solution procedure. It may be noted here that the experimental values for K were calculated from $\overline{u^2}$ with the assumption of $\tilde{v} = \tilde{w} = 0.6\,\tilde{u}$ which may be inadequate, particularly in the present case with a considerable region of recirculation, and is partly attributing for the differences between the calculated and measured

kinetic energy of turbulence.

5.6.3 The Calculation of the Flow in G2 With Swirl

The calculations presented here correspond to the measurements of Chapter 4 for a 0.93 swirl number. The inlet values of the axial and tangential velocity components were available from the experiments and are shown in Figs. 4.10 and 4.12: the radial velocity component at the intake section was presumed zero. This assumption is reasonably realistic since the outer diameter of the swirler is equal to the pipe diameter up to the entry section. The experimental values of the mean axial and tangential velocities were available at different x-locations together with the corresponding normal stresses: the kinetic energy of turbulence was obtained from the sum of the individual normal stresses with $\tilde{v}$ is assumed equal to 0.6 $\tilde{u}$. The comparisons with the calculations are presented in Figs. 5.16 to 5.18 for the mean axial and tangential velocities and the turbulence kinetic energy.

Fig. 5.16 presents the calculated and the measured radial profiles of the axial mean velocity at five x-locations. In the upstream two stations, the figure indicates good agreement which reflects the accuracy of the assumptions for the conditions at the inlet section. The width of the central recirculation zone is accurately predicted within 8%. At Station 4 the two regions of recirculation are predicted with the maximum velocity value is slightly shifted to higher value of the radius. Further downstream and at Stations 7 and 8 the discrepancies between experiments and calculations were increased: while the width of the recirculation is overpredicted, its intensity is underestimated.

Comparisons of the calculated and measured values of the tangential velocity are presented in Fig. 5.17 and indicate an

agreement within 20% at high radii while in the vicinity of the centre-line the velocity gradient is underpredicted. The calculated values of the kinetic energy of turbulence, Fig. 5.18, exhibits discrepancies in the downstream stations: these correspond to the discrepancies in the axial mean velocity.

The discrepancy between prediction and experiments may be attributed, at least in part, to the streamline curvature effects. As shown from Fig. 5.16, the flow changes rapidly in the axial direction and so resulting in high turbulence production and significant turbulent transport terms. These rapid changes led to increasing the magnitude of the extra strain rates (any rate of strain other than $\partial\overline{U}/\partial y$) in addition to new rates of strain introduced by swirl. As shown in Chapter 3, even the case of non-swirling flows where τ_{xy} is the only existing shear stress the effect of these extra strain rates on the shear and normal stresses is not correctly presented by Boussinesq equation. In swirling flows, the shear stresses, $\tau_{y\theta}$ and $\tau_{x\theta}$ are finite and are also expected to be incorrectly represented (see Bradshaw, 1975). It has been shown, see Habib and Whitelaw (1980), that these effects led to incorrect representation of low swirling flows (S = 0.23) and the velocity of near-zero was not predicted. In the present context, the swirl number was high enough to initiate a central recirculation and was correctly represented by the present calculation at the upstream stations. However, the comparison showed discrepancies in the calculations of $\overline{U}$, $\overline{W}$ and K particularly near the centre-line and these can be minimized by the treatment of the swirl effects in terms of the "anisotropy of eddy viscosity" so as to define $\nu_{y\theta}$ and $\nu_{x\theta}$ as functions of the corresponding shear stresses which are in turn to be obtained from algebraic relations (Koosinlin and Lockwood, 1973) or from an algebraic stress-model

approach (Rodi, 1976). As shown by Rodi (1976), the lack of dependence of the dominant parameter, c_μ, upon the rate of strain and rotation invariants suggests that the $K \sim \varepsilon$ model becomes inaccurate as the flow departs from homogeneity and plane shear, respectively. The discrepancies may be also reduced by specifying empirical formulae for the different constants as functions of value of $\overline{W}/\overline{U}$ (Rubel, 1972) or of Richardson number (Rodi, 1979).

5.6.4 The Effect of Swirl Number

The comparisons between the calculations and experiments in the preceding two subsections showed that the present calculation procedure was able, although with some discrepancies, to predict flows with and without swirl. The main features of the flow field in both cases were correctly predicted and allow a qualitative investigation of the influence of the swirl number on the different flow properties corresponding to furnace geometries to be done. Thus, in the present subsection, the effect of swirl number on the flow properties in G2 is presented and discussed for five different swirl numbers; 0.0, 0.2, 0.4, 0.6 and 0.93. The mass flow rate was the same for the five cases. The inlet distributions of the axial mean velocity were not available (except for S = 0.0 and 0.93) and so interpolated from the present measurements, Chapter 4, and those of Beltagui and MacCallum (1976): the distributions are shown in Fig. 5.19. The inlet values of the tangential mean velocity and kinetic energy of turbulence were interpolated from those of 0.0 and 0.93 swirl number results.

The calculations are shown in Figs. 5.20 to 5.27 and allow comparisons of the contours of the axial and tangential mean velocities, mean pressure, stream functions and velocity vector distributions and kinetic energy of turbulence. As indicated from Fig. 5.20, in the

case of no swirl, the flow separates at the throat of the expanding conduit. The effect of swirl is to create an adverse pressure gradient along the radius and the axis of the jet as can be shown from Figs. 5.21a and 5.21b. As the degree of swirl is increased, the radial-pressure gradient causes the flow to fill out the cross-sectional area of the divergence until at a value of swirl number of 0.4 there was no separation before the exit from the divergent nozzle. With the increase in the swirl number, the forces due to the axial pressure gradient exceed those of the forward inertia forces and reverse flow is set up on the axis; this is clearly shown from Fig. 5.20c. Fig. 5.20 indicates also that the increase in the swirl number increases the size and strength of the core recirculation zone: the positions of flow separation and maximum negative velocity value are also transferred towards the inlet section. The forward mass flow is increasing owing to the entrainment from the central and peripheral recirculation zones while the net flow area between them is decreasing. This was also indicated by Beltagui and MacCallum (1976).

Fig. 5.21 presents the contours of the mean pressure and shows that the pressure decreases suddenly downstream of the inlet section ($X/R_1 \tilde{} 0$) and recovers with increasing X, but with lower values in the recirculation region. As the swirl number increases, adverse radial and axial gradients are formed due to the centrifugal forces and these are shown by Figs. 5.21b, 5.21c, 5.21d and 5.21e.

Fig. 5.22 presents the contours of the tangential velocity component. In general the distributions of $\overline{W}$ are similar for all swirl numbers above 0.4 with higher values of $\overline{W}$ in higher swirl number cases. The position of maximum tangential velocity moves rapidly towards the walls: for the low swirl number, S = 0.2, the $\overline{W}$-velocity is distributed in a way that there is a considerable annular area over

which the tangential velocity component is almost uniform. At high swirl numbers, the jet spread is rather high and the rate at which the maximum values of the axial and tangential velocity components along the length of the jet decay is faster and increases with the increase in the swirl number, see Fig. 5.23. This is in accord with the experimental observations of Chigier and Beér (1964) and indicates higher rates of mixing with the increase in the swirl number. This is again clarified by the rather uniform distributions of the turbulent kinetic energy in the cases of higher swirl numbers with the transfer of the maximum values towards the inlet section, Fig. 5.24.

Figs. 5.25 and 5.26 represent the distributions of the stream functions ψ_1 and ψ_2 defined as:-

$$\psi_1 = \frac{1}{\dot{m}_o} \int_R^r (2\rho\, \bar{U}\, \pi\, r\, dr) \quad \text{and} \quad \psi_2 = \frac{1}{\dot{m}_o} \int_O^r (2\rho\, \bar{U}\, \pi\, r\, dr) \tag{5.24}$$

where $\dot{m}_o$ is the input mass flow rate. It is shown from Fig. 5.25 that the core of the outer recirculation zone is transferred towards the inlet section with increasing the swirl number. The maximum value of the reverse flow rate is increased also from swirl number above 0.2.

Finally, Fig. 5.27 represents the velocity vector distribution of the $\bar{U}$ and $\bar{V}$ components. The increase in the size of the central recirculation and decrease in the outer one are clearly shown; the main stream entrainment from the two regions is also well represented.

5.7 Summary and Concluding Remarks

The calculation procedure described in the preceding sections of this chapter has been applied to the prediction of the flow properties of two different geometries with different angles of expansion and swirl numbers and the results compared with the corresponding experimental data of Chapter 4; comparison indicates that

the general features of the flow field are correctly predicted.

In this calculation method, the elliptic form of the continuity and momentum equations and equations for the kinetic energy of turbulence and its rate of dissipation were represented in orthogonal curvilinear coordinates and developed to calculate the properties of turbulent recirculating flows. With only a small penalty of computer storage, the method allows flows bounded by curved surfaces to be calculated more easily and accurately than is possible in Cartesian coordinates.

For the flows with zero swirl number the mean velocity was represented accurately by the present calculations: some discrepancies were indicated in the calculation of the kinetic energy of turbulence and were attributed to streamline curvature effects. For swirling flows the problem was compounded by further extra strain rates and discrepancies were increased. However, the calculation procedure is reasonably accurate, flexible and economical to use in many engineering purposes.

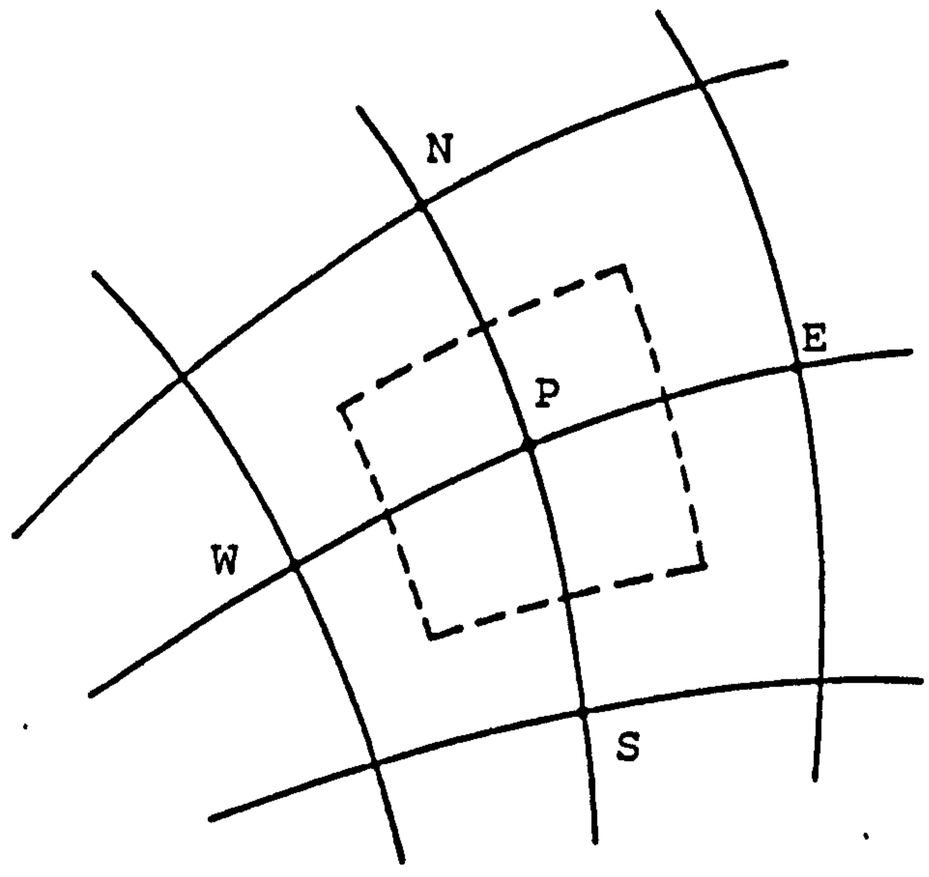


Fig. 5.1 Finite Difference Grid

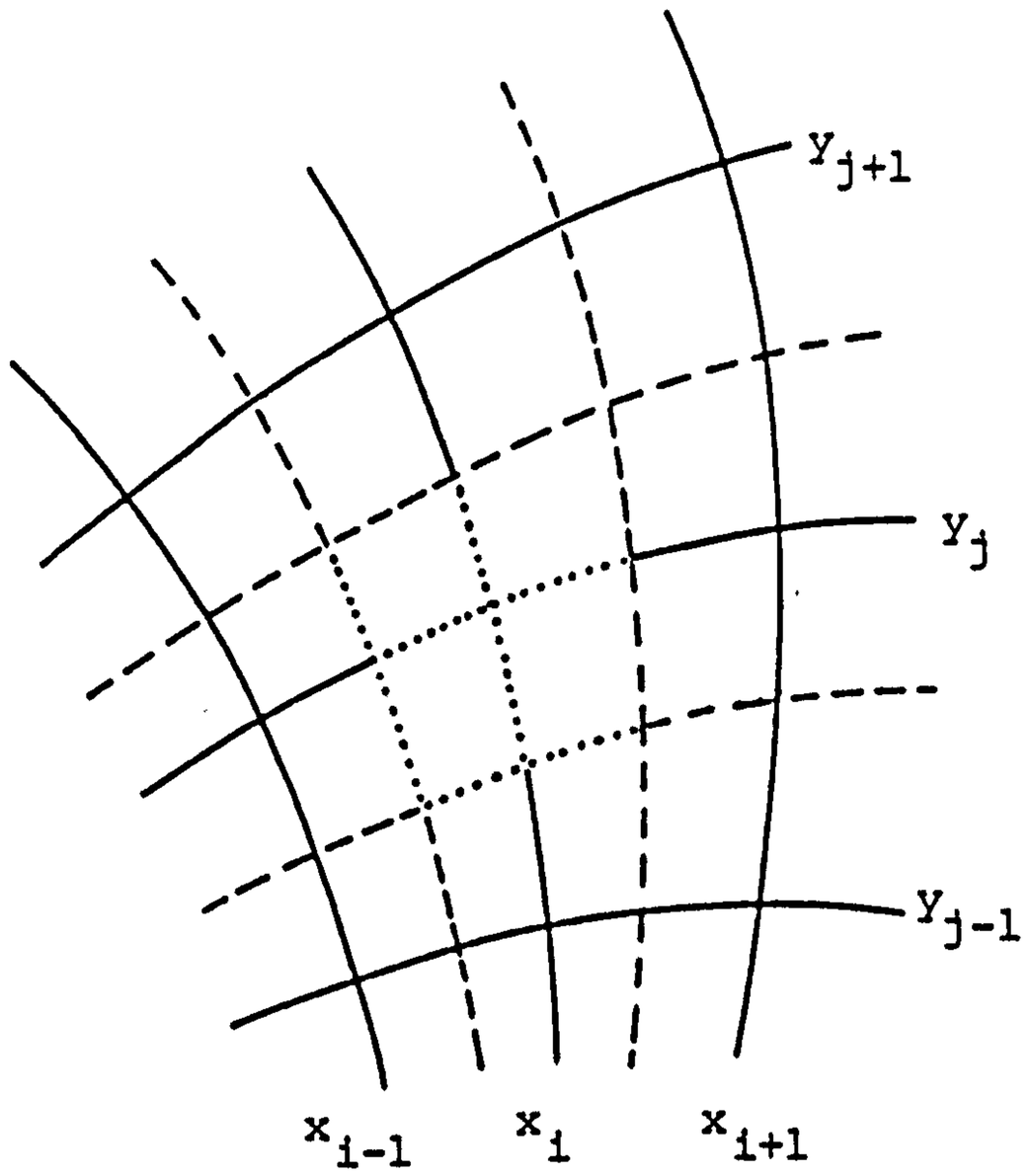


Fig. 5.2 Finite Difference Grid Representation

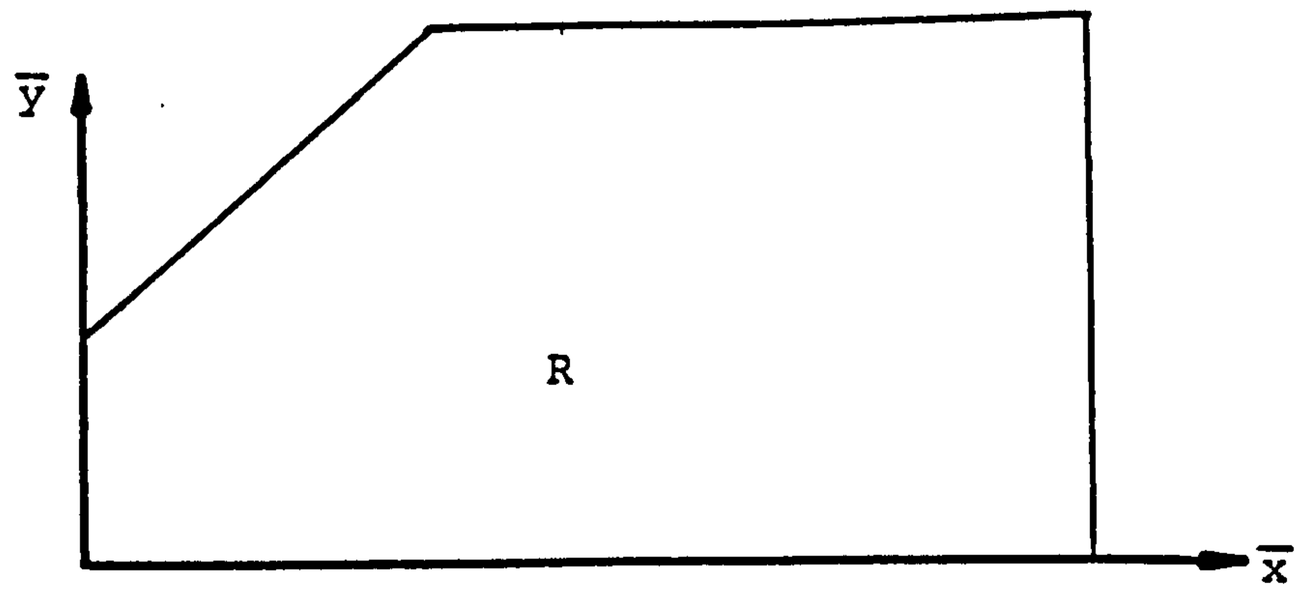


Fig. 5.3 (a) Definition Sketch of the Physical Region, R (Solution Domain in Cartesian Coordinates)
(b) Mesh Structure in the Transformed Space, R' (Solution Domain in Orthogonal Space)

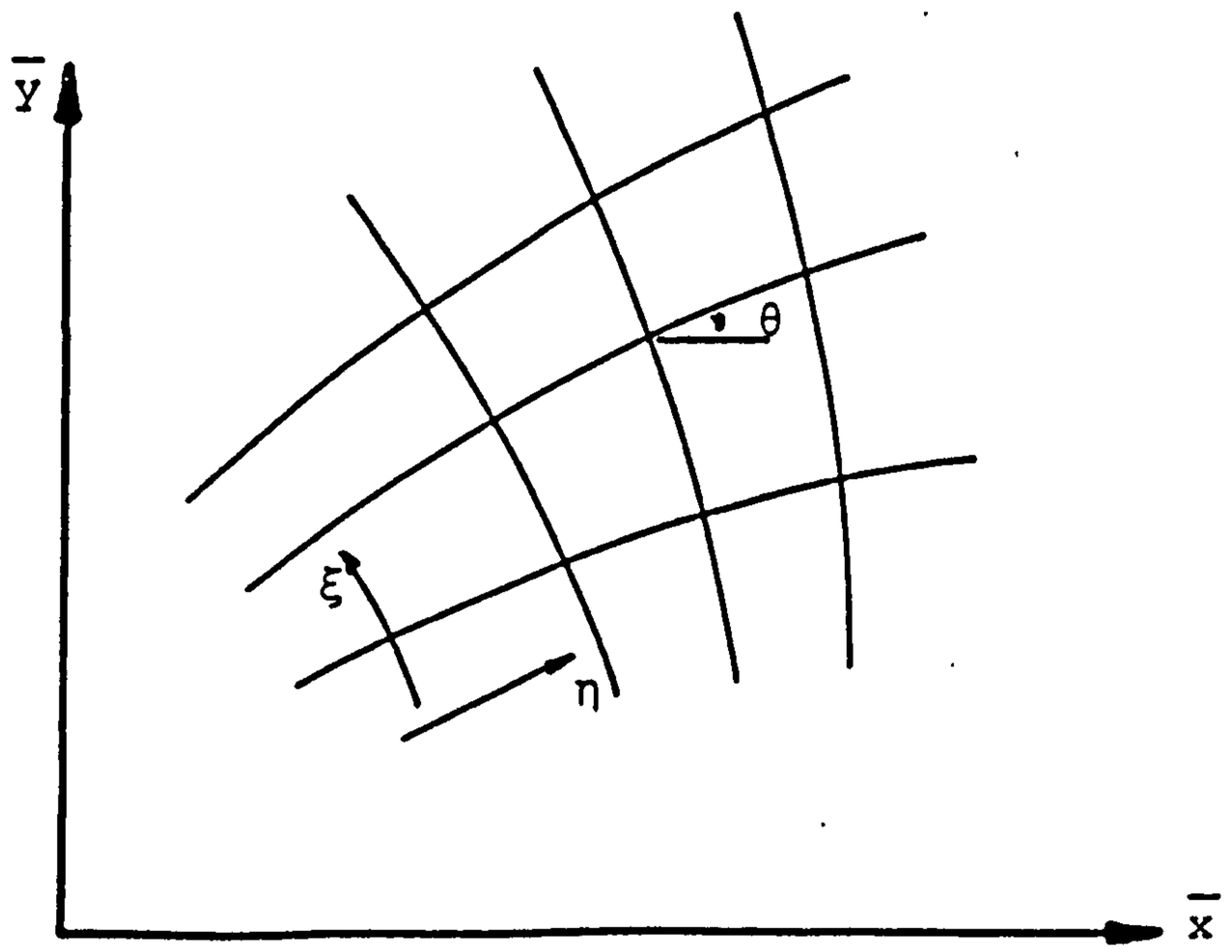


Fig. 5.4 Orthogonal Coordinate Lines in Cartesian Coordinates

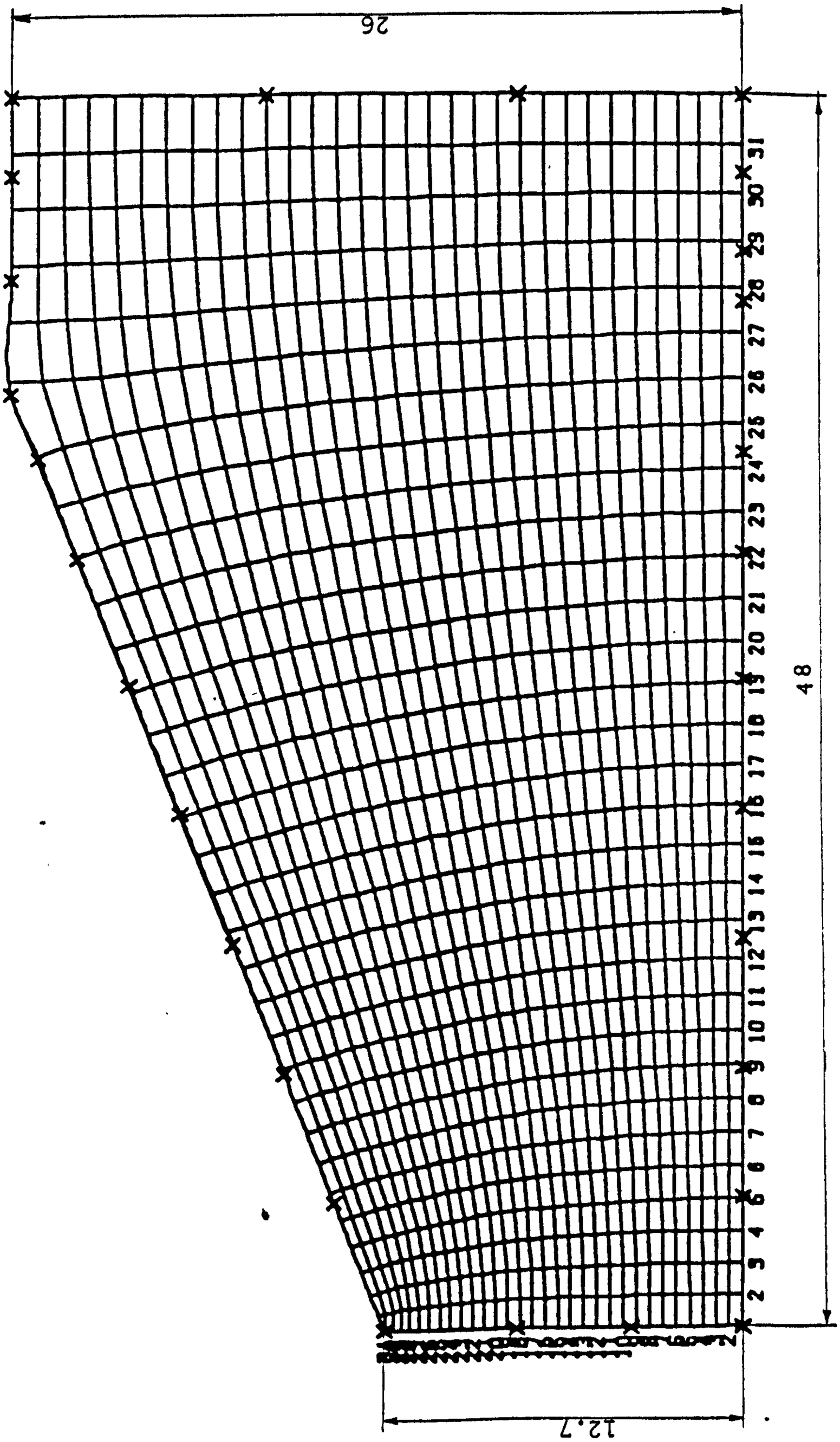
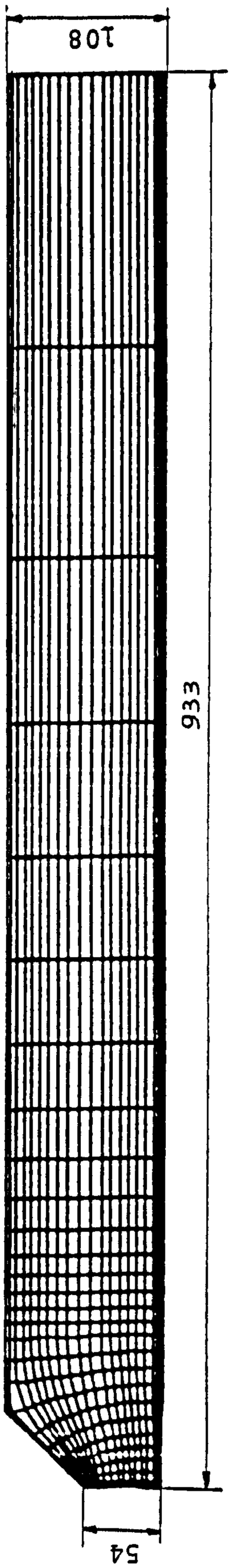
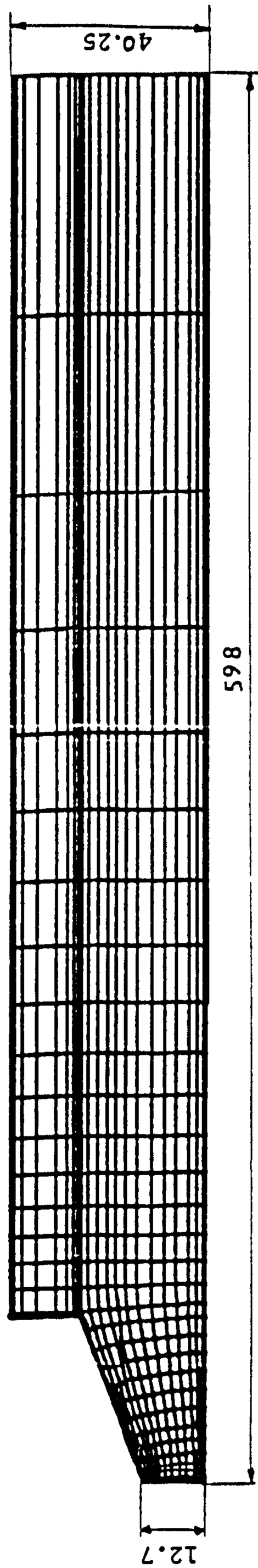


Fig. 5.5 Example of a Computer Generated Orthogonal Grid



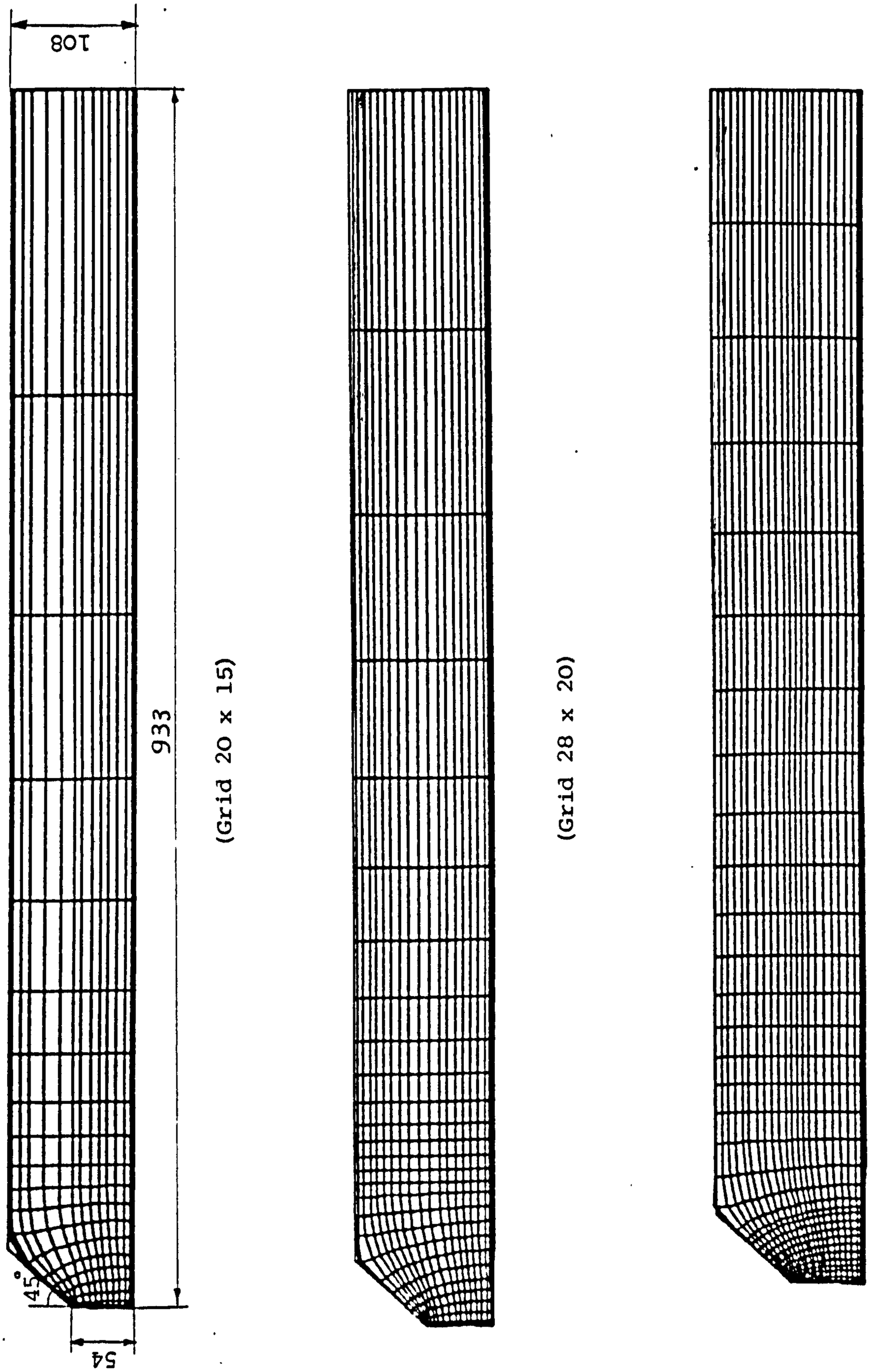
(i)



(ii)

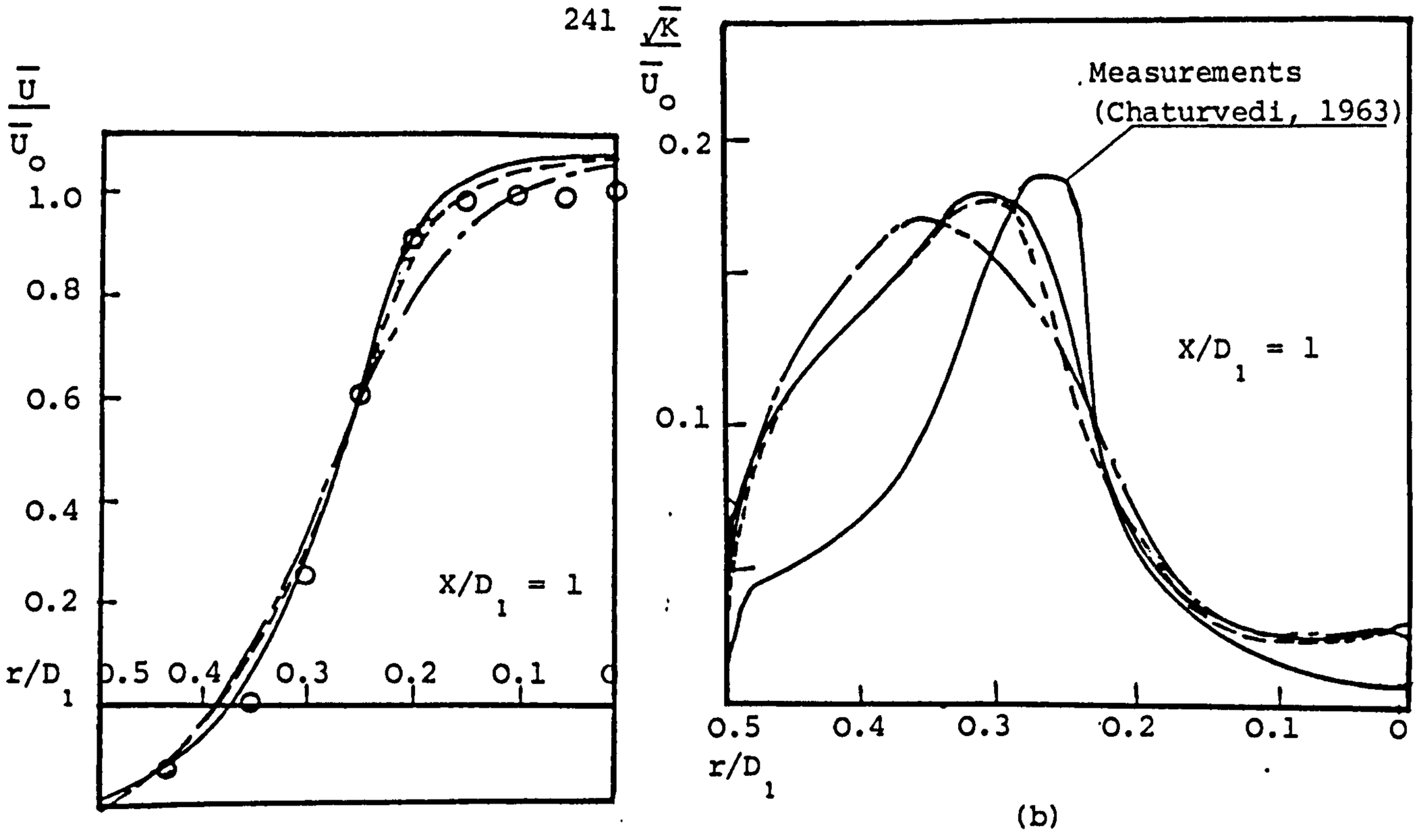
Dimensions in mm

Fig. 5.6 Examples of the Grid Distributions; (i) Test Case 2, (ii) Test Cases 3 and 4



Dimensions in mm

Fig. 5.7 Sample of the Grid Distributions used in the Grid-Independence Test



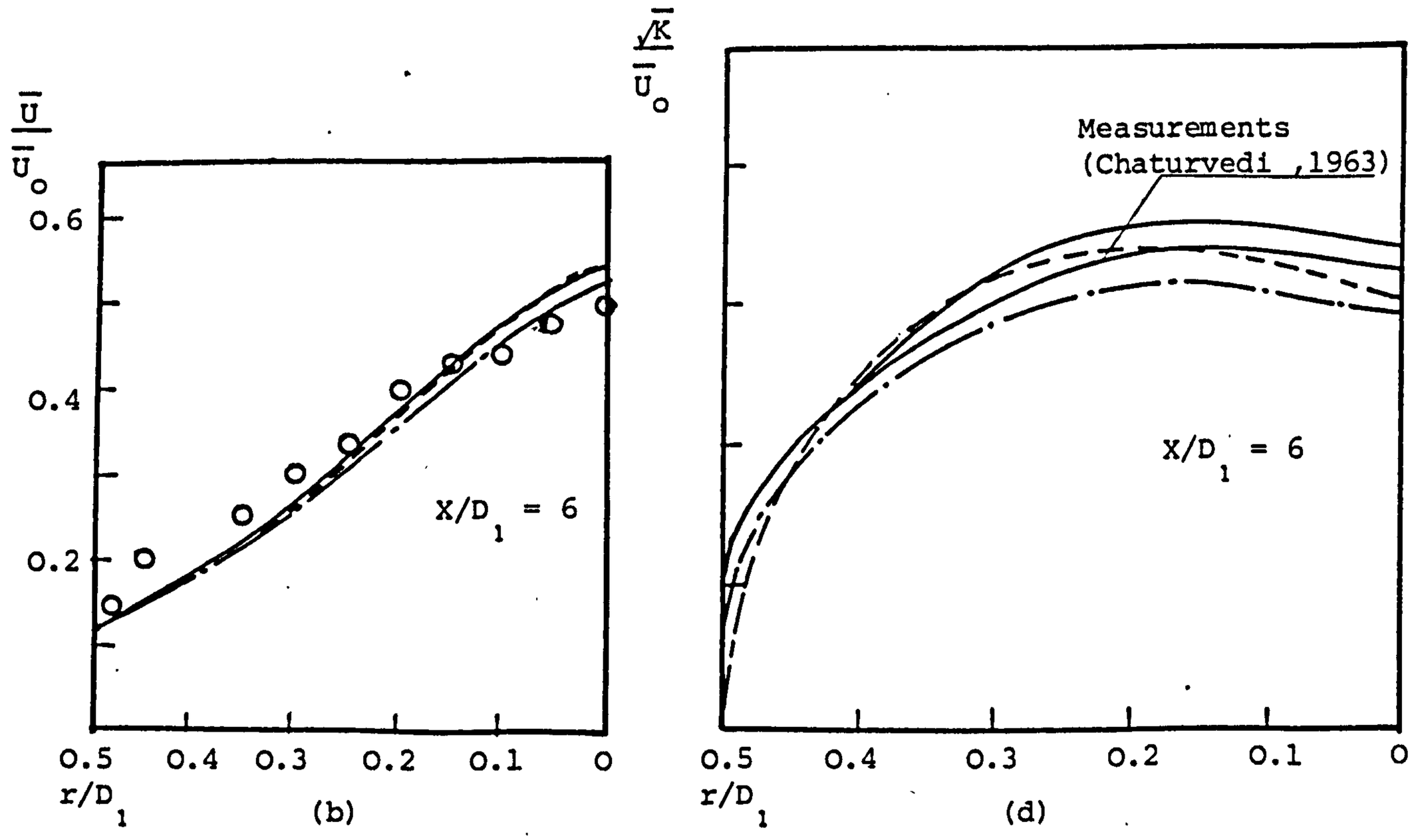


Fig. 5.8 Effect of Grid Size on Calculated Flow Properties
———, 34 x 24; - - - -, 28 x 20; ——— - —, 20 x 15;
O, Measurements (Chaturvedi, 1963)

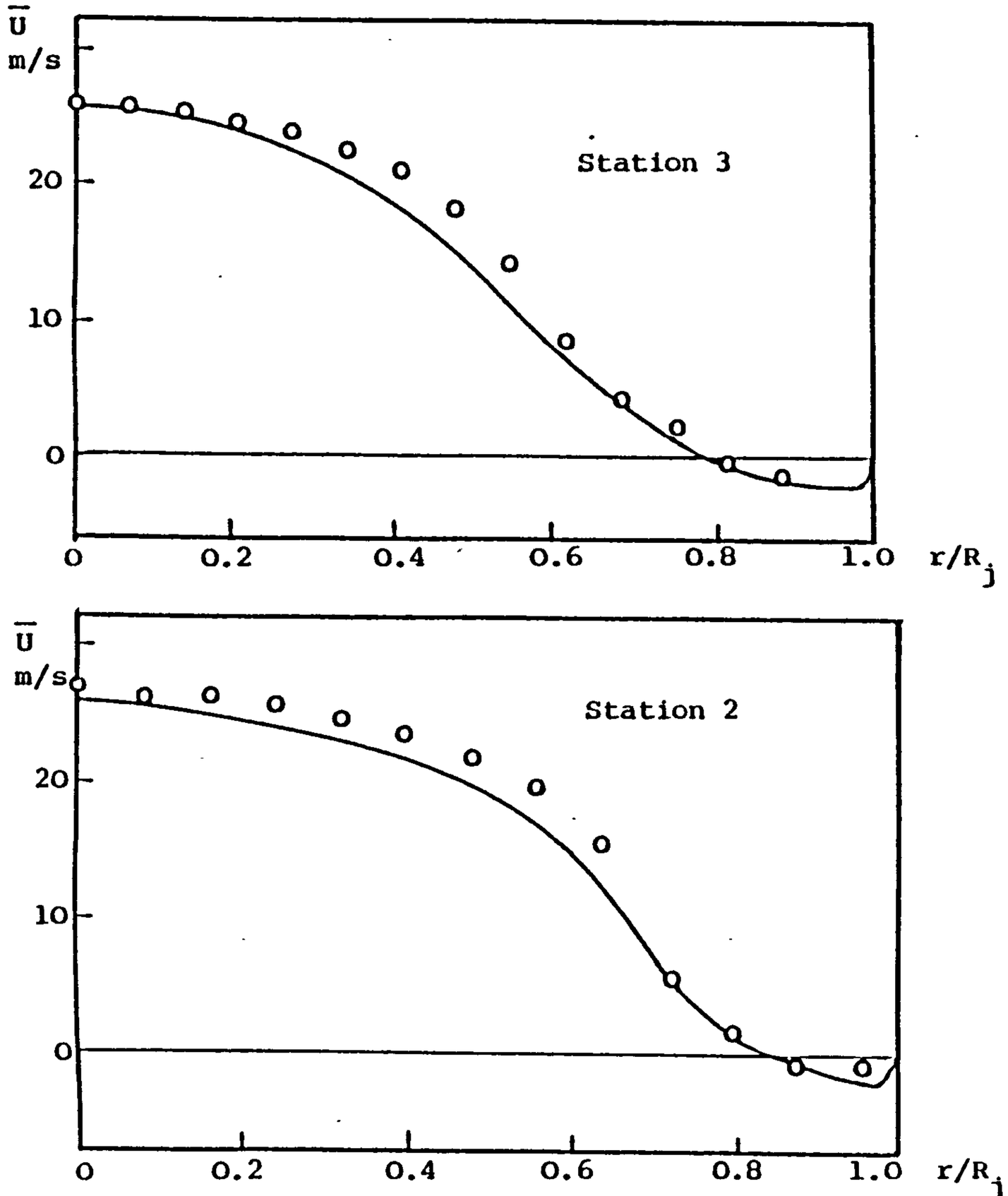


Fig. 5.9 Measured and Calculated Radial Profiles of Axial Mean Velocity in G1 (S = 0.0)
Calculations; Present Measurements

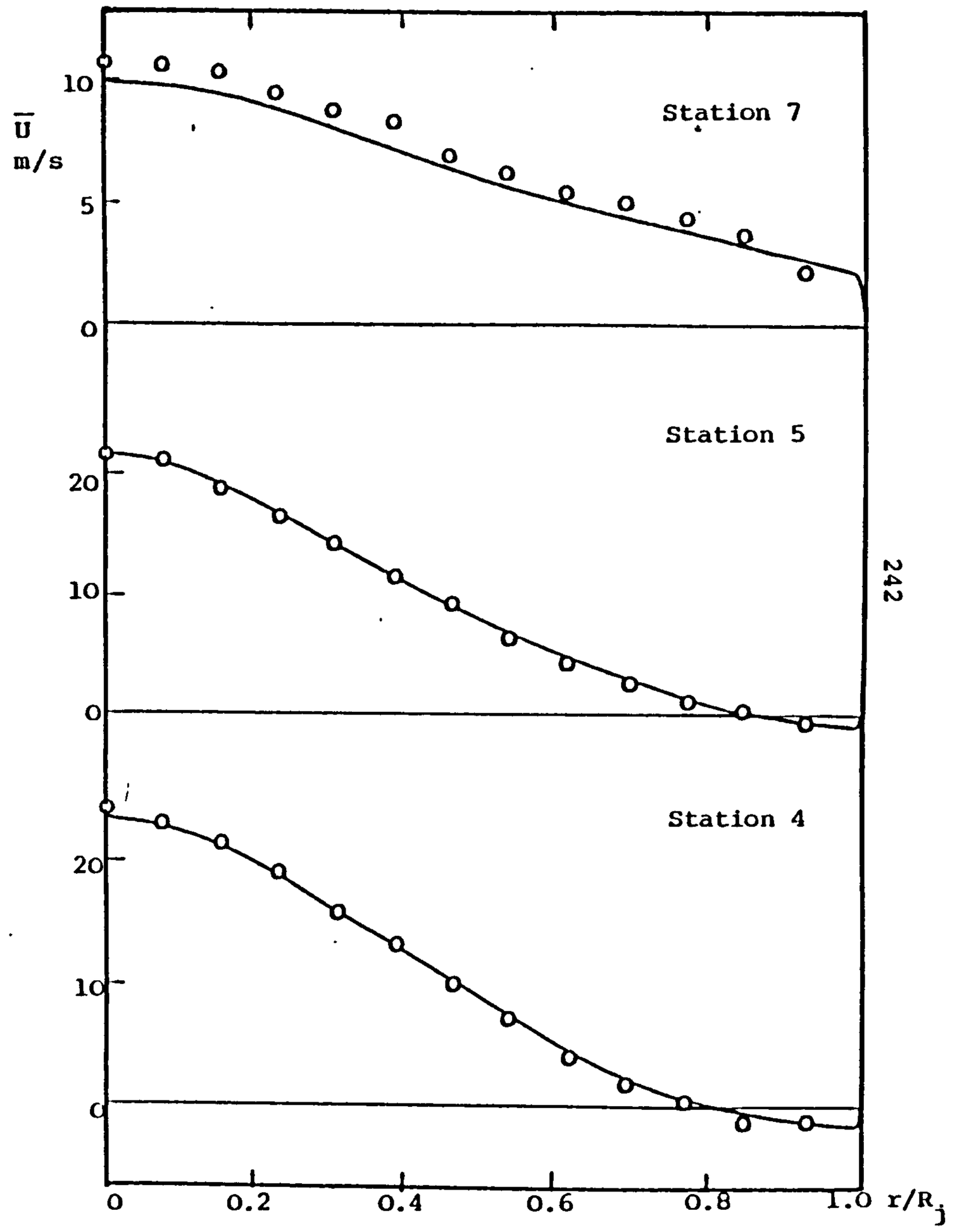


Fig. 5.9 (Continued)

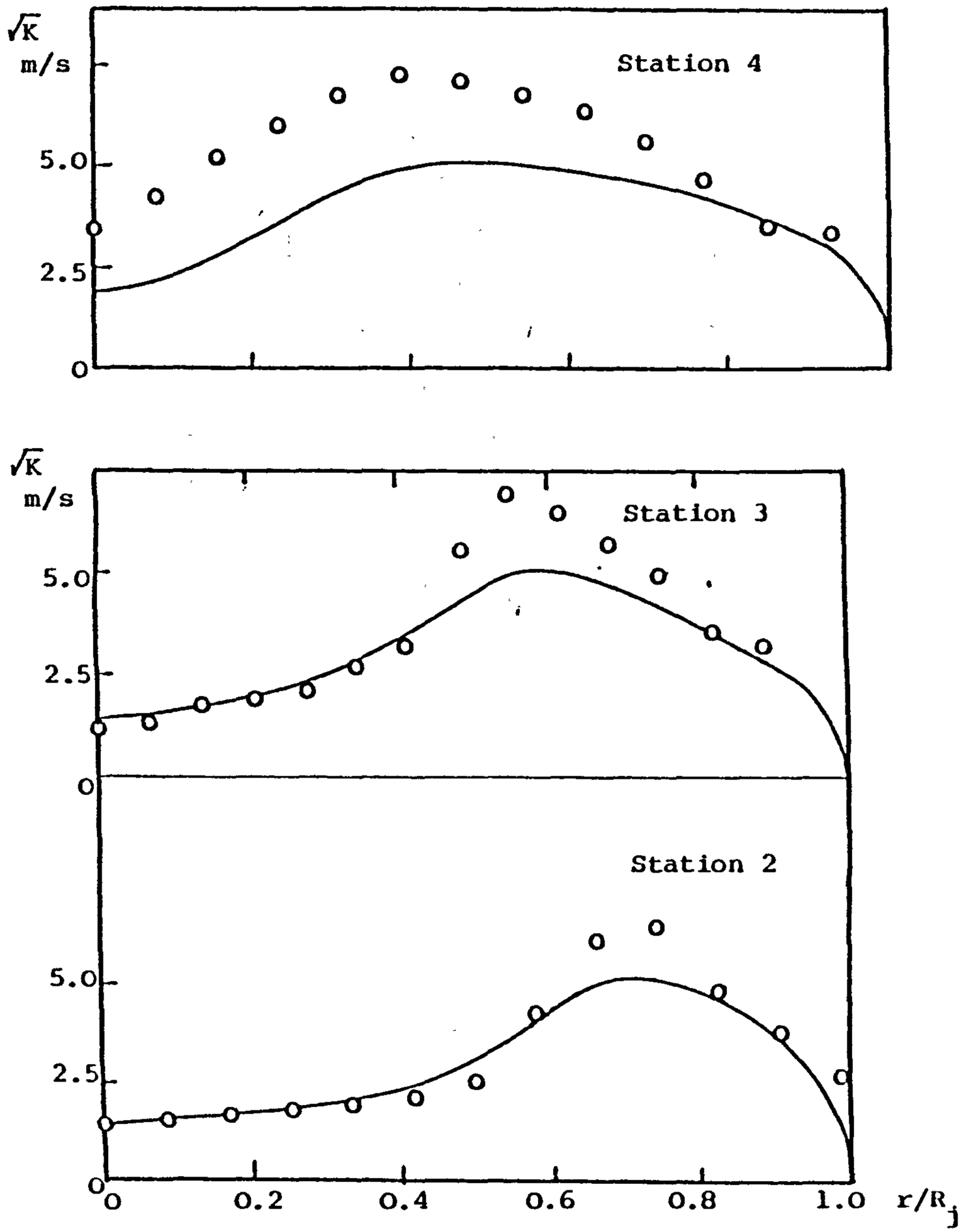


Fig. 5.10 Measured and Calculated Radial Profiles of Kinetic Energy of Turbulence in Gl (S = 0.0)
Calculations; Present Measureemtns

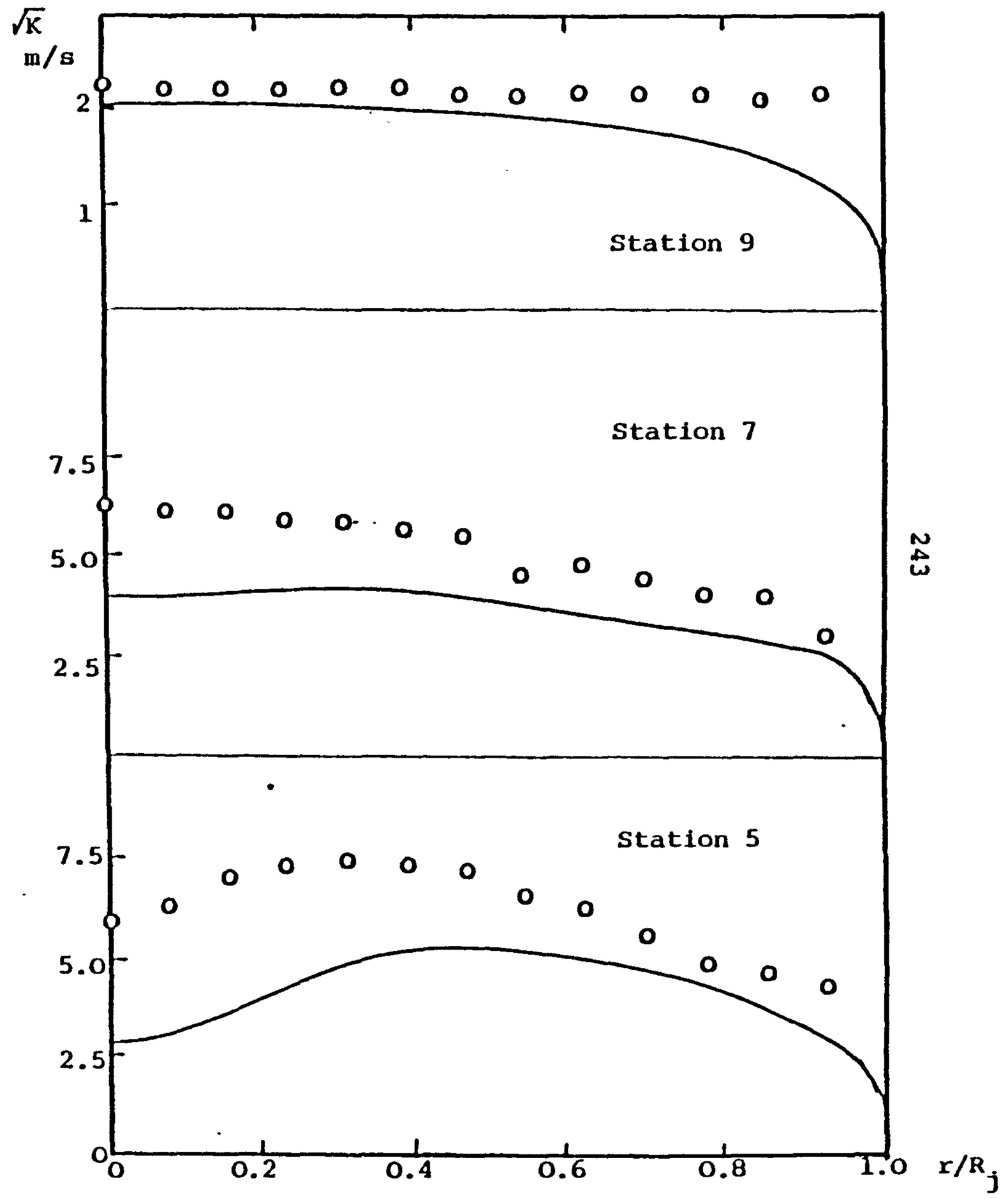
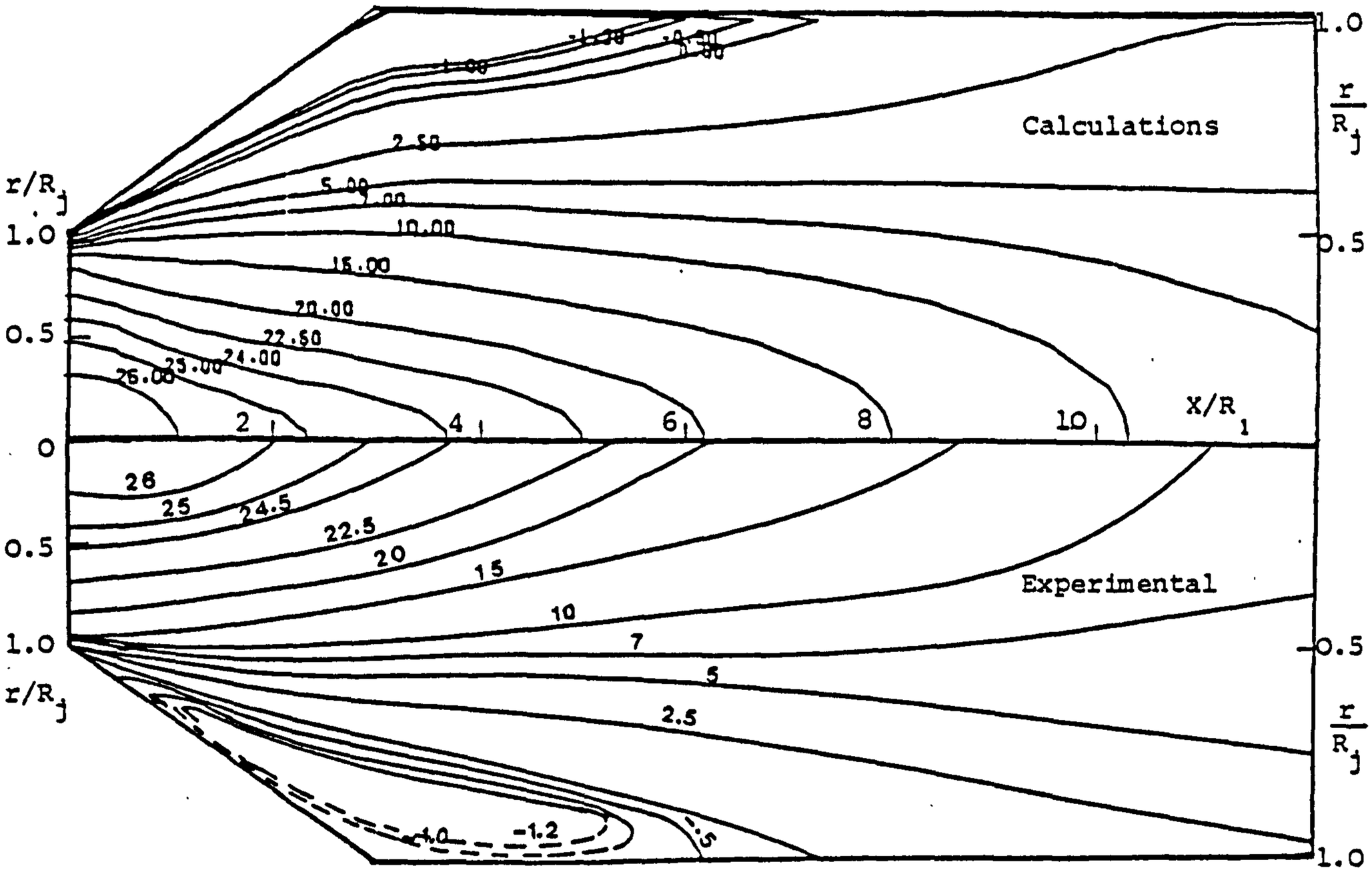
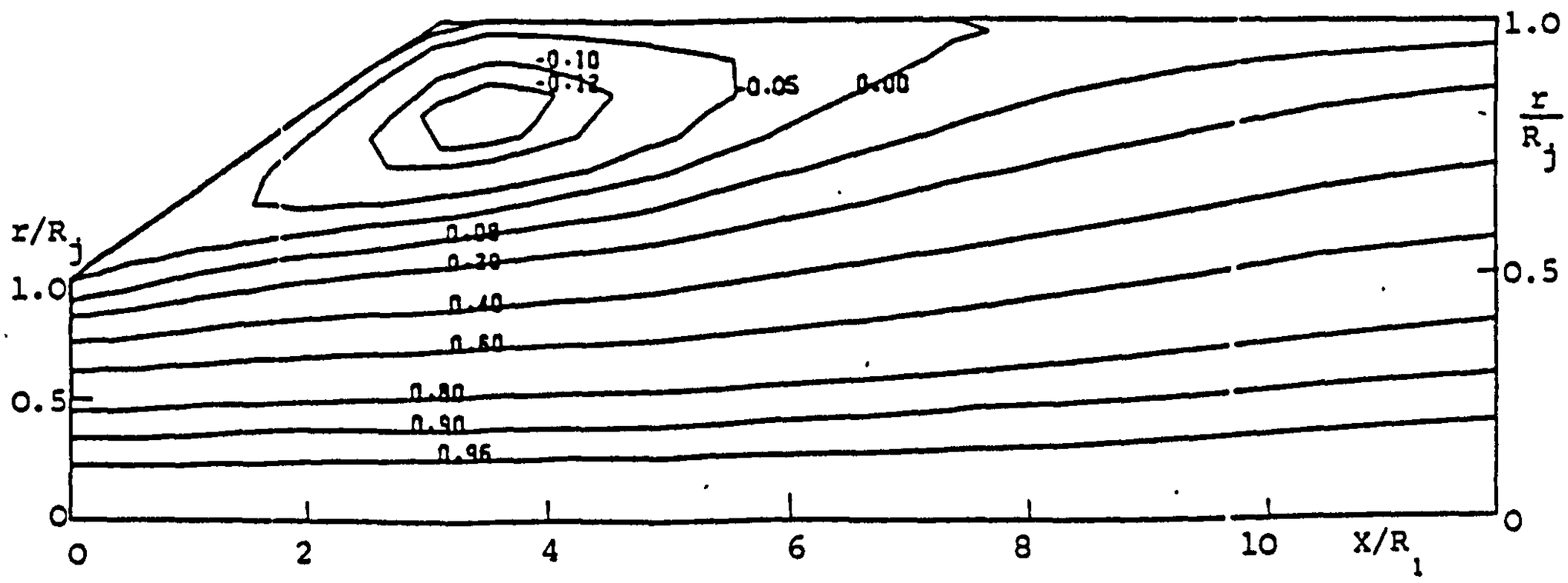


Fig. 5.10 (Continued)

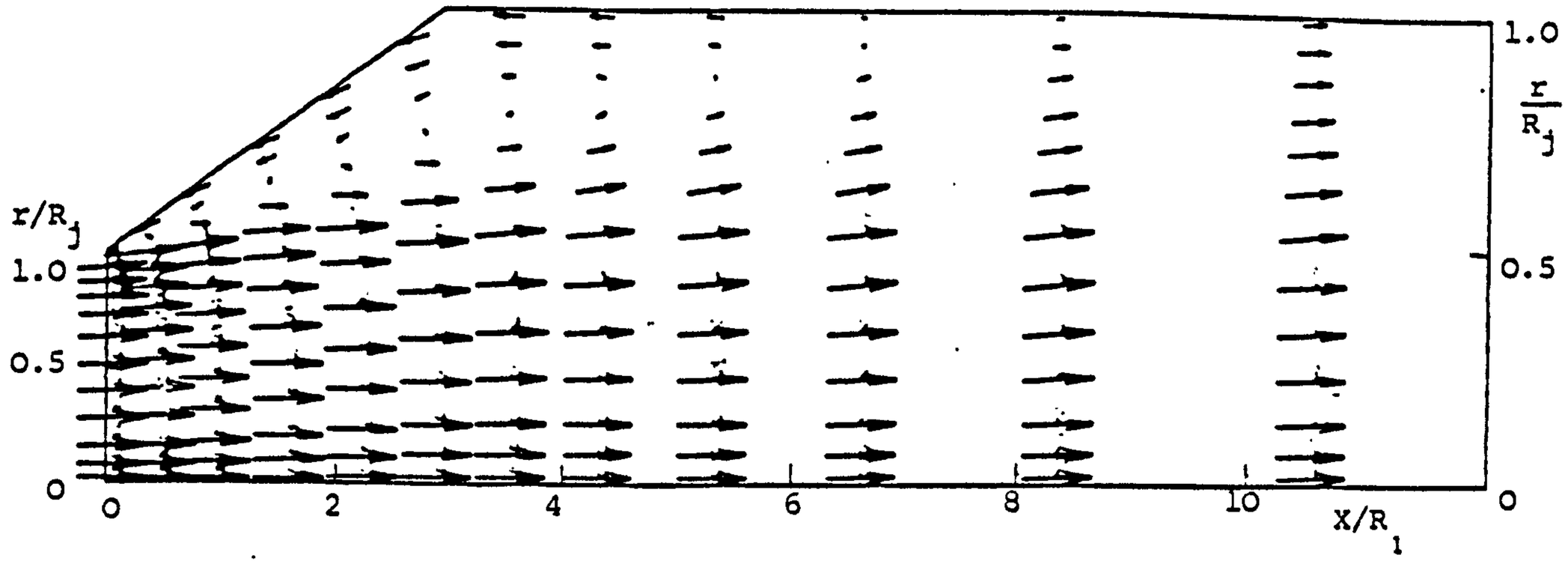


(a) Axial Mean Velocity



(b) Stream Function

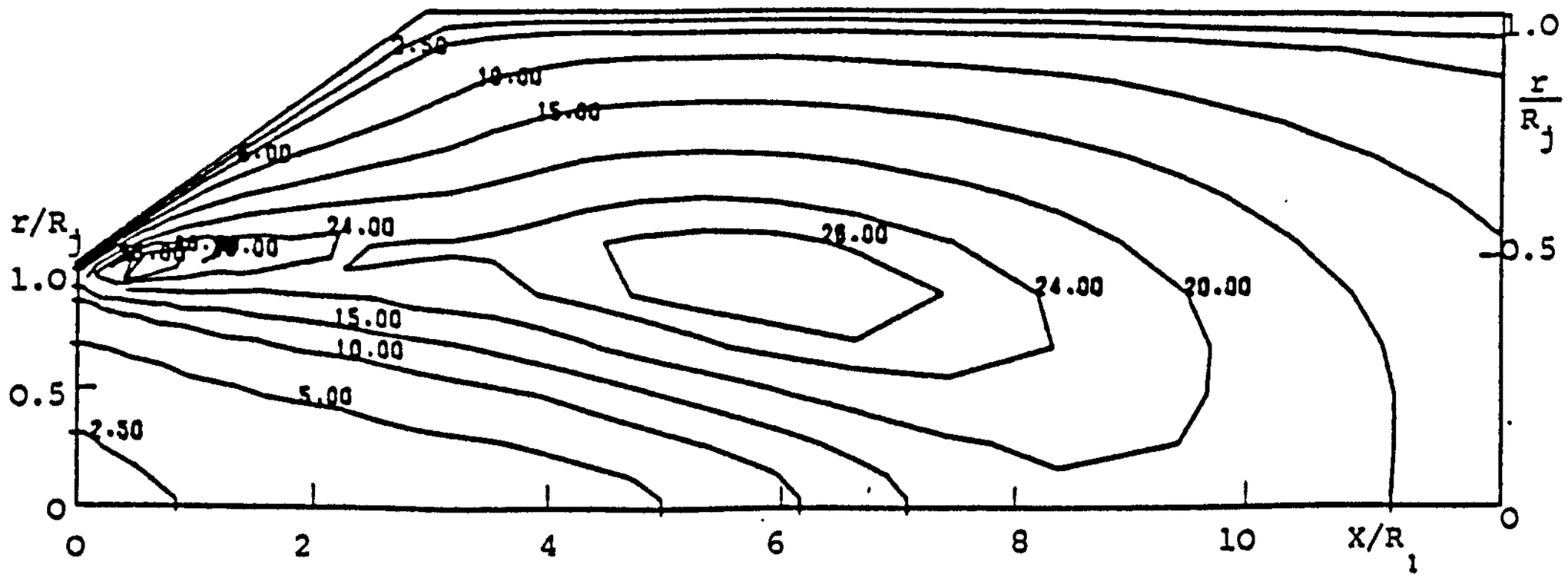
Fig. 5.11 Contours of Flow Properties in G1



(c) Velocity Vector

K (m^2/s^2)

26.0 24.0 20.0 15.0 10.0 5.00 2.50



(d) Kinetic Energy of Turbulence

Fig. 5.11 (Continued)

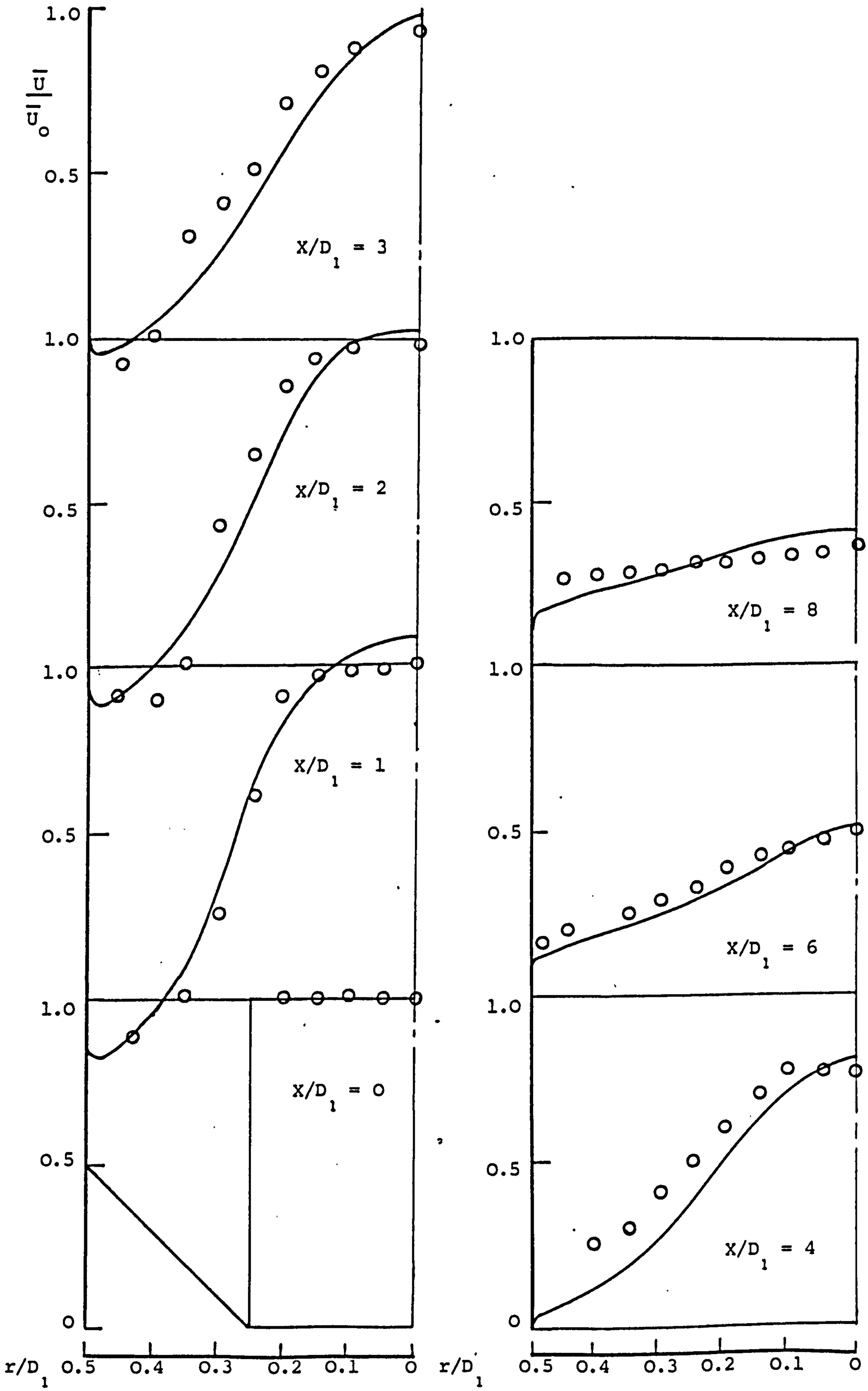


Fig. 5.12 Measured and Calculated Mean Velocity
———,Calculations; O, Measurements (Chaturvedi, 1963)

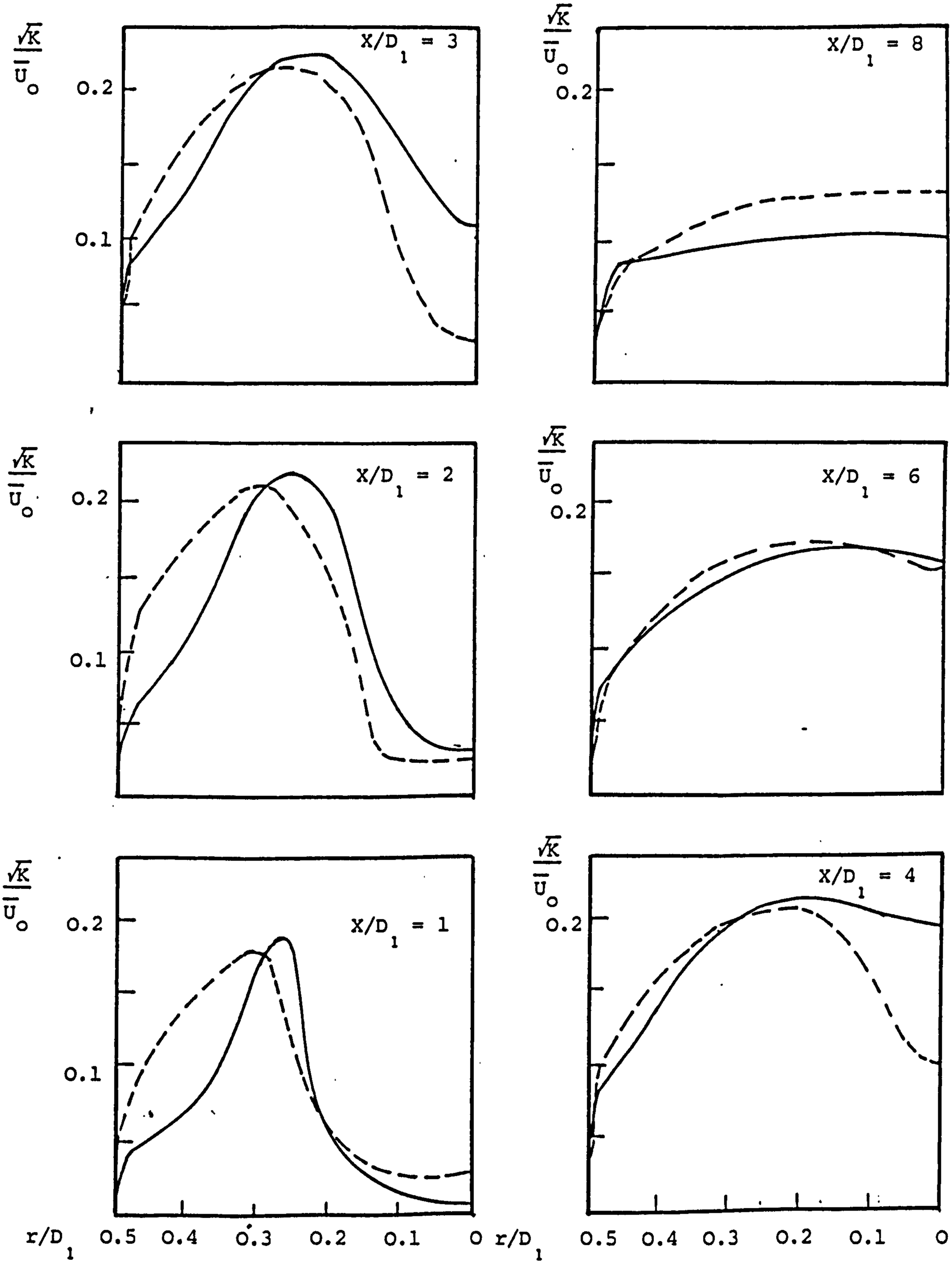


Fig. 5.13 Measured and Calculated Kinetic Energy of Turbulence, Test Case 2

— — — —, Calculations; ———, Measurements (Chaturvedi, 1963)

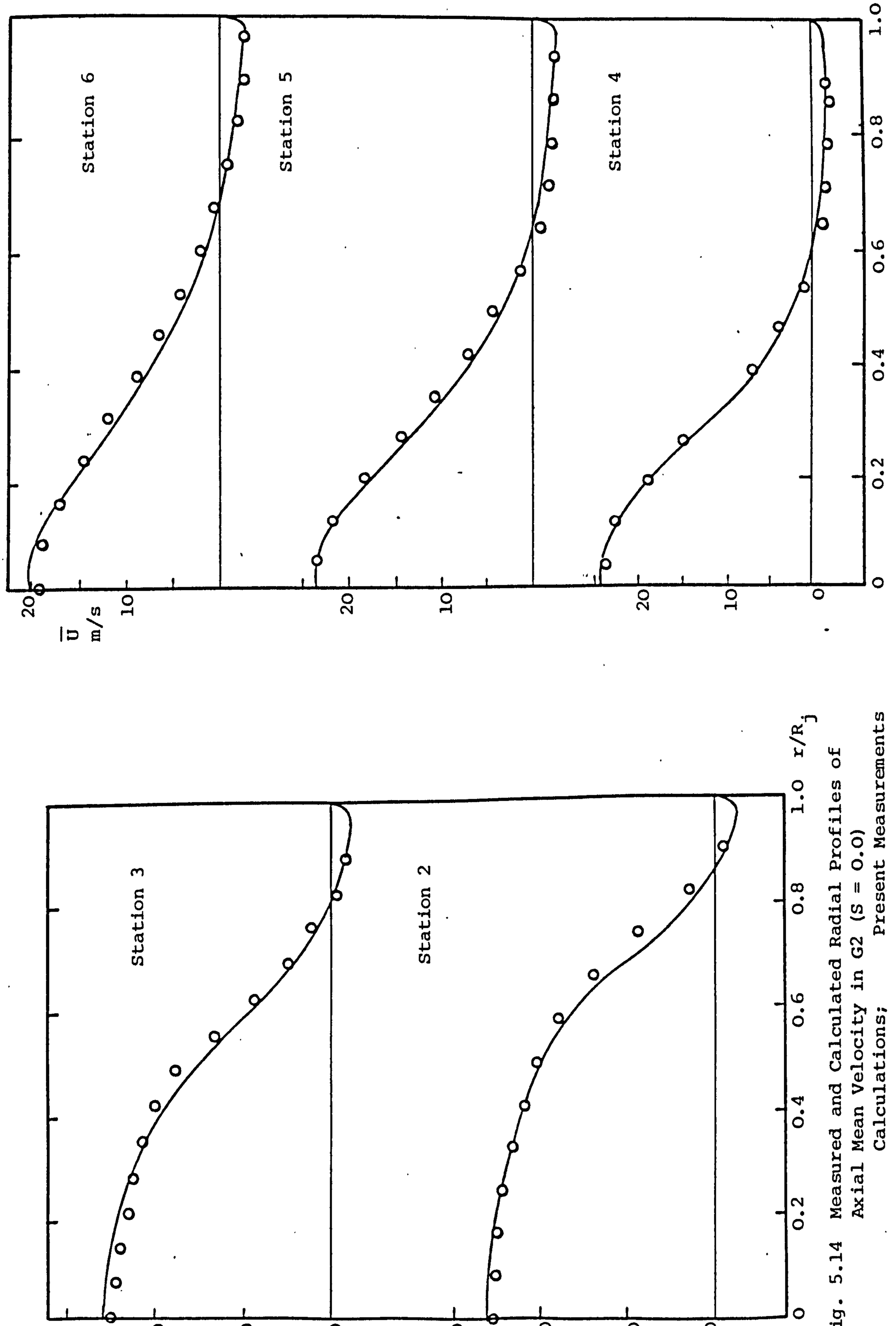


Fig. 5.14 (Continued)

Fig. 5.14 Measured and Calculated Radial Profiles of Axial Mean Velocity in G2 (S = 0.0)
Calculations; Present Measurements

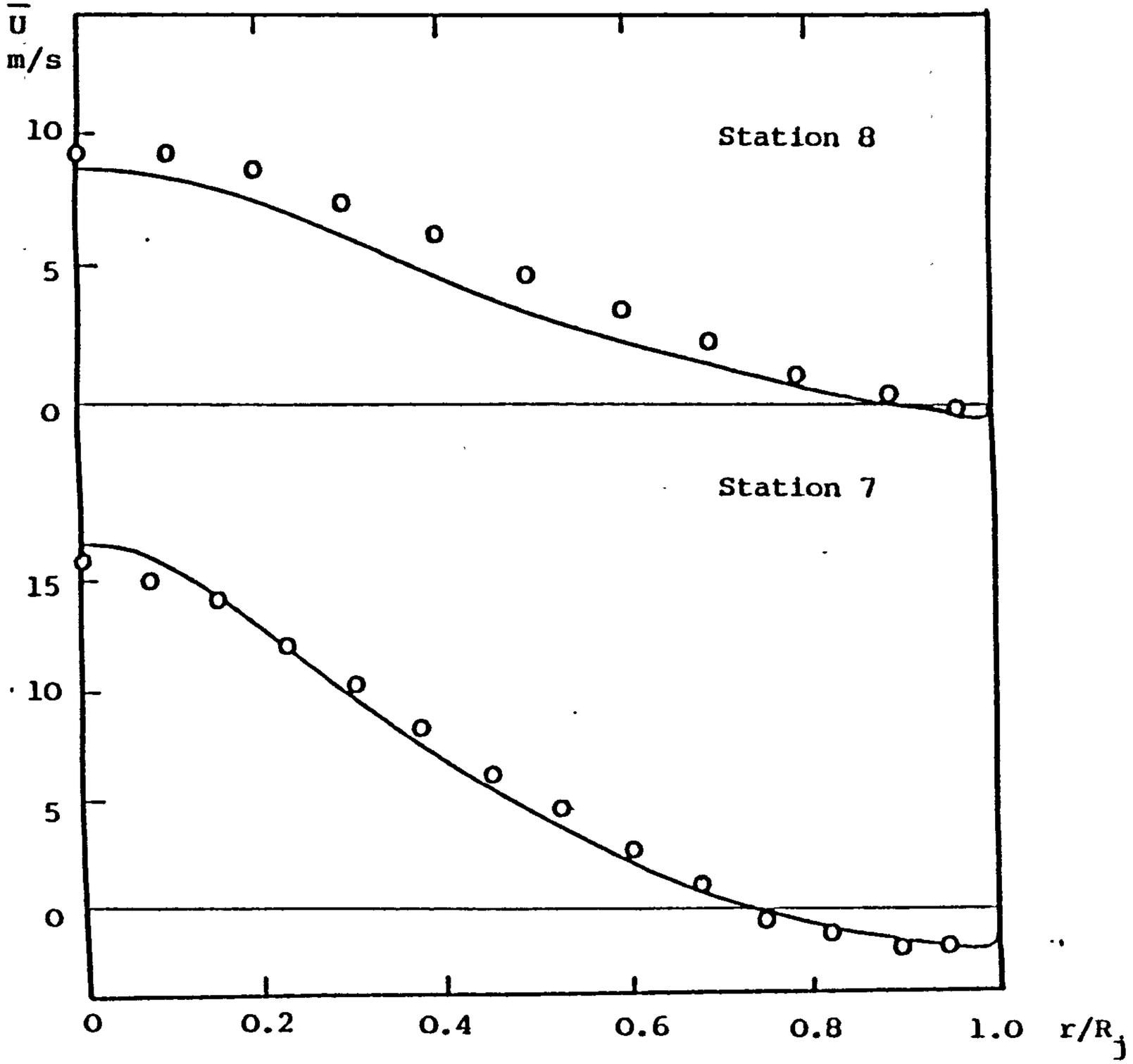


Fig. 5.14 (Continued)

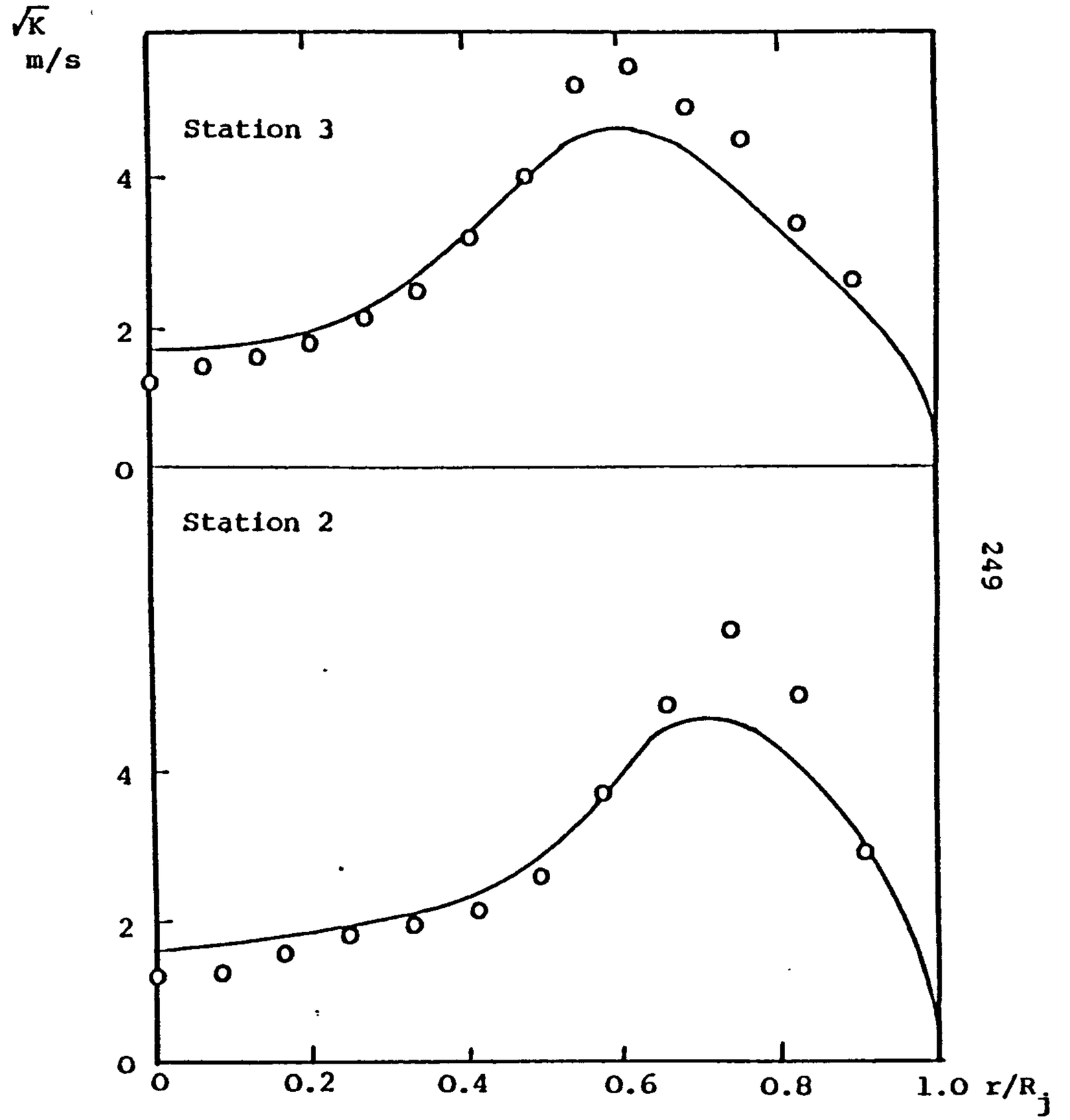


Fig. 5.15 Measured and Calculated Radial Profiles of Kinetic Energy of Turbulence in G2 (S = 0.0)
Calculations; Present Measurements

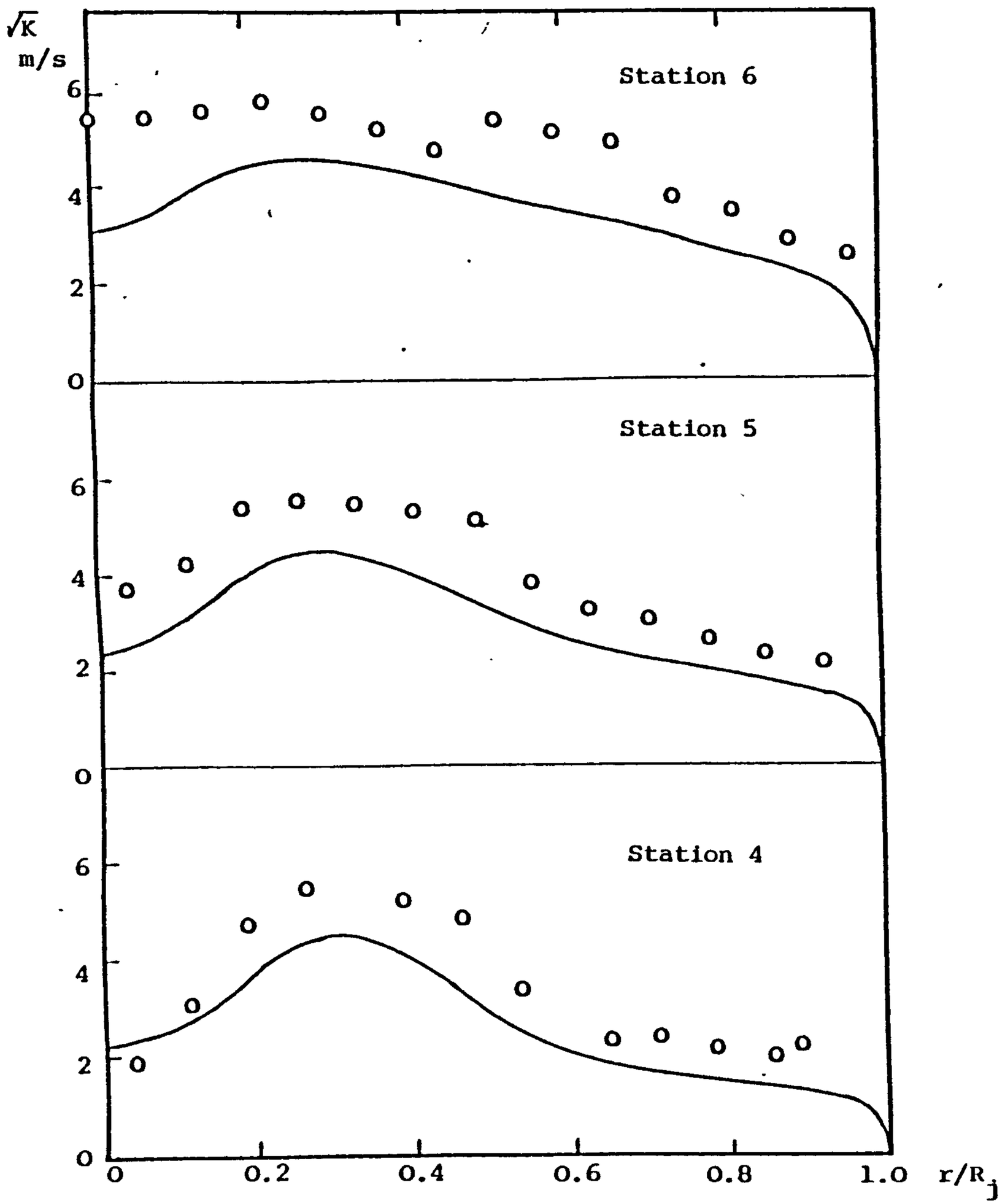


Fig. 5.15 (Continued)

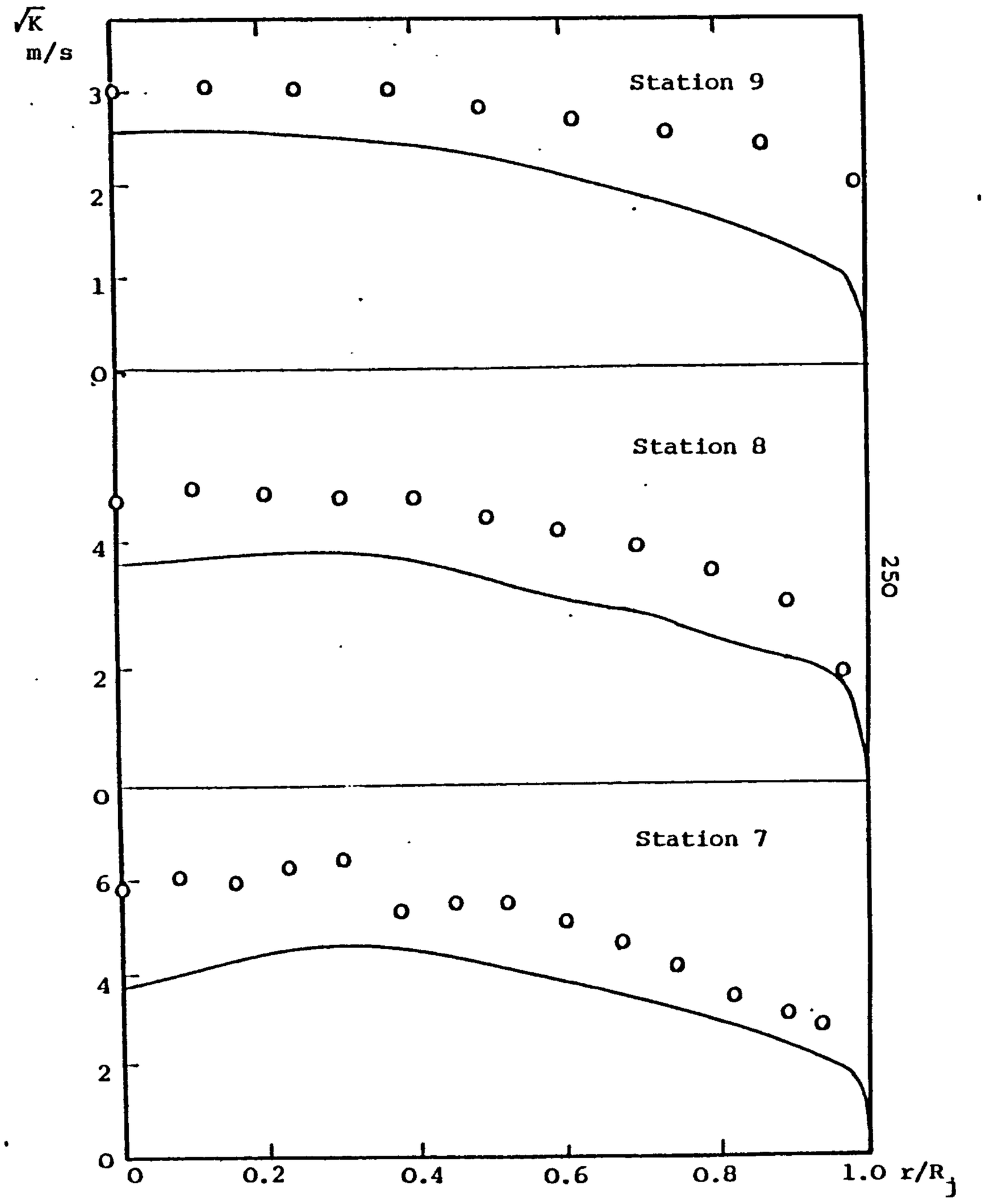


Fig. 5.15 (Continued)

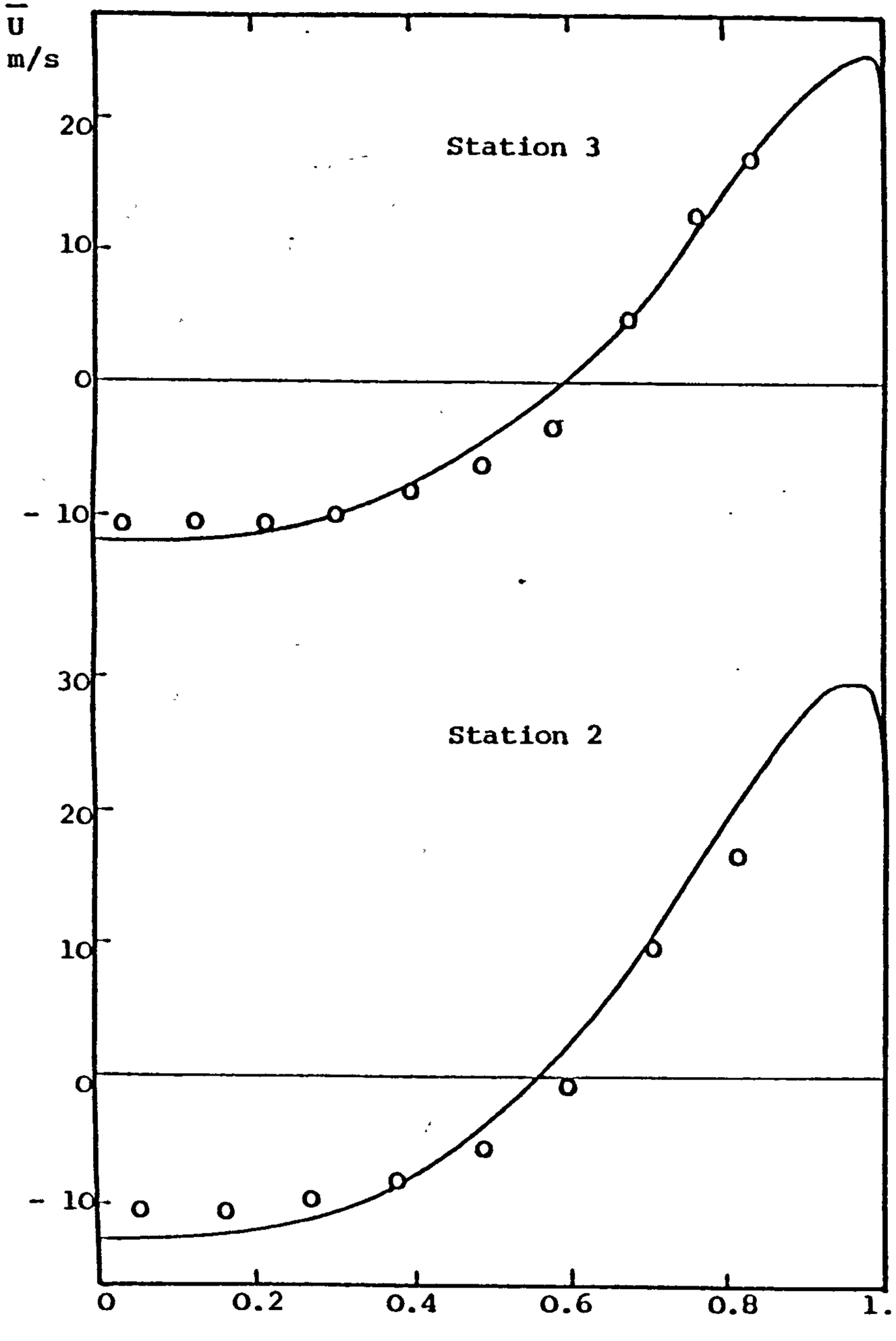


Fig. 5.16 Measured and Calculated Radial Profiles of Axial Mean Velocity in G2 (S = 0.93)
Calculations; Present Measurements

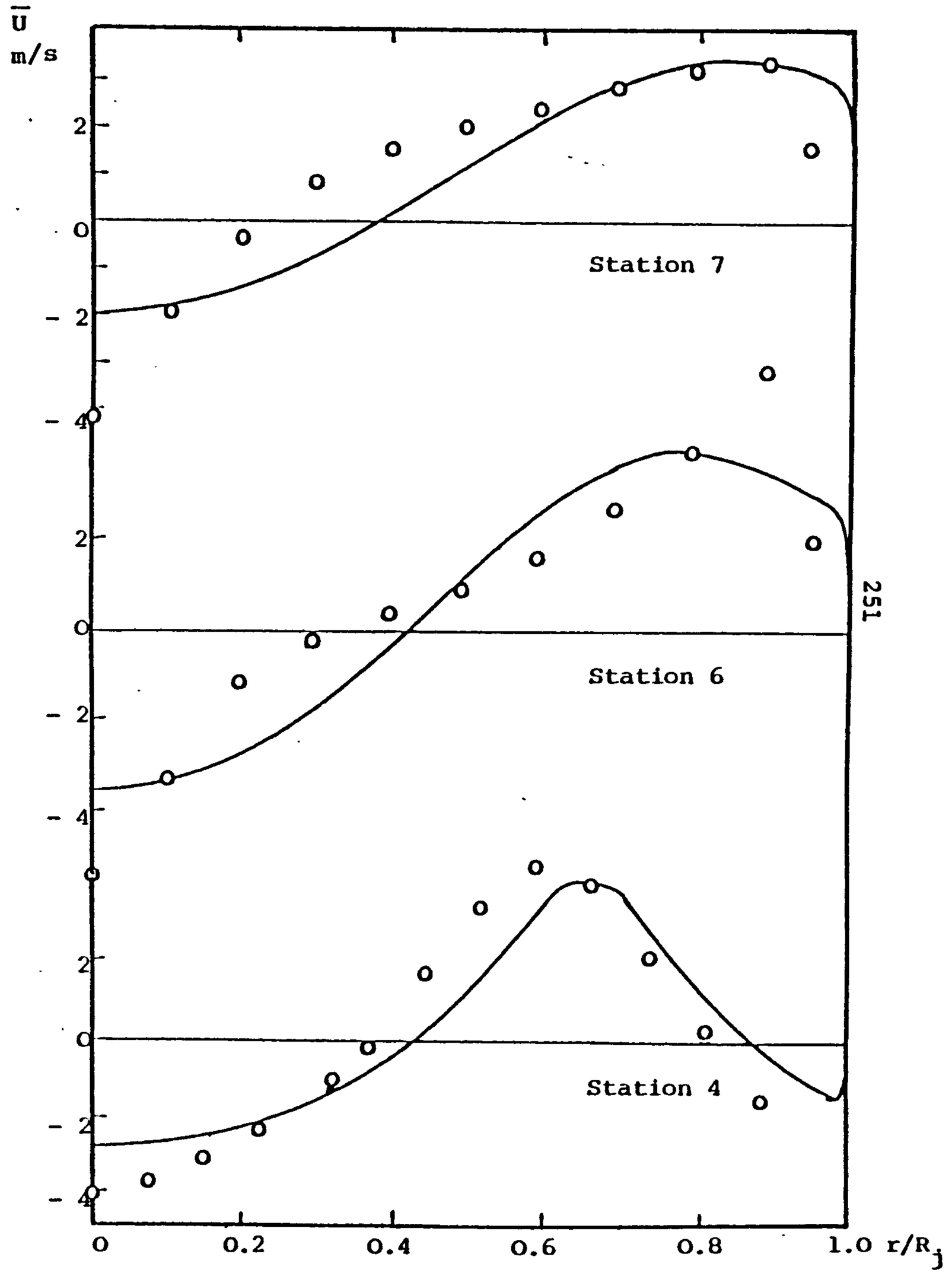


Fig. 5.16 (Continued)

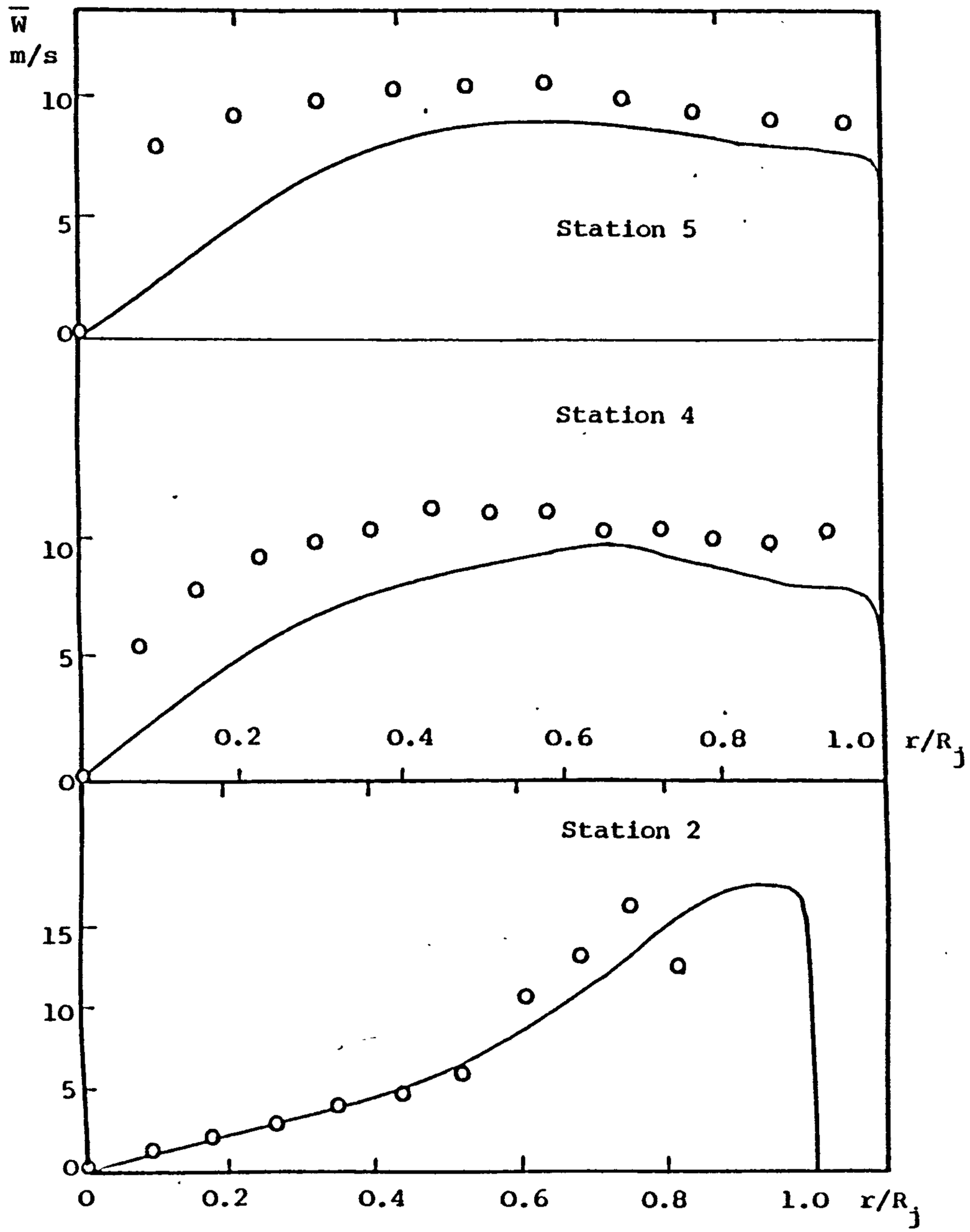


Fig. 5.17 Measured and Calculated Radial Profiles of the Tangential Mean Velocity in G2 (S = 0.93)
Calculations; Measurements

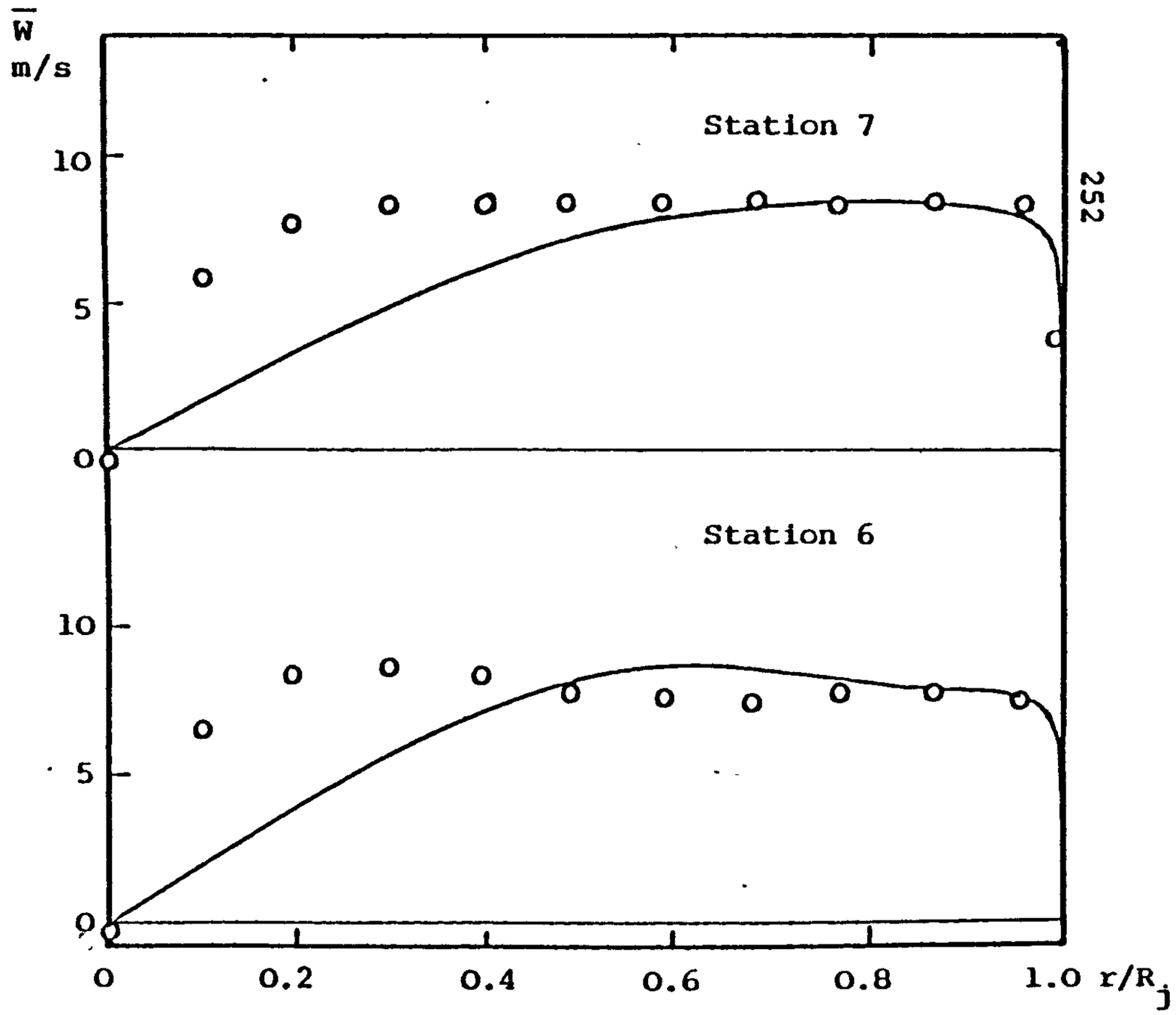


Fig. 5.17 (Continued)

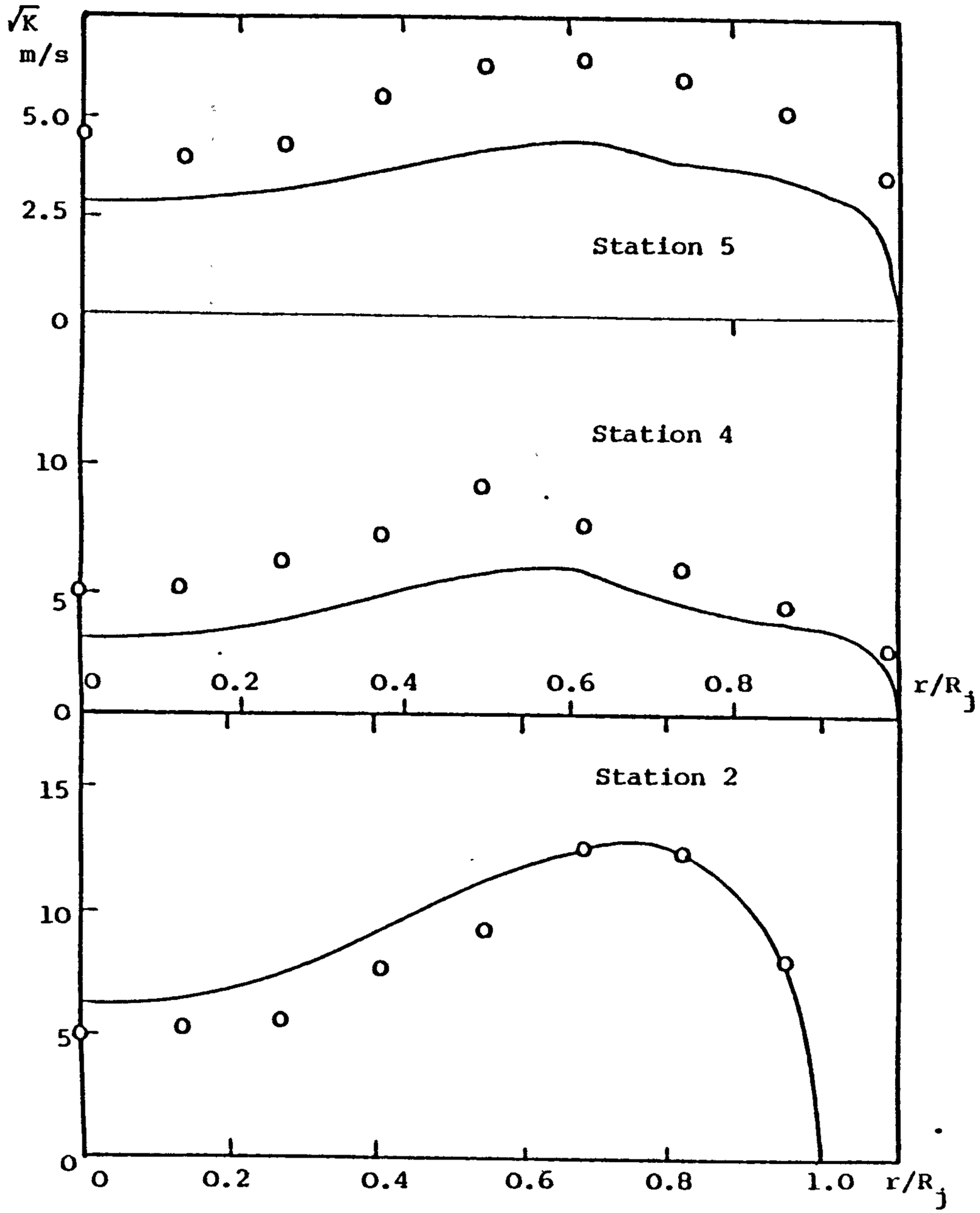


Fig. 5.18 Measured and Calculated Radial Profiles of Kinetic Energy of Turbulence in G2 (S = 0.93)
Calculations; Present Measurements

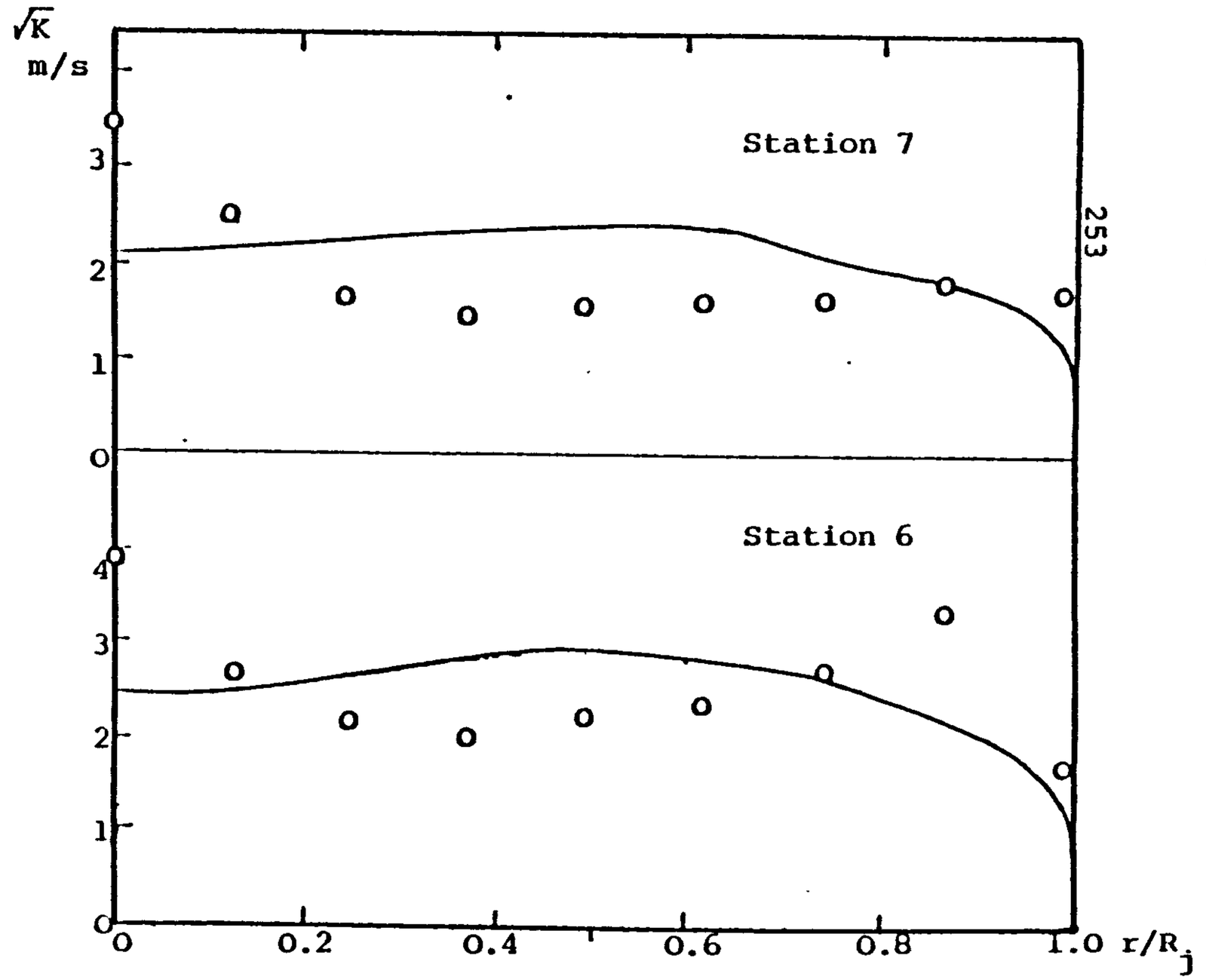
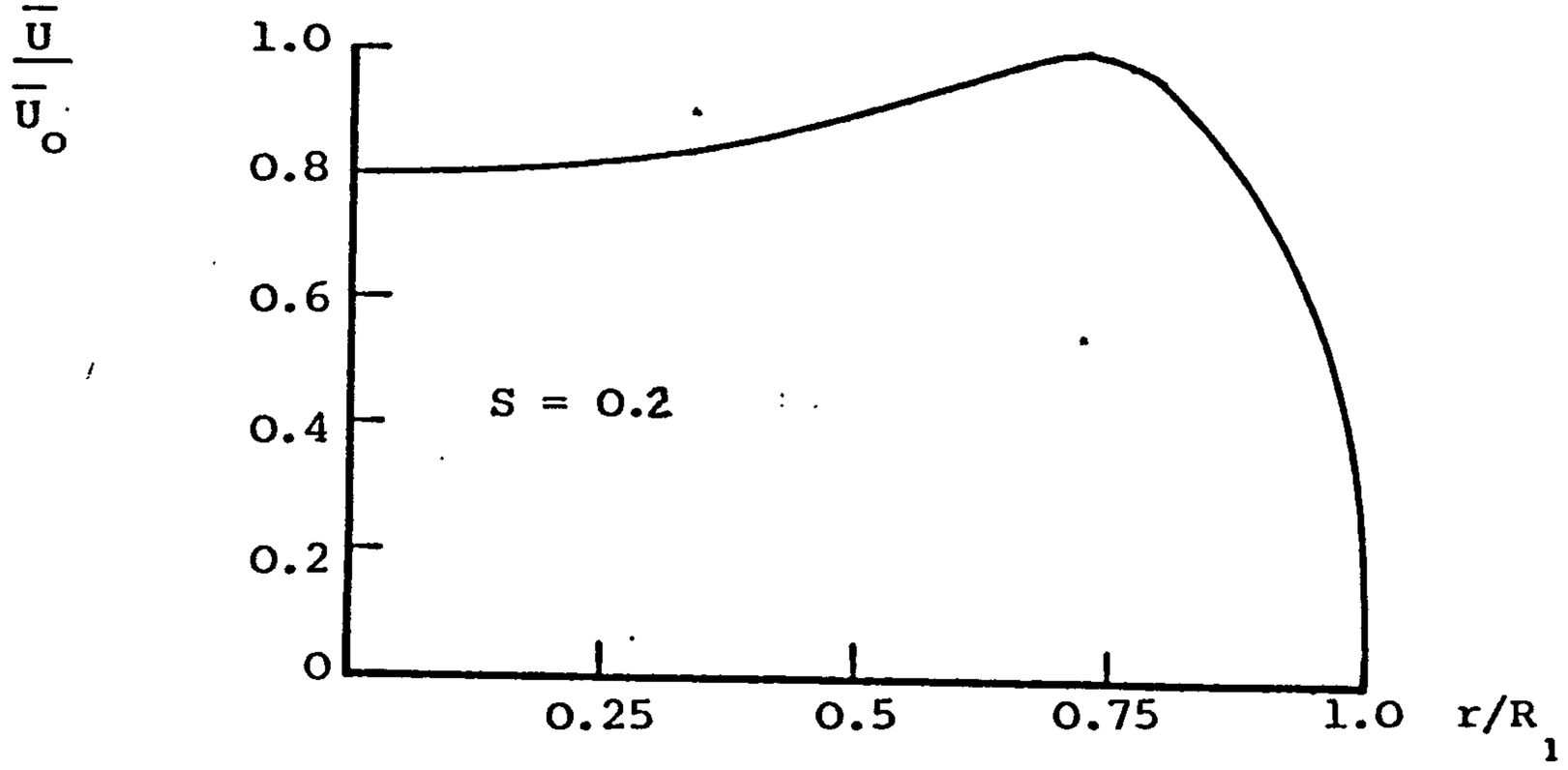
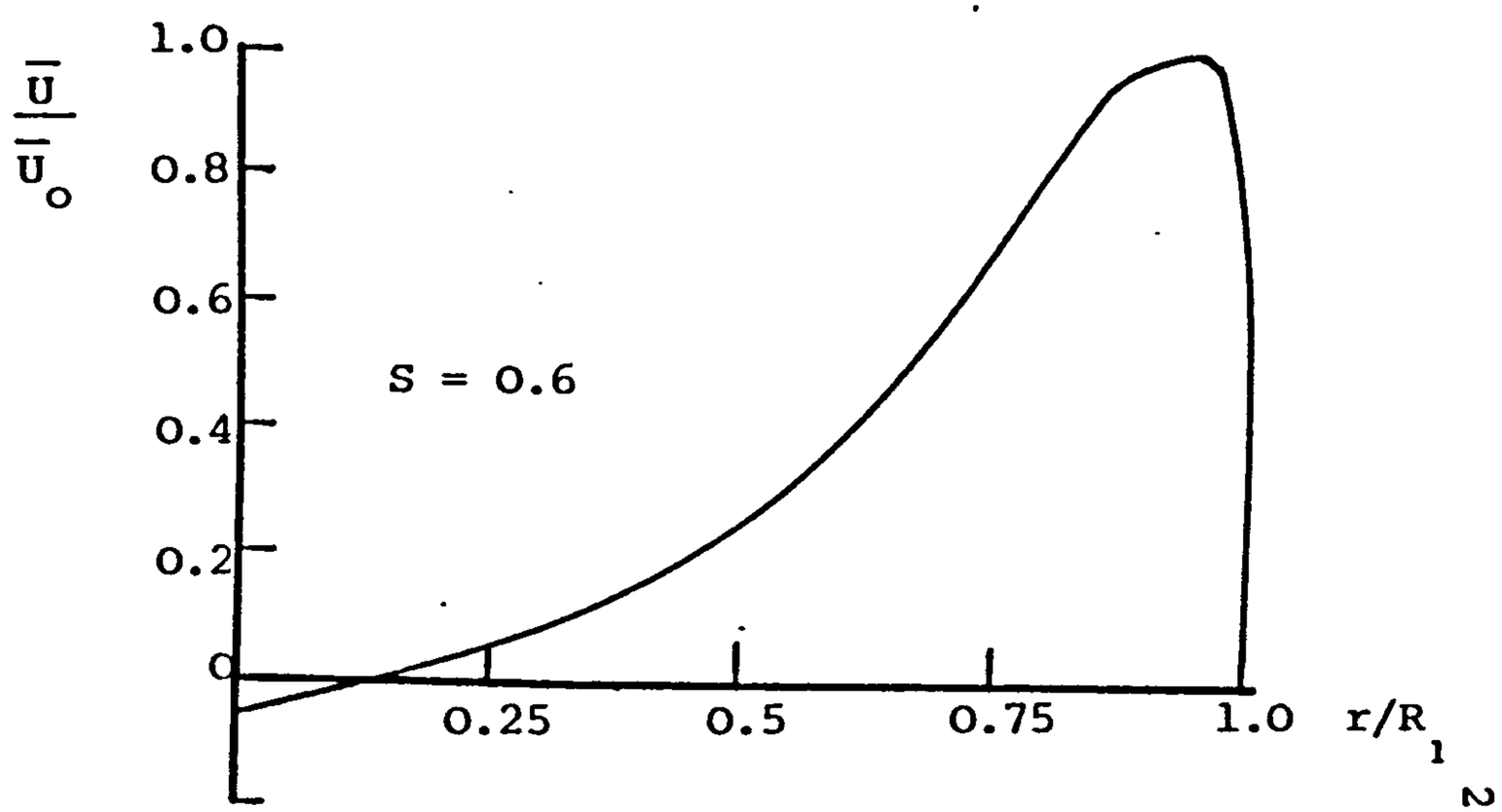
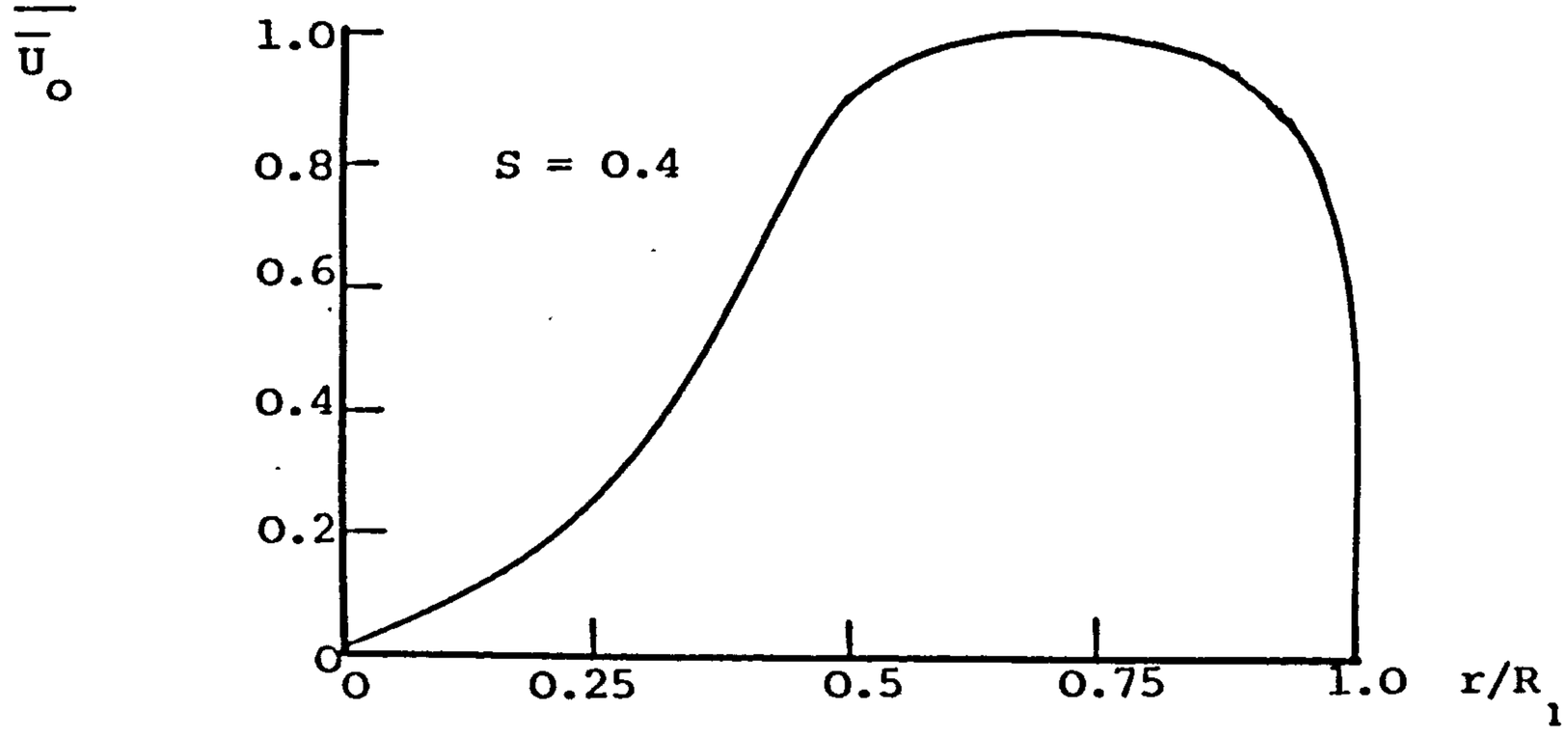


Fig. 5.18 (Continued)







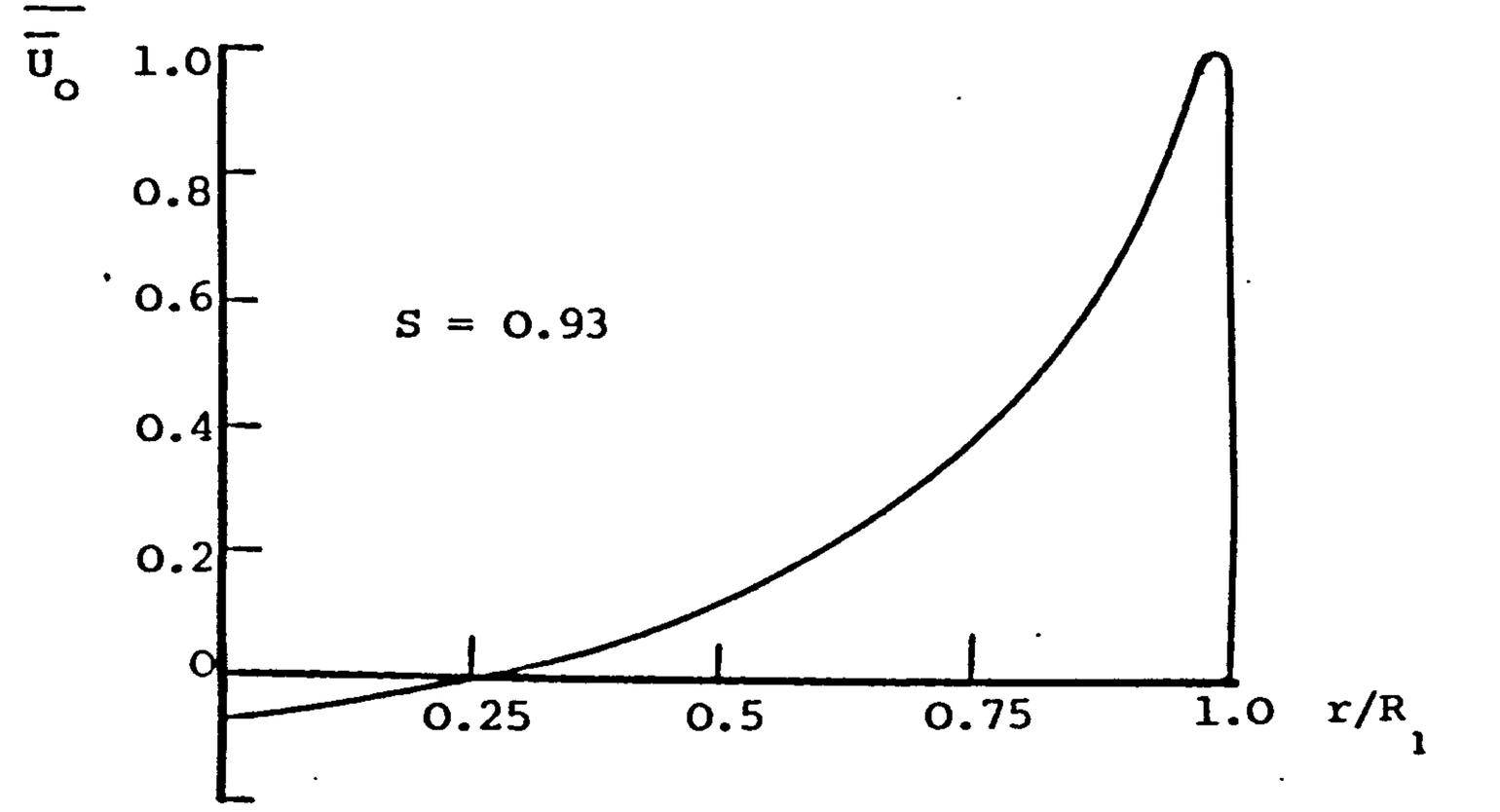
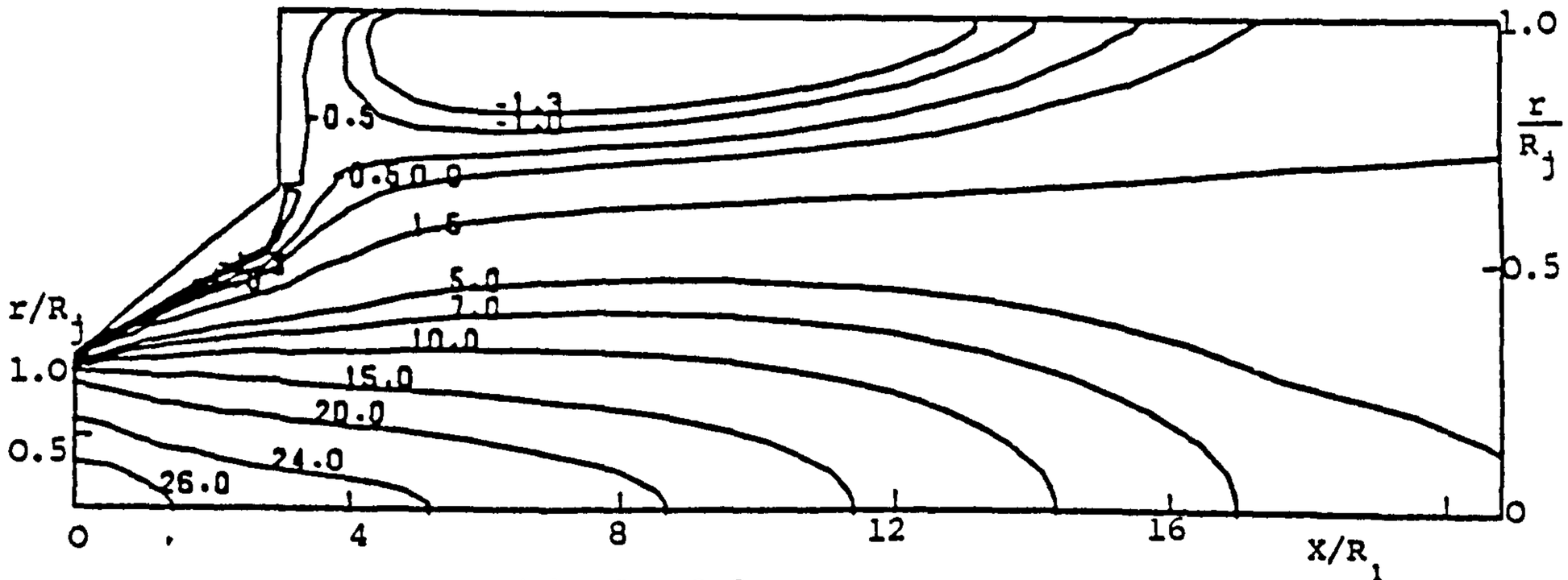
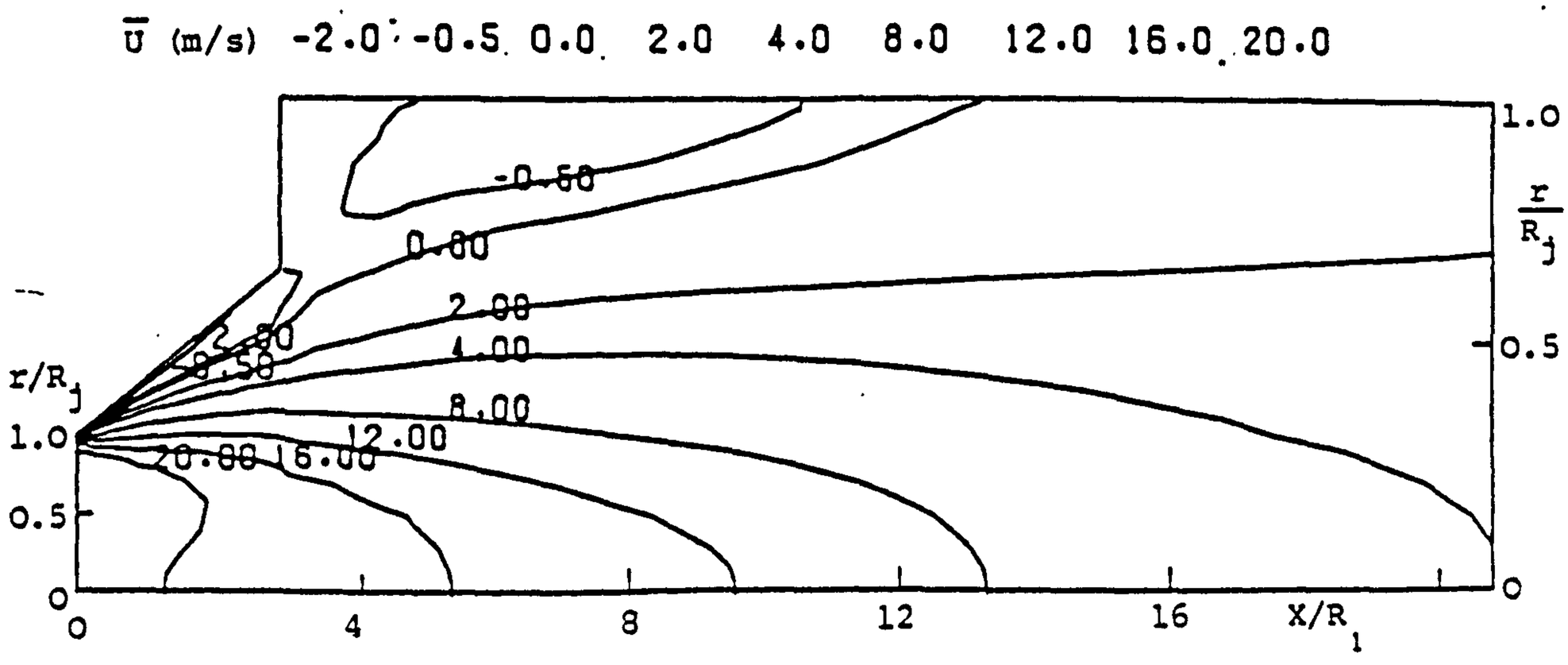


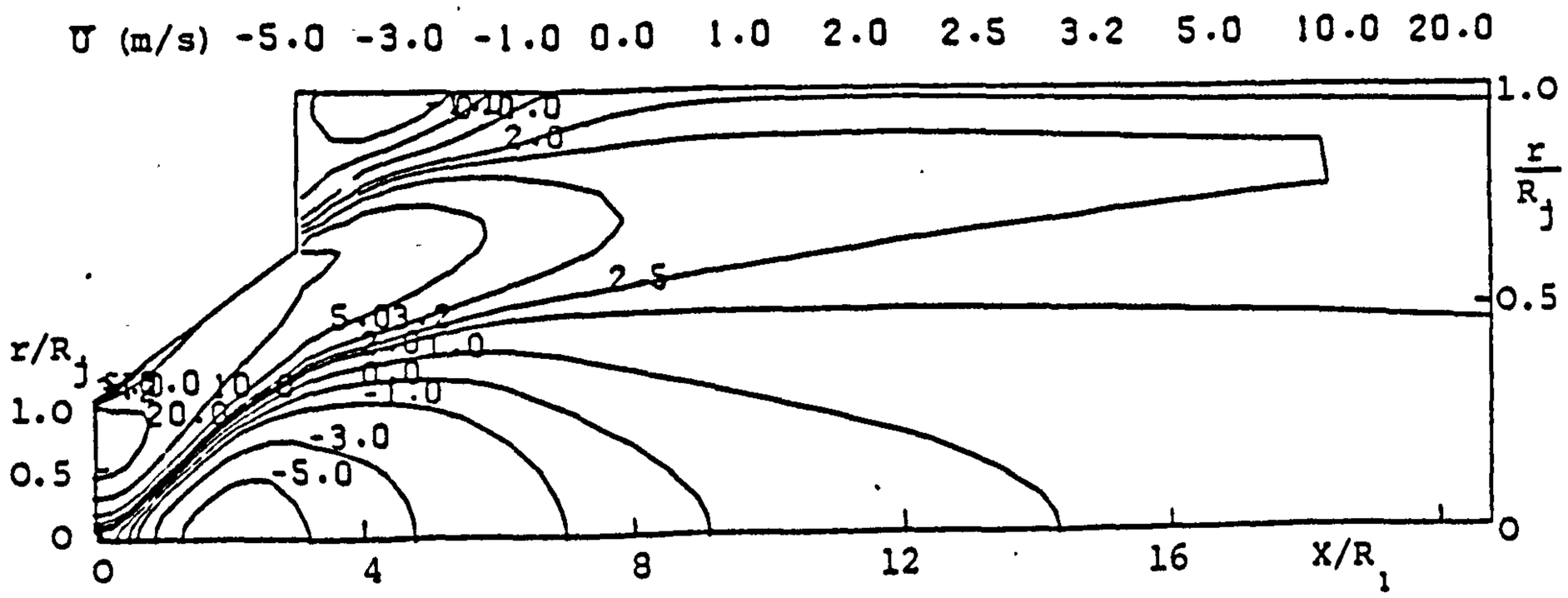
Fig. 5.19 Inlet Distributions of the Axial Mean Velocity



(a) S = 0.0

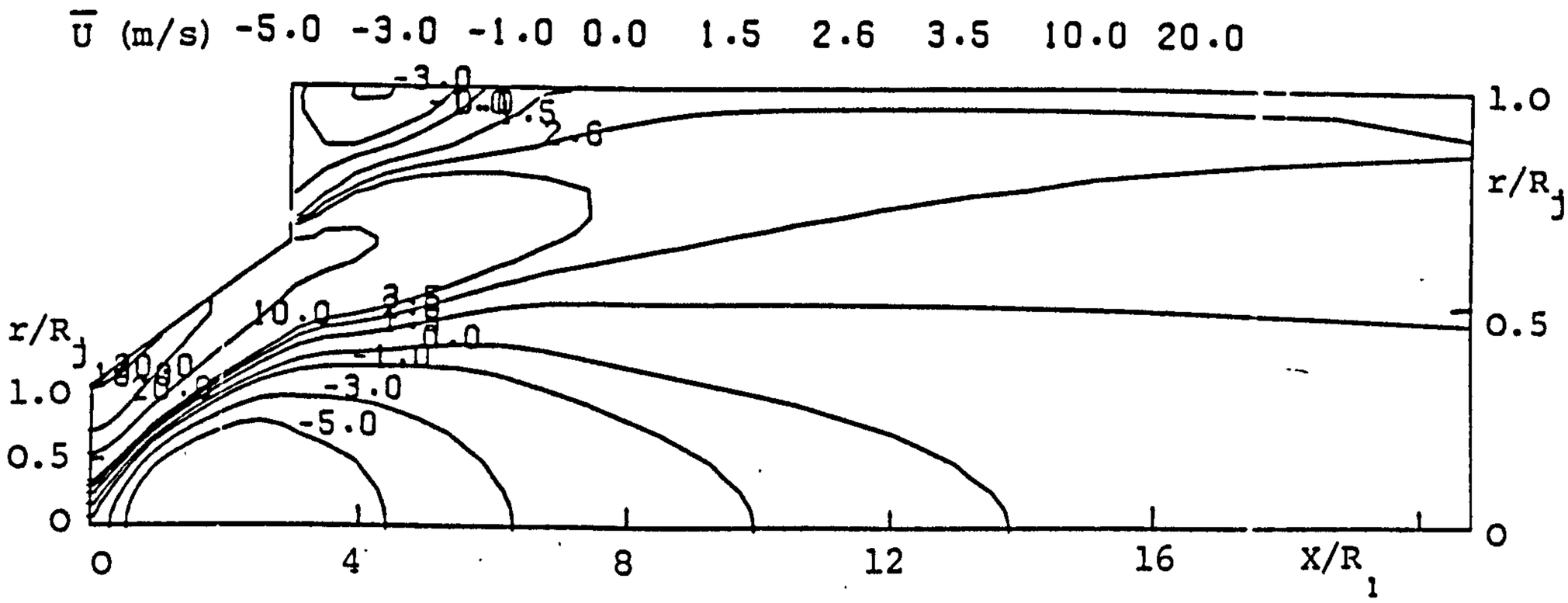


(b) S = 0.2

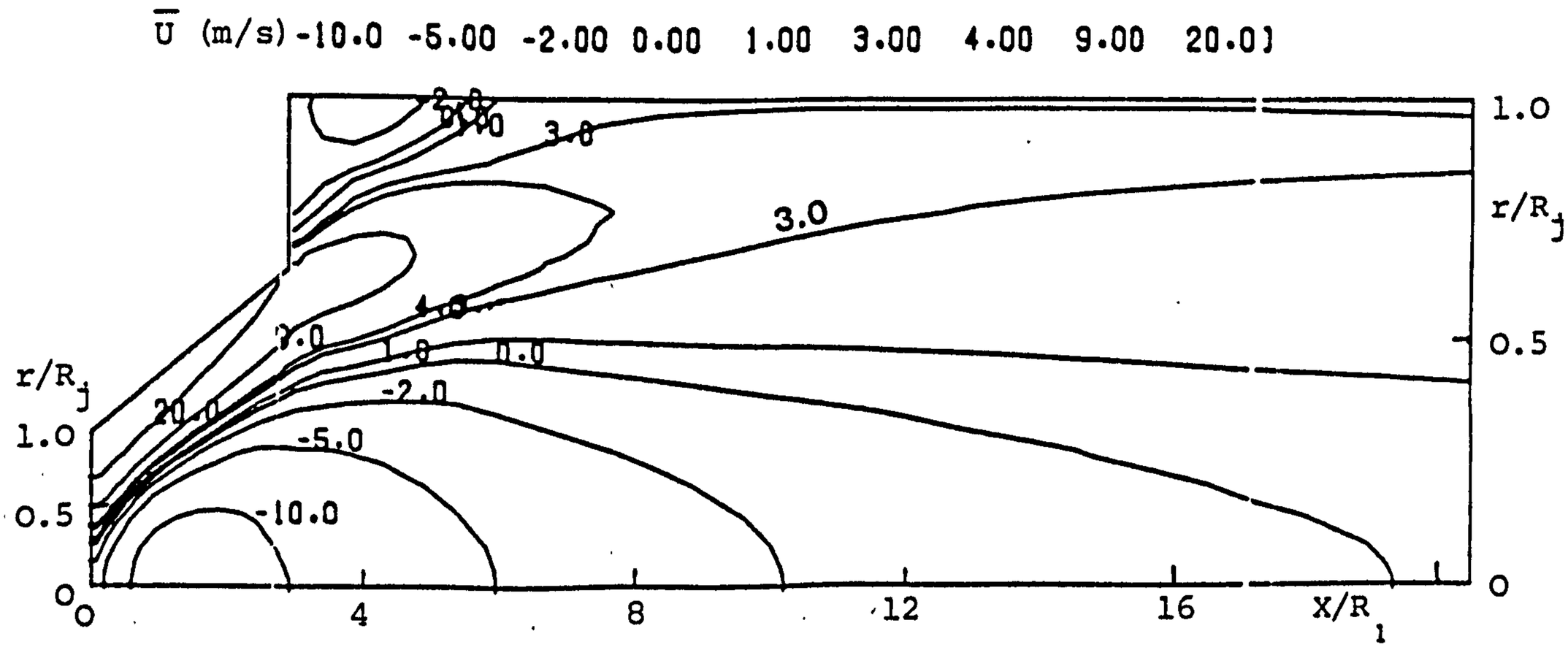


(c) S = 0.4

Fig. 5.20 Contours of the Calculated Axial Mean Velocity in G2

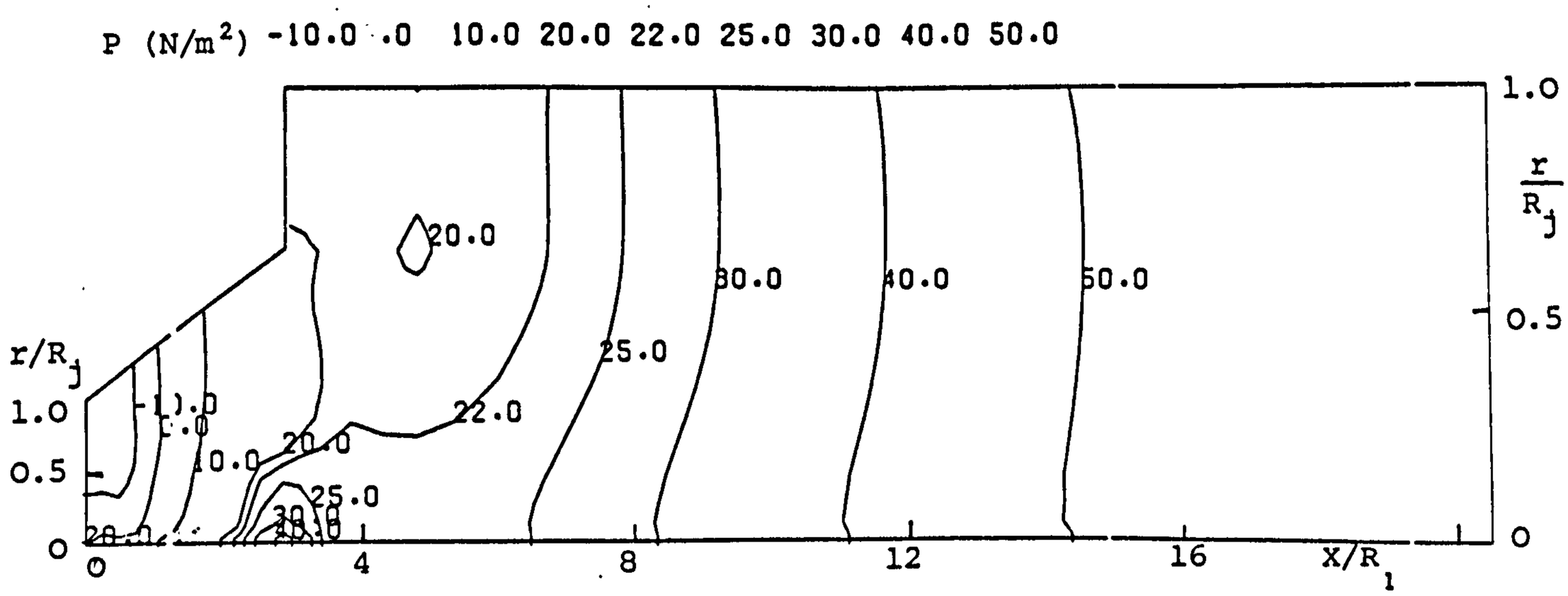


(d) S = 0.6

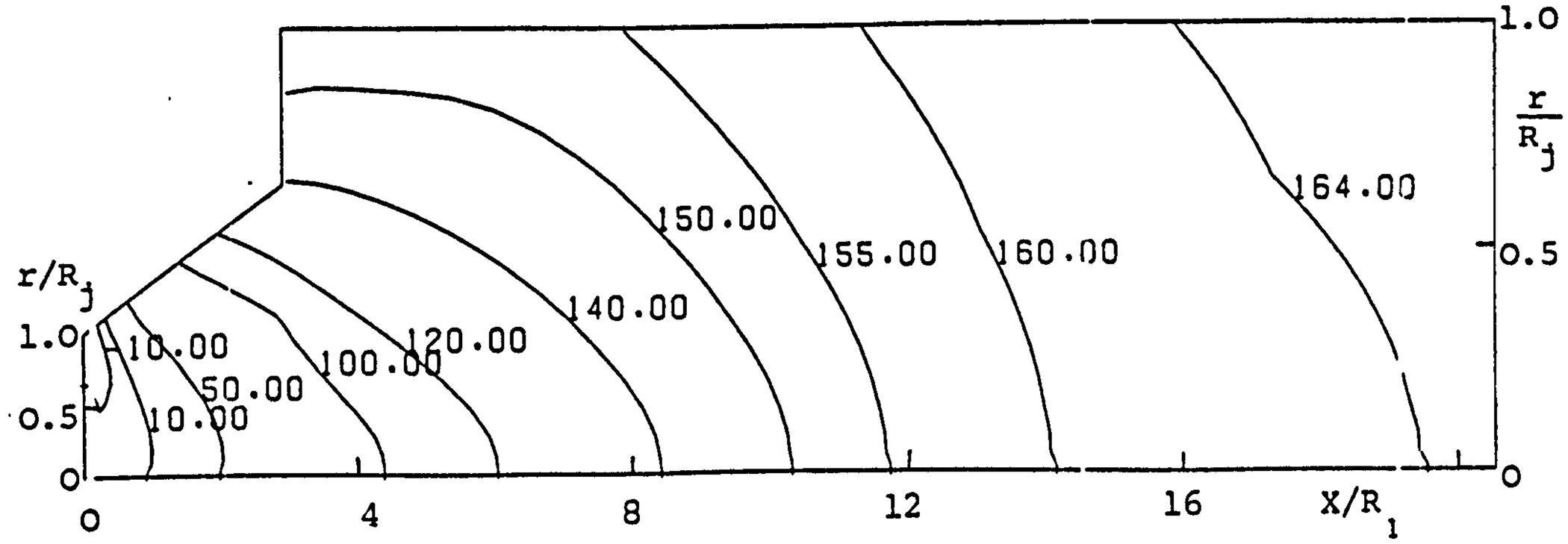


(e) S = 0.93

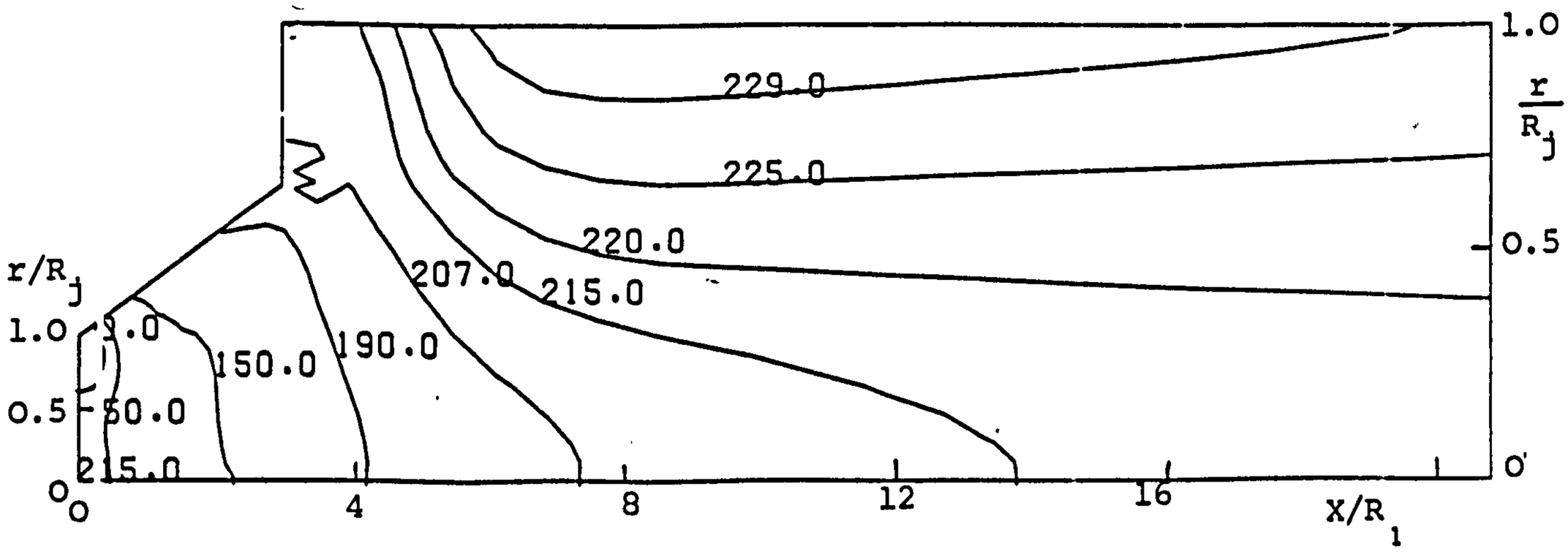
Fig. 5.20 (Continued)



(a) S = 0.0

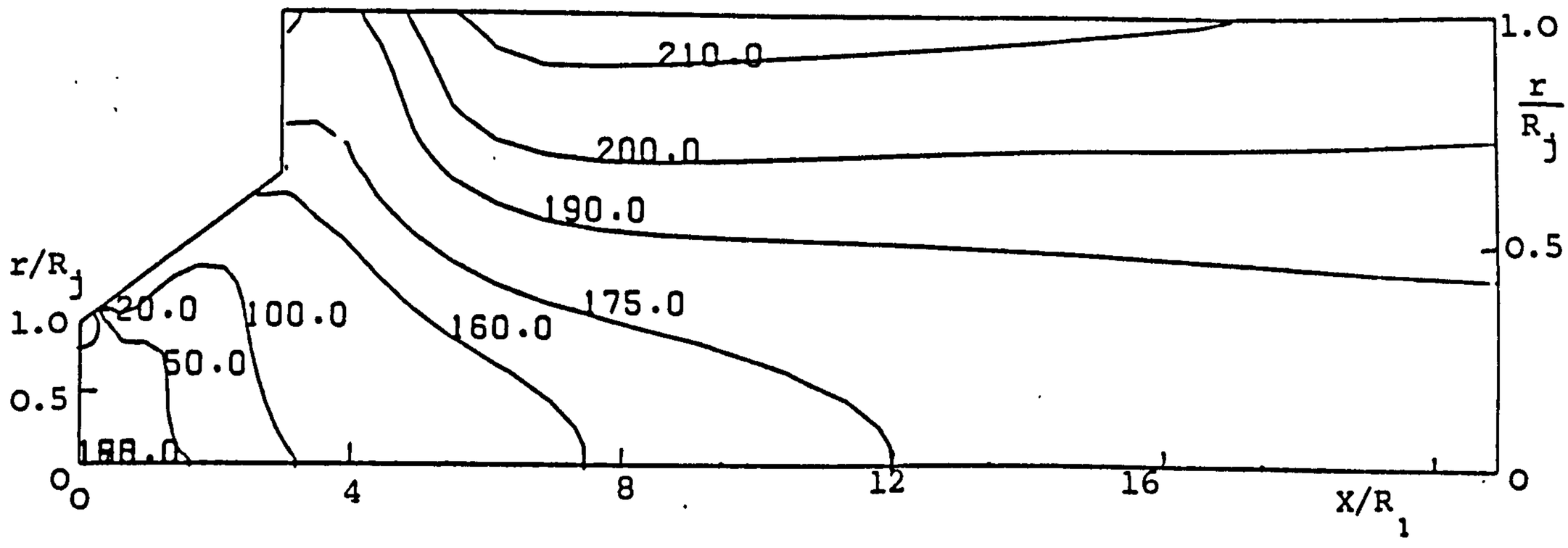


(b) S = 0.2

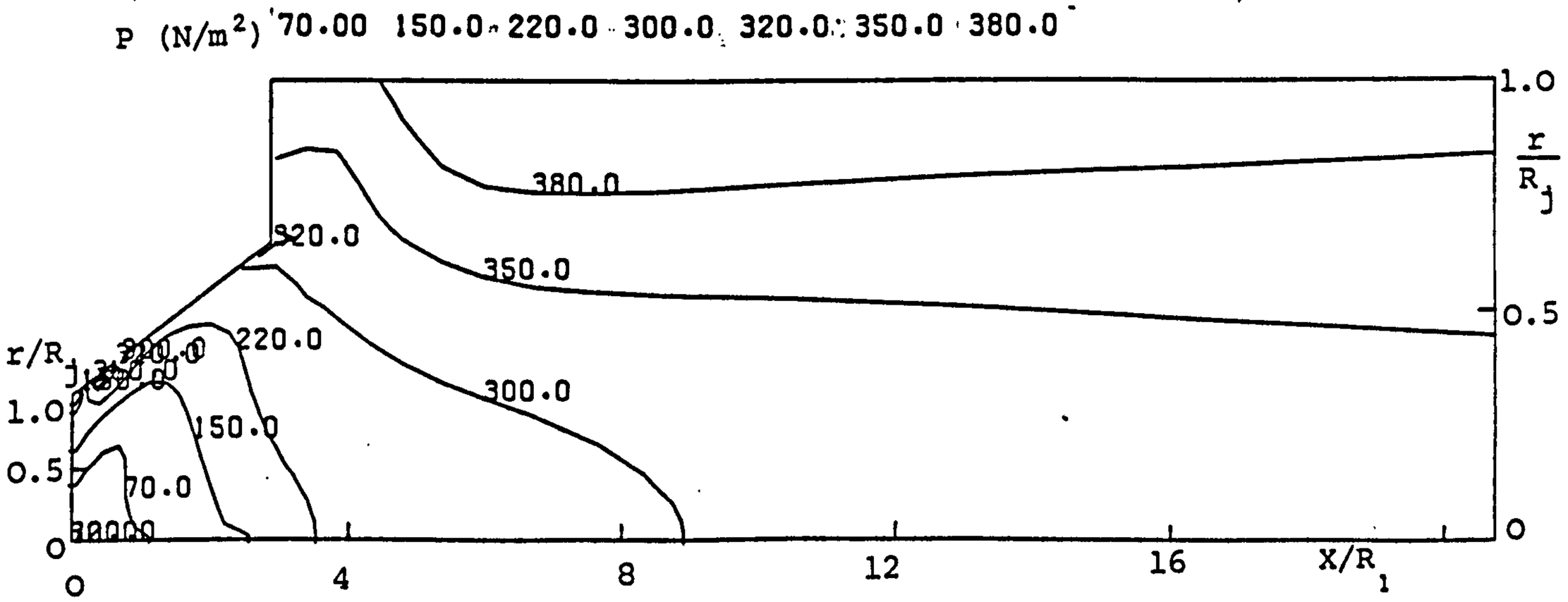


(c) S = 0.4

Fig. 5.21 Contours of the Calculated Static Pressure

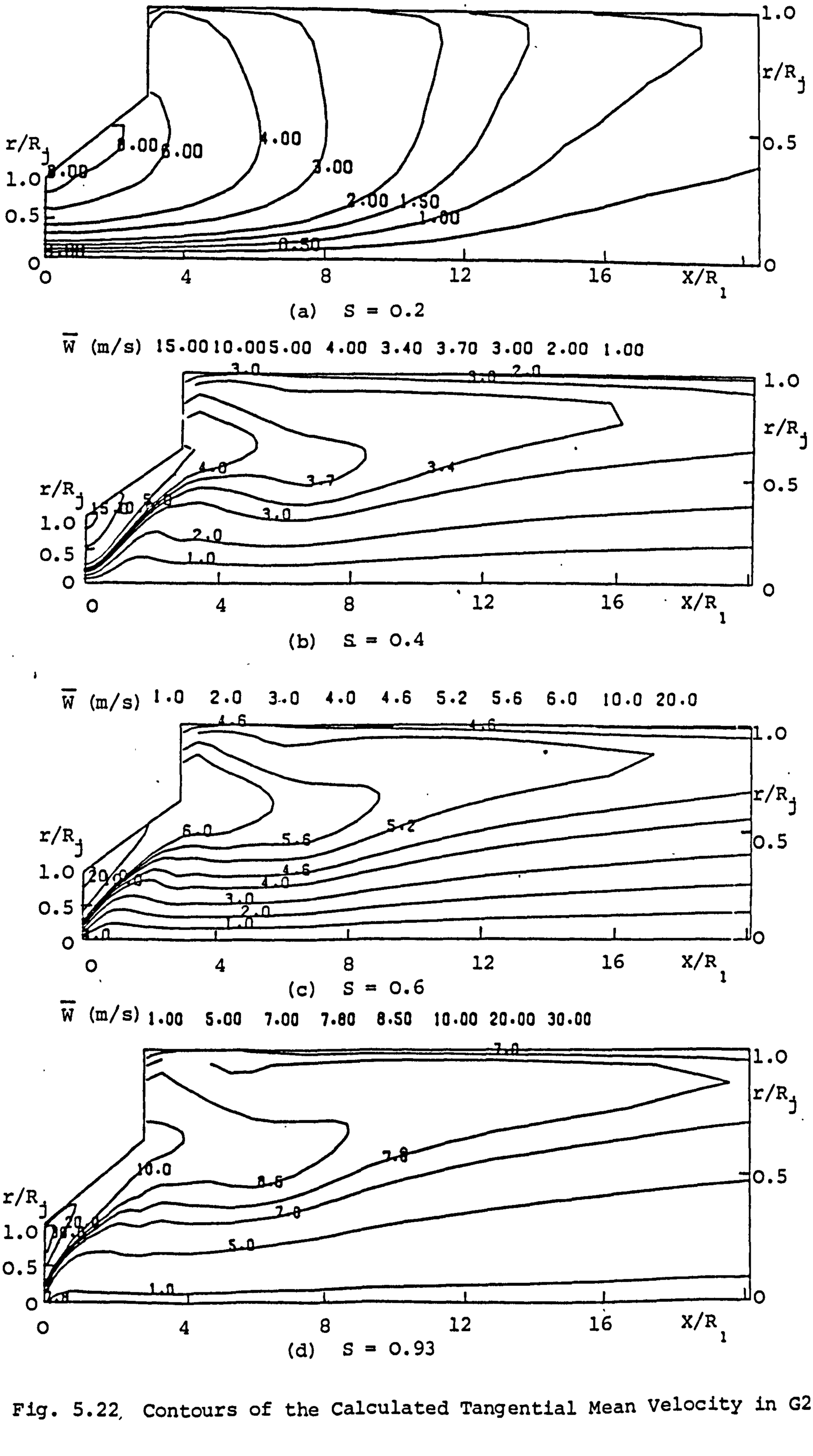


(d) S = 0.6



(e) S = 0.93

Fig. 5.21 (Continued)



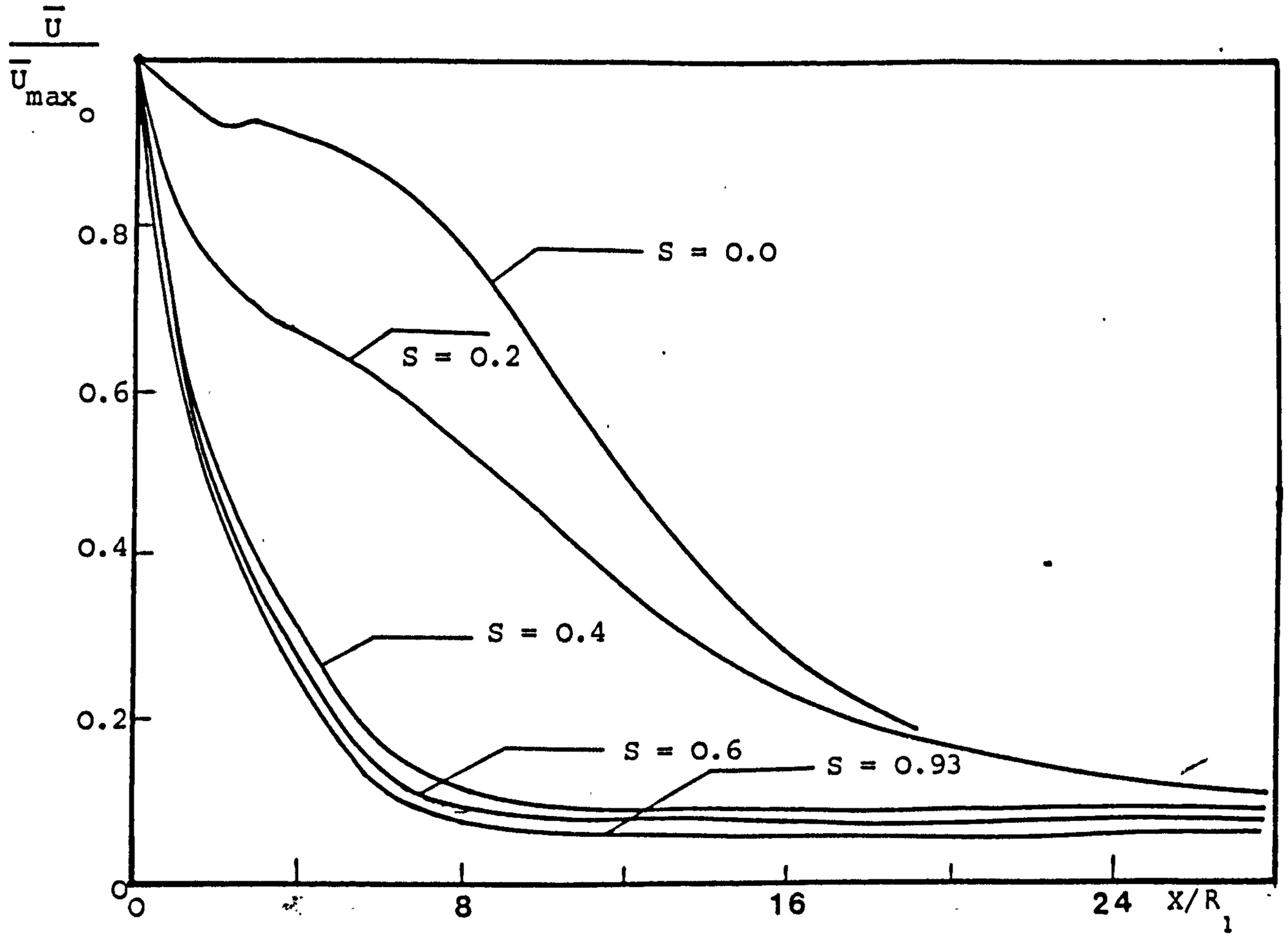
(a) S = 0.2

(b) S = 0.4

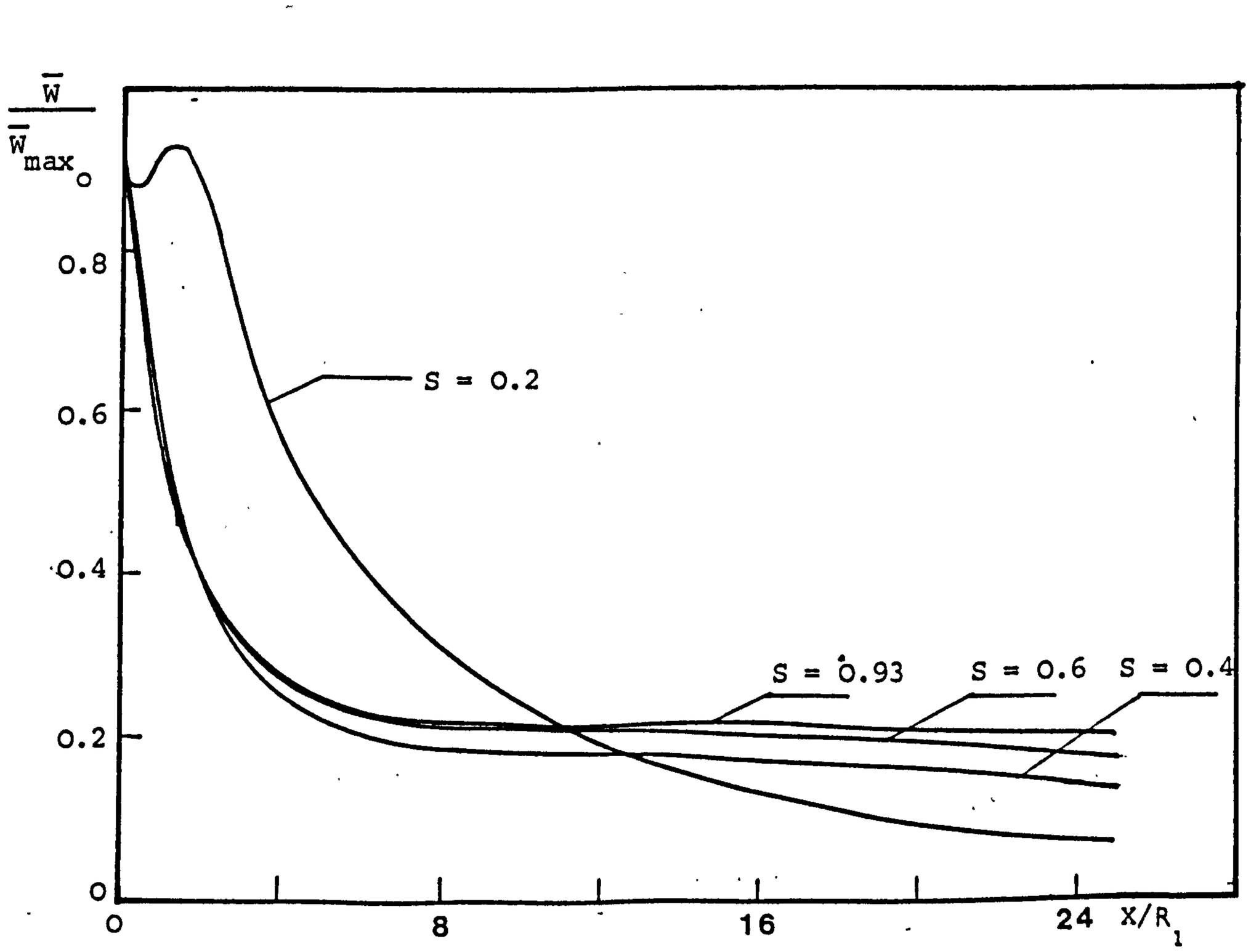
(c) S = 0.6

(d) S = 0.93

Fig. 5.22 Contours of the Calculated Tangential Mean Velocity in G2

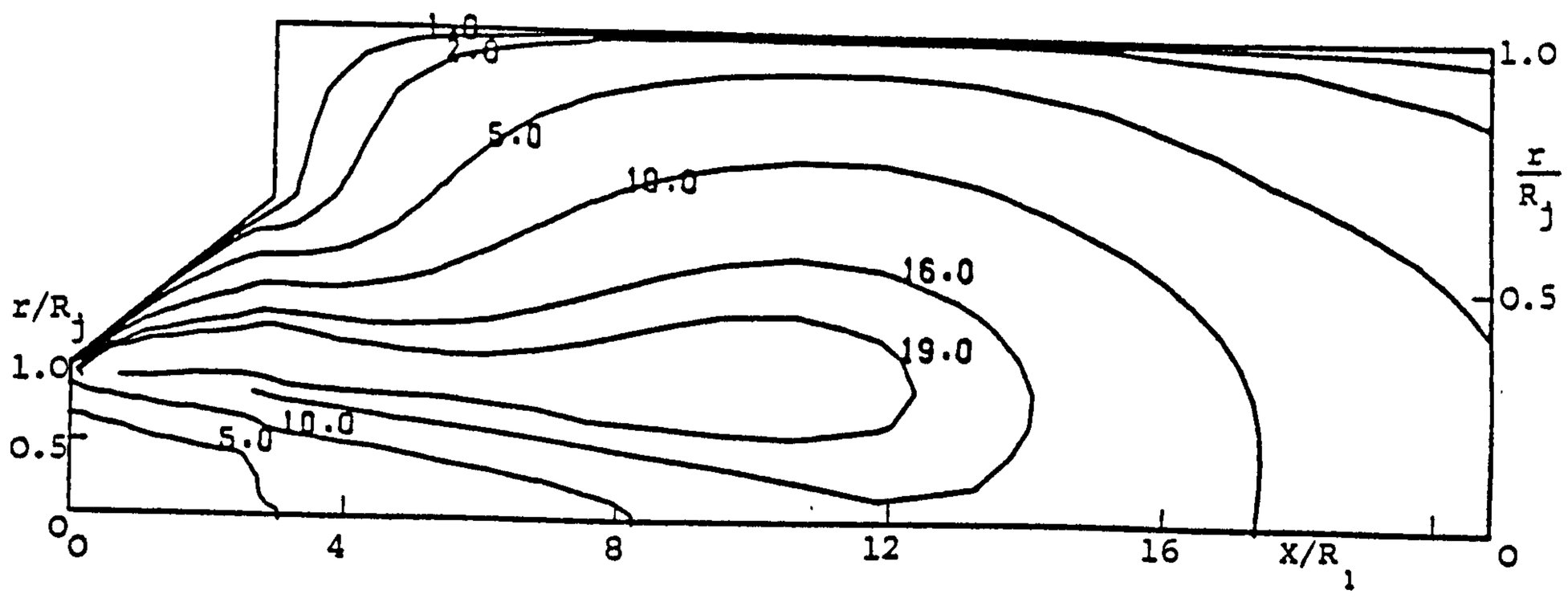


(a)

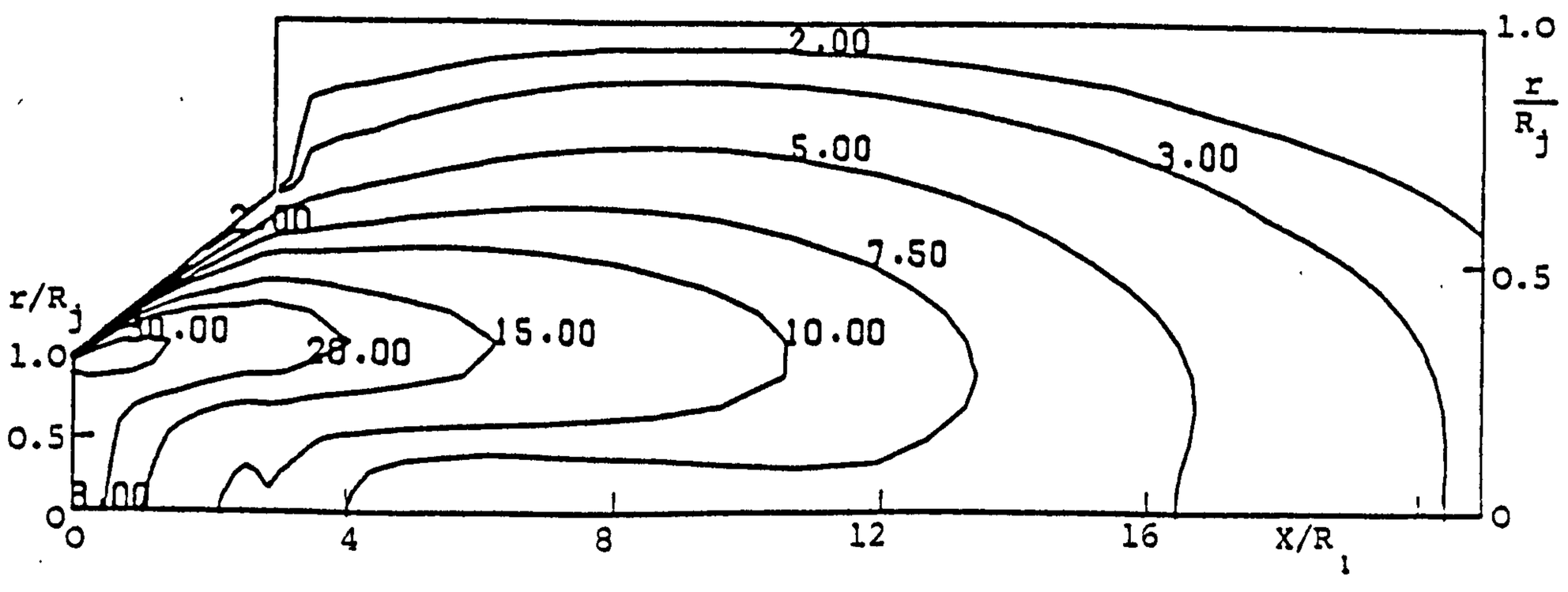


(b)

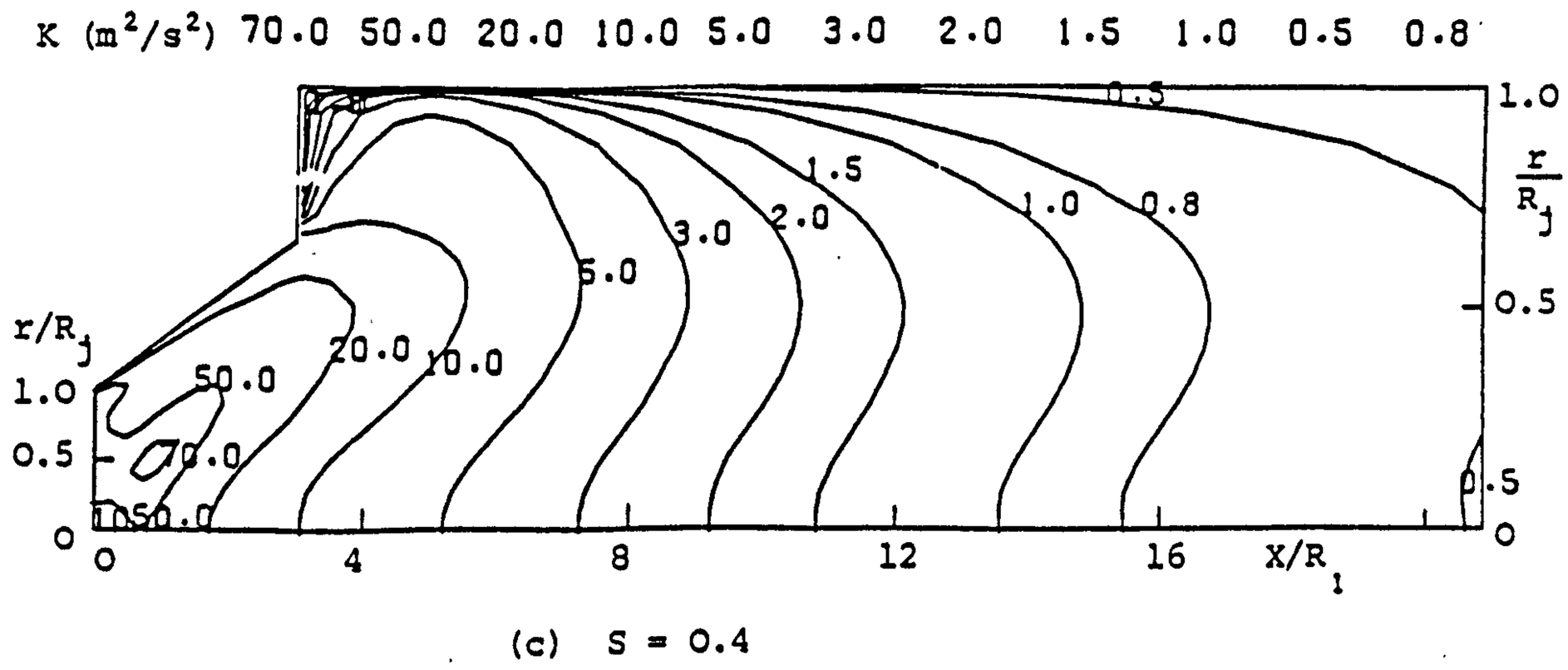
Fig. 5.23 Decay of Axial and Tangential Mean Velocities with the Increase in the Swirl Number
(a) Axial Velocity; (b) Tangential Velocity



(a) S = 0.0

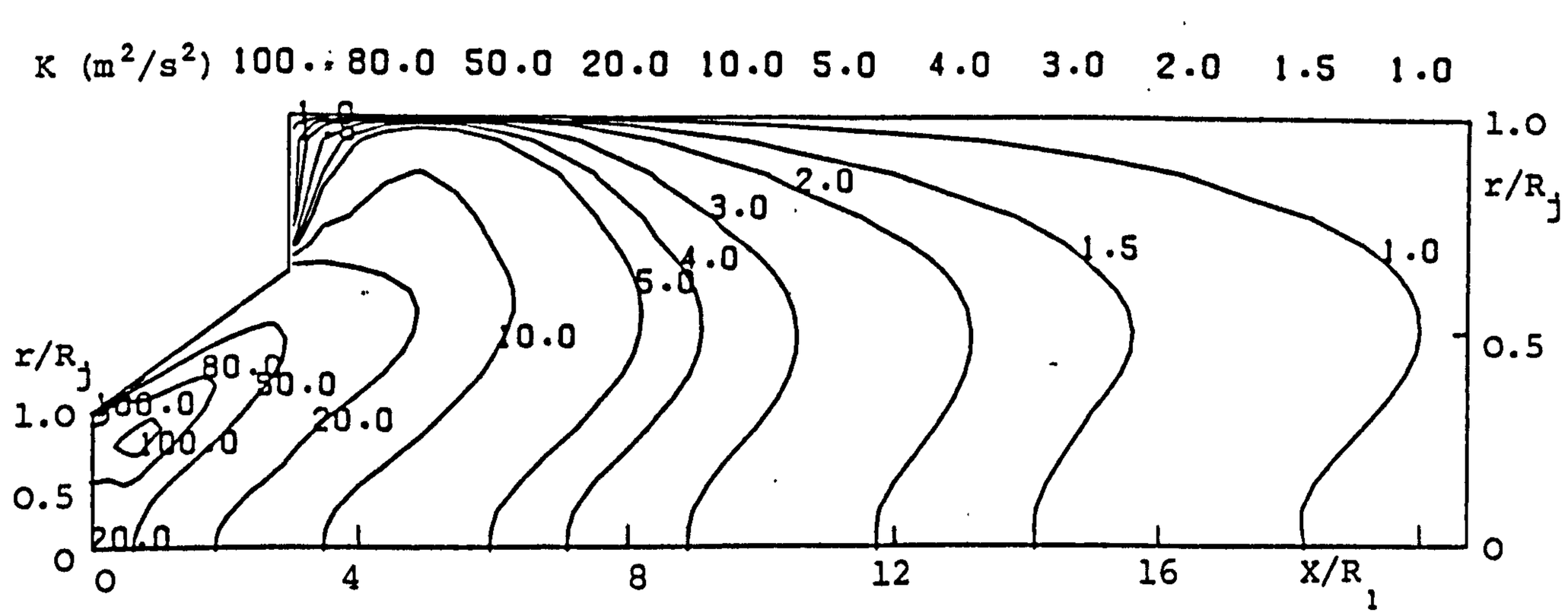


(b) S = 0.2

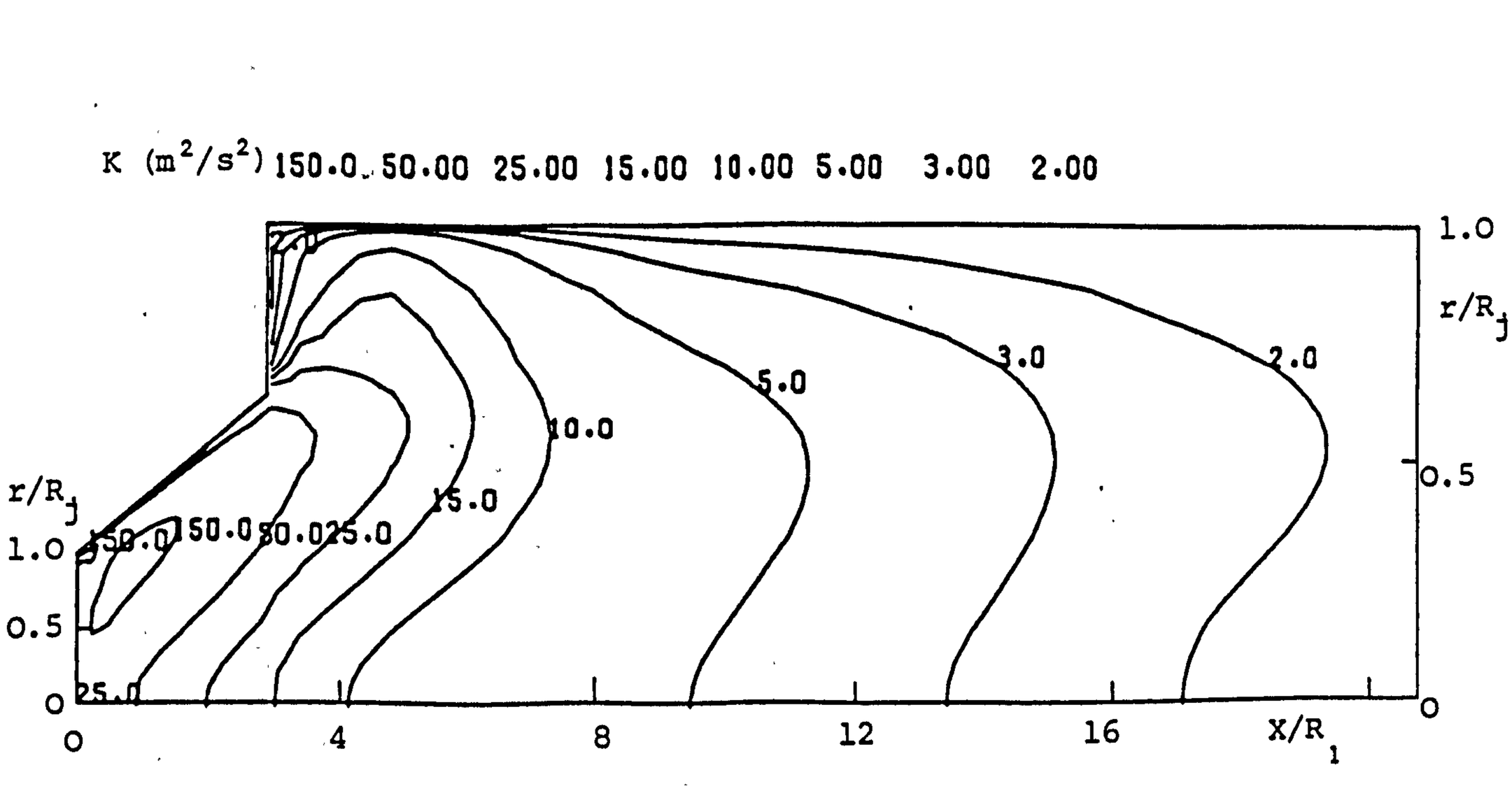


(c) S = 0.4

Fig. 5.24 Contours of the Calculated Kinetic Energy of Turbulence in G2

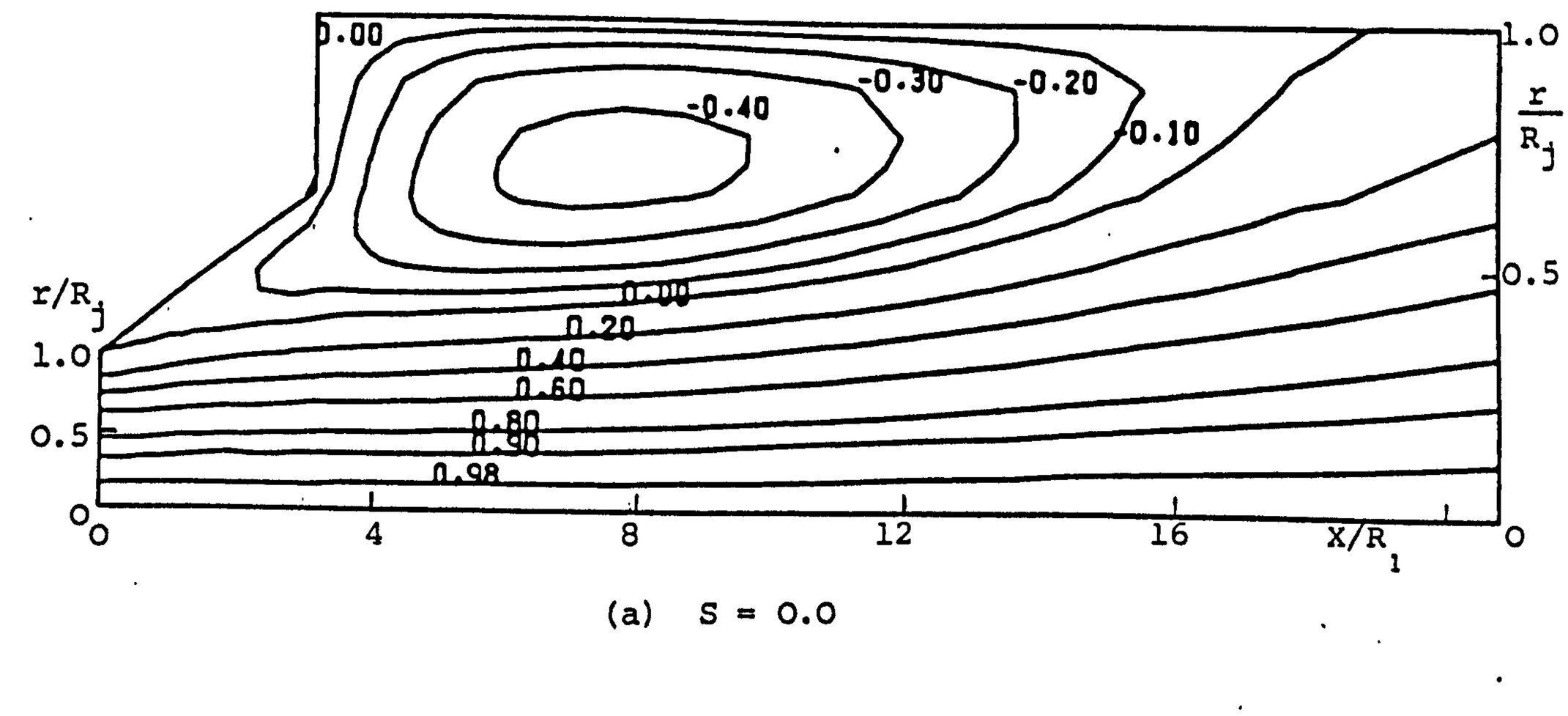


(d) S = 0.6

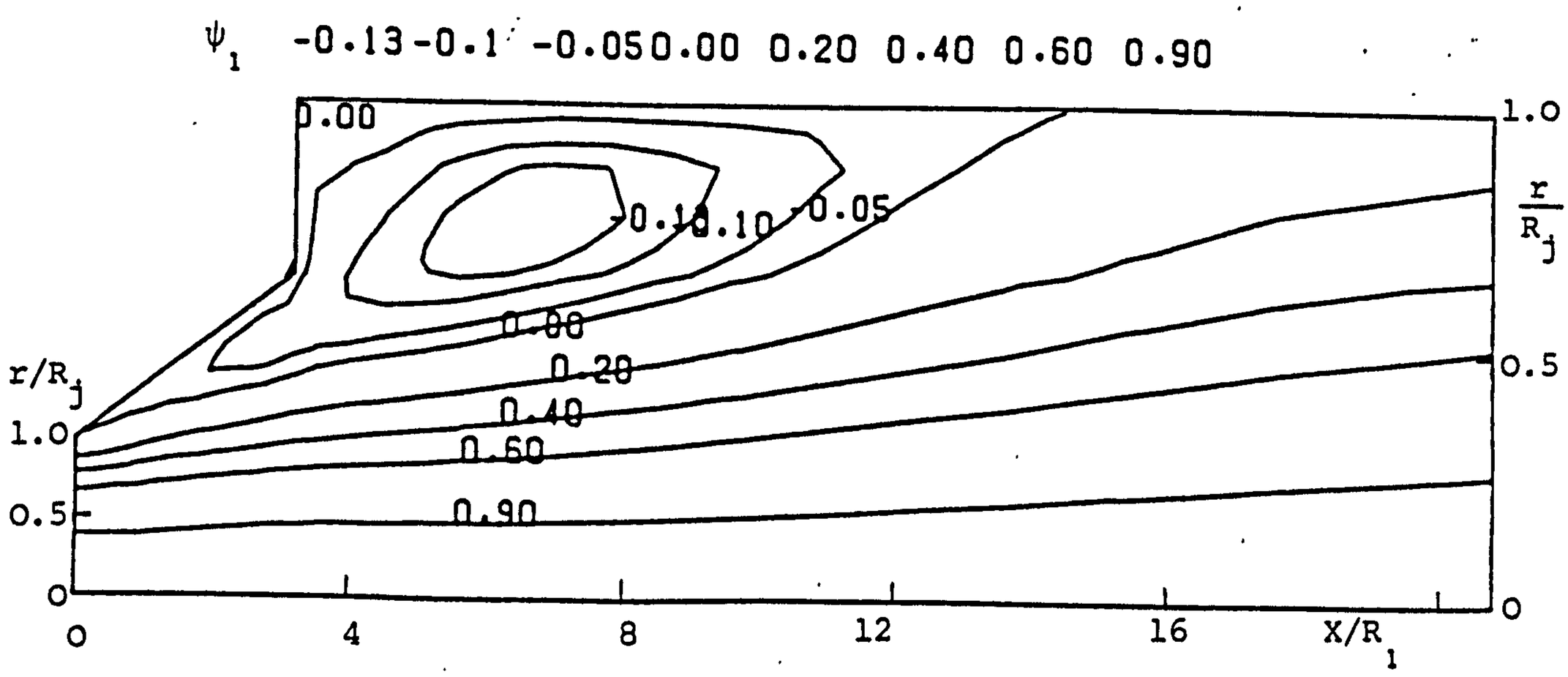


(e) S = 0.93

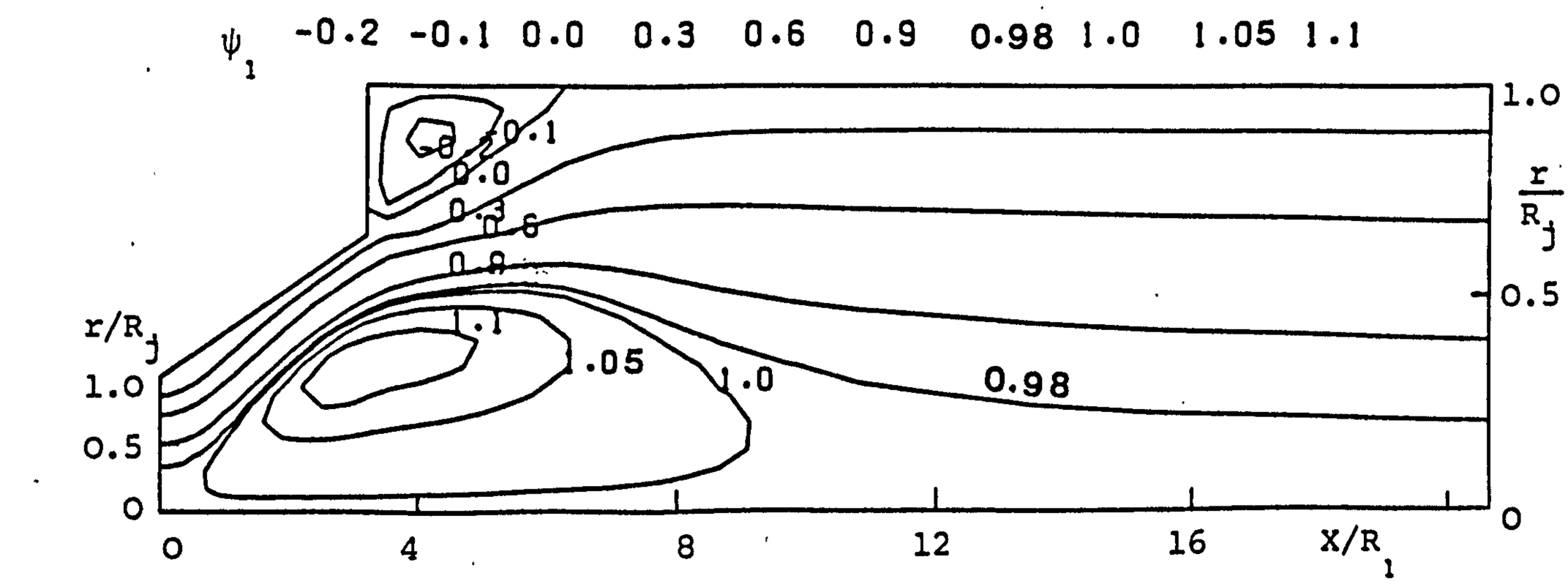
Fig. 2.24 (Continued)



(a) S = 0.0

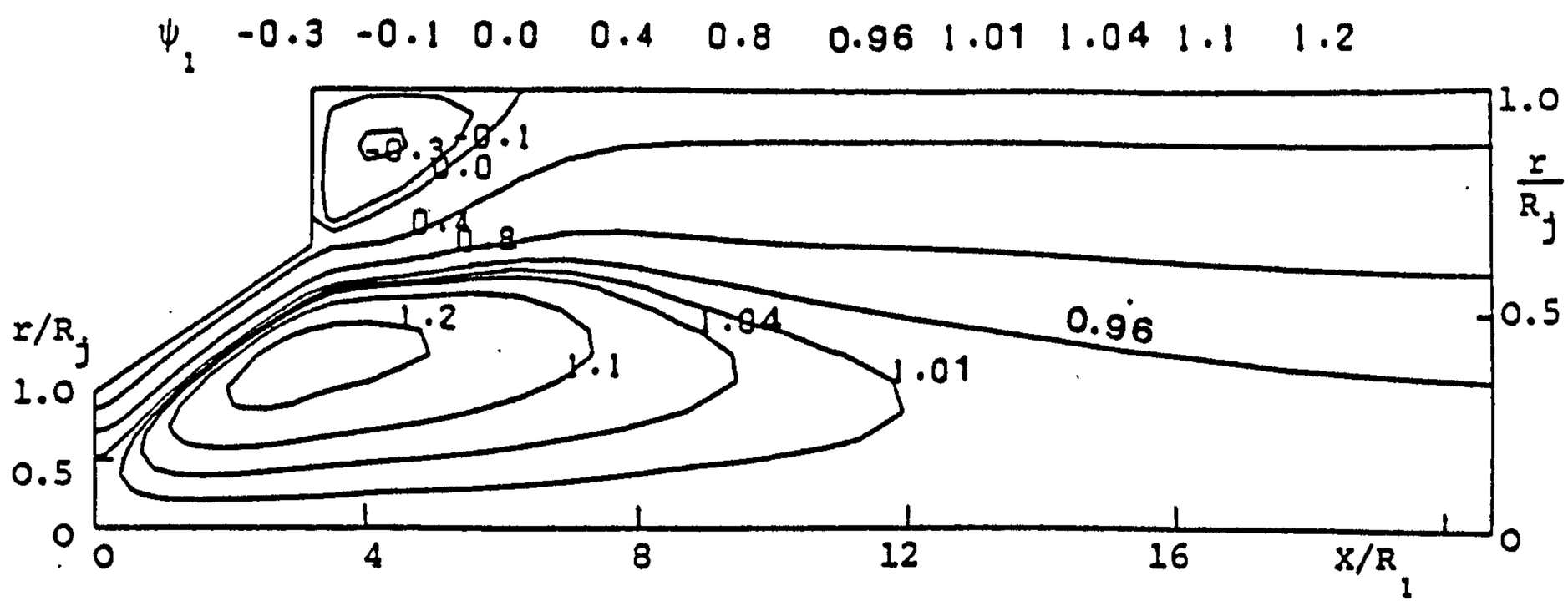


(b) S = 0.2

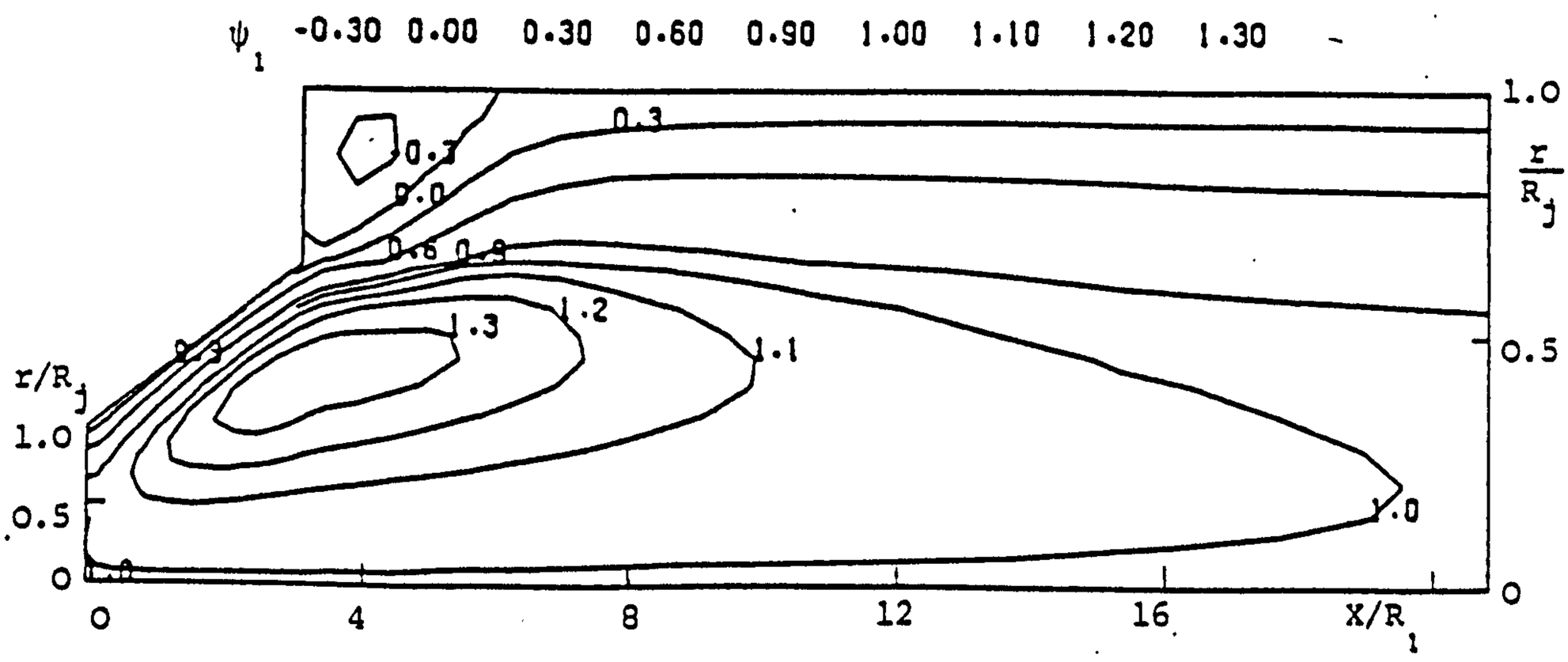


(c) S = 0.4

Fig. 5.25 Contours of the Calculated Stream Function, ψ_1, in G2



(a) S = 0.6



(b) S = 0.93

Fig. 5.25 (Continued)

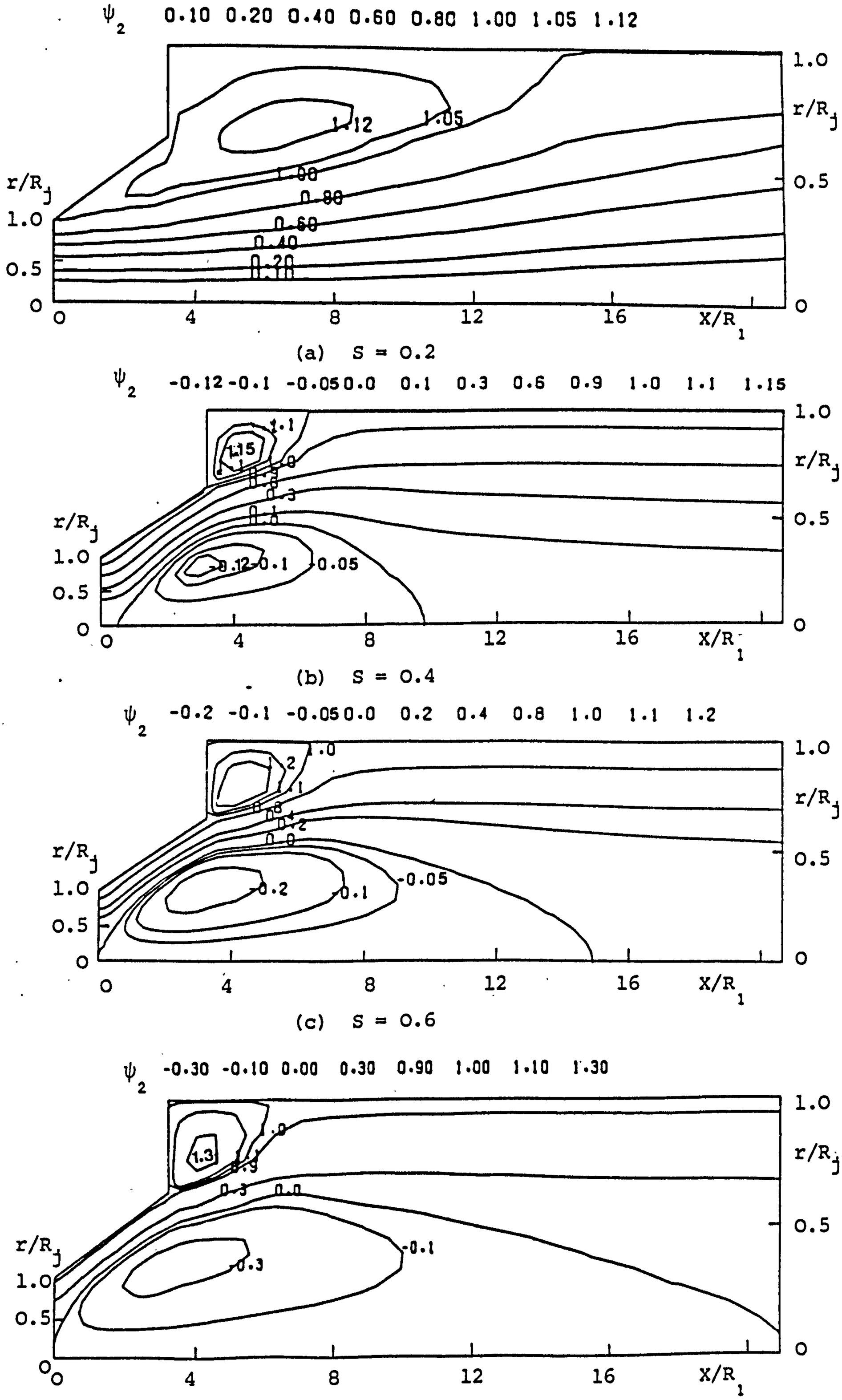
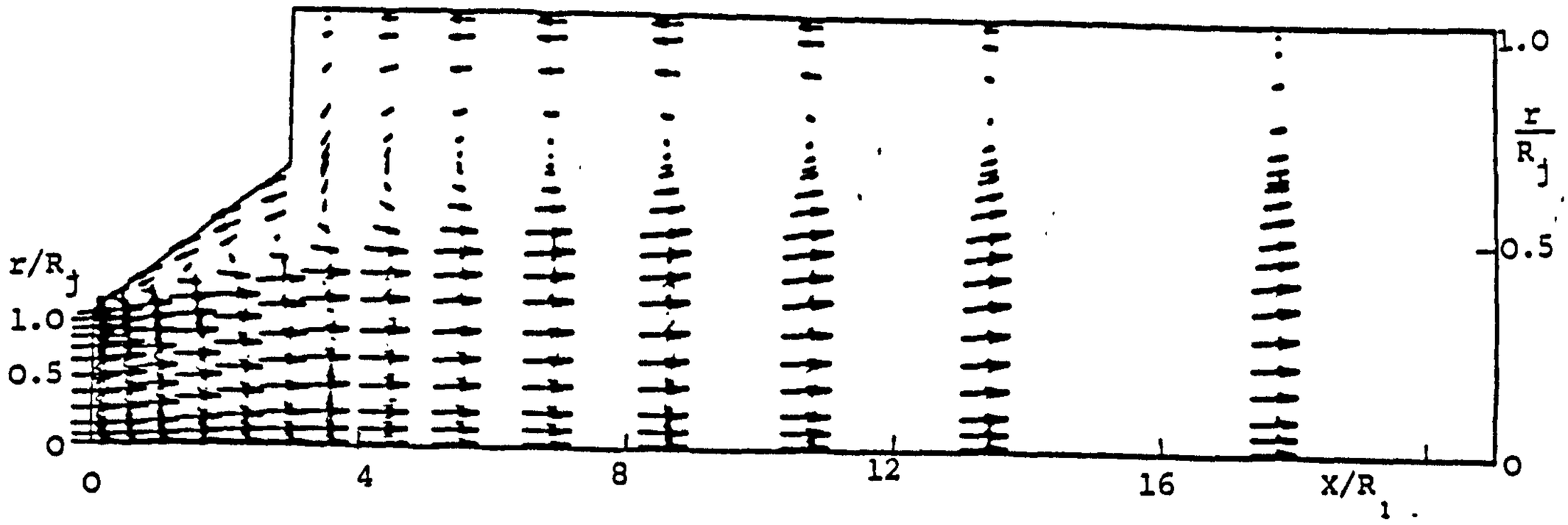
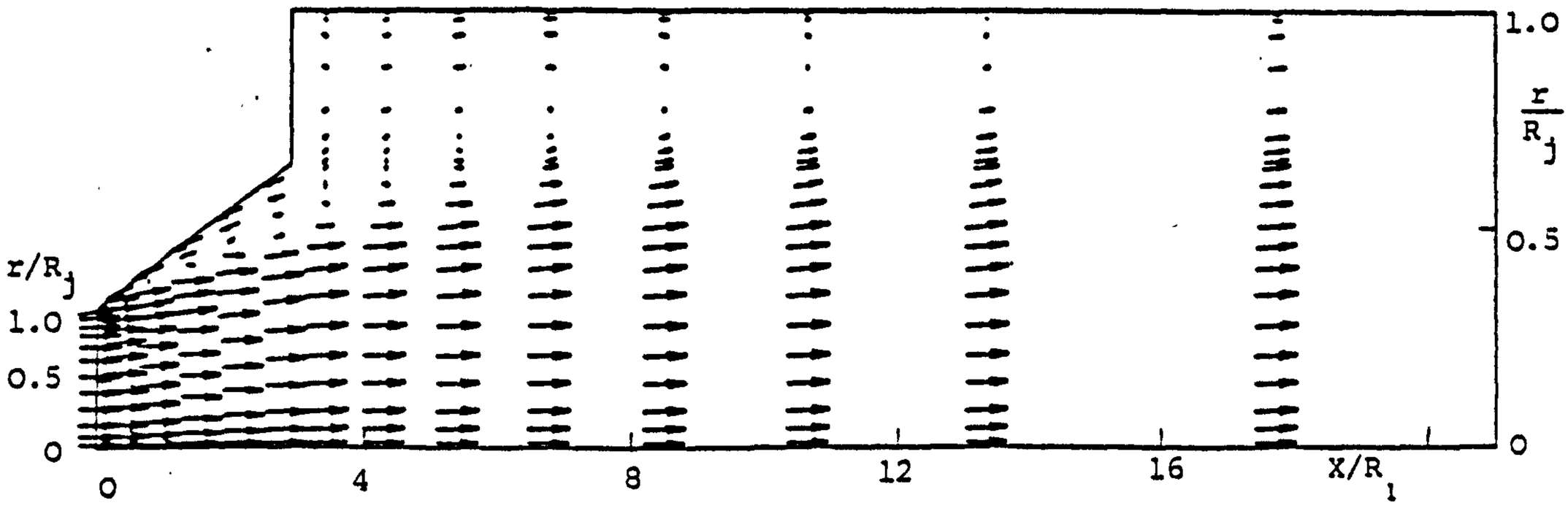


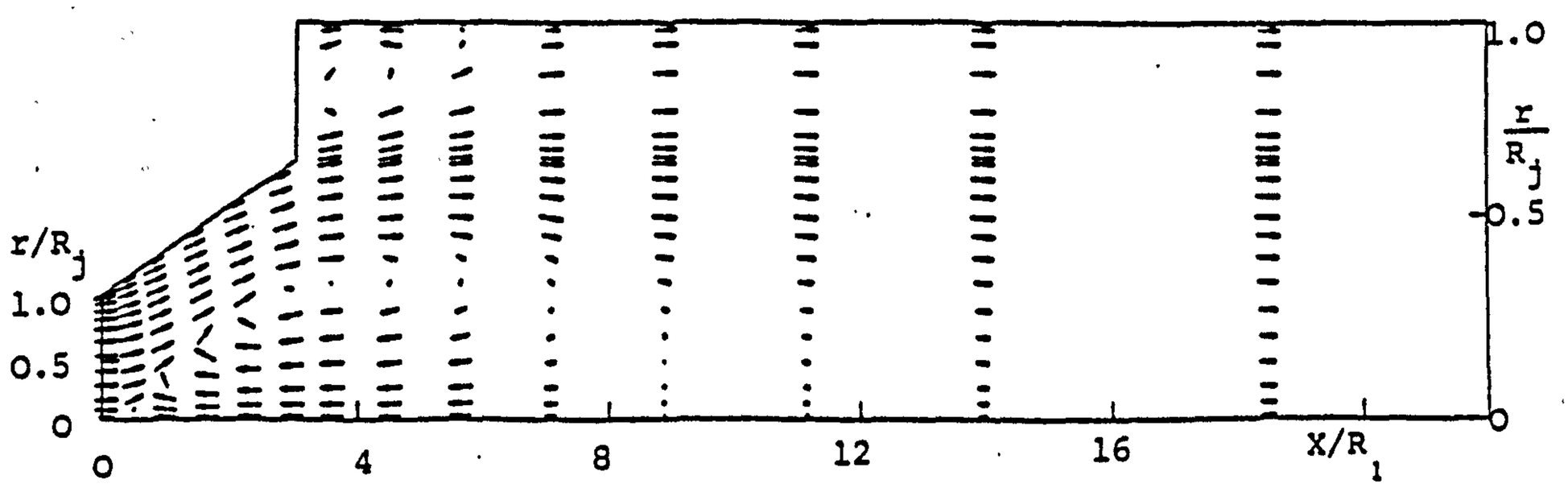
Fig. 5.26 Contours of the Calculated Stream Function, ψ_2, in G2



(a) S = 0.0

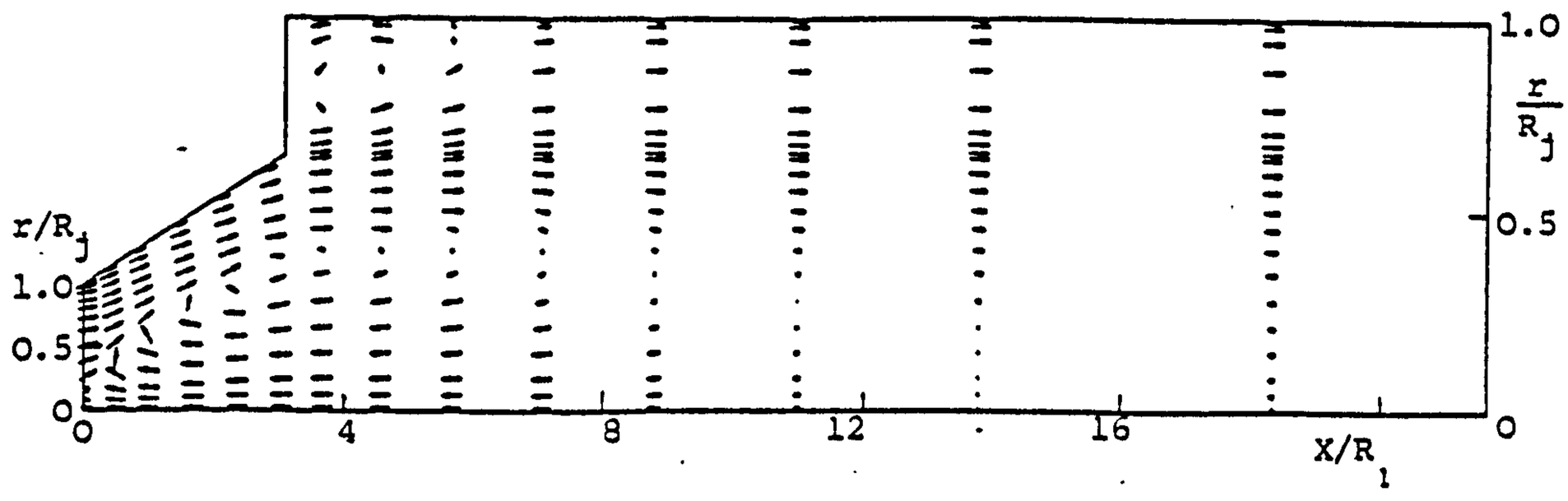


(b) S = 0.2

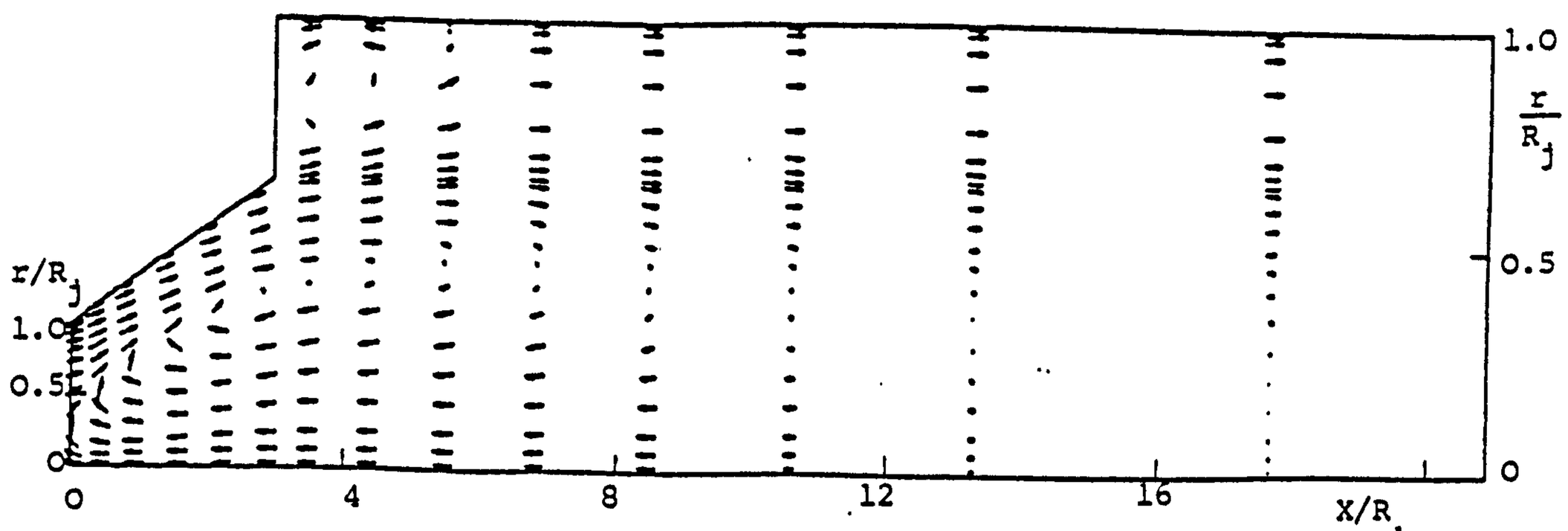


(c) S = 0.4

Fig. 5.27 Calculated Velocity Vector Distributions in G2



(d). S = 0.6



(e) S = 0.93

Fig. 5.27 (Continued)

CHAPTER 6

CLOSURE

A summary of the main conclusions of the present investigation is given in the first section of this chapter. Recommendations for future experimental and theoretical work are discussed in the second section.

6.1 Achievements of the Present Work

The main achievements of the present study and the conclusions thereof may be summarized as follows:-

(1) Measurements of mean velocity and turbulence characteristics were achieved in confined double coaxial jets for two velocity ratios and with and without swirl. The results provide new and valuable experimental information which can be used to test the extension of turbulence models to strongly elliptic flows.

The measurements were obtained by hot-wire anemometer, laser anemometer and pitot tube and so allow a comparison between two obtrusive and one unobtrusive measuring techniques. The comparison was obtained in regions of low and high turbulence intensity and in reverse flow regions and thus the accuracy of each technique in such flows was discussed and better assessment and precision of the results were achieved. The comparison indicated discrepancies between the results of the three techniques particularly in the recirculating flow and that their magnitudes were seldom sufficiently great to permit erroneous fluid mechanic conclusions.

The results without swirl have shown that the larger velocity ratio gives rise to steeper mean velocity gradients and so larger

values of normal stress in the mixing region and immediately downstream of the recirculating flow; the corresponding intensities are also larger. Comparison with the previous results for unconfined flow indicates that the confinement leads to increased values of turbulence intensity in the region downstream of the mixing region. In the upstream region, the mixing of the two streams dominates the central region of the flow and the flow properties are not greatly influenced by the confinement.

The results with swirl of 0.23 in the outer jet for the 3.0 velocity ratio indicate a region of near-recirculation on the centre-line between one and three furnace diameters downstream of the exit plane.

2. Measurements of mean velocity, Reynolds stresses and probability density distributions were achieved in four developing expanding flows in two different geometries with swirl numbers of 0.0 and 0.93. The measurements were obtained by laser Doppler anemometry and present accurate data which help in understanding the properties of the flow field which simulates that of high intensity combustion furnaces and assist the improvement of turbulence-modelling procedures for increasingly complex flows.

The results for zero swirl number showed that the Reynolds-stress generation is connected to the main strain, $\partial\overline{U}/\partial y$, in the upstream region. This connection breaks down in the downstream region and the production of the kinetic energy of turbulence is connected to the maximum value of the Reynolds stresses. The results also showed the importance of the extra strain terms on the generation of the kinetic energy of turbulence particularly in the case of swirl. The effect of these high strain rates on the Reynolds stresses are not well

presented by any of the present turbulence models and suggests that these models are inadequate to represent such flows.

3. A solution procedure was presented and applied to the prediction of the flow properties in the confined double coaxial jet with sudden expansion. Elliptic equations, obtained for the continuity, momentum and the rate of turbulence dissipation equation were solved numerically together with either an equation for the kinetic energy of turbulence (mean-flow closure) or equations for four Reynolds stresses (Reynolds-stress closure).

The comparison between the experimental and predicted results for the two velocity ratios indicates that the general features of the flow fields are correctly predicted by the three models of turbulence used. The Reynolds-stress models showed better agreement near and inside the recirculation zone than the two-equation model. The comparison with experiments showed also that significant discrepancies exist between experiments and predictions; the size of the recirculation zone was underpredicted by the three models with the Reynolds-stress models performing rather better. The axial normal stress was underestimated by the three models particularly near the centre-line and the rate of dissipation along the centre-line overpredicted; again the Reynolds stress models gave better results. The discrepancies were attributed partly to incorrect form of the equation of the rate of dissipation and partly to streamline curvature of which the effects are not correctly represented by any of the three models.

4. A calculation method for the prediction of the properties of swirling and non-swirling turbulent recirculating flows bounded by curved surfaces in orthogonal curvilinear coordinates was presented.

The procedure was tested for the calculations of wide angle diffusers with different expansion angles and for zero and 0.93 swirl numbers. The comparison between experimental and predicted results showed that the procedure represented the mean flow field in the zero swirl case very accurately. Discrepancies were shown in the calculated kinetic energy of turbulence which were attributed to the inappropriate assumptions in the effective viscosity hypothesis. In the swirl case, the discrepancies were larger and attributed to the inability of the effective viscosity hypothesis to predict flows with high streamline curvature and high extra rates of strain.

6.2 Recommendations for Future Work

6.2.1 Experimental Work

It is suggested that experiments can be extended to cover the points stated below:-

(i) More extensive measurements of $\overline{U}$, $\overline{V}$ and $\overline{uv}$ are required to aid the assessment and improvement of the calculation method in the presence of extra rates of strain; and to provide a better understanding of the velocity and turbulence characteristics in the confined double coaxial jets. These measurements will be specifically helpful in examining the extent of the ability of the Boussinesq equation to represent the relation between stresses and rates of strain in recirculating flows.

(ii) More extensive measurements of the rate of dissipation of the kinetic energy of turbulence in the confined double coaxial jets are required as a basis for evaluation and improvement of the turbulence

models. The rate of dissipation may be obtained from one-dimensional spectral density as described in Chapters 2 and 3 (see also Lawn, 1971) or from measurement of temporal derivatives and transformation to spatial derivatives in the flow direction (see Laufer, 1954, and Wygnanski and Fiedler, 1969).

(iii) In the confined double coaxial jet with swirl, measurements of the shear stresses, $\overline{uv}$, $\overline{uw}$ and $\overline{vw}$ and $\overline{V}$ and $\overline{v^2}$ are required to form with the present measurements of $\overline{U}$, $\overline{W}$, $\overline{u^2}$ and $\overline{w^2}$ a complete set of information which will help in better understanding of the turbulent processes occurring in swirling flows and to provide a basis for improvement of turbulence models. In this context, the laser Doppler anemometer is unnecessarily time-consuming and a combination of hot-wire anemometer and pulsed hot-wire anemometer (Bradbury, 1976) in regions of low and high turbulence intensities, respectively, may be preferred but at the expense of accuracy due to blockage effects. The incorporation of mini-computers in the analysis of the signals is also advantageous.

(iv) In the case of the flows in quarl-angle expansion geometries, the present measurements were achieved for one angle and one swirl number. Further measurements with different expansion angles and swirl numbers are also required to aid the understanding of the various physical processes. The study of the influence of these parameters represents a series of flows with gradually increased extra rates of strain and so also represents useful data for turbulence modelling. Measurements of the distribution of the mean pressure are also required.

6.2.2 Theoretical Work

The comparisons with experimental data made in the present

work suggest that the present turbulence models require improvements to increase the accuracy and generality of the calculation procedure. In particular, the isotropic viscosity hypothesis and the source of the rate of dissipation are probable causes of inaccuracy and are worthy of further investigation.

A fresh approach is needed to deal with the rate of dissipation of the turbulent kinetic energy. Trials to increase the ability of the present approach to predict flows with rotation (Launder et al, 1977, and Rodi, 1979) by replacing the constants in the ε-equation with specified empirical constants which are functions of Richardson number may be helpful. A more promising approach to the closure problem is based on devising stress equations for different slices of wave number space in the way described by Tchen (1973) and Hanjalic et al (1979).

The present calculations for zero swirl with the existence of streamline curvature and with swirl (see also Habib and Whitelaw, 1980) suggest the need for application of the Reynolds stress-models which require the solution of equations for all six Reynolds stresses. An algebraic-stress model approach (see Rodi, 1976, and Gibson, 1978) may provide a more palatable solution, if the time consumption and storage requirements by the Reynolds-stress models are considered large.

The extension of the calculation procedure of Chapter 5 to combusting flows and furnaces will provide a more general calculation procedure for the calculation of flows bounded by complex geometries than procedures which use Cartesian coordinate system.

PART III

SUPPLEMENTARY INFORMATION

APPENDIX A1

REFERENCES

ABBOTT, D. E. and KLINE, S. J. (1962)
"Experimental investigations of subsonic turbulent flow over single and double backward facing steps".
J. Basic Eng., D 84, p. 317.

ARIE, M. and ROUSE, H. (1956)
"Experiments on two-dimensional flow over a normal wall".
J. Fluid Mech., 1, p. 129.

ARIS, R. (1965)
"Vectors, tensors and the basic equations of fluid mechanics".
Prentice-Hall.

BAKER, R. J., HUTCHINSON, P., KHALIL, E. E. and WHITELAW, J. H. (1974)
"Measurements of three velocity components in a model furnace with and without combustion".
15th Symposium (Int.) on Combustion, p. 553.

BAKER, R. J., HUTCHINSON, P. and WHITELAW, J. H. (1974a)
"Velocity measurements in the recirculation region of an industrial burner flame by laser anemometry with light frequency shifting".
Combustion and Flame, 23, pp. 57-71.

BARFIELD, W. D. (1970)
"Numerical method for generating orthogonal curvilinear meshes".
J. Computational Phys., 5, pp. 23-33.

BECKER, H. A. and BROWN, A. P. G. (1974)
"Response of pitot probes in turbulent streams".
J. Fluid Mech., 62, pp. 84-114.

BELTAGUI, S. A. and MacCALLUM, N. R. L. (1976)
"Aerodynamics of vane-swirled flames in furnaces".
J. Inst. Fuel, 49, p. 183.

BOUSSINESQ, J. (1877)
"Théorie de l'écoulement tourbillant".
Mem. Pres. Acad. Sci., 23, p. 46.

BRADBURY, L. J. S. (1976)
"Measurements with a pulsed-wire and a hot-wire anemometer in the highly turbulent wake of a normal flat plate".
J. Fluid Mech., 77, pp. 473-497.

BRADBURY, L. J. S. and CASTRO, I. P. (1971)
"A pulsed wire technique for velocity measurements in highly turbulent flow".
J. Fluid Mech., 49, pp. 657-691.

BRADLEY, C. I. and COCKRELL, D. J. (1971)
"The response of diffusers to conditions at their inlet".
Paper 5, Section A, Symposium on Internal Flows, University of Salford, U.K., April.

BRADSHAW, P. (1973)
"Effect of streamline curvature on turbulent flow".
AGARDograph, 169.

BRADSHAW, P. (1975)
"Calculation methods for complex flows".
VKI Short Course on Prediction Methods for Turbulent Flow, March 3 - 7.

BRADSHAW, P. (Editor) (1976)
Topics in applied physics.
Vol. 19, "Turbulence", Springer-Verlag.

BRADSHAW, P. and WONG, F. Y. F. (1972)
"The reattachment and relaxation of turbulent shear layer".
J. Fluid Mech., 52, p. 113.

BUCHHAVE, P. (1975)
"Biasing errors in individual particle measurements with the LDA-counter signal processor".
Proceedings of LDA-Symposium, Copenhagen.

CEBECI, T., KHALIL, E. E. and WHITELAW, J. H. (1979)
"Calculation of separated boundary-layer flows".
AIAAJ, Vol. 17, No. 12, p. 1291.

CHAMPAGNE, F. H. and SLEICHER, C. A. (1967)
"Turbulence measurements with inclined hot wires. Part 2: Hot-wire response equations".
J. Fluid Mech., 28, pp. 77-182.

CHATURVEDI, M. C. (1963)
"Flow characteristics of axisymmetric expansions".
J. of the Hydraulics Division, Proceedings of the American Society of Civil Engineers, Vol. 89, No. HY3, p. 61.

CHEDAILLE, J., LEUCKEL, W. and CHESTERS, A. K. (1966)
Aerodynamics studies carried out on turbulent jets by the International Flame Research Foundation.
J. Inst. Fuel, 39, p. 311.

CHIGIER, N. A. and BEÉR, J. M. (1964)
"Velocity and static-pressure distributions in swirling air jets issuing from annular and divergent nozzles".
ASME J. Basic Eng., D86, p. 788.

COOK, N. J. and REDFEARN, D. (1976)
"The calibration and use of a hot wire probe for highly turbulent and reversing flows".
J. Ind. Aerodyn., 1, p. 221.

CORRSIN, S. and UBEROI, M. S. (1951)
"Spectrum and diffusion in a round turbulent jet".
NACA Report 1040.

CRABB, D., DURÃO, D. F. G. and WHITELAW, J. H. (1978)
"Velocity characteristics in the vicinity of a two-dimensional rib".
Imperial College, Mech. Eng. Report FS/78/34.

DALY, B. J. and HARLOW, F. H. (1970)
"Transport equations of turbulence".
J. Phys. Fluids, 13, p. 2634.

DAVIES, T. W. (1969)
"A study of the aerodynamics of the recirculation zone formed in a free annular air jet".
Ph.D. Thesis, University of Sheffield.

DIMOTAKIS, Paul E. (1976)
"Single scattering particle laser Doppler measurements of turbulence".
AGARD Conference Proceedings No. 193 on Applications of Non-Intrusive Instrumentation in Flow Flow Research, France, May 3 - 5.

DOWNING, P. M. (1972)
"Reverse flow sensing hot-wire anemometer".
J. Phys. E., Sci. Instrum., 5, p. 849.

DURÃO, D. (1971)
"Turbulent mixing of coaxial jets".
M.Sc. Thesis, University of London.

DURÃO, D. F. G. (1976)
"The application of laser anemometry to free jets and flames with and without recirculation".
Ph.D. Thesis, Mech. Eng. Dept., Imperial College.

DURÃO, D. F. G., LAKER, J. and WHITELAW, J. H. (1978)
"A microprocessor controlled frequency analyser for laser Doppler anemometry".
Imperial College, Mech. Eng. Report FS/78/21.

DURÃO, D. F. G., LAKER, J. and WHITELAW, J. H. (1980)
"Bias effects in laser Doppler anemometry".
Imperial College, Mech. Eng. Report FS/79/5. See also J. Phys. E: Sci: Instrum., 13, p. 442.

DURÃO, D. and WHITELAW, J. H. (1973)
"Turbulent mixing in the developing region of coaxial jets".
ASME J. Fluids Engng., 95, p. 467.

DURÃO, D. and WHITELAW, J. H. (1975)
"The performance of acousto-optic cells for laser Doppler anemometry".
J. Phys. E. Sci. Instrum., 8, p. 776.

DURÃO, D. F. G. and WHITELAW, J. H. (1978)
"Velocity characteristics of the flow in the near-wake of a disc".
J. Fluid Mech., 85, p. 369.

DURÃO, D. F. G. and WHITELAW, J. H. (1979)
"Relationship between velocity and signal quality in laser Doppler anemometry".
J. Phys. E., 12, p. 47.

DURST, F., MELLING, A. and WHITELAW, J. H. (1976)
"Principles and practice of laser Doppler anemometry".
Academic Press.

DURST, F. and RASTOGI, A. K. (1979)
"Theoretical and experimental investigations of turbulent flows with separation".
Proc. of the First Symposium on Turbulent Shear Flows, (Eds. F. Durst, B. E. Launder, F. W. Schmidt and J. H. Whitelaw).

DURST, F. and WHITELAW, J. H. (1971)
"Integral optical units for laser Doppler anemometry".
J. Phys. E., Sci. Instrum., 4, p. 804.

DURST, F. and WHITELAW, J. H. (1971a)
"Optimisation of optical anemometers".
Proc. Roy. Soc., A324, p. 157.

GIBSON, M. M. (1978)
"An algebraic stress and heat-flux model for turbulent shear flow with streamline curvature".
Int. J. Heat Mass Transfer, 21, pp. 1609-1617.

GOLDSTEIN, S. (1936)
"A note on the measurements of total head and static pressure in a turbulent stream".
Proc. Roy. Soc. London, 155A, p. 570.

GOSMAN, A. D. and IDERIAH, F. J. K. (1976)
"Teach-T; A general computer program for two-dimensional, turbulent, recirculating flows".
Dept. of Mech. Eng., Imperial College, London.

GOSMAN, A. D., KHALIL, E. E. and WHITELAW, J. H. (1979)
"The calculation of two-dimensional turbulent recirculating flows".
Proc. of the First Symposium on Turbulent Shear Flows. (Eds. F. Durst, B. E. Launder, F. W. Schmidt and J. H. Whitelaw).

GOSMAN, A. D. and PUN, W. M. (1974)
"Lecture notes for course entitled - Calculation of recirculating flows".
Imperial College, Mech. Eng. Dept. Report HTS/74/2.

GOSMAN, A. D., PUN, W. M., RUNCHAL, A. K., SPALDING, D. B. and WOLFSTEIN, M. (1969)
"Heat and mass transfer in recirculating flows".
Academic Press, London and New York.

HABIB, M. A. and WHITELAW, J. H. (1979)
"Velocity characteristics of a confined coaxial jet".
ASME J. Fluids Engng., 101, p. 521.

HABIB, M. A. and WHITELAW, J. H. (1980)
"Velocity characteristics of a confined coaxial jet with and without swirl".
ASME J. Fluids Engng., 102, p. 47.

HANJALIC, K. and LAUNDER, B. E. (1972)
"A Reynolds stress model of turbulence and its application to thin shear flows".
J. Fluid Mech., 52, pp. 609-638.

HANJALIC, K., LAUNDER, B. E. and SCHIESTEL, R. (1979)
"Multiple-time-scale concepts in turbulent transport modelling".
2nd Symposium on "Turbulent Shear Flows", July 2 - 4, Imperial College, London.

HARLOW, F. H. and NAKAYAMA, P. I. (1967)
"Turbulence transport equations".
J. Phys. Fluids, 10, (11), pp. 2182-2189.

HIETT, G. F. and POWELL, G. E. (1962)
"Three-dimensional probe for investigation of flow patterns".
The Engineer, 213, p. 165.

HINZE, J. O. (1959)
"Turbulence".
McGraw-Hill, New York.

HOESEL, W. and RODI, W. (1977)
"New biasing elimination method for laser Doppler velocimeter counter processing".
Rev. Sci. Instrum., Vol. 48, No. 7, p. 910.

HUNG, T. and BROWN, T. D. (1977)
"An implicit finite-difference method for solving the Navier-Stokes equation using orthogonal curvilinear coordinates".
J. Computational Physics, 23, pp. 343-363.

HUTCHINSON, P., KHALIL, E. E. and WHITELAW, J. H. (1977)
"Measurement and calculation of furnace-flow properties".
J. of Energy, 1, p. 212.

HYDE, D. J. and SYKES, J. (1979)
"A finite difference method for the solution of turbulent, combusting flows in enclosures with a divergent burner quarl".
HTFS AERE R5262.

KALINSKE, A. A. (1946)
"Conversion of kinetic to potential energy in fuel expansions".
Trans. ASCE, 111, pp. 355-390.

KHALIL, E. E., SPALDING, D. B. and WHITELAW, J. H. (1975)
"The calculation of local flow properties in two-dimensional furnaces".
Int. J. Heat Mass Transfer, 18, pp. 775-791.

KLINE, S. J., ABBOTT, D. E. and FOX, R. W. (1959)
"Optimum design of straight-walled diffusers".
ASME J. Basic Engng., 81, p. 321.

KOLMOGOROV, A. N. (1942)
"Equations of turbulent motion in an incompressible fluid".
IZV. Akad. Nuak. SSSR, Ser. Phys., Vol. I, No. 1-2, pp. 56-58.
(English translation: Imperial College, Mech. Eng. Report ON16, 1968).

KOOSINLIN, M. L. and LOCKWOOD, F. C. (1973)
"The prediction of axisymmetrical turbulent swirling boundary layers".
Imperial College, Mech. Eng. Dept., Report HTS/73/1.

LAKER, J. (1979)
Private communication.

LAUFER, J. (1954)
"The structure of turbulence in fully developed pipe flow".
NACA Report 1174.

LAUNDER, B. E., MORSE, A., RODI, W. and SPALDING, D. B. (1972)
"The prediction of free shear flows - a comparison of the performance of six turbulence models".
NASA Conference on Free Shear Flow, Langley Field, Hampton, July.

LAUNDER, B. E., PRIDDIN, C. H. and SHARMA, B. I. (1977)
"The calculation of turbulent boundary layers on spinning and curved surfaces".
ASME, J. Fluids Engng., 99, p. 231.

LAUNDER, B. E., REECE, G. J. and RODI, W. (1975)
"Progress in the development of a Reynolds-stress turbulence closure".
J. Fluid Mech., 68, pp. 537-566.

LAUNDER, B. E. and SPALDING, D. B. (1972)
"Mathematical models of turbulence".
Academic Press.

LAUNDER, B. E. and SPALDING, D. B. (1973)
"The numerical computations of turbulent flows".
Imperial College, Dept. of Mech. Eng. Report HTS/73/2. See alos Computer Methods in Applied Mechanics and Engineering, 3, p. 269.

LAUNDER, B. E. and WHITELAW, J. H. (1977)
"Turbulent flow modelling".
Heat Transfer and Fluid Flow Service, AERE Harwell and National Engineering Laboratory, Report AERE-R8635.

LAWN, C. J. (1971)
"The determination of the rate of dissipation in turbulent pipe flow".
J. Fluid Mech., 48, pp. 477-505.

LIVESEY, J. L. and TURNER, J. T. (1965)
"The dependence of diffuser performance upon inlet flow conditions".
J. Roy. Aero. Soc., 69, 11, pp. 794-795.

MATHUR, M. L. and MacCULLUM, N. R. L. (1967)
"Swirling air jet issuing from vane swirlers. Part 2: Enclosed jets".
J. Inst. Fuel, 40, p. 238.

MATTHEWS, L. and WHITELAW, J. H. (1973)
"Plane jet flow over a backward facing step".
Proc. of Institution of Mech. Eng., Vol. 187, p. 447.

McDONALD, A. T., FOX, R. W. and VAN DEWOESTINE, R. V. (1971)
"Effects of swirling inlet flow on pressure recovery in conical diffusers".
AIAA J., 9, pp. 2014-2018.

McDOUGALL, T. J. (1980)
"Bias correction for individual realisation LDA measurements".
J. Phys. E. Sci. Instrum., 13, p. 53.

McLAUGHLIN, D. K. and TIEDERMAN, W.G. (1973)
"Biasing correction for individual realization of laser Doppler anemometer measurements in turbulent flows".
J. Phys. Fluids, 16, p. 2082.

MELLING, A. (1975)
"Investigation of flow in non-circular ducts and other configurations by laser Doppler anemometry".
Ph.D. Thesis, Mech. Eng. Dept., Imperial College, London.

MOORE, C. A. and KLINE, S. J. (1958)
"Some effects of vanes and of turbulence in two-dimensional wide-angle subsonic diffusers".
NACA TN 4080.

MORSE, A. (1979)
Private communication.

MOSS, W. D., BAKER, S. and BRADBURY, L. J. S. (1979)
"Measurements of mean velocity and Reynolds stresses in some regions of recirculating flow".
Proc. of the First Symposium on Turbulent Shear Flows. (Eds. F. Durst, B. E. Launder, F. W. Schmidt and J. H. Whitelaw).

MUELLER, T. J. and ROBERTSON, J. M. (1963)
"Modern developments in theory".
Appl. Mech., 1, p. 326.

MURAKAMI, M. and KIKUYAMA, K. (1976)
"Effects of rotation on diffuser flow".
Bulletin of the JSME., Vol. 19, No. 137, p. 1294.

NAOT, D. and LAUNDER, B. E. (1975)
"Numerical calculations of the turbulent swirling and recirculating flows with a Reynolds stress closure".
Ben Gurion University of the Negev, Mech. Eng. Dept., Report No. ME-22/75.

OTA, T. (1975)
"An axisymmetric separated and reattached flow on a longitudinal blunt circular cylinder".
ASME J. of Applied Mech., 42, p. 311.

OTA, T. and ITASAKA, M. (1976)
"A separated and reattached flow on a blunt flat plate".
ASME J. Fluid Engng., 98, pp. 79-86.

OWEN, F. K. (1976)
"Measurements and observations of turbulent recirculating flows".
AIAA J., 14, p. 1556.

PAI, B. R., RICHER, W. and LOWES, T. M. (1975)
"Flow and mixing in confined axial flows".
J. Inst. Fuel, 48, p. 185.

PATANKAR, S. V. and SPALDING, D. B. (1972)
"A calculation procedure for heat, mass and momentum transfer in three-dimensional parabolic flows".
Int. J. Heat Mass Transfer, Vol. 15, pp. 1787-1806.

POPE, S. B. (1976)
"The calculation of turbulent recirculating in general orthogonal coordinates".
Mech. Eng. Dept., Imperial College Report CHT/76/7.

POPE, S. B. and WHITELAW, J. H. (1976)
"The calculation of near-wake flows".
J. Fluid Mech., 73, pp. 9-32.

PRANDTL, L. (1925)
"Bericht über Untersuchungen zur ausgebildeten Turbulenz".
ZAMM, 5, p. 136. Translation to English by D. B. Spalding (1980), Imperial College, Mech. Eng. Dept., Report HTS/TN/80/1.

RAITHBY, G. D. (1976)
"A critical evaluation of upstream differencing applied to problems involving fluid flow".
Comp. Meth. Appl. Mech. Eng., 9, p. 75.

REECE, G. J. (1976)
"A generalized Reynolds-stress model of turbulence".
Ph.D. Thesis, University of London.

REYNOLDS, A. J. (1974)
"Turbulent flows in engineering".
John Wiley & Sons.

RIBEIRO, M. M. (1976)
"The turbulence structure of free jet flows with and without swirl".
Ph.D. Thesis, University of London.

RIBEIRO, M. M. and WHITELAW, J. H. (1980)
"Coaxial jets with and without swirl".
J. Fluid Mech., 96, pp. 769-795.

RIBEIRO, M. M. and WHITELAW, J. H. (1980 a)
"The structure of turbulent jets".
Proc. R. Soc. Lond., A370, pp. 281-301.

RODI, W. (1972)
"The prediction of free turbulent boundary layers by use of a two-equation model of turbulence".
Ph.D. Thesis, Mech. Eng. Dept., Imperial College.

RODI, W. (1974)
"A new method of analysing hot-wire signals in highly turbulent flow, and its evaluation in a round jet".
DISA Information 17, 9 and Report No. ET/TN/B/10, Mech. Eng. Dept., Imperial College.

RODI, W. (1976)
"A new algebraic relation for calculating the Reynolds stresses".
Z. ANG. MATH., 56, p. 219.

RODI, W. (1979)
"Influence of buoyancy and rotation on equations for the turbulent length scale".
2nd Symposium on Turbulent Shear Flows, July 2 - 4, Imperial College, London.

ROTTA, J. (1951)
"Statistische Theorie nichthomogener Turbulenz".
Zeitsch. für Physik, 129, p. 547 and 131, p. 51.

ROTTA, J. C. (1979)
"A family of turbulence models for three-dimensional thin shear layers".
Proc. of the First Symposium on Turbulent Shear Flows. (Eds. F. Durst, B. E. Launder, F. W. Schmidt and J. H. Whitelaw).

RUBEL, A. (1972)
"Some effects of swirl on turbulent mixing and combustion".
NASA CR-1956.

SAKAMOTO, H., MORIGO, M. and ARIE, M. (1975)
"Study of the flow around bluff bodies immersed in turbulent boundary layers".
Bulletin of the JSME, Vol. 18, No. 124, p. 1126.

SANDBORN, V. A. and KLINE, S. J. (1961)
"Flow models in boundary-layer stall inception".
ASME J. Basic Engng. Trans., 83, pp. 317-327.

SENOO, Y., KAWAGUCHI, N. and NAGATA, T. (1978)
"Swirl flow in conical diffusers".
Bulletin of the JSME., Vol. 21, No. 151, p. 112.

SHEMER, L. and EINAV, S. (1979)
"Sensing volume and biasing corrections for dual counter LDA processors".
Rev. Sci. Instrum., 50(7), p. 879.

SIMPSON, R. L., STRICKLAND, J. H. and BARR, P. W. (1977)
"Features of a separating turbulent boundary layer in the vicinity of separation".
J. Fluid Mech., 79, pp. 553-594.

SMITHSON, I. K. (1969)
"Characteristics of free and confined vortex flow".
Ph.D. Thesis, University of Sheffield.

SPALDING, D. B. (1975)
"Turbulence modelling: Solved and unsolved problems".
Turbulent mixing in non-reactive and reactive flows, Ed. by S. N. B. Murthy.

SPALDING, D. B. (1980)
Private communication.

SPANGENBERG, W. G., ROWLAND, W. R. and MEESE, N. E. (1967)
"Fluid mechanics of internal flow".
Ed. G. Sovran, Elsevier, pp. 110-150.

SYRED, N. and BEÉR, J. M. (1974)
"Combustion in swirling flows: A review".
Combustion and Flame, 23, pp. 143-201.

TCHEN, C. M. (1973)
"Repeated cascade theory of homogeneous turbulence".
J. Physics of Fluids, Vol. 16, 1, p. 13.

TENNEKES, H. and LUMLEY, J. L. (1972)
"A first course in turbulence".
M.I.T. Press.

TILLMAN, W. (1945)
"Investigations of some particularities of turbulent boundary layers on plates".
British Ministry of Aircraft Production, Translation Map-VG-34-45 T.

TOWNSEND, A. A. (1956)
"The structure of turbulent shear flow".
Cambridge University Press.

WAITMAN, B. A., RENEAU, L. R. and KLINE, S. J. (1961)
"Effect of inlet conditions on performance of two-dimensional subsonic diffusers".
J. Basic Eng., D83, pp. 349-360.

WARSI, Z. U. A. and AMLICKE, B. B. (1976)
"Improved algebraic relation for the calculation of Reynolds stresses".
AIAAJ, Vol. 14, No. 12,

WILSON, N. M. (1978)
"Digital signal-processing techniques for laser Doppler velocimetry".
J. Phys. E. Sci. Instrum., Vol. 11, p. 555.

WINGFIELD, G. A. (1967)
"Mixing and recirculation patterns from double concentric jet burners using an isothermal model".
J. Inst. Fuel, 40, p. 456.

WOLFSHTEIN, M. (1969)
"Convection processes in turbulent impinging jets".
Ph.D. Thesis, University of London.

WYGNANSKI, I. and FIEDLER, H. (1969)
"Some measurements in the self-preserving jet".
J. Fluid Mech., 38, pp. 577-612.

YANTA, W. J. (1973)
"Turbulence measurements with a laser Doppler velocimeter".
Naval Ordnance Laboratory, Maryland, Report TR73-94.

ZAMAN, O. and LUMLEY, J. L. (1979)
"Buoyancy effects in entraining turbulent boundary layers: A second-order closure study".
Proc. of the First Symposium on Turbulent Shear Flows (Eds. F. Durst, B. E. Launder, F. W. Schmidt and J. H. Whitelaw).

APPENDIX A2

EXPERIMENTAL DATA OF QUARL ANGLE EXPANSION WITH SWIRL

The results of the flow properties in the confinement with an expanding entry, G1, with swirl number of 0.93 are presented in this appendix in the form of radial profiles at different axial locations. These results serve as a reference to the contour plots presented in Chapter 4 and allow the reader to extract the experimental data of interest with much ease.

The radial profiles of the axial mean velocity and corresponding normal stress are shown in Figs. A2.1 and A2.2, respectively. Figs. A2.3 and A2.4 represent the radial profiles of the mean and rms of the tangential velocity fluctuations.

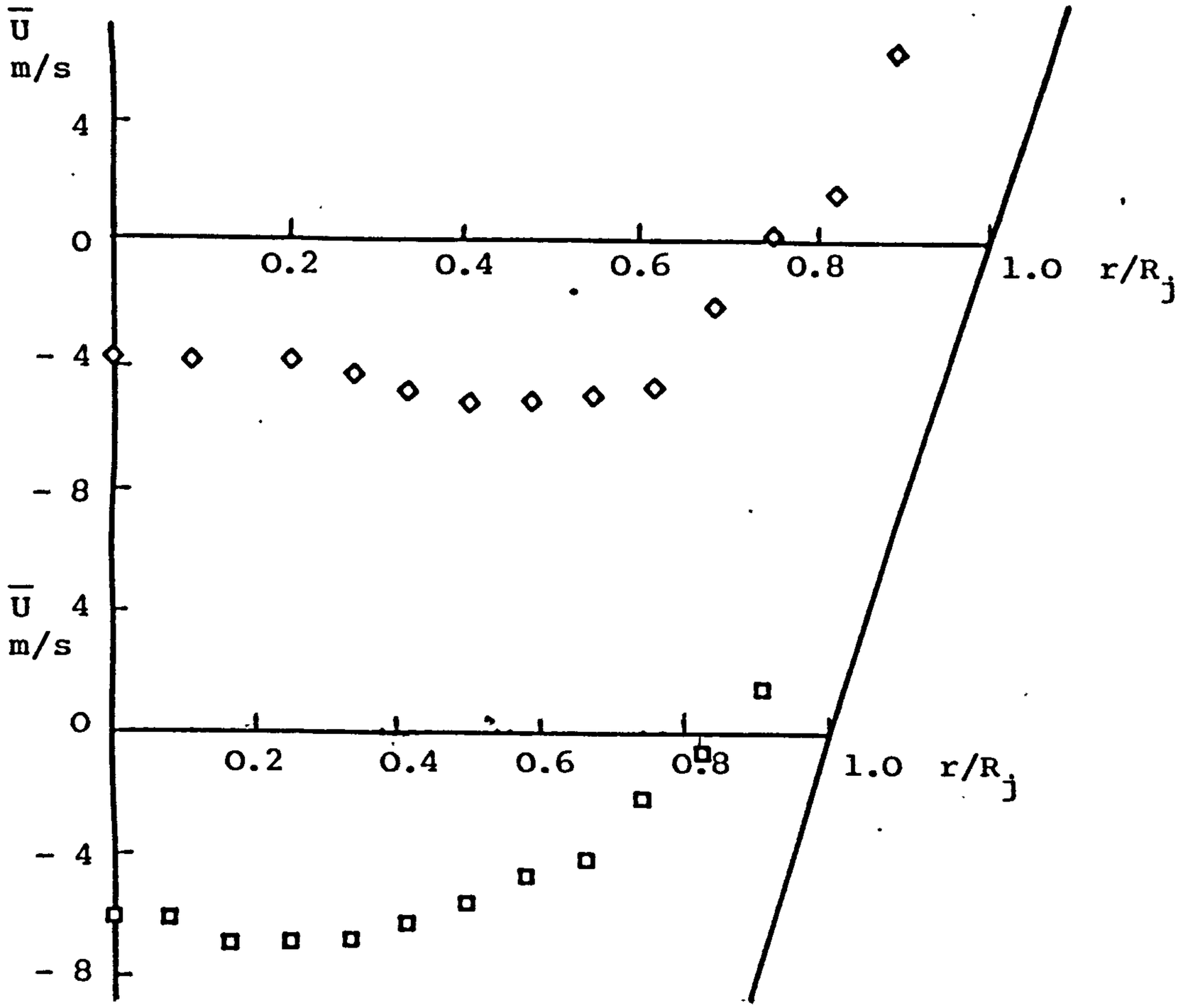


Fig. A2.1 Development of Axial Mean Velocity Profiles Across the Centre-Line of G1 (S = 0.93)

Symbol	○	□	◇	▽	△
Station	1	2	3	4	5
Symbol	●	■	◆	▼	▲
Station	6	7	8	9	10

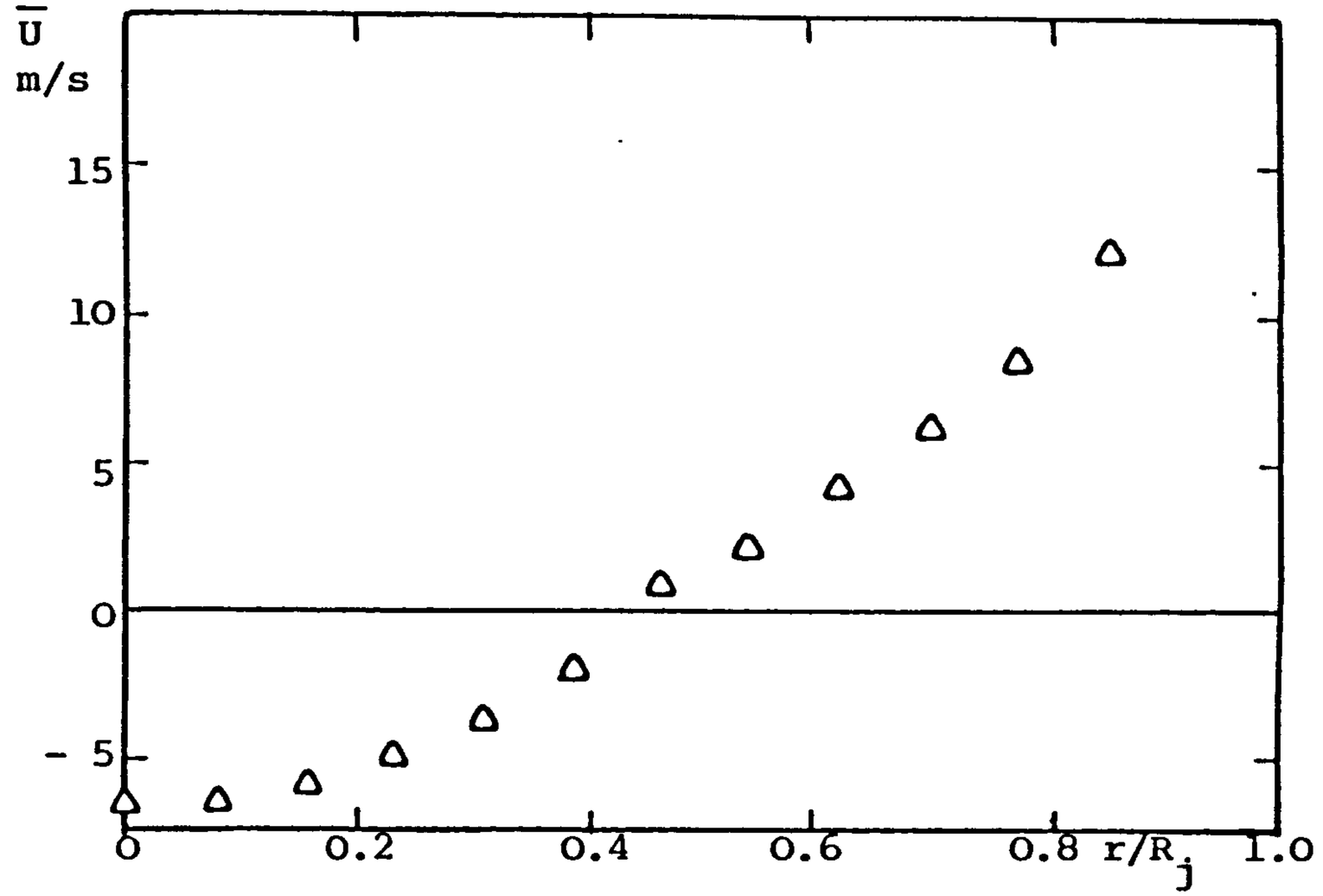


Fig. A2.1 (Continued)

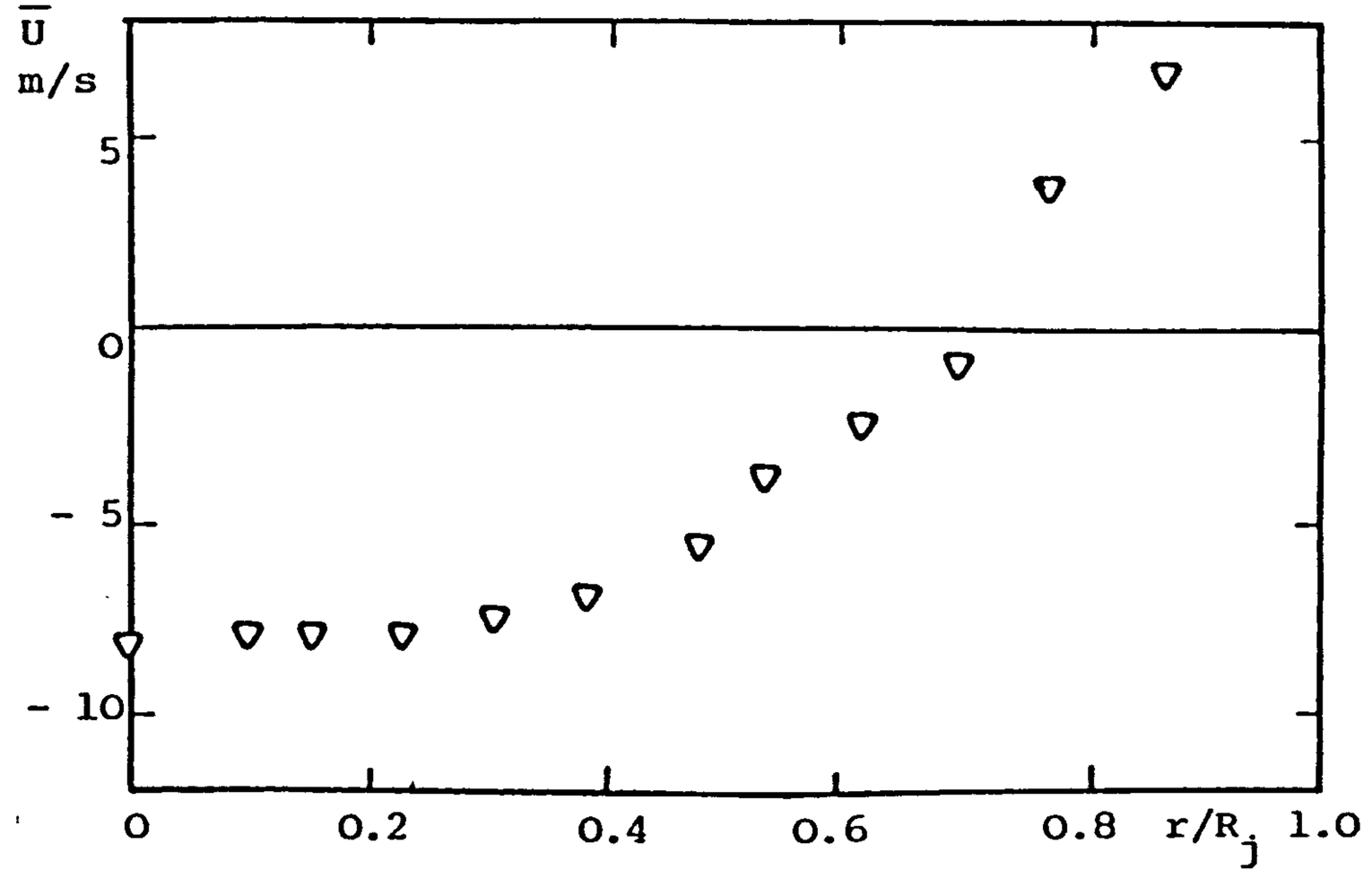


Fig. A2.1 (Continued)

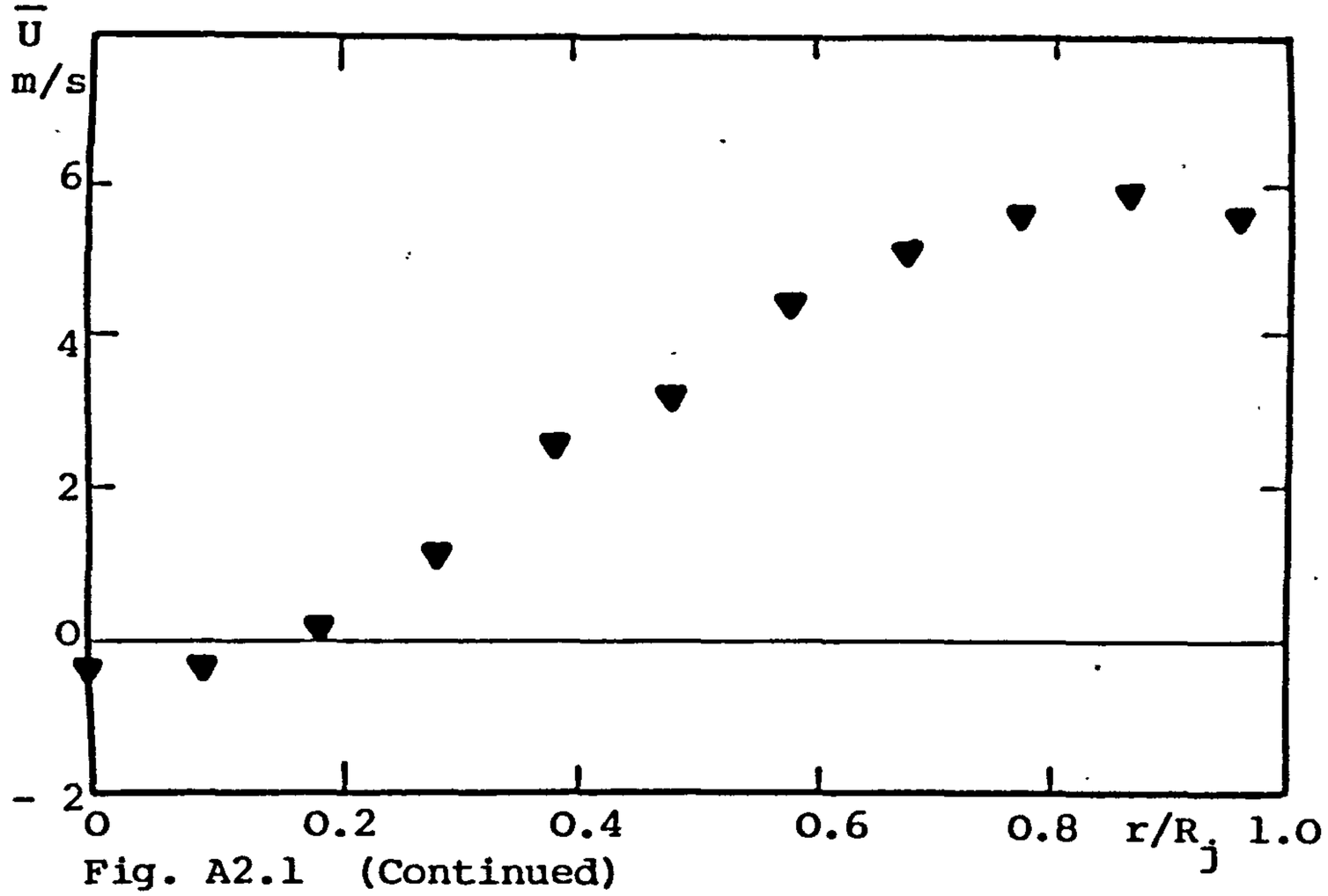


Fig. A2.1 (Continued)

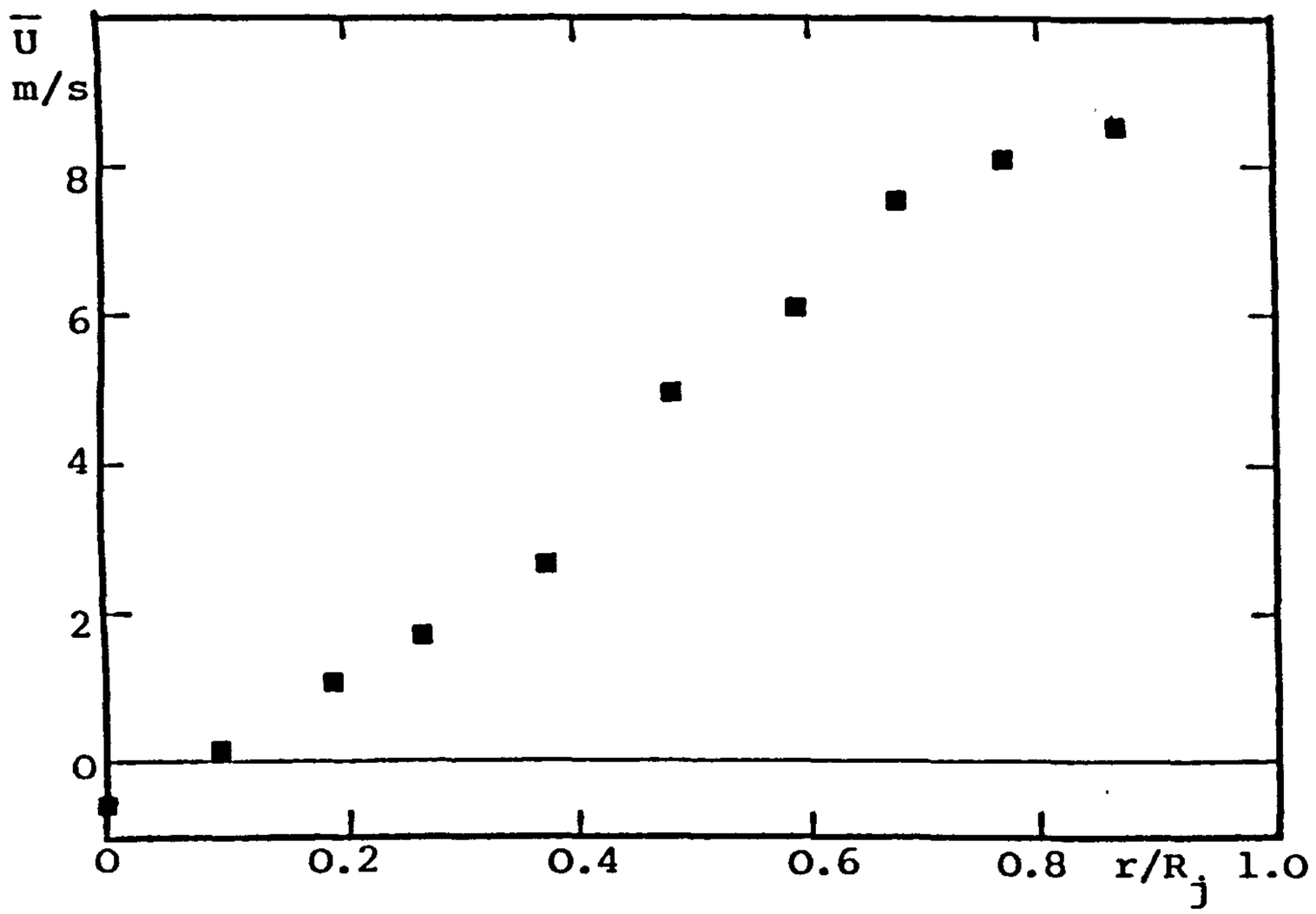


Fig. A2.1 (Continued)

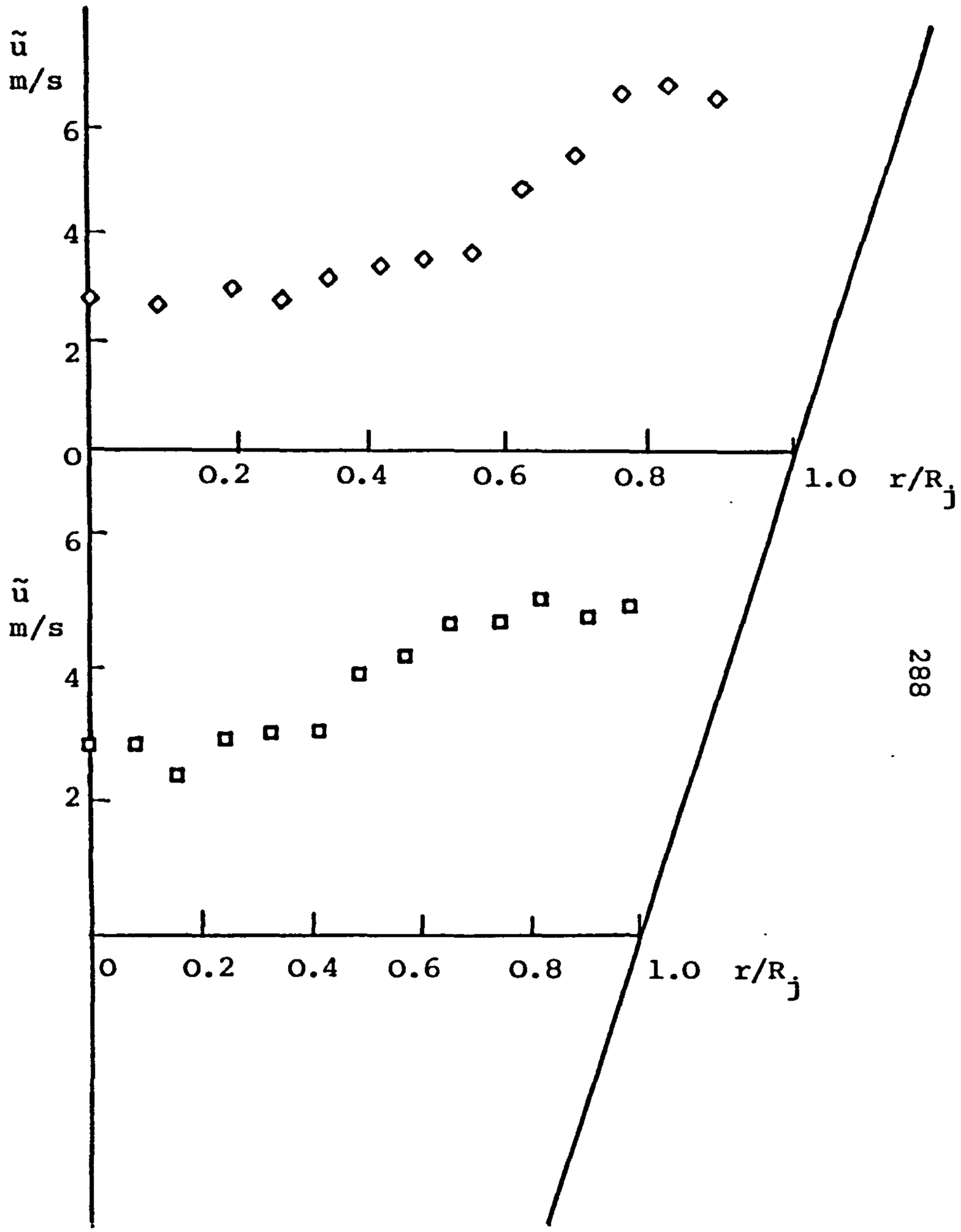


Fig. A2.2 Development of the Axial Normal Stress Across the Centre-Line of G1 (S = 0.93); Notation as in Fig. A2.1

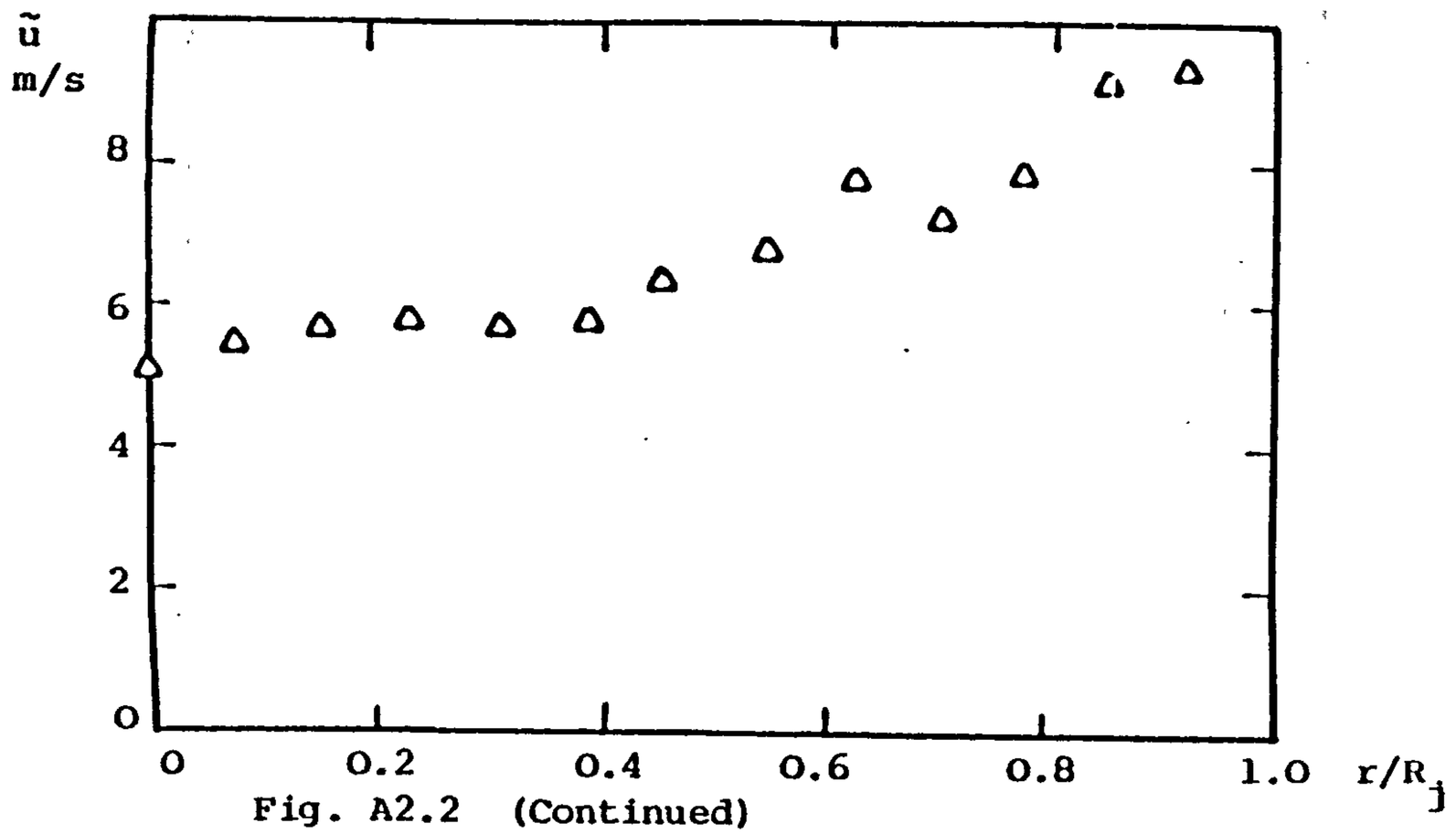


Fig. A2.2 (Continued)

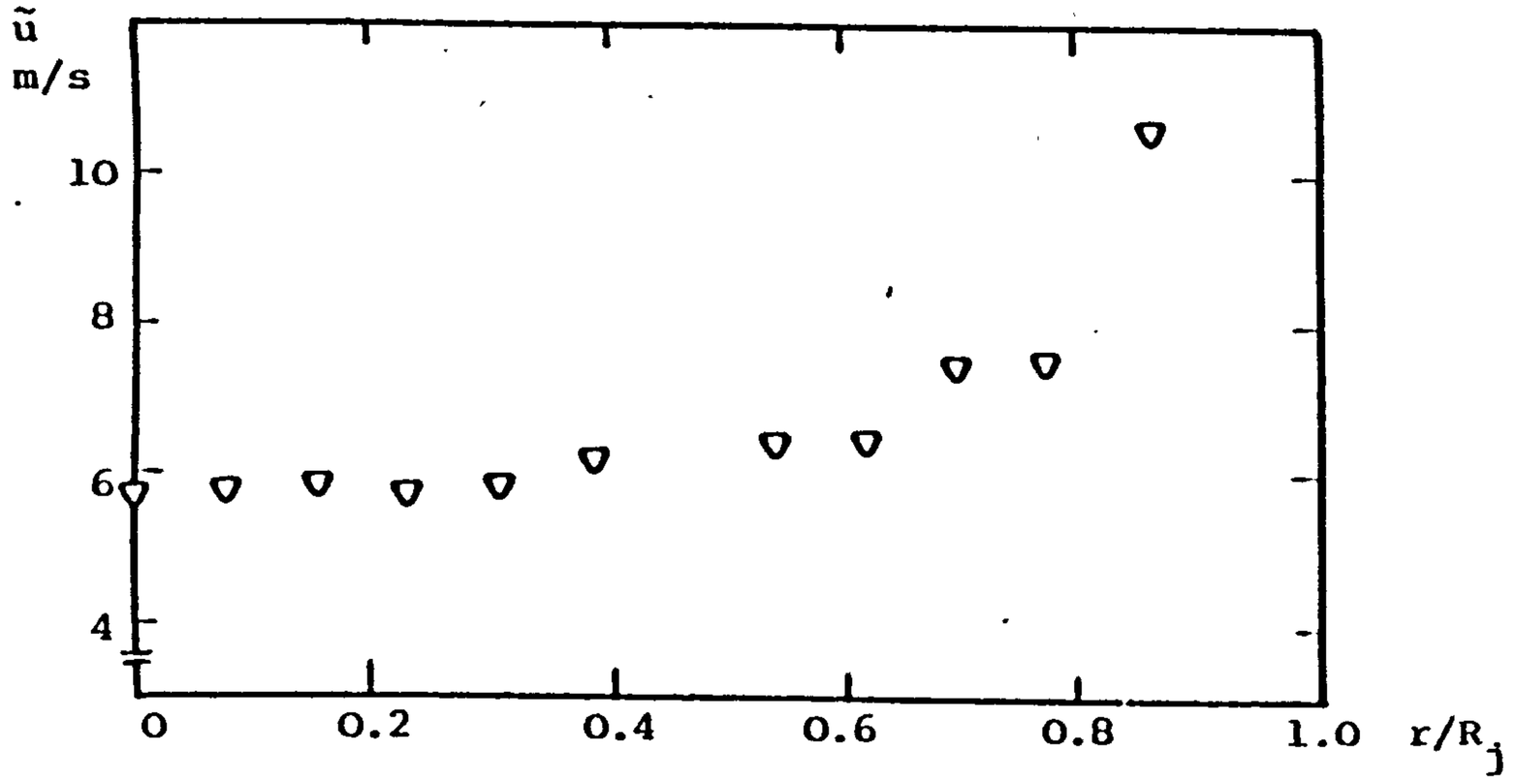
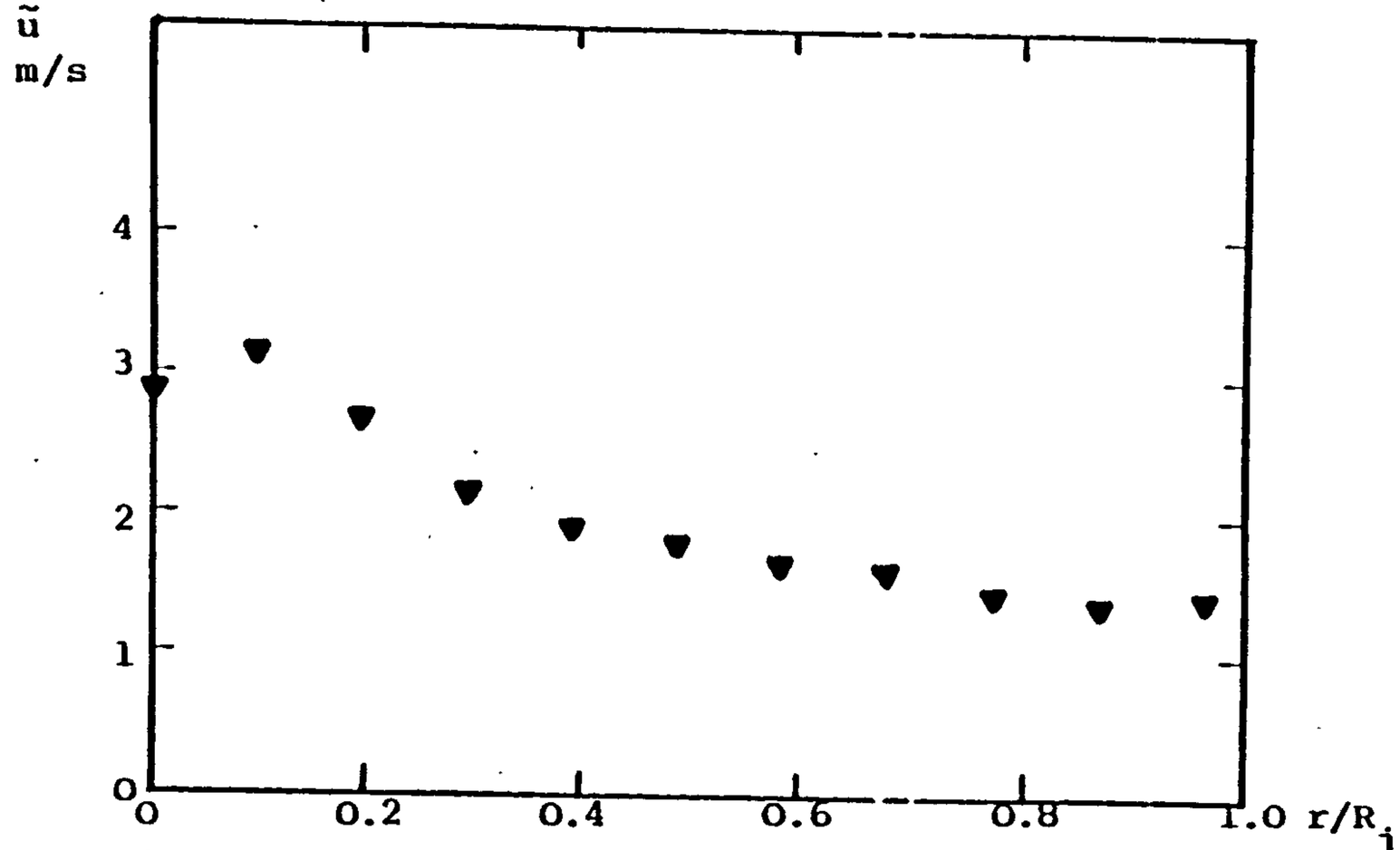


Fig. A2.2 (Continued)



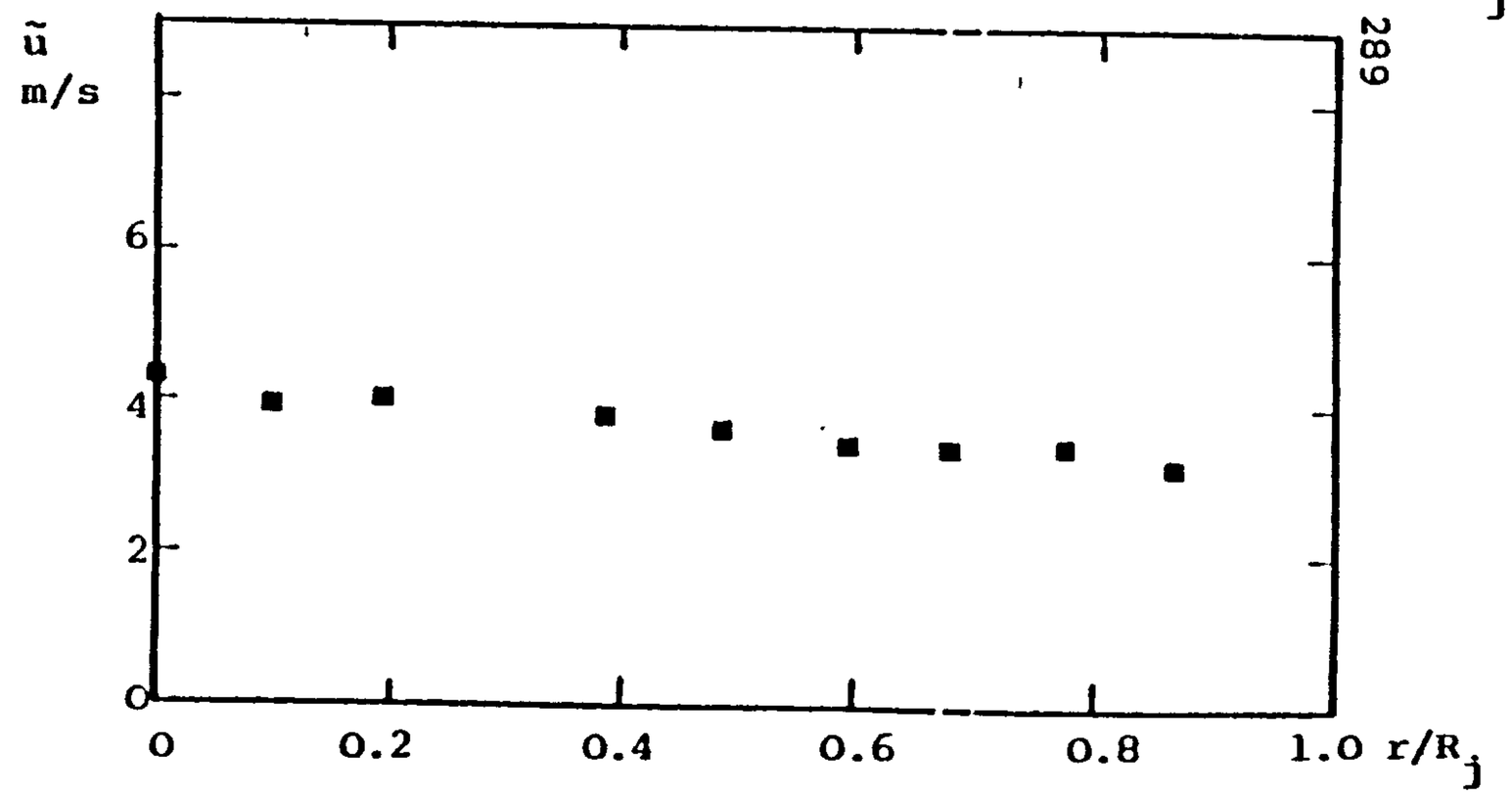


Fig. A2.2 (Continued)

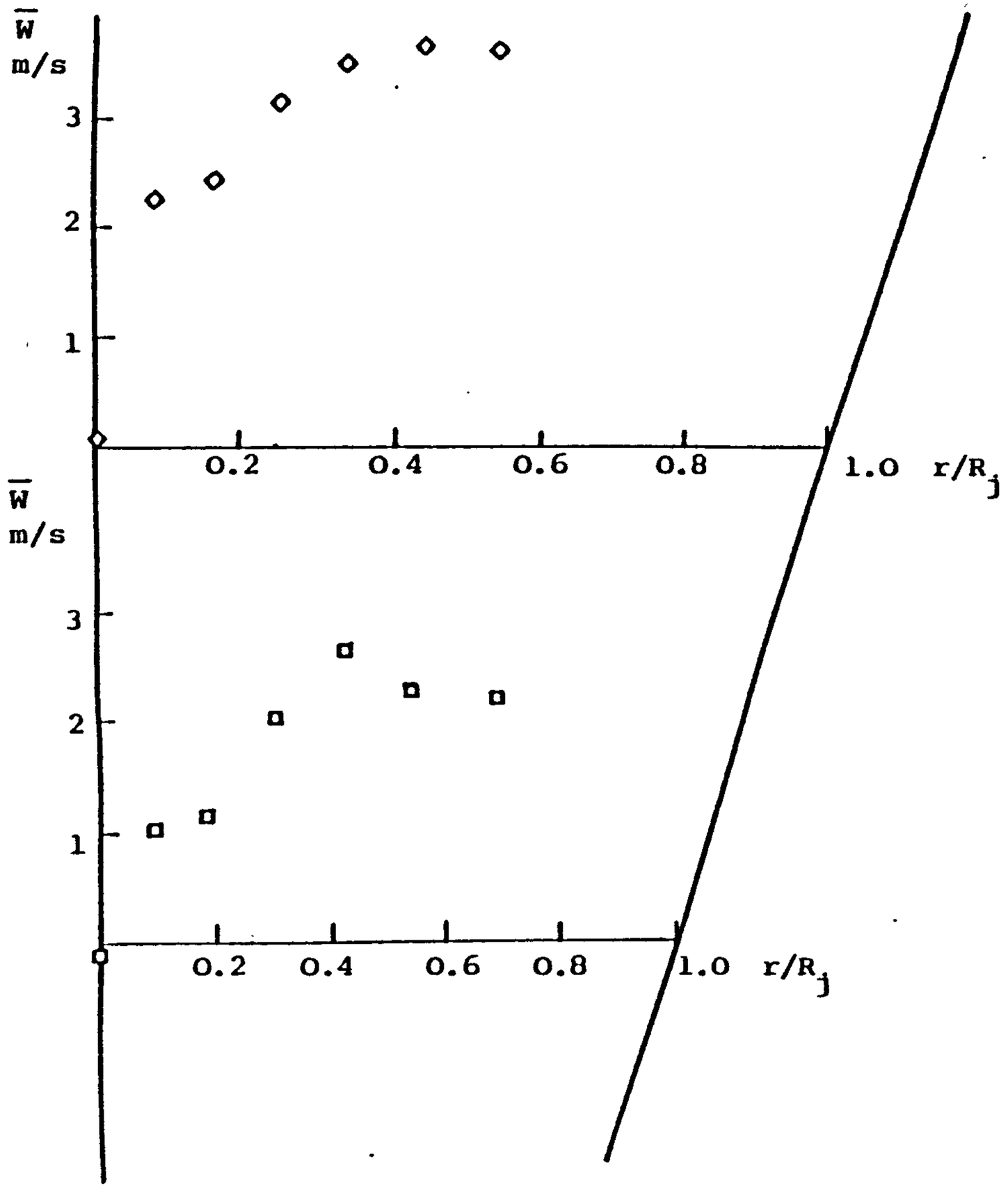


Fig. A2.3 Development of the Tangential Mean Velocity Profiles Across the Centre-Line of G1 (S = 0.93); Notation as in Fig. A2.1

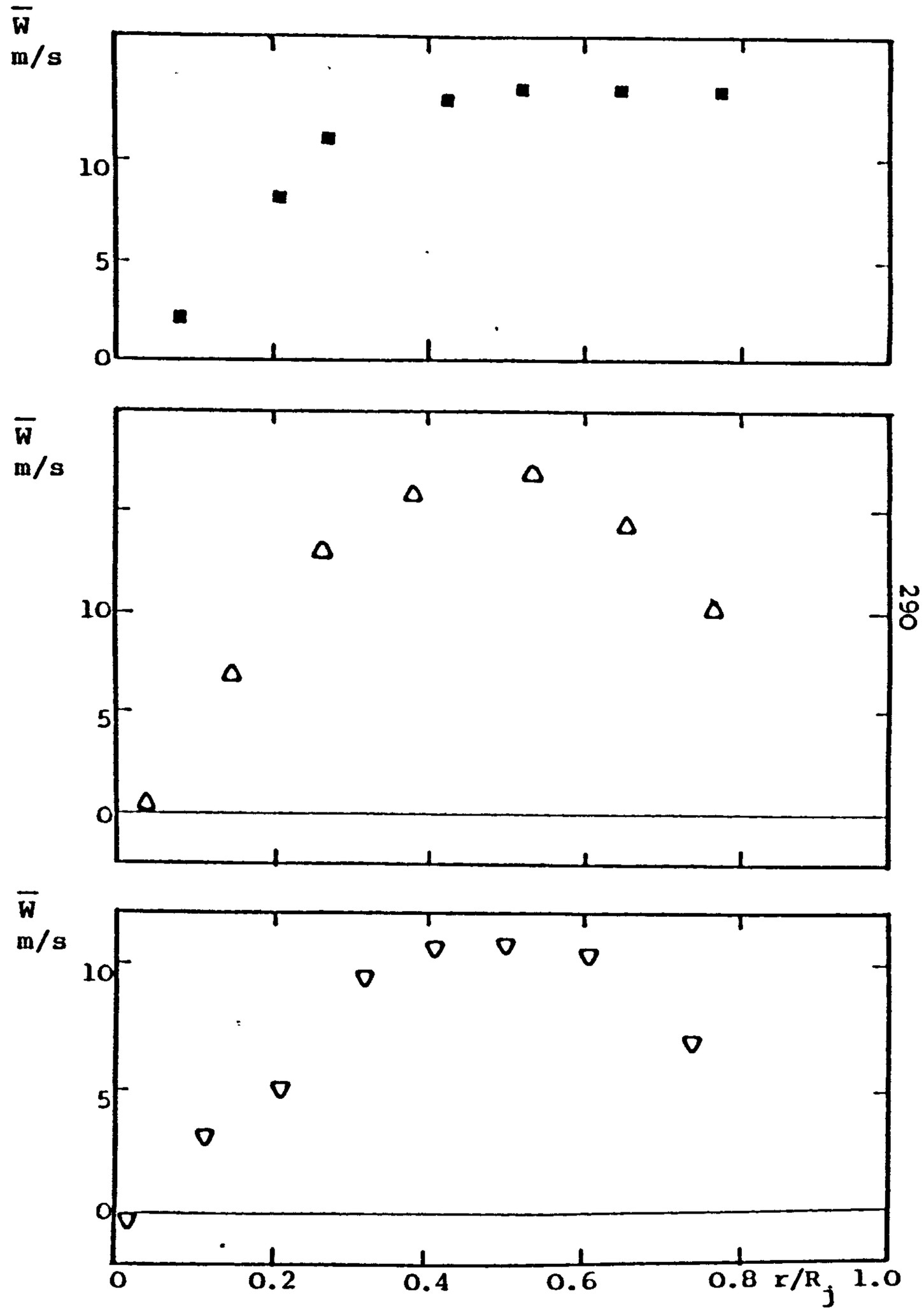


Fig. A2.3 (Continued)

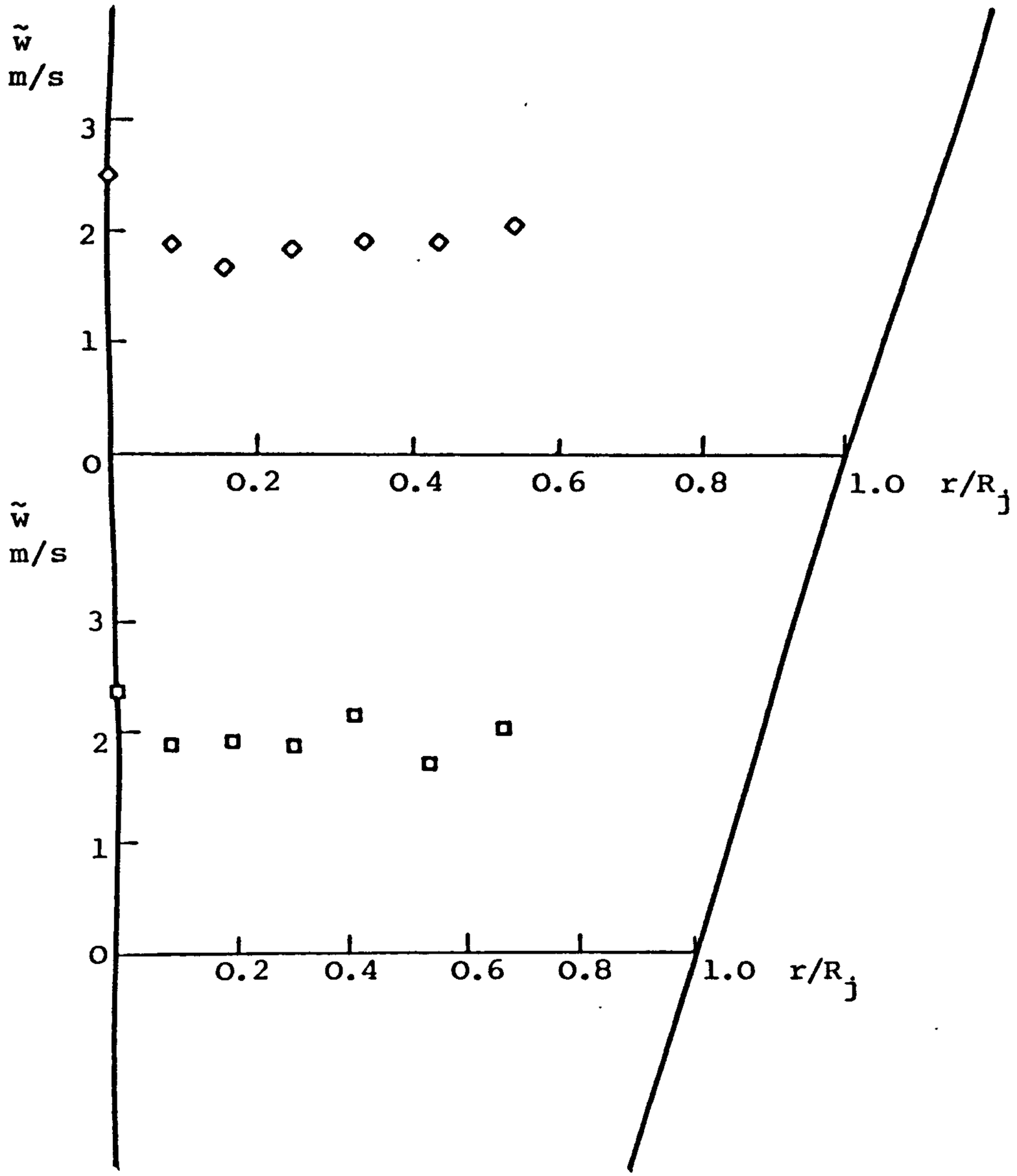


Fig. A2.4 Development of Tangential Normal Stress Profiles Across the Centre-Line of G1 (S = 0.93); Notation as in Fig. A2.1

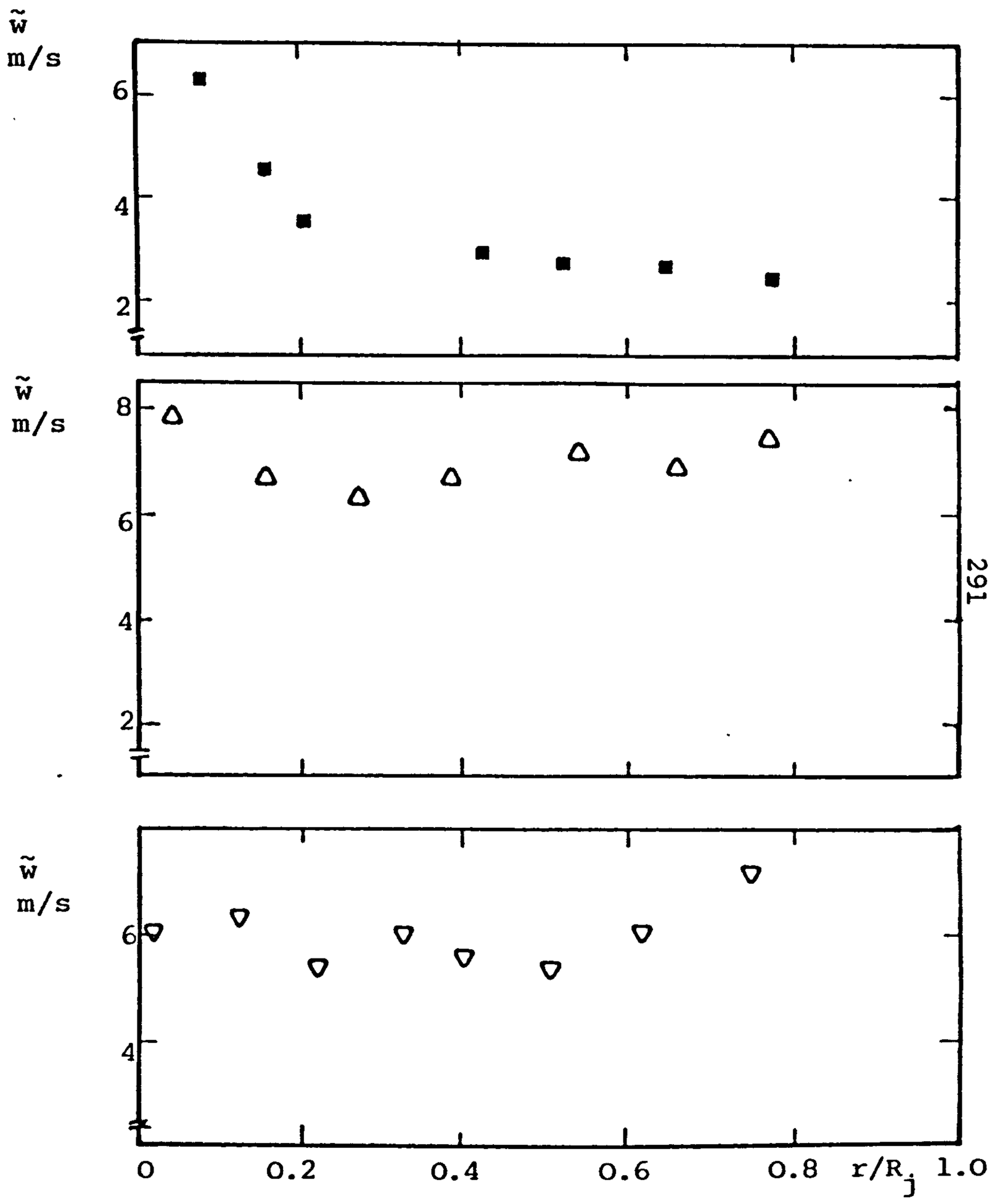


Fig. A2.4 (Continued)

APPENDIX A3

EQUATIONS IN ORTHOGONAL CURVILINEAR COORDINATES

The equations of the dependent variables presented in Chapter 5 are derived in this appendix. In this derivation, the equations of the two-dimensional fluid motion of Chapter 3, expressed in Cartesian tensor form, are used to arrive at a set of equations represented in an orthogonal coordinate system. The reader is referred to Aris (1965) and Bradshaw (1973) for details of the definitions mentioned throughout the derivations.

(i) Definitions

If we consider a coordinate system x^i (i = 1, 2, 3), the transformation to another coordinate system $\bar{x}^j$ (j = 1, 2, 3) can be written as:-

$$d\bar{x}^j = \frac{\partial \bar{x}^j}{\partial x^i} dx^i \qquad \text{(sum over i)} \qquad \text{(A3.1)}$$

Contravariant and covariant transformations are defined respectively as:-

$$\bar{a}^j = \frac{\partial \bar{x}^j}{\partial x^i} a^i \quad \text{and} \quad \bar{a}_j = \frac{\partial \bar{x}^i}{\partial x_j} a_i \qquad \text{(A3.2)}$$

Using this, the length of the line element in any transformed coordinates $\bar{x}^i$ is given by:-

$$(ds)^2 = \sum_{i=1}^{3} (d\bar{x})^2 =$$

$$= \sum_{i=1}^{3} \left[\frac{\partial \bar{x}^k}{\partial x^i} dx^i \cdot \frac{\partial \bar{x}^k}{\partial x^j} dx^j \right]$$

$$= g_{ij} \, dx^i \, dx^j \qquad \text{(A3.3)}$$

g_{ij} relates physical distance to the infinitesimal coordinate increments of a space arithmetised, hence its name, metric tensor. When the off-diagonal terms of g_{ij} are zero, the coordinates corresponding to g_{ij} are called orthogonal since, at any point in space, they are at right angles to one another.

A covariant index can be converted into a contravariant one by the relation:-

$$a^j = g^{ij} \, a_i \qquad \text{(A3.4)}$$

where:-

$$g^{ij} = \frac{1}{g_{ij}} \qquad \text{(A3.5)}$$

Covariant differentiation of a contravariant vector a^i with respect to x^j is given by:-

$$a^i{}_{,j} = \frac{\partial a^i}{\partial x^j} + \left\{ \begin{matrix} i \\ k \quad j \end{matrix} \right\} a^k \qquad \text{(A3.6)}$$

where $\left\{ \begin{matrix} i \\ j \quad k \end{matrix} \right\}$ is the Christoffel symbol of second kind and is given by

(for orthogonal coordinate system):-

$$\left\{ \begin{matrix} i \\ j \quad k \end{matrix} \right\} = 0 \qquad \text{if } i, j, k \text{ are all different}$$

$$= h_m \, H_\ell(m) \qquad \text{if } i = j = k = \ell = m$$

$$\text{or } i = j = \ell,\ k = m$$

$$\text{or } i = k = \ell,\ j = m$$

$$= - \left\{ \frac{h_\ell^{\,2}}{h_m} \right\} H_\ell(m) \qquad \text{if } j = k = \ell,\ i = m \qquad \text{(A3.7)}$$

where $H_\ell(m)$ are the coordinate variation terms and are defined as:-

$$H_\ell(m) = \frac{1}{h_\ell \, h_m} \frac{\partial h_\ell}{\partial x_m} \qquad \text{(A3.8)}$$

and h_ℓ are the scale factors:-

$$h_\ell = \sqrt{g_{\ell\ell}} \qquad \text{(no sum on } \ell) \qquad \text{(A3.9)}$$

Since some coordinate systems do not all have dimensions, it has been necessary to distinguish between the quantities that appear in the equations of motion written in general tensor notation, and their physical components in a given coordinate system. Equation (A3.6) is expressed as (see Bradshaw, 1973):-

$$a(i, m) = h_i \, h_m \, g^{\ell m} \left[\frac{\partial}{\partial x_\ell} \left\{ \frac{a(i)}{h_i} \right\} + \left\{ \begin{matrix} i \\ n \quad \ell \end{matrix} \right\} \frac{a(n)}{h_n} \right] \qquad \text{(A3.10)}$$

where:-

$$a(j) = (g_{jj})^{1/2}\, a^j = h_j\, a^j \qquad \text{(A3.11)}$$

Now to derive the differential equation in any chosen system, the equation for Cartesian coordinates is written in general tensor notation. Then Equation (A3.6) is to be worked out and the physical components of vectors and tensors are recovered by using Equations (A3.10) and (A3.11). Finally, the Christoffel symbols are to be substituted for according to Equation (A3.7).

(ii) Equation of Continuity

Equation of continuity may be expressed as:-

$$U^{\ell}{}_{,\ell} = 0$$

Substituting from Equation (A3.10), it can be written as:-

$$\frac{\partial}{\partial x_\ell}\frac{U(\ell)}{h_\ell} + \begin{Bmatrix} \ell \\ n\ \ \ell \end{Bmatrix}\frac{U(n)}{h_n} = 0 \qquad \text{(A3.12)}$$

Substituting for Christoffel symbol from Equation (A3.7):-

$$\frac{\partial}{\partial x_\ell}\frac{U(\ell)}{h_\ell} + h_n\, H_\ell(n)\, \frac{U(n)}{h_n} = 0 \qquad \text{(A3.13)}$$

Also it can be reduced to:-

$$\nabla(n)\ U(n) = 0 \qquad \text{(A3.14)}$$

where $\nabla(n)$ is the divergence operator, defined as:-

$$\nabla(n) = \frac{1}{\sqrt{g}} \sum_{n} \frac{\partial}{\partial x_n} \frac{\sqrt{g}}{h_n} U(n) =$$

$$= \frac{\partial}{\partial x^n} \frac{U(n)}{h_n} + \frac{1}{h_\ell} \frac{\partial h_\ell}{\partial x_n} \frac{U(n)}{h_n} \qquad \text{(A3.15)}$$

(iii) The Momentum Equation

Equation of momentum may be written as:-

$$U^\ell \, U^i,_\ell = - \frac{1}{\rho} P,i \qquad \text{(A3.16)}$$

Operating Equation (A3.10):-

$$h_i \, h_\ell \, g^{\ell\ell} \left[U(\ell) \frac{\partial}{\partial x_\ell} \left(\frac{U(i)}{h_i} \right) + U(\ell) \left\{ \begin{matrix} i \\ n \quad \ell \end{matrix} \right\} \frac{U(n)}{h_n} \right] = - \frac{1}{\rho} h_i \, g^{ii} \frac{\partial P}{\partial x_i} \qquad \text{(A3.17)}$$

Substituting for $\nabla(\ell)$ from Equation (A3.15):-

$$\nabla(\ell) \, U(\ell) \, U(i) + \frac{h_i}{h_\ell} U(\ell) \left[\left\{ \begin{matrix} i \\ i \quad \ell \end{matrix} \right\} \frac{U(i)}{h_i} + \left\{ \begin{matrix} i \\ \ell \quad \ell \end{matrix} \right\} \frac{U(\ell)}{h_\ell} \right] = - \frac{1}{\rho} h_i \, g^{ii} \frac{\partial P}{\partial x_i}$$

(A3.18)

Substituting for the Christoffel symbols from Equation (A3.7) and recovering the physical components from Equation (A3.11), the momentum equation reduces to:-

$$\nabla(\ell) \, U(\ell) \, U(i) + H_i(\ell) \, U(i) \, U(\ell) - H_\ell(i) \, U(\ell) \, U(\ell) = - \frac{1}{\rho} \frac{\partial P}{\partial x(i)} \qquad \text{(A3.19)}$$

Putting $U = \overline{U} + u$ and averaging, therefore:-

$$\nabla(\ell)\left[\rho\bar{U}(\ell)\ \bar{U}(i) + \rho\overline{u(\ell)\ u(i)}\right] = -\frac{\partial P}{\partial x(i)} + H_{\ell}(i)\left[\bar{U}(\ell)\ \bar{U}(\ell) + \overline{u(\ell)\ u(\ell)}\right]$$

$$- H_{i}(\ell)\left[\bar{U}(i)\ \bar{U}(\ell) + \overline{u(i)\ u(\ell)}\right] \qquad \text{(A3.20)}$$

(iv) Boussinesq Equation

$$-\rho\overline{u(i)\ u(j)} = \mu_{t}\left(\frac{\partial\bar{U}_{i}}{\partial x_{j}} + \frac{\partial\bar{U}_{j}}{\partial x_{i}}\right) - \frac{2}{3}\left(\rho K + \mu_{eff}\frac{\partial U_{\ell}}{\partial x_{\ell}}\right)\delta_{ij} \qquad \text{(A3.21)}$$

Substituting from Equation (A3.10):-

$$-\rho\overline{u(i)\ u(j)} = \mu_{t}\left[\frac{h_{i}}{h_{j}}\frac{\partial}{\partial x_{j}}\frac{\bar{U}(i)}{h_{i}} + \frac{h_{j}}{h_{i}}\frac{\partial}{\partial x_{i}}\frac{\bar{U}(j)}{h_{j}} + \frac{\bar{U}(n)}{h_{n}}\left(\frac{h_{i}}{h_{j}}\begin{pmatrix} i \\ n\ \ j \end{pmatrix} + \frac{h_{j}}{h_{i}}\begin{pmatrix} j \\ n\ \ i \end{pmatrix}\right)\right]$$

$$- \frac{2}{3}\left[\rho K + \mu_{eff}\ \nabla(\ell)\ U(\ell)\right]\delta_{ij} \qquad \text{(A3.22)}$$

Substituting for Christoffel symbols, for example:-

$$\left.\begin{aligned}
&\begin{pmatrix} i \\ n\ \ j \end{pmatrix} = \begin{pmatrix} i \\ i\ \ j \end{pmatrix} + \begin{pmatrix} i \\ j\ \ j \end{pmatrix} + \begin{pmatrix} i \\ n\ \ j \end{pmatrix}\delta_{ij} = \\
&= h_{j}\ H_{i}(j) - \frac{h_{j}^{2}}{h_{i}}H_{j}(i) + h_{n}\ H_{i}(n)\ \delta_{ij} \qquad \text{(A3.23)} \\
&\text{also:}\quad \frac{h_{i}}{h_{j}}\frac{\partial}{\partial x_{j}}\frac{U(i)}{h_{i}} = \frac{\partial U(i)}{\partial x(j)} - H_{i}(j)\ U(i)
\end{aligned}\right\}$$

and compacting the terms, Equation (A3.22) can be written as:-

$$- \overline{\rho u(i)\ u(j)} = \mu_t \left[\frac{\partial \bar{U}(i)}{\partial x(j)} + \frac{\partial \bar{U}(j)}{\partial x(i)} - H_j(i)\ \bar{U}(j) - H_i(j)\ \bar{U}(i) + 2H_i(n)\ \bar{U}(n)\ \delta_{ij} \right]$$

$$- \frac{2}{3} \left[\rho K + \mu_t\ \nabla(n)\ \bar{U}(n) \right] \delta_{ij} \qquad \text{(A3.24)}$$

(v) Equations of Kinetic Energy of Turbulence and its Rate of Dissipation

The equations of scalar quantities can be represented in general form:-

$$\frac{\partial \rho \bar{U}_j \Phi}{\partial x_j} - \frac{\partial}{\partial x_j} \frac{\mu_{eff}}{\sigma_\Phi} \frac{\partial \Phi}{\partial x_i} = S_\Phi \qquad \text{(A3.25)}$$

Substituting for:-

$$\frac{\partial \Phi}{\partial \bar{x}_i} \rightarrow \frac{\partial \Phi}{\partial x(i)} \qquad \text{(A3.26)}$$

the equation in a general orthogonal curvilinear form can be written as:-

$$\nabla(i) \left[\rho \bar{U}(i) \Phi - \frac{\mu_{eff}}{\sigma_\Phi} \frac{\partial \Phi}{\partial x(i)} \right] = S_\Phi \qquad \text{(A3.27)}$$

The production of the kinetic energy of turbulence is the only term that needs to be transformed:-

$$G = \sum_{\substack{i=1 \\ j=1}}^{\substack{i=3 \\ j=3}} - \rho u(i)\ u(j) \frac{\partial \bar{U}(i)}{\partial x_j} \qquad \text{(A3.28)}$$

Substituting for $\partial \bar{U}_i / \partial x_j$ and $- \overline{\rho u(i)\ u(j)}$ from Equations (A3.21) and

(A3.24) respectively:-

$$G = \sum_{\substack{i=1 \\ j=1}}^{\substack{i=3 \\ j=3}} \frac{1}{2}\mu_t \left[\frac{\partial \bar{U}(i)}{\partial x(j)} + \frac{\partial \bar{U}(j)}{\partial x(i)} - \bar{U}(i)\ H_i(j) - \bar{U}(j)\ H_j(i) + 2\bar{U}(n)\ H_i(n)\ \delta_{ij}\right]^2$$

(A3.29)

Finally, the set of equations derived above can be summarised* in the general form:-

$$\nabla_x \left(\rho\bar{U}\Phi - \Gamma_{eff}\frac{\partial\Phi}{\partial x}\right) + \nabla_y \left(\rho\bar{V}\Phi - \Gamma_{eff}\frac{\partial\Phi}{\partial y}\right) = S_\Phi \qquad \text{(A3.30)}$$

where:-

$$\nabla_x = \frac{1}{h_2}\frac{\partial}{\partial x}h_2 \qquad \text{and} \qquad \nabla_y = \frac{1}{rh_1}\frac{\partial}{\partial r}rh_1 \qquad \text{(A3.31)}$$

The source terms of the different dependent variables are shown in Table A3.1.

---

* x(i), i = 1, 2 are expressed as x, y

U(i), i = 1, 2, 3 are expressed as $\bar{U}$, $\bar{V}$ and $\bar{W}$

TABLE A3.1

CONSERVATION EQUATIONS CORRESPONDING TO EQUATION (A3.30)

Φ	Γ	S_Φ
Mass	0	0
$\bar{U}$	μ_{eff}	$-\frac{\partial P}{\partial x} + \nabla_x \left[\mu_{eff}\left(\frac{\partial \bar{U}}{\partial x} + 2\bar{V}\, H_1(2)\right)\right] + \nabla_y \left[\frac{\partial \bar{V}}{\partial x} - H_1(2)\ \bar{U} - H_2(1)\ \bar{V}\right] + H_2(1)\left[\rho\bar{V}^2 - \mu_{eff}\left(2\frac{\partial \bar{V}}{\partial y} + 2\bar{U}H_2(1)\right)\right] + H_3(1)\left[\rho\bar{W}^2 - \mu_{eff}\left(2\bar{U}H_3(1) + 2\bar{V}H_3(2)\right)\right] - H_1(2)\left[\rho\bar{U}\bar{V} - \mu_{eff}\left(\frac{\partial \bar{U}}{\partial y} + \frac{\partial \bar{V}}{\partial x} - H_1(2)\bar{U} - H_2(1)\ \bar{V}\right)\right]$
$\bar{V}$	μ_{eff}	$-\frac{\partial P}{\partial y} + \nabla_y \left[\mu_{eff}\left(\frac{\partial \bar{V}}{\partial y} + 2\bar{U}\, H_2(1)\right)\right] + \nabla_x \left[\mu_{eff}\left(\frac{\partial \bar{U}}{\partial y} - H_2(1)\ \bar{V} - H_1(2)\ \bar{U}\right)\right] + H_1(2)\left[\rho\bar{U}^2 - \mu_{eff}\left(2\frac{\partial \bar{U}}{\partial x} + 2\bar{V}H_1(2)\right)\right] + H_3(2)\left[\rho\bar{W}^2 - \mu_{eff}\left(2\bar{V}H_3(2) + 2\bar{U}H_3(1)\right)\right] - H_2(1)\left[\rho\bar{U}\bar{V} - \mu_{eff}\left(\frac{\partial \bar{V}}{\partial x} + \frac{\partial \bar{U}}{\partial y}\right) - H_2(1)\ \bar{V} - H_1(2)\ \bar{U}\right]$

.... Continued

TABLE A3.1 (CONTINUED)

Φ	Γ	S_Φ
$\bar{w}$	μ_{eff}	$-\nabla_x \left(\mu_{eff} H_3(1) \bar{w}\right) - \nabla_y \left(\mu_{eff} H_3(2) \bar{w}\right)$ $- H_3(1) \left(\rho\bar{u}\bar{w} - \mu_{eff} \frac{\partial \bar{w}}{\partial x} + \mu_{eff} H_3(1) \bar{w}\right)$ $- H_3(2) \left(\rho\bar{v}\bar{w} - \mu_{eff} \frac{\partial \bar{w}}{\partial r} - \mu_{eff} H_3(2) \bar{w}\right)$
K	μ_{eff}/σ_K	$G - \rho\varepsilon$
ε	$\mu_{eff}/\sigma_\varepsilon$	$\frac{\varepsilon}{K} (c_{\varepsilon_1} G - c_{\varepsilon_2} \rho\varepsilon)$

where:-

$$G = \mu_{eff} \left(2 \left(\frac{\partial \bar{u}}{\partial x} + \bar{v} H_1(2)\right)^2 + 2 \left(\frac{\partial \bar{v}}{\partial y} + \bar{u} H_2(1)\right)^2 + 2 \left(\bar{u} H_3(1) + \bar{v} H_3(2)\right)^2 \right.$$
$$\left. + \left(\frac{\partial \bar{u}}{\partial y} + \frac{\partial \bar{v}}{\partial x} - \bar{u} H_1(2) - \bar{v} H_2(1)\right)^2 + \left(\frac{\partial \bar{w}}{\partial x} - \bar{w} H_3(1)\right)^2 + \left(\frac{\partial \bar{w}}{\partial r} - \bar{w} H_3(2)\right)^2 \right)$$

APPENDIX A4

EQUATIONS IN CYLINDRICAL COORDINATES

In this appendix, a tabulation of the equations of motion presented in Chapter 3 for the two-equation model is provided. They are derived from those in Appendix A3 by carrying out the following steps:-

(i) The metric tensor in cylindrical coordinates is given by:-

$$g_{ij} = \begin{pmatrix} 1 & 0 & 0 \\ 0 & r^2 & 0 \\ 0 & 0 & 1 \end{pmatrix} \qquad (A4.1)$$

(ii) All the coordinate variation terms are zero except:-

$$H_3(2) = \frac{1}{r} \qquad (A4.2)$$

(iii) The divergence operator:-

$$\nabla_x = \frac{\partial}{\partial x} \quad \text{and} \quad \nabla_y = \frac{1}{r}\frac{\partial}{\partial r} r \qquad (A4.3)$$

Thus the differential equations can be expressed as:-

Continuity Equation

$$\frac{\partial}{\partial x}\rho\bar{U} + \frac{1}{r}\frac{\partial}{\partial r}\rho\bar{V} = 0 \qquad (A4.4)$$

U-Momentum Equation

$$\frac{\partial}{\partial x}(\rho\bar{U}^2) + \frac{1}{r}\frac{\partial}{\partial r}(\rho r\bar{U}\bar{V}) - \frac{\partial}{\partial x}\mu_{eff}\frac{\partial\bar{U}}{\partial x} - \frac{1}{r}\frac{\partial}{\partial r}\mu_{eff}\, r\frac{\partial\bar{U}}{\partial r}$$

$$= -\frac{\partial P}{\partial x} + \frac{\partial}{\partial x}\left(\mu_{eff}\frac{\partial\bar{U}}{\partial x}\right) + \frac{1}{r}\frac{\partial}{\partial r}\left(\mu_{eff}\, r\frac{\partial\bar{V}}{\partial x}\right) \qquad \text{(A4.5)}$$

V-Momentum Equation

$$\frac{\partial}{\partial x}(\rho\overline{UV}) + \frac{1}{r}\frac{\partial}{\partial r}(\rho r\bar{V}^2) - \frac{\partial}{\partial x}\left(\mu_{eff}\frac{\partial\bar{V}}{\partial x}\right) - \frac{1}{r}\frac{\partial}{\partial r}\left(\mu_{eff}\, r\frac{\partial\bar{V}}{\partial r}\right)$$

$$= -\frac{\partial P}{\partial r} + \frac{1}{r}\frac{\partial}{\partial r}\left(\mu_{eff}\, r\frac{\partial\bar{V}}{\partial r}\right) + \frac{\partial}{\partial x}\mu_{eff}\frac{\partial\bar{U}}{\partial r} + \frac{\rho\bar{W}^2}{\partial r} - 2\mu_{eff}\frac{\bar{V}}{r^2} \qquad \text{(A4.6)}$$

W-Momentum Equation

$$\frac{\partial}{\partial x}(\rho\bar{U}\bar{W}) + \frac{1}{r}\frac{\partial}{\partial r}(r\rho\bar{V}\bar{W}) - \frac{\partial}{\partial x}\mu_{eff}\frac{\partial\bar{W}}{\partial x} - \frac{1}{r}\frac{\partial}{\partial r}\left(\mu_{eff}\, r\frac{\partial\bar{W}}{\partial r}\right)$$

$$= -\frac{1}{r}\frac{\partial}{\partial r}\left(\mu_{eff}\frac{\bar{W}}{r}\right) - \frac{\rho\bar{V}\bar{W}}{r} + \frac{\mu_{eff}}{r}\frac{\partial\bar{W}}{\partial r} + \mu_{eff}\frac{\bar{W}}{r^2} \qquad \text{(A4.7)}$$

K-Equation

$$\frac{\partial}{\partial x}(\rho\bar{U}K) + \frac{1}{r}\frac{\partial}{\partial r}(\rho r\bar{V}K) - \frac{\partial}{\partial x}\left(\mu_{eff}\frac{\partial K}{\partial x}\right) - \frac{1}{r}\frac{\partial}{\partial r}\left(\mu_{eff}\, r\frac{\partial K}{\partial r}\right) = G - \rho\varepsilon$$

(A4.8)

ε-Equation

$$\frac{\partial}{\partial x}(\rho\bar{U}\varepsilon) + \frac{1}{r}\frac{\partial}{\partial r}(\rho r\bar{V}\varepsilon) - \frac{\partial}{\partial x}\left(\mu_{eff}\frac{\partial\varepsilon}{\partial x}\right) - \frac{1}{r}\frac{\partial}{\partial r}\left(\mu_{eff}\, r\frac{\partial\varepsilon}{\partial r}\right)$$
$$= \frac{\varepsilon}{K}(c_{\varepsilon_1} G - c_{\varepsilon_2}\rho\varepsilon) \qquad \text{(A4.9)}$$

where:-

$$G = \mu_{eff}\left[2\left(\left(\frac{\partial\bar{U}}{\partial x}\right)^2 + \left(\frac{\partial\bar{V}}{\partial y}\right)^2 + \left(\frac{\bar{V}}{r}\right)^2\right) + \left(\frac{\partial\bar{U}}{\partial r} + \frac{\partial\bar{V}}{\partial x}\right)^2 + \left(\frac{\partial\bar{W}}{\partial x}\right)^2 + \left[r\frac{\partial}{\partial r}\left(\frac{\bar{W}}{r}\right)^2\right]\right]$$

(A4.10)

APPENDIX A5

REYNOLDS STRESS EQUATIONS

This section is concerned with the presentation of the Reynolds stress equations of which the general form is presented in Chapter 3. The equations are presented in cylindrical coordinates and include four Reynolds stresses and the rate of dissipation of kinetic energy of turbulence.

The differential equations may be expressed in the general form:-

$$\frac{\partial}{\partial x}(\rho\bar{U}\Phi) + \frac{1}{r}\frac{\partial}{\partial r}(r\rho\bar{V}\Phi) - c_\Phi \frac{\partial}{\partial x}\frac{\rho K}{\varepsilon}\left[u^2\frac{\partial\Phi}{\partial x} + \overline{uv}\frac{\partial\Phi}{\partial y}\right]$$

$$- \frac{c_\Phi}{r}\frac{\partial}{\partial r}\frac{r\rho K}{\varepsilon}\left[\overline{uv}\frac{\partial\Phi}{\partial x} + \overline{v^2}\frac{\partial\Phi}{\partial y}\right] = G_\Phi + S_\Phi \qquad \text{(A5.1)}$$

The momentum equations which are solved with the Reynolds-stress equations are:-

$$\frac{\partial}{\partial x}(\bar{U}^2) + \frac{1}{r}\frac{\partial}{\partial r}(r\overline{UV}) = -\frac{1}{\rho}\frac{\partial P}{\partial x} - \frac{\partial}{\partial x}(\overline{u^2}) - \frac{1}{r}\frac{\partial}{\partial r}(r\overline{uv})$$

$$\frac{\partial}{\partial x}(\overline{UV}) + \frac{1}{r}\frac{\partial}{\partial r}(r\bar{V}^2) = -\frac{1}{\rho}\frac{\partial P}{\partial y} - \frac{\partial}{\partial x}(\overline{uv}) - \frac{1}{r}\frac{\partial}{\partial r}(r\overline{v^2}) + \frac{w^2}{r}$$

The values of c_Φ, G_Φ and S_Φ are presented in Table A5.1. The values of the constants, B_1, B_2, B_3 and c_{Φ_2} are taken as follows:-

In Model II

$$B_1 = B_2 = B_3 = 0 \qquad \text{and} \qquad c_{\Phi_2} = c_2$$

In Model III

$$c_{\Phi_2} = 0 \qquad B_1 = \frac{c_2 + 8}{11} \qquad B_2 = \frac{30c_2 - 2}{55} \qquad B_3 = \frac{8c_2 - 2}{11}$$

TABLE A5.1

CONSERVATION EQUATIONS CORRESPONDING TO EQUATION (A5.1)

Φ	c_Φ	G_Φ	S_Φ
$\overline{u^2}$	c_s	$-2\rho\left(\overline{u^2}\frac{\partial\bar{U}}{\partial x}+\overline{uv}\frac{\partial\bar{U}}{\partial y}\right)$	$-c_1\ \rho\frac{\varepsilon}{K}\left(\overline{u^2}-\frac{2}{3}K\right)-(c_{\Phi_2}+B_1)\left(G_{\overline{u^2}}-\frac{2}{3}G_K\right)-2B_2\ \rho K\frac{\partial\bar{U}}{\partial x}$ $+2B_3\left(\rho\overline{u^2}\frac{\partial\bar{U}}{\partial x}+\rho\overline{uv}\frac{\partial\bar{V}}{\partial x}+\frac{1}{3}G_K\right)-\frac{2}{3}\rho\varepsilon$
$\overline{v^2}$	c_s	$-2\rho\left(\overline{uv}\frac{\partial V}{\partial x}+\overline{v^2}\frac{\partial V}{\partial y}\right)$	$-c_1\ \rho\frac{\varepsilon}{K}\left(\overline{v^2}-\frac{2}{3}K\right)-(c_{\Phi_2}+B_1)\left(G_{\overline{v^2}}-\frac{2}{3}G_K\right)-2B_2\ \rho K\frac{\partial\bar{V}}{\partial y}$ $+2B_3\left(\rho\overline{v^2}\frac{\partial\bar{V}}{\partial y}+\rho\overline{uv}\frac{\partial\bar{U}}{\partial y}+\frac{1}{3}G_K\right)-\frac{2}{3}\rho\varepsilon-2\rho\frac{c_s K\overline{w^2}}{\varepsilon}\frac{\overline{(v^2-w^2)}}{r^2}$

.... Continued

TABLE A5.1 (CONTINUED)

Φ	c_Φ	G_Φ	S_Φ
$\overline{w^2}$	c_s	$-2\rho\,\overline{w^2}\,\frac{\overline{V}}{r}$	$-c_1\,\rho\,\frac{\varepsilon}{K}\left(\overline{w^2}-\frac{2}{3}K\right)-(c_{\Phi_2}+B_1)\left(G_{\overline{w^2}}-\frac{2}{3}G_K\right)-2B_2\,\rho K\,\frac{\overline{V}}{r}$ $+2B_3\left(\rho\,\frac{\overline{w^2V}}{r}+\frac{1}{3}G_K\right)-\frac{2}{3}\rho\varepsilon+2\rho\,\frac{c_s K\,\overline{w^2}}{\varepsilon}\,\frac{\overline{(v^2-w^2)}}{r^2}$
$\overline{uv}$	c_s	$-\rho\left(\overline{v^2}\,\frac{\partial\overline{U}}{\partial y}+\overline{u^2}\,\frac{\partial\overline{V}}{\partial x}-\frac{\overline{uv}}{r}\overline{V}\right)$	$-c_1\,\rho\,\frac{\varepsilon}{K}\,\overline{uv}-(c_{\Phi_2}+B_1)\,G_{\overline{uv}}-B_2\,\rho K\left(\frac{\partial\overline{U}}{\partial y}+\frac{\partial\overline{V}}{\partial x}\right)+B_3\rho\left[\overline{u^2}\,\frac{\partial\overline{U}}{\partial y}\right.$ $\left.+\overline{v^2}\,\frac{\partial V}{\partial x}+\overline{uv}\left(\frac{\partial\overline{U}}{\partial x}+\frac{\partial\overline{V}}{\partial y}\right)\right]-\rho\,\frac{c_s K\,\overline{w^2}}{\varepsilon}\,\frac{\overline{uv}}{r^2}$
ε	c_ε	$c_{\varepsilon_1}\,\frac{\varepsilon}{K}\,G_K$	$-c_{\varepsilon_2}\,\rho\,\frac{\varepsilon^2}{K}$

where $G_K=-\rho\left[\overline{uv}\left(\frac{\partial\overline{U}}{\partial y}+\frac{\partial\overline{V}}{\partial x}\right)+\overline{u^2}\,\frac{\partial\overline{U}}{\partial x}+\overline{v^2}\,\frac{\partial\overline{V}}{\partial y}+\overline{w^2}\,\frac{\overline{V}}{r}\right]$